Toward Nanoscale Rapid Prototyping: Development and Characterization of DNA-Based Platforms for Multivalent Interactions and Locomotion

Dissertation

Luzia Kilwing

Munich, 2021

Toward Nanoscale Rapid Prototyping: Development and Characterization of DNA-Based Platforms for Multivalent Interactions and Locomotion

Luzia Kilwing

Dissertation

at the Faculty of Physics
Ludwig-Maximilians-Universität München

at the
Dana-Faber Cancer Institute
and the
Wyss Institute for Biologically Inspired Engineering
at Harvard University

submitted by
Luzia Kilwing

Munich, 10.09.21

Primary Reviewer (Erstgutachter): Prof. Dr. Tim Liedl
Secondary Reviewer (Zweitgutachter): Prof. Dr. William M. Shih
Defense date (Tag der mündlichen Prüfung): 25th of October 2021

To my beloved parents.

Zusammenfassung

DNA Nanotechnologie nutzt die quaternäre Logik der Watson-Crick Basenpaarung von DNA und ihre damit einhergehende, molekulare Programmierbarkeit für die Selbstassemblierung von Objekten auf Nano-Ebene. Basierend auf einer Auflösung von 6 nm, zeichnen sich diese durch ihre strukturelle Komplexität und chemische Adressierbarkeit aus. Eine große Anzahl an bereits demonstrierten Hochpräzisions-Anwendungen zeigt die Vielfältigkeit des Forschungsgebietes. Die sogenannte DNA-Origami Faltung ist eine etablierte Technik des Fachgebietes, um DNA-Nanostrukturen zu designen und zu synthetisieren. Dabei wird ein langer DNA-Einzelstrang als Gerüst für die Anlagerung vieler kurzer Oligonukleotide verwendet. Die Anlagerung kann auf Grund der Watson-Crick Basenpaarung so programmiert werden, dass die kleinen DNA Fragmente an lokal entfernten Stellen entlang des Gerüststrangs binden und diesen damit in 2D- und 3D-Formen bringen. Durch gesteuerte DNA-Strangmigration, ein Prozess der in der Fachliteratur als *DNA strand displacement* bekannt ist, können den DNA-Origami Strukturen dynamische Eigenschaften verliehen werden.

Über die letzten Jahrzehnte demonstrierten verschiedene Formen des 3D-Drucks den revoluzionären Charakter einer solchen Technologie und deren gewinnbringenden Anwendungen für Forschung und Industrie. Dies motiviert Ideen zu entwickeln, um zum Zwecke eines ähnlich positiven Einflusses, eine Form der schnellen Prototypenentwicklung auf die Nano-Ebene zu übertragen.

Die vorliegende Arbeit präsentiert Machbarkeitsnachweise, die zeigen, dass sich die Techniken der DNA-Selbstassemblierung, wie die DNA-Origami Technik, für diese Herausforderung besonders gut eignen.
Sich am Beipiel des 3D-Drucks orientierend, wird sich dieser Idee aus zwei Richtungen angenähert. Es bedarf erstens Plattformen, die die Koordination einer Vielzahl von Interaktionen zur selben Zeit erlauben und zweitens reversible und repetierende Transport-Mechanismen, die die benötigten molekularen Bausteine an die gewünschten Zielorte bringen.
Dies zum Ziel, präsentiert der erste Teil dieser Arbeit die Entwicklung und Validierung dreier, neuer Design-Strategien zur Oberflächenmaximierung von DNA-Origami Strukturen, um deren Kapazitäten für Funktionalisierungen und Wechselwirkungen zu steigern. Die neuen Ansätze wurden dabei auf sogenannten quadratischen (square-), hexagonalen (honeycomb-) und quadratisch-löchrigen (square-holey-) DNA-Gittern implementiert. Herausforderungen bezüglich der Stabilität der generierten Strukturen werden diskutiert und Lösungen präsentiert. Eine Reihe von definitiven Design-Empfehlungen als auch verfeinerte Aufreinigungsprotokolle für die Erstellung von Strukturen mit bis zu 200 individuell adressierbaren, funktionalen Anlagerungstellen wurden in diesem Zusammenhang entwickelt.

Im zweiten Teil der Arbeit wird gezeigt, dass die entwickelten DNA-Strukturen polyvalent miteinander wechselwirken und gesteuert werden können. Dies wird erreicht durch einen neuartigen Mechanismus, der im Zuge dieser Arbeit entwickelt wurde. Eine zyklische Aktivierung und Deaktivierung eines Sets bestehend aus sechs orthogonalen DNA-Einzelsträngen wird benutzt, um eine kontrollierte Vorwärts- und Rückwärtsbewegung der großen DNA-basierten Plattformen auf festen DNA-Origami Straßen zu induzieren. Der Mechanismus wurde mittels Gelelektrophorese und Transmissionselektronenmikroskopie validiert. Die Validierung der implementierten, kleinen Schrittgröße von 3.4 nm steht dabei noch aus und wird durch die Anwendung höher-auflösender Detektionsmethoden angestrebt.
Eine Rapid-Prototyping-Technologie auf Nano-Ebene wird als vielversprechender Ansatz zur Entwicklung zukünftiger, atomisch-präziser Herstellungsprozesse für die Industrie angesehen und ist einer der Hauptmotivatoren der vorliegenden Arbeit.

Abstract

DNA nanotechnology exploits the quaternary logic of DNA and uses its molecular programmability for the directed self-assembly into nanoscale objects. Those exhibit outstanding structural complexity and chemical addressability with a resolution down to about 6 nm. Launching a vast number of high-precision applications has demonstrated the versatility of the field. DNA origami folding is a popular technique to design and assemble DNA nanostructures using a long single DNA scaffold strand that is brought into 2D and 3D shapes by programming hundreds of short oligonucleotides to bind at locally distant regions on the scaffold based on Watson-Crick base-pairing. Programmed DNA strand displacement reactions are a useful tool to render DNA origami structures dynamic.

Witnessing the great achievements of the 3D printing technology on the macroscale motivates one to explore ideas of how to transfer the concept of rapid prototyping to the nanoscale to achieve a similar impact.
This thesis presents proof-of-concept data showing that the techniques of DNA self-assembly provide a demand-meeting toolbox for this challenge.
The idea is approached from two sides. Implementation of rapid prototyping requires platforms for the simultaneous coordination of numerous interactions as well as reversible and repetitive mechanisms to transport material to designated locations.

The first part of the thesis thus presents three new design strategies for the assembly of multi-layer DNA-origami architectures with maximized surface areas for a high number of functional sites. The approaches are implemented on square-, honeycomb-, and square-holey lattices and challenges with respect to the stability of the structures are addressed. This resulted in a considerate set of definite design recommendations as well as refined purification protocols. Structures with up to 200 individually addressable, functional sites are going to be presented.
The second part of the thesis shows that these architectures can undergo polyvalent interactions and a novel mechanism to displace their surfaces with respect to each other is implemented. Data will be discussed showing the promotion of large DNA arrays along rigid DNA origami tracks based on the cyclic activation and deactivation of a set of six, orthogonal fuel strands for a controlled forward and backward motion. The mechanism was validated using gel electrophoresis and transmission electron microscopy. The small step size of 3.4 nm remains to be confirmed by deploying higher-resolution detection methods. Rapid prototyping on the nanoscale is believed to be a promising pathway toward future technologies for atomically precise manufacturing which is one of the main incentives for the presented studies.

Acknowledgements

In all beginnings dwells a magic force,
for guarding us and helping us to live.

– *Hermann Hesse*

Science means constantly walking a tightrope
between blind faith and curiosity; between expertise and creativity;
between bias and openness; between experience and epiphany;
between ambition and passion; and between arrogance and conviction -
in short, between an old today and a new tomorrow.

– *H. Rohrer*

I consider myself as one of those fortunate people who as scientist are given the chance to walk along that tightrope and experience new beginnings with each new thought, each new idea, each new experiment and each new result revealing the beauty of nature and life. This journey would not be possible and as rich without the many people who I am blessed to know and work with. In these last hours of my PhD journey it is thus of uttermost importance to me to express my deep gratitude.

First and foremost, I like to thank both my PhD advisors, Prof. Tim Liedl and Prof. William Shih.

I like to thank **Prof. Tim Liedl** for his trust and all the invaluable advice throughout the years we worked together, his continuous support in realizing my research ideas, the much appreciated feedback and for the constant openness to all my questions at any time. The freedom he gave, coupled to his constructive guidance allowed me to thrive on my challenges and let me grow into an independent thinker. Thank you for bearing with me through the wild idea to pursue my doctoral studies half-time in Munich and half-time in Boston and making it possible for me to experience research in both groups.

I like to give my special thanks to **Prof. William Shih** for his invaluable mentorship, for keeping me balanced along the tightrope of scientific discovery, for his strong sensitivity, mindfulness and openness with which he leads a fantastic research group generating a remarkable atmosphere for everyone where innovative ideas and problem solving can flourish and elevate. Thank you, for many hours of joint philosophizing and creative brain picking that inspired my inner enthusiasm and passion for exceptional and big ideas. Thank you for lots of invaluable advice that shaped me as a young scientist, for the opportunity to learn from you and your group and for making this collaboration between two groups possible.

I highly appreciate to have had the opportunity to work at great institutions such as the Chair for Soft Condensed Matter at the Faculty of Physics at the **LMU Munich**, the **Center for Nanoscience (CeNS)**, the **Wyss Institute for Biologically Inspired Engineering at Harvard University** and the **Dana-Faber Cancer Institute** who provided invaluable resources and an extremely rich, interdisciplinary and unique atmosphere to work and grow in.
Being part of two research groups blessed me with a countless number of fantastic colleagues.
I like to thank my collaborators at Oxford University **Prof. Andrew Turberfield**, **Dr. Erik Benson**, **Dr. Jonathan Bath** and **Rafael Carrascosa Marzo** for the great cooperation toward our shared vision of molecular 3D printers, for many nourishing transatlantic meetings, inspiring discussions and progress reports. Special thanks to Erik who contributed the oxDNA simulations to this work.

Special thanks to:
Dr. Bhavik Nathwani from the Shih lab and **Jasleen K. D. Singh** from the Wickham lab at the University of Sydney for fruitful teamwork, great discussions and for the opportunity to exchange and learn from each other's expertise.

Dr. Richard Guerra, **Dr. Dionis Minev** and **Chris Wintersinger**. In particular, thank you Rick and Dio for introducing me to MeRPy-PCR and for an exciting, joint exploration of the technique. Thank you Rick for always being available to generate and provide MeRPy-strands and thank you Dio and Chris for sharing your expertise on TEM imaging.

Susanne Kempter and **Gerlinde Schwake** in Munich for their constant and highly appreciated organization of the lab space making lab work enjoyable for everyone.

The whole secretary team at the Rädler chair for constant availability and support.

Margaret Ivins and **Jessica Rodriguez** in Boston for invaluable support on any visa-, travel- and orientation-related issues and for making my arrivals at the Wyss and the Dana-Faber so welcoming.

Thank you to all past and current members of the Liedl and Shih group. They all have contributed in their own way to make my research journey fruitful and to render my multiple re-integrations into the groups and labs due to the alternating changes of sites smooth and enjoyable. Thank you to everyone for being always available for questions and great scientific exchange.

I gratefully acknowledge financial support of the **Deutsche Forschungsgemeinschaft (DFG)** through **SFB1032** "Nanoagents"and funding from the **U.S. Department of Energy (DOE)** through the **Advanced Manufacturing Office**.

On a more personal note, my PhD journey would not have been the same without some special people who are very dear to me.
I like to express my endless thanks to **Dr. Gloria Lee**, **Dr. Joseph Tavacoli** and **David Bianchi** for your cherished support on proofreading this work and my dear friend

Maxim Wandrowski for technical support.
Lily Iglehart, thank you for each warmhearted welcome and fare-well to Boston. Your friendship and hospitality made Boston a second home to me and is something I count to my blessings.

I am endlessly grateful to life for being blessed with the most wonderful parents one can wish for. Thank you for your unconditional support on anything I wish to pursue and for continuously accompanying me along the sometimes very unpredictable roads of this journey.
My love and gratitude also goes to my brother. Thank you, Julian, for always encouraging me to keep my head up, for being my example every day and teaching me to always believe in myself and never give up.

Contents

1. Introduction **3**

2. Biochemical and -physical background **7**
2.1. Reaction kinetics and rates . . . 7
2.1.1. Thermodynamics vs. kinetics . . . 7
2.1.2. Reaction rates . . . 8
2.1.3. Reaction orders . . . 9
2.1.4. Kinetics of DNA duplex formation . . . 10
2.2. DNA according to Watson-Crick . . . 12
2.2.1. Chemical structure of nucleotides . . . 12
2.2.2. The generation of the DNA double helix . . . 13
2.3. Non-canonical base pairing . . . 18
2.4. Holliday junctions and branch migration . . . 21
2.5. Thermodynamic and mechanical stability of DNA . . . 22
2.6. DNA as building source material . . . 24

3. Design strategies of structural DNA nanotechnology **25**
3.1. Branched DNA molecules . . . 25
3.2. The DNA origami technique . . . 26
3.3. Scaffold-free DNA nanostructures . . . 32

4. Dynamic DNA nanotechnology **35**
4.1. DNA switches . . . 35
4.2. DNA stepper motors . . . 37
4.3. Current challenges of DNA walker systems and how to address them . . . 42

5. Theoretical and experimental methodology **45**
5.1. Tools supporting the design process . . . 45
5.1.1. Sequence generation with caDNAno . . . 45
5.1.2. OxDNA . . . 47
5.2. Experimental methods . . . 48
5.2.1. Toehold mediated strand displacement . . . 48
5.2.2. Gel electrophoresis . . . 49
5.2.3. Purification methods . . . 53
5.3. Transmission electron microscopy . . . 55
5.4. Methanol-responsive polymer PCR . . . 57

6. DNA-based platforms for multivalent interactions **59**
6.1. Overview of the studied design approaches . . . 59
6.2. **Design approach 1:** Diagonal-cut, square-lattice designs for a decreased functional-site distance . . . 63
6.2.1. Design and folding of diagonal-cut architectures . . . 63

6.2.2. Stability of diagonal-cut architectures . . . 64
6.2.3. Conclusion . . . 69
6.3. **Design approach 2:** Maximized surface areas through reduced helical depth 72
6.3.1. Design and folding of flat DC-DNA arrays with a high aspect ratio . 72
6.3.2. Redesign cycle of high aspect ratio-arrays for less supertwisting . . . 73
6.3.3. Conclusion . . . 76
6.3.4. Design and experimental evaluation of flat DC-DNA arrays with a low aspect ratio . . . 76
6.3.5. Conclusion . . . 82
6.3.6. Design and folding of square-shaped DC-DNA arrays . . . 83
6.3.7. Conclusion . . . 87
6.3.8. Implementation of design approach 2 into hexagonal-shaped honeycomb-lattices . . . 88
6.3.9. Conclusion . . . 92
6.3.10. Implementation of design approach 2 into square-shaped honeycomb-lattices . . . 93
6.3.11. Conclusion . . . 95
6.4. **Design approach 3:** Square-holey lattices and the combination of multiple scaffolds for a larger design space . . . 96
6.4.1. Square-holey lattice architecture . . . 96
6.4.2. Incorporation of MeRPy-strands for the addition of further DNA layers . . . 98
6.4.3. Conclusion . . . 100
6.5. Summary . . . 103

7. Symmetric, three-phase DNA origami stepper 105
7.1. General design considerations . . . 105
7.1.1. Architectural premises . . . 105
7.1.2. Functional mechanism . . . 107
7.1.3. Clip strand design for forward and backward control . . . 108
7.2. Mini-stepper . . . 110
7.2.1. Design and functionalization . . . 110
7.2.2. Dimerization of mini-stepper monomers . . . 110
7.2.3. Conclusion . . . 116
7.3. Falcon-stepper . . . 118
7.3.1. Design and functionalization . . . 118
7.3.2. Folding and purification of falcon-stepper monomers . . . 119
7.3.3. Dimerization of falcon-stepper monomers . . . 121
7.3.4. Conclusion . . . 125
7.3.5. Three-phase actuation of falcon-steppers . . . 126
7.3.6. Symmetric actuation across two RGB cycles . . . 129
7.3.7. Backward stepping . . . 133
7.3.8. Optimization of the TEM staining protocol for a higher image contrast 134
7.3.9. TEM verification of PRGBR-stepping . . . 139
7.3.10. Strand interaction specificity . . . 144
7.3.11. Conclusion . . . 145
7.4. Summary . . . 146

8. Summary and outlook **149**

A. Materials and methods **153**
A.1. Buffers 153
A.2. Reagents 154
A.3. Methods 155

B. Additional data **159**
B.1. DNA-based platforms for multivalent interactions - Additional Data 159
B.2. Symmetric, three-phase DNA origami stepper - Additional Data 166

C. Sequences and designs **181**

Bibliography **217**

List of Figures **227**

List of Tables **231**

Acronyms

AGE	agarose
APS	ammonium persulfate
bp(s)	base pair(s)
conc.	concentration
DC	Diagonal-cut
ddH$_{2}$O	doubled-distilled water
dsDNA	double-stranded DNA
EtBr	Ethidium bromide
EtBr	Ethidium bromide
EtOH	ethanol
h	hour
HC	honeycomb
HJ	Holliday junction
K	Kelvin
kb	kilobase
MgCl_{2}	Magnesium chloride
min	minute
NaOAc	sodium acetate
NaOH	sodium hydroxide
nt(s)	nucleotide(s)
PAGE	polyacrylamide
PCR	polymerase chain reaction
ppt	precipitation
R12	Falcon-rails with an interacting handle length of 12 nt
RGB	red, green, blue
RT	room temperature
Rx	rail with an interacting handle length of x nt
sc	scaffold
scaf	scaffold
SH	square-holey
ssDNA	single-stranded DNA
Sx(-)	sliders with an interacting handle length of x nt
Sx(+)	sliders with an interacting handle length of x nt and bearing purple clip strands
TEM	Transmission electron microscopy
TEMED	Tetramethylethylenediamine
TMSD	toehold mediated strand displacement
UFO	uranylformate
v"x"	version "x"
WS	working solution

1. Introduction

The impact of climate change on everyday life manifests in many different ways ranging from rising temperatures and sea levels, unusual weather phenomena, and decreased biodiversity to food and water shortages [1]. Approaches to address the causes of climate change demand re-thinking the ways of producing goods, approaching mobility, generating energy, and managing waste [2].
According to the World Resource Institute, about 76% of greenhouse gas emissions originate from energy consumption, of which 12.6% are ascribed to the manufacturing industry. Notably, emissions from manufacturing grew by 56% since 1990. Electricity and heat generation, on the other hand, which owes for the largest contribution within the energy sector, grew by 78% between 1990 and 2013, but the increased use of renewable energy sources and abandoning of coal have managed to reduce the growth to 2.3% between 2013 and 2016. [3]
Rendering current manufacturing techniques, as one of the fastest-growing contributions to greenhouse gas emissions, more energy efficiency thus plays a critical role to succeed with the goal to reach net-zero towards the middle of the century.

Besides the constant praising for renewable energies, electric vehicles and food alternatives that, undeniably, are powerful measures that will be decisive for the next 20 years, it is crucial to understand that our manufacturing techniques have reached an intrinsic limit in terms of energy conservation even though renewable energy sources such as wind or solar power will be introduced.
This limit reveals, in particular, reflecting upon the manufacturing flagship - the semiconductor industry. Gordon Moore extrapolated in 1965 that the number of transistors implemented on a chip is going to double every 12-24 months [4]. This prediction is known as Moore's law and became the defining trajectory of how the semiconductor industry economized.
In 1983, Norio Taniguchi predicted that commercial manufacturing precision will have increased by a factor of 100 000 by the end of 1999 with regard to the past 100 years. His chart (shown in figure 1.1) thereby already included correct predictions for ultra-precise machinery which he anticipated to have reached atomic accuracy of about 0.3 nm by the end of 2020. His predictions can be seen as the machinery complement to Moore's law [5]. It is important to realize that both predictions are closely related in the sense that the fulfillment of Moore's law strongly relies on ever-increasing manufacturing precision. This encourages the hypothesis that the next stage in Taniguchi's chart, which is the control of manufacturing on the atomic level, offers an interesting pathway to increase not only the performance efficiency of our manufacturing techniques but also their energy efficacy.

However, atomically precise manufacturing (APM) was not approached in the semiconductor industry for long due to the outdated persuasion of handling endlessly divisible matter. Matter is quantized and simply does not provide further orders of magnitude for an improvement of precision following the classical approaches. [6]

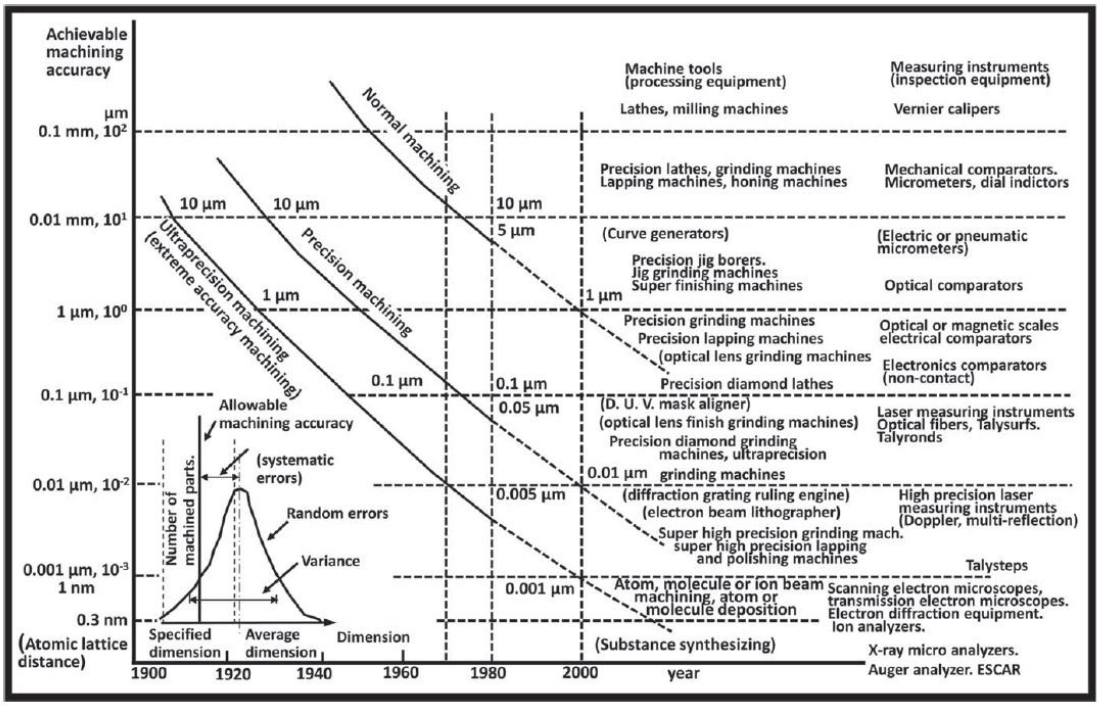

Figure 1.1.: The development of machine accuracy according to Norio Taniguchi [5].

Photolithography, like many other manufacturing techniques, has reached its maximal spatial resolution due to the diffraction limit and quantum effects arising from ever-smaller length scales, which render it even more sensitive to structural defects. Trying to find ways around the quantized nature of matter has resulted in energy- and cost-intensive casting or subtractive processes that dissipate a lot of heat and often involve highly processed base materials. An APM technology that could place each atomic building block at designated locations is proposed to hold the potential of greatly reducing energy costs in manufacturing mainly due to the fact that addressing individual atoms offers an immense reduction of and control about generated waste products [7].
Reducing the energy costs of manufacturing processes, such as in the semiconductor industry, goes hand-in-hand with reduced financial costs. This can have game-changing effects on the production of devices such as photovoltaics or technical units for carbon dioxide removal, but also innovative fuel cells and new materials.

The discussion so far leaves no doubt about the feasibility of such a technology that is capable to arrange individual atoms on a large-scale manufacturing level. However, scientists are trained to think critically and should consider this as a duty. Thus, this introduction should not end without a critical thought about APM and its disruptive character before the proof-of-concept studies presented within this thesis are outlined.
It should be mentioned that there is a controversy about whether APM is at all possible. Advocates of APM are mainly convinced by the example set out by nature's complex machines such as ribosomes. Also, the first technological demonstrations of APM, such as scanning tunneling or atomic force microscopy, are considered convincing forerunners. Assuming APM is feasible, it is thought to revolutionize everyday life to a similar extent as the industrial and digital age. As with every new technology, this disruptive character

comes along with the potential of being misused. In general, a major reduction in manufacturing costs is not only beneficial for the environmental sector but could also boost advances in the production of high-precision weapons or surveillance devices impacting societal security. These trains-of-thoughts can lead in many different directions and a proper, overarching debate about them is pivotal to responsible decision-making and to ensure the development of APM in the right direction. Umbrello et al. attempted to analyze the potential benefits and harms of APM on our society. They conclude that it remains hard to predict the impact of APM since it has not been developed so far but, based on their analysis, however, they express their mild tendency toward APM having a net beneficial impact on our society. Learning how to hold proper debates about futuristic technologies like APM is key to enable early guidance of their development. Inducing these debates early can be crucial to a reduction of the potential risks. [7]

We are at the very early stages of incorporating APM into prototype systems. To hold its promises, an implementation of APM needs to address the following requirements:
APM needs an easily accessible building material, a mechanism for the exact addressing of the building blocks and an implemented ability to perform repetitive actions to realize processes such as error correction.
This thesis suggests DNA and DNA self-assembly as a prototype system to implement APM. DNA is a biomolecule whose synthesis itself is atomically precise. The synthesis of DNA was made possible thanks to studies of Caruthers et al. in 1985 [8] and has developed into a technological standard that, nowadays, it is easy to generate any desired sequence up to certain lengths commercially. The quaternary logic of Watson-Crick base pairing places the molecule into a computation-like context where it is not seen as the molecule of heritage but as a highly programmable building material.
These are key premises that enabled DNA nanotechnology, a field that explores the programmed and directed DNA self-assembly. The field has launched many techniques that can generate nanostructures with an outstanding level of accuracy and addressability. DNA origami folding, the technique of choice in this thesis, uses a long, single-stranded DNA strand ("scaffold") that can be brought into any desired shape by the complementary binding of hundreds of short oligonucleotides ("staples") to locally distant regions on the scaffold. DNA origami structures are highly tolerant of structural defects. [9]
The folding process exhibits an intrinsic error correction pathway since non-complementary binding or sequences with secondary structures are kinetically and thermodynamically outcompeted by the binding of the complementary strand [10].
Each strand is specifically addressable at a resolution of around 6 nm. The production of the self-assembled objects is highly scalable since it produces a trillion copies at the same time as long as enough building blocks are present to be recruited from the solution [9].

Thesis' objectives:

This thesis aims to show that DNA combined with the available techniques of nanoscale, controlled self-assembly provide a demand-meeting toolbox to implement APM in the long run. The presented strategies are ground on the understanding that molecular additive manufacturing is a promising approach for this implementation.
Besides subtractive manufacturing and material forming, additive manufacturing is one of the three main techniques to produce goods where the individual building blocks are transported and placed at designated positions to build the desired shape layer by layer.

The best-known example for additive manufacturing on the macroscale is 3D printers. [5] This thesis presents first data on how the concept of rapid prototyping could be transferred to the nanoscale by developing a DNA-origami based 1D symmetric, three-phase actuator with the potential to be extended into a further dimension. Thereby, three new ideas are explored that make it outstanding compared to already reported stepper systems. It is novel that the presented system manages to actuate whole DNA arrays along rigid DNA-origami tracks, that the actuation relies on the cyclic activation and de-activation of a symmetric set of signal DNA strands and the relatively short step size that will be particularly interesting for high precision applications in the future.
The main research question was whether it is possible to generate DNA-based platforms that allow multiple interactions between DNA origami surfaces to happen in tandem for the purpose of high cooperativity stepping.
Cooperativity thereby should be understood as the degree to which intermediate stepping states are disfavored and is suggested to support high operation efficiency and tolerance toward defects.
This question was explored by testing different design innovations for the self-assembly of large DNA arrays. In total, 13 different designs and their experimental realization will be presented, four of which are used to implement the proposed stepping mechanism.
The thesis presents proof-of-concept data aiming to inspire further studies on the implementation of APM to DNA self-assembly as it believes in such a technology's potential to bring the required, revolutionizing change to our manufacturing industry in the long run. Thereby it is clear that this is only the beginning of a long trajectory toward this goal, but at the same time understands the urge to get started with the development of prototype systems.

Thesis' structure:

The thesis starts reviewing a considerate selection of biochemical and physical topics in chapter 2 and presents the state-of-the-art research on structural as well as dynamic DNA nanotechnology in chapters 3 and 4. This should ensure that the reader is equipped to understand the research presented in the subsequent chapters. Chapter 5 gives an overview of the key methods used to study the developed systems. Chapter 6 presents new design strategies for the self-assembly of large DNA arrays using the DNA origami folding technique and suggests design rules that can provide helpful guidance for other researchers approaching DNA origami design with a focus on square lattices. Chapter 7 shows how some of these structures can be used to realize stepping based on multi-leg coordination. The final summary will provide insight into ongoing research to extend the presented 1D stepper system from chapter 7 into 2D and how the concept of cooperativity could have an interesting impact on the steppers' performance.

2. Biochemical and -physical background

2.1. Reaction kinetics and rates

Thermodynamic and kinetic properties can contribute to the understanding of the processes in a system under study. Although thermodynamics provide powerful insights about a system, a discussion of the kinetics and reaction rates is inevitable for a proper prediction and design of the involved processes under study. This section provides a distinct differentiation of the terms thermodynamics and kinetics before introducing the concept of chemical reaction rates. It should be mentioned that thermodynamics and kinetics are both highly diverse and rich research fields. The following discussions focus on a subset of aspects helpful to the understanding of the research contents presented within this thesis.

2.1.1. Thermodynamics vs. kinetics

Non-equilibrium systems favor to transition to states of lower free energy in order to maximize entropy. Thermodynamics thereby determine whether this transition is energetically allowed or even favorable by describing the involved energy transfers, while the kinetics of a system predict how fast a reaction will proceed. Some important quantities to describe the difference between thermodynamics and kinetics are the free energy ΔG and the activation energy ΔE_A, whereby ΔG is a thermodynamic quantity and ΔE_A a kinetic one. The difference can be explained by considering the following reaction:

$$A \rightleftharpoons B \tag{2.1}$$

where a reactant A is converted to a product B and vice versa. The energy profiles of both the forward and backward reaction are shown in figure 2.1, with the free energy G plotted on the y-axis, and the reaction time t plotted on the x-axis. The energy levels of reactant A and product B are indicated as horizontal bars. Let us start with the forward reaction (2.1 (i)) where we assume that the reactant A has a higher free energy G compared to the product B. The reactant could thus reduce its free energy through the transition to the product. By definition, the difference between both energy levels ΔG is negative. This type of reaction is called a spontaneous reaction since it proceeds without the addition of further energy. The energy stored in A is released throughout the process of the reaction. Reactants involved in the reverse, non-spontaneous reaction (2.1 (ii)) are at lower energy levels compared to their products. Here ΔG is positive and energy has to be added to come back to the initial state A.
Indicated in purple, figure 2.1 shows the different activation energies E_A for the two reactions. In general, every chemical reaction needs an initial energy input. This energy is called the activation energy E_A and imposes a kinetic energy barrier to the system. Once added for example in the presence of pressure or heat, this energy lifts the system to a higher, unstable transition state T from which the system quickly drops to the next available level. This activation energy is analogous to a push a ball needs to roll down a hill, or a topological configuration a molecule must form before chemical bonds can be broken.

Figure 2.1 shows that in non-spontaneous reactions (ii) the energy barrier that has to be overcome is much higher compared to spontaneous reactions (i). Activation energy directly determines reaction speed, with lower E_A resulting in faster reactions. Thus it is very important to consider not only the thermodynamic energy transfers involved in a reaction but also its kinetic energy barriers. A system's transition could be thermodynamically favored but kinetically trapped, which is why a consideration of both is necessary to understand and predict the processes of a macroscopic system [11].

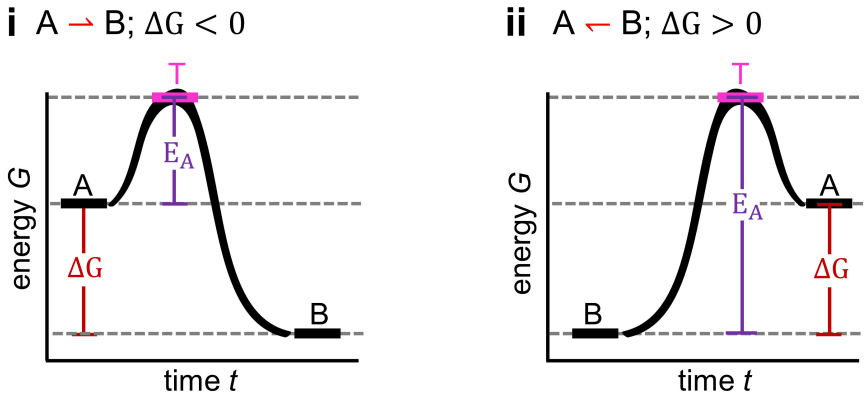

Figure 2.1.: Energy profiles of spontaneous vs. non-spontaneous reactions. y-axis refers to the free energy, x-axis refers to the time. (i) A spontaneous reaction is characterized by a negative change in free energy ΔG (red) and proceed without further energy input, while non-spontaneous reactions (ii) exhibit a positive change in free energy ΔG and require additional energy to proceed. Activation energies (purple) impose kinetic energy barriers that need to be overcome first before reactions can proceed. High-energy, unstable transition states (pink) are reached through the addition of the activation energy from which the systems quickly drop to the next available energy level. [11]

2.1.2. Reaction rates

The previous section explained that kinetics introduce a time quantity to the thermodynamic discussion of a system's energy landscapes and can predict the speed of a chemical conversion. In chemistry, this speed is described by reaction rates. They are expressed using an intensive variable, very often the concentration of the involved substances, that changes over time. The mathematical description of rates is the time derivative of the concentrations. Given the above scenario where A is converted to B (2.1), the rates can be written as follows:

$$Rate_A = \frac{d[A]}{dt}$$

$$Rate_B = \frac{d[B]}{dt}$$

Here, the square brackets indication the concentrations of A and B.

So called *rate laws* are used to describe the relation between the rates and changes in concentrations. For the given example the rate laws for the forward and backward reaction

are as follows:

$$Rate = \frac{d[A]}{dt} = -k_+[A] + k_-[B] \tag{2.2}$$

$$Rate = \frac{d[B]}{dt} = -k_-[B] + k_+[A] \tag{2.3}$$

Here, k_+ and k_- are the so called *reaction rate constants*. They are characteristic quantities for the description of biological processes. In combination with the so called *Arrhenius equation* (see equation 2.4), an empirical law that describes the dependency of the rate constant on temperature and activation energy, valuable information about the actual reaction mechanism can be extracted.

$$k = A_f exp(-E_A/RT) \tag{2.4}$$

with E_A the activation energy, R the gas constant, T the temperature and A_f the frequency factor describing the frequency of collision of molecules that have the required orientation to trigger the chemical reaction. Note that higher T yields higher rate constants. Also the equation confirms the initial statement that at lower activation energies the rates are higher and thus the reactions proceed faster [12]. Rate constants can only be determined experimentally and are specific to each reaction.

2.1.3. Reaction orders

The above definition of reaction rates shows that rates in general depend on changes of the concentration of a reactant or product and that this change can be captured by rate laws. Reaction orders give slightly more details on that dependency. Most common orders are first-order and second-order reactions. The above discussion is an example for a first-order reaction. Another example would be radioactive decay. The central characteristic of first-order reactions is that the reaction rates change in the same way as the concentration of the reactants do. Meaning, if for example the concentration of reactant A is doubled, the reaction rate would also double. Thereby, it can happen that a second-order reaction is first-order with respect to a subset of involved substances. The unit of a first-order reaction is s^{-1}, for second-order reactions it is $M^{-1}s^{-1}$.

Fist-order reactions

2.1 is a typical first-order reaction. The derived set of differential equations 2.2 and 2.3 can be solved by separating the variables and integration. Considering that the forward reaction is typically much faster, it can be claimed that $k_+ \gg k_-$. This results in the following expression:

$$[A] = [A]_0 \exp -k_+ t \tag{2.5}$$

with A_0 refers to the concentration of [A] at the beginning of the reaction. The solution shows that A decays exponentially. The half-life is another quantity that can be determined from this solution. It states the time required for half of the initial concentration

of A to have reacted and is defined as follows:

$$t_{1/2} = \frac{\ln 2}{k_+} \tag{2.6}$$

It is interesting to see, that the half-life only depend on the forward rate [12].

Second-order reactions

To give an example for a second-order reaction, let us consider a reaction as follows:

$$A + A \rightarrow B$$

A rate law can be found as follows:

$$-\frac{1}{2}\frac{d[A]}{dt} = k[A]^2 \tag{2.7}$$

Similar to first-order reaction rate laws, one can find a solution to this equation via integration.

$$\frac{1}{[A]} = \frac{1}{A_0} + 2kt \tag{2.8}$$

where A_0 is the concentration of A at $t = 0$.
2.5 and 2.8 are fundamental equations to judge whether a process under study follows the laws of a first- or second-order reaction.
If the natural logarithm of [A] is linear in t, one can conclude that the reaction is first-order with respect to A. The experimental data should follow a graph with a slope of $-k$. In contrast, if the $\ln \frac{1}{[A]}$ is linear in t, the reaction is second-order in A and the slope can be determined as double the second-order reaction rate constant. [12]

2.1.4. Kinetics of DNA duplex formation

DNA hybridization follows the law of a second-order reaction and is an interesting application of what has been described above. Since this thesis heavily relies on concepts of DNA hybridization, this section aims to provide some details about the reaction kinetics of duplex formation.
A DNA helix (H) forms upon the interaction of two complementary, DNA single strands A and B:

$$A + B \rightarrow H$$

The appropriate rate-law for this type of reaction can be described as follows:

$$\frac{d[A]}{dt} = -k[A][B] \tag{2.9}$$

Assuming that there is only one copy of each complementary species one can equate [A] with [B] and 2.10 reduces to

$$\frac{d[A]}{dt} = -k[A]^2 \tag{2.10}$$

yielding the same equation as in 2.7 and which can be solved with the only difference being the factor of 2 that cancels out. An expression for the fraction of strands that is hybridized, gives valuable insights for the interpretation of DNA hybridization reactions. The fraction bound f can be defined as follows:

$$f = \frac{[A]}{A_0} \tag{2.11}$$

where A_0 is the total amount of strand A. Using the solution for second-order reactions 2.8, f can be rewritten as

$$f = \frac{1}{1 + A_0 kt} \tag{2.12}$$

Another important aspect is that one can apply the pre-equlibirum approximation to the mechanism of DNA hybridization that helps to eliminate a first approximation for its rate constant. Doing so, one has to acknowledge that hybridization starts with the formation of an unstable complex of two base pairs. These two base pairs prefer to dissociate rather then grow into a larger complex, meaning that $k_{-1} > k_2$. As a consequence, the formation of the unstable, two base pair stretch happens more frequently before the critical nucleus consisting of three or more base pairs is formed to initiate the actual growth. Figure 2.2 illustrates this process and highlights the involved reaction rates.

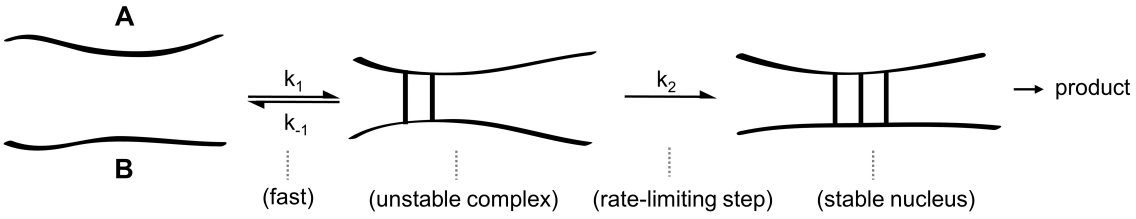

Figure 2.2.: Kinetics of DNA duplex formation. Two complementary DNA single strands A and B interact with each other at a rate k_1 to form an unstable product connected via two base pairs. Rates to dissociate k_{-1} at this point is smaller than rate k_2 leading to a stable nucleus. Thus pre-equilibrium assumption holds true for the initial step. Once the rate-limiting step of adding a third base is overcome, growth into the whole product is continued. Although simplified, this picture of DNA hybridization can be used to approximate the rate constant for base-pairing k_2. [12]

The process can be described via a bimolecular rate law:

$$\frac{d[P]}{dt} = k_2[\text{unstable helix}] \tag{2.13}$$

where P is the the unstable double-helical product.
Following the pre-equilibrium approximation one can obtain an expression for the rate constant K_1:

$$K_1 = \frac{[\text{unstable helix}]}{[A][B]} \tag{2.14}$$

Combining 2.13 and 2.14 results in the following expression for the rate at which the DNA

helix is produced:

$$\frac{d[P]}{dt} = k_2 K_1 [A][B] \tag{2.15}$$

This is a central finding that allows to conclude that rate constant for DNA hybridization is $k = k_2 K_1$. Experimentally it has been found that $k \simeq 10^6 M^{-1} s^{-1}$ and $K_1 \simeq 10^{-1} 1 M^{-1}$ [12] which can be used to calculate the rate constant for base pairing $k_2 \simeq 10^7 s^{-1}$.

2.2. DNA according to Watson-Crick

DNA (**d**eoxyribose **n**ucleic **a**cid) is well known as the molecule that stores and passes on the genetic information of all living organisms on Earth. Its chemical properties and associated functionalities of storing and processing information are unique and crucial for the existence, evolution, and diversity of life.
This chapter provides background on the chemical nature of DNA and how its chemistry conveys thermodynamic properties. The basics described in this chapter will later be consulted for the introduction of the concepts of DNA nanotechnology and will thus focus on the structural and physical properties of DNA rather than its biological meaning.

2.2.1. Chemical structure of nucleotides

Key to understanding the presented content within this work is that DNA is a charged, linear and most importantly directional polymer [13].
In general, polymers are materials composed of multiple periodically repeated subunits [14].
In the case of DNA these subunits are the nucleotides (nt). They are made of a phosphoric acid coupled to a sugar molecule (β-D-2-Deoxyribose) that binds to one of the four existing chemical bases: adenine (A), guanine (G), thymine (T) and cytosine (C). Since their structures chemically originate in purines and pyrimidines, all bases share a characteristic planar aromatic ring (see figure 2.3 A). Purine bases such as A and G have an additional imidazole group attached to the main ring and incorporate four instead of two nitrogen atoms compared to pyrimidine bases such as T and C [13].
The numbering (red) of the carbon atoms in figure 2.3 A shows that carbon atoms at positions 2 and 5 are the only positions shared in purines and pyrimidines. The numbering becomes important when describing the creation of nucleosides, an intermediate compound consisting of the base and the deoxyribose molecule. Figure 2.4 explains how purine bases connect their nitrogen at position 9 to the deoxyribose's carbon at position 1. Pyrimidine bases on the other hand connect their nitrogen 1 atom to the desoxyribose. The connection between bases and sugar molecules is a β-glycosidic bonds.
A nucleotide is characterized by a phosphoric acid that connects to the nucleoside through esterification of the hydroxyl group at the carbon 5 site of the deoxyribose. [15]
Multiple nucleotides are connected to each other via their phosphate groups that establish ester bonds between the deoxyribose's carbon 5 of one nucleotide and the desoxyribose's carbon 3 of the following nucleotide. This results in two chemically different ends of a nucleotide chain. Figure 2.4 shows that the chain starts with the so called 5'-end at the top which exhibits a free phosphate group and ends with the 3'-end at the bottom with the hydroxyl group at the carbon 3 of the last deoxyribose. This generates directionality in the nucleic acid chain. [15]

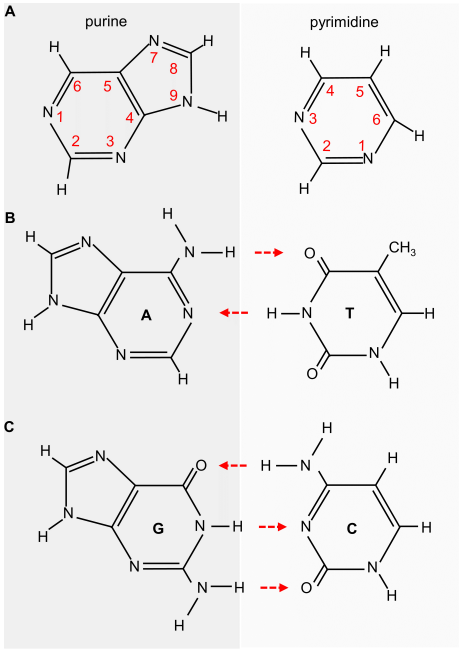

Figure 2.3.: Chemical structure of the four DNA bases and their binding partners. **A** DNA bases chemically originate in purines and pyrimidines. Characteristic to these structures is the planar, aromatic carbon ring. Purines and pyrimidines only share carbon position 2 and 5 indicated by the red numbering. **B** A and G are purine bases. They have an additional imidazole group attached to the main aromatic ring and incorporate four nitrogen atoms. Pyrimidine bases such as T and C hold two nitrogen atoms. Red dashed arrows indicate the hydrogen bonds between the bases. The arrow heads point toward the direction of the hydrogen acceptor. In the context of Watson-Crick base pairing adenine connects to thymine via two hydrogen bonds, while guanine pairs with cytosine via three hydrogen bonds. [15]

In summary, the varying component of nucleotides are the incorporated bases A, T, C, and G. Nucleotides form a single DNA strand upon the interaction of their sugars and phosphate groups. A chain of connected nucleotides is known as the primary structure of DNA. The primary structure is conventionally represented as a string of the base letters A, T, C and G and reads from the 5' to the 3' end [15].

2.2.2. The generation of the DNA double helix

The Watson-Crick model describes DNA under physiological conditions where it adopts a double helical structure. The following explains the assembly of a DNA double helix with a focus on the involved molecular forces.
In general, two complementary and antiparallel DNA single strands are required to assemble the DNA double helix. The natural configuration of DNA is the so called B-form. It is the configuration of DNA in living cells and characterized by a clockwise rotation of the double helix and a well distinguishable major and minor groove.
In the context of Watson-Crick base pairing, the four bases have a designated partner each, to whom they establish hydrogen bonds. A pairs with T and G pairs with C. This binding affinity is due to three reasons. First, it manifests in the chemical structure of the bases themselves that cause directed hydrogen bonds between them. Second, the sugar-

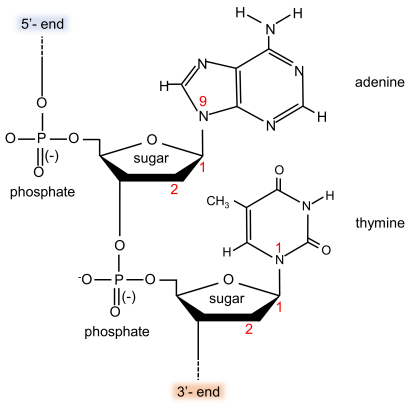

Figure 2.4.: Sugar-phosphate backbone of DNA. Nitrogen 1 of purine bases (here: adenine) form a β-glycosidic bond with the carbon 1 of the deoxyribose. A compound consisting of a nitrogenous base and a deoxyribose is called a nulceoside. This becomes a nucleotide when the hydroxyl group on carbon 5 of the sugar esterifies with a phosphoric acid. Nucleotides assemble into a polymer chain via ester bonds established by the phosphate groups bridging from the deoxyribose's carbon 5 of one nucleotide to the desoxyribose's carbon 3 of the following nucleotide. This results in two chemically different ends of the chain. One end exhibits a free phosphate group (5'-end), the other end displays the hydroxyl group at carbon 3 of the last deoxyribose. [15]

phosphate backbone of the DNA aligns the bases toward each other and third, the sizes of the purine and pyrimidine bases and the space available in the helical geometry limits the possible combinations of the bases. [16]

Hydrogen bonds

Hydrogen bonds are non-covalent bonds. They form if two electronegative atoms interact with each other over a hydrogen atom. Typical examples for electonegative atoms that interact via hydrogen bonds are nitrogen and oxygen atoms.
Figure 2.5 A(i) revises the location of nitrogen and oxygen within the periodic table and the associated values of their electronegativity of 3.04 and 3.44, respectively. The elements listed in the periodic table exhibit increased electronegativity going from left to right. Nitrogen and oxygen are placed on the far right of the periodic table, to the left of fluorine, known as the element with the highest electronegativity. [17]
Figure 2.5 B(ii) explains the partial charge distribution in a hydrogen bond demonstrated for the most common cases. It shows how the electronegative atoms on the left of the chemical equations act as hydrogen donators (orange) by withdrawing the electron from the covalently bound hydrogen (black line). The hydrogen atom gains a positive partial charge σ_+ upon this interaction and is thus available for an interaction with the electron acceptor (green) which is the electronegative atom on the right. This establishes the hydrogen bond between the two atoms (green dashed lines). [13] With this in mind, a second look at figure 2.3 B reveals that the chemical structure of the DNA bases offer an ideal setting for hydrogen bonds. The red dashed arrows indicate the directionality of the hydrogen bonds pointing toward the direction of the electron acceptor atoms that provide the required free electron pair. The two base pairs AT and GC share the central hydrogen bond N-H→N, however they point in opposite directions for each base pair. The N-H→O

bond is pointing toward the carboxyl group in both cases, always opposite to the central N-H→N bond. Compared to the AT base pair, GC establishes a third hydrogen bond (see figure 2.3 C).
While the directionality of the hydrogen bonds carry information about the specific binding affinity of the four bases, that alone is not enough to determine selectivity. The size difference between purines and pyrimidine bases combined with the limited space within a double helix favors the combination of a purine with a pyrimidine base since the combination of two purines or two pyrimidines would either take up too much or too little space within the helical gap. This reinforces the binding affinity of A to T and G to C. [16]
Compared to covalent interactions, hydrogen bonds are only weak with a binding energy of 4–20 kJ mol^{-1}. However, in a chain of multiple nucleotides the amount of hydrogen bonds sums up and results in a stable polymer. The distance between the electronegative atoms that contribute to a hydrogen bond is around $0.24 - 0.35$ nm. Hydrogen bonds do not contribute too much to the formation of the double helix itself, but as described above are a key contributor to the specific binding affinity of the bases to each other. The fact that A only pairs with T and G only with C is a defining propriety of Watson-Crick base pairing and is called base complementarity. [13]
A DNA double helix consists of two complementary DNA single strands. If the DNA sequence of one of the two strands is known, the sequence of the second DNA strand can easily be predicted based on the rules of complementarity.

Glycosidic bond

Glycosidic bonds in DNA are established between the bases and their sugar molecules. Each base pair exhibits two glycosidic bonds on opposite sites integrating the bases into both sites of the sugar-phosphate backbone. Thereby the glycosidic bonds are not perfectly aligned with respect to each other due to the different sizes of the purine and pyrimidine bases. This causes the base pairs to have asymmetric sites that globally result in a so called major and minor groove.
Figure 2.5 C(i) shows an atomic model of a DNA double helix. Major grooves are highlighted orange, minor gooves are shown in yellow. Figure 2.5 C(ii) depicts the position where the glycosidic bonds connect the bases to the deoxyribose for the two base pairs AT and GC. The orange part of the outlining ellipse highlights the larger distance between the two gycosidic bonds, the yellow part corresponds to the smaller distance. It also shows that major and minor grooves exhibit nitrogen and oxygen atoms (colored pink) that are available for potential hydrogen bonds with other molecules. The latter is important since it offers attachment sites for proteins or other molecules. [13]

Van-der-Waals interaction

Van-der-Waals (VdW) interactions are present between the stacked bases and additionally stabilize the double helix. In general, VdW interactions arise due to fluctuations in the electron distributions of an atom. An asymmetric electron cloud can disturb the electron clouds of adjacent atoms through ion interactions and leads to a similarly asymmetric electron distributions in the neighbor atoms. These distributions result in attractive forces between the two atoms as long as their distance is larger then the so called Van-der-Waals

contact distance. Once distances become smaller then the contact distance, the electron clouds of the adjacent atoms overlap and repulsion forces predominate. Similar to hydrogen bonds, the binding energy of an individual VdW interaction is small (2-4 kJ mol^{-1}). In a large molecular complex however, these small binding energies sum up and make a decent contribution to the molecule's stability. Figure 2.5 C(i) shows how the attractive energy of VdW interaction predominates the repulsive energy with increasing distances between two neighboring atoms. Repulsive forces however predominate at distances smaller than the VdW-contact radius. Figure 2.5 C(ii) depicts how bases stack on top of each other due to VdW forces between them. [13]

Hydrophobic effect

The hydrophobic effect becomes important during the alignment of the bases within the double helix. Due to the non-polar nature of the bases, they prefer to point toward the inner of the double helix and adapt the dense base stacking to avoid as much contact with water as possible. The sugar-phosphate backbone builds the outer shell of the double helix. [13]

Ionic interactions in DNA

Each phosphate group of the DNA backbone exhibits a negative charge at neutral pH. During DNA hybridization, the process where two DNA single strands form a double helix, these negative charges lead to repulsive forces between the single strands. Under physiological conditions these repulsive forces can be counterbalanced with the high dielectric constant of water and present cations such as Na^+ and Mg^{2+}. When working with synthetic DNA strands it is thus of great importance to buffer the reactions to help the DNA strand to anneal with their binding partners. [13]

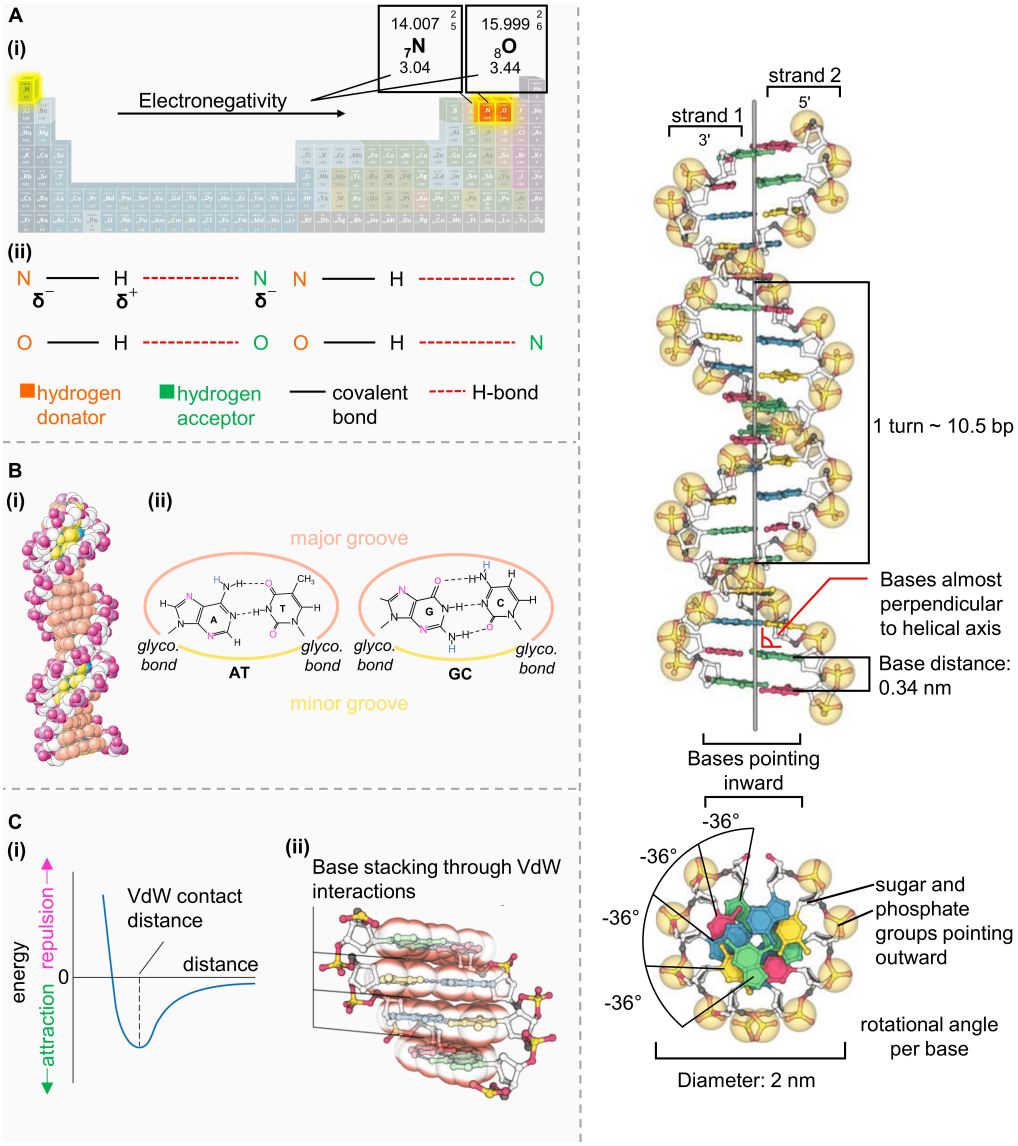

Figure 2.5.: The DNA double helix - involved forces and geometry. **A** Concept of hydrogen bond formation. **i** Nitrogen and oxygen exhibit a high electronegativity suitable to contribute to hydrogen bond formation. Electronegativity values in the periodic table increase from left to right [18]. **ii** Examples for prominent hydrogen bond formations. Hydrogen donators are indicated orange, hydrogen acceptors in green. The high electronegativity of nitrogen or oxygen induce a partial, positive charge in the covalently bound hydrogen atom. Thus, the hydrogen atom can interact with the electronegative hydrogen acceptor atom. Red dashed lines indicate the established hydrogen bonds. **B** Major and minor groove formation in DNA. **i** Atomic model of the DNA double helix highlighting major (orange) and minor (yellow) grooves. **ii** Chemical structure of the base pairs AT and GC and the glycosidic bond location. Asymmetric alignment of the bonds result in a larger distance between the bonds causing the major groove (orange) while the smaller distance causes the minor groove (yellow). Pink atoms are available for the interaction with molecules.**C** Van-der-Waals interactions between DNA base pairs. **i** Potential energy between two atoms plotted against the distance. Potential energy is repulsive at distances closer than the VdW contact distance. At distances larger than the VdW contact distance atoms attract each other. **ii** Side view of the DNA double helix showing the VdW interactions between the basepairs that leads to base pair stacking.**D** 3D model of the DNA double helix highlighting some key geometric features. [13]

Geometric properties of the DNA double helix

The chemical structure of the bases and the interaction forces result in a DNA double helix with characteristic geometric parameters. While there are three known configurations of DNA (B-form, A-form, and Z-form) [13], the following discussion addresses the B-configuration.
Figure 2.5 D(i) despicts the side view of a DNA double helix with the key parameters of B-DNA highlighted. A DNA double strand (dsDNA) consists of two antiparallel and complementary single strands - strand 1 and strand 2. Bases are aligned in a way that they point inward and are stacked on top of each other in an almost 90° angle. The sugar-phosphate backbone faces outward. The inter-base distance is 0.34 nm. The double helix completes a full turn after 10.5 basepairs (bps) which corresponds to roughly 3.6 nm. The rotational angle of the double helix is visualized in figure 2.5 D(ii). With each base the double helix turns -36°. The diameter of B-DNA is around 2 nm. [13]

2.3. Non-canonical base pairing

So far, the presented discussions have focused on the Watson-Crick base pairing mechanism. Non-canonical base pairing are interactions of DNA bases beyond the standard model of Watson-Crick base complementarity. This widens opportunities to work with DNA as a programmable building material and will thus be explained briefly in the following sections. Although non-canonical base pairing mainly occurs in RNA [19], there are some phenomena in DNA used in DNA nanotechnology that are worth mentioning at this point.

Twelve basic geometric families

To access non-canonical base pairing, it is worth taking a second look at the chemical structure of nucleotides. Figure 2.6 shows that each nucleotide has three faces available for interaction with other bases via hydrogen bonds. Besides the standard Watson-Crick binding site, purine bases exhibit a so called hoogsteen edge and the sugar edge. Pyrimidine bases as well have those three faces for potential interaction, the hoogsteen edge however is really a C-H edge but is commonly called hoogsteen edges as well. This configuration space expands with further possible configurations originating from the *cis* and *trans* forms of the sugar molecules within a nucleotide. *Cis* and *trans* configurations refer to the orientation of the glycosidic bond of the bases shown in figure 2.7. Combining the three edges for possible interactions with the two available configurations of the sugar molecules results in a total amount of 12 possible ways for bases to pair with each other. These are known as the "twelve basic geometric families" which are listed in 2.1. [20]

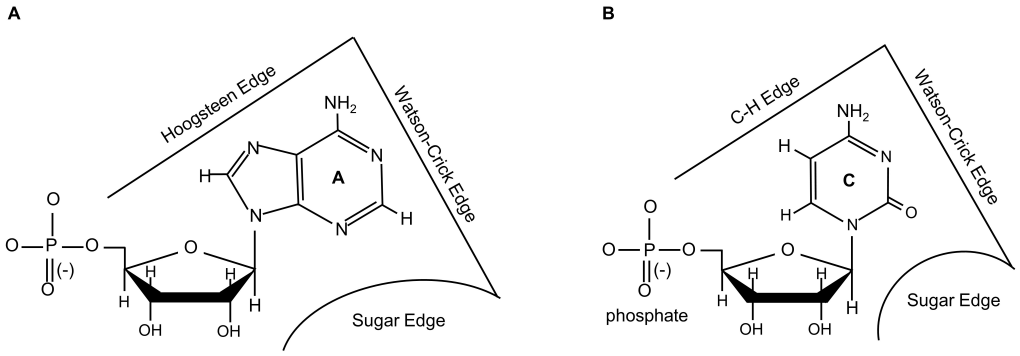

Figure 2.6.: Bases can interact with other bases via three faces: The standard Watson-Crick edge, the Hoogsteen edge and the sugar edge. **A** Three possible faces for a nucleotide with the purine adenine (A). **B** Three possible faces for a nucleotide with the pyrimidine cytosine (C). The hoogsten edge for pyrimidine bases is the C-H edges but generally called hoogsten edge as well. [20]

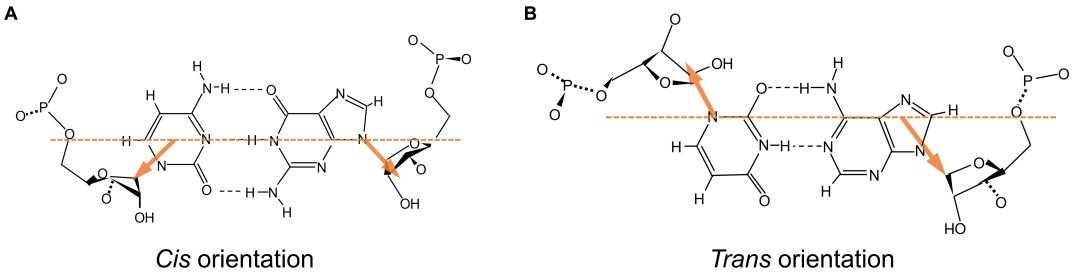

Figure 2.7.: *Cis* and *trans* orientation of the glycosidic bond in DNA base pairs. The orange, dashed line parallel to the hydrogen bonds is used to visualize the different orientations. Arrows point toward the direction of the glycosidic bonds. **A** In *cis*-orientation the glycosidic bond is oriented in a way that both phosphate-sugar groups are pointing in the same direction below the parallel line. **B** Glycosidic bonds in *trans* orientation force the phosphate-sugar goups to face opposite directions, one above and one below the orange line. [20]

No.	Glycosidic bond orientation	Interacting edges
1	Cis	Watson–Crick/Watson–Crick
2	Trans	Watson–Crick/Watson–Crick
3	Cis	Watson–Crick/Hoogsteen
4	Trans	Watson–Crick/Hoogsteen
5	Cis	Watson–Crick/Sugar Edge
6	Trans	Watson–Crick/Sugar Edge
7	Cis	Hoogsteen/Hoogsteen
8	Trans	Hoogsteen/Hoogsteen
9	Cis	Hoogsteen/Sugar Edge
10	Trans	Hoogsteen/Sugar Edge
11	Cis	Sugar Edge/Sugar Edge
12	Trans	Sugar Edge/Sugar Edge

Table 2.1.: List of the "twelve basic geometric families". Bases can interact with each other via three faces. The sugars of the nucleotides can adapt *cis* or *trans* configuration. This adds up to twelve possible geometries for a base pair. [20]

Hoogsteen base pair

The purine bases rotate 180° around their glycosidic bond to be able to engage over their hoogsteen edge with other bases. This is one central characteristic for hoogsteen (H) base pairs. In general, the hoogsteen base arrangement employs the standard Watson-Crick (WC) pairing mechanism (A-T, C-G) but occurs in different geometries. Figure 2.8 shows the hoogsteen base pairs H-AT on the left and H-GC on the right. Thereby, the glycosidic bonds are in cis configuration in both cases (indicated by the orange arrow). There are further variations of hoogsteen base pairs where the bonds are in trans configuration. Figure 2.8 shows that the A of the H-AT pair has rotated and uses its imidazole group to accept a hydrogen bond. The second hydrogen bond is established via the NH_2 group of the main aromatic ring. [16]
Compared to the standard WC-GC pair, the H-GC pair forms two instead of three hydrogen bonds. WC-GC pairs and H-GC pairs share the hydrogen bond between guanine O6 and cytosine N4. The second hydrogen bond of the H-GC pair however establishes between guanine N7 and cytosine N3 [21]. The cytosine in a H-GC pair is protonated and thus properly termed G-C^+. The protonation causes the H-GC pair to prefer a lower pH. [16]

DNA motifs

It is the hoogsteen base pairing that allows the formation of secondary structures in DNA such as the so called G-quadruplex and the intercalated-motif (i-motif) [16]. They can arise if longer, continuous strings of G or C bases are incorporated within a DNA sequence. The G-quadruplex is a symmetric structure formed upon the presence of G-rich regions on a DNA strand. It can involve one to four strands arranged in G-tetrads and adopts a helical geometry. Typically, mono- or divalent cations gather in the center of the G-tetrads [22]. Figure 2.8 A illustrates the structural features of a G-quadruplex. The i-motif requires continuous runs of C bases. It is characterized by a hemi-protonation where the N-atoms

of two C bases highlighted in red in figure 2.8 B interact over one proton. Multiples of these CC^+ base pairs come together in a 90° angle [16] and form an i-motif. The majority of investigated i-motifs have been found to be most stable at low pH [23]. Both motifs have been exploited for the development of DNA switches in DNA nanotechnology due to their sensitivity toward certain pH. Chapter 4 will explain how DNA motifs are implemented to realize configurational changes in DNA nanostructures.

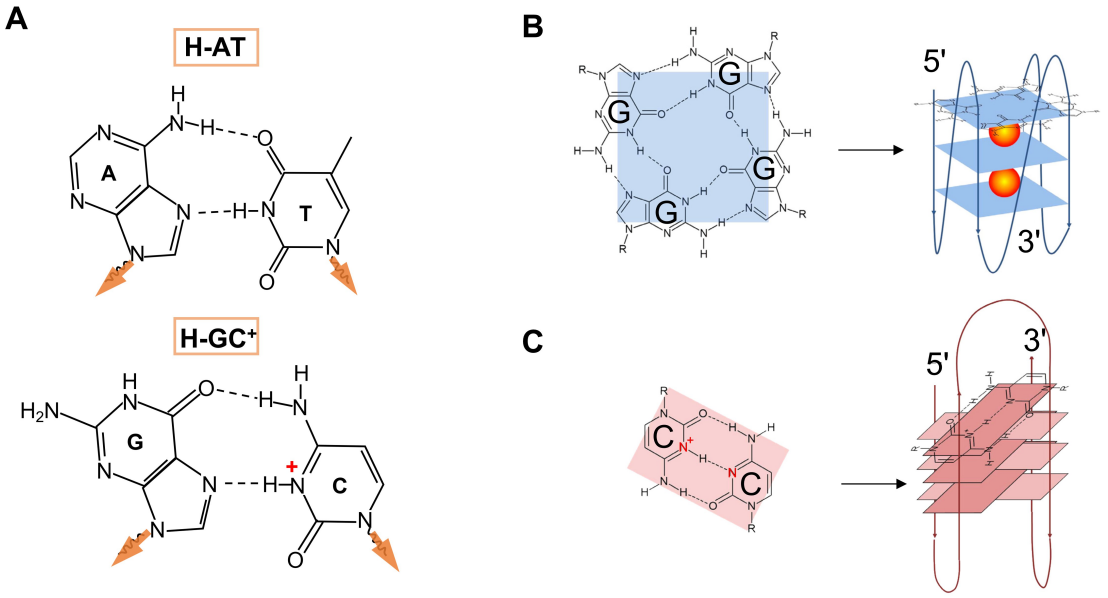

Figure 2.8.: A Hoogsteen base pairs (AT and GC^+) (cf. text) [21]. **B** G-quadruplex formed by consecutive repetition of G bases. G-tetrads are arrangend in a helical configuration and capture mono-or divalent cations in their center. **B** I-motifs are formed upon C-rich DNA sequences. CC base pairs hemi-protonate and stack on top of each other in 90° angles. [24]

2.4. Holliday junctions and branch migration

Holliday junctions are intermediate structural motifs formed during DNA recombination [25, 26]. There are many conformers exhibiting different coaxial stacking phenomena that fall under the term Holliday junctions and whose existence depend on buffer conditions and the level of complementarity around the crossing point. In general however, a Holliday junction is characterized by four double-stranded arms as shown in figure 2.9.
Sequence symmetry around the crossing point (indicated in pink) can cause the Holliday junction to travel along the horizontal or vertical axis resulting in different conformers. This dynamic feature is called *branch migration*. The fact that nucleic acids can assemble dynamic junctions is heavily exploited in the field of DNA nanotechnology. [16]
Its applications are discussed in chapter 3.

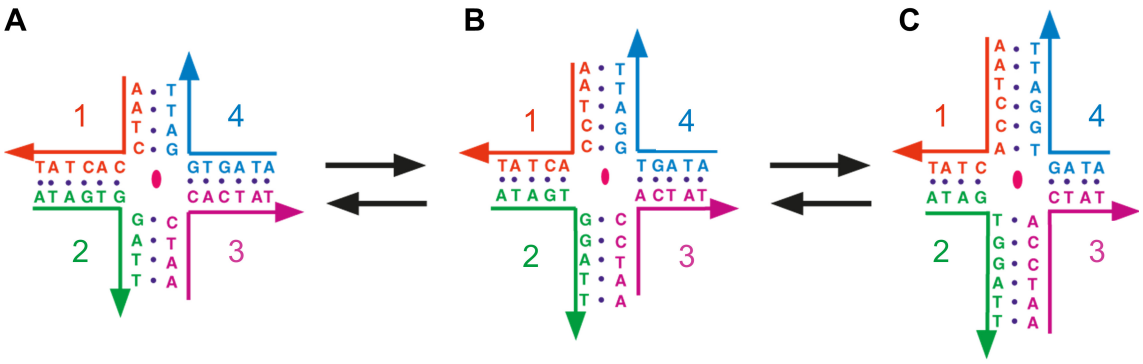

Figure 2.9.: Holliday junctions and branch migration. **A** A Holliday junction is characterized by four double-stranded DNA arms. Base pairs can be interchanged around the crossing point depending on the sequence symmetry in the center (pink dot) and thus forming conformers with growing vertical and shrinking horizontal arms shown in **B** and **C**. [16]

2.5. Thermodynamic and mechanical stability of DNA

Denaturation of DNA

Denaturation describes the process of unwinding and separating a DNA duplex. In its natural habitat, DNA is a stable polymer held together by the intermolecular forces described above. However, external triggers such as heat, basic or acidic buffers, and chemical reagents such as formamide or urea can lead to denaturation of the double helix. The hyperchromic effect is used to observe and study this process. The effect describes the decreased absorption of double stranded DNA compared to the individual single strands when measured at a wavelength λ of 260 nm, which is the wavelength of maximal absorpotion capacity for DNA. A sigmoidal curve is characteristic when measuring the absorption of a DNA double strand under heating conditions and thus allows indirect observation of the denaturing process. Once the strand is fully separated, the curve plateaus. This spectro-photometrical method also showed that DNA denaturation is a reversible process. The DNA single strands find their complementary counterparts again upon cooling. [15]
Another important parameter that should be mentioned in the context of thermodynamic stability is the melting temperature. It is the quantity describing the temperature at which half of the DNA strands are denatured while the other half is still in its double-stranded configuration. It can be determined using the sigmoidal curves provided by the absorption measurements at $\lambda = 260nm$ or alternatively calculated using the following formula:

$$T_m = \frac{\Delta H^0 \cdot 1000}{\Delta S^0 + R \cdot ln(\frac{C_T}{4})} - 273.15, \tag{2.16}$$

where ΔH^0 is the change in enthalpy in $[kcal/mol]$, ΔS^0 is the change in entropy in $[cal/mol \cdot K]$, C_T is the total molar strand concentration in $[M]$ and R is the gas constant in $[cal/mol \cdot K]$ [27].
It is interesting that for synthetic DNA sequences the resistance to denaturation can be tuned by targeted insertion of GC-base pairs. This is because the three hydrogen bonds in a GC base pair stores more binding energy, thus leading to higher melting temperatures. Conversely, the sigmoidal curves as well as experimentally obtained melting temperatures can be used to judge the GC-content of a give DNA samples. [15]

Persistence length and worm-like chain model

The persistence length is a quantity that describes the mechanical properties of polymers such as their bending stiffness. The flexibility of a polymer is closely related to its mechanical stability and thus crucial for its function. Polymers with a higher persistence length are more rigid compared to polymers with a lower persistence length. Very often, the individual subunits of polymers are quite rigid themselves and could be described as single rods. Especially for DNA however, once multiples of these subunits join together to form the polymer, the system gains flexibility and in order to maximize entropy adopts a random coil conformation. [28]
Theoretical models that exclusively focus on non-interactive, single rods are not sufficient anymore to describe the behavior of the polymer as a whole. The worm-like chain model (WLC model) is so far the most suitable way to describe a semi-flexible polymers such as single-stranded (ss) and double-stranded (ds) DNA. It extends simpler models by treating the polymer as an elastic continuum (see figure 2.10) that is inextensible with a linear bending energy and is subject to thermal fluctuations. [28]

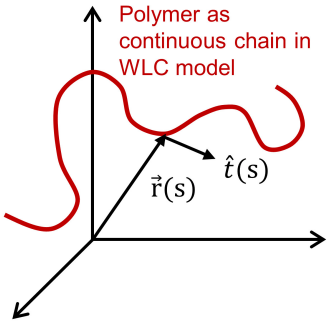

Figure 2.10.: The WLC-model describes polymers as continuum which can be parameterized using the tangent vector $\hat{t}(s) = \partial\vec{r}(s)/\partial s$ along the contour length of the polymer. Thereby, $\vec{r}(s)$ is the position vector for any point along the contour. [29]

The ability to bend comes with an energy cost. To find a simple description for the bending energy, one first introduces an arc length s spanning a certain distance L which is also known as the contour length of the polymer. The tangent vector $\hat{t}(s) = \partial\vec{r}(s)/\partial s$ can be chosen as parametrization along the polymer's contour, with $\vec{r}(s)$ being the position vector for any point along the contour. $\partial\hat{t}(s)/\partial s$ is the mathematical description of the tangent vector's change which is an analogue to the curvature of the polymer. [28]
In a scenario of only small bends and forces that are linear, one can follow Hooke's law and results in the following description for the free energy:

$$H = \frac{\kappa}{2}\int_0^L \left(\frac{\partial\hat{t}(s)}{\partial s}\right)^2 ds \tag{2.17}$$

Thereby, κ is the bending stiffness of the polymer that can be defined as follows:

$$\kappa = L_p \cdot k_b T,$$

with L_p being the persistence length, k_b the Boltzmann constant and T the temperature. A more intuitive definition of the persistence length can be obtained looking at the corre-

lation of the tangent vectors at the polymer's coordinates $t(s)$ and $t(s')$:

$$\langle \hat{t}(s) \cdot \hat{t}(s') \rangle = \langle \cos(\Theta_{s'} - \Theta_s) \rangle = e^{-\frac{s-s'}{L_p}} \tag{2.18}$$

Thereby, $s - s'$ can be interpreted as the polymer contour length. The correlation between the two tangent vectors, which is determined by the cosines of the angles between them, decreases exponentially. Thus, the persistence lengths can also be described as the measure that quantifies the length scale over which the correlation between the two tangent vectors exists. The WLC model allows us to determine the persistence length for DNA. Under physiological conditons the persistence length of dsDNA and ssDNA is $L_p^{dsDNA} = 50nm$ and $L_p^{ssDNA} = 1.3nm$. [28]
To get a clearer picture about the size of the polymer, the mean square end-to-end distance can be derived from the WLC-model. The derivation begins with the calculation of the end-to-end distance of the polymer which is done via the integral of the tangent vector along the contour length:

$$\overrightarrow{R} = \int_0^L \hat{t}(s) ds \tag{2.19}$$

Based on this, the means squared end-to-end distance can be stated as follows:

$$\langle R^2 \rangle = \int_0^L ds \int_0^L ds' \langle \hat{t}(s) \cdot \hat{t}(s') \rangle \tag{2.20}$$

The integrand is the previously derived correlation 2.18 between the two tangent vectors and can be inserted in 2.20. With this the integral can be performed and leads to:

$$\langle R^2 \rangle = 2L_p \Big(\frac{L}{L_P} - 1 + e^{\frac{-L}{L_p}} \Big) \tag{2.21}$$

In the case of $L >> L_p$ the mean square end-to-end distance reduces to $\langle R^2 \rangle \approx 2LL_p$. [28]

2.6. DNA as building source material

The quaternary logic implemented through Watson-Crick base-pairing, coupled with the physical and thermodynamic properties of DNA, make this biological molecule an ideal building material. It is a flexible polymer that can bend while maintaining enough stability to retain structure. Further, the denaturation of DNA is a reversible process, and rates of re-annealing can be tuned by varying the length of single strands, GC content, and presence of repetitive sequences of bases. [15]
In addition, the studies by Caruthers et al. [8] in 1985 presented a new and cost-effective technique to produce synthetic DNA strands at high yields based on the use of phosphoramidites. The following chapter will show why these properties are crucial and how they can be exploited for the programmed self-assembly of DNA nanostructures.

3. Design strategies of structural DNA nanotechnology

DNA nanotechnology is the research field that investigates and develops the programmed and controlled self-assembly of nanoscale objects made from DNA. Thereby, it deprives DNA from the established context as the molecule of heredity and instead focuses on its programmabitily offered by the Watson-Crick base pairing mechanism. This chapter outlines some of the most prominent design strategies that have evolved throughout the early years of the discipline and that belong to the state-of-the-art techniques of the field.

3.1. Branched DNA molecules

In the 1980s, Nadrian Seeman laid the theoretical groundwork for DNA nanotechnology and performed pioneering, experimental work. He employed the concept of Holliday junctions (HJs) to create the first synthetic DNA nanostructures. To recapitulate, figure 3.1 A (i) shows the typical outline of the four-arm junction that can adapt various conformations by branch migrating around the junction's node. Seeman and coworkers proposed a modified HJ that could be immobilized [30] and extended with further arms [31] (see figure 3.1 A (ii) and B). Sequence symmetry minimization of the involved DNA strands was thereby key to halt branch migration within the HJ that usually would enable the junctions' node to travel in all directions [30].
These synthetic DNA junctions serve as excellent building blocks. Complementary single-stranded overhangs, so called "sticky ends", on the HJ tiles allow them to interact with each other and form higher-order structures. [16]
Chen at al. have been the first to show that the HJ tiles can be used to form a 3D cube made from six DNA strands for each face and whose vertices rely on immobilized three-arm junctions [32]. These concepts inspired the development of further DNA motifs yielding diverse geometries. Variations of the HJ tiles achieved the more rigid double-crossover (DX) and triple crossover (TX) motifs shown in figure 3.1 D that were used to assemble μm sized, 2D periodic patterns [33, 34]. Further examples for motifs are cross motifs [35, 36] and 3-point-star motifs [37] that also are capable to assemble lattices whose structural properties have been studies in more detail by He et al. [38].
Further studies showed that the different motifs could also be used for the creation of 3D objects such as 3D lattices [39] and different polyhedral structures [40–42].
Overall, early DNA nanostructures worked with only a few short oligonucleotides (typically around 100 nt) whose sequences were highly tuned and that generated the basic building blocks for higher-order assemblies. [16]
However, researchers also pursued ideas of a templated assembly. Shih et al. used a long DNA single strand as a scaffold that only requires five 40mer DNA "helper" strands capable of shaping the template into an octahedron [43]. Yan et al. demonstrated that they can program DX DNA tiles to attach to a long DNA scaffold strand to form an information carrying lattice [44]. Typically the scaffold strands used for such templated

assemblies were generated via the enzymatic ligation of shorter oligonucleotides. The most prominent example for templated assembly of DNA nanostructures is the DNA origami technique developed in 2006 by P. Rothemund [9]. As this is the main method used within this work, the following chapter explains its basic concepts and some of the main design rules that have been empirically eliminated for this approach so far.

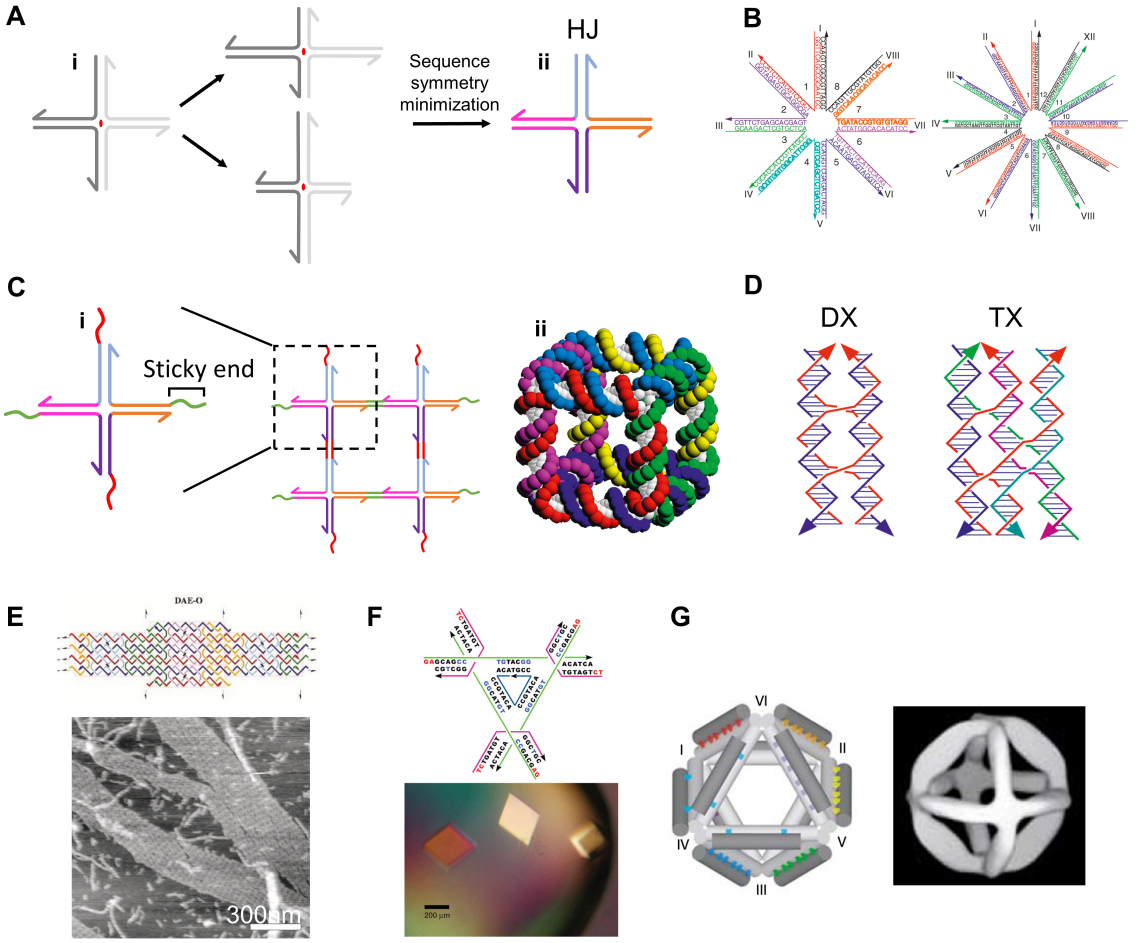

Figure 3.1.: A (i) HJs adapt different conformations upon branch migration at the junction node. (ii) HJs can be immobilized through sequence symmetry minimization [16]. **B** Extension of a four-arm junction to 8-12 arm junctions [31]. **C** (i) Sticky ends at the arms of a HJ enable the junctions to interact with each other and (ii) turn them into ideal building blocks for higher-order assembly such as the assembly of a cube [32]. **D** Double and triple crossovers are examples for DNA junction motifs with higher rigidity [16]. **E** Use of the DX motif for the construction of lattices [33]. **F** 3D crystal based on a DNA tensegrity triangle motif [39]. **G** Templated assembly of an DNA octahedron based on a 1.7kb long scaffold strand [43].

3.2. The DNA origami technique

DNA origami structures are generated using a circular, 8 kb long viral genome extracted from the M13 bacteriophage. The scaffold is complemented with hundreds of 20-60 bp

long oligonucleotides ("staples") that are designed complementary to locally distant binding sites on the scaffold. They mould the scaffold strand into large arrays of antiparallel DNA helices as shown in figure 3.2 B. Helices are connected by staple or scaffold crossovers that adapt junction motifs similar to the ones described in the previous section. Figure 3.2 C shows that the structural complexity of DNA origami is not restricted to rectangular arrays of antiparallel helices but instead can be designed to yield numerous shapes. [9]

Key to DNA origami is that single stranded extensions, or in technical jargon "handles", can be incorporated at a spatial resolution of 6 nm [9]. Handles can either contribute to a specific pattern on top of the structure [9] as shown in the last row in figure 3.2 C, serve as attachment sites for functional units such as gold particles [45], proteins [46, 47] or dye molecules [48] or can be addressed by other incoming DNA sequences that initiate further chemical processes [49]. Crossovers can only occur at locations where adjacent helices are in closest proximity [9].

Figure 3.2 illustrates the folding process of an origami structure over the course of a temperature ramp. Scaffold strand and staples are usually mixed at a fixed stoichiometry such as in a 5×to 20×excess with respect to the scaffold. Because DNA is a negatively charged polymer, origami folding usually needs to include cations such as magnesium chloride ($MgCl_2$) to screen the repulsion forces that originate from the negatively charged backbones. [9]
It is so far best practice to start the ramp with a high temperature at around 95°C to make sure all individual strands are separated and potentially present secondary structures that would hamper the folding process are dissolved. The reaction volume then is subjected to an incremental decrease in temperature down to around 20°C. Among other design-specific and experimental parameters, the temperature ramp is key to successful folding at appropriate yields. [10]

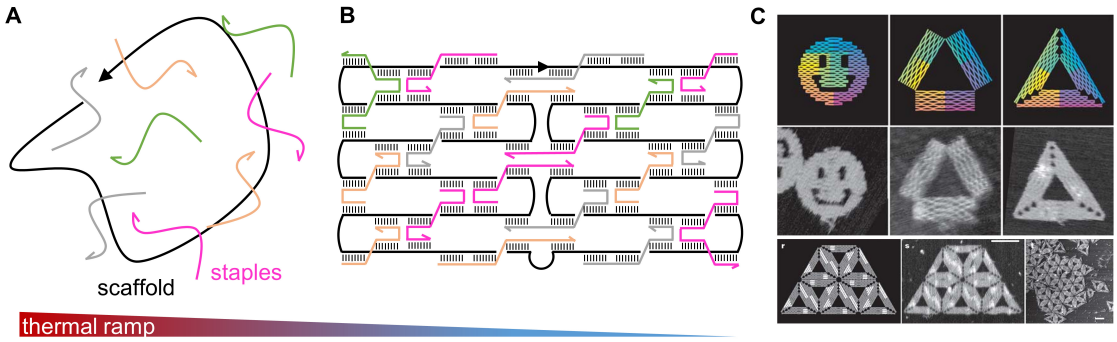

Figure 3.2.: Folding of DNA origami structures. **A** A long, circular scaffold strand (black) is complemented by staples - short oligonucleotides - that mold the scaffold into a desired shape based on their complementarity to different regions on the scaffold. **B** DNA arrays are generated by connecting multiple, adjacent DNA helices via scaffold and staple crossovers. **C** The DNA origami method yields a vast portfolio of different structures with a spatial resolution of 6 nm. The structures can be precisely addressed. Patterns can be generated using handles extruding from the plane. [9]

It has been shown that the folding of DNA origami structures is a highly cooperative process. This means that starting the folding ramp at high temperatures lets staples with highest melting temperatures, such as staples with a high GC content, to hybridize with the scaffold first. It was found that they then act as seeds promoting the hybridization of adjacent staples with a lower melting temperature. The cooperative nature of the process is also an explanation for the hysteretic trend observed for cooling and heating curves. [50–52]

Several techniques to extend DNA origami into three dimensions have been reported [53–57]. These include the combination of several 2D sheets to form a cube with a controllable lid [53], the honeycomb-like [54] and square-lattice like [55] arrangement of DNA double helices, gridiron structures [56] as well as helices packed on hexagonal and hybrid lattices [58]. Liedl et al. realized a highly stable 3D architecture implementing the concept of tensegrity into the designs [57]. Using triangulated DNA origami structures has proven to assemble polyhedral shapes of various geometries [59–61]. Curved 3D DNA origami structures have been achieved by the combination of concentric DNA rings [62] or by the controlled incorporation of basepair insertions and deletions in the origami designs [63].

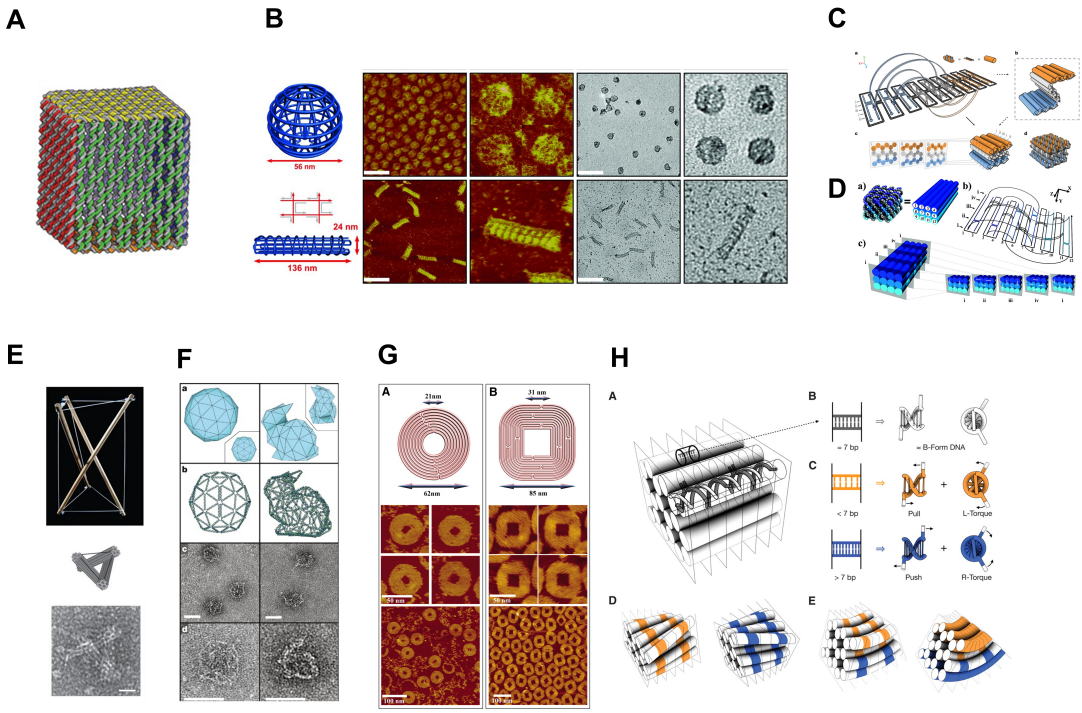

Figure 3.3.: Methods to extend DNA origami into 3D. **A** Combination of multiple 2D DNA origami sheets to a 3D cube with a switchable lid component [53]. **B** Gridiron folding of DNA strands generates meshes that can be assembled into spheres and tubes [56]. **C** Arrangement of DNA helices on a honeycomb-lattice [54] and **D** square lattice [55] to fold into 3D objects. **E** 3D tensegrity structures made from 13 helix bundles [57]. **F** 3D meshes can generate polyhedral shapes of different geometries [59]. **G** Curved DNA origami structures assemble upon the combination of multiple concentric rings [62]. **H** Explicit curvature is introduced by targeted basepair deletions and insertions [63].

This thesis implies a profound understanding of the honeycomb- and square-lattice design concepts and as such the following subsections will provide a more detailed description of these ideas. By the end, some of the main definite design rules are summarized, that have been accumulated by the field throughout years of empirical and theoretical data acquisition. This will serve as basis for the discussions of experiments presented in chapter 6.

Honeycomb-pleat-based vs. square-lattice DNA origami structures

The honeycomb-pleat based [54] and square-lattice designs [55] are the two main strategies to generate 3D DNA origami. The main difference is the helix arrangement each of which comes with its own design challenges. Both approaches exploit the helicity of the helices and that shifting crossover patterns can force them to arrange in space rather than within one plane (see figure 3.4 A and C). In a honeycomb-lattice, helices are placed in a 120° angle with respect to its three nearest neighbors while in a square-lattice design helices are placed in 90° angles toward each other resulting in a rectangular unit cell with four nearest neighbors. [54, 55]
Proper DNA origami design requires the knowledge about the geometric parameters of B-DNA presented in chapter 2 which impose constraints on the possible crossover positions. The general rule is that antiparallel crossovers can connect two neighboring helices only at positions where the respective peaks of the helices' backbones are facing towards each other. Additionally, one has to take into consideration that the distance between two crossover positions can only be an integer number of bases. Since natural B-DNA helices complete one full turn after 10.5 bps, finding proper crossover positions that would allow attachment of helices to each other without straining them is challenging. This can be approached however by arranging the helices at suited angles with respect to each other as is going to be explained in the following paragraphs. [64]
In honeycomb-lattices one typically uses every seventh bp on a staple helix as possible crossover positions as this allows the addition of an adjacent helix at an angle of 120° without straining the helices (see figure 3.6) [54].
Crossover positions that do not induce strain will be referred to as "relaxed" and are basically positions where the bases of two adjacent helices align [64].
Aiming for crossovers at relaxed distances, eliminates three specific sets of crossover positions that repeat every $0 + 21n$ bps shown in figure 3.4 B. These allow the helices to maintain their preferred, natural twist of 10.5 bps per turn. [54]

This is a major difference to the square-lattice approach [55]. A square-lattice arrangement of helices imposes strain onto the helices to make them fit into the square-like assembly (see figure 3.4 C). Relaxed crossover positions in a square-lattice staple helix would arise every 7.88 bps as shown in figure 3.6. Since crossovers can only be placed after an integer number of bases one chooses 8 bps as crossover distance in square-lattices. A shared set of crossovers for the connection of adjacent helices in square-lattices occurs every $0+32n$ bps as shown in figure 3.4 D. Rounding up the relaxed crossover distance leads to a deviation from the helices' natural geometric parameters and forces the average helical twist to 33.75° per bp instead of the naturally arising 34.3° per bp. A full turn adds to a total number of 10.67 bps instead of the 10.5 bps which causes an underwinding of the helices. Interestingly, the structures still assemble but exhibit a right-handed global supertwist that needs to be counteracted *via* a specific pattern of bp deletions to re-establish the 10.5

bp per turn. [55]
Intentional increase or decrease of bps per helical turn can also be used to the benefit of achieving curved structures [63].

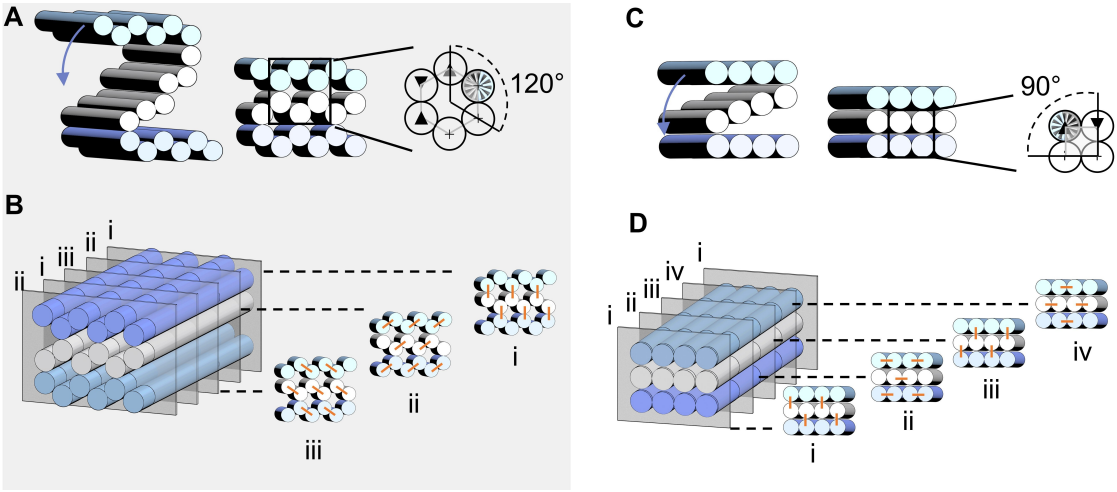

Figure 3.4.: Honeycomb-pleat-based vs. square-lattice design. **A** Shifting the crossover positions within a single layer DNA origami sheet can force it to adopt a three dimensional arrangement with a honeycomb-pleated unit cell. Helices can align in a 120° angle with respect to each other. [54] **B** At intervals spaced apart every 7 bps, possible crossover patterns occur. This results in three distinct sets of crossover positions patterns (i)-(iii) that repeat after 21 bps [54]. **C** In square-lattice designs helices of a single layer DNA origami sheet are arranged at 90° angles with respect to each other and exhibit possible crossover positions every 8bp [55]. **D** A set of four distinct crossover patterns (i)-(vi) repeats every 32 bps [55].

Figure 3.5 demonstrates the impact of deviating from the natural 10.5 bps per turn with a single-layer, square-lattice sheet. Red elements in the schematic view in the top row refer to right-handed twist, blue to left-handed. If no measures are taken to correct the accumulated 10.66 bp per turn in a crude square-lattice design, structures will be massively twisted as shown in panel A by CanDo simulations. Reducing the amount of bps per turn to 10.33 by alternating bp deletions as shown in B, results in the opposite, left-handed twist. Deleting every fourth bp in a regular pattern as shown in C manages to re-establish the natural 10.5 bps per turn and results in a flat sheet as predicted by canDo. [64]
As a side note, CanDo is a modeling software specifically developed for the prediction of DNA origami folding. It is based on a finite-element approach and provides quick insights into the flexibility and thermal stability of the structures that can be submitted online. [65]
The above example of the bending sheet shows how delicately square-lattice designs are influenced by changes on the single bp-level. Although the design process as well as the experimental fine-tuning requires more effort, square-lattice structures offer the advantage of a higher resolution of spatial addressing and a different geometry for placing functional handles compared to honeycomb-lattices [55].
This is and incentive to study square-lattice structures in more detail and find definite design rules to render their folding processes more reliable and robust. Extracting definite design rules however, can be challenging, since they very often are architecture-dependent and not trivial to generalize.

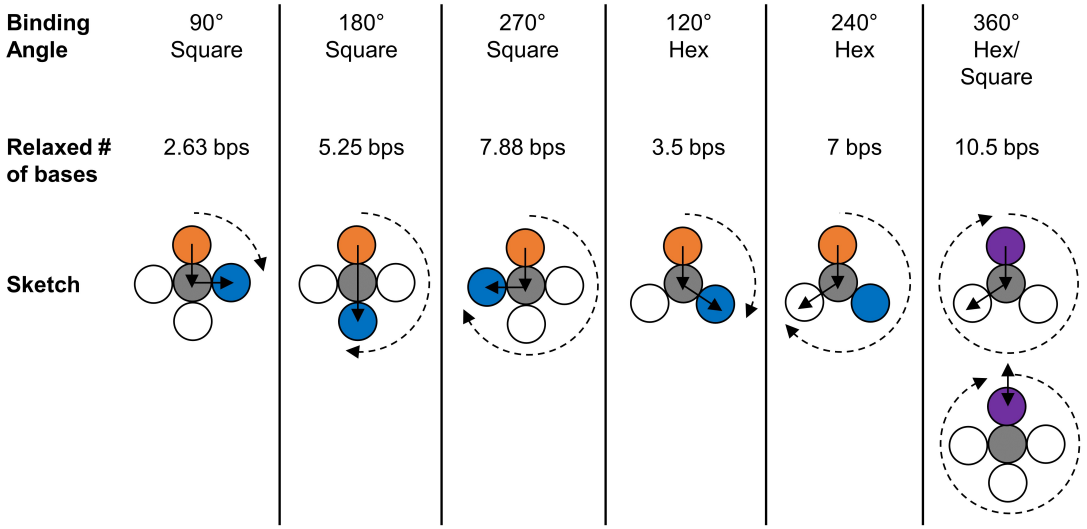

Figure 3.5.: Crossovers between adjacent helices need to be placed after an integer number of bps. Due to the helicity, this number dictates a certain set of angles between the helices to result in a relaxed assembly. Figure based on [64]

Ke et al. systematically analyzed the effects of bp insertions close to crossover positions, as well as the foothold length with which staples attach to the scaffold. They found that these features had effects on the folding yields of honey-comb designs with helix bundles of varying sizes [66]. The effect on folding yields by adjusting the staple length at the seam of honeycomb-based structures was studied by Dunn et al. [52].
Analogous studies on the effect of design tweaks on square-lattice architectures however are almost none existent. Reported square-lattice designs so far are quite delicate structures, highly-tuned for the desired application. The lack of generalized design recommendations concerning square-lattice designs was one incentive to systematically study the effect of varying crossover densities, helix length and aspect ratios on the assembly of square-lattice structures presented in chapter 6 of this thesis.

Advantages of the DNA origami assembly technique

DNA origami structures do not only stand out with their highly resolved addressability. Another key advantage of DNA origami compared to the previously presented methods to assemble DNA nanostructures is that DNA origami folding is highly tolerant toward variations in strand stoichiometry. Staple strands are added in excess and successful folding can still be achieved if individual staple strands are missing within the structure. Additionally, purification of DNA strands may only be required for those that should bind to a target or perform another functional task which further facilitated the experimental process. [16]
Finally, natural branch migration serves as an error correction mechanism within DNA origami meaning that non-complementary binding or sequences with secondary structures are kinetically and thermodynamically outcompeted by the binding of the complementary strand [10].

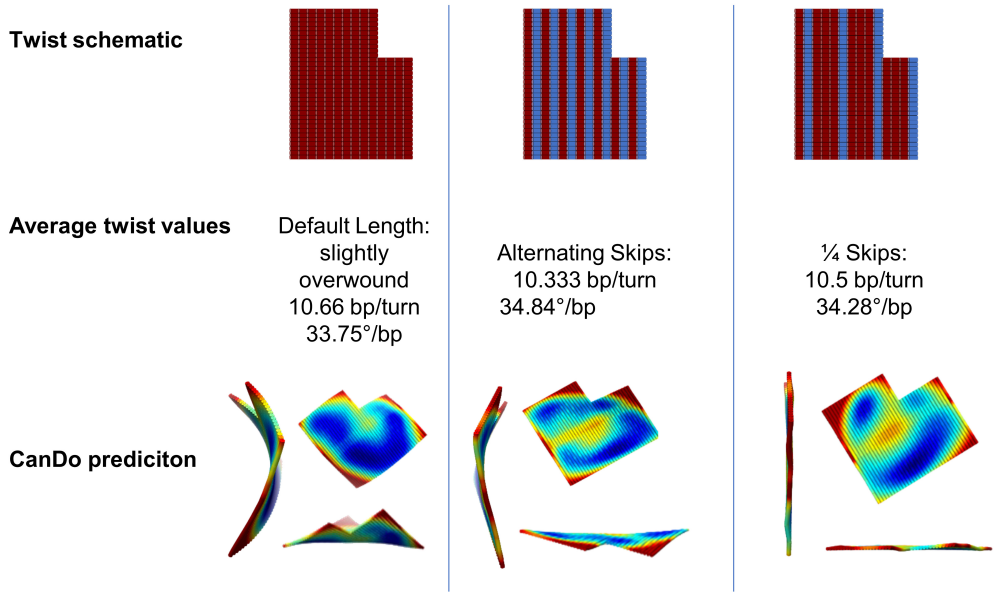

Figure 3.6.: Counteracting twist in a single-layer, square-lattice DNA origami sheet. **A** Uncompensated square-lattice structures result in 10.66 bp/turn and a pronounced right-handed twist. **B** Inducing alternating skips leads to 10.33 bp/turn and reduced twist. **C** Skipping every fourth bp re-establishes the natural geometry of 10.5 bp/turn and results in flat sheets. Figure based on [64]

The dependency on a present scaffold on the one hand limits the assembly to a finite number of structures but on the other hand also provides a neat control over the nucleation process.
Together, all these properties render DNA origami folding exceedingly labor- and time-efficient as well as robust compared to non-scaffolded assembly approaches and enabled the elevation of structural complexity.

3.3. Scaffold-free DNA nanostructures

The previous section outlined the advantages of DNA origami. However for some purposes, DNA origami presents drawbacks that have been tackled by alternative design approaches. DNA origami tile [67] and brick [68] assembly offer a far more modular design procedure. This means that instead of designing a completely new set of staple strands for each new design, tile and brick assembly relies on a set of a few unique building blocks that can be combined to build up structures. [68]
The concept of tile assembly was used to generate a huge amount of versatile structures both in 2D [69] and 3D [70]. The concept revived with the published data from Wei et al. [67] who managed to extend to larger scales the concept of uniquely addressed tiling that was first introduced by Rothemund and Winfree in 2000 [71].
Wei et al. [67] designed tiles, single-stranded DNA segments of 42 nt, in a way that their four unique binding sites bind four further tiles themselves presenting further binding sites (see figure 3.7 A). Combining a certain amount of tiles can be designed to assemble rectan-

gular, 2D lattices. By skipping specific binding regions those 2D lattice can be sculptured to different 2D outlines. This design concept allows for the generation of a variety of different shapes based on a very restricted amount of unique, single-stranded tiles. The robustness and complexity of the presented structures were astonishing to the scientific community since earlier approaches of tiling were highly sensitive to strand stoichiometry. It was a prevailing opinion that assembly of tile-structures would halt once a certain set of tile strands had been exhausted. The reasons for the success of the technique are still under investigation but can be most likely attributed to deviating kinetics of the nucleation and growth phase during assembly. [67]

The same research group developed DNA brick assembly. Here they used 32 nt-components with again four binding sites that assemble to a 3D cube that can act as canvas from which various shapes can be carved (see figure 3.7 B) [68]. By increasing the binding domains to 13 nts the DNA brick approach was able to generate structures of giga-dalton size (see figure 3.7 C) and demonstrated one of the main advantages compared to DNA origami whose size is limited by the scaffold length [72].

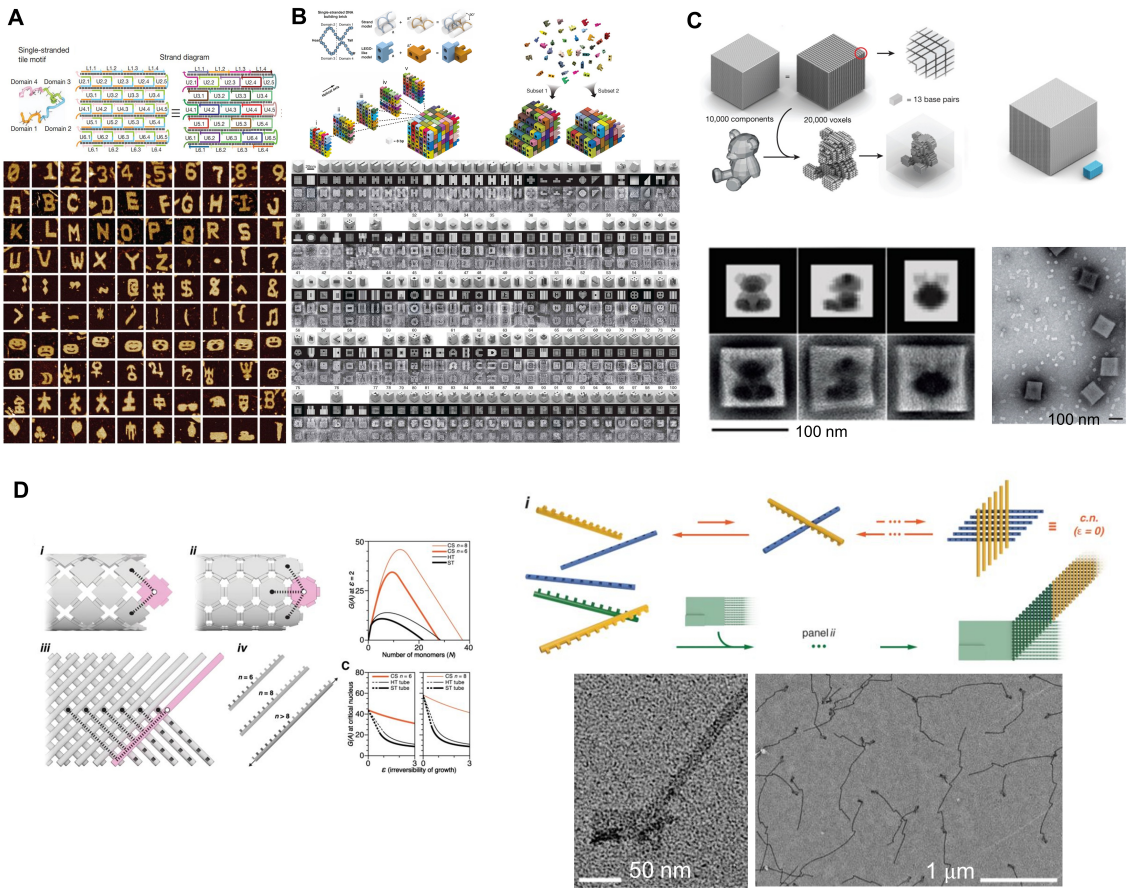

Figure 3.7.: Scaffold-free assembly of DNA nanostructures. **A** Assembly of 2D shapes using DNA tiles [67]. **B** Assembly of 3D structures from DNA bricks [68]. **C** Assembly of giga-dalton 3D structures from DNA bricks [72]. **D** Crisscross assembly of DNA slats into micrometer sized ribbons [73].

Many years of research on different approaches how to direct the assembly of DNA strands has shown that each approach, whether it be scaffold-based or scaffold-free, has its advantages and drawbacks.
A very recent study by Minev at al. [73] combines the advantages of DNA origami folding having tight control over nucleation and the DNA tile or brick approach being capable to grow infinitely. They introduce what is called crisscross polymerization using DNA slats, single-stranded DNA, capable to bind not only to their nearest neighbors which results in an assembly with high coordination numbers (see figure 3.7 D). This is key to implement a strict control over nucleation. Slats are recruited from solution exclusively upon the introduction of a DNA origami seed that they show is essential to overcome the intrinsic kinetic energy barrier to induce fast growth of ribbons on the order of microns. By fine-tuning the assembly pathways they achieved an implementation of cooperative behavior resulting in a switch-like behavior of structure growth. [73]

4. Dynamic DNA nanotechnology

Continuous structural refinement using the methods of structural nanotechnology outlined in the previous chapter led to an immense pool of DNA nanostructures with intricate geometries and highly organized sites for functional attachments. Dynamic nanotechnology takes on the challenge introducing dynamic features to these DNA nanostructures to render them responsive to the environment. This opens up many, new avenues for the applications of DNA nanostructures including DNA switches and artifical DNA motors.

4.1. DNA switches

One of the first examples for configurational switching was demonstrated by Pohl et al. [74] who demonstrated rotary motion of a DNA double strand by switching from conventional B-DNA to Z-DNA configuration. This behavior was achieved with $(CG)_n$ runs in the sequences that adopt Z-DNA configuration upon high salt concentration and low temperatures [74].
Salt and temperature dependent switching was also implemented into DNA origami structures that are capable of changing between open and cross-like configurations [75]. Using the pH responsiveness of G or C-rich DNA sequences inspired a large variety of switches that cyclically contract and extend i-motif sequences [76–78] or circular DNA constructs [79]. In order to increase the range of pH-sensitivity the parallel Hoogsteen-motif has been used to induce switch-like transition from duplex to triplex DNA conformations [80].
pH-switches also have been studied *in vivo* where they could indirectly detect endosomal pathways based on the pH variations in the different endosomal states [81]. Through the incorporation of azobenzenes in DNA duplexes reversible separation of the duplexes was achieved once configurational change of the azobenzenes from cis to trans states has been introduced upon exhibition to UV, and visible light [82]. This photo-induced mechanism of conformational change was implemented among others in DNAzyme for the controlled cleavage of RNA [83].

DNA as fuel

In 2000 Yurke et al. demonstrated that DNA molecules can not only be designed to respond to chemical changes but that DNA strands themselves can act as fuel to induce motion to DNA nanostructures [49]. Their proof-of-concept system was a DNA tweezer that was actuated from open to closed states based on toehold mediated strand displacement (TMSD) reactions.
The concept of this DNA tweezer is explained in figure 4.1 A. It illustrates the system made of three strands. Two of them partially hybridize with the main strand forming double-stranded regions but still exhibiting single-stranded extensions at their other end. This is referred to as the open state of the system. The tweezer can be closed by an incoming "set" strand that hybridizes to the single-stranded regions forcing the double strand into a denser configuration. A toehold sequence on the "set" strand can then be

addressed with an "unset" strand whose hybridization with the toehold induces strand displacement. This re-establishes the open state.
Each cycle of opening and closing produces double-stranded waste. The tweezer can be actuated as long as unbound set and unset strands are available. [49] This study initiated

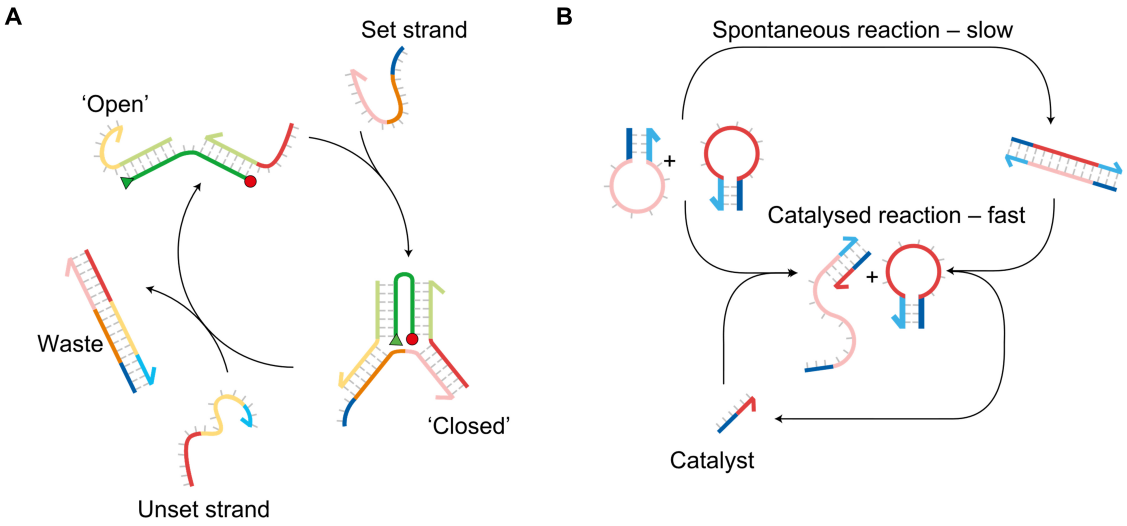

Figure 4.1.: Using DNA as fuel for nanodevices. **A** DNA tweezer actuated between open and closed states through toehold mediated strand displacement. Fuel strand binds to incorporated toehold sequences highlighted in yellow and blue. [49] **B** The kinetic energy barriers involved in switching mechanisms can be finetuned by including hairpin structures, secondary structures that interact at lower reaction rates. An incoming DNA strand complementary to one of the loops of the hairpins can act as a catalyst to open the hairpin. [84]
Images from [85]

a cascade of further investigations including theoretical considerations to understand the reaction kinetics of the tweezer [86], modified tweezers with different ground states [87] as well as three state tweezers [88]. Ouldridge et al. [86] used a coarse-grained model to simulate hybridization, stacking, as well as hairpin formation of two single DNA strands. Thereby, they considered key physical properties of DNA in their model which helped to generate a suitable representation of both, single- and double-stranded DNA molecules and could then be used to determine the free energy landscape of the DNA tweezer. They found that the closing "set" strand would complete its hybridization to one arm of the tweezer first before it hybridizes to the second one. For the opening "unset" strand they found that it interacts much slower with the first arm than it does with the second one. Their study also suggests that potential hairpin formation of the long signaling DNA strand slows down the process of strand displacement. Such studies provide better understanding of the variables that influence the performance of DNA switches. [86]
Besides the tweezer there have been many other examples of dynamic nanostructures that use DNA as a fuel for their motion.
Yan et al. managed to twist connecting links of a linear string of DNA tiles by 180° through the introduction of appropriate removal and replacement DNA strands causing a transition of the string's subunits from cis to trans states [89]. This switch has later been included in the assembly of a 2D DNA lattice that then could be similarly actuated to achieve larger scale switching [90]. Similar actuation of a 2D array was achieved by Feng and coworkers

[91] who designed an array made from three-arm HJ molecules equipped with a stem loop. With the aid of an appropriate "unset" strand the stem loop can be released which leads to an increased lattice spacing [91]. TMSD was also applied to generate DNA logic gates for biosensing applications [92].

4.2. DNA stepper motors

Non-autonomous walkers

Early demonstrations of DNA walker architectures have been provided by Sherman et al. [93] as well as Shin et al. [94] and will be explained in the following. Their systems relied on toehold mediated strand displacement to promote a biped as the dynamic module with two, single-stranded legs along linear, double-stranded DNA tracks that exhibited single-stranded extensions as anchor points (see figure 4.2 A). Set strands that bound the bipeds to the track exhibited a toehold region that could be addressed by an unset strand to induce TMSD. This liberated one leg at a time that then became available to bind to the subsequent binding site. In that way they showed that the biped legs alternatingly acted as locked and forward stepping leg. Their walkers remained attached to the track by at least one leg at all times. While the architecture and strategy for actuation of both their walker modules were quite similar the execution of the stepping was different. Sherman et al. demonstrated an inchworm-like stepper with one leg being the forward stepping leg and the other being dragged. Shin et al. realized a hand-over-hand stride where the rear leg is pulled forward with each step that is taken. These walkers were limited to a few steps due to the flexibility of the tracks. [93, 94]

Autonomous walkers

Different approaches have been presented throughout the last decade to render DNA nanodevices autonomous meaning independent of an external energy source. The following will give a brief overview on what has been achieved to that regard.
The stored energy of a single stranded loop domain of a DNA hairpin was determined to be 1.4 kcal mol^{-1} at 20°C [95]. Based on this finding, DNA hairpins have been demonstrated as suitable energy sources to power nanodevices [84, 96–98].
Hairpins are secondary structures of DNA single strands with a double-stranded neck and single-stranded loop domain (see figure 4.1 B). Two hairpin loop domains interacting with each other form a so called kissing loop [97].
It was found that the topological constraints imposed by hairpins or kissing loops cause DNA systems to reside in a state away from the global energy minimum but can be forced to transition to their equilibrium state by catalyst strands that resolve the topological constraint (see figure 4.1 B) [84, 96].
Turberfield et al. [84] exploit this mechanism that is described in the following, to render their device autonomous. Two hairpin structures whose neck sequences are the same (blue) and loop sequences are complementary (red) are able to slowly form a double stranded end product by spontaneous hybridization. Introducing a catalyst strand however that is complementary to one half of the hairpins' neck and to some non-hybridized bases within the loop renders the reaction much faster. In fact, they found that reaction rates can be up to $10^4\times$faster for catalyzed reactions than for spontaneous reactions. [84]

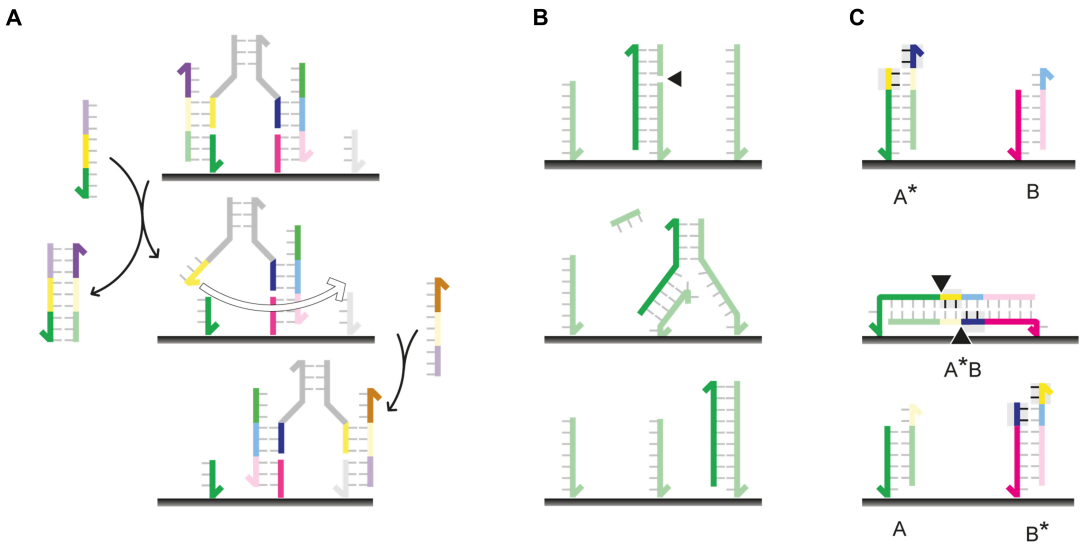

Figure 4.2.: DNA strand displacement and enzymatically driven DNA walkers. **A** Biped walking along double-stranded DNA tracks driven by toehold mediated strand displacement [93, 94]. **B** Biped walker driven by nicking enzymes and based on the "burnt-bridge" approach [99]. **C** DNA walker powered by enzymatic restriction and ligation [100]
Images from [85]

Green et al. [98] provided a detailed study on the kinetics and thermodynamics of spontaneous interactions of two hairpins versus the catalyzed reaction. They have shown that spontaneous reactions can be further suppressed by a decrease in hairpin loop length and simultaneous increase in neck length. This provides even more control over the kinetics of the system. Additionally, they found that the location of the toehold sequence is crucial. According to their data, external toeholds increase the opening reaction rates by 10-100×while internal toeholds impose an entropic activation barrier that drastically slows down the reaction speed. [98]
These insights have been used to develop further bipedal DNA walkers [70, 101, 102].

Other ideas to render DNA-based stepping autonomous involved using the energy liberated through enzymatic reactions such as with nicking enzymes [99], restriction and ligation enzymes [100] (see figure 4.2 B and C, respectively) as well as DNAzymes [103].
Common among enzyme-based DNA walkers is that they rely on the “burnt-bridge approach” which describes a walking mechanism that damages the track and makes the motion irreversible [99, 104].
To implement reversibility of the performed motion, researchers have investigated chemically [105, 106] and photo- [107, 108] controlled DNA-walkers.

Increasing efficiency of walkers

The thusfar reviewed bipedal walkers are limited to short travel distances usually taking no more than 3-4 steps. This motivated further studies to increase the efficiency of walkers.

Tomov et al. [109] showed that the number of steps taken could be increased to 32 steps if bipedal walkers are actuated along a DNA origami surface that exhibits the appropriate

single-stranded footholds and is embedded in a microfluidic chamber that can be flushed with 64 individual fuel strands in sequence (see figure 4.3 C). The microfluidic device allowed them to study the walkers' efficiency and found that removing used DNA strands from the system positively impacts the overall performance of the walker with respect to its speed and travel distance. [109]
Shortly after, Khara et al. [110] analyzed the same system in detail using coarse-grained computer simulation. Förster resonance energy transfer measurements (FRET) were additionally performed and showed that the simulated data is in good agreement with the experiments. They were able to determine a maximum step length of 40 nm for their walker, a sensitivity of the walker toward its surrounding such as the DNA origami template as well as information on the kinetics of the walker. [110]

Another interesting pathway toward longer travel distances is based on so called DNA spiders constructed by Pei et al. [111]. These exhibit a core component made from streptavidin and three DNAzyme-legs and were shown to move across a substrate decorated with DNA. [111]
This behavior was exploited by Lund et al. [112] to promote the DNA spiders accross a 2D DNA origami sheet (see figure 4.3 A). Walking was achieved by a diffusion-based random walk along the origami sheet that provides anchor sites in the form of single-stranded DNA substrates that can be cleaved through the enzymatic activity of the spiders. They have shown that based on this mechanism spiders can traverse 100 nm from one end to the other end of the DNA origami sheet. Thereby, the directionality of the movement is not controlled. The movement was characterized by multiple back stepping and revisiting of anchor sites. Nevertheless, the net movement toward the end of the tracks manages to push 70% of the spiders to the end of the tracks. They used AFM and fluorescence microscopy to detect the spiders, the resolution however was only sufficient enough to capture three distinguished positions of the spiders on their way to the end of the track. [112]

Wickham et al. [113] developed a walker that can, as in the case of the spiders, traverse 100 nm but in a directed fashion. Thereby, nicking enzymes cut footholds that are arranged on a 2D DNA origami sheet. The footholds are hybridized to a DNA single strand that reveals a toehold after the cutting process. The toehold enables the single strand to interact with the next available anchor site and eventually completely engages with it after a completed cycle of branch migration (see figure 4.3 B). Using real-time AFM imaging and fluorescence microscopy they were able to show that the walker can be promoted in the programmed direction at constant stepping rates. [113]

Studies by Bazrafshan et al. [114] recently reported on a DNA origami motor that manages to combine many of the desired motor features such as autonomy, directionality, long travel distances and high speed. However, the motor goes back to the burnt-bridge approach and thus lacks the feature of reversibility. Their presented motor is based on a DNA origami tube that is functional with multiple DNA single/strand that can connect to a substrate that is covered with RNA single strands. Once connected, a RNase enyzme recognizes the double/stranded regions and exclusively cuts the legs from their footholds and induces a rolling motion of the DNA origami tube. Their DNA origami motor offered an ideal platform to study the impact of the motor form and the leg pattern, amount and density. They found that motors with a high structural rigidity and leg density perform longest

and fastest. These motors have traveled up to micron distances with up to 100 nm/min. [114]
By replacing the DNA origami tube with a 50 nm gold nanoparticle they managed to increase the previously discussed motor performance up to speeds of 50 nm/sec [115]. Without the need of labeling the motor for detection it was possible for them to elucidate that this motor architecture performs Lévy-like motion. According to their data, more legs in close proximity result in higher travel speed while longer legs favor traveling in one set direction. Still the motion of this motor is irreversible. [115]

Reverse rolling of plasmonic constructs, but with the sacrifice of lower speed, was shown by Zhou et al. [116]. Here, two gold nanorods are organized in a 90° angle to each other and separated by a multi-layer DNA origami structure that exhibits six anchor sites. Their rods were functionalized with DNA single-strands complementary to the anchor sites. Only one of the two nanorods performs the motion and thus changes its orientation toward the fixed nanorod. They detected this conformational change via circular dichroism (CD) measurements and thus indirectly tracked the motion. Based on TMSD, their system is capable of walking across 2D and 3D geometries without destroying the tracks. [116]
Following the same approach, the movement of two individual nanorods on a DNA origami template could be directed and detected via CD measurement [117].
Additionally, very recently the same group extended this system so that both a rotary and straight motion are executed within the same motor complex. Multiple of these complexes could be combined to achieve large scale motion. [118]

Walkers for molecular cargo transport and synthesis

Transporting cargo using a DNA-based walker is one of many interesting applications that have been reported. The following will describe two representative examples.
Gu et al. [119] demonstrated a system that allows a DNA walker to collect gold nanoparticles from designated sites and transport them across a DNA origami track (see figure 4.4 A). Their walker component consisted of four DNA single strands that were supposed to perform the motion along the track, and three DNA single strands that were rendered capable to interact with the gold nanoparticles. Thereby, they programmed their walker to proceed in a rotary motion completing 120° rotation with each taken step, reaching the cargo site after two steps. The rotation thereby is responsible to bring the cargo accepting strands in close proximity to the cargo sites. Both the cargo transfer as well as the promotion are mediated through DNA strand displacement reactions. They implemented a mechanism that allowed to control the cargo site in a way that the walker does not have to accept a cargo each time the cargo site is visited. This control allowed them to produce eight different states at the end of the track. [119]

He et al. [120] used a DNA walker to collect molecules from a track for the synthesis of a higher-order molecular complex (see figure 4.4 B). Thereby they used a DNAzyme based walker architecture that carried an amine group that could chemically interact with a substrate distributed on a single DNA strand. Each time the walker reaches the substrate, the amine group is close enough to interact with the substrate, generating a product that is transported to the next interaction site and used for the further synthesis. In this way they managed to autonomously produce an oligoamide in a single-pot reaction which they argue is more efficient compared to other synthesis techniques using DNA-templates. [120]

Another interesting realization of nanoparticle transport was presented by Cha et al. [121]. Based on a DNAzyme motor they demonstrate walking along a carbon nanotube and achieved travel distances of 3 μm at speeds of 1nm/min (see figure 4.4). [121]

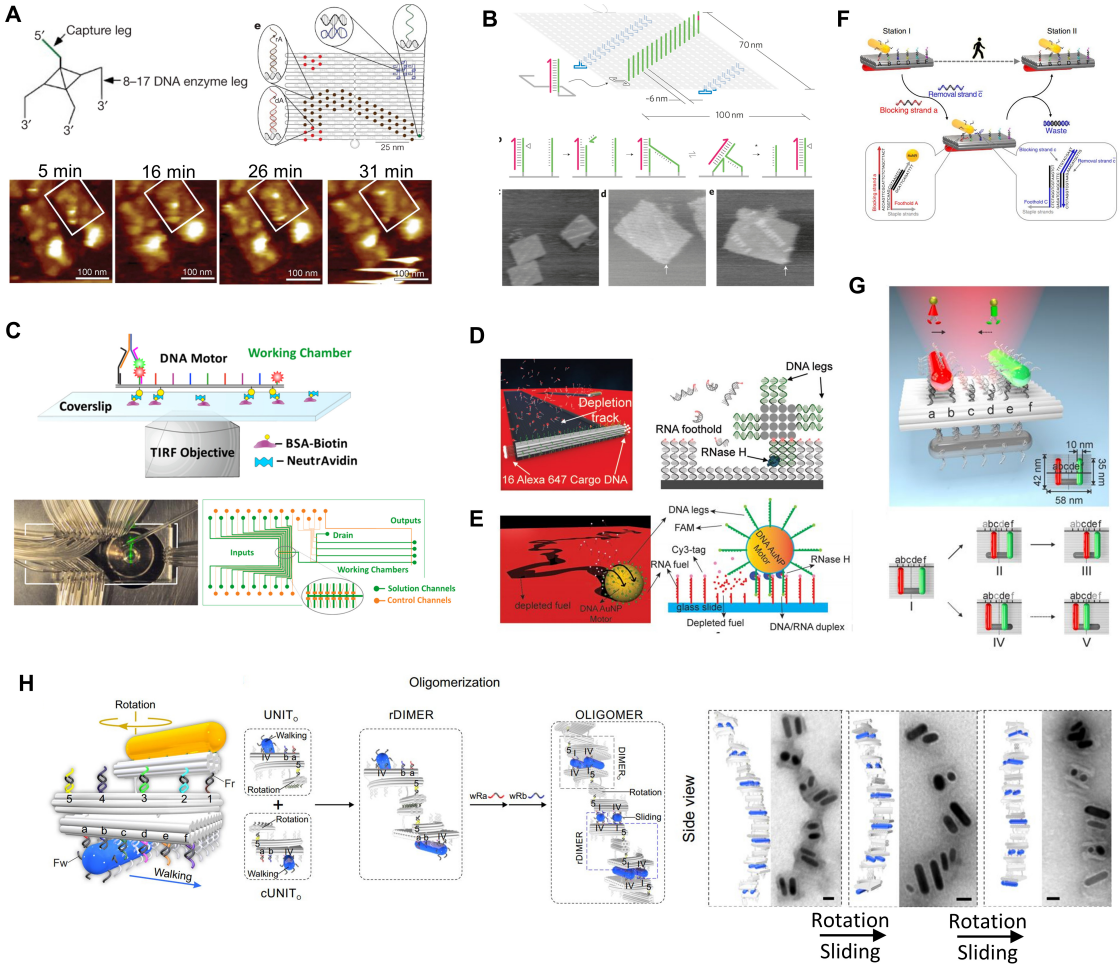

Figure 4.3.: Boosting DNA walkers toward higher efficiency. **A** DNA spiders executing a diffusion-based random walk on a 2D DNA origami sheet [112]. **B** Directed motion of a DNA walker across a 2D DNA origami sheet [113], **C** Bipedal DNA walkers embedded in a microfluidic chamber [109], **D** DNA origami tube traveling micron distances on a depletable RNA substrate [114]. **E** Irreversible rolling of gold nanoparticle based on interactions between RNA substrate and DNA functionalizations on the gold particle [115]. **F** Rolling of gold nanorod across a multi-layer DNA origami structure [116]. **G** Coordinating the movement of two nanorods across a multi-layer DNA origami structure [117]. **H** Combining rotary and straight motion of nanorods within the same DNA origami complex [118].

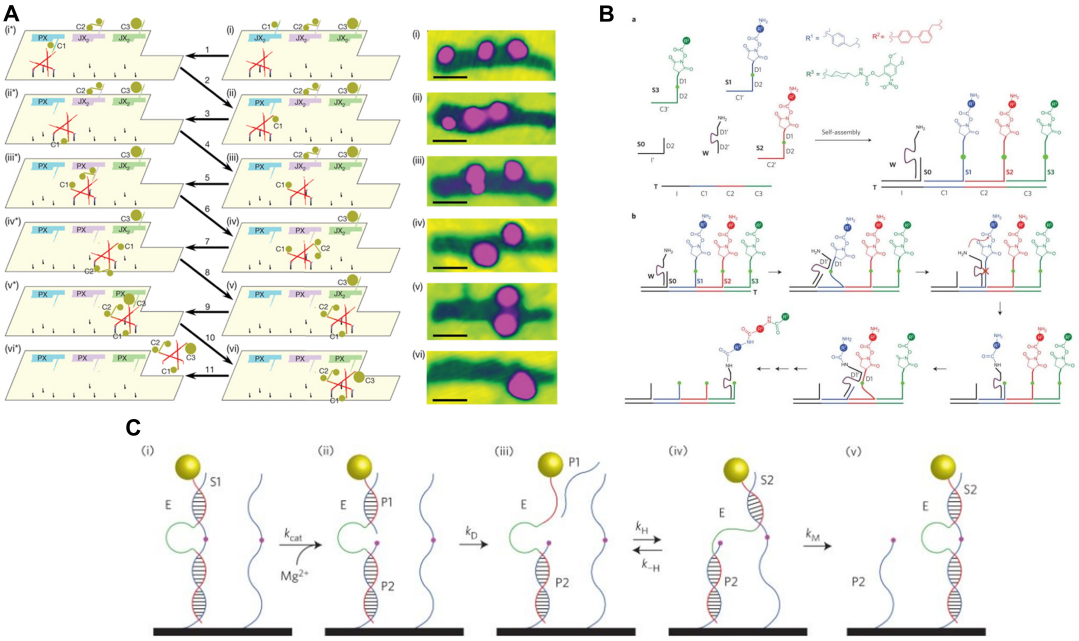

Figure 4.4.: DNA walkers for cargo transport. **A** A DNA walker tranporting gold nanoparticles across a DNA tile [119]. **B** DNAzyme driven walker collecting components for the synthesis of a complex consisting of multiple amides [120]. **C** Nanoparticle transport along a carbon nanotube [121].

4.3. Current challenges of DNA walker systems and how to address them

Research on DNA walker systems conducted throughout the past years and partially recapitulated in this chapter has helped to define the central requirements imposed on the architectures and mechanisms to render them suited for a versatile spectrum of applications. These requirements can be summarized as follows: DNA stepper systems should be able to ensure that the dynamic modules stay bound to the track during the promotion, perform autonomous and directed locomotion, travel long distances at high speed and should traverse without damaging their tracks to establish reversibility of the motion [122].

However, it has been challenging so far to develop mechanisms that meet all requirements at once. Rather the walkers are tuned for the application of interest.

Thereby, it is notable that the two features most demanding to combine seem to be long travel distances with a mechanism for reverse action.

Additionally, the majority of the presented walkers provide limited room for the attachment of cargo since the systems most of the time rely on single DNA molecules as dynamic components that can hold only one functional unit. Displacement of larger surfaces such as the DNA origami tube [114] or gold nanoparticles [115] so far have only been demonstrated to perform a rolling motion which makes use of all functional sites along their surfaces for the locomotion and thus cannot be exploited for functional attachments.

In the case of strand displacement driven motors another challenge is that for each step taken a new orthogonal sequence has to be introduced (i.e. sequences that are unique and

only bind to the designated target). This imposes a design challenge for everyone who pursues to promote the motors for a high number of steps.
These are challenges that, if resolved, can further increase the efficiency of present DNA motors and open up a new scope of applications.
Aiming to transfer the concepts of rapid prototyping to the nanoscale, as initially set out as incentive for the present thesis, requires confronting these challenges. The work presented within this thesis addresses these with a new stepping mechanism that is capable to displace DNA origami surfaces with respect to each other and that based on its design innovation gets on with only six orthogonal sequences that are applied in cycles for a controlled forward and backward motion.
Using DNA origami structures as both - the walking component and the track - provides a surface with numerous attachment sites.
Multiple leg interaction can improve the walker efficiency in terms of speed and travel distance as confirmed by studies of Bazrafshan et al. [115]. The stepping mechanism suggested in this thesis is based on a fourfold leg interaction which is also believed to render the stepping more reliable in the sense of a higher tolerance toward missing footholds along the DNA origami surface due to the backup-legs.
Although the approach presented within the scope of this thesis addressed many challenges outlined above the fact that it is based on strand displacement will cause it to fall short on stepping speed. This remains to be addressed by using approaches such as microfluidic-devices or by rendering the steppers purely fuel strand concentration based. The latter is explained in more detail in the final summary of this work.

5. Theoretical and experimental methodology

The following sections provide an overview about software tools and biochemical methods that have been primarily used to generate and analyze the results presented in chapter 6 and chapter 7. First, methods for designing sequences and testing design efficacy using the DNA origami simulation tool oxDNA will be briefly discussed. The rest of the chapter is dedicated to describing theoretical and practical aspects of the central experimental methods employed in the context of the presented studies.

5.1. Tools supporting the design process

5.1.1. Sequence generation with caDNAno

All core sequences for the DNA nanostructures presented within this thesis are generated with the aid of caDNAo version 1. Thereby, "core" refers to the DNA sequences required to build up the main body of the DNA architectures. Functional sequences such as handles have been partly generated with python scripts or were manually designed.
CaDNAo is a computer software with a graphical user interface developed by Douglas et al. [123] in 2009. In their paper they describe how caDNAo can be used and which design rules are implemented. This will be briefly recapitulated in the following paragraphs.
CaDNAo helps researchers find appropriate scaffold routing and corresponding staple strands for their desired DNA structures. Thereby, it can be individually chosen whether to arrange DNA helices on a honeycomb- or square-lattice. Depending on the chosen outline, the appropriate design constraints imposed by the geometry and arrangement of DNA double helices are already implemented in the software to avoid topological traps in the designs.
The user interface of caDNAno is divided into three panels as shown in figure 5.1 A: the slice panel displacing the cross-section of the desired structure on the far left, the path diagram in the middle, and a 3D view of the final structure on the far right. The design process starts with the slice panel. Here, the designer can sketch an outline of the structure by adding or removing helices that are represented as orange circles (see figure 5.1 A). The neighboring path diagram can then be consulted for a rolled-out view of the helices with all strand details shown. This is the panel where most of the design work is performed. The designer first performs the scaffold routing, which sets how the scaffold passes through the structure. Subsequently, staple helices are added and adjusted and the appropriate crossover positions are implemented. [123]

Staple crossovers, which are connections between staple helices, are shown in red in figure 5.1 B, while scaffold crossovers, which are connections between scaffold helices, are shown in blue. An empirical rule of the field is that one should ensure that staples have at least 8 bps long footholds that attach to the scaffold. This will provide sufficient binding energy

for stable incorporation into the structure. [123]

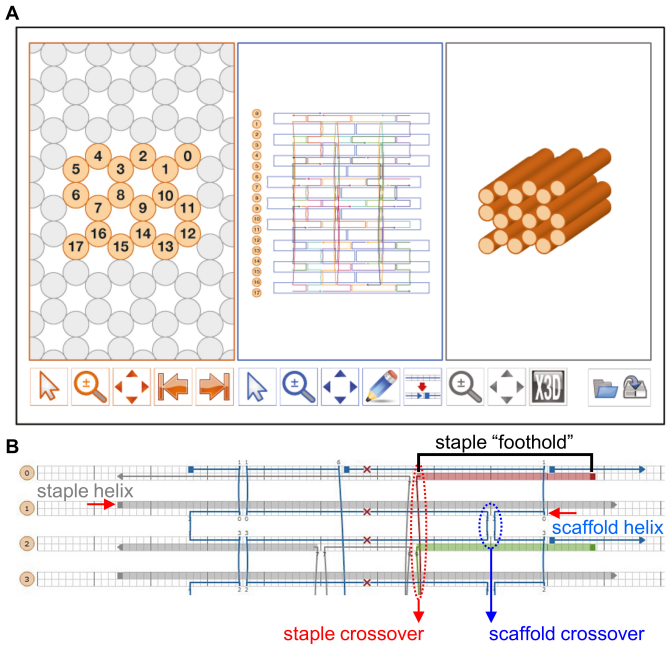

Figure 5.1.: CaDNAno user interface and path diagram for caDNAno version 1. **A** Slice panel (left) showing the cross-section of the target structure, path diagram (middle) and 3D view of target structure. **B** Close-up of path diagram showing staple and scaffold helices as well as staple and scaffold crossovers. [123]

CaDNAno offers a pre-selected variety of possible crossover positions between helices that would maintain the prescribed geometry of B-DNA. Although crossover positions can be manually forced, it is recommended to either stick with the options suggested by caDNAno or to make considerate choices to avoid a deviation from the natural geometry of DNA, which may otherwise lead to strained and twisted structures. [123]

The general rule is that antiparallel staple strand crossovers are only allowed at positions where the backbones peaks of two neighboring DNA helices face each other. On a honeycomb-lattice this is true every 7 bps, generating three crossover patterns that repeat every 21 bps assuming a helical turn of 10.5 bps. These geometric parameters are slightly different for a square-lattice arrangement. Once the square-lattice is selected as a template in caDNAno, crossovers can be implemented every 8 bps resulting in the first crossover patterns that reoccurring after 32 bps. There are four possible crossover patterns for square lattice designs. [54]

More details on DNA origami design considerations are described in chapter 3.

Scaffold crossovers are allowed every 5 bps away from staple crossover of the respective staple helix in order to avoid kinetic traps. CaDNAno also allows users to add base pair deletions or insertions. [123]

CaDNAno has been further developed to caDNAno 2 (see `https://cadnano.org/`) and most recently scadnano, an online software with many upgrades facilitating the user experience [124].

5.1.2. OxDNA

oxDNA is a coarse-grained model that simulates DNA origami structures [125]. It is a helpful tool for gaining initial insights into the designs prior to experimental investigation.

oxDNA simulates nucleotides as rigid bodies that are influenced by various factors. Those include the backbone potential, which is the potential caused by the hydrogen bonds between bases, the stacking forces between the bases, the electrostatic repulsion between the backbones of the helices, and cross-stacking interactions between bases that are placed diagonally from each other. [126]

Figure 5.2 illustrates the points of action of the considered forces. Implementing these interactions enables to simulate among others the actual structure of the DNA origami design, the twisting and bending phenomena and the elasticity of the structures [126].

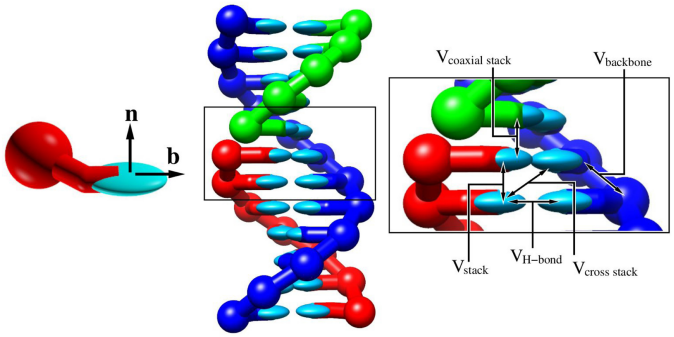

Figure 5.2.: Nucleotides as rigid bodies and with various sites for interactions. **b** is the "base" vector that aligns with the stacking and hydrogen-bond directions, **n** is the normal vector to the base plane. Illustration on the right marks all centers of interaction that are considered in oxDNA simulations. [126]

Doye et al. outline some pitfalls related to oxDNA simulations that need to be considered when interpreting the results. First, they point out that oxDNA prioritizes an accurate model of the bending and twisting behavior of the simulated structure over the extensional modulus. This could impact the predictions concerning the mechanical response of DNA origami structures. Second, the electrostatic potential is approximated via a simple Debye-Hückel relation and is strongly connected to the presence of ions in reaction buffers. The basis of the fit used in oxDNA simulations is the Na^+ concentration that is needed to drive hybridization of DNA duplexes.

However, DNA origami structures are typically folded in the presence of MgCl2. Both NaCl and $MgCl_2$ impact duplex stability, thus affecting the stability of DNA origami in different ways. Although it is known that the ionic strength of $MgCl_2$ is much higher compared to NaCl, there is no straightforward conversion from a given $MgCl_2$ concentration to a comparable NaCl concentration. Thus experimental results could deviate from oxDNA simulations because of different buffer conditions. [126]

oxDNA simulations shown within this work have been performed by Dr. Erik Benson using the following set of parameters: 500 mM Na^+ at 20° C and for 100 M timesteps, corresponding to around 1.5 µs.

5.2. Experimental methods

5.2.1. Toehold mediated strand displacement

Early studies investigated DNA strand displacement primarily in the context of genetic recombination [127–131]. The demonstration of a switchable DNA tweezer by Yurke et al. in 2000 [49] based on toehold mediated strand displacement (TMSD) initiated a cascade of studies showing strand displacement based locomotion of DNA walkers [131].
As the stepper system presented in this thesis relies on TMSD, the following section describes the overall working mechanism to provide the required background knowledge for the discussions in chapter 7.

TMSD broadly speaking is the externally induced exchange of one binding single strand

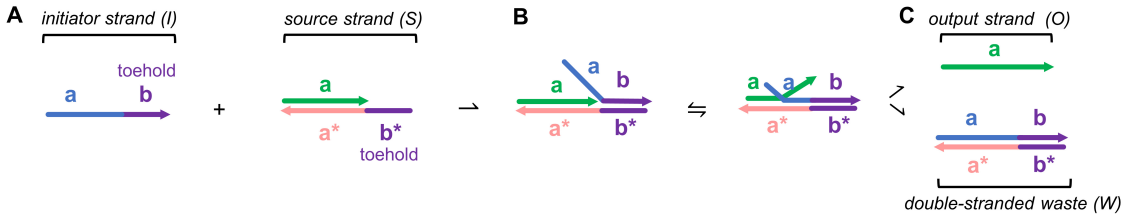

Figure 5.3.: Working principle of toehold mediated strand displacement. Image based on [131]

within a DNA duplex. This process is based on DNA branch migration [131], a mechanism that has been described in chapter 2. Figure 5.3 displays the working mechanism of TMSD. TMSD, as the name already suggests, involves a DNA double strand (S) (pink and green) that exhibits a toehold sequence (**b*** on the pink strand), meaning an unpaired region that extrudes from the DNA double strand and is available for an initiator strand (blue) to bind to via a complementary region (**b** on the blue strand) (shown in **A**). The initiator strand (I) attaching to the toehold initiates branch migration where the blue and green strands are competing to bind to the pink template (shown in **B**). Eventually, the green strand is completely displaced and the reaction results in the unbound, green single strand (O) and a new duplex (W) consisting of the pink and blue strand (shown in **C**). This forward reaction Simmel et al. [131] state the ratio of strand concentrations as follows:

$$\frac{[W]}{[S]} = \sqrt{\frac{k_f}{k_r}} = \exp(-\Delta G^\circ / 2RT), \tag{5.1}$$

with k_f being the rate constant for the forward reaction $S + I \rightarrow W + O$, k_r being the rate for the reverse reaction, ΔG° the free energy for the binding of the toehold **b*** to its complement **b**, R the gas constant and T the temperature. This expression assumes that all involved strands are at equal concentrations. Longer toeholds result in more negative values for the free energy ΔG° and based on the above expression 5.1 this predicts a bias of the reaction to proceed toward the end state shown in figure 5.3 **C**.
The two latter statements suggest that TMSD reactions can be tuned via the integrated toehold length and concentration of the involved DNA strands. Figure 5.4 is an assembly of data on forward reaction rates of TMSD with respect to the used toehold length. It shows that reaction rates increase with increasing toehold length before plateauing at a length of around 8-10 bps. [131]

Theoretical [132] and computational [86, 133] studies of TMSD show how the reaction kinetics of strand displacement may be leveraged to generate more efficient reactions.

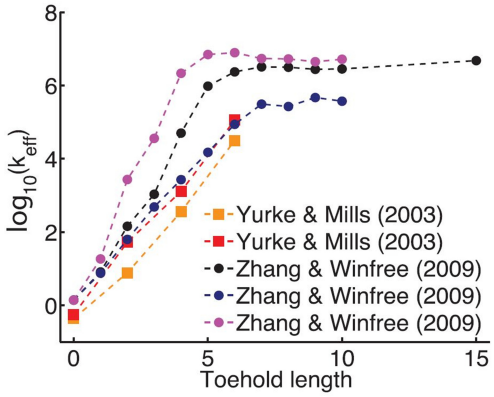

Figure 5.4.: Dependency of toehold mediated strand displacement reaction rates on the toehold length. Data is assembled from different studies experimentally investigating displacement reaction rates for different toehold lengths. [131]

5.2.2. Gel electrophoresis

Gel electrophoresis is one of the most established biochemical analysis tools. In brief, gel electrophoresis exploits the fact that charged molecules of different molecular weight exhibit different mobility when traveling through a porous gel once an electric force is applied. As a negatively charged molecule, DNA fragments can be separated using the methods of electrophoresis. [13]
Gel electrophoresis is a key method of this work, thus a slightly more elaborated view on the specifics of the working principle is included at this point. An overview about the physical basics as well as the abilities and limits of the method will be given.

Much of the following discussion is based on a detailed article written by J-L. Viovy [134], which describes the working mechanisms underlying electrophoresis.
At first glance, the theory behind gel electrophoresis can appear rather challenging. A comprehensive theory of electrophoresis requires profound understanding of polyelectrolytes and their dynamics in ionic solutions. This topic is itself subjected to ongoing polymer physics research and in some areas still not completely understood. It will become evident however, that gel electrophoresis is very often conducted in scenarios that allow to drastically reduce the complexity of the theoretical framework. [134]
First the physical forces exerted on a charged molecule that is surrounded by an ion-containing solution are considered. Upon entering the solution, the charged molecule will disturb the distribution of ions, resulting in layers of counterions that gather around the molecule. Thereby, one generally differentiates between what is called the *Stern layer* and the *diffuse layer*. The *stern layer* refers to counterions that are subjected to higher attraction forces by the molecule's charge simply because they are closer to the molecule. The stern layer is thus the contiguous layer around the molecule's surface. Its counterions are considered immobile. The diffuse layer adjoins the stern layer and consists of ions that are still capable of moving. Stern and diffuse layers are also known as the *electric*

double layer The stern layer can be characterized by its thickness which is described *via* the *Bjerrum length*:

$$l_b = \frac{e^2}{4\pi\epsilon_b\epsilon_0 kT}, \tag{5.2}$$

with e being the elementary charge, ϵ_b being the dielectric constant of the fluid, ϵ_0 being the vaccum permittivity, k being the Boltzmann constant and T being the temperature. A general description of mobile ions and their equilibrium distribution in solutions is provided by the Poisson-Boltzmann equation:

$$\epsilon_b\epsilon_0\nabla^2 V_p = -e\sum_k Z_k C_k \exp\left(\frac{-ez_k V_p}{kT}\right), \tag{5.3}$$

where k refers to the ions and ez_k and C_k describe their charge and bulk concentration. The Gouy-Chapman model provides a valid solution to the Poisson-Boltzmann equation. The diffuse layer however, is sufficiently described by the linearized version of 5.3, also know as the Debye-Hückel theory which provides a description for the screening potential $V_p(x)$ that affects the external fields within a electrolyte as follows:

$$V_p(x) = V_s \exp(-\kappa X). \tag{5.4}$$

This expression is associated with a Debye-screening length κ^{-1} which is defined as:

$$\kappa^{-1} = \sqrt{\frac{\epsilon_b\epsilon_0 kT}{e^2\sum_k z_k^2 C_k}}, \tag{5.5}$$

with z_k being the ionic valency. [134]

So far, we have seen that an electric double layer is generated once a charged object is embedded in a solution of ions. The presence of such an electric double layer and the changes induced to it by an external electric field are key to describe electrophoresis (see figure 5.5). This force generated by the electric field causes a displacement of both the counter-ion cloud surrounding the molecule and the molecule itself. However, the ion cloud will be displaced in the opposite direction of the molecule which affects the hydrodynamic motion of the molecule. Calculating this motion is quite sophisticated, but solutions can be obtained in the limits of the Debye- length κ^{-1}. Assuming a sphere-like molecule of radius R, one finds that for $\kappa^{-1} >> R$ at equilibrium the electric force equals the Stokes'sche friction and one can find an expression for the drift velocity as follows:

$$v = \frac{qE}{6\pi\eta R}, \tag{5.6}$$

with q being the charge and R the radius of the molecule, E the strength of the electric field and η the viscosity of the medium. Based on this, one can state the electrophoretic mobility:

$$\mu = \frac{v}{E} = \frac{q}{6\pi\eta R}. \tag{5.7}$$

In the case of $\kappa^{-1} << R$ it is necessary to solve the Navier-Stokes equation:

$$\eta \Delta V_p = -\rho E, \tag{5.8}$$

with ρ being the solution of the Debye-Hückel model for cases within the Debye-layer, that cancels out in cases outside the layer. [134]
Calculations by Smoluchowski in 1903 [135] showed that this velocity is independent of the size and shape of the molecule and the expression for the electrophoretic mobility reduces to:

$$\mu = \frac{\epsilon_b \epsilon_0 \zeta}{\eta}, \tag{5.9}$$

where one introduces a ζ-potential describing the potential at which friction causes individual ions to shear off the layer. A more intuitive approach to modeling the electrophoretic velocity stated in 5.9 can be generated by expressing the electrophoretic mobility using the surface charge density:

$$\mu = \frac{\sigma}{4\pi\eta\kappa} \tag{5.10}$$

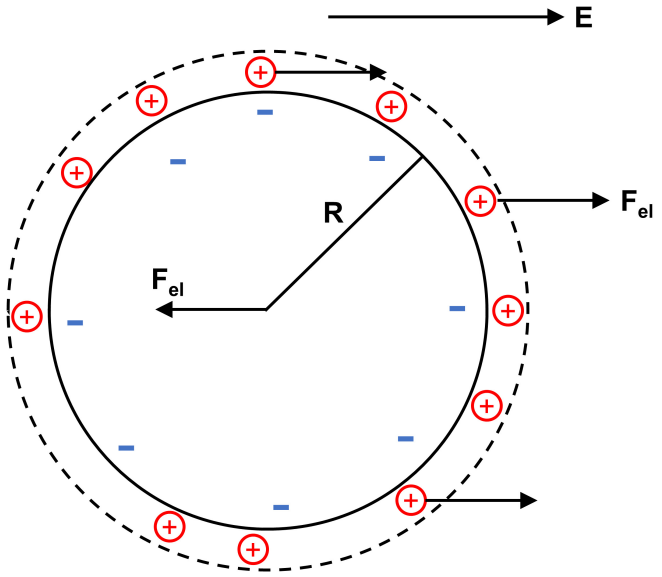

Figure 5.5.: Schematic representation of the involved forces on a negatively charged sphere in an ionic solution subjected to electrophoresis. It is assumed that the spheres radius R is larger than the Debye-length κ^{-1}. [134]

The key message of the previous discussions is that according to Smoluchowski, the electrophoretic mobility of a charged object is independent of its size and shape [135].

Viovy highlights the implications of this size-independence in the electrophoretic separation of charged molecules as summarized below:

Once the Smoluchowski limit is reached, which is the case for small κ^{-1}, the screening effects imposed by counterions are larger than the Debye-length. This results in shearing forces that can only affect a cylinder-like object of diameter $d + 2\kappa^{-1}$ and the resulting mobility is again described by equation 5.9. This together with the size-independency predicts that electrophoresis for long and flexible polyelectrolytes such as DNA molecules is impossible in free solutions, but instead requires a medium such as a gel that limits its freedom to move. [134]

To describe the limited mobility of DNA molecules in gels one can refer to the biased reptation model [136] that provides the following expression:

$$\frac{u}{u_0} \approx \frac{1}{3}(\frac{1}{N} + \frac{\epsilon^2}{3}), \tag{5.11}$$

with u_0 being the mobility in free solution and N the length of the polymer. ϵ is the quantity describing a reduced, electric field that depends on parameters such as the gel-pore size.
According to Slater et al. [136] the reptation model allows the following central conclusions. For small molecules, Brownian motion dominates over the motion generated by an applied electric field. For large molecules however, the electric field has the higher impact on the mobility compared to Brownian motion. Fine-tuning the pore size of the gel as well as the applied field strengths determines the diffusion-dependent term of biased reptation in such a way that polymers of constant charge density can be separated based on their lengths. Hence, molecules that are smaller travel faster through a gel than molecules that are larger. [136]

Common materials used to separate DNA via gel electrophoresis include agarose or polyacrylamide (PAGE). The latter is a flexible and neutral polymer and requires a bifunctional cross-linker such as bis-acrylamide to polymerize. [134]

Bio-Rad Laboratories provides useful manuals on gel casting and running [137]. The cross-linking reaction needs to be induced by a free-radical source such as ammonium persulfate (APS) and a stabilizing reagent such as tetramethylethylene-diamine (TEMED). The gel is usually cast vertically between two glass plates. The concentration of acrylamide applied typically ranges between 5-25% , with higher acrylamide concentrations better suited for resolvingsmaller molecules.
In general, PAGE gels are used to separate smaller DNA (up to 500 bps). PAGE gels are appreciated for their ability to detect size differences as low as 1 bp. [137]

Agarose (AGE) is a rigid polysaccaride with lower resolution but is suitable for separating larger DNA samples such as DNA origami structures. To prepare an AGE gel one typically dissolves agarose in a buffered solution at percentages between 0.5 - 2% and heats it up to dissolve it. AGE gels are poured in horizontal casting systems while they are still in a liquid phase, where they polymerize upon cooling. [134]

For both gel types, combs are used during the casting process to generate wells where samples are loaded. An electric field is then applied causing the negatively charged DNA samples to travel to the anode of the system. During the running process, the gels are placed in an electrophoresis chamber that is filled with a suitable buffer.

Although the gel percentage is the general, determining factor for the separation of the samples, one knows that there are many more parameters that can influence the gel mobility of DNA. Interpretation of gel electrophoresis results thus needs to be performed carefully and under consideration of all possible influences. The mobility of DNA for instance is influenced by its adapted conformation. It is known that, although of the same size, linear DNA runs at different speeds compared to circular DNA of the same sequence length. Applied voltage, temperature, and ionic strength of the buffer are other parameters that influence migration speed. Since single-stranded DNA is especially prone to adapting various conformations, it is common lab technique to dissolve these secondary structures using denaturing agents such as urea or formamide prior to gel loading. [137]
As an assembly of multiple DNA double helices, DNA origami structures are subjected to the same influences when run on gels and an estimate of their migration speed only makes sense in reference to a control of well-known behavior. Denaturing conditions to overcome the lack of predictability are not worth considering since the structures would disassemble. This means that there is always a slight chance that the detected signal on the gels does not necessarily correspond to the DNA origami with the predicted structural conformations. Thus it is recommended to always include a second route of verification such as electron microscopy for the very initial assessment of a new DNA origami design.
In general, the readout of a gel electrophoresis experiment is performed through judging the sharpness, intensity and purity of so called gel bands - horizontal bars on gels each referring to species of the same size.
To make DNA gel bands visible, intercalating fluorescent dyes that render DNA visible upon excitation at the appropriate wavelength are most commonly used. One of the most widely used dyes is ethidium bromide (EtBr). The limits of detection are usually directly correlated to the sensitivity of the dyes. [138]

In this work agarose gel electrophoresis is used to analyze the feasibility of different proposed DNA origami designs. A sharp and intense gel band indicates a DNA origami design that behaves well and is capable of generating the desired structures. Once design success is confirmed via another technique such as electron microscopy, gel bands can also be used to estimate the purity and structural stability of DNA origami structures. Meanwhile, a lack of bands, smeared backgrounds, or higher order bands in sample containing only one DNA origami structure indicate unsuitable folding conditions or failed designs.
The buffers used in gel electrophoresis were complemented with 10-11 mM $MgCl_2$ to maintain the reaction conditions required for the stability of the analyzed DNA origami structures. The analysis of single-stranded DNA was based on gel casting and running buffers that contained 8.3 M urea to denature the samples. Besides AGE gel electrophoresis, this work relies on electrophoresis using PAGE gels to purify DNA single strands. This method will be discussed in more detail in section 5.2.3. More details on the experimental parameters of the performed electrophoreses are stated in the captions of respective gel data in the upcoming chapters as well as in appendix A.3.

5.2.3. Purification methods

Within the context of this work, purification is not only used for the obvious reason of purifying the structures from residual strands that have been applied in excess, but also serve as an indicator for the structural stability of new DNA origami architectures. The following explains the different purification techniques and which task they perform. It

should be mentioned that successful purification of DNA origami structures can be highly architecture-dependent, and often it is necessary to finetune the individual protocols for the individual structures. Wagenbauer et al. provides a suitable guide to get started with the many different techniques and can serve as a good starting point for parameter finetuning.

PAGE purification

PAGE purification was used to purify functional handles that extrude from DNA origami structures with their 5'-end and are designed to fullfill a certain task such as binding a specific target. The main motivation to perform PAGE purification only on 5'-end extruding oligonucleotides is to remove all truncated sequences which is a common left-over product from the synthesis [139]. Since synthesis is performed from the 3'- to the 5'-end, truncations - if present - appear on the 5'-end. These sequences would interfere with the interactions that the handles are designed to undergo. PAGE gels are used to separate single-stranded handles according to their size. Thereby, 2 nmol of each individual sequence was applied across multiple gel pockets of a 15% denaturing PAGE gel. Denaturing conditions were established with gel casting and running buffers containing 8.3 M urea as well as formamide containing sample buffer. The gel bands of interest have been cut under UV-shadowing and extracted from the gel using ethanol precipitation. Details on the protocol can be found in appendix A.3.

Agarose gel purification

Native AGE gel electrophoresis is used in DNA nanotechnology mainly to separate excess staple strands from the folded DNA origami structures. Staple strands are on the order of around 30-60 nt and thus run much faster through the gel compared to the folded structures. Once the gel is imaged, staples appear as dark clouds on the bottom of the gel. The different gel mobilities make it easy to cut the gel band that is ascribed to the structures of interest. Samples are then usually extracted from the gel by squeezing the sample though a glass slide or through centrifugation. Gel purification is a suitable method to achieve a homogeneous sample containing only the desired species of structures such as only the monomers or dimers. One drawback of gel purification is the low recovery yields that is, if performed correctly and with diligence, around 30%.
Gel purification in the context of this thesis was mainly used to generate a homogeneous sample for TEM imaging. It turned out that for some structures it was crucial to gel purify them before imaging to achieve suitable image contrast. This will be explained in more detail in chapter 7. Information on the protocol can be found in appendix A.3.

Amicon filtration

Amicon filtration uses commercially available molecular weight cut-off filter units that consist of a microcentrifuge tube and a vertical membrane made from regenerated cellulose (see figure 5.6). It can be used for various purposes such as purification, sample concentration or buffer exchange. Filters are chosen such that their pore size is not larger than the samples to be purified. The sample is placed in the filter membrane, usually complemented with buffer, and is then centrifuged. All particles that are smaller than the pore size will travel through the membrane and collected at the tube bottom as shown in figure 5.6. This process can be repeated as needed. In the last step the sample is eluted

from the membrane by centrifuging the inverted filter placed on a fresh microcentrifuge tube once more.

Amicon filtration can be an efficient way to purify DNA origami structures from excess staple strands and usually results in higher yields compared to gel purification. However, parameters such as the dilution buffer, centrifugation time, temperature, membrane size, and membrane pre-treatment can significantly affect the outcome. [140]
In case of low recovery yields, it is a good measure to analyze the flow-through. Samples detected in the flow-through indicate that the pore size was not chosen correctly or that other parameters require further finetuning. If the flow-through does not contain samples but the recovery yields are low then this suggests samples interacted with the filter membrane in a manner that prevented their eventual elution.
More details on amicon purification and how the parameters can be tuned are presented in chapter 6 and appendix A.3.

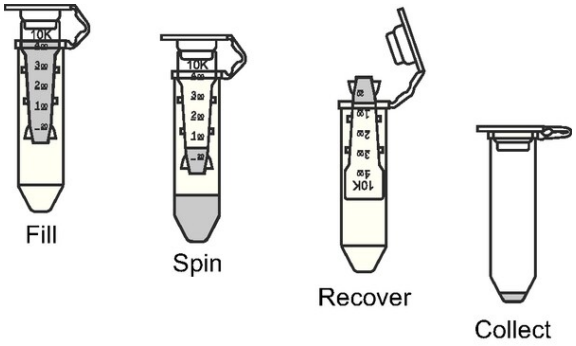

Figure 5.6.: Amicon®Ultra filter system and the process of sample filtration. [141]

PEG purification

PEG purification is another method for separating DNA origami structures from the excess staple strand and can also be used to concentrate the samples. It is based on precipitating DNA with the aid of polyethylenglykol (PEG). The structures are subjected to a PEG precipitation buffer that is the buffer of the structures of interest complemented with up to 20% w/v PEG-8000 as well as sodium chloride. Through centrifugation the structures are collected in a pellet at the tube bottom whereas the supernatant contains single-stranded DNA. Analyzing both the pellet and the supernatant can be useful to judge how much sample material got lost in the supernatant. Recovery yields are usually higher compared to gel purification. One drawback of this purification method is that final products exhibit PEG residues from the precipitation protocol.

5.3. Transmission electron microscopy

Compared to conventional light microscopy, transmission electron microscopy (TEM) provides much higher image resolution with magnifications in the range of 10^3 to 10^6. The key difference is exposing a thin specimen to an electron beam instead of visible light. To understand the reason for the increased resolution, one needs to go back to the theoretical work of two scientists that majorly contributed to the field of optics. Right after Einstein

proposed the wavelike character of electrons, Louis de Broglie was able to come up with the mathematics to calculate their wavelength using:

$$\lambda = \frac{\hbar}{p} = \frac{\hbar}{(mv)}, \tag{5.12}$$

with $\hbar = 6.626x10^{-34}$ being the Planck constant and p, m, and v being the momentum, mass and velocity of the electron. Assuming electrons are released from a heat source and accelerated by a difference in the electric potential of around 50 V, the velocity v and wavelength λ calculates to $v \approx 4.2 \cdot 10^6 \ \frac{m}{s}$ and $\lambda \approx 0.17$ nm. This assumes the processes are executed in vacuum. This is a drastic decrease in wavelength compared to visible light spectrum of 300 - 700 nm. [142] The powerful consequences for microscopy only become clear when looking at Abbe's formula for the diffraction limit that defines the maximum resolution. Resolution refers to the minimal possible distance d between points that still allows them to be individually detectable. According to Abbe this minimal distance depends on the wavelength λ of light and the aperture NA of the optical lens used in the microscope. The latter itself depends on the refractive index of the medium used between specimen and objective and half of the opening angle α. This leads to the following definition:

$$d = \frac{\lambda}{2n\sin(\alpha)} = \frac{\lambda}{2NA} \tag{5.13}$$

A maximum resolution of 0.3 μm for a wavelength in the middle of the visible light spectrum ($\approx$ 500 nm) can be calculated assuming a large aperture lens where $\sin(\alpha) = 1$ and imaging on air with $n = 1$. Using the reduced wavelength of electrons for the calculation of the minimal distance d results in much higher resolution values. [142]
In a TEM, electron are usually emitted from a V-shaped filament through the process of thermionic emission. A common material used for the filament are tungsten wires that can be heated up to 2500 K by a direct current before it starts releasing electrons. Based on the fact that electrons can also be regarded as negatively charged particles they are thus responsive to electric and magnetic fields. This is exploited to accelerate and focus the electron beam once subjected to an electric field. Thereby, higher acceleration voltages can tune the electron wavelengths to even higher resolution. The electron beam is typically focused *via* a system of at least three lenses before it penetrates the specimen. As the name suggests, only electrons that have transmitted through the probe are detected. Detection is usually done on a CCD camera. [142]

Although TEM ensures a certain level of resolution, image quality by itself is highly impacted by the way the probe is prepared. In general, samples of interest suspended on a mesh grid. Thereby, grids of various mesh sizes and coatings are available and have to be chosen according to the specific needs of the probe. Many biological probes such as DNA exhibit a low contrast when imaged and require specific staining with heavy metals such as uranylformate or -acetate. The staining procedure is another factor that can influence the image quality to a large extent. As TEM is the second main technique used to study the developed DNA origami architectures, staining procedures have been studied in more detail and results are presented in chapter 7. Further, appendix A.3 can be consulted for the specific parameters involved in staining and imaging.

5.4. Methanol-responsive polymer PCR

Methanol-responsive polymer PCR (MeRPy-PCR) was recently developed by the Shih laboratory and extends the method of standard polymerase chain reaction (PCR) to generate high-purity, single-stranded DNA of various lengths and at high yields. Commercial synthesis of DNA strands larger than 200 bps are typically associated with high costs and poor purity. [143]

The following explains the working mechanism of classic PCR before MeRPy-PCR will be explained.
PCR is used to amplify a given DNA sequence of interest that is embedded in a double-stranded DNA probe. This requires that the sequences of the regions adjacent to the section of interest are known, as well as the presence of a thermostable polymerase and sufficient nucleoside triphosphates (dNTPs), the building blocks for the DNA amplification. Based on the known flanking regions one designs complementary primers that then hybridize adjacent to the section of interest. This helps the polymerase find its starting point for synthesis. The typical length of the primers is between 20-30 nts. A PCR-cycle

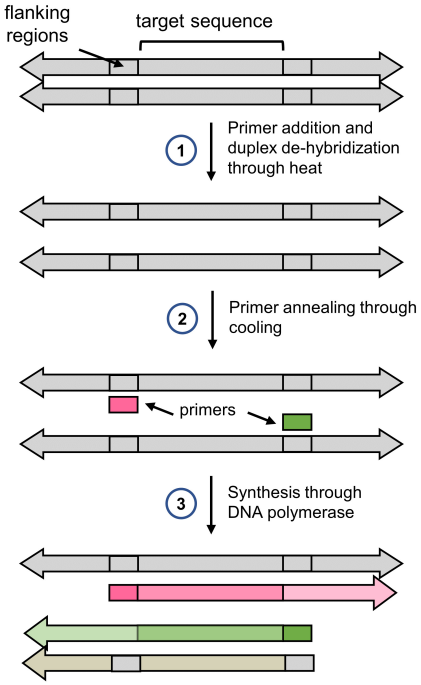

Figure 5.7.: First cyle of a standard PCR. Image based on [13]

consists of three main steps (see figure 5.7). First the double-stranded probe is heated to around 95°C to induce disassembly of the double strand. Second, the probes are cooled down to around 54°C to allow the primers to hybridize with the 3'-ends of the section of interest. This implies that the primers do not attach to the same single strand, but due to the directionality of the strands there is one primer for each individual single strand of the duplex. This provides the right conditions for the taq-DNA-polymerase to start synthesizing from the primer toward the section of interest. Synthesis proceeds from the 5'- to 3'-end at around 72°C and does not stop once the section of interest is synthesized but continues till the ends of the templates. Thus, after the first cycle the sections of interest

are still incorporated within a longer DNA single strand (see pink and green strands in figure 5.7). After the second cycle, four double-strands will be generated, two of which exhibit the shorter sequence of interest hybridized to a longer DNA segment. This process can be repeated as needed and leads to the exponential amplification of the short, desired sequence. It is important to note that PCR always amplifies the target sequence but in a double strand configuration. [13]

For many applications however it is of interest to separate the double-stranded PCR end-product and instead have two single-stranded DNA sequences ready to use. Minev et al. addressed this need by MeRPy PCR that manages to isolate the single DNA strands from PCR duplexes. The key invention of MeRPy-PCR is to incorporate a linear polyacrylamide-co-acrylate tag into one of the two primers that are subsequently used in standard PCR (shown in figure 5.8 A). This way the PCR end-product is equipped with a tag that is responsive toward methanol and allows users to separate the two strands through precipitation (shown in figure 5.8 B first step). Tagged primers can additionally include deoxyuridine (dU) which can be used to create an abasic site. This can later be cleaved and allows the recovery of the reverse strand (see figure5.8 B second step). The MeRPy-PCR technique takes advantage of robust DNA amplification through standard PCR that is also applicable to long DNA strands and succeeds in eliminating both single DNA strands from the PCR duplexes at high yields. [143]

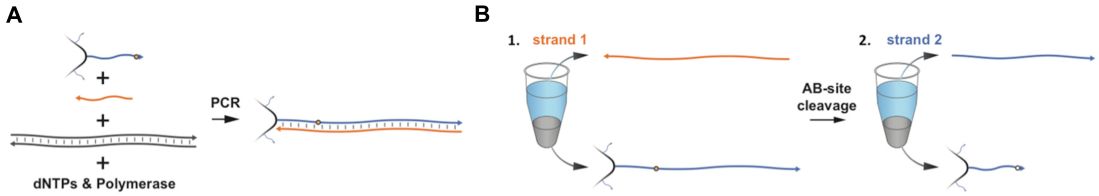

Figure 5.8.: Working principle of MeRPy-PCR. [143]

6. DNA-based platforms for multivalent interactions

The scaffold in DNA origami folding limits its growth to a certain size and thus to a finite number of possible functional sites. Hence, for many applications the amount of interactions possible along a DNA origami surface is too low to induce the desired effects. This chapter presents three novel design strategies to maximize the surface areas of DNA origami structures for an increased number of functional sites and to minimize the distance between them. These three design approaches all come with their own set of challenge questions and working hypotheses as outlined below. Definite design recommendations are going to be eliminated and insights are provided to support other researchers in their design processes.

6.1. Overview of the studied design approaches

Design approach 1: Diagonal-cut arrangement of helices on a square-lattice for a reduced functional site-distance

The first design approach investigates multi-layer DNA-origami architectures with helices bundled in a diagonal-cut arrangement on a square-lattice. This arrangement displays the ends of alternating helices with a 3.4 nm spacing as shown in figure 6.1. Compared to a 4.8 nm spacing in conventional square-lattice arrangements, the diagonal-cut yields a reduction of that spacing by 1.3 nm. The above considerations only take helices sharing the same scaffold directionality (i.e. parity) into account. Scaffold parity and the resulting functional-site distances are visualized in figure 6.1. The scaffold starts routing through the structure by going into the plane, jumping to the next adjacent helix and returning out of the plane as illustrated by the red arrows in figure 6.1 and the grey loops.
Challenge question: Does a deviation from the square-lattice norm result in properly folded nanostructures?
Working hypothesis: The diagonal arrangement does not impact the helix density and thus does also not change the charge density imposed by the helices' backbones. Thus, it is expected that this kind of helix arrangement is not increasing the repulsion forces within the design and should lead to properly folded structures.

Design approach 2: Shortened DNA helix depth

The goal of design approach 2 is to minimize the scaffold used per helix to a minimum of 50 bps for the benefit of assembling it into further helices that contribute to a maximization of the surface area. The helix density within the arrays is thereby increased which is desired in the context of surface maximization. However, the short helices and the high density impose the following design challenges.

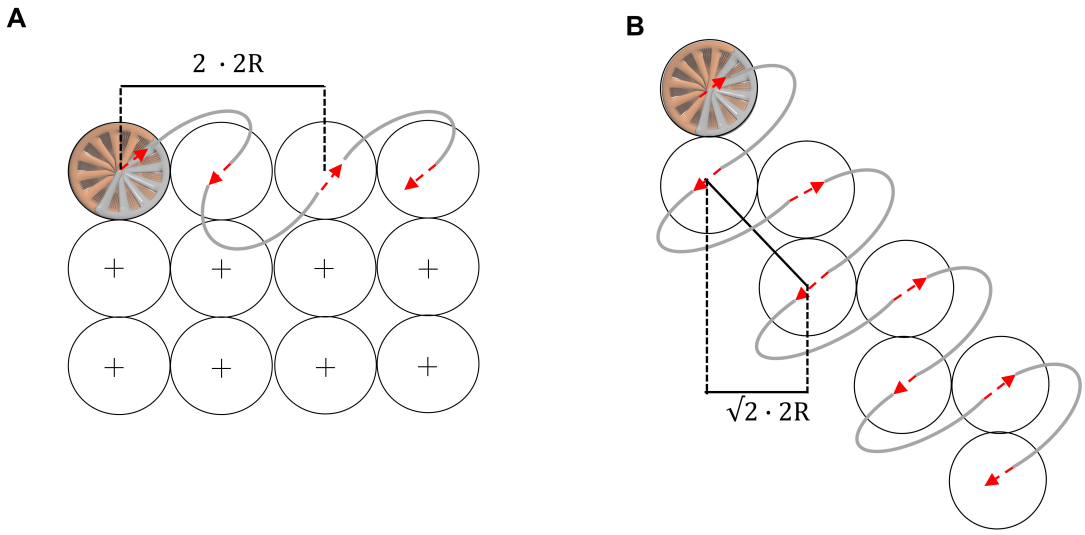

Figure 6.1.: A diagonal-cut arrangement of helices on a square-lattice reduces the distance between functional sites. Thereby, helices that share the same scaffold direction (indicated by red arrows) are considered as potential functional sites. Arrows pointing in the same direction refer to shared scaffold directionality. **A** Conventional arrangement of helices on a square-lattice yields a distance of $2 \cdot 2R = 4.8$ nm with R being the radius of a DNA double helix (1.2 nm). **B** Diagonal-cut arrangement of helices on a square-lattice exhibit a reduced distance of $\sqrt{2} \cdot 2R = 3.4$ nm between functional sites with R being 1.2 nm.

As such, dense arrays of 50 bps short helices exhibit a high density of staple crossovers that generates two problems given that they are incorporated every 8 bps to follow the baseline design rule of the field. First, the short foothold of the staple strand is not able to generate sufficient binding energy to interact with the scaffold leading to inefficient incorporation of the staple strand into the middle of the structure. Staple strand incorporation will have a high risk of failure. Second, the short foothold will cause staples to be also weakly bound along the edges of the structure rendering the overall complex highly unstable. In general, one can predict that the densely packed arrangements will not assemble if no measures are taken to reduce the staple crossover density by replacing them with higher energy interactions.

Baked into the very foundation of DNA nanotechnology, it is the recommendation to connect two adjacent helices in a DNA origami structure via two crossovers. The reason can be understood quite intuitively. Helices connected via a single crossover, have a much higher degree of freedom and result in a much more dynamic construct compared to a double crossover connection. The latter will result in a much stiffer complex and is thus regarded crucial to the structural integrity of DNA origami structures. This led to another baseline design rule in the field according to which a staple crossover should be incorporated every three helical turns and traverse to the adjacent helix at least 2 x. A helical depth of only 50 bps makes satisfying this convention difficult. In essence, the challenge for design approach 2 lies with the question how to reduce the staple crossover density and whether structures with only one crossover per interface will result in proper folding. The chapter will present two design innovations to address this challenge. First, a subset of staple crossovers are replaced with scaffold crossovers which introduces a scaffold seam

within the structures. Second, mini-scaffold strands (mini-scafs) are introduced that are around 80 bps long and incorporate mainly along the edges of the structures. This saves additional staple crossovers and is hypothesized to further stabilize the structures' outline. The design innovations are implemented on diagonal-cut, square-lattices as well as on honeycomb-lattices.
Challenge questions: Is it possible to reduce the staple crossover density by the suggested design innovations and does a deviation from the established design rule of having at least two crossovers per helical interface result in proper folding?
Working hypothesis: Global twist inherent to designs on square-lattices is hypothesized to become more prominent with shorter helices and reducing crossover density might destabilize the structures. This needs to be counterbalanced with specific bp deletion patterns throughout the whole design, considerate choice of crossover positions and/or potential adaptation of the aspect ratios. Honeycomb-lattice based designs are predicted to behave better since the helix arrangement better matches the natural, geometric properties of B-DNA helices and the staple crossover density is inherently lower compared to square-lattice designs.

Design approach 3: Square-holey lattices and the combination of multiple scaffolds for a larger design space

Design approach 3 introduces so called square-holey (SH) lattice architectures as another strategy to establish a larger design space. SH lattices designs yield multi-layer DNA origami structures assembled on a conventional square-lattice and are characterized by a regular pattern of skipping every second helix on the grid. This approach conserves scaffold that can be deployed in a longer helix length. In contrast to design approach 2 where structures grow exclusively perpendicular to the helical axes, maximization of surface area in design approach 3 is realized along the helical axis through increased helix lengths and perpendicular to the helical axis through the addition of further DNA layers. The latter is realized by the incorporation of a medium sized scaffold ("midi-scaf") that complements the standard, M13 derived scaffold. Midi-scaffolds are typically in the size range of 3000 bps and are synthesized using the MeRPy-PCR protocol described in chapter 5.
Challenge question: Does the square-holey lattice design strategy result in stable structures and can multiple scaffolds be combined to result in structures exceeding the size limits of conventional DNA origami?
Working hypothesis: There will be a balance number between fully occupied DNA layers and holey layers to result in stable structures and it is predicted that further stabilizing layers can be added to the main body through the incorporation of midi-scaffold strands. Overall, the helix density in a square-holey lattice is reduced compared to conventional square-lattices. Thus global twist phenomena should be much less of a concern compared to architectures from design approach 2.
The following presents the DNA architectures that have been developed to study the three individual design approaches described above. A graphical overview on all designs that are going to be discussed within this chapter is given in figure 6.2.
Two key features have been the focus of the attention to evaluate the feasibility of the architectures: First, the overall folding yields and related question about experimental parameters that would maximize the yields and purity of the folding. Yield and purity of the folded structures are accessed using gel electrophoresis and TEM imaging. Second, the stability of the structures toward changes in reaction conditions. The tool of choice to

test the stability has been either amicon or PEG purification. oxDNA simulations have been additionally used to support decision making in the re-design cycles for the structures. Finally, it may be pointed out that providing efficient purification protocol is key when introducing novel DNA architectures, not only to access their stability but also to generate pure starting material for further applications. Purification of DNA structures becomes especially challenging, the larger the surfaces are. Not only do these surfaces allow multi-site interactions with desired binding partners, but also hold a higher potential for unspecific interactions among each other. It is thus inevitable to evaluate a potential tendency of these structures to unspecifically interact with each other and come up with strategies to avoid this. Only if these questions are addressed, novel design strategies are a valuable addition to the pool of expertise of the field. Two final comment to the following discussions. First, indications on the DNA origami dimensions can only be estimates. Distances between the helices can vary due to different inter-helical gap measurements that depend on the helix arrangement, buffer conditions and temperature [144]. In the following discussions the helical radius (R) is fixed at 1.2 nm.

Second, TEM images were generated following the protocol provided in appendix A.3 unless otherwise stated.

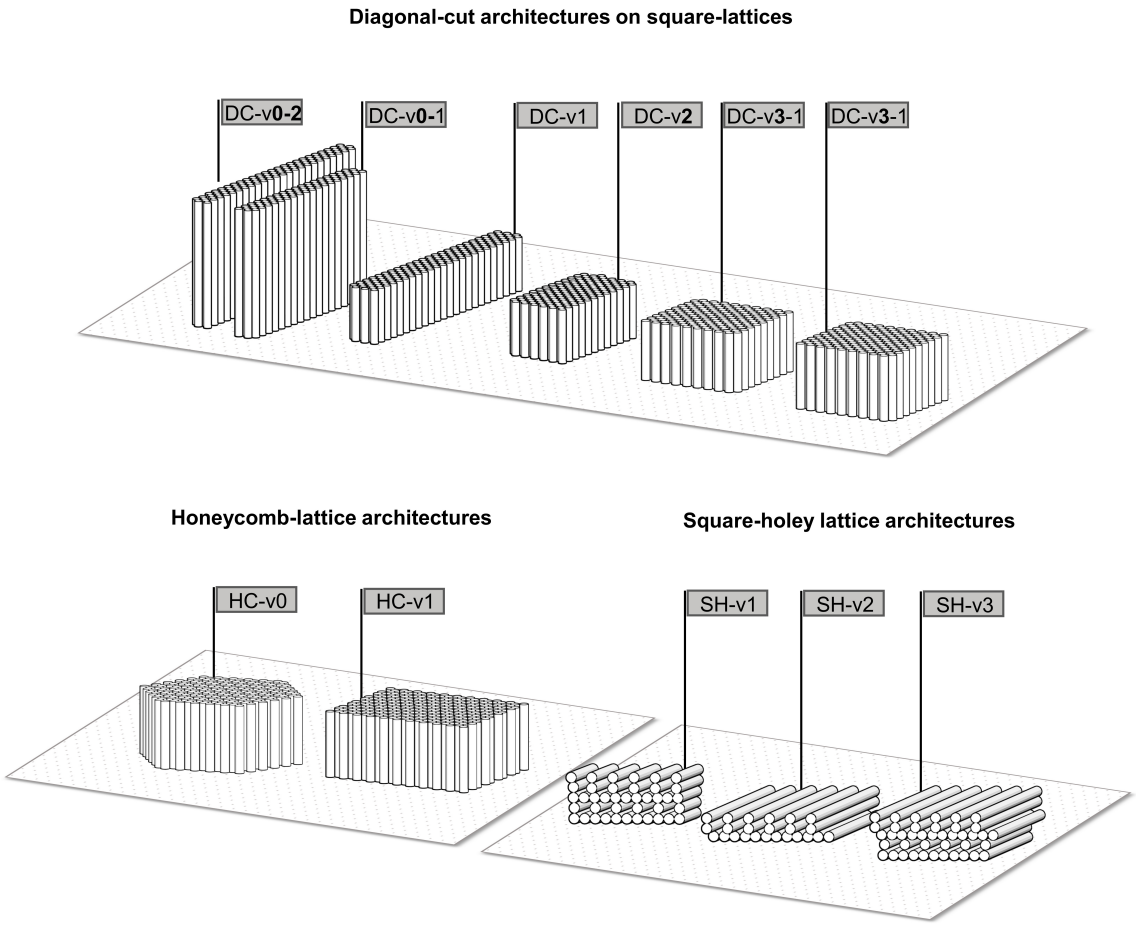

Figure 6.2.: Overview of the designed and evaluated architectures presented within this chapter

6.2. Design approach 1: Diagonal-cut, square-lattice designs for a decreased functional-site distance

6.2.1. Design and folding of diagonal-cut architectures

Design features of DC-v0

For design approach 1, structures exhibited a diagonal-cut (DC) helix placement pattern based on the square-lattice. Figure 6.3 explains how the diagonal-cut arrangement is implemented. It shows one candidate of the developed DC-v0 structures that consists of 84 helices with a length of 118 bps. Instead of growing the DNA-array into east direction as is done in conventional square-lattice designs, the helices are added into north-east direction.
The DC pattern is also reflected in the scaffold routing between the helices. The blue areas in figure 6.3 B highlight the helices that are connected by scaffold crossovers. Additional, non-highlighted helices are connected to the main body via staple crossovers. Figure 6.3 C displays a subsection of the path diagram from cadnano highlighting the scaffold crossovers (blue) as well as the bp-deletion patterns (red dashed boxes). The latter are crucial for any design based on square-lattices to counteract the global twist that originates from the dense packing of helices. Here, two bp-deletions are included at a distance of 53 bps on each helix.
DNA origami monomers in general can exhibit a tendency to stick to each other due to the freely exposed and hydrophobic helical ends. This unintended interactions are approached by including either extruding scaffold loops at the sites of the structures or extruding staple strands. [64]
Thus the structures do not exhibit blunt ends but single stranded overhangs (black dashed boxes in figure 6.3 C). This was implemented for all designs presented in this chapter and are supposed to act as steric brushes to prevent DNA origami monomers from sticking to each other.
Two versions of DC-v0 have been investigated, a slightly smaller version based on the p7308 scaffold (DC-v0-1) equipped with 18 handles and a larger one based on the p8064 scaffold (DC-v0-2) and equipped with the maximum amount of 48 possible handles. Handles are distributed along the edge-helices of shared scaffold parity (see red indications in figure 6.3). The handles consisted of 21 bps with a 2T linker acting as a spacer between the structure and the handle. It was found that the number of attached handles plays a role in purification protocols for these structures which is why the experiments presented were performed with the maximal number of handles attached to detect the effect they have on folding and purification. The following presents the folding procedure and the key steps on the way to a proper purification protocol of the structures.

Folding of DC-v0

Folding of DC-v0 follows the protocol provided in the appendix A.3. A final $MgCl_2$ concentration of 10 mM and the 6025-18h temperature ramp was used. The structures have been analyzed using native AGE gel electrophoresis and TEM imaging. The native AGE gel analysis shown in figure 6.4 A resulted in sharp product bands for both DC-v0-1 and v0-2. These have been further confirmed with TEM using the standard TEM protocol described in appendix A.3. TEM images in 6.4 B show overview TEM images as well as a close-ups of the top and side view of DC-v0-1 and v0-2. Both observed configuration

match the expectations toward the designed dimensions of the structures.

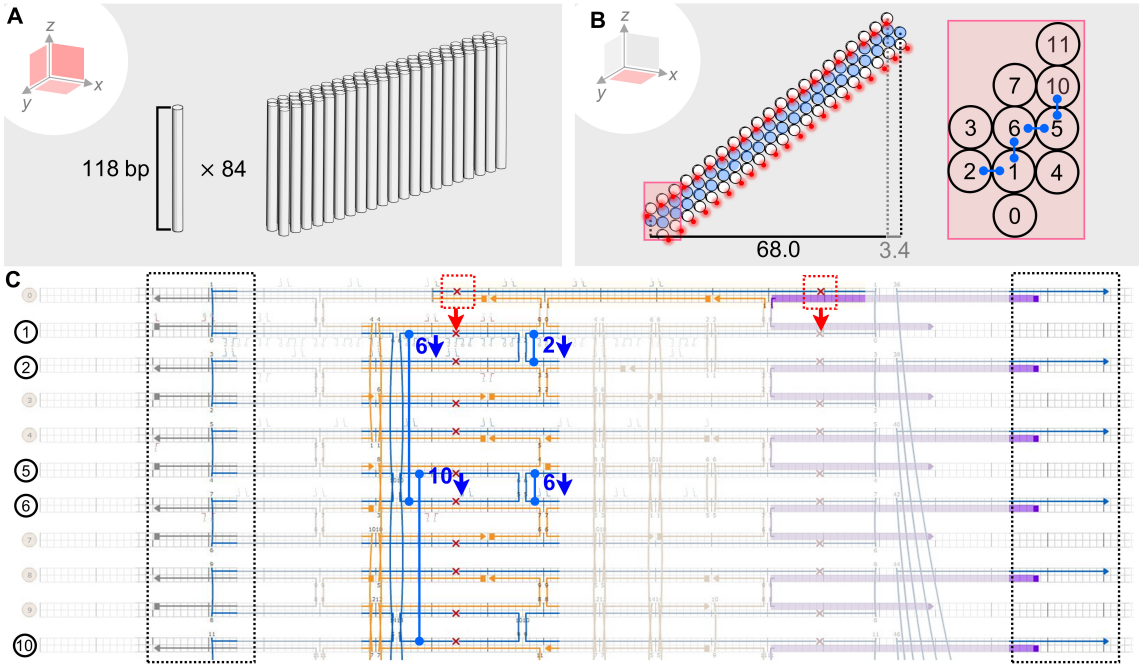

Figure 6.3.: Design approach 1: Diagonal-cut architectures based on a square-lattice (DC-v0). **A** 3D view DC-v0-2 showing the amount and length of the helices. **B** Top view outlining the dimensions (left) and the scaffold routing through the helices in blue (right). The scaffold routes through the middle layer of the structure. The structure offers room for 42 handle attachments in total (red dots). **C** Path diagram shows a rolled out view on the helices highlighting the positions of the scaffold crossovers by arrows. The number next to the arrows indicates the helix destination. Red crosses indicate bp deletions. The structure is streaked by a regular pattern of bp deletions. Dashed black boxes indicate the single stranded overhangs at the edges that are used to reduce the risk of multimerization.

6.2.2. Stability of diagonal-cut architectures

Typically, staple strands are applied to the folding mixture in a 10-20×excess with respect to the used scaffold concentration to avoid early growth termination. Although for many applications it is not necessary to purify the structures from the staple strand excess, there are applications where freely diffusing staple strands especially functional ones such as handles, could interfere with a proper execution of the designed task. As described in the introduction, structures presented within this thesis, are developed to realize multivalent interaction along their surfaces. Thus it is crucial at this point to provide proper protocols for purification that eliminate the excess of functional handles. Hence, rather than focusing on eliminating body staple, the focus lies on removing handles that lend function to the structure.

Purification of DC-v0 structures turned out to be challenging. It was hypothesized that the more functional handles extruded from the structures, the stickier the become. This made especially DC-v0-2 (48 handles) prone to multimerization and aggregation, a char-

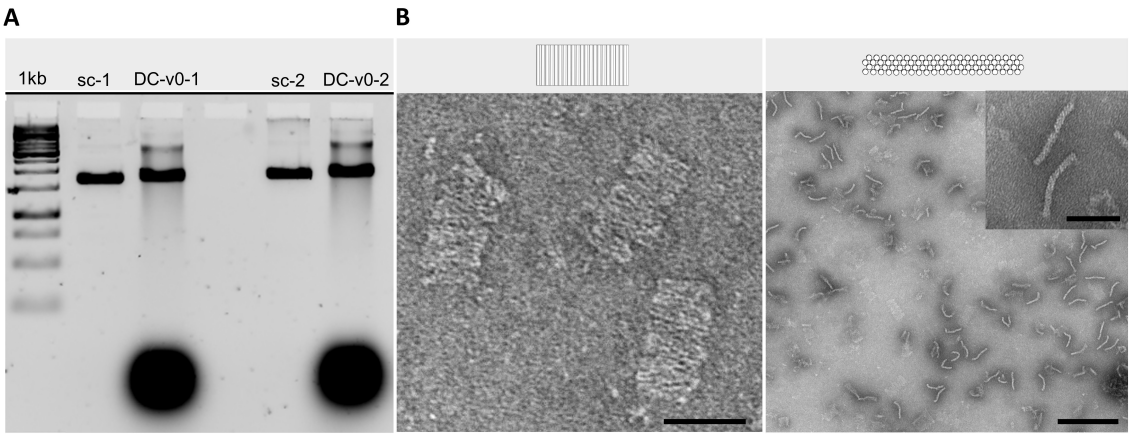

Figure 6.4.: Folding evaluation of diagonal-cut arrangement of helices on a square-lattice. **A** 2% native AGE gel: (1) 1kb ladder, (2) p7308 scaffold control for DC-v0-1, (3) Raw DC-v0-1, (4) empty, (5) p8064 scaffold control for DC-v0-2, (6) Raw DC-v0-2. **B** TEM images of DC-v0-1 (left) and DC-v0-2 (right) showing different orientations of the structures. Scale bars TEM (left, right, inset): 50 nm, 200 nm, 50 nm.

Gel running parameters: 0.5×TBE buffer with 10 mM $MgCl_2$, EtBr 0.5 $\mu g/mL$, 65V for 2h at RT.

acteristic that complicates the search for a proper purification protocol. Investigations of different purification methods have eliminated filtration through a molecular cut-off membrane as the one with the highest potential for successful purification.

It is important to point out at this point that the cut-off filter system used within this work is designed and sold by Merck Millipore. The type of filter system used here is sold under the name Amicon®Ultra-0.5 mL Centrifugal Filters. The following filtration procedures using the filter units from Merck Millipore will be referred to as "amicon purification/filtration".

The following presents the milestone experiments along the route to an efficiently working purification protocol for the DC-v0 structures. Purification protocols were tested with the maximum number of functional handles attached to the structures. The following discussions are based on the standard protocol for amicon purification (see appendix A.3) and present the findings that resulted from slight parameter adaptions in the standard procedure.

Tween in dilution buffer reduces multimerization

Figure 6.5 A shows the results for an amicon purification of DC-v0-2 using the standard protocol. It was found in separate experiments that it is necessary for the DC structures to repeat the amicon filtration 4 x in order to result in a decent removal of staple strand excess. After each spin an aliquot has been collected and analyzed on native 2% AGE gels (see figure 6.5 A and B, lanes (4)-(7)). The smeared background in the product bands on lane (7) on the gel is an indication for a high degree of impurity. These impurities can be misfolded structures, freely diffusing DNA strands or multimerized structures. Additionally, one observes a prominent multimer band when comparing the raw sample with the amicon purified sample. This effect increased with each performed spin. It is

important to note that the concentrations of the loaded samples on the gels in figure 6.5 are not normalized to the raw folding control in lane (3) on both gels. 3.3×more amicon purified product has been loaded on the gels compared to the raw sample control. This has to be taken into consideration when judging the recovery yields. The gel band of amicon purified and raw sample are of almost equal intensity. If the sample volumes would have been normalized one could conclude a 100% recovery yields. However, since 3.3×more amicon purified samples have been loaded this estimate has to be scaled down to a recovery yield of around 30%. This means that almost 70% of the structures are lost throughout the purification procedure. In order to identify the origin of the material loss, the flow through samples that have been collected during amicon purification have been analyzed. Gel analysis of the flow-through samples did not result in a product band. This suggested that most of the structures got caught in the filter membranes. This motivated using TWEEN 20, a common, membrane-detaching reagent used in the lab, to rinse the membranes of the filter units first before applying the sample. It was hypothesized that this would decrease the affinity of the structures to stick to the membranes.
It was found that pre-rinsing the amicon filter membrane with TWEEN 20 does avoid aggregation of the sample in the membrane. It seemed though, that the TWEEN 20 washes out over the course of the four spins and the sample quality decreases in the 3rd and 4th spin. For this reason, instead of just pre-rinsing the membranes with TWEEN 20, the dilution buffer was complemented with 0.05% TWEEN 20 so that membranes were subjected to TWEEN in each spin. This approach showed a drastic increase in the purity of the product bands as shown by much cleaner product bands in figure 6.5 B in lanes (4)-(7). Adjusting the $MgCl_2$ in the dilution buffer to a final concentration of 20mM further improved the purity and performed better compared to lower $MgCl_2$ concentrations.
These findings suggest in general that the structures are quite sensitive toward the dilution buffer applied and that they can not be treated with the standard amicon purification protocol. Also $MgCl_2$ seems to have a profound influence on the recovery yields. Despite resulting in much cleaner product bands when a combined buffer of TWEEN 20 and $MgCl_2$ is applied, the recovery yields are still much lower compared to the standard protocol. Also, staple strands are removed less efficiently compared to the standard protocol judging by the staple clouds that reduce much slower for samples treated with TWEEN 20. This motivated further investigations of parameters that potentially influence the purification efficacy.

Lower magnesium concentrations in dilution buffers increase recovery yields

The fact that experiments showed that 20mM $MgCl_2$ included in the dilution buffer helped to reduce the multimerization motivated a systematic investigation of the effect of different $MgCl_2$ concentrations in the dilution buffers on the recovery yields. $MgCl_2$ concentrations in dilution buffers have been varied from 6 mM up to 17 mM in steps of 1 mM. Final $MgCl_2$ concentrations slightly vary due to the fact that the dilution buffers are added to the samples that themselves are buffered in 10 mM $MgCl_2$. Native AGE gel electrophoresis was used to detect the impact of the different $MgCl_2$ concentrations on the recovery yields. ImageJ was used to measure the gel band intensities of teh individual gel bands and plotted against the respective $MgCl_2$ concentration (see figure 6.6). The complete dataset used to generate figure 6.6 can be found in appendix B.1. In general, yields decrease with increasing $MgCl_2$ concentration in dilution buffers. 6 mM $MgCl_2$ resulted in highest recovery yields close to 30%, while the yields start to collapse at 10 mM $MgCl_2$ with

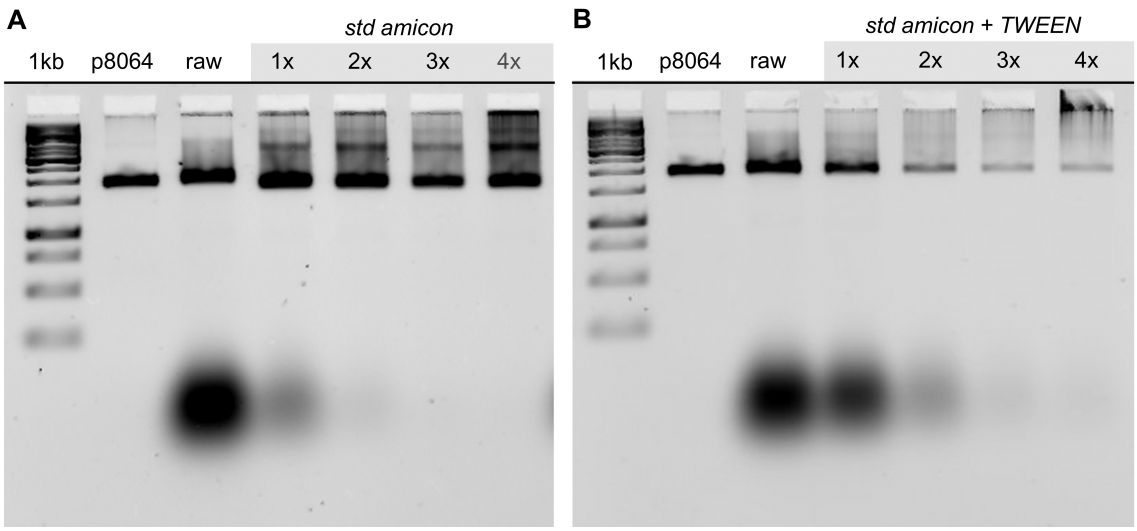

Figure 6.5.: Effect of TWEEN 20 and $MgCl_2$ on recovery yields of DC-v0-2 in amicon purification evaluated with 2% native AGE gels. Concentrations of loaded samples are not normalized. Sample amounts in lanes (4)-(7) are 3.3×higher compared to the controls p8064 and the raw folding samples. **A** (1) 1 kb ladder, (2) p8064 scaffold control, (3) Raw DC-v0-2, (4)-(7) Sample aliquots collected after subsequent spins with amicon filters. **B** Amicon purification of the same samples but including 0.05% TWEEN 20 and 20mM $MgCl_2$ in the dilution buffer.

Gel running parameters: 0.5×TBE buffer with 10 mM $MgCl_2$, EtBr 0.5 $\mu g/mL$, 65V for 2h at RT

yield of 17.8% down to only 1.9% for 17mM $MgCl_2$. As a result the standard amicon protocol was adjusted to use dilution buffers with a reduced $MgCl_2$ concentration of 6 mM. TWEEN 20 was excluded from dilution buffers at the cost of a less pure product but at much higher yields.

Masking strands

Although it was found that there is an optimal $MgCl_2$ concentration, recovery yields remained at a low level of around 30%. This was incentive to develop a strategy that could increase the yields. One approach to do so, was to introduce so called "masking" strands, strands that could bind to the handles of the DC structures and later be removed via strand displacement. The hypothesis is that double-stranded handles would render the structures less accessible for unspecific interactions and less sticky supporting a better elution from the filter membranes. Masking strands of different lengths (i.e. 19, 22 and 24 bps) covering different subsets of the handle sequences have been tested. Thereby, masking strands have been added in a 2x excess over the staple strands right after folding and incubated for 1h at room temperature (RT).
Figure 6.7 shows the result of the native AGE gel analysis. Again, aliquots have been taken after each spin and analyzed in comparisons to the raw folding sample. The far left of the gel shows results for samples that have been purified using the updated amicon purification protocol with 6 mM $MgCl_2$ in the dilution buffer. The monomer bands are populated at yields that have been typically observed using this protocol. Still there is a decent degree of multimerization and smeared background that, as presented above, can be treated with TWEEN 20 for the sacrifice of lower yields. The question was whether masking strands

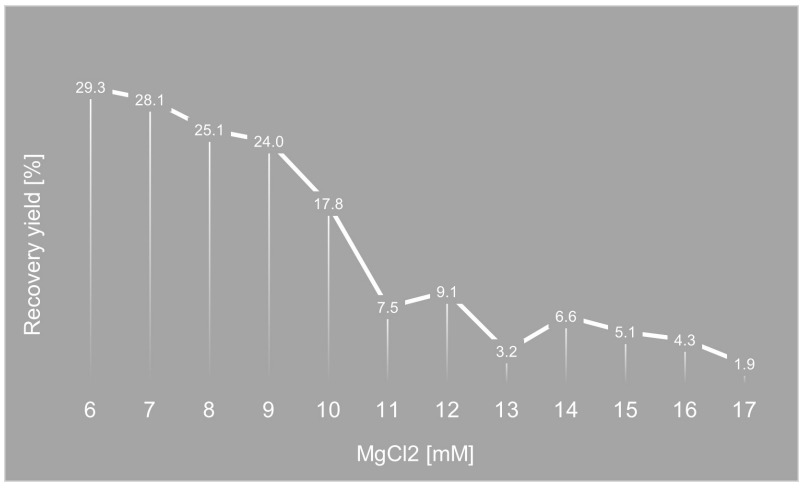

Figure 6.6.: Magnesium screening for dilution buffers in amicon purification. 2% native AGE gels have been used to analyze the effect of different $MgCl_2$ concentrations. Gel band intensities have been measured and plotted against the respective $MgCl_2$ concentration revealing a distinct dependency of the recovery yields on the $MgCl_2$ concentration.

can combine both, the desire to have clean product and reasonably high yields. Looking at the gel in figure 6.7 shows that this approach failed to meet these challenge. The level of multimerization drastically increased upon addition of the masking strands and led to aggregation of the structures in the gel pockets. 19mer masking strands thereby caused almost all monomers to either multimerize or aggregate whereas 22mer and 24mers did have a slightly less drastic impact. It was not possible at this point to draw a hard conclusion from this data. Possible reasons for this behavior however could be that either multimerization is not caused by the stickiness of the handles or that the masking strand induce some unspecific binding of the structures to each other. Masking the handles does not lead to the desired output and the approach was thus set aside.

Core strands added back

The previous experiment did not result in an improvement of multimerization. However, it allows one tentative conclusion that is that the reason for multimerization could not arise from the stickiness of the handles alone. If that would be the case, masking the handles would have resulted in less multimers on the gel. This indicates that there are other reasons why the structures tend to interact with each other. One hypothesis is, that the harsh reaction conditions of the amicon purification destabilizes the structure in a way that individual staple strand might leave the assembly and the structures become holey and exhibit open binding regions for mutual interaction. To evaluate this hypothesis, 100nM of core staple strands - strands that are only incorporated into the main body and do not carry additional function - have been added to 25uL of DC-v0-1 and v0-2 right after amicon purification and incubated at 37°C for 1h. The goal was to fill up potential holes within the structures that might have been created during purification. Adding core staples after amicon purification further reduced the final $MgCl_2$ concentration which is why the $MgCl_2$ concentration was first adjusted to 12mM again before core staples were added. Thereby it was assumed that the samples are at 6mM $MgCl_2$ concentration after amicon purification.

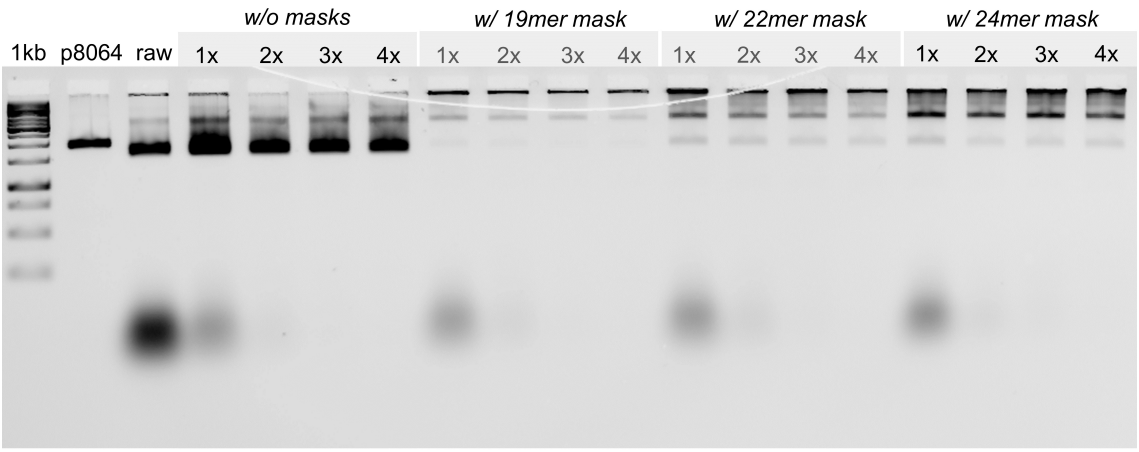

Figure 6.7.: 2% native AGE gel showing the impact of handle masking on recovery yields and purity in amicon purification of DC-v0-2. (1) 1 kb ladder, (2) p8064 scaffold control, (3) Raw DC-v0-2, (4)-(7) Sample aliquots collected after subsequent spins with amicon filters using the updated standard protocol. No masking strand applied. (8)-(11) Sample aliquots collected after subsequent spins with amicon filters using the updated standard protocol, but with 19mer masking strands, (12)-(15) with 22mer masking strands, (16)-(19) with 24mer masking strands applied.

Gel running parameters: 0.5×TBE buffer with 10 mM $MgCl_2$, EtBr 0.5 $\mu g/mL$, 65V for 3h at RT

Figure 6.8 A and B show the gel characterization of this approach for DC-v0-1 and DC-v0-2, respectively. Comparing the raw folding sample in lane (1) with the amicon purified version in lane (2) exhibits the usual degree of multimerization and smeared bands. Interestingly, adding back core staple strands to the structures right after amicon purification drastically improves the purity of the gel product bands and was capable to eliminate the creation of multimers completely. TEM imaging (see figure 6.8 C) was used to verify that the observed product bands for core supported structures indeed correspond to the expected structures. These first indications that adding back core staples strands after amicon purification is a highly effective measure to protect the structures from multimerization and aggregation raised the question whether the situation gets similarly improved when including more core staple strands in the folding reaction already. Thus, structures have been folded at a 20×staple strand excess instead of 10×and the amount of added core strands was reduced to 50nM for 25uL amicon purified samples. Amicon purification of structures folded with a 20×staple strand excess and subsequent addition of 50nM core staples strands resulted in best yields for both the DC-v0-1 and v0-2.
Minimum recovery from amicon purification can be observed for samples folded with a 10×staple strand excess and without subsequent core strand addition. This was again true for both the DC-v0-1 and v0-2.

6.2.3. Conclusion

Large-scale, high-precision, nanoscale applications require precisely addressable platforms for multivalent interactions and pure base material. This requirement imposes special demands on the developed DNA nanostructures and explains why it is not only important to develop new design strategies that work on a proof-of-principle basis but structures that

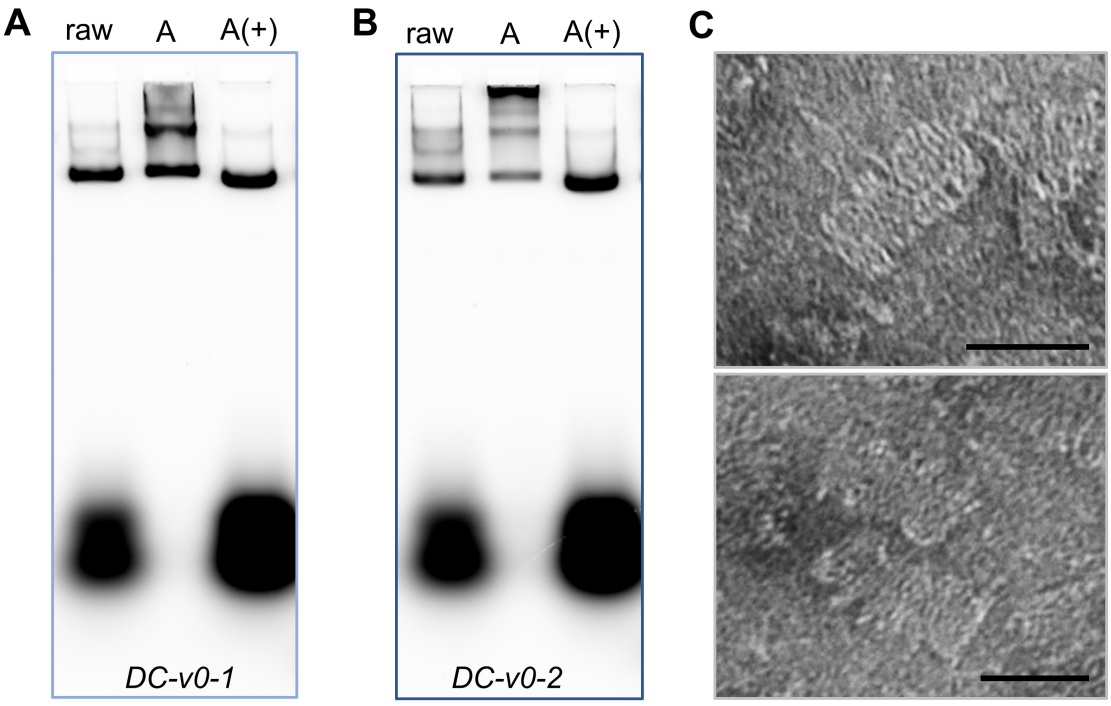

Figure 6.8.: 2% native AGE gel to evaluate the effect of added back core strand on recovery yield and purity in amicon purification of DC-v0-1 and v0-2. **A** Gel for DC-v0-1 (18 handles): (1) Raw DC-v0-1, (2) amicon purified DC-v0-1 (A), (3) core supported, amicon purified DC-v0-1 (A+). **B** Gel for DC-v0-2 (48 handles): (1) Raw DC-v0-2, (2) amicon purified DC-v0-2 (A), (3) core supported, amicon purified DC-v0-2 (A+). **C** TEM images of DC-v0-1 (top) amd DC-v0-2 (bottom), scale bars for the 50nm.

Gel running parameters: 0.5×TBE buffer with 10 mM $MgCl_2$, SYBR gold pre-staining 1:10 000 dilution, 65V for 3h at RT

are stable and can be purified.

It was possible to develop DNA nanostructures with a close packing of functional sites by deviating from conventional square-lattice arrangements and establishing a diagonal-cut arrangement of helices on a square-lattice. This reduced the distance between functional sites from 4.8 nm to 3.4 nm. The well defined assembly of DC structures confirms the working hypothesis of design approach 1. Additionally, work has been presented that addressed the challenge of multimerization and aggregation of the structures during purification. It was observed that large surface areas are prone to unspecifically interact with each other once subjected to harsh reaction conditions. This effect increases the more handles are included which is why the effect was most pronounced with DC-v0-2 structures that carried a maximum amount of 42 handles. Amicon filtration has been chosen as the method of purification. Systematic investigation of reaction parameters, such as the composition of the dilution buffer and stabilizing the structures with additional core staples resulted in a proper purification protocol.
In conclusion, amicon purification is able to remove excess interacting, functional handles from DC structures. It is crucial to use 6 mM $MgCl_2$ in the dilution buffer, to adjust the $MgCl_2$ concentration to 12 mM after amicon purification and to complement the structures with 2.5 pmol of core staple strands. It is recommended to fold DC structures

with a 20×staple strand excess. This way it is only necessary to complement amicon purified structures with 1.25 pmol core staples strand instead of 2.5 pmol.

6.3. Design approach 2: Maximized surface areas through reduced helical depth

Aiming for a maximization of the surface area, design approach 2 investigates whether it is possible to minimize the assigned scaffold per individual helix to 50 bps in order to provide more scaffold material for the assembly of further helices. Such a high density of short helices however, comes with certain design challenges. As described in the introduction of this chapter, one major challenge that needs to be addressed is the high number of staple crossovers. Figure 6.9 illustrates the axes along which crossovers need to be established in a square-lattice (A) versus a honeycomb-lattice design (B). Helix 0 in a square-lattice design has four surrounding helices to connect to while in a honeycomb-lattice those reduce to three. This also means that switching to honeycomb designs inherently reduces the amount of required staple crossovers by a factor of two.
Switching to another lattice however, should not be the only presented solution to reduce staple crossover density. Different applications require different geometries and spacing between functional sites. This motivates developing high density arrays and addressing the challenge of high staple crossover densities, not only on honeycomb-lattices but also on square-lattices.
One of the design innovations for a reduced staple crossover density is to satisfy two of the above mentioned axes by scaffold crossover. For square-lattices this means that staple crossovers only have to address the two residual axes. In case of the honeycomb-lattice staple crossovers are only established in one direction. Additionally, so called mini-scaf strands are introduced at the edges of the structures which replace further staple crossovers.
The short depth of the helices imposes the second design challenge. Contradicting the baseline rule to have a crossover every three helical turns, there is only room for one crossover per interface within 50 bp short arrays.

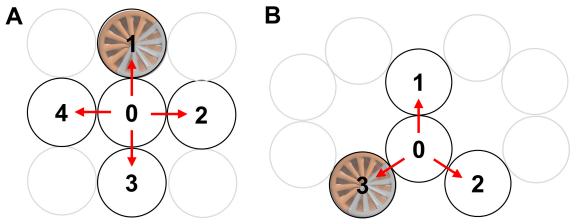

Figure 6.9.: Axes of crossover connections and nearest neighbors in square- vs. honeycomb-lattices. **A** On square-lattices each helix has four nearest neighbors and establishes crossovers in four different directions. **B** On honeycomb-lattices each helix has three nearest neighbors and thus only three axes along which crossovers are established. This leads to an inherently lower crossover density compared to square-lattice architectures.

6.3.1. Design and folding of flat DC-DNA arrays with a high aspect ratio

Design features of DC-v1-1

Design approach 2 was implemented for DC-v1-1 shown in figure 6.10. The previous design DC-v0 was used as starting point. By shortening the helix length from 118 bps to 50 bps,

scaffold becomes available to fold into 60 more helices for DC-v1-1 compared to DC-v0. The additional helices have been added in a third layer resulting in a 24×3 array (see figure 6.10 A). Figure 6.10 B includes a top view of the array showing the expected dimensions as well as a close-up of a subsection of the array on the far right with the scaffold routing highlighted blue and the staple routing highlighted pink. The whole array is divided into scaffold domains (gray) meaning that helices within gray domains are exclusively connected via scaffold crossovers. Staple crossovers connect between the domains. A 12 nt flexible scaffold linker additionally connects between gray and white domains. The path diagram in figure 6.10 C shows that DC-v1-1 exhibits two scaffold crossovers per interface but only one staple crossover per interface. This is not to confuse with the fact that all four crossover directions of the square-lattice are addressed. Demonstrated with helix 2 in 6.10 C one can see that the scaffold traverses via a double crossover to helix 2 and 3, while staples traverse via a single crossover to helix 7 and 9. This pattern is repeated throughout the whole structure. Crossovers are highlighted by arrows, the number next to the arrows indicates the targeted helix. Due to the short helix length, the deletion pattern from DC-v0 reduced to only one bp deletion per helix in DC-v1 indicated as cross in the red, dashed box.

Folding of DC-v1-1

DC-v1-1 is based on the p8064 scaffold. Figure 6.11 summarizes the data on initial folding experiments. 6.11 A shows a 2% native AGE gel that was used to analyze the optimal $MgCl_2$ concentration for the folding reaction and to compare two folding ramps 6025-18h and 5040-18h. From the gel one can conclude that a $MgCl_2$ concentration of 10 mM results in best folding judging from a clean, monomeric product band. Any $MgCl_2$ concentration above that results in aggregated material indicated by the black bands in the gel pockets. The gel does not depict a difference between the folding ramps. Both ramps yield similarly clean products. Overall, the product bands appear sharp and distinct which are indications for a proper folding of the structure. oxDNA simulations of the structures have predicted a pronounced, global, right-handed twist as shown in figure 6.11 C (i). TEM imaging confirmed these predictions as DC-v1-1 structures looked highly twisted on TEM grids and, also predicted by simulations, exhibit partially dissolved ends (figure 6.11 B and C (ii), (iii)). It is important to note, that oxDNA might not result in a correct prediction for the 12 nt flexible scaffold linker that also might have impact on the structures' twisting behavior. Thus the oxDNA predictions for these structures have to be interpreted carefully and can only serve as a rough guidance for design decisions.
In general, the experiments allow the conclusion that twist inherent to square-lattice designs seems to become even more pronounced when helices are shortened to 50 bps. Subsequent efforts focused on the evaluation of design changes to counteract the global twist and are going to be described in the following subsection.

6.3.2. Redesign cycle of high aspect ratio-arrays for less supertwisting

The path diagrams in figure 6.12 shows how the crossover positions have changed in DC-v1-2 compared to the previous design DC-v1-1. The overall crossover density is kept constant but half of the total amount of crossovers are swapped to result in an alternating offset. For explanatory purposes this is demonstrated for helix 2 in figure 6.12. Instead of having the staple crossing over to helix 7 and then helix 9 as in DC-v1-1, staple crossovers

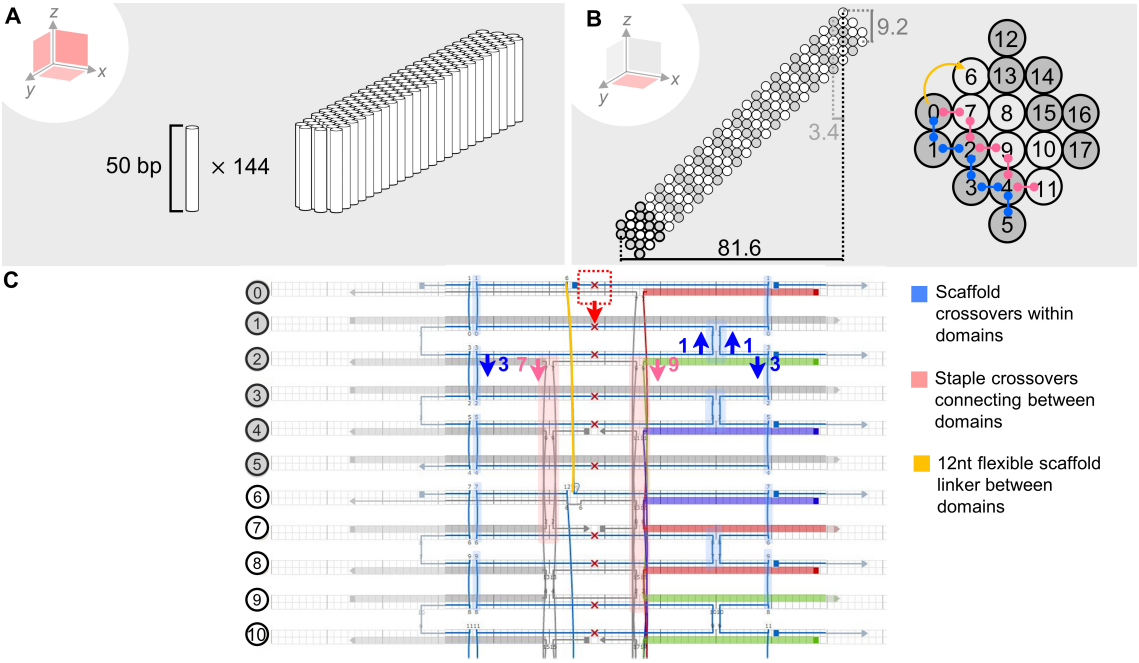

Figure 6.10.: Design approach 2: Helices shortened to 50 bps in a 24×3 array (DC-v1-1). **A** 3D view DC-v1-1 showing the amount and length of the helices. **B** Top view outlining the dimensions (left), scaffold and staple routing through the helices in blue and pink (right). The design is divided into gray and white domains. The far right close-up of the helices shows that scaffold crossovers (blue) connect within gray domains, staple crossovers (pink) connect between domains. Additionally, a 12 nt flexible scaffold linker connects between domains. **C** Path diagram highlighting the scaffold and staple crossovers with blue and pink arrows, respectively. Numbers next to the arrows indicate the helix targeted by the respective crossover. Demonstrated for helix 2, there are two scaffold crossovers for each of the interfacing helices 1 and 3 and only one staple crossover for the interfacing helices 7 and 9. This pattern is repeated throughout the whole structure.

in DC-v1-2 first jump to helix 9 and then to 7. Also the bp deletion pattern is slightly changed. Bp deletions are placed with an offset of 12 bps on each helix (see red, dashed boxes).

Folding of DC-v1-2

As all DC-v1 designs, DC-v1-2 is also based on the p8064 scaffold. Figure 6.13 shows a 2% native AGE gel analyzing the magnesium screening that has been again tested for two folding ramps, 6025-18h and 5040-18h. The same screening has been included for DC-v1-1 on the far left on the gel to have a direct comparison between both designs. $MgCl_2$ concentrations were varied from 10 mM to 16 mM in steps of 2 mM. In general, DC-v1-2 exhibits a higher level of multimerization as indicated by higher-order bands on the gel that get more pronounce with increasing $MgCl_2$ concentrations. The monomer gel bands for DC-v1-2 are also slightly broader compared to the 6025-18h gel bands in lanes (3)-(6) for DC-v1-1. A broader gel band could be an indication for a larger variety of partially folded structures. Overall, gel bands seem to be slightly broader for the 5040-18h

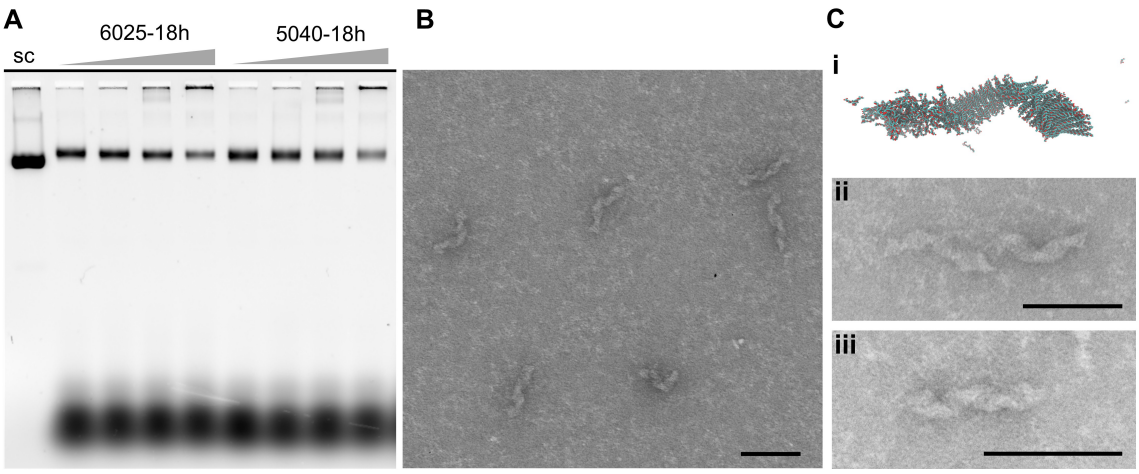

Figure 6.11.: Folding evaluation of DC-v1-1. **A** 2% native AGE gel for the analysis of a $MgCl_2$ screening from 10 mM to 16 mM final concentration tested for the two folding ramps 6025-18h and 5040-18h. (1) p8064 scaffold control, (2)-(5) DC-v1-1 folded with the 6025-18h ramp at increasing $MgCl_2$ concentrations starting from 10mM (2) up to 16 mM (5) in steps of 2mM. (6)-(9) DC-v1-1 folded with the 5040-18h ramp at increasing $MgCl_2$ concentrations starting from 10mM (6) up to 16 mM (9) in steps of 2mM; **B** Overview TEM image of DC-v1-1. Scale bar at 100 nm; **C** (i) oxDNA simulation of DC-v1-1 showing pronounced, right-handed twist (Data courtesy: Dr. Erik Benson); (ii), (iii) Close-up TEM images of DC-v1-1. Scale bars at 100 nm. TEM images show gel purified DC-v1-1 folded at 12mM $MgCl_2$ with 5040-18h.

Gel running parameters: 0.5×TBE buffer with 10 mM $MgCl_2$, EtBr 0.5 $\mu g/mL$, 60V for 4h at RT

ramp for both designs that suggests a tentative preference for the 6025-18h in both cases. Figure 6.13 B (i) is an oxDNA simulation of DC-v1-2 and predicts significantly less twisted structures compared to the predictions given on DC-v1-1 above. Figure 6.13 B (ii)-(iv) provides some representative TEM images of the DC-v1-2. In (iii) one can see a close-up TEM image of structures that seem to be much less twisted compared to the previous design. However, a second population of structures that looked very different (see (iv)) was observed. Those exhibited a "horseshoe"-like outline. At this point it is not clear whether this is a matter of how the structures are landing on the TEM grid or whether we observed topologically different structures. Further investigations revealed that these "horseshoe" structures also appear for DC-v1-1 but are much more populated for DC-v1-2. Overall, swapping half of the crossover positions helped to drastically reduce the supertwist and results in a straighter structural outline. However, the fact that there are structures that tend to bend into "horseshoe" like configurations motivates to further investigate a way to render the structures even straighter.

Folding of DC-v1-3

To further reduce the twist observed for the previous DC-v1 candidates, DC-v1-3 explores whether an increased staple crossover density for a higher structural stability. The crossover density was increased to an average of 1.7 staple crossovers per interface. This means that some helices connect to their neighbors via two staple crossovers instead of one. Additionally, the average staple strand length is increased compared to the previous designs. The increased crossover density reduces supertwisting in the oxDNA simulation

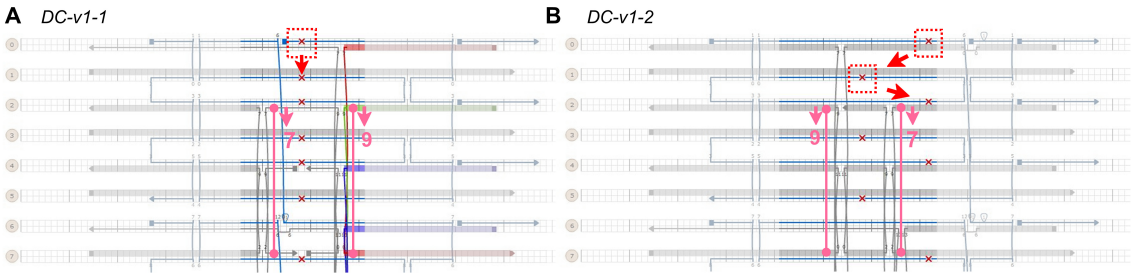

Figure 6.12.: Swapping crossover position for less supertwisting (DC-v1-2). **A** Cadnano path diagram of DC-v1-1 highlighting the staple crossover positions (pink) and their respective helix destination. Bp deletions are marked in red, dashed boxes. **B** Cadnano path diagram for DC-v1-2 showing how the crossover positions are swapped. Instead of crossing over to helix 7, the first staple crosses over to helix 9. This swapping has been performed for half of the crossovers of the structures as a measure to counteract the global twist.

shown in figure 6.14 B (i). Most intense gel product bands have been observed for 16 mM final $MgCl_2$ concentration for both temperature ramps (see figure 6.14 A). Samples folded with the 5040-18h ramp however, resulted in broader gel bands for the higher magnesium range and suggest that the 6025-18h ramp might be a better fit for this design. Despite promising product bands on the gel, TEM imaging revealed that the structures did not fold into the desired geometries. Misfolded structures and aggregated material has mainly been observed on the TEM grids (figure 6.14). Approaches to fold structures at even higher $MgCl_2$ concentration and with an extended ramp over the course of three days did not improve the folding of DC-v1-3 structures. The experiments performed for DC-v1-3 allow to conclude that an increased crossover density seems to deeply impact the stability of the structures and is thus not a suitable measure to reduce supertwisting.

6.3.3. Conclusion

Studies on design approach 2 have shown that in general it is possible to reduce the helix length of DNA origami structures to a minimum of 50 bps and still result in folded structures despite having only one staple crossover per interface. The working hypothesis that global twist that is inherent to square-lattice designs will be even more pronounced for these designs is something that has been indeed observed. As study platforms for new design rules, DC-v1 structures exhibited a global, right handed twist that can be slightly decreased by swapping half of the existing staple crossover positions in the design and by introducing a 12 bps offset of bp deletions. Increasing the staple crossover density does not - as initially hypothesized - support the stability of the structures or counteract the global twist, but sabotages the folding completely.

6.3.4. Design and experimental evaluation of flat DC-DNA arrays with a low aspect ratio

The second part of the design approach 2-working hypothesis stated above was that global twist could be balanced by adjusting the aspect ratio of the structures. It was of interest to find out whether global twisting across lower aspect ratios would be reduced compared to higher aspect ratios. This motivated the development of DC-v2 structures.

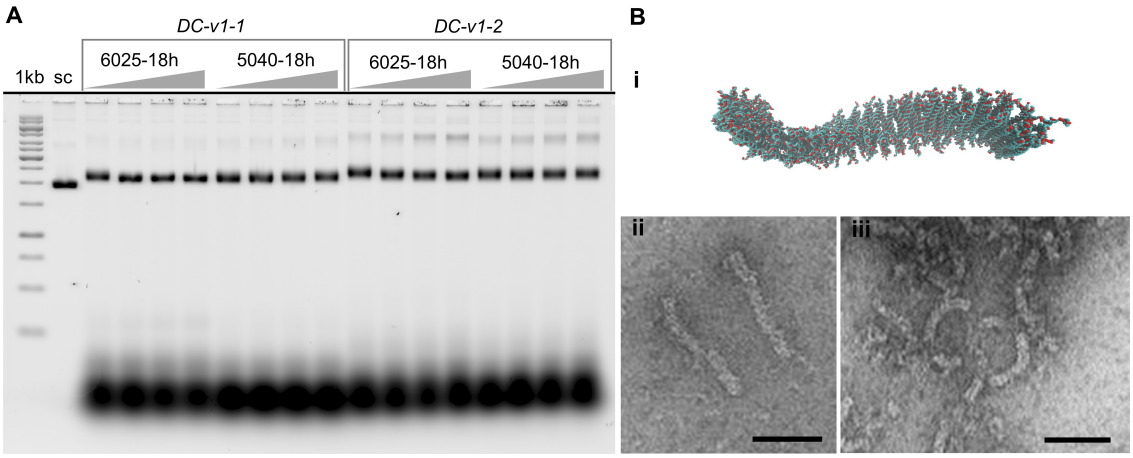

Figure 6.13.: Folding evaluation of DC-v1-2. **A** 2% native AGE gel for the analysis of a $MgCl_2$ screening from 10 mM to 16 mM final concentration tested for the two folding ramp 6025-18h and 5040-18h. (1) 1kb ladder, (2) p8064 scaffold control, (3)-(6) DC-v1-1 folded with the 6025-18h ramp at increasing $MgCl_2$ concentrations starting from 10 mM (3) ranging up to 16 mM (6) in steps of 2mM. (7)-(10) DC-v1-1 folded with the 5040-18h ramp at increasing $MgCl_2$ concentrations starting from 10mM (7) ranging up to 16 mM (10) in steps of 2mM, (11)-(14) DC-v1-2 folded with the 6025-18h ramp at increasing $MgCl_2$ concentrations, (15)-(18) DC-v1-2 folded with the 5040-18h ramp at increasing $MgCl_2$ concentrations (Data courtesy: Dr. Bhavik Nathwani). **B** (i) oxDNA simulation of DC-v1-2 predicting a drastic decrease in twist (Data courtesy: Dr. Erik Benson). (ii) and (iii) Close-up TEM images of DC-v1-2 folded at 12mM $MgCl_2$ with 5040-18h. Scale bars indicate 50 nm.

Gel running parameters: 0.5×TBE buffer with 10 mM $MgCl_2$, SYBR safe 0.5 $\mu g/mL$, 60V for 4h at RT

Design features of DC-v2-1 and DC-v2-2

As for DC-v1 structures, DC-v2 also consists of 144 helices that are 50 bps short and arranged on a diagonal-cut square-lattice. The main difference is, that instead of a 24×3 array, helices will assemble in a 12×6 array. DC-v2 thus exhibits a lower aspect ratio compared to the previously discussed DC-v1 structures.

Figure 6.15 A provides a 3D model of DC-v2. The top view in figure 6.15 B outlines the expected dimensions of DC-v2 as well as the scaffold and staple routing through the domains. The design features are equal to those already introduced for DC-v1. Two scaffold crossovers per interface connect helices within the gray domain, while one staple crossover connects helices between gray and white domains.

It has been shown for DC-v1-2 that swapping half of the crossover positions is an efficient way to reduce supertwisting. This design lesson was directly implemented for DC-v2 structures as well. DC-v2-2, a second DC-v2 candidate, exhibits half of the staple crossovers shifted by 10.5 bps to the left and right (see figure 6.15 C on the right). Also following the design strategies of DC-v1-2, an offset in the bp deletion pattern was incorporated for DC-v2-2 structures indicated in the dashed, red boxes aiming to reduce the strain of the structures.

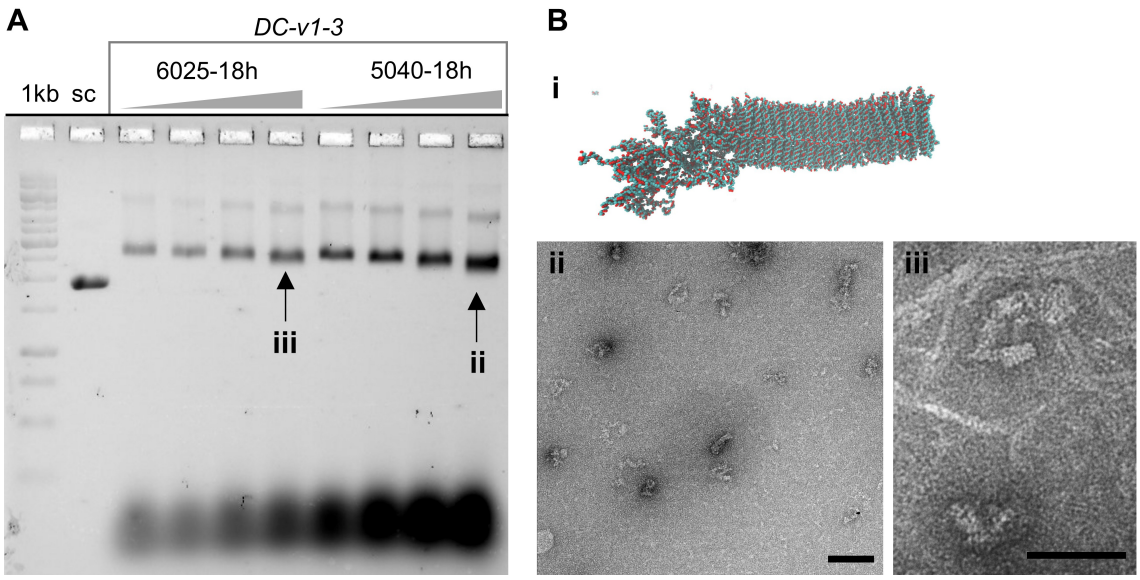

Figure 6.14.: Folding evaluation of DC-v1-3. **A** 2% native AGE gel for the analysis of a $MgCl_2$ screening from 10 mM to 16 mM final concentration tested for the two folding ramp 6025-18h and 5040-18h. (1) 1kb ladder, (2) p8064 scaffold control, (3)-(6) DC-v1-3 folded with the 6025-18h ramp at increasing $MgCl_2$ concentrations starting from 10 mM (3) ranging up to 16 mM (6) in steps of 2mM. (7)-(10) DC-v1-3 folded with the 5040-18h ramp at increasing $MgCl_2$ concentrations starting from 10mM (7) ranging up to 16 mM (10) in steps of 2mM (Data courtesy: Dr. Bhavik Nathwani); **B** (i) oxDNA simulation of DC-v1-2 predicting a drastic decrease in twist (Data courtesy: Dr. Erik Benson). (ii) Overview TEM image of DC-v1-3 folded at 16mM $MgCl_2$ with 5040-18h. Scale bar at 100 nm. (iii) Close-up TEM images of DC-v1-3 folded at 16mM $MgCl_2$ with 6025-18h. Scale bar at 50 nm.

Gel running parameters: 0.5×TBE buffer with 10 mM $MgCl_2$, SYBR safe 0.5 $\mu g/mL$, 60V for 4h at RT

Folding of DC-v2-1 and DC-v2-2

Figure 6.16 A shows the results for DC-v2-1 and v2-2 folded at a 12mM final $MgCl_2$ concentration and with the 5040-18h ramp. The folding parameters have been eliminated in prior standard experiments that included a magnesium screening and the comparison of different temperature ramps. Further experimental data for DC-v2-1 and DC-v2-2 are shown in figure 6.16 B and C, respectively.

The design process for DC-v2-2 was supported by oxDNA simulations that predicted a decent decrease of the global twist for DC-v2-2 structures. Screenshots taken from the oxDNA simulations for DC-v2-1 and DC-v2-2 in figure 6.16 B (i) and C (i) show a bottom (left) and front view (right) of the structures. DC-v2-1 exhibits a pronounced right-handed twist across the whole array. This is particularly visible looking at the front view where instead of having all helices aligned within one plane, one observes the back helices being tilted to the right compared to the front helices. It is remarkable how this global twist reduces for DC-v2-2 where the simulated front view of the structure is an almost perfect square meaning that all helices have the same orientation within the array. Gel electrophoresis can inform about the homogeneity of the sample and give indications of the overall structural stability. However, it is not possible to extract information about the twisting behavior of the structures from the gel. Thus, TEM images are included in

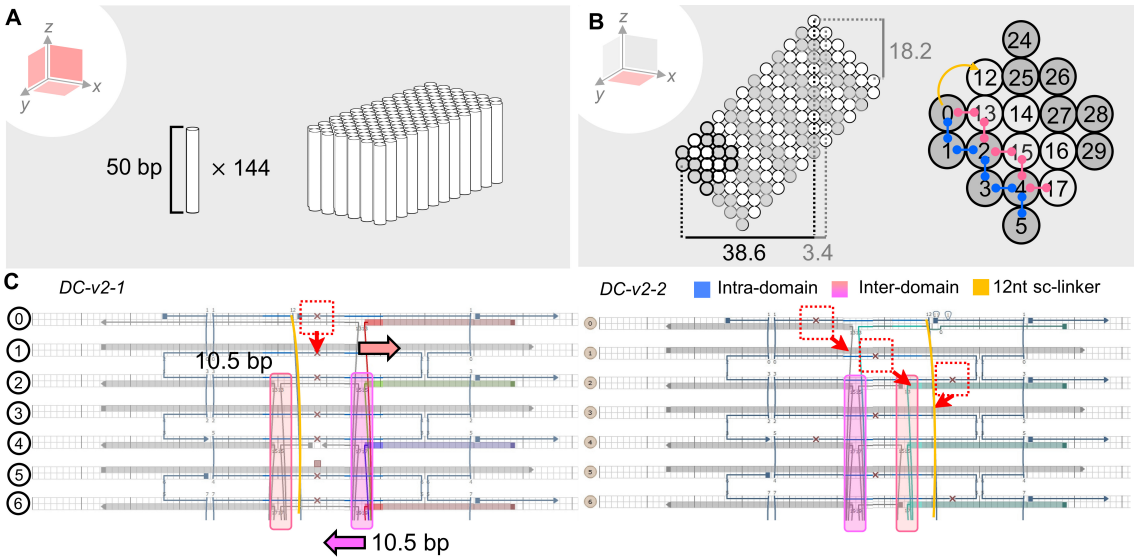

Figure 6.15.: Design approach 2: Lowering the aspect ratio for less supertwisting (DC-v2).**A** 3D view DC-v2 showing the amount and length of the helices. **B** Top view outlining the dimensions (left), scaffold and staple routing through the helices (right). It is divided into gray and white domains. The far right close-up of the helices shows that scaffold crossovers (blue) connect within domains, staple crossovers (pink) connect between domains. Additionally, a 12 nt flexible scaffold linker connects between domains. **C** Path diagram for DC-v2-1 on the left and DC-v2-2 on the right. Staple crossover positions for DC-v2-2 are shifted by 10.5 bps. For DC-v2-2 structures an offset in the bp deletion pattern (red, dashed boxes) is incorporated.

figure 6.16 B (ii) and C (ii).
Analyzing a larger amount of TEM images for DC-v2-1 and DC-v2-2 revealed that DC-v2-1 exhibits a higher population of misfolded or bent structures compared to DC-v2-2. Some examples of bent DC-v2-1 structures are shown in the close-up images in 6.16 B (iii). DC-v2-1 tends to kink close to its middle axis (indicated by the red arrow). This is something that has been observed less frequently for DC-v2-2 structures. Overall, DC-v2-2 structures seem to result in slightly straighter structures (see 6.16C (iii)) and appear less flexible on TEM images. The analysis of TEM images concerning the global twist of the structures is only an empirical one. So far, these TEM images serve as first indications that DC-v2-2 seems to be less twisted as predicted by the simulations. However, further investigations using a visualization technique that allows more insight into the twisting behavior of the structures will be necessary to draw a definite conclusion. Such a technique could be Cryo-EM imaging.

Purification of DC-v2-1 and DC-v2-2

New architectures are only of interest for further applications if they can maintain their structural integrity over time while subjected to purification procedures. Purification of the structures acts as an indirect tool to test the structures' stability. PEG purification was the method chosen for DC-v2 structures. For explanatory purposes, the following discussion on purification is split into two parts individually dealing with DC-v2-1 and v2-2.
Figure 6.17 is dedicated to DC-v2-1. **A** shows a 2% native AGE gel comparing the raw

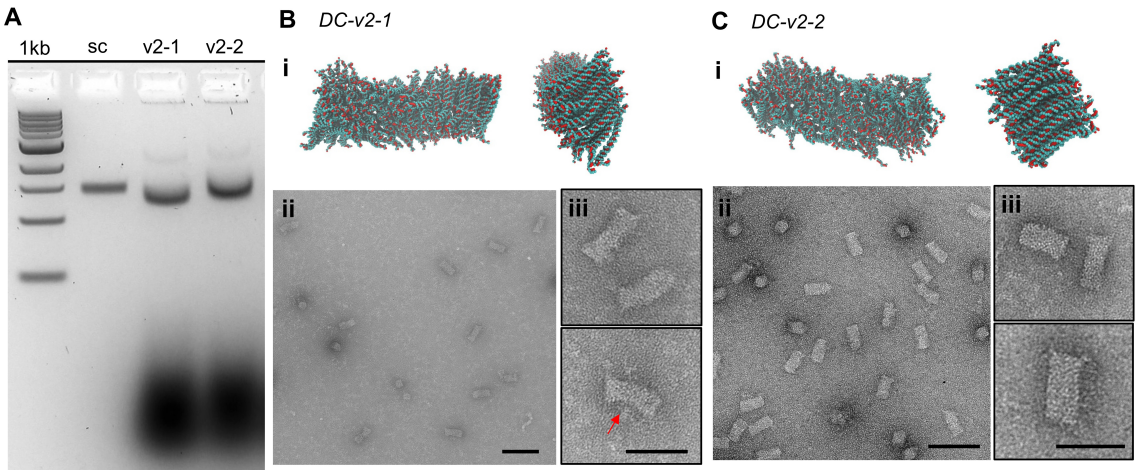

Figure 6.16.: Experimental data on DC-v2-1 and v2-2 folding. **A** 2% native AGE gel for the analysis of DC-v2-1 and v2-2 folding at 12 mM final $MgCl_2$ concentration and the 5040-18h ramp. (1) 1kb ladder, (2) p8064 scaffold control, (3) DC-v2-1 raw product, (4) DC-v2-2 raw product. **B** Screenshots were taken from oxDNA simulations and TEM analysis of DC-v2-1. (i) Simulated bottom (left) and front (right) view (Data coutesy: Dr. Erik Benson), (ii) Overview TEM image with scale bar at 100 nm, (iii) Close-up TEM image with scale bar at 50 nm. Red arrow pointing to the position at which DC-v2-1 structures tend to bend. **C** Screenshots were taken from oxDNA simulations and TEM analysis of DC-v2-2. (i) Simulated bottom (left) and front (right) view (Data courtesy: Dr. Erik Benson), (ii) Overview TEM image with scale bar at 100 nm, (iii) Close-up TEM image with scale bar at 50 nm (Data courtesy: Dr. Bhavik Nathwani)

Gel running parameters: 1×TAE buffer with 11 mM $MgCl_2$, SYBR gold pre-staining 1:10 000 dilution, 65V for 2.5 h at RT

folding sample in lane (3) with a sample that has been PEG purified using the standard protocol listed in appendix A.3. The gel confirms that the excess staple strands have been properly removed however the recovery yield is very low. This motivated the search for the optimal parameters for the PEG precipitation of DC-v2 structures that would result in high and pure yields. Thereby it has been found that the structures are highly sensitive toward the final magnesium concentration used in the PEG ppt buffer. Best results have been obtained when the final $MgCl_2$ concentration have been matched with the $MgCl_2$ used for folding which has been 12mM in this case. Lower or higher $MgCl_2$ concentrations led to a decent and up to a complete loss of structures in the supernatant.
Strategies such as titrating the percentage of PEG 8000 in the PEG precipitation (ppt) buffer or diluting the samples before being applied to the PEG buffer neither improved the recovery yield. Yields increased when PEG ppt buffers have been prepared fresh right before usage. Also it was found to impact the recovery yields when the $MgCl_2$ was added to the PEG ppt buffer first, followed by the addition of another equal amount of ppt buffer to balance the added magnesium. Only after that, the folding solution was added to the ppt buffer. Recovery yields were also found to be sensitive toward the sample volumes. For the refined protocol, the sample volumes that have been precipitated were fixed at 200 µL Mixing and equilibration time impacted the outcome as well. More details on the standard and refined PEG purification protocols are listed in appendix A.3.
Judged by the gel band intensity, figure 6.17 shows a pronounced increase in recovery yield for samples treated with the refined protocol. Image J analysis of the gel band intensities

in figure 6.17 B indicated a 53% recovery yield. However, samples that have been PEG purified using the refined protocol seem to be unstable over time. Lane (4) in figure 6.17 C contains the same sample as in lane (4) in B but having rested at 4°C over a week. One observes a high level of multimerization and aggregation for the rested sample which indicates a instability of the structures. Another reason subsequently hypothesized for the

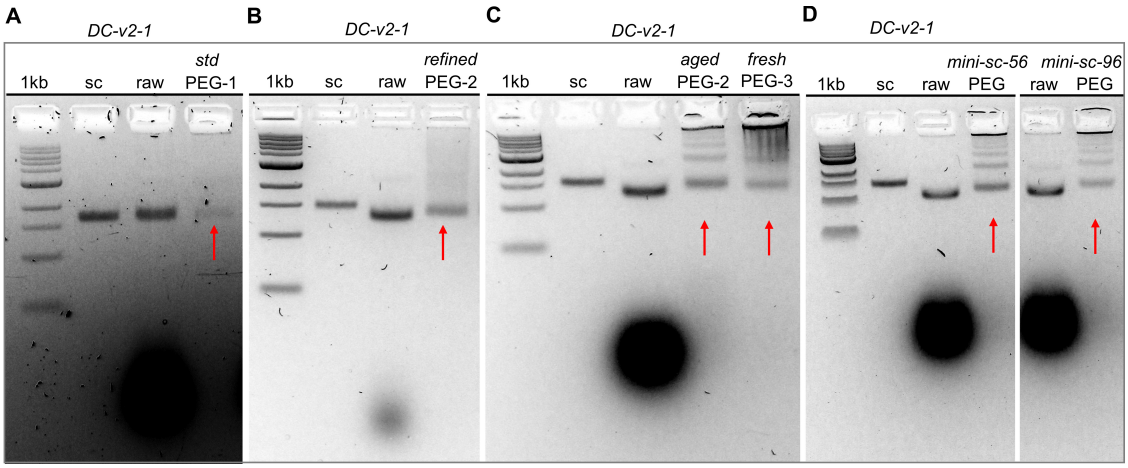

Figure 6.17.: Experimental evaluation of approaches to enhance the stability of DC-v2-1 structures toward PEG purification. 2% native AGE gels to analyze recovery yields of DC-v2-1 structures in different PEG ppt protocols, (1) 1kb ladder, (2) p8064 scaffold control, (3) raw DC-v2-1 folding sample. **A** (4) DC-v2-1 purified using the standard PEG ppt protocol. **B** (4) DC-v2-1 purified using a refined PEG ppt protocol. **C** (4) DC-v2-1 has have been purified with the refined PEG ppt protocol but analyzed after one week at 4°C, (5) DC-v2-1 purified with the refined PEG ppt protocol but purified right after folding. **D** (4) DC-v2-1 with 56 bps mini-scafs and purified with refined PEG ppt protocol, (6) DC-v2-2 with 96 bps mini-scafs and purified with refined PEG ppt protocol.

Gel running parameters: 1×TAE buffer with 11 mM $MgCl_2$, SYBR gold pre-staining 1:10 000 dilution, 65V for 2.5 h at RT

instability was that the folding of the structures might not have gone to completion and that some staples have not been incorporated quite yet. This could be one explanation for the observed instability of PEG purified samples. The hypothesis was validated twofold. First, it was tested whether some amount of equilibration time after folding could render the structures more tolerant toward purification. This would imply that freshly folded structures generally result in lower or less pure recovery yields.
The last lane in figure 6.17 C shows the results testing this hypothesis. PEG purified, fresh DC-v2-1 structures result in lower and less pure yields compared to "aged" DC-v2-1 that have had some time to equilibrate after folding shown in lane (4) in 6.17 B.
These experiments conclude that there is a rather small time window in which the structures have completely settled for their equilibrium after folding and purified structures start to multimerize.
The second approach to evaluate the above-stated hypothesis, was to fold DC-v2-1 and v2-2 structures over a longer folding ramp of 66h and investigate whether this affects recovery yields in PEG purification. The results for this experiment, however, did not show any indication that longer folding ramps would make the structures more stable. The samples have been run on 2% native AGE gels right next to PEG purified samples that have been folded using the standard 18h folding ramp. Gels can be found in the appendix

B.3. Another idea tested to support the stability of the structures toward purification was to include longer mini-scaf strands along the structures' edges. Lane (4) and lane (6) in figure 6.17 D contain PEG purified structures with either short (56 bps) or long (96 bps) mini-scaf strand, respectively. The same multimer bands show as in previous gels indicating that the length of mini-scaf strands does not influence the stability of the structures. Also, PAGE purification of the mini-scaf strand prior to use in folding did not improve the stability of the structures in PEG precipitation.
The same experiments have been performed for DC-v2-2 and are shown in 6.18. The trends are almost the same, but much more pronounced. Unlike with DC-v2-1, refined PEG purification protocols did not result in better yields. Also, DC-v2-2 seem to be unstable over time and different lengths of mini-scaf strands did not benefit the stability of the DC-v2-2 structures.

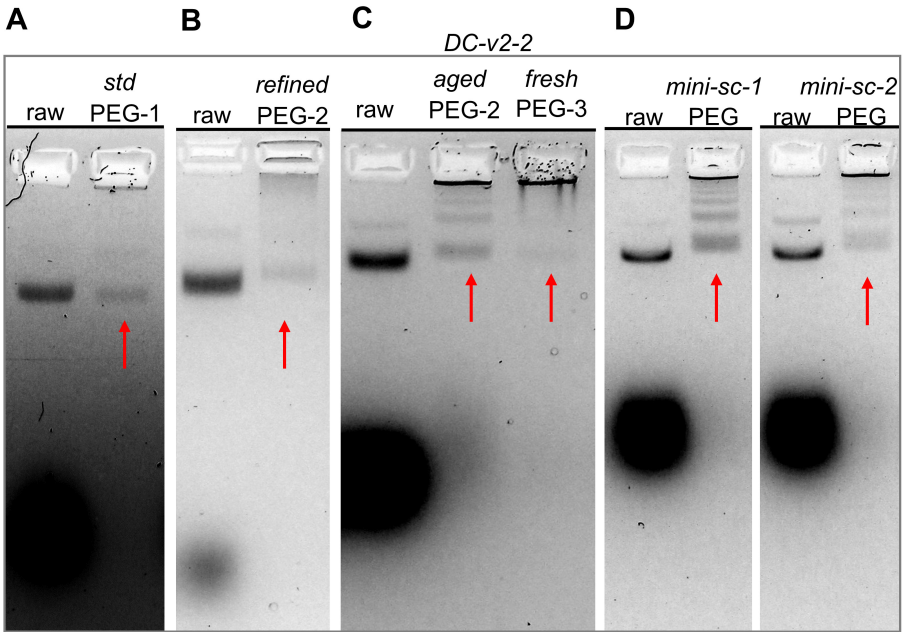

Figure 6.18.: Experimental evaluation of approaches to enhance the stability of DC-v2-2 structures toward PEG purification. 2% native AGE gels to analyze recovery yields of DC-v2-2 structures in different PEG ppt protocols, (1) raw DC-v2-2 folding sample. **A**(2) DC-v2-2 purified using the standard PEG ppt protocol. **B** (2) DC-v2-2 purified using a refined PEG ppt protocol. **C** (2) DC-v2-2 that has been purified with the refined PEG ppt protocol but again analyzed after one week at 4C, (3) DC-v2-2 purified with the refined PEG ppt protocol but purified right after folding. **D** (left) (2) DC-v2-1 with 56 bps mini-scafs and purified with refined PEG ppt protocol, (right) (2) DC-v2-2 with 96 bps mini-scafs and purified with refined PEG ppt protocol. General note: Only a subset of the gels is shown for a better overview of the key samples. Appendix B.4 and B.5 provides the whole data set.

Gel running parameters: 1×TAE buffer with 11 mM $MgCl_2$, SYBR gold pre-staining 1:10 000 dilution, 65V for 2.5 h at RT

6.3.5. Conclusion

Studies on DC-v2 structures confirmed the initially proposed hypothesis that global twists across shallow arrays of densely packed helices can be reduced by a reduction of the as-

pect ratio. Compared to 24×3 arrays (DC-v1 structures) that lead to highly supertwisted structures, 12×6 arrays (DC-v2 structures) exhibited a drastic decrease in global twists both in simulation and experimentally observed on TEM images. This is going to be further validated through higher resolution visualization techniques in the future. However, the data presented allows us to say that the twist decrease can presumably be attributed to a higher moment of torsional inertia that results from a smaller aspect ratio. Recovery yields in PEG precipitation were low for the standard protocol but can be increased through delicate changes in the purification procedure and the preparation of fresh PEG buffer. Despite an improvement of the recovery yield, the fact that the structures respond so sensitively to changes in the purification protocol is concerning. Purified DC-v2 structures also revealed an instability as they start to multimerize with time. Despite fine-tuning of the purification protocols and slight adaptations of the design, structures remained unstable.

Motivated by these results, a new re-design cycle was initiated aiming for more stable structures. The lesson learnt from studies on DC-v2 structures that lower aspect ratios are indeed a valid strategy to reduce global twists was thereby taken into consideration.

6.3.6. Design and folding of square-shaped DC-DNA arrays

Design features of DC-v3

Now that strategies have been found to reduce the internal twist of shallow structures, the challenge addressed in this design cycle was to find suitable design features that could stabilize these structures and render them tolerant toward purification. This is approached by going back to the baseline rule of having two staple crossover positions per interface, by an even lower aspect ratio compared to the previously discussed DC-v2 architectures as well as by a slight increase of the helical depths.

DC-v3 structures are square-shaped, 9×9 arrays and consist of 200 helices as illustrated in figure 6.19 A. Hence they exhibit a 38% larger surface area compared to DC-v2 structures. Within the DC-v3 category, two design strategies have been evaluated. The scaffold routing thereby remained the same as well as the bp deletion pattern. However, they differ in staple crossover patterns, scaffold length, and helix depth.

DC-v3-1 is 50 bps short and relies on the p8064 scaffold that is not completely used up for the main body of the structure. The residual 595 nt of the p8604 scaffold are thus designed to fold into a six-helix bundle that is 33 nm long.

DC-v3-1 uses both of the two possible crossover directions. To understand the cross-sectional view in 6.19 B should be consulted. As an example, helix 2 has two remaining axes for staple crossovers pointing to helix 21 and helix 23. The main characteristic of DC-v3-1 is that it crosses over both helices via two staple crossovers per interface. This is highlighted for helix 2 in the path diagram in figure 6.19 C. As a consequence, DC-v3-1 exhibit four staple crossovers per interface. DC-v3-2, on the other hand, only uses one of the two possible directions for staple crossovers and relies on the larger scaffold p8634. Figure 6.19 B shows which one is used by the non-opaque, pink connections. In the case of helix 2, staples only crossover to helix 23 via two crossover positions. This is hypothesized to lead to a slight deviation from the square-shaped outline. The fact that DC-v3-2 only uses three axes for crossovers turns it into an intermediate architecture between a square- and honeycomb-lattice.

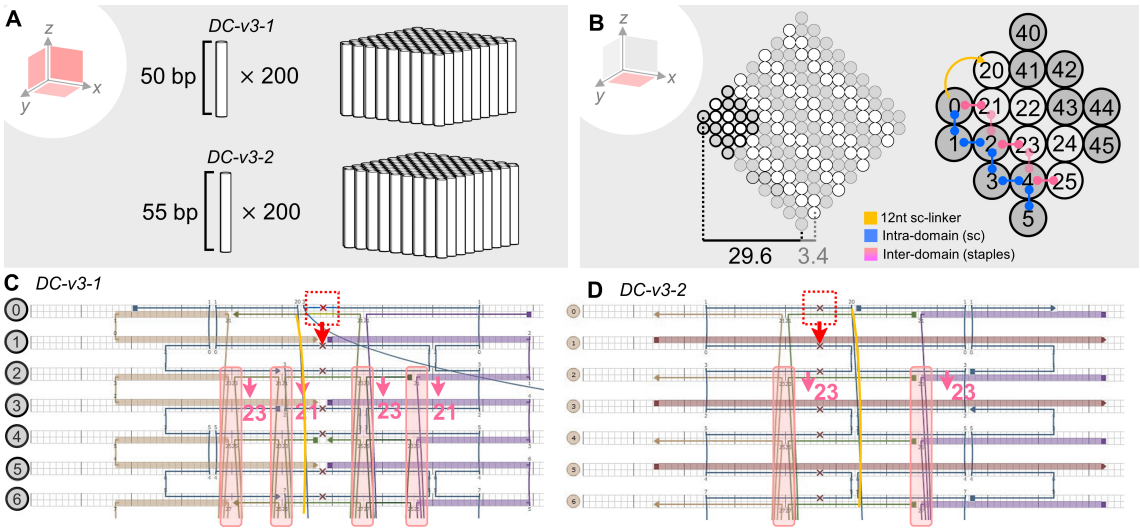

Figure 6.19.: Re-design cycle of DC-v2 for higher stability: Design features of DC-v3. **A** 3D model of DC-v3-1 and v3-2. Both are 9x9 arrays consisting of 200 helices. DC-v3-1 is 50 bps short, DC-v3-2 is 55 bps short. **B** Top view of the sqaure-shaped architecture. Close-up view on a subset of the structure showing the scaffold and staple pattern. Two of the four possible crossover axes are occupied by scaffold crossovers (blue routing in gray domain). DC-v3-1 is using both remaining axes for staple crossovers while DC-v3-2 is only using one axis (non-opaque, pink). **C** Subset of the path diagram for DC-v3-1 (left) and DC-v3-2 (right) showing four crossover positions for DC-v3-1 (two per possible direction) and two crossover positions for DC-v3-2 (two for only one possible direction). Bp deletion pattern is unchanged and no offset is incorporated.

Folding of DC-v3-1 and DC-v3-2

Figure 6.20 displays the result of a magnesium screening and TEM analysis for the DC-v3-1 architecture. Folding was performed at different final $MgCl_2$ concentrations ranging from 6 mM to 18 mM and using the two folding ramps 5040-18h and 6025-18h. The different folding conditions were analyzed and compared on a 2% native AGE gel. A sharp and intense monomer band is typically an indication for successful folding at high yields. Gel band intensities dropped for both temperature ramps at $MgCl_2$ concentrations of 14 mM to 18 mM. The product bands for the 6025-18h ramp overall exhibited a decent gel shift which usually is an indication of incomplete folding. The p8064 scaffold control in lane (2) displays higher order bands that most likely originate from a pipetting error that caused some material of the 1kb ladder in lane (1) to leak to the second gel pocket. DC-v3-1 is a good example to show how important it is to consult a second technique for verification such as TEM imaging. Although the folding of DC-v3-1 resulted in sharp gel bands, TEM imaging of the 10 mM $MgCl_2$ sample for both ramps revealed that those gel bands did not correspond to properly folded structures. Instead one observes lumps of aggregated material. This is evidence enough to conclude that the DC-v3-1 design strategy does not assemble into well-behaved structures. Thus DS-v3-1 was set aside and studies continued with the DC-v3-2 architecture.

Figure 6.21 summarizes experimental data on the folding of DC-v3-2. As before, a 2% native AGE gel was used to analyze a magnesium screening and to compare the performance

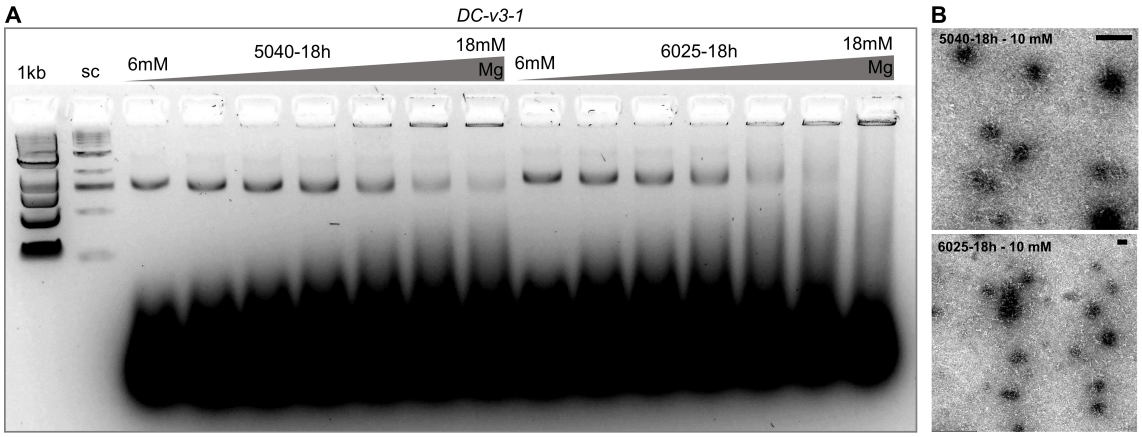

Figure 6.20.: Experimental data on DC-v3-1 folding. **A** 2% native AGE gel analysis of the $MgCl_2$ screening for DC-v3-1.$MgCl_2$ concentrations range from 6 mM to 18 mM in steps of 2 mM. (1) 1 kb ladder, (2) p8064 scaffold control, (3)-(9) DC-v3-1 folding using the 5040-18h temperature ramp and at increasing $MgCl_2$ concentrations ranging from 6 mM to 18 mM in steps of 2 mM, (10)-(16) DC-v3-1 folding using the 5040-18h temperature ramp and at increasing $MgCl_2$ concentrations ranging from 6 mM to 18 mM in steps of 2 mM. **B** TEM imaging of DC-v3-1 folded with 5040-18h at 10 mM $MgCl_2$ concentration (top), TEM imaging of DC-v3-1 folded with 6025-18h at 10 mM $MgCl_2$ concentration (bottom); scale bars at 100 nm.

Gel running parameters: 1×TAE buffer with 11 mM $MgCl_2$, SYBR gold pre-staining 1:10 000 dilution, 70V for 2h 20min cooled in ice bath

of the two folding ramps 5040-18h and 6025-18h. Two controls of DC-v3-1 were included to have a direct comparison between the two designs. The gel ran a day after the one for DC-v3-1. The fact that the gel band intensity of DC-v3-1 controls on this gel dropped remarkably, shows again that the structures are not well-behaved and probably keep on dissolving or forming higher-order complexes. The gel bands for DC-v3-2 are quite diffused for all conditions tested except for the 6025-18h ramp at $MgCl_2$concentrations of 14 mM and 16 mM (red arrows). Here, one observes gel bands that are of low intensity, however quite sharp. Figure 6.21 B shows TEM images of DC-v3-2 folded at 14 mM final $MgCl_2$ concentration and over the course of 66h. The particles exhibit the expected outline, however they appear more diamond-shaped than square-shaped. This effect is attributed to using only one of the two possible crossover directions that might cause strain along the unoccupied crossover axis. However, the effect does not conflict with the design goals and can thus be left uncorrected.

Purification of DC-v3-2

The stability of the structures has been again accessed via PEG purification. Section 6.3.4 presented a refined PEG purification protocol with conditions that are more suited for the square-lattice structures in question. Thus, the following experiments are based on the refined protocol. Details can be found in appendix A.3 Testing longer folding ramps like 66h was motivated fourfold. First, the low folding yields observed on the gel in 6.21 A were thought to be improved by 66h folding. Second, it was interesting to investigate whether one could spot a difference in the purification recovery yield. Since it has been found in studies on DC-v2 structures that higher recovery yields do not necessarily correlate with

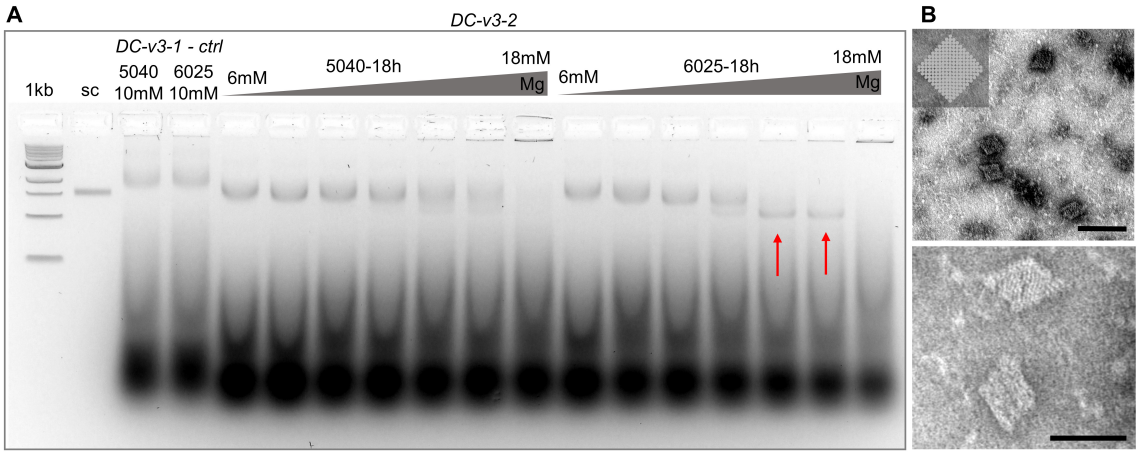

Figure 6.21.: Experimental data on DC-v3-2 folding. **A** 2% native AGE gel analysis of the $MgCl_2$ screening for DC-v3-2. (1) 1 kb ladder, (2) p8064 scaffold control, (3) Raw folding of DC-v3-1 at 10 mM $MgCl_2$ using the 5040-18h temperature ramp, (4) Raw folding of DC-v3-1 at 10 mM $MgCl_2$ using the 6025-18h temperature ramp, (5)-(11) DC-v3-2 folded with the 5040-18h temperature ramp and at increasing $MgCl_2$ concentrations ranging from 6 mM to 18 mM in steps of 2 mM, (12)-(18) DC-v3-2 folded with the 6025-18h temperature ramp and at increasing $MgCl_2$ concentrations ranging from 6 mM to 18 mM in steps of 2 mM. **B** TEM imaging of DC-v3-2 folded at 14 mM $MgCl_2$ with the 6025-66h folding ramp. Illustrated top view in the upper left corner. Overview image (top) with scale bar at 100 nm and close-up image (bottom) with scale bar at 50 nm. Comparison of the TEM results with the illustration shows the expected deviation of the observed particles from the square-shaped outline due to the crossovers that are only going in one direction.

Gel running parameters: 1×TAE buffer with 11 mM $MgCl_2$, SYBR gold pre-staining 1:10 000 dilution, 70V for 2.5h cooled in ice bath

the long-term stability of the DC structures it was a third question whether the DC-v3 structures gain higher stability toward PEG purification when folded over longer time scales and fourth whether this stability is time-sensitive. Results of the PEG purification for DC-v3-2 have been analyzed on a 2% native AGE gel shown in figure 6.22. The gel pieces shown originate from two large gel that have been cut for a better presentation of the key findings. For the complete data set, the reader is forwarded to the appendix B.6.

The gel band intensities for the raw samples in lanes (3) and (5) are equally low meaning that with respect to folding yields there is not detectable difference between 18h and 66h folding ramps. However, the gel does show a higher recovery yield for DC-v3-2 structures that have been folded over the course of 66h. The monomer band for the PEG purified sample in lane (4) is less intense compared to the monomer band in lane (6). Both PEG purified samples however, do show slight multimerization and aggregation in the gel pockets whereby the trend was more pronounced for 66h folded samples. The main improvement of this design approach compared to earlier described architectures is that this multimerization does not increase over time as indicated by the last four lanes in 6.22. These gel lanes correspond to the same samples shown in lanes (3)-(6), but have rested at 4°C overnight before they have been analyzed again on the gel. Previous designs have shown a drastic increase in multimerization and aggregation once rested overnight. This seems not to be the case with DC-v3-2 structures which is an overall indication for better

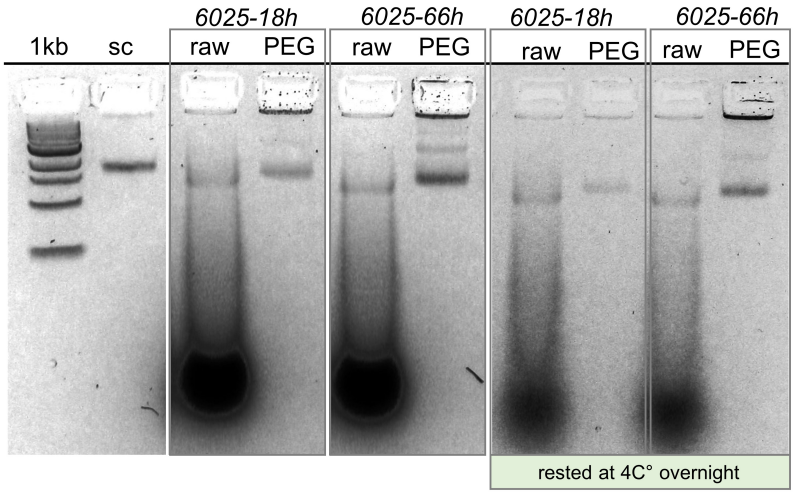

Figure 6.22.: Gel evaluation of PEG purification of DC-v3-2. 2% native AGE gel comparing the recovery yields of PEG purified DC-v3-2 folded over the course of 18h vs. 66h. (1) 1kb ladder, (2) p8634 scaffold control, (3) Raw DC-v3-2 folded at 14 mM $MgCl_2$ with the 6025-18h ramp, (4) PEG purified DC-v3-2 that had been folded at 14 mM $MgCl_2$ with the 6025-18h, (5) Raw DC-v3-2 folded at 14 mM $MgCl_2$ with the 6025-66h, (6) PEG purified DC-v3-2 that had been folded at 14 mM $MgCl_2$ with the 6025-66h, (7)-(10) Same samples as in (3)-(6) but rested at 4°C overnight.

Gel running parameters: 1×TAE buffer with 11 mM $MgCl_2$, SYBR gold pre-staining 1:10 000 dilution, 65V for 2h cooled in ice bath

stability of the structures once PEG purified. It is to note that the last four lanes originate from a separate gel meaning that one has to be cautious about a direct comparison of the overall yields. Deviations in gel band intensity could have many reasons related to the fact that the last samples ran on a different gel. However, in terms of multimerization, it is indeed possible to say that the degree of multimerization did not increase with the resting time of the sample.

6.3.7. Conclusion

The DC-v3 architectures exemplify how crucial it is to fine tune crossover density within DNA origami structures and show how this design parameter can even cause a complete failure of the folding performance. Figure 6.23 summarizes again the design difference between DC-v3-1 and v3-2 in terms of the occupied crossover axes. While DC-v3-1 uses two axes for staple crossovers, DC-v3-2 only uses one of the possible two directions. Additionally, these designs come back to the baseline rule of having at least two crossover positions per interface. Using both possible crossover axes thus results in four staple crossovers per interface for DC-v3-1. Efforts to design the staple toeholds as long as possible to generate enough binding energy generates less straightforward staple paths compared to the ones in DC-v3-2 structures. It was found that these design choices led to an all-or-nothing response in terms of folding. The DC-v3-1 design did not achieve any proper assembly, while DC-v3-2 resulted in the expected structures. The refined PEG purification protocol that has been optimized for the DC-v2 architectures and discussed in the previous section resulted in reasonable recovery yields for DC-v3-2 structures. Longer folding ramps did not improve the folding yields of DC-v3-2 structures but did have a positive impact on

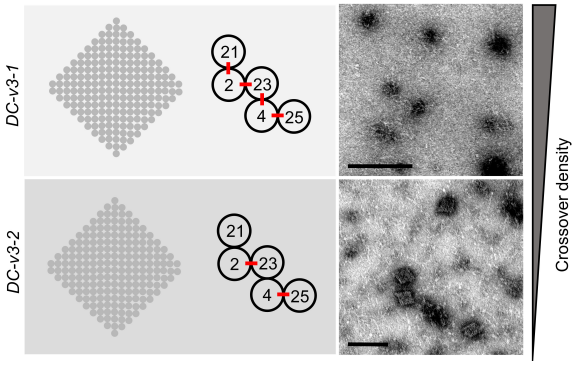

Figure 6.23.: Crossover density is crucial for shallow square-lattice based, diagonal-cut structures. Four staple crossover positions per interface leads to a complete failure of the folding process. Reducing this density down to two crossovers per interface helps to re-establish proper folding.

the recovery yields in PEG purification. The degree of multimerization observed for PEG purified structures remained constant over time which is a sign for a much more stable architecture compared to previously studied DC-v2 structures. These studies conclude the following for square- lattice, diagonal-cut arrays. It is indeed possible to shrink the helical depth down to 50 bps. However, it is recommended to slightly increase this depth to around 55 bps to provide enough room for two crossover positions per interface as this drastically improves the stability of the structures.

6.3.8. Implementation of design approach 2 into hexagonal-shaped honeycomb-lattices

Design features of HC-v0-1 and HC-v0-2

The DC-v3 architectures, despite being designed on a square-lattice, can be understood as an intermediate between square- and honeycomb-lattices since it is not using all four axes for possible crossovers offered by the square-lattice. Rather they are using three of them two axes are occupied by scaffold crossovers and one is reserved for staple crossovers. This is one way to reduce staple crossover density which we have seen in section 6.3.6 is crucial for successful folding. Honeycomb-lattices, per definition, only have three axes for possible crossovers thus reducing the staple crossover density by the factor of two compared to square-lattice designs. Since the subject of reducing staple crossover density by addressing only three axes has shown promising results in section 6.3.6, the goal of further design work was to transfer the design challenge of maximizing surface areas to honeycomb-lattices. The following presents three honeycomb-based architectures that investigate strategies to assemble large and stable arrays consisting of helices with a minimum depth of 55-56 bps and three staple crossovers per interface but restricted to one of the three axes.
Figure 6.24 A illustrates the overall outline of the honeycomb-lattice architecture HC-v0. It is made from 182 helices with a depth of 55 bps arranged to a hexagonal disc. A top view of the disc in 6.24 B on the left shows its dimensions. Shifting from diagonal-cut arrangements to a honeycomb-lattice increased the functional site-distance to 4.2 nm. Along the north-south axis the disc measures around 33.0 nm, along the east-west axis is 44.4 nm. Scaffold and staple routings are shown in the close-up illustration next to the top

view in 6.24 B. Two of the three axes of the honeycomb unit cell are occupied by scaffold crossovers shown in blue, while the vertical axis is reserved for staple crossover highlighted in pink. A 12 nt, flexible scaffold linker shown in yellow connects the individual layers. Figure 6.24 C shows the path diagrams for two candidates of HC-v0. Both exhibit three crossover positions per interface. Demonstrated for helix 1, one can see that in the first version HC-v0-1 the middle staple of the three staples is circular, meaning it comes back to helix 1 once it visited helix 14. This is the main and only difference to the second candidate HC-v0-2 where all three staples are linear. The second candidate is hypothesized to lead to faster and more robust folding compared to the first version. No specific bp deletion pattern is necessary for honeycomb-lattice structures since this arrangement of helices per se better fits the natural geometry of B-DNA.

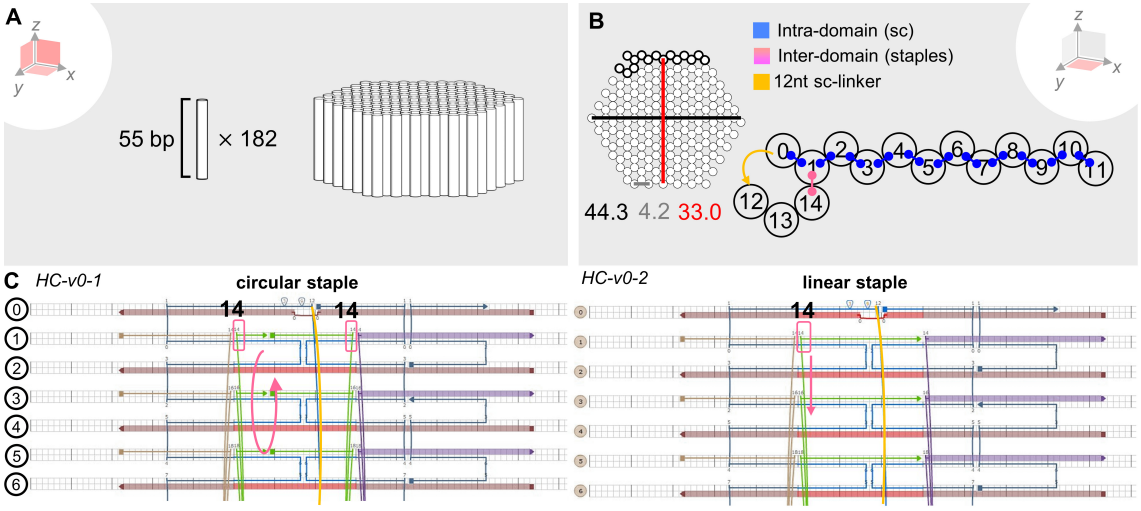

Figure 6.24.: Design approach 2 on a honeycomb-lattice: Design features of HC-v0-1 and v0-2. **A** 3D illustration of HC-v0. 182 helices assemble into a 55 bps short hexagonal disc. **B** Top view of the hexagonal disc outlining the dimensions. The functional-site distance is 4.2 nm, the north-south axis measures 33.0 nm, the east-west axis 44.4nm. Two of the three available axes per helix for crossovers are occupied by the scaffold (blue) and one by the staples (pink). The routing is depicted in the close-up illustration next to the top view. A 12 nt, flexible scaffold linker connects the layers.**C** Path diagram for HC-v0-1 on the left and HC-v0-2 on the right highlighting the different staple paths for the middle staple. On each helix three crossovers are realized in one direction. The middle one follows a circular path for HC-v0-1 and a linear path for HC-v0-2.

Folding of HC-v0-1 and HC-v0-2

Figure 6.25 shows experimental data of the folding and TEM imaging of the HC-v0-1 candidate which is the one with the circular staple path. A 2% native AGE gel was used to analyze the magnesium screening and compare the two temperature ramps 5040-18h and 6025-18h. Judging from band sharpness and brightness, the best folding conditions have been achieved for 5040-18h ramps at $MgCl_2$ concentrations between 10-14 mM and for 6025-18h at $MgCl_2$ concentrations of 12 and 14 mM. TEM images in 6.25 B verify that the observed gel band indeed correspond to properly folded monomers.

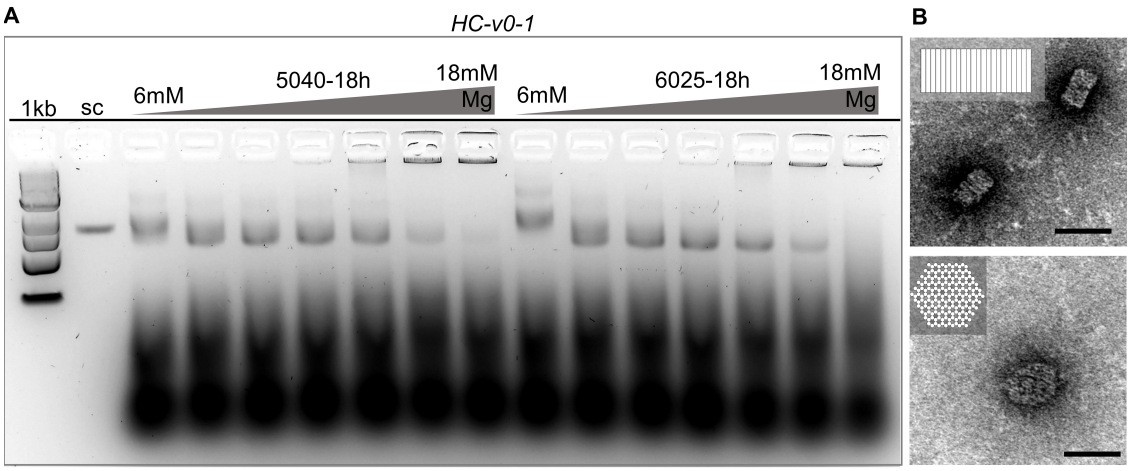

Figure 6.25.: Experimental data on HC-v0-1 folding. **A** 2% native AGE gel analysis of different folding conditions. (1) 1 kb ladder, (2) p8064 scaffold control, (3)-(9) Raw HC-v0-1 folded with the 5040-18h ramp at $MgCl_2$ concentrations ranging from 6 to 18 mM in steps of 2 mM, (10)-(16) Raw HC-v0-1 folded with the 6025-18h ramp at $MgCl_2$ concentrations ranging from 6 to 18 mM in steps of 2 mM. **B** (top) TEM image of HC-v0-1 folded with the 6025-18h ramp at 14 mM $MgCl_2$ concentration; (bottom) TEM image of HC-v0-1 folded with the 5040-18h ramp at 10 mM $MgCl_2$ concentration; scale bars at 50 nm.

Gel running parameters: 1×TAE buffer with 11 mM $MgCl_2$, SYBR gold pre-staining 1:10 000 dilution, 70V for 2h 20min cooled in ice bath

The same folding parameters were tested for HC-v0-2 and are shown in figure 6.26. Similar to HC-v0-1 but more pronounced, this design revealed a distinct preference for the 6025-18h folding ramp and $MgCl_2$ concentrations between 10-14 mM. At these conditions, folding resulted in very sharp and intense gel bands running at the same height as the HC-v0-1 controls in lanes (2) and (3). Control 1 refers to HC-v0-1 folding with the 5040-18h ramp at 10 mM $MgCl_2$ concentration. Control 2 refers to HC-v0-1 folding with the 6025-18h ramp at 14 mM $MgCl_2$ concentration. Ran side by side shows that ctrl 2 exhibits a sharper gel band compared to ctrl 1 which again confirms that also HC-v0-1 seems to fold better using the 6025-18h folding ramp. HC-v0-2 folded at 6 mM $MgCl_2$ concentration ran with a pronounced gel shift which is a general indication for misfolded or incomplete structures. Gel bands for the 5040-18h folding ramp are very diffuse and broad. TEM imaging shown in 6.26 B shows HC-v0-2 folded over the course of 66h and confirm that the design results the in proper assembly of the hexagonal disc. The top TEM image shows a top view of the disc, the bottom TEM image shows a side view. Both views match the theoretical expectations according to shape and dimension.

Purification of HC-v0-1 and HC-v0-2

Purification of HC-v0-1 and v0-2 was performed with the refined PEG ppt protocol developed in section 6.3.4. Details can be found in A.3. As it was shown that 66h folding ramps have the potential to render the large square-lattice arrays more stable toward PEG purification, it was interesting to see whether this heolds true for honeycomb-based architectures as well. Figure 6.27 shows the 2% native AGE gel analysis of the purified HC-v0-1 and v0-2 folded over the course of 18h vs 66h. Lanes (3)-(10) refer to the purification of HC-v0-1. Lanes (11)-(18) refer to the purification of HC-v0-2. Lanes labeled as "PEG"

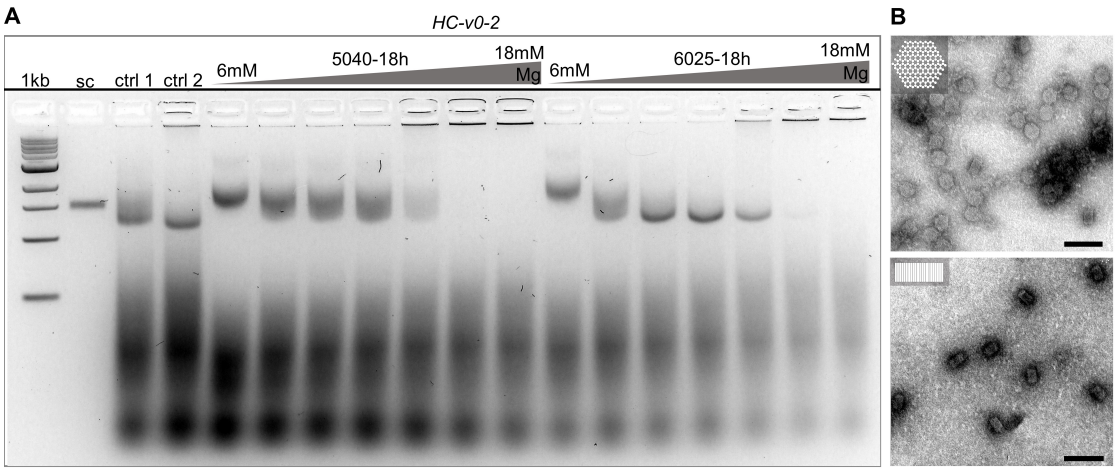

Figure 6.26.: Experimental data on HC-v0-2 folding. **A** 2% native AGE gel analysis of different folding conditions. (1) 1 kb ladder, (2) p8064 scaffold control, (3) Control 1: HC-v0-1 folded with 5040-18h at 10mM $MgCl_2$ concentration, (4) Control 2: HC-v0-1 folded with 6025-18h at 14mM $MgCl_2$ concentration, (5)-(11) Raw HC-v0-2 folded with the 5040-18h ramp at $MgCl_2$ concentrations ranging from 6 to 18 mM in steps of 2 mM, (12)-(18) Raw HC-v0-2 folded with the 6025-18h ramp at $MgCl_2$ concentrations ranging from 6 to 18 mM in steps of 2 mM. **B** TEM images of HC-v0-2 folded with the 6025-66h ramp at 14 mM $MgCl_2$ concentration, scale bars at 100 nm.

Gel running parameters: 1×TAE buffer with 11 mM $MgCl_2$, SYBR gold pre-staining 1:10 000 dilution, 70V for 2h 20min cooled in ice bath

refer to the PEG purified samples and are normalized to the "raw" samples with respect to the loaded sample amount. Lanes labeled as "PEG-2" also contain PEG purified samples but double the amount compared to the raw samples. This was done as a precautionary measure in case yields of PEG purification would be so low that they are hard to resolve on the gels. Since the normalized "PEG" lanes are all detecable, "PEG-2" lanes can be ignored for this discussion. Overall, one has to point out that PEG purified samples for both designs show no or very little multimerization, though some aggregation in the gel pockets. Recovery yields for both designs are improved with a preceding 66h folding ramp. It is noticeable that for all conditions there is a detectable amount of structure lost in the supernatant ("SN"). This could be caused by a less efficient capturing mechanism in the pellet during PEG precipitation and could be tackled by further fine tuning of the PEG ppt protocol. These samples were separately investigated on a native AGE gel after resting at 4°C overnight to see whether PEG purified structures remain stable. Results show that this is the case and can be found in appendix B.7.

TEM imaging was performed for both designs, HC-v0-1 and v0-2, before and after PEG purification to first judge whether gel bands observed in figure 6.27 correspond to distinct, monomeric structures and second to see whether structures maintain their structural integrity after PEG precipitation. Figure 6.28 shows TEM images of HC-v0-1 on the left and HC-v0-2 on the right. Top view shows a distinct honeycomb-lattice. Structures before and after PEG ppt did not look different which concludes that structure are well-behaved and stable upon PEG ppt.

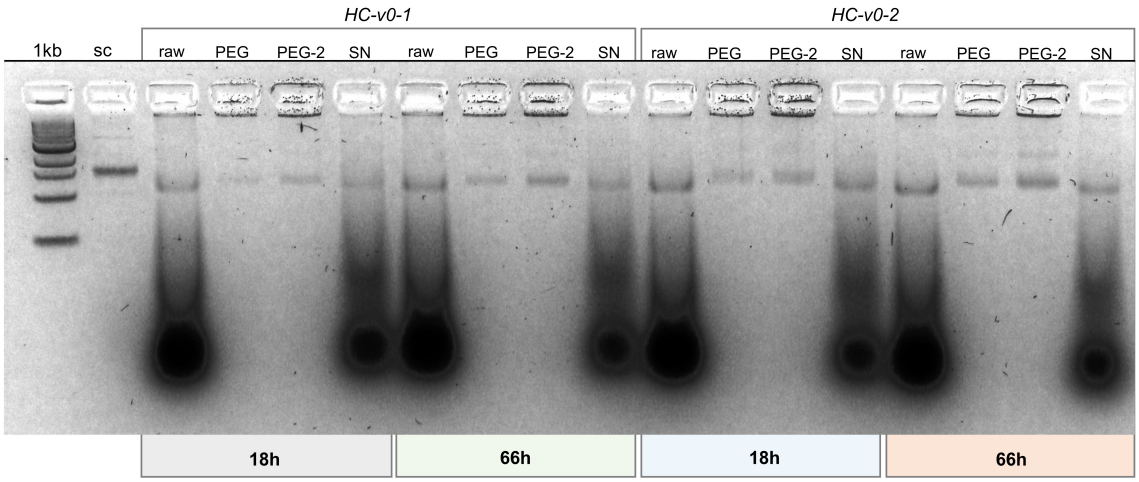

Figure 6.27.: Gel evaluation of PEG purification of HC-v0. 2% native AGE gel comparing the recovery yields of the two PEG purified HC-v0 candidates folded over the course of 18h vs. 66h. (1) 1kb ladder, (2) p8064 scaffold control, (3) Raw HC-v0-1 folded at 14 mM $MgCl_2$ with the 6025-18h ramp, (4) PEG purified HC-v0-2 that had been folded at 14 mM $MgCl_2$ with the 6025-18h, sample volume normalized to lane (4), (5) PEG purified HC-v0-2 that had been folded at 14 mM $MgCl_2$ with the 6025-18h, double the sample amount compared to lane (4), (6) supernatant from PEG ppt of HC-v0-1, (7)-(10) Same conditions as in lane (3)-(4) but with HC-v0-1 folded over the course of 6025-66h, (11)-(14) Same conditions as in lane (3)-(4) but with HC-v0-2 folded over the course of 6025-18h, (15)-(18) Same conditions as in lane (3)-(4) but with HC-v0-2 folded over the course of 6025-66h.

Gel running parameters: 1×TAE buffer with 11 mM $MgCl_2$, SYBR gold pre-staining 1:10 000 dilution, 70V for 2h cooled in ice bath

6.3.9. Conclusion

Studies on HC-v0 architectures have shown that it is possible to implement design approach 2 of having short helices for the benefit of larger surface areas on honeycomb-lattices, too. Honeycomb-lattices, by definition, tackle one of the major design challenges imposed by design approach 2 which is the reduction of staple crossover density. Since there are only three instead of four axes of possible crossover directions, honeycomb-based structures reduce the crossover density by a factor of 2 simply caused by the hexagonal arrangement of the helices and the three nearest neighbors that arise from that. This inherent reduction of crossover density and the arrangement of helices that lines up with the natural geometry of B-DNA is also the reason why HC-structures require less attention concerning twist compensations compared to the previously discussed DC structures.
Since the conclusion on DC structure was that sticking to the baseline rule of having at least two staple crossover positions per interface, HC structures exhibited three staple transitions along the north-south axis. It was found through gel and ImageJ analysis that the single crossover junctions in HC-v0-2 perform slightly better in PEG precipitation compared to the circular staple path of HC-v0-1.
Folding works similarly well for both architectures. HC-v0-1, however, falls short recovery-wise in PEG purification when folded over the course of 18h. Only 6% were recovered from the original sample. Longer folding ramps slightly increase the recovery yields for HC-v0-1. For Hc-v0-2 no difference in folding or stability was detected when comparing 18h vs. 66h folding ramps. Recovery yields for PEG ppt remained stable at around 35%. These

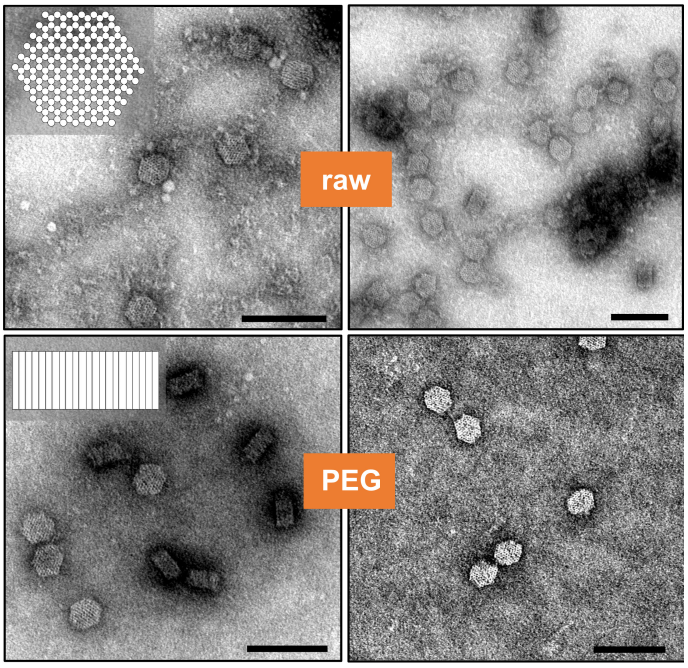

Figure 6.28.: TEM imaging of HC-v0 structures before and after PEG precipitation. The left side refers to HC-v0-1, the right side refers to HC-v0-2 structures.

results enable a clear recommendation for HC-v0-2 as a design strategy to implement design approach 2 on honeycomb-lattices. These results enable a clear recommendation for HC-v0-2 as design strategy to implement design approach 2 on honeycomb-lattices.

6.3.10. Implementation of design approach 2 into square-shaped honeycomb-lattices

Design features of HC-v1

The promising results on the previously discussed honeycomb-based arrays motivated the development of further architecture. Thereby, the same design rules as already presented for HC-v0 have been applied but the overall geometry has been adjusted. HC-v1 assembles 200 helices into a square-shaped array that is 56 bps deep. Figure 6.29 A shows a 3D illustration of HC- v1. Dimensions are shown in 6.29 B. The array is around 42 nm wide and exhibits the functional-site distance of 4.2 nm that is allowed by the honeycomb arrangement. The scaffold and staple routing is shown in the close-up view on the right in 6.29 B and is very similar to that applied for HC-v0 architectures. The main difference is that HC-v1 structures rely on the larger p8634 scaffold and that 10 helices (labeled as "x" in 6.29) are constituted by mini-scaf strands alone. A 12 nt, flexible scaffold linker is included to connect the layers with each other. Figure 6.29 C shows the path diagram with the three crossover positions per interface, whereby only one of the three possible directions for staple transitions is addressed. This means, demonstrated for helix 1, that there are three crossovers to helix 20. Staple paths are kept linear.

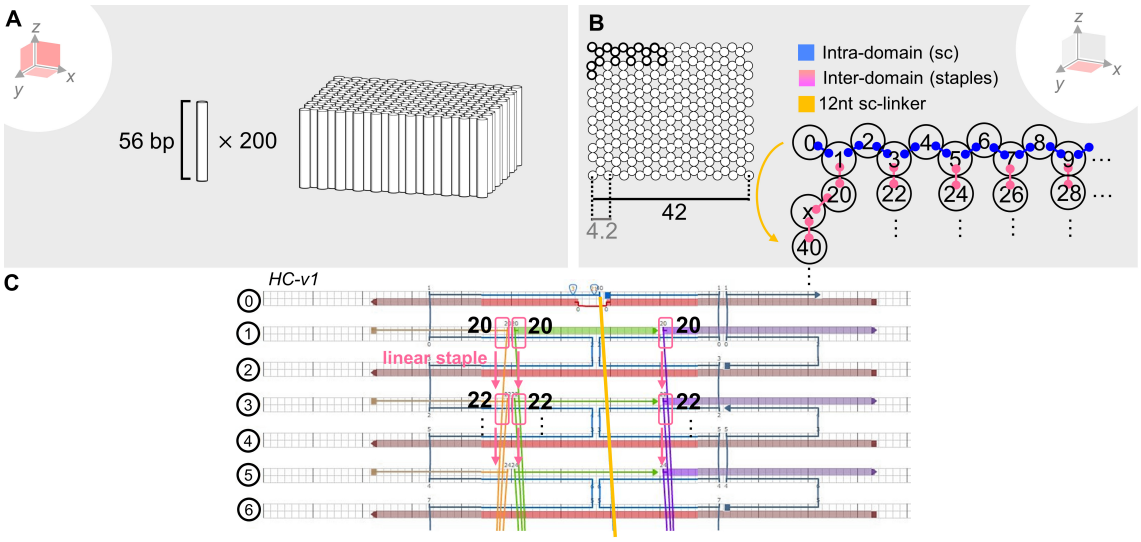

Figure 6.29.: Design approach 2 on a honeycomb-lattice: Design features of square-shaped HC-v1. **A** 3D illustration of HC-v1. 200 helices assemble into a 56 bps short square-shaped array. **B** Top view of the array outlining the dimensions. The functional-site distance is 4.2 nm. HC-v1 arrays are 42 nm wide. Two of the three available axes per helix for crossovers are occupied by the scaffold (blue) and one by the staples (pink). The routing is depicted in the close-up illustration next to the top view. A 12 nt, flexible scaffold linker connects the layers. **C** Path diagram for HC-v1. Staples per helix are only using one of the possible three directions and crossover 3 x per helix. Staple paths are linear.

Folding of HC-v1

2% native AGE gel was used to eliminate optimal folding conditions. A magnesium screening revealed the sharpest gel bands for $MgCl_2$ concentrations of 12-14 mM. Anything lower or higher lead to pronounced gel shifts or a complete loss of product bands, respectively. Analyzing samples that have been subjected to different temperature ramps shows a clear preference for 6025-18h. Lanes (15)-(17) in figure 6.30 yielded the sharpest product bands among all other tested conditions. HC-v1 was also imaged with TEM. 6.30 B depicts images collected from HC-v1 samples folded over the course of 66h. It was possible to resolve a crisp honeycomb pattern when structures landed on the TEM grids with the helices standing up.

Purification of HC-v1

PEG purification was used to access the structural stability of HC-v1 architectures. Figure 6.31 shows experimental data collected. A 2% native AGE gel shown is used to analyze PEG purified samples and compare them with the raw folding sample. Lanes labeled with "PEG-2" contain double the amount of sample compared to the raw folding sample. Lanes labeled "PEG" contain a sample amount normalized to the raw folding sample and can thus be used to draw direct conclusions on the recovery yields in comparison with the gel band intensity yielded by raw folding samples. The recovery yields for HC-v1 overall are outstanding compared to what has been observed for all the other architectures so far. Again, recovery yields could be further increased by folding the samples over the course of

66h. The amount of multimerization or aggregation in the gel pockets seems to remain at a constant and low level for both temperature ramps tested. Structures remained stable also after resting at 4°C overnight as can be observed in data presented in the appendix B.7. It is to note that almost no sample amount got lost in the supernatant which indicates that HC-v1 are better captured in a pellet during PEG ppt compared to HC-v0 structures.

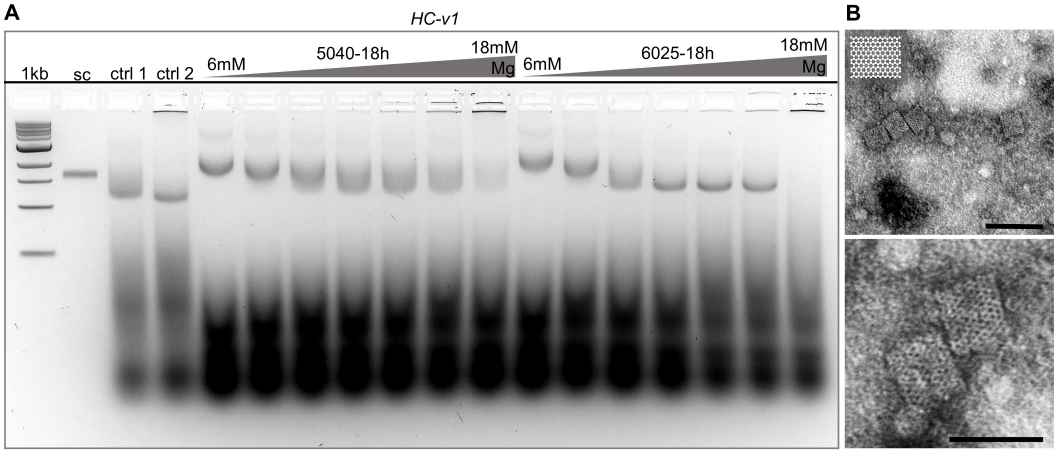

Figure 6.30.: Experimental data on HC-v1 folding. **A** 2% native AGE gel analysis of different folding conditions. (1) 1 kb ladder, (2) p8634 scaffold control, (3) Control 1: HC-v0-1 folded with 5040-18h at 10mM $MgCl_2$ concentration, (4) Control 2: HC-v0-1 folded with 6025-18h at 14mM $MgCl_2$ concentration, (5)-(11) Raw HC-v1 folded with the 5040-18h ramp at $MgCl_2$ concentrations ranging from 6 to 18 mM in steps of 2 mM, (12)-(18) Raw HC-v1 folded with the 6025-18h ramp at $MgCl_2$ concentrations ranging from 6 to 18 mM in steps of 2 mM. **B** TEM images of HC-v1 folded with the 6025-66h ramp at 14 mM $MgCl_2$ concentration, (top) overview image with scale bar at 100 nm, (bottom) Close-up image with scale bar at 50 nm.

Gel running parameters: 1×TAE buffer with 11 mM $MgCl_2$, SYBR gold pre-staining 1:10 000 dilution, 70V for 2h cooled in ice bath

6.3.11. Conclusion

HC-v1 shows that the design lessons learnt can be applied for the design of other geometries that might be more beneficial as well depending on the intended application of the structures. Folding of HC-v1 works best with the 6025-18h temperature ramp at $MgCl_2$ concentrations of 12- 14 mM. Using the refined protocol for PEG purification resulted in decent recovery yields and multimerization or aggregation phenomena remained at a constant, low level. Recovery yields could be further increased by folding the samples over the course of 66h. However, this is the first architecture that does not necessarily require longer folding ramps to result in a reasonable amount of purified sample.

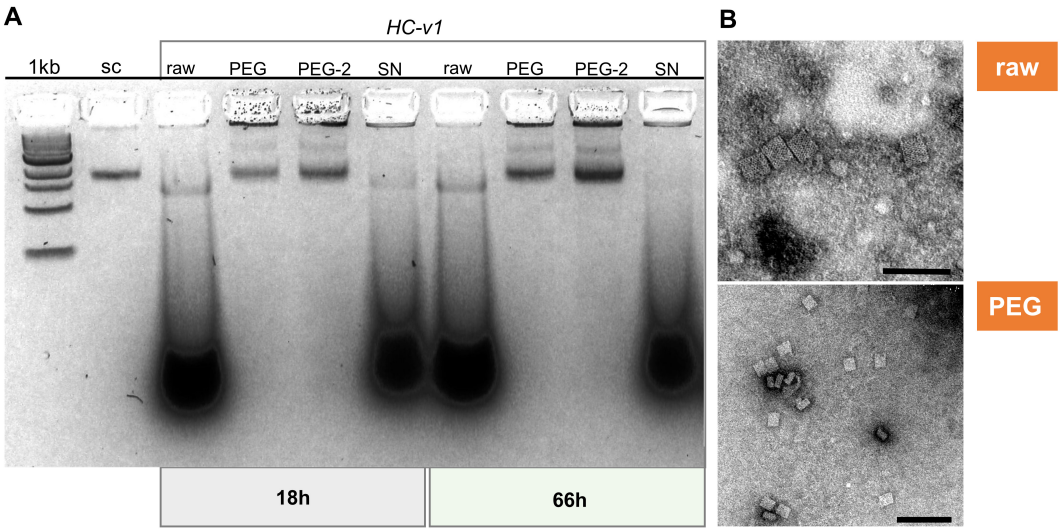

Figure 6.31.: Gel evaluation of PEG purification of HC-v1. 2% native AGE gel comparing the recovery yields of HC-v1 folded over the course of 18h vs. 66h. (1) 1kb ladder, (2) p8634 scaffold control, (3) Raw HC-v1 folded at 14 mM $MgCl_2$ with the 6025-18h ramp, (4) PEG purified HC-v1 that had been folded at 14 mM $MgCl_2$ with the 6025-18h, sample volume normalized to lane (4), (5) PEG purified HC-v1 that had been folded at 14 mM $MgCl_2$ with the 6025-18h, double the sample amount compared to lane (4), (6) Supernatant from PEG ppt of HC-v1, (7)-(10) Same conditions as in lane (3)-(4) but with HC-v1 folded over the course of 6025-66h. Gel running parameters: 1×TAE buffer with 11 mM $MgCl_2$, SYBR gold pre-staining 1:10 000 dilution, 70V for 2h cooled in ice bath

6.4. Design approach 3: Square-holey lattices and the combination of multiple scaffolds for a larger design space

This section discusses an alternative way to approach the goal of surface maximization for multi-layer DNA nanostructures. In contrast to design approach 2 from the previous section where helices were shortened to release scaffold material, design approach 3 investigates a whole new design strategy called the square-holey lattice. The design technique is still based on a square-lattice, however, DNA origami structures exhibit an alternating pattern of fully occupied and holey layers. Skipping every second helix on the square-lattice releases a scaffold that can be deployed for the helix length. Thus, the surface maximization this time is not realized perpendicular to the helical axes but along their axes. It will be discussed how square-holey lattices can be implemented demonstrated with two SH-candidates, SH-v1 and SH-v2. Additionally, it will be shown how the incorporation of medium-sized scaffold strands and further mini-scaf strands extend the design space and have an additional stabilizing effect on the square-holey lattice architectures.

6.4.1. Square-holey lattice architecture

Figure 6.32 illustrates the overall outline of a square-holey lattice compared to a conventional square-lattice. Instead of visiting every helix lattice point with the scaffold routing, layers are incorporated where every second helix is skipped. Typically, the SH structures

include one or two fully occupied layers that act as a stabilizing core body. Through the alternation of fully occupied and holey layers, it is possible to generate multi-layer structures such as in design approach 2, but with an overall reduction of the helix density. This inherently solves two design challenges that otherwise need to be addressed. First, it circumvents the problems arising from a high crossover density in densely packed square-lattice designs that required intricate solutions as shown in the previous section. Second, the lower helix density should lead to a reduction of global twist phenomena that are typically the main concern when designing on a square-lattice.

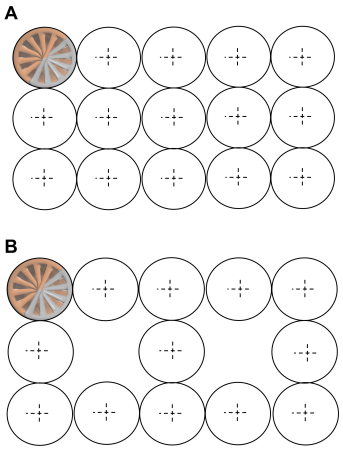

Figure 6.32.: A Helix arrangement conventional square-lattice architectures. Each lattice point of the individual DNA layer is occupied. **B** Helix arrangement in square-holey-lattices. Alternating patterns of fully occupied DNA layers and layers that skip every second lattice point.

Design and experimental evaluation of square-holey lattice structures

Figure 6.33 depicts a first SH candidate: SH-v1. 6.33 A shows a 3D model of the assembled structure. It consists of five DNA layers. The first layer is fully occupied and is followed by a layer with only every second lattice point occupied. To avoid potential stability issues the proceeding layer is fully occupied again before two further, holey layers are introduced (see figure 6.33C).
The scaffold used is the p8064 and is used to assemble 89 nm long helices on the top and 67 nm long helices at the base. Layers add up to a 12 nm depth. With 11 helices assembled next to each other, the surface of SH-v1 calculates to a total of 2314 nm^2.
Folding of SH-v1 was performed at a final $MgCl_2$ concentration of 10 mM and using the 5040-18h temperature ramp. The folded samples have been analyzed on a 2% native AGE gel shown in 6.34 A. SH-v1 resulted in a sharp monomer band at a high yield. TEM imaging verified that the observed gel band corresponds to SH-v1 monomers. Figure 6.34 B shows an overview TEM image at the top and close-up images of the two landing positions of SH-v1. The left one observes SH-v1 that landed on its side, the rightTEM image depicts top views of the structure with a crisp outline of the individual helices (white). Dark lines in between the helices refer to the holey areas in the design.
A subsequent design effort aimed for an increase of the 89 nm surface of SH-v1. It was also of interest whether 5 layers are needed to result in stable structures. To study these

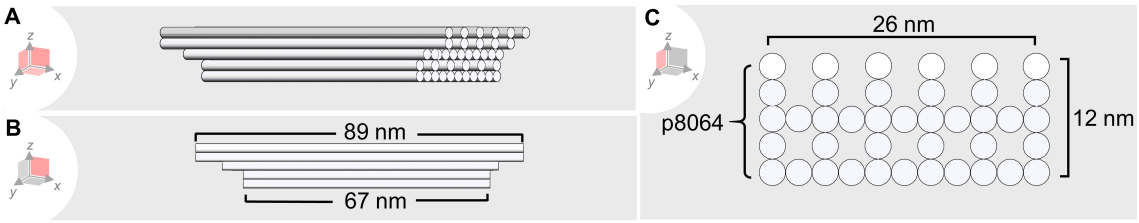

Figure 6.33.: Design approach 3: Square-holey lattice architecture SH-v1. **A** 3D rendering of SH-v1. **B** Side view of SH-v1 showing the 89 nm surface and the 67 nm base of the structure. **C** Front view of SH-v1 illustrating the five layers. Two of them are fully occupied whereas the residual ones skip every second helix lattice point. The helices add up to a width of 12 nm and are assembled with the p8064 maxi-scaffold. 11 adjacent helices result in 26 nm width of SH-v1.

questions a second SH candidate was designed (SH-v2). More scaffold material was made available by switching to the longer scaffold p8634. Also, reducing the number of layers provided scaffold material that could contribute to the length of the surface helices. Figure 6.35 provides a 3D illustration of SH-v2 in A, a side view in B and a front view in C. p8634 is designed to assemble in a three-layered structure that has only one fully occupied layer at the bottom, followed by two layers that skip every second helix. This adds up to a 7nm width. Surfaces are now 138 nm long, whereas the base is 93 nm long. SH-v2 has a surface area of around 4002 nm^2. Overall this is an increase in surface area of around 58%.

Folding of SH-v2 has been evaluated with a 2% native AGE gel and TEM imaging. Figure 6.36 A shows results for the $MgCl_2$ screening subjected to two different temperature ramps, 5040-18h and 6025-18h. Folding performed much better for the 6025-18h ramp as indicated by sharper and more intense gel product bands. $MgCl_2$ concentrations ranged from 8-12mM in steps of 2 mM. TEM images in 6.36 B show SH-v2 folded with the 6025-18h ramp at 12 mM $MgCl_2$. Although particles have been observed matching the expectations with respect to shape and dimensions, it is to emphasize that a decent population of particles was present that adapted a curled up and distorted configuration.

This indicated that the three-layered structures are quite flexible and lack the required rigidity to adapt a straight outline. This motivated to go back to five layered structures as it has been shown with SH-v1 that five layers seem to provide the necessary rigidity to avoid the curling of the structures.

6.4.2. Incorporation of MeRPy-strands for the addition of further DNA layers

In order to maintain the maximized surface area of SH-v2 also for SH-v3, besides the p8634 maxi-scaffold, a 3158 nt, DNA single-stranded scaffold as well as further 40-48 nt mini-scaf strands were incorporated into the design. This combination of multiple scaffolds allowed the addition of two further DNA layers without having to reduce the surface of the DNA origami structure. Figure 6.37 provides an overview of the geometric properties of SH-v3. 6.37 A shows a 3D model of the structure. In B one can see that the surface of the DNA origami structure remained the same. 6.37 C shows how the three DNA layers from SH-v2 are extended by two further DNA layers. The blue layer thereby is

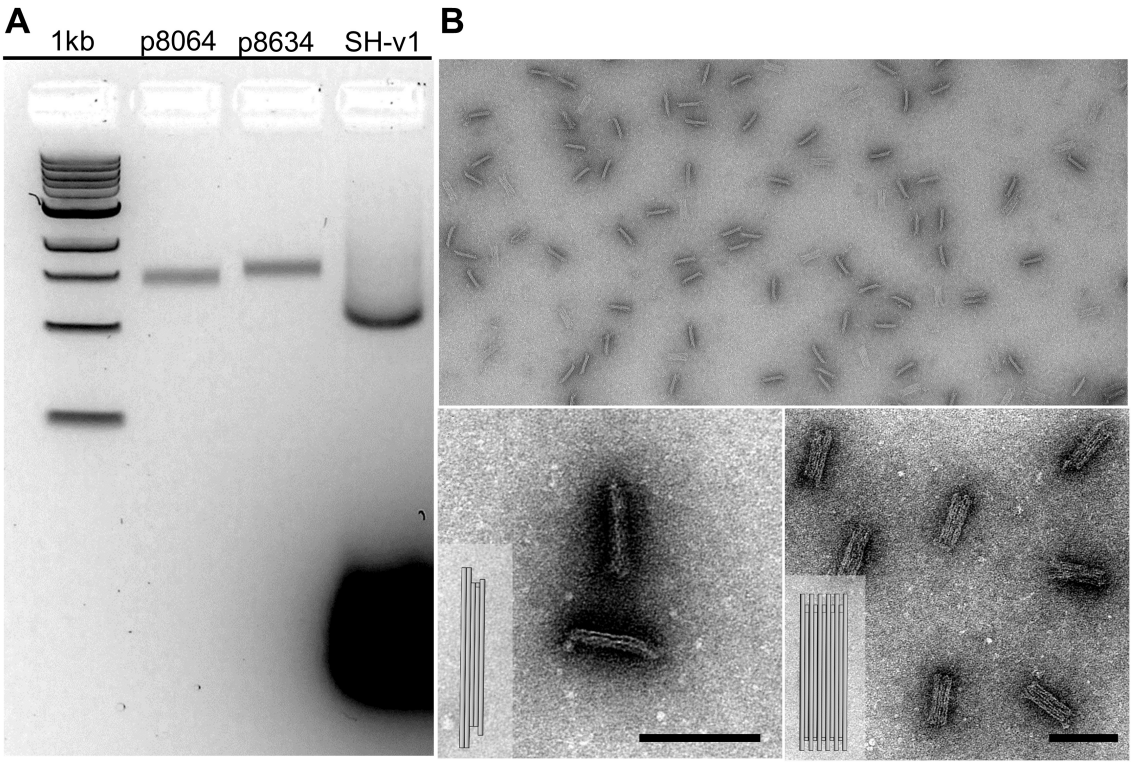

Figure 6.34.: Experimental data on SH-v1 folding. **A** 2% native AGE gel analysis of the folding of SH-v1 was performed at 10 mM $MgCl_2$ final concentration and using the 5040-18h temperature ramp. (1) 1kb ladder, (2) p8064 scaffold control used for SH-v1 folding, (3) p8634 scaffold, (4) Raw folding of SH-v1. **B** TEM imaging of SH-v1. (top) overview image of SH-v1, (bottom left) Close-up image of SH-v1 landing on their sides, illustration of the landing configuration on the left, (bottom right) Close-up image of SH-v1 facing up, illustration of the top view on the left; scale bars at 100 nm.

Gel running parameters: 1×TAE buffer with 11 mM $MgCl_2$, SYBR gold pre-staining 1:10 000 dilution, 70V for 2.5h cooled in ice bath

constituted by 36 mini-scaf strands that have a length between 40 and 48 nts. The white layer refers to the one assembled by a 3158 nt long midi-scaffold that is synthesized using the MeRPy-protocol described in chapter 5. The additional scaffold strands are connected to the p8634 maxi-scaffold by additional 148 staple strands. For the assembly of the first three layers (shown in gray in figure 6.37 C), the same set of handles can be used as for SH-v2 which makes this design highly modular.

The results for the magnesium screening and the comparison of the two folding ramps 5040-18h and 6025-18h have been analyzed using a 2% native AGE gel and TEM imaging. The results are depicted in figure 6.38 A. SH-v3 structures show a clear preference for the 6025-18h folding ramp. A gel product band for the 5040-18h at 8 mM $MgCl_2$ is pretty much non-existent and for higher $MgCl_2$ concentrations bands are quite diffuse. Folding with the 6025-18h achieves much better results. Gel product bands appear for all three $MgCl_2$ concentrations, however, 10 mM $MgCl_2$ seems to work best. Figure 6.38 B shows some TEM images of SH-v3 folded with the 6025-18h ramp at 10 mM $MgCl_2$. The structures observed on the TEM grids all appeared much more rigid compared to SH-v2. No population of curled or distorted looking particles has been observed.

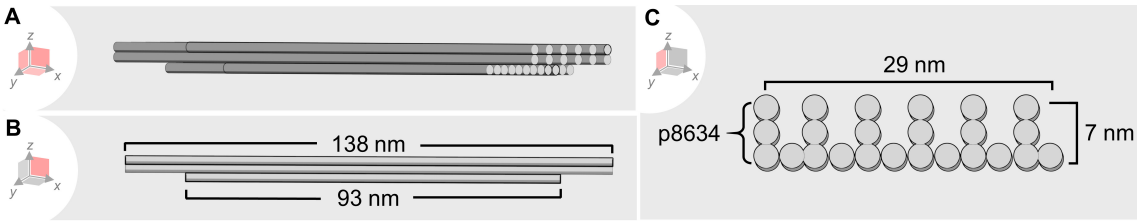

Figure 6.35.: Design approach 3: Square-holey lattice architecture SH-v2. **A** 3D rendering of SH-v2. **B** Side view of SH-v2 showing the 138 nm surface and the 93 nm base of the structure. **C** Front view of SH-v2 illustrating the three layers. One is fully occupied whereas the residual ones skip every second helix lattice point. The helices add up to a width of 7 nm and are assembled with the p8634 maxi-scaffold. 12 adjacent helices result in 29 nm width of SH-v2. This leads to a 58% increase in surface area compared to SH-v1.

6.4.3. Conclusion

The data collected on SH-v3 folding allows us to conclude that introducing two more layers to SH-v2 stabilizes the structure and prevents it from curling. The results are preliminary indications that it is possible to extend the design space through the combination of multiple scaffolds. These insights provide interesting future perspectives for further designs that could exceed the size limitation of DNA origami that exclusively rely on the common maxi-scaffolds. The MeRPy-technique provides the basis for those as it allows to generate a variety of medium-sized single strands whose commercial synthesis has yet to be addressed.

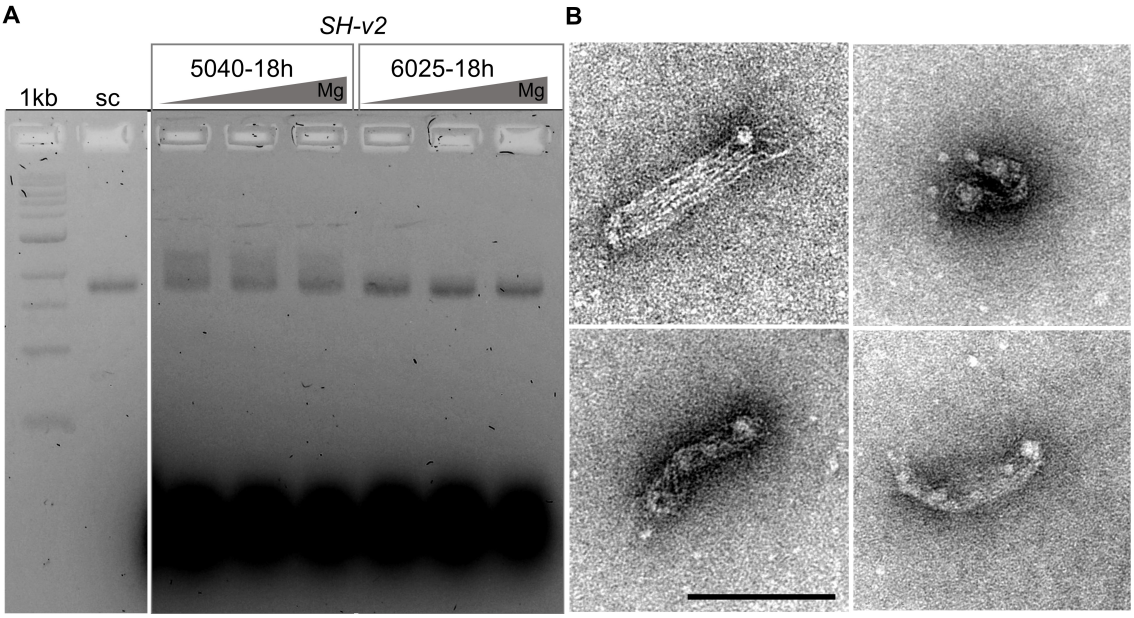

Figure 6.36.: Experimental data on SH-v2 folding. **A** 2% native AGE gel to analyze the magnesium screening for SH-v2 folding and to compare the two temperature ramps 5040-18h and 6025-18h. $MgCl_2$ concentrations ranged from 8-10 mM $MgCl_2$ in steps of 2 mM. (1) 1kb ladder, (2) p8634 scaffold control, (3)-(5) SH-v2 folded with 5040-18h ramp at $MgCl_2$ ranging from 8-12 mM, (6)-(8) SH-v2 folded with 6025-18h ramp at $MgCl_2$ ranging from 8-12 mM. **B** TEM images for SH-v2 folded with the 6025-18h ramp at 12 mM $MgCl_2$, scale bars at 100 nm.

Gel running parameters: 1×TAE buffer with 11 mM $MgCl_2$, SYBR safe 0.5 $\mu g/mL$, 65V for 4h at RT

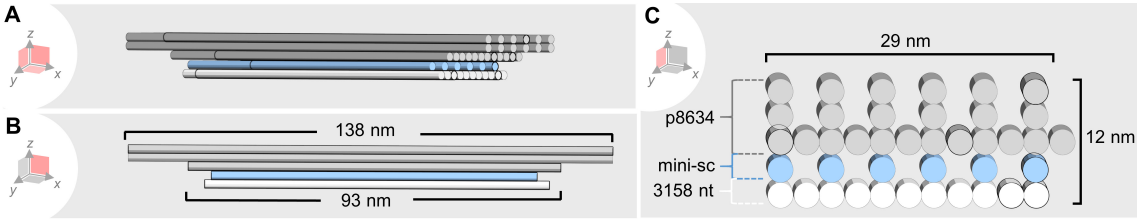

Figure 6.37.: Design approach 3: Square-holey lattice architecture SH-v3. **A** 3D rendering of SH-v3. **B** Side view of SH-v3 showing the same surface area measurements as for SH-v2. **C** Front view of SH-v3 illustrating extension of the original three layers to five layers. In SH-v3 two layers are fully occupied, the residual ones skip every second helix lattice point. The original three layers from SH-v2 are consituted by the p8634 maxi-scaffold. The blue layer is made from 36 mini-scaf strands that are 40-48 nt long. The white, base layer is made from a 3158 nt long midi-scaf strand. The helices add up to a width of 12 nm. 12 adjacent helices result in 29 nm width.

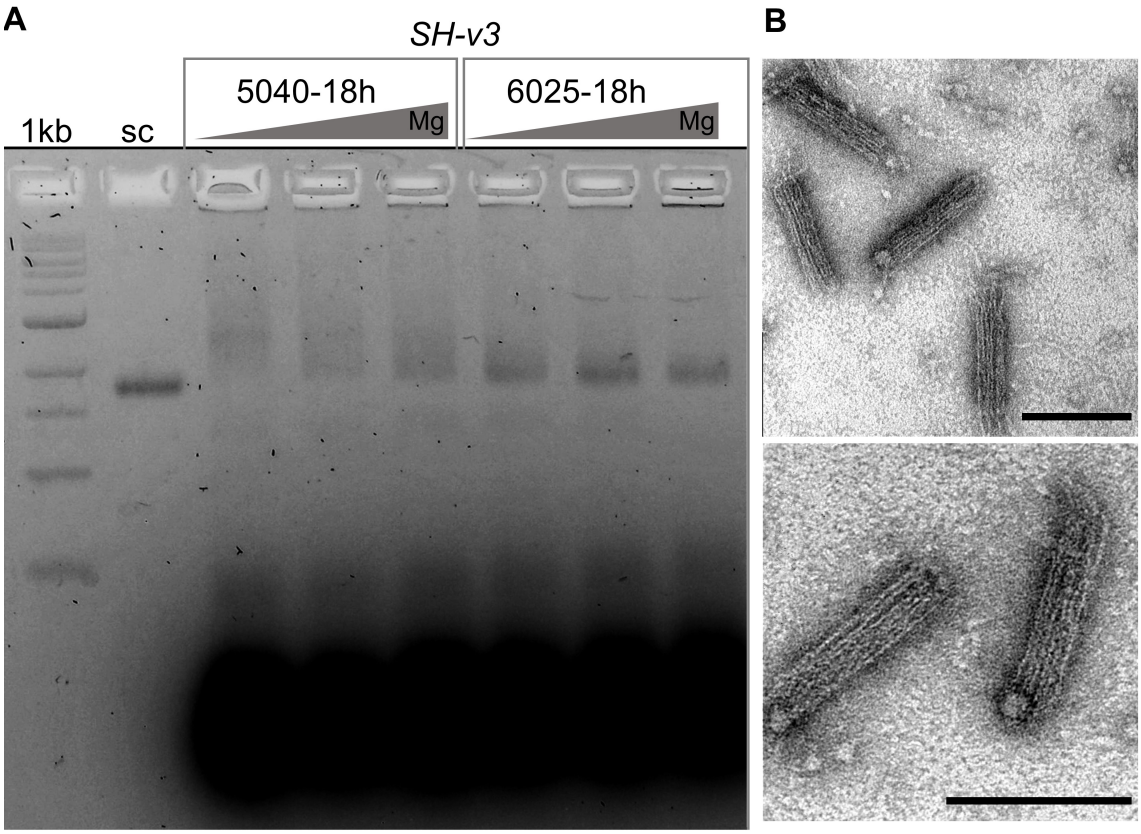

Figure 6.38.: Experimental data on SH-v3 folding. **A** 2% native AGE gel to analyze the magnesium screening for SH-v3 folding and to compare the two temperature ramps 5040-18h and 6025-18h. $MgCl_2$ concentrations ranged from 8-10 mM $MgCl_2$ in steps of 2 mM. (1) 1kb ladder, (2) p8634 scaffold control, (3)-(5) SH-v3 folded with 5040-18h ramp at $MgCl_2$ ranging from 8-12 mM, (6)-(8) SH-v3 folded with 6025-18h ramp at $MgCl_2$ ranging from 8-12 mM; **B** TEM images for SH-v3 folded with the 6025-18h ramp at 10 mM $MgCl_2$, scale bars at 100 nm.

Gel running parameters: 1×TAE buffer with 11 mM $MgCl_2$, SYBR safe 0.5 $\mu g/mL$, 65V for 4h at RT

6.5. Summary

The studies presented within this chapter aimed to develop platforms for multi-site interactions. These architectures provide a solid base to implement the ever-growing complexity of ideas on how to engineer processes on the nanoscale. Defining the reasons and motivation to pursue these studies was guided by the inspiring processes brought forward by nature that show extraordinary efficiency when multiple components are orchestrated to achieve large-scale effects. Nanoscale engineering is often strongly focused on the implementation of isolated processes in one prototype system. The power of the DNA origami technique per se is that it allows to finetune the individual components in a theoretical design framework and once completed to generate a trillion copies of these prototypes at the same time through the process of programmed self-assembly. Boosting the functionality of these prototype systems as well as the efficacy with which processes can be realized within the designed frameworks thus promotes the powerful concepts of DNA nanotechnology even further and extends the scope of possible applications.
However, multi-site interactions are only possible if a structural framework for it is given. This chapter introduced three novel design approaches based on the DNA origami technique to maximize the surface areas of DNA origami structures to increase the number of addressable functional sites for the realization of multi-site interactions. Through a systematic study of various design features of square-lattice and honeycomb-pleated based architectures, it was possible to eliminate definite design recommendation that provide helpful support for the development of future DNA nanostructures. The studied approaches and associated results manage to transform empirical knowledge of the field into certain guidelines.

Design approach 1 introduced an alternative arrangement of helices on a square-lattice for a reduced functional site-distance of 3.4 nm given that only helices of shared scaffold parity are considered. This corresponds to a 1.4 nm shorter functional site distance compared to conventional square-lattice architectures and is particularly interesting for high-precision applications where the close proximity of attachment sites is required.

Results associated with design approach 2 provide meaningful insights into the importance of crossover densities as well as the deliberated choice of crossover and bp deletion positions.
The goal of design approach 2 was to generate DNA arrays of even higher helix density that can provide more functional sites. Minimizing the scaffold to 50 bps per individual helix supplies released scaffold for the assembly of further helices. The main challenge imposed by this approach is a problematic increase of staple crossover density that would, if remaining untreated, result in unstable structures due to low binding energies of the staples. Developing strategies to reduce the high staple crossover density within these shallow structures has been the focus of the studies associated with design approach 2. Two design innovations to do so have been introduced and evaluated. First, a scaffold seam was introduced that would traverse the structure in two of the four directions that are present in square-lattice designs. That way half of the total amount of available crossover directions are covered by the longer scaffold with toeholds of higher binding energy. Second, so-called mini-scaf strands are designed along the edges of the structures for more stabilization and to save further staple crossovers. It has been additionally tested whether neglecting the baseline rule of having at least two crossover positions along one

helical interface would be a further way to save crossover positions.
The implementation of these design premises in architectures of high aspect ratios fails. These structures exhibit pronounced supertwisting that can be partially balanced by the deliberated choice of crossover positions but overall does not fulfill the desired requirements.
Reducing the aspect ratios of these structures does enable proper assembly based on the suggested design innovations which are attributed to the higher moment of torsional inertia that results from a smaller aspect ratio. However, these structures turned out to be unstable over time once purified which is a sign for some unspecific interactions between the structure, such as domain swapping.
Investigation of further designs revealed that shortening helices to a minimum depth are possible nevertheless, by implementing an intermediate representation of a square- and honeycomb-lattice. These designs use only three of the four crossover axes of the square-lattice and thus mimic the conditions of a honeycomb-lattice although helices are arranged in 90° angles. Also, these designs go back to having at least two crossovers per interface. Based on these adjustments of the initially-posted design strategies, it was possible to successfully implement the original idea of design approach 2 and assemble stable DNA arrays with 200 individually addressable helices of 55 bps depth.
To generate a greater selection of geometries, design approach 2 has been applied to honeycomb-based architectures too. Applying the design rules that have been thoroughly investigated, enabled the development of two further 55-56 bps deep architectures consisting of 182-200 helices. Thereby the helices were assembled into stable hexagonal discs as well as into square-shaped arrays.

Design approach 3 presents another strategy to achieve large surface areas on DNA origami. It shows that multi-layer structures fold well although every second helix lattice point is unoccupied. It turned out that these structures however need at least two fully occupied layers to result in rigid outlines. Structures with only one fully occupied base layer exhibited extensive curling. It was shown that most of the maxi-scaffold can be used for surface maximization, and the additional layers required for stabilization can be assembled through the incorporation of a medium-sized scaffold and multiples of mini-scaffolds. This combination of scaffolds is an interesting design approach with the potential to yield even larger assemblies.

In summary, it should be pointed out that shortening helices to a minimum is indeed a possible strategy to maximize the surface area of DNA origami structures. However, it is recommended to use slightly longer helices than 50 bps if it is the desire to stick to square-lattice architectures. Honeycomb-lattices seem to be more tolerant toward such a short helix length and are thus supposed to be more suitable for this approach. Although many different architectures have been presented within this chapter, none of them can really be treated as superior to one to the others. The choice for a particular design is subjected to the targeted application. The studies discussed present a variety of geometries that themselves provide many opportunities to address the functional sites. It is also possible to address only every second or third of the functional site which results in different spacing and could be preferred in one or the other applications. The following chapter will use some of the presented architectures to implement a multi-leg stepping mechanism - an application that hugely benefits from structural features developed here.

7. Symmetric, three-phase DNA origami stepper

This chapter demonstrates how the platforms discussed in the previous chapter can be used to elevate current demonstrations for nanoscale stepping based on DNA. With the developed DNA arrays at hand, the possibility to realize multi-site interactions will be used to implement three novel ideas for a stepping mechanism, making it stand out from already-reported ones. It is novel in the approach that stepping will be performed by a marching formation through coordinating multiple legs along large and rigid tracks, stepping is promoted by a three-phase actuation of short bridge strands for a controlled forward and backward motion and the relatively short step size of 3.5 nm. Two DNA origami-based motor candidates - the mini-stepper and the falcon-stepper - will be discussed. Thereby, mini-steppers rely on the DC-v0-1 and v0-2 architectures discussed in section 6.2.1, while falcon-steppers will use the SH-v1 designs from section 6.4.1. It has been shown that DC-v0 structures are prone to multimerization under certain reaction conditions. This was the main motivation to shift the focus of the work to the falcon- stepper. However, some of the most central challenge questions have been investigated with the mini-stepper system. The associated findings have a direct impact on the falcon- stepper system and helped guide the route of investigation. Thus, a considerate selection of results on the mini-steppers system will be presented despite the fact that stepping has never been realized with the mini-stepper system. Prior to describing the experimental findings of the steppers, key design considerations will be discussed.

7.1. General design considerations

7.1.1. Architectural premises

Monomeric stability and high yield

The motion of the steppers is driven by DNA strand displacement reactions. Thereby, stepping relies on a cyclic activation and deactivation of incoming unset and set strands that lift the stepping legs and establishes bonds at the designated binding sites, respectively. With each step taken, the addition of unset and set strands further dilutes the reaction solution. Stepping across longer distances will highly dilute the concentration of the steppers, which conflicts with the detection limits of gel electrophoresis and TEM imaging, the detection tools of choice for this work. Measures are necessary to meet the detectable concentrations.

An excellent monomer folding yield is thus desirable to already start the stepping process at high concentrations. Additionally, it holds interest to work with structures that do not need extensive purification as these protocols typically come with a loss of material and harsh reaction conditions that might affect structural integrity. Monomers should also be stable in the presence of multiple DNA single strands and other DNA origami structures.

Dimeric stability

It is equally important that the monomers are able to interact with their designated binding partners and form stable dimeric complexes. There are several factors that can support dimerization of DNA origami structures, including the buffer conditions, final magnesium concentration, the amount of unused waste material in the reaction mix, the set strand design as well as the axis of interaction. The latter is strongly influenced by the charge distribution of DNA double helices, which is crucial to take into account when designing the DNA monomers and their platforms of interactions.
This stability is influenced by the repulsion forces becoming increasingly critical for a larger number of combined helices. It is interesting to see that successful dimerization can be realized along as well as perpendicular to the helical axis.

Sufficient room for handle incorporation

The stepper components need to provide sufficient room for the incorporation of handles. The motivation for this is three-fold. First, the steppers developed within this work are based on a multi-leg approach and are supposed to move a whole DNA array instead of simply a biped DNA molecule. This per se requires more than just one or two handles. Second, once stepper mechanisms like the one investigated here are fully developed, it will hold central interest to integrate additional functional units for various applications, e.g. molecular cargo such as proteins or print-heads for nanoscale patterning of surfaces. Thus, the slider — as the dynamic component of the system — should not only incorporate the functional handles required for the stepping mechanism itself but should also provide sufficient room for further attachments. Third, the rail determines the number of steps that could be taken and thus the operating range of the stepper. A rail architecture that allows a periodic repetition of handles is desirable to achieve long travel distances.

Small step size

Another central goal is to develop an architecture that allows a small step size. This is in particular interesting for high-precision applications in the future. In the context of 3D printing on the nanoscale, a small step size is key to the degree of operational accurateness of material deposition.
The step size is determined by the proximity of DNA helices in the DNA origami assembly as well as the positions allowed for handles to extrude from the helix. Figure 7.1 shows ways to arrange helices on a square-lattice (**A**), on a honeycomb-lattice (**B**) and a diagonal-cut square-lattice (**C**). The latter is introduced in chapter 6 which should be consulted for further information on this particular design style. DNA double helices are represented as cylinders. The black arrows show the directionality of the scaffold routing through the design space. Although it is possible to embed handles extruding from the structures on each helix, it is more common using only helices that share the same scaffold parity. Consequently, all handles extruding from the structures will have the same directionality, which makes addressing them with their complementary counterparts much easier. The distances considered in figure 7.1 thus refer to the distances of helices with shared scaffold parity.
For the mini-stepper, interacting handles are designed to extrude from the ends of the helices. Thus, the step size is determined by the distance between even or odd parity helices arranged on the diagonal-cut square-lattice. On the other hand, falcon-stepper

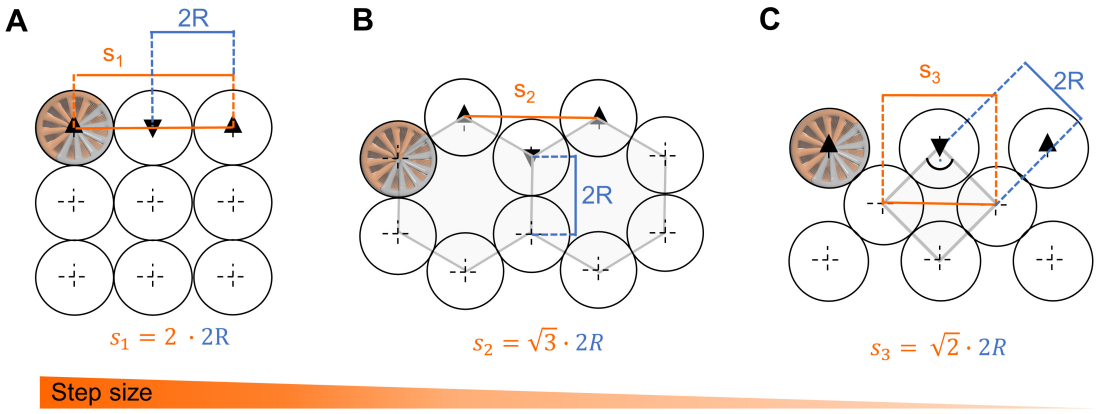

Figure 7.1.: Variations in step size depending on chosen lattice designs. The step size refers to the distance between two helices that share the same scaffold parity indicated by black arrows. Step sizes decrease going from left to right. R refers to the radius of B-DNA of 2.4 nm. **A** Square-lattice designs allow a step size of 4.8 nm. **B** The geometry of honeycomb-lattice arrangement of helices results in a step size of 4.2 nm, **C** step sizes on diagonal-cut square lattices reduce to 3.4 nm.

interacting handles extrude along the sides of the helices. Step size is thus determined by the helical turn.

7.1.2. Functional mechanism

The steppers divide into two functional units: the component that performs the actual stepping ("slider") and the platform of stepping ("rail"). Both are equipped with interacting handles, staples that extrude from the surfaces of the origami structures in a regular pattern and that can interact with complementary sequences. So-called clip and clip-removal strands act as the set and unset strands, respectively. They are designed to be complementary to the extruding parts of the handles on the sliders and rail and mediate a connection between the DNA origami surfaces.

Multi-leg coordination

As reviewed in chapter 4, there are many examples in the literature showing the actuation of single-stranded DNA molecules along a track. The approaches presented within this work aim to extend those mechanisms to realize stepping of DNA arrays through the control of multiple legs. Each state of the system relies on a fourfold binding of sliders to rails via four clip strands that bind simultaneously.

It is hypothesized that this renders the artificial DNA motor more tolerant towards assembly defects, or towards missing interacting handles. From other studies, it is known that handle incorporation is successful in up to 80% of the cases [145]. Relying on four handles for each step provides an efficient backup in case handles are left out during the folding process of sliders and rails. We believe that the multi-leg approach makes the stepping mechanism less error prone and more robust.

Sequence symmetry

Key to the design and function of the stepper system is the underlying sequence symmetry of interacting handle and clip strand sequences. The design involves three groups of handles and clip strands that are highlighted red (R), green (G) and blue (B) in figure 7.2. Each group comprises two unique sequences that add up to six sequences required for stepping. This is innovative compared to other approaches that require a new sequence for every step taken.
Figure 7.2 shows a side view of engaged sliders and rails and explains how the three handle/clip strand groups mediate stepping. It is important to note that the RGB handle patterns for the slider and rail are different. While both structures start off with the red handle group in state 1, the subsequent handle group for rail structures is the blue one, whereas it is the green one for the slider. The pattern deviation is key to enabling movement of the slider on the rail. Strand displacement reactions applied to an equal alignment of handle groups would only result in an interchanging of RGB bonds rather than forward movement. State 1 in figure 7.2 is achieved once red clip strands are applied to a solution containing sliders and rails. The slider binds to the rail occupying the first four attachment points on the rail. Applying the green clip strands and red clip-removal strands subsequently causes the sliders to proceed to state 2. Thereby, the system reaches an intermediate state 1-2, in which both the red and green clip strands are mediators of the slider-rail connection, until red-removal strands cause the slider to completely engage with the green handles. Sliders can reach state 3 in the same way, but with blue clip strands and green clip-removal strands. Intermediate states occur with each step. In the case of stepping to state 3, sliders will reside on the rail in an intermediate state 2-3 with green and blue clip strands engaged simultaneously. Once sliders have reached state 3 with the aid of green clip-removal strands, they have completed the three phases of the first RGB stepping cycle. The RGB cycle is repeated by adding the same red clip strands but blue-removal strands. This forces the slider to proceed to the second red handle set on the rail and allows continuing with a second cycle of three-phase actuation. Continuous progression of the slider on the rail is thus realized by the recurring addition of the set of six unique RGB clip and clip-removal strands and it eliminates the need to introduce a new sequence for every step taken.

7.1.3. Clip strand design for forward and backward control

Clip strands are key components of the system in two ways: first, they are the mediators of the connections between slider and rail components, and second they are the driving force of the actuation itself. Considerate design and a thorough investigation of the clip and clip-removal strand interactions are thus crucial for a successful implementation of the mechanism described above.
One central requirement that the clip strands need to fulfill is a balanced length. They should be sufficiently long to master the implemented step size while at the same time providing enough rigidity to hold the sliders and rails in place. A suited clip strand length is additionally important to embed a bias of the steppers towards shorter bridging distances as a control element for forward and backward motion. This concept is explained in figure 7.3, which depicts that a slider and rail that are originally engaged via red clip strands and subsequently subjected to green clip strands have the choice to attach to the green handles placed in front of the original red attachment site or the one behind. f and b in figure 7.3

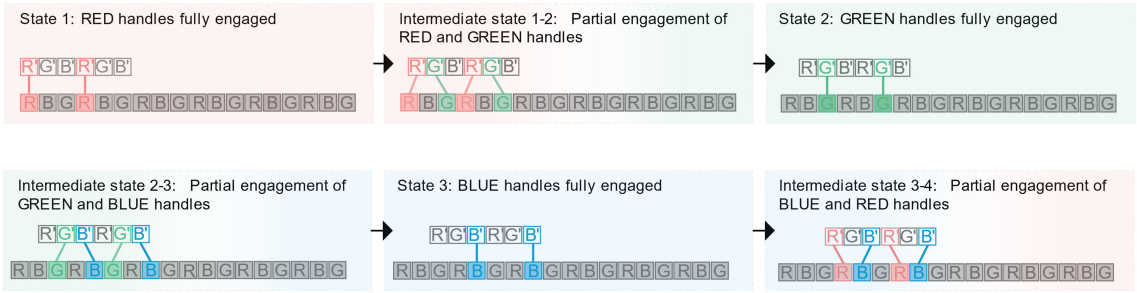

Figure 7.2.: Schematic explaining the symmetric, three-phase stepping mechanism. The slider proceeds on the rail upon the symmetric cycling of RGB clip strand engagement and removal. One cycle comprises the three phases of consecutive addition of red, green, blue clip and clip-removal strands and is repeated upon completion of the three phases. After the initial heterodimerization of the slider and rail via purple initialization handles and clip strands, the slider starts in state 1, where it is engaged via the set of red clip strands. To proceed, the green clip strands are applied, which force the slider into an intermediate state 1-2 of red and green clip strands engagement. Followed by a red clip-removal strand displacement reaction, the slider fully engages with the green handles. This scheme is repeated for the transition from green to blue (i.e. state 2 to state 3). The slider-rail systems can step into a second cycle of three-phase actuation after purifying from left over clip-removal strands and applying the same RGB clip strands (i.e. state 3-4).

refer to the distance that sliders have to travel in case of a forward or backward promotion, respectively. The systems are designed in such a way that displacement is controlled by a bias towards lower energetic cost that the system needs to invest when it overcomes shorter distances. This bias helps to control the directionality of the displacement and works similarly for the backward motion. Backward stepping follows a BRG pattern instead of the RGB pattern for the forward stepping.

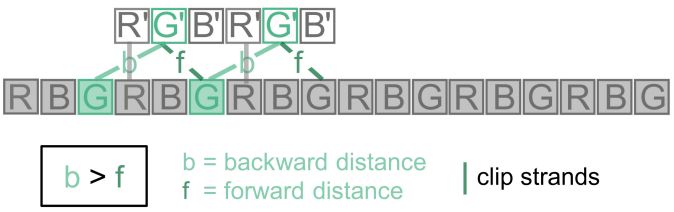

Figure 7.3.: Illustration showing the slider bound to the rail via red clip strands (shown grayed out). Once green clip strands are applied, the system has two choices to step to the next green attachment site crossing either the distance f or b. Based on the clip strand design, the system will favor overcoming the shorter distances. In this demonstrated case of forward stepping, the shorter distance is f, which will trigger the system to step to the right.

7.2. Mini-stepper

7.2.1. Design and functionalization

For the mini-stepper system, DC-v0-1 has been chosen as the slider and DC-v0-2 as the rail component. Both architectures are described in detail in chapter 6 and from now onwards they are referred to as the mini-slider and mini-rail, respectively.
Figure 7.4 provides an overview on how the above described stepping mechanism is implemented into the architecture. A mechanism for initial hybridization of the two monomers is programmed to occur via six purple clip strands shown in the 3D model in figure 7.4 A. It is also shown that handles extrude from the main body along the helical axes. Helices that carry the interacting RGB handles are highlighted correspondingly. Figure 7.4 B is a top view of the slider and rail showing more details about the handle distribution. Sliders exhibit twelve RGB interacting handles where each color quartet comprises two unique sequence. Rails comprise the same quartets but repeated multiple times along the surface. Looking closely, one can see that handles on the slider follow a R**G**B pattern while rails follow a R**B**G pattern. This is key to enable proper displacement of the slider as described above. For explanatory reasons, figure 7.4 A also includes engaged red clip strands whose connection to the handles is further described in 7.4 C. Slider as well as rail handles are 21 nt long single strands extruding from the main body with their 5'-ends or 3'-ends, respectively.
The close-up in figure 7.4 C shows that unlike a standard vertical handle-antihandle interaction, the clip strands bind to the rail handles with their 5'-end (indicated as a square) and cross over to the slider handle. The 3'-end of the clip strand – illustrated as an arrow – holds a 10nt long toehold sequence for strand displacement reactions.
The system is designed to generate dimers that interact along the helical axes of the monomers. Through the diagonal-cut arrangement of the helices, it is possible to implement a step size of 3.4 nm.

7.2.2. Dimerization of mini-stepper monomers

Titrating clip strand final concentration

Successful folding of mini-stepper monomers has been shown in section 6.2.1. The first trials to dimerize mini-stepper monomers have been performed with slightly varied rail architectures, MR-v0-6. These were based on the same scaffold as mini-sliders (MS-v0), thus exhibiting the same molecular weight and running at the same height on agarose gels. Moreover, only a subset of six interacting handle pairs have been included for MR-v0-6. The highlighted helices in figure 7.5 A refer to the handle set that has been included for sliders and rail.
Rail interacting handles have been PAGE purified and included in the folding mixture at a 4×excess with respect to the scaffold. In this case, final handle concentrations were at 80 nM. Appendix A.3 can be consulted for more details on the folding protocol. The material was folded using the 5040-18h ramp and 12 mM final $MgCl_2$ concentration. The experiment focused on one isolated clip strand interaction, in this case interactions mediated by the green clips. The clip strands have been included in the slider folding mixture at varying concentrations. The structures used for the dimerization experiment were amicon purified prior to use following the standard amicon purification protocol provided in appendix A.3. Since MR-v0-6 did not exhibit all possible handles, the rails

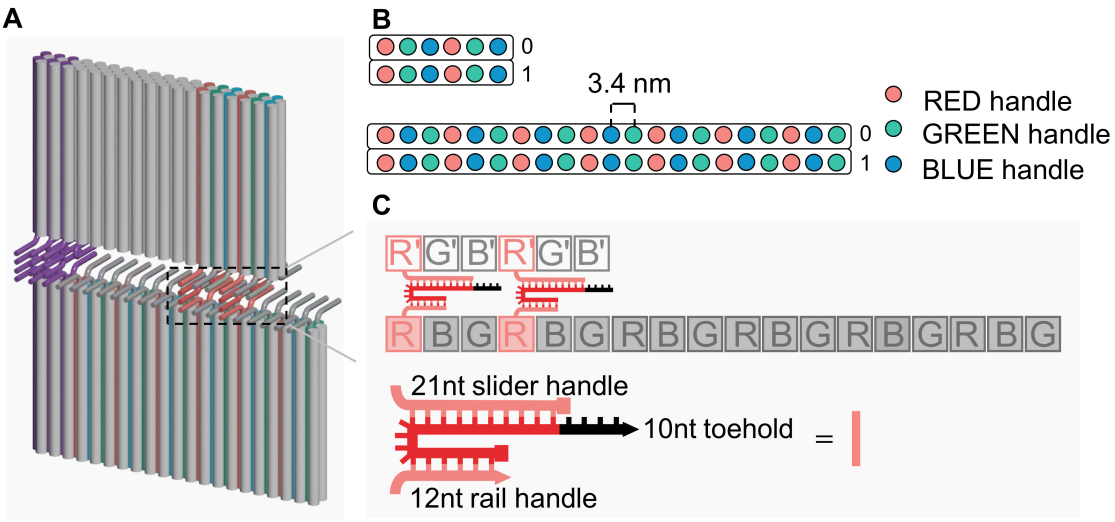

Figure 7.4.: Mini-stepper design and functionalization. **A** 3D model of engaged mini-slider and mini-rail via red clips stands. A program for very initial heterodimerization is programmed to occur via six purple handles extruding at one end of the structures. **B** Interacting, RGB handle distribution on the slider (top) and the rail (bottom). **C**Detailed illustration of the handle-clip strand interaction demonstrated for the red engagement. Slider and rail handles are 21 nts long and extrude with their 5'- or 3'-end, respectively. 5'-ends are indicated with a square, and 3'-ends with an arrow. Complementary clip strands bind antiparallel to the handles and include a 10 nt toehold sequence for DNA strand displacement reactions.

were much less sticky and could thus be treated with the standard amicon purification protocol. The reduced number of handles on the rail limited the possible attachment point for the slider and thus allowed predicting where the slider attaches on the rails.
The handle-clip interactions result in a configuration where the end of the slider attaches to the beginning of the rail. A 3D render of the expected configuration is shown as an inset in figure 7.5 D.
Concentrations of clip strands and monomers after the respective purification have been accessed with nanodrop measurement. Sliders and rails have been mixed in a 1:1 ratio at increasing concentrations of green clip strands. Lower clip strand concentrations were tested within a range of 2-14 nM in steps of 2 nM (see figure 7.5 B), and upper clip strand concentrations ranged from 10-40 nM in steps of 5 nM (see figure 7.5 C). Dimerization was performed at 10 µL final reaction volumes and incubated at 37°C overnight. The results have been analyzed on a 2% native AGE gel. Negative controls were included where the slider and rail have been combined but no clip strands were included in the reaction mixture (ctrl (-)). The experiment resulted in distinct dimer bands with the highest gel band intensities for clip strand concentrations between 6-15 nM. Figure 7.5 B shows that for clip strand concentrations higher than 15 nM, dimer band intensities continuously decline. The same trend is observable for clip strand concentrations lower than 6 nM. Another phenomenon detected on the gels is a higher-order band appearing above the dimer band. This multimer band was also most pronounced for clip strand concentrations between 6-15 nM. TEM images were taken from raw dimerization samples, showing constructs with the expected dimeric configuration (see figure 7.5 D top and bottom). However, other configurations have also been observed. The first two TEM images

in figure 7.5 E show constructs that have been observed besides the dimers, which could provide an explanation for the higher-order bands. The encircled complexes on the first image of figure 7.5 E are higher-order assemblies containing up to four slider and rail monomers, while the second image shows an assembly made from three monomers. The TEM image on the far right in figure 7.5 E shows another population observed. Thereby, perfectly aligned sliders and rails are stacked on top of each other, which does not correspond to the configuration that the designed clip strand interaction aims for. It should be highlighted that this configuration was also observed in the negative control samples, which explains the faint dimer band that is already visible in the negative control sample in lanes (5) on the gels. The negative controls do not contain clip strands and should thus not result in any dimerization. One hypothesis for the fact that one does observe dimeric structures in the control sample is that sliders and rail have a tendency to interact unspecifically. This would coincide with the experiences on the multimerization of DC structures described in 6.2.2.

Finally, a comment should be made about the monomer bands in the dimerization samples, which are of higher intensity compared to the monomer bands of the raw folding samples. This indicates that the two types – the slider and rail – have been combined. However, it is not possible to judge whether one of the monomers is depleted more or whether one monomer is underrepresented. The latter would lead to a premature stop of the dimerization and would be a reason for low dimerization yields. This motivated implementing a mini-rail with a slightly larger molecular weight to distinguish the two monomers on a gel.

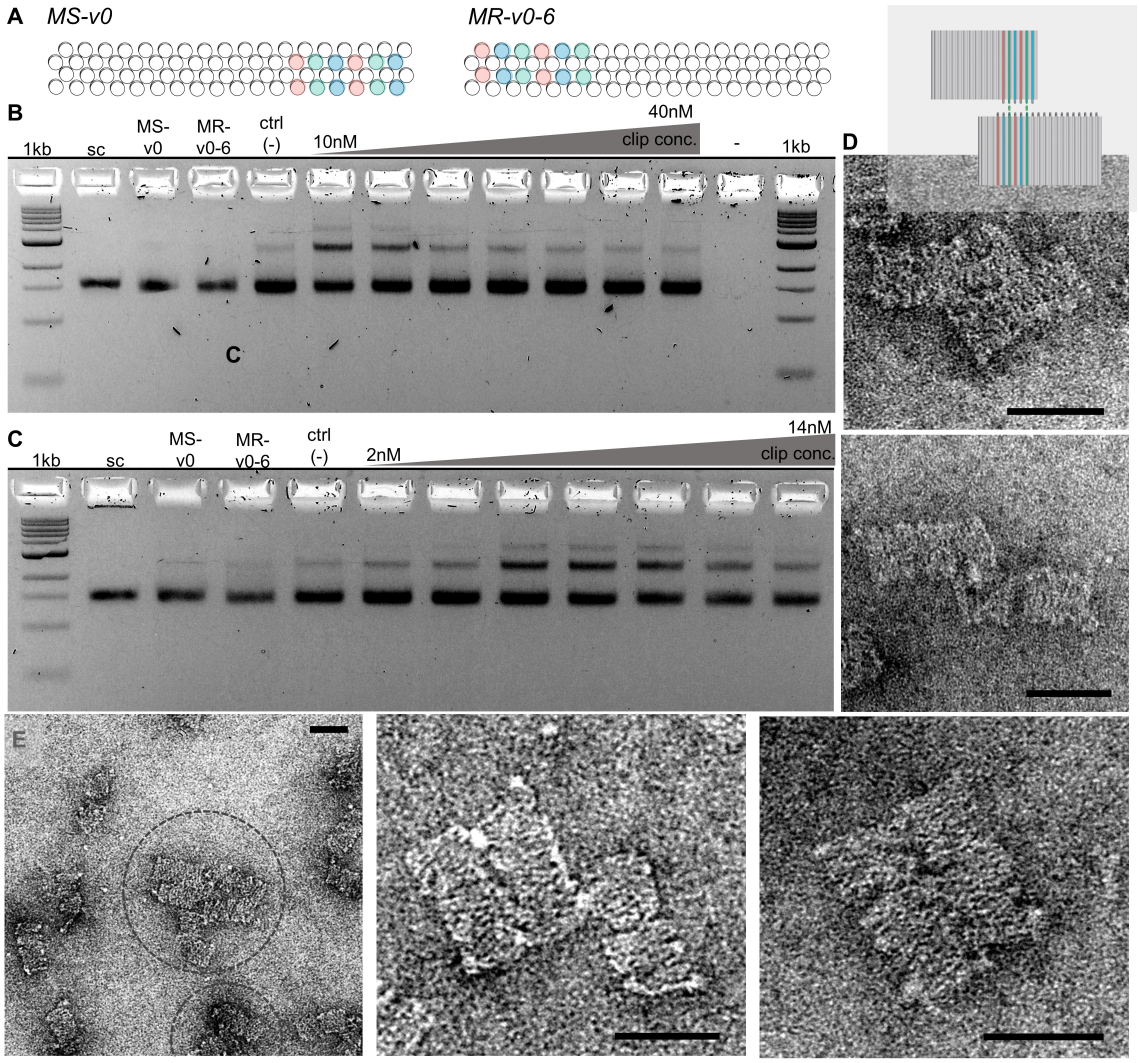

Figure 7.5.: Clip strand titration for mini-monomer dimerization. **A** Top view on mini-slider (MS-v0) and mini-rail (MR-v0-6) a reduced set of six handle pairs for MR-v0-6 and the common six handle pairs for MS-v0. Both rely on the p7308 scaffold. **B** 2% native AGE gel to analyze the results of dimerization at varying clip strand concentrations, (1) 1kb ladder, (2) p7308 scaffold control, (3) amicon purified MS-v0, (4) amicon purified MR-v0-6, (5) Negative control sample with combined MS and MR but without clip strands, (6)-(12) dimerization of MS-v0 with MR-v0-6 at increasing clip strand concentrations from 10-40 nM in steps of 5 nM, (13) empty, (14) 1kb ladder. **C** 2% native AGE gel to analyze the results of dimerization at varying clip strand concentrations, (1) 1kb ladder, (2) p7308 scaffold control, (3) amicon purified MS-v0, (4) amicon purified MR-v0-6, (5) Negative control sample with combined MS and MR but without clip strands, (6)-(12) dimerization of MS-v0 with MR-v0-6 at increasing clip strand concentrations from 2-14 nM in steps of 2 nM. **D** TEM imaging of raw dimerization sample that wass bjected to 10 nM clip strand concentration, scale bars at 50 nm, E TEM images of higher-order assemblies observed in the same sample as in D, scale bars at 50 nm. **E** TEM images of higher order assemblies observed in the same sample as in **D**, scale bars at 50 nm.

Titrating the monomer ratio

In order to better estimate depletion rates and ratios, the slightly larger DC-v0-2 introduced in 6.2.1 has been used for the mini-rail candidate MR-v1 to result in a distinguishable doublet gel band once the mini-slider and -rails are combined and analyzed on a gel. MR-v1 exhibits a larger molecular weight compared to the mini-slider since it is based on the p8064 scaffold. Moreover, in MR-v1 all 48 possible attachment sites have been occupied with interacting handles. The larger MR-v1 structures have been analyzed on a 2% native AGE gel. Furthermore, it was investigated how the ratios between applied mini-sliders and -rails influence the dimerization yields. The top view of MR-v0 and the adjusted version MR-v1 in figure 7.6 A outline the handle distribution. Since MR-v1 now exhibits multiples of the handle sets, purple handles have been included at the beginning of the rail and slider structures for an initial heterodimerization via six purple clip strands of a unique sequence. Figure 7.6 B shows a 2% native AGE gel analyzing dimerization yields via these purple initialization handles when purple clip strand concentrations were varied from 6-10 nm and the ratios between MS-v0 and MR-v1 were titrated in ratios of 1:1, 2:1, and 1:2, respectively.
It is to note that this investigation used mini-sliders and -rails that have been purified using a glycerol gradient and ultra-centrifugation instead of amicon purification. The gel in 7.6 clearly shows the expected gel shift between MS-v0 and MR-v1. Purified monomers in lane (4) and (7) exhibited a pronounced higher-order band. These higher-order bands also appear in the negative control in lane (8) where MS-v0 and MR-v1 have been combined but not subjected to purple clip strands. The distinct separation between slider and rails becomes even more evident in the control since one observed the expected doublet band for the monomers as well as the higher-order bands. Multimerization of the monomers makes it difficult to argue that the higher-order bands in dimerization samples indeed correspond to dimers. However, one can observe that the higher-order double in lane (7) dissolves upon dimerization and is replaced with a more intense single gel band in all following lanes (8)-(16). This indicates that the higher-order bands observed for the samples that have been dimerized are not a product of the unspecific multimerization of sliders and rails observed in lane (4) and (7).
One can conclude that the intensity of the dimer bands remains constant independent of the titrated ratios. Looking at the monomer doublet band in lane (8)-(16) reveals that the titration worked well. Gel band intensities of the individual bands within the doublet are equal for the 1:1 ratio. Moreover, the 2:1 and 1:2 ratios coincide with expectations. The 2:1 ratios show a higher band intensity for the slider band matching the fact that the slider has been applied in a 2x excess compared to the slider. Lane (14)-(16) correspond to samples that contain double the number of rails compared to the slider, which is also depicted by the much more intense rail band within the doublet. However, multimerization and aggregation are much more pronounced compared to the other samples. This might originate from the fact that the rail always tends to multimerize to a stronger extent compared to the sliders. Now that the rail is in excess, this effect increases. Purple clips were added after folding and not – as before – included in the folding mixture. Dimerization was performed at 20 mM final $MgCl_2$ at 37°C overnight.

Conclusively, it can be said that the deviations from a 1:1 ratio of applied monomers are not the reason for limited dimerization yields. However, the problem of multimerization of the monomer that conflicts with an induced dimerization remains present. The following

approach tests whether shortening the interacting handle length would be able to reduce unwanted multimerization and – if so – whether it would further increase the dimerization yields.

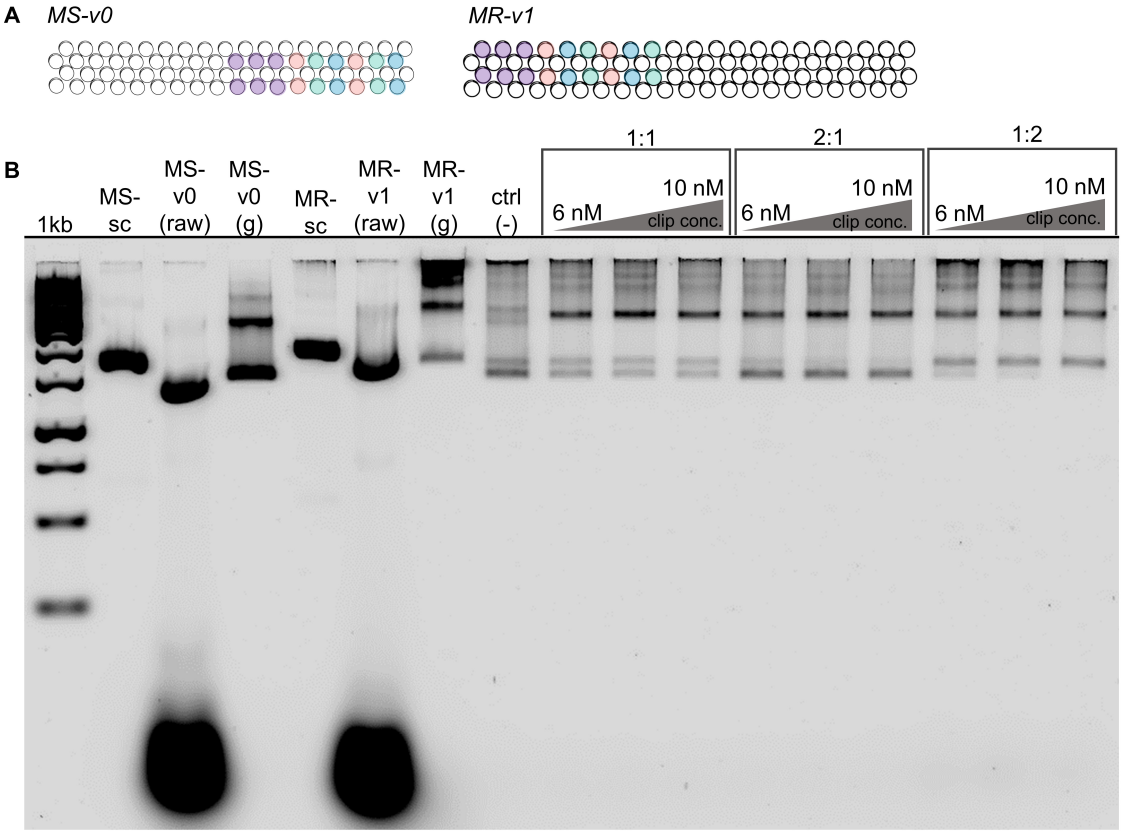

Figure 7.6.: Titration of the ratio between mini-sliders and -rails in dimerization. **A** Top view of MS-v0 (left) and MR-v1 (right) showing the RGB handle pattern for sliders and the RBG handle pattern for the rail. Purple handles are included at the beginnings of the structures for a initial hybridization and to designate the slider to a fixed position on the rail. **B** 2% native AGE gel to analyze the gel shift between MS-v0 and MR-v1 and the effect of different ratios between sliders and rail on the dimerization yield. (1) 1kb ladder, (2) p7308 scaffold control for MS-v0, (3) Raw MS-v0, (4) Glycerol gradient purified MS-v0, (5) p8064 scaffold control for MR-v1, (6) Raw MR-v1, (7) Glycerol gradient purified MR-v1, (8) MS-v0 and MR-v1 combined without addition of purple clip strands, (9)-(11) MS-v0 and MR-v1 combined in a 1:1 ratio at different clip strand concentrations ranging from 6-10 nM in steps of 2 nM, (12)-(14) MS-v0 and MR-v1 combined in a 2:1 ratio of slider to rail at different clip strand concentrations ranging from 6-10 nM in steps of 2 nM, (15)-(17) MS-v0 and MR-v1 combined in a 1:2 ratio at different clip strand concentrations ranging from 6-10 nM in steps of 2 nM.

Investigation of different interacting handle lengths

MS-v0 and MR-v1 have been purified with the refined amicon purification protocol listed in A.3. This included folding the monomers using the 6025-18h temperature ramp, 12 mM $MgCl_2$ concentration, a 20x staple strand excess and adding back core staple strands after amicon purification. Eight different monomers have been folded exhibiting different

handle lengths of either 12, 13, 16 or 21 nts. The latter was thereby the standard handle length used thus far and it serves as a control. The following combinations have been tested. Sliders equipped with 21 nt handles have been incubated with rails exhibiting either 12, 14, 16 or 21 nt handles (see lanes (7), (9), (11), (13) 7.7 respectively).
Additionally, sliders that were equipped with 16 nt handles incubated with rails exhibiting 16 nt handles and following the same scheme for the 12 nt and 14 nt handles (see lanes (15), (17), (19)). Purple clip strands had been included in the folding mixture at a 40x excess compared to the scaffold. Clip strands as well as interacting handles of the rail have been PAGE purified prior to use. Dimerization was performed at 20 mM final $MgCl_2$ concentration and at 37°C overnight.
Figure 7.7 shows the 2% gel analysis of dimerization yields for mini-sliders and -rails that interacted via differently long handles. As introduced above, samples that contain both sliders and rails appear as a doublet band on gels. However, the doublet band is not visible in 7.7. One explanation could be the slight sample overloading of the gel pocket that results in a signal overlapping of the individual monomer gel bands. Lanes labeled with a minus correspond to samples that did not contain clip strands, and thus are expected not to result in a dimer band. Lanes labeled with a plus contained clip strands and should exhibit dimer bands. The gel detects dimer bands for all conditions, whereas the dimer bands for samples that contained clip strands are more pronounced, indicating that the clip strand reinforced the dimerization. Thereby, it is quite evident judging from the dimer band intensity that the combination S21+R12 results in the highest dimerization yields. Combinations that included rails with a 14 nt handle (lane (10) and (16)) resulted in the lowest yields.
Although the negative controls exhibit dimerization, it can be concluded very generally that interacting handle length influences the dimerization behavior. If a careful conclusion can be made, then it is that the sliders with a 21 nt handle react best with rails exhibiting 12 nt handles. However, one cannot conclude whether the different handle length counteract the tendency of the monomers to go through unspecific multimerization. Additional data showing the amicon purification of each individual slider and rail candidate is included in appendix B.2. No reduction in multimerization could be detected. In conclusion, different handle lengths do not reduce unwanted multimerization, but show potential to increase the dimerization yields of mini-sliders and -rails.

7.2.3. Conclusion

Overall, it was possible to show that despite the repulsion forces exerted due to densely packed DNA arrays, monomers can interact with each other along helical axes.
The mini- stepper system was a suitable platform to learn that there are parameters and reaction conditions that influence the dimerization behavior and once fine-tuned they can increase the dimerization yields. It was found that there is an optimal clip strand concentration and that deviating from it can lead to almost complete suppression of the dimerization process. The optimal range for the mini-slider to -rail dimerization was constrained to 60- 150 fmol. In general, it is helpful to design the stepper components with slightly different molecular weights to distinguish them on a gel. This helps to estimate the level of depletion of the individual components, which has practical benefits such as easier predictions about what to expect on TEM grids and whether one of the two monomers had been underrepresented and thus leads to a premature termination of the reaction. The binding length of the interacting handles has been found to influence

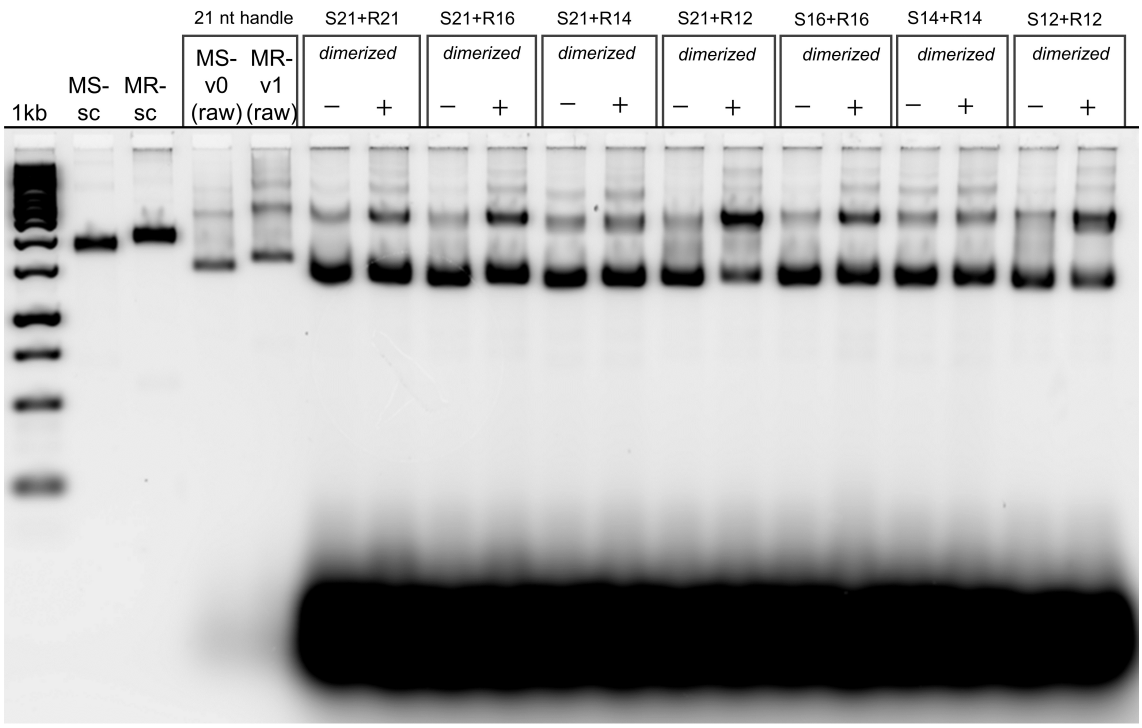

Figure 7.7.: 2% native AGE gel showing the effect of different interacting handle length on dimerization yields for mini-stepper. (1) 1kb ladder, (2) p7308 scaffold control for MS-v0, (3) p8064 scaffold control for MR-v1, (4) raw MS-v0 (21nt handles), (5) raw MR-v1 (21 nt handles), MS-v0 (21 nt handles) combined with MR-v1 (21 nt handles) without (6) and with (7) clip strands, MS-v0 (21 nt handles) combined with MR-v1 (16 nt handles) without (8) and with (9) clip strands, MS-v0 (21 nt handles) combined with MR-v1 (14 nt handles) without (10) and with (11) clip strands, MS-v0 (21 nt handles) combined with MR-v1 (12 nt handles) without (12) and with (13) clip strands, MS-v0 (16 nt handles) combined with MR-v1 (16 nt handles) without (14) and with (15) clip strands, MS-v0 (14 nt handles) combined with MR-v1 (14 nt handles) without (16) and with (17) clip strands, MS-v0 (12 nt handles) combined with MR-v1 (12 nt handles) without (18) and with (19) clip strands.

the dimerization yield and thus is a parameter that needs to be re-accessed for all new designs. For the mini-stepper system, slider handles length of 21 nt in combination with a rail handle length of 12 nt resulted in the highest yields.
Despite the fact that a proper purification protocol was developed for mini-sliders and -rails, multimerization that has been observed and successfully treated in section 6.2.2, kicked in again once the mini-sliders and -rail were combined for dimerization. It was not possible to suppress the constant level of multimerization despite many more design and experimental efforts that have been made but not shown here. Ambiguous results caused by multimerization of the structure render it challenging to derive meaningful conclusions and forced stopping further investigating mini-stepper systems. Instead, it was important to switch to an architecture that provides more robust monomers, shows less unspecific interactions and allows a higher and more precise external control of the interactions involved. The upcoming section shows how this is possible by switching to an SH-structure as stepper components.

7.3. Falcon-stepper

The falcon-stepper comprises two DNA origami monomers, called the falcon- slider ("FS") and falcon-rail ("FR"). Thereby, the five-layered, square-holey architecture presented in section 6.4.1 is used as falcon-rails. Based on the square-holey lattice design approach, falcon-sliders have been designed to be slightly larger compared to the rails and they exhibited two wing-like overhangs from the main body. This satisfies what has been found to be useful in the previous section, namely having different molecular weights for sliders and rails to render them distinguishable on the gel. Moreover, for TEM imaging it is helpful to dimerize structures that do not completely resemble each other but instead have some distinguishable features. The following section introduces the design features of the falcon-stepper and shows how the symmetric, three-phase stepping mechanism described above is successfully implemented in this architecture.
To support the comprehensibility of the discussions below, the following terminology is introduced. Dimers and dimerization that are mediated through purple clip strands will be called purple dimers and purple dimerization. This will be handled in the same way for interactions mediated via any other type of the red, green and blue clip strands, which will be often abbreviated as with the letters "R", "G" and "B". Disassembly reactions upon the addition of clip-removal strands will be termed accordingly.

7.3.1. Design and functionalization

Figure 7.8 summarizes the architectural features of the falcon-stepper. The falcon-slider and -rail rely on different DNA scaffold strands (p8634 and p8064), which fold into a core structure comprising 40 helices. The residual 570 unpaired bases of the slider scaffold are used for the addition of a wing part to the slider's core structure. This extends the slider structure to 90 helices in total. This is illustrated in 7.8 A by cross-sections of the falcon-slider (top), and a cross-section of the falcon-rail (bottom). The assembly generated falcon-sliders that are 75 nm wide and 39 nm long, while falcon-rails are only 27 nm wide but 89 nm long.
The helices that are designed to interact with each other and carry the RGB handles are highlighted in red, green an blue. Handle distribution patterns are shown in the roll-out out view below the cross-sections. Due to the completely different architecture compared to the mini-steppers, the layer of interaction is extended from two adjacent helices to six helices. Through the SH design style, the helices on the highlighted layer in figure 7.8 A share scaffold parity and thus can be equipped with uni-directional, interacting handles placed at a step size of 3.4 nm. As shown, the handle distribution pattern is spread out to six adjacent helices. Looking from the bottom to the top, sliders again follow a R**G**B pattern, while rails follow a R**B**G pattern.
Eighteen handles for the slider and 48 handles for the rail extrude perpendicular to the helical axis on the fifth layer of the core structures. The 3D model in 7.8 B shows how the design and functionalization of the individual components assemble to a multi-origami complex. B shows the falcon-rail and -slider attached to each other via the purple initialization handles and clips – designed to define a designated starting point for the stepping – and via the red clip strands. Details on the handle-clip strand interaction are provided in figure 7.8 C.
Slider handles are 21 nt long single strands extruding from the core structure with their 5'ends. Rail handles are 12 nt long single strands extruding with their 3'ends. Studies

that eliminated the optimal handle lengths will be presented in the following. Clip strands interact with the handles in the same way as described for the mini-stepper system. A 10 nt toehold sequence is attached to the 3'end of the clip strand for later strand displacement reaction.

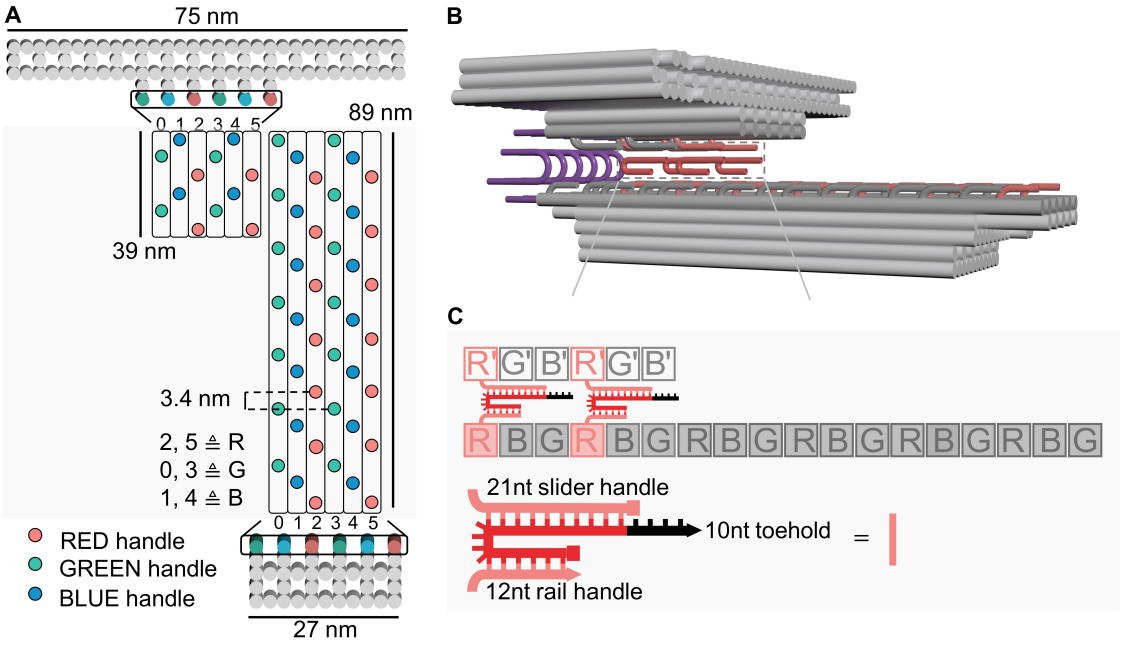

Figure 7.8.: Falcon-stepper design and functionalization. **A** Cross-section of falcon-slider (top) and -rail (bottom) showing the architectural outline and measurements of the structures. Helices that carry interacting handles are highlighted in red, green and blue. Rolled-out view (middle) showing the distribution of 18 interacting, RGB handles on the slider and 48 for the rail. **B** 3D model of engaged falcon-slider and -rail *via* red clips stands. A program for initial heterodimerization is programmed to occur *via* six purple handles extruding at the ends of the structures. **C** Detailed illustration of the handle-clip strand interaction demonstrated for the red engagement. Slider handles are 21 nts long and extrude from the main body with their 5'-ends, while rail handles are 12 nts long and extrude with their 3'-ends. 5'-ends are indicated with a square, 3'-ends with an arrow. Complementary clip strands bind antiparallel to the handles and include a 10 nt toehold sequence for DNA strand displacement reactions.

7.3.2. Folding and purification of falcon-stepper monomers

Successful folding of falcon-rails has been shown in 6.4.1. Falcon-sliders folding was also performed at a final $MgCl_2$ concentration of 10 mM and using the 50-40-18h ramp. However, slider folding slightly varied from rail folding in the sense that all interacting handles have been PAGE purified before including them in the slider folding solution. Furthermore, PAGE purified purple clip strands have been included in the slider folding mixture in a 40x excess with respect to the scaffold used. Folding was analyzed on a 2% native AGE gel as well as with TEM imaging. Lane (5) in figure 7.9 A shows a distinct and clean product band for falcon-sliders that had been folded with purple clip strands. The inset in figure 7.9 B is an illustration of the slider showing what the slider monomers are expected to look like when facing up. Indeed, this is what was observed with TEM imaging. An

overview TEM image as well as a close-up image of the sliders are provided in 7.9 B.
It was noticed that the middle section of the slider appears darker compared to the wing portions. One reason for this could be that the core body of the sliders is made from five DNA layers compared to the wings, which are built from three layers only. In this way, sliders accumulate more staining solution in the middle area that thus appears darker. This will be important later when TEM staining protocols are studied in detail to achieve suitable image contrast.
Figure 7.9 C shows that falcon-monomers are much less challenging to purify. The purification technique tested was amicon filtration. Thereby, the refined amicon purification protocol that has been developed during the studies on DC-v0 structures in section 6.2.1,was used as a base to start with. The step of adding back core staple strands has been excluded since this was a measure specifically addressing the multimerization behavior of DC-v0 structures. In a first trial of falcon monomer amicon purification, it was assumed that the structures should be more tolerant towards purification and that additional support by added back core staple strands is not required. Indeed, this procedure led to successful purification of falcon-monomers. Lanes (6) and (7) in figure 7.9 show the results of 2% native AGE gel analysis of amicon purified falcon-rail and -sliders, respectively. The purification resulted in sharp and clean monomer bands for both structures. No aggregation in the gel pockets has been observed as well as yields at reasonable levels judging from gel band intensities and their comparison with the raw folding samples in lane (4) and (5). Recovery yields for sliders were higher compared to the rail. Staple strands have been removed to a strong extent. Only a slight staple cloud on the bottom remains after purification.

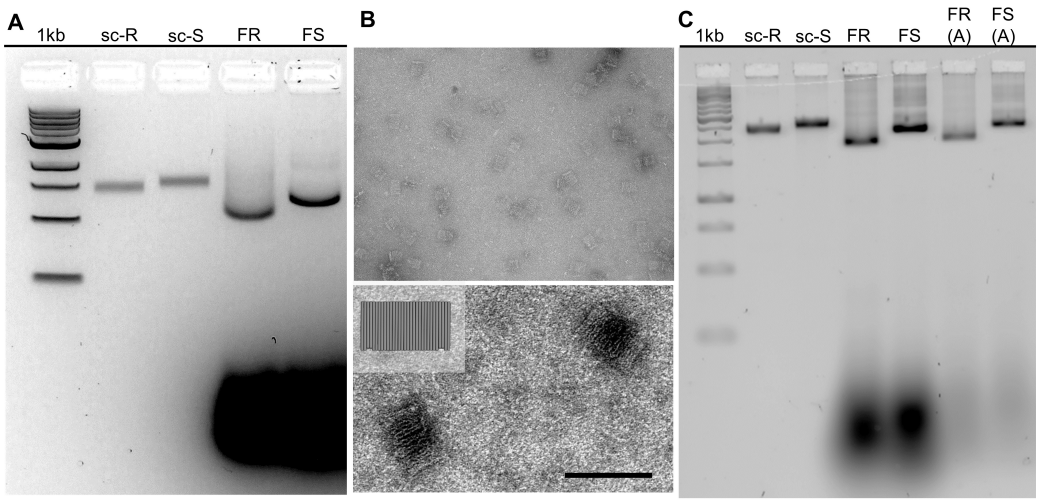

Figure 7.9.: Falcon monomer folding and purification. **A** 2% native AGE gel analysis of falcon-rail and -slider folding at 10 mM $MgCl_2$ concentration and using the 5040-18h temperature ramp. (1) 1kb ladder, (2) p8064 scaffold control for falcon-rail, (3) p8634 scaffold control for falcon-slider, (4) Raw falcon-rail, (5) Raw falcon-slider, **B** TEM overview image of raw falcon-sliders (top). Close-up view of falcon-sliders (bottom), inset in the top left corner illustrating the expected geometry of the falcon-sliders, scale bar at 100 nm.

Gel running parameters: (A) 1x TAE + 11 mM $MgCl_2$ + SYBR gold pre-staining 1:10 000 dilution; 70V for 2h 20min in ice bath; (B) 0.5x TBE buffer with 10 mM $MgCl_2$, SYBR safe staining 0.5 $\mu g/mL$; 70V for 4h at RT.

7.3.3. Dimerization of falcon-stepper monomers

Similar to the mini-stepper system, a mechanism for initial heterodimerization was programmed to occur via six purple clip and handle strands extruding from the end of falcon-sliders and -rails. This initial heterodimerization was found to be influenced by various parameters, as already implied by studies on the mini-steppers from the previous section. The parameter tuning for the initial heterodimerization of falcon-slider and -rails was partly conducted with amicon purified monomers. Later, it will be shown that the same findings also hold true for unpurified monomers, rendering the falcon-architecture even more favorable for the desired stepping application.

Length of handle binding regions

First, different lengths of the binding region on sliders' and rails' interacting handles have been investigated. Initially, the handles for both monomers were 21 nts long. The goal was to ascertain whether a shorter handle length – meaning a reduced binding region between the slider and rail handles – would influence the dimerization yields and – if so – to what extent. For this purpose, four handle length variations for the rail monomer have been tested. Slider handles remained at 21 nt, as it was found for the mini-stepper system that shortening the handle length for both monomers tends to reduce the dimerization yields. This results in the folding of one slider candidate with 21 nt long handles and four rail candidates, each of which exhibit either 21 nt, 16 nt, 14 nt or 12 nt handles. It should be highlighted again that this refers to purple initialization handles. Purple clip strands have been included in the slider folding mixture at a 40x excess with respect to the scaffold used. As negative controls, sliders have also been folded without purple clip strands to observe whether the interactions between the sliders and rails upon purple clip strand addition are specific. Dimerization reaction has been performed at 20 mM final $MgCl_2$ concentration and at 37°C overnight. The results have been analyzed with a 2% native AGE gel shown in figure 7.10.
The raw sliders ("S21") and rails ("R21") with the standard 21 nt handle length were analyzed in lane (4) and (5). The amicon purified versions are shown in lane (6) and (7). The gel band intensity for amicon purified R21 was lower than for S21. This corresponds to a slightly lower recovery yield for rail monomers, which provides an explanation for a slightly less intense rail monomer band within the doublet band in the subsequent lanes. The gel lanes labeled with a minus ("-") correspond to the negative controls meaning these samples lack purple clip strands. For these samples, it is expected that besides the two gel bands for the respective monomers, nothing else should be detected. This is the case for all negative controls and confirms that falcon-sliders and -rails do not interact unspecifically with each other, as has been the case for the mini-stepper monomers. This is a huge improvement compared to the previous stepper system. It allows concluding that dimer bands that appear for the other conditions tested on the gel in figure 7.10 are a product of specifically induced interactions.
It is interesting to observe the drastic differences in dimerization yields once different handle lengths are involved. Successful dimerization was judged upon an appearing dimer band running above the monomer bands. While an equal handle lengths of 21 nt shown in lane (9) resulted in almost no dimerization, the combination of sliders with 21 nt handles ("S21") and rails with 12 nt handles ("R12") led to a complete depletion of rails. The rail monomer band for the S21+R12 sample in lane (15) vanished completely and the

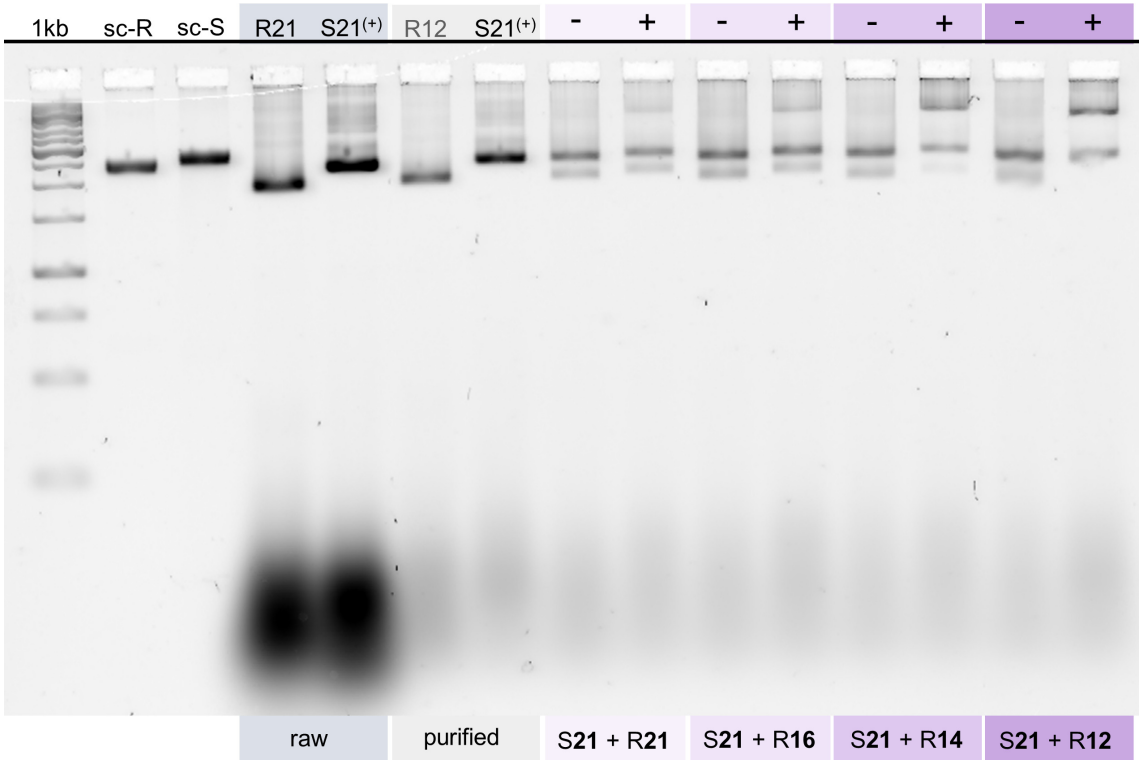

Figure 7.10.: 2% native AGE gel to analyze the effect of handle length variations on the heterodimerization of falcon-sliders and -rails. (1) 1kb ladder, (2) p8064 scaffold control for falcon-rails, (2) p8634 scaffold control for falcon-sliders, (3) Raw falcon-rail exhibiting 21 nt handles (R21), (4) Raw falcon-slider exhibitin 21 nt handles and with purple clip strands included in the folding ($S21^+$), (5) Amicon purified R21, (6) Amicon purified $S21^+$, S21+ R21 without clip strand (7) and with clip strands (8), (9) S21 without purple clip strands incubated with rails that exhibit 16 nt handles (R16), (10) $S21^+$ incubated with R16, (11) S21 without purple clip strands incubated with rails that exhibit 14 nt handles (R14), (12) $S21^+$ incubated with R14, (13) S21 without purple clip strands incubated with rails that exhibit 12 nt handles (R12), (14) $S21^+$ incubated with R12.

Gel running parameters: 0.5x TBE buffer with 10 mM $MgCl_2$, SYBR safe pre-staining 0.5 $\mu g/mL$; 60V for 4h at RT.

appearing dimer band had the highest intensity compared to all other conditions. The gel shows an increasing dimerization yield with a decreasing rail handle length.

These findings motivated switching to a 12 nt rail handle length and keeping 21 nt for the slider handle for all subsequently-presented experiments.

It remained to be shown whether different handle lengths also influence the clip strand removal reaction. To investigate this, the same samples from the above discussion have been subjected to purple clip-removal strands that could initiate DNA strand displacement upon binding to the toehold region of the clip strands. Clip strand removal reactions have been performed at 37°C for 1h applying 1 pmol of purple clip-removal strands to the reaction volume. The results have been analyzed on a 2% native AGE gel. Successful DNA strand displacement of purple clip strands would lead to disassembly of the dimers. An indication for disassembled dimers is a vanishing dimer band on the gel in a sample that had previously shown a dimer band and was combined with the appropriate clip-removal

strands. This was indeed observed for all samples on the gel shown in figure 7.11.
It should be highlighted again that the samples analyzed on the gel in 7.11 are the same as in 7.10. They rested for some days at 4C. A subsection of those were then used for the removal reactions. The negative controls shown in lanes labeled with ("-") showed very minor higher-order bands. This could be attributed to the fact that these samples already rested for some time and might have formed some complexes that are not detectable. However, the overall trend that dimerization yields increase with decreasing rail handle length was reproducible looking at lanes (4), (5), (8), (9), (12), (13), (16) and (17). The effect of the removal strands is thus most pronounced in the samples where dimerization yields were highest and dimer bands were quite intense. Thus, one observes a vanishing dimer band especially for the samples S21+R14 and S21+R12. It can also be shown that the structures successfully adopt a monomeric state upon clip strand removal, as indicated by increasing monomer band intensities in lanes (15) and (19) compared to lanes (13) and (17).
These experiments allow concluding that purple clip-removal strands are capable of dissolving the dimers that had been formed using purple clip strands. Together with the negative controls that did not include any clip strands, these results indicate a second time that the interaction between the falcon-monomers is specific.

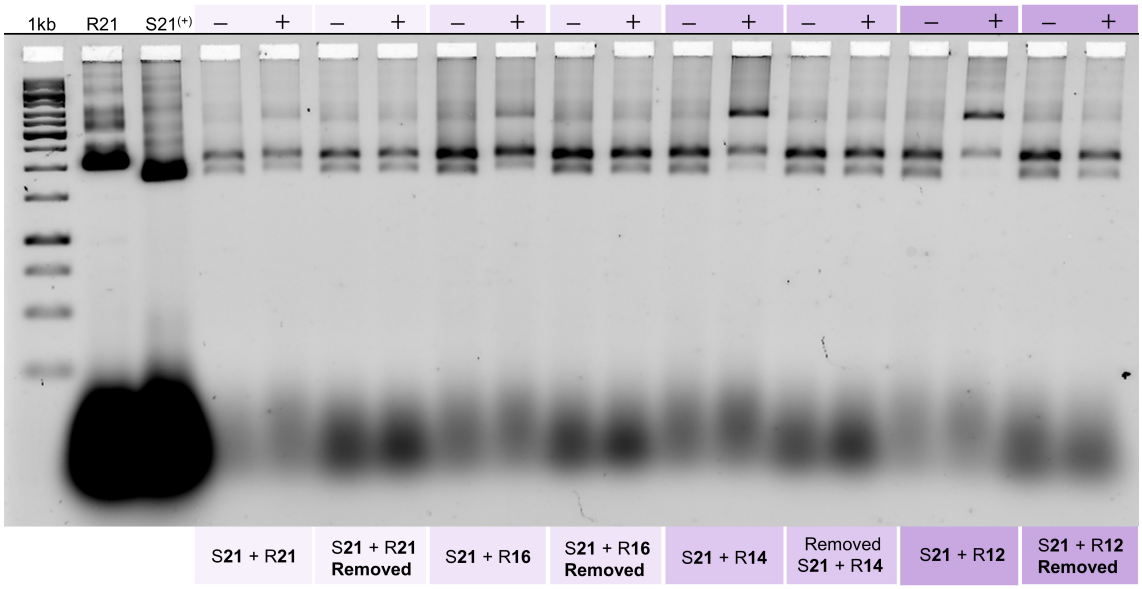

Figure 7.11.: 2% native AGE gel to analyze the effect of handle length variations on purple clip strand removal reactions. (1) 1kb ladder, (2) Raw falcon-rail exhibiting 12 nt handles (R21), (3) Raw falcon-slider exhibiting 21 nt handles and with purple clip strands included in the folding ($S21^{+}$), S21+R21 dimerization without (4) and with (5) purple clip strands, (6)-(7) Purple clip-removal strands applied to samples from lane (4) and (5), respectively, S21+R16 dimerization without (8) and with (9) purple clip strands, (10)-(11) Purple clip-removal strands applied to samples from lane (8) and (9), respectively, S21+R14 dimerization without (12) and with (13) purple clip strands, (14)-(15) Purple clip-removal strands applied to samples from lane (12) and (13), respectively, S21+R12 dimerization without (15) and with (17) purple clip strands, (18)-(19) Purple clip-removal strands applied to samples from lane (15) and (17), respectively.

Gel running parameters: 0.5x TBE buffer with 10 mM $MgCl_2$, SYBR safe pre-staining 0.5 $\mu g/mL$; 60V for 4h at RT.

Dimerization without pre-purification of monomers

It was suspected that even though falcon-monomers have tested much more robust towards purification, amicon purification was the reason why the negative controls in 7.11 showed slight indications for multimerization over time. This motivated testing whether falcon-monomers could be dimerized without pre-purification.
Figure 7.12 shows results on the purple dimerization of unpurified falcon-rails and -sliders at 37°C overnight. One can observe a complete depletion of the rail monomers indicated by a vanishing rail monomer band in lane (6) and an appearing sharp dimer band. Successful heterodimerization of falcon-monomers can thus be achieved without the need for their pre-purification. Purification is thus no longer a concentration-limiting step, which is especially helpful for the upcoming stepping experiments. For all upcoming experiments, purification has been left out and falcon-monomers were used unpurified.

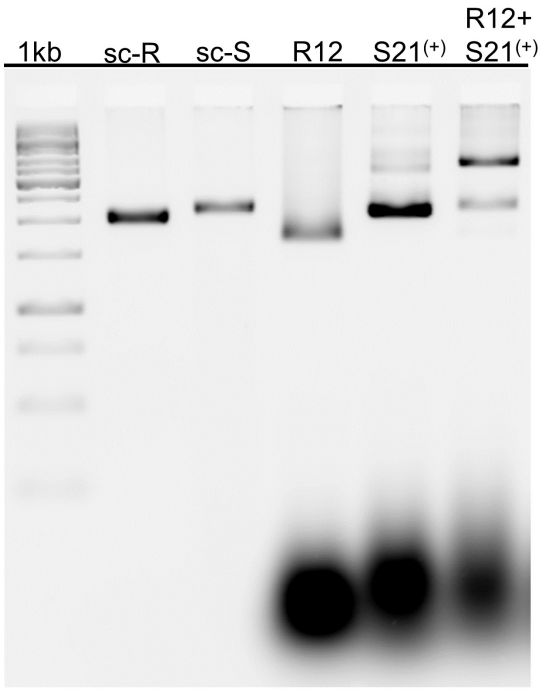

Figure 7.12.: 2% native AGE gel to analyze heterodimerization of unpurified falcon-sliders and -rails. (1) 1kb ladder, (2) p8064 scaffold control for falcon-rails, (2) p8634 scaffold control for falcon-sliders, (3) Raw falcon-rail exhibiting 12 nt handles (R21), (4) Raw falcon-slider exhibiting 21 nt handles and with purple clip strands included in the folding ($S21^{+}$), (5) Heterodimerization of unpurified R12 and $S21^{+}$.

Gel running parameters: 0.5x TBE buffer with 10 mM $MgCl_2$, ethidium bromide 0.5 $\mu g/mL$, 60V for 210 min at RT

Time and temperature dependency of dimerization yield

The presented purple dimerization experiments have shown that falcon-monomers can be specifically triggered to attach and detach by the introduction of appropriate clip or clip-removal strands. Slight changes in the handle length have shown a dramatic impact on the heterodimerization yields. The reaction kinetics of the interaction between two components is generally subjected to environmental parameters. It is known that temperature

and time can be crucial to the efficacy of the reaction. Thus, it was important to study the extent to which the heterodimerization yields of falcon-monomers are influenced by the temperature and time.

Thus far, falcon-monomers have incubated overnight at 37°C. Figure 7.13 presents results found on different incubation times and temperature. Thereby, dimerization yields associated with an overnight incubation at 37°C were compared with 2h and 1h incubation. Lane (6) on the 2% native AGE gel in 7.13 A shows that the overnight incubation results in a dimer band with the highest band intensity compared to the dimer bands corresponding to the 2h and 1h incubation in lanes (7) and (8), respectively. The fact becomes even more evident when inspecting the monomer bands of the samples. Rail monomers are almost completely depleted when incubated overnight while the doublet gel band is still clearly visible for the shorter incubation times.

Figure 7.13 B investigates whether the yields for an overnight incubation change with temperatures of 37, 45 and 50°C. Higher temperatures were not tested to avoid disassembly of the origami structures. Lanes (6)-(8) show that the temperature does not have a huge impact on dimerization yields judges by an almost equal dimer band intensity for all three conditions. Lanes (10)-(12) test the clip strand removal reactions for the samples that had been incubated at different temperatures. Removal reactions were performed at 37°C for 1h and show that that although samples had been dimerized at different temperatures, they can be efficiently disassembled. Since all purple dimers were dissembled equally well upon the addition of purple clip-removal strands, one can assume that the observed dimers generated at different temperatures do not exhibit differently strong interactions. Lane (13) shows again that a 1h incubation is not capable of driving the dimerization reaction to completion even at a higher temperature of 50°C.

7.3.4. Conclusion

The studies presented thus far on falcon-sliders and -rails have shown that the falcon design is a much more robust architecture compared to the mini-sliders and -rails. This became particularly evident when first amicon purification of the falcon-monomers resulted in clean and stable products without the need for fine-tuning of the protocol, and second when it was found that purification of the falcon-monomers is not required for good dimerization yields. The 21 nt handle length for mini-stepper monomers has also been implemented into the falcon design and thus served as a starting point for handle length variations. Deviations from 21 nt handle length showed a drastic impact on purple dimerization yields. The best dimerization yields have been achieved for a 12nt overlap between interacting handles of the falcon-sliders and -rails. The design thus settled for a 12 nt handle length of rail monomers and a 21 nt handle length for the sliders. Purple dimerization that involves six clip strand interactions requires overnight incubation to reach completion. Thereby, the yields seem to be independent of the temperature applied.

In any case, clip strand removal reactions at 37°C for 1h achieved proper disassembly of the purple dimers upon the addition of 1 pmol of purple clip-removal strands. Slider handles as well as purple clip strands have been PAGE purified prior to use. It should be emphasized that these findings simply refer to the very initial heterodimerization mediated via six purple clip strands.

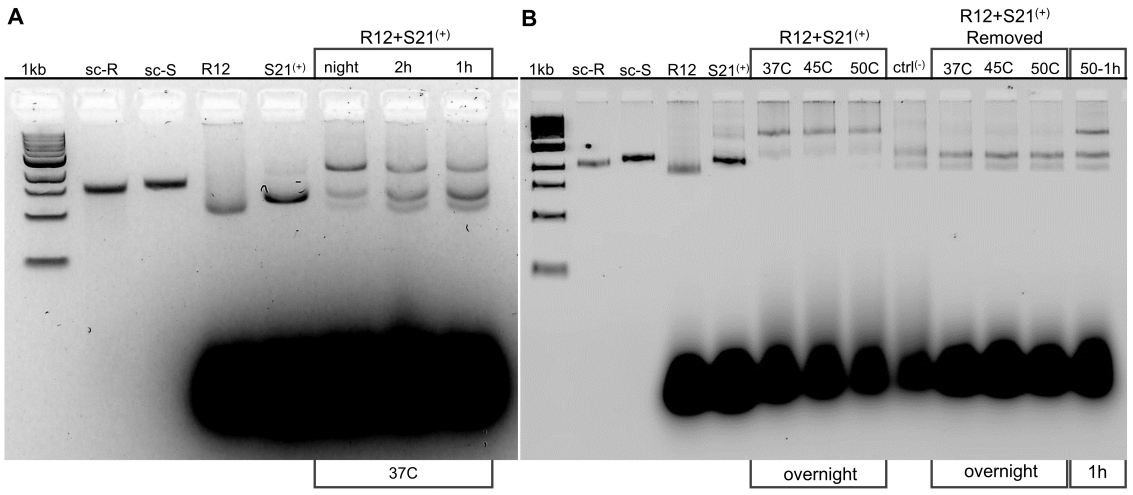

Figure 7.13.: A 2% native AGE gel analyzing the impact of an overnight incubation of falcon monomers versus a 2h and 1h incubation. (1) 1kb ladder, (2) p8064 scaffold control for falcon-rails, (3) p8634 scaffold control for falcon-sliders, (4) Raw falcon-rail exhibiting 12 nt handles (R21), (5) Raw falcon-slider exhibiting 21 nt handles and with purple clip strands included in the folding ($S21^+$), Heterodimerization of unpurified R12 and $S21^+$ at 37°C overnight (6), for 2h (7) and for 1h (8); **B** 2% native AGE gel analyzing the impact of different temperatures on the overnight heterodimerization of falcon-monomers. (1) 1kb ladder, (2) p8064 scaffold control for falcon-rails, (3) p8634 scaffold control for falcon-sliders, (4) Raw R21, (5) Raw $S21^+$, Overnight heterodimerization of unpurified R12 and $S21^+$ at 37°C (6), at 45°C (7) and at 50°C, (8) Combination of R12 + S21 without clip strands (9), clip strand removal reactions for R12+$S21^+$ that were incubated at 37°C (10), at 45°C (11) and at 50°C (12), purple heterodimerization of R12 and $S21^+$ at 50°C over the course of 1h (Data courtesy for gel in B: Dr. Bhavik Nathwani)

Gel running parameters: (A) 1x TAE + 11 mM $MgCl_2$ + SYBR gold pre-staining 1:10 000 dilution; 70V for 2h 20min in ice bath; (B) 0.5x TBE buffer with 10 mM $MgCl_2$, SYBR safe staining 0.5 $\mu g/mL$; 70V for 3h at RT.

7.3.5. Three-phase actuation of falcon-steppers

The following section covers key experiments investigating whether it is possible to actuate the falcon-sliders along the rails through symmetric, three-phase RGB cycles by the subsequent addition of red, green and blue clip and clip-removal strands. Native AGE gel electrophoresis as well as TEM imaging have been used again to detect the reactions. Thereby, it should be reminded that falcon-steppers that transit from one clip strand engagement to the subsequent one reach an intermediate state where both of the clip strands are engaged. The removal of the previous clip strand is only then induced once the system has reached the intermediate state. This ensures that dimers that are detected are not a product of a detaching and re-attaching process, but an actual forward actuation. Each clip engagement and clip-removal reaction was performed at 37°C over the course of 2h and 1h, respectively. Clip strands were thereby applied at a final concentration of 800 nM, and clip-removal strands at a final concentration of 2 µM.

At the beginning of this chapter in section 7.1.3 it has been proposed that clip strands need a balanced length to fulfill the designed functions. They should be sufficiently long

to overcome the 3.4 nm distance between the RGB attachment sites, but short enough to ensure rigid attachment of the sliders to the rails. If clip strands are too long, they can easily skip attachment sites and the control over forward and backward motion is lost. Too short clip strands will not be able to stretch sufficiently to induce motion. The length and concomitant flexibility of the clip strands were fine-tuned through implementing stretches of T-bases – so-called T-linkers – within the transition space between the slider and rail handles. In the following, the effect of different T-linker lengths embedded in clip strands on the performance of RGB actuation is investigated. Thereby, clip strands with a T-linker of 2T and 6T have been compared to clip strands without a T-linker (0T).

For purple heterodimerization, it has been found that the best results were achieved with clip strands that included no T-linker. The corresponding data can be found in appendix B.9. This is different to what has been found for RGB clip strands, which exhibit best stepping performance for a clip strand-linker length of 6T. Figure 7.14 displays one gel for each individual state of the RGB cycle analyzing the efficacy of stepping upon different linker lengths. Details on the individual states have been provided in section 7.1.2. As a reminder, after heterodimerization of the falcon-sliders to the rails via six purple clip strands, the dimers are first subjected to red clip strands that bind the red slider handles to the first for red attachment points along the rail leaving the system engaged via both the purple and red clip strands. This is referred to as "state 0-1", highlighted in purple-red in figure 7.14 A. The addition of purple clip-removal strands dissolves the purple slider handles from the purple rail handles, resulting in a dimer that is purely engaged via the four red clip strands that still appear as a dimer band on an agarose gel. By that time, the slider has completed one 3.4 nm step along the rail. The same process is repeated for states 2 and state 3, which are achieved by green and blue clip strand interactions. A RGB cycle refers to two steps along the rail completed by a slider, from red to green and from green to blue.

The gels in figure 7.14 visualize this process by detecting the dimer bands for each state. Figure 7.14 A starts with a proper heterodimerized falcon-stepper shown in lane (6). Lane (7) and (8) are control samples corresponding to a purple dimer disassembled upon the addition of a purple clip-removal strand and rails and sliders that have been mixed without a clip strand present, respectively. These controls confirm that the dimer band in lane (6) originates from a specific interaction of sliders and rails upon the addition of purple clip strands. This sample has been subjected to red clip strands exhibiting no T-linker (0T) in lane (9), a 2T-linker in lane (10) and a 6T-linker in lane (11). The dimer band was maintained for all three clip strand variations. The subsequent gel lanes (12) to (14) correspond with the same samples subjected to purple clip-removal strands. ImageJ analysis of the gel band intensities revealed an average decrease in gel band intensity of 57%, whereby the intensity for the 0T sample in lane (12) showed the highest decrease. This indicates that clip strands without T-linkers provide the least stable binding via the four clip strands compared to clip strands that include T-linkers. Moreover, the sample shows an increasing population of the rail monomer band, meaning that some rails have left the assembly with the sliders due to insufficiently strong binding. This trend also continues for the other states. While clip strands with a 2T- and 6T-linker result in consistent dimer band intensities through the whole RGB cycle, 0T-linker samples continue to disassemble especially once the removal of the preceding clip strand is induced. It should be noted that the overall intensity of all dimer bands drops down to an average of 25% when more

steps are taken. In case the clip strands exhibit a 6T-linker (see lane (13) in figure 7.14 C), around 35% of the original dimer material is able to step all of the way through the RGB cycle. By contrast, only 13% of the dimers that are based on clip strands without T-linkers (see lane (11) in figure 7.14 C) make it through one RGB cycle. All generated dimers can be specifically disassembled upon the addition of the appropriate clip-removal strand shown in the last three lanes of each gel. It should be noted that the clip-removal strands do not include T-linkers. ImageJ analysis of the gel band intensities as well as the gels of figure 7.14 with the uncut staple clouds can be found in appendix B.2. The analysis of different T-linker length within clip strands has shown that a 6T-linker included in the RGB clip strands achieves the best responses to the three-phase actuation and is thus implemented in the clip strand design.

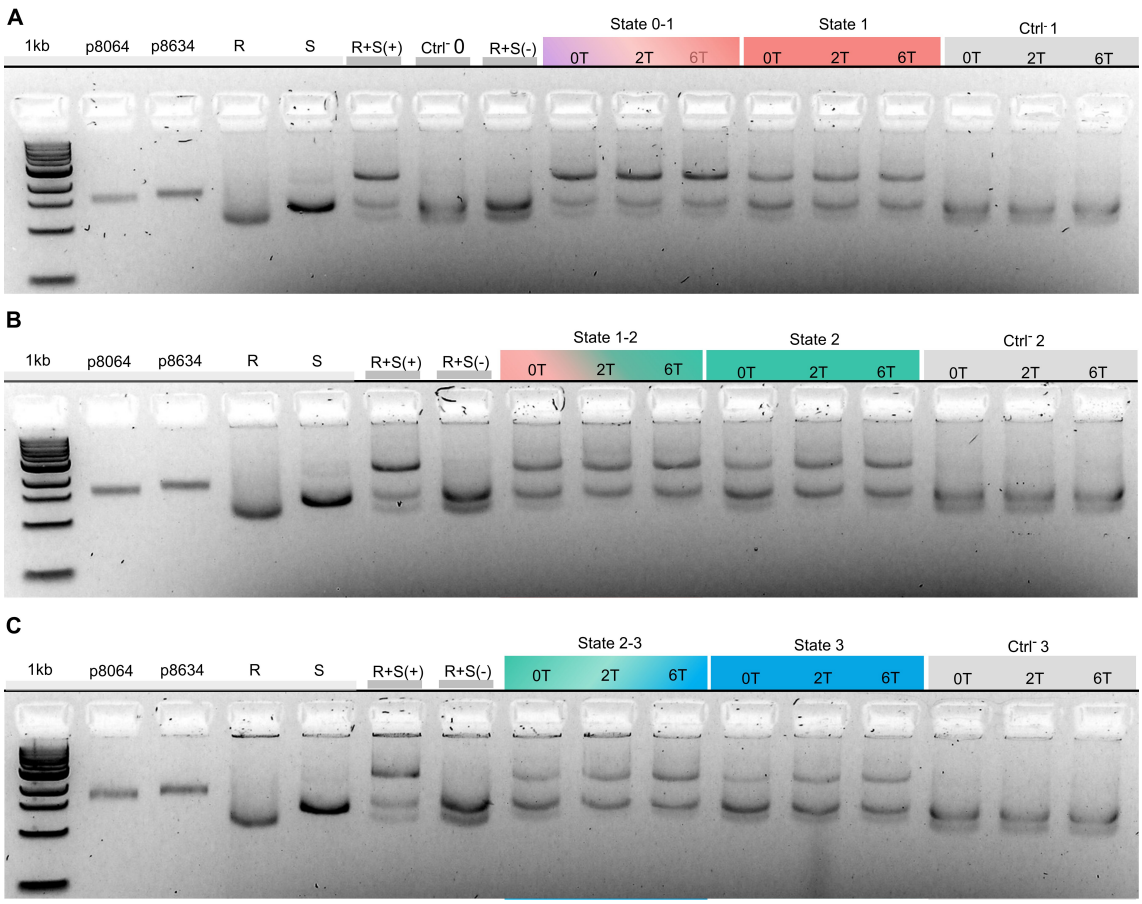

Figure 7.14.: 2% native AGE gel analysis of the effect of T-linker length in clip strands on the performance of RGB stepping. Shared lanes across all gels: (1) 1kb ladder, (2) p8064 scaffold control for falcon-rails, (3) p8634 scaffold control for falcon-sliders, (4) Raw R12, (5) Raw S21^{+}, (6) R12+S21^{+} heterodimers. **A** Analysis of 0T- vs. 2T- vs. 6T-linkers embedded in red clip strands. (7) Disassembled heterodimers R12+S21^{+} upon addition of purple clip-removal strands (ctrl$^{(-)}$), (8) Combined R12 and S21 without clip strands, (9)-(11) Dimers mediated *via* purple and red clip strands (state 0-1). Red clip strands exhibit 0T-, 2T- and 6T-linkers, (12)-(14) Dimers from lanes (9)-(11) but treated with purple clip-removal strands (state 1), (15)-(17) Dimers from lanes (9)-(11) treated with red clip-removal strands (ctrl^{-}). **B** Analysis of the effect of 0T-, 2T- and 6T-linkers embedded in green clip strands on state 1-2- and state 2-dimers. **C** Analysis of the effect of 0T-, 2T- and 6T-linkers embedded in blue clip strands on state 2-3- and state 3-dimers.

Gel running parameters: 1x TAE + 11 mM $MgCl_2$ + SYBR gold pre-staining 1:10 000 dilution; 65V for 2h 30min in ice bath

7.3.6. Symmetric actuation across two RGB cycles

The mechanism for the three-phase actuation was experimentally verified with gel electrophoresis in the previous section. However, symmetric actuation remains to be confirmed. Symmetric within this context means that sliders can step into a second cycle of RGB actuation relying on the same clip and handle sequences. Reaction solutions with falcon-steppers that have reached state 3 via one RGB cycle contain all four flavors of clip-removal strands. Since the same clip strands are used to promote the slider even fur-

ther, it is necessary to first purify the solutions from the clip-removal strands that would otherwise interfere with a second engagement of the slider and rail with the clip strands. For this purpose, clip-removal strands have been equipped with a biotin-modification that could interact with streptavidin-coated magnetic beads. In this way, the beads can bind all biotinylated clip-removal strands on their surfaces. The magnetic beads can be separated from solution by subjecting it to a magnetic field. Beads carrying clip-removal strands are collected at the tube bottom and form a pellet. The supernatant solution thus contains falcon-stepper residing in state 3 and can be further processed. The purification technique using magnetic beads is illustrated in figure 7.15 E. Details on the protocol are listed in the appendix A.3.

For native AGE gel evaluation of two-cycle stepping, the dimer band is the indicator for successfully-induced interactions between the falcon-slider and -rails. Observing dimer bands of intermediate states in which a falcon-slider is attached to the rail via two clip strand flavor right before it can fully engage with the subsequent anchor point ensures that the detected steppers are not a result of the slider detaching and re-attaching to the rail, but rather it is dragged along the rails' surfaces by the RGB clip strands. Thus, it is expected to see dimer bands for both the intermediate states and the actual states. These dimer bands should be specifically dissolvable upon the addition of the clip-removal strands. Thereby, one should keep in mind that with each introduced component, the reaction volume further dilutes, which reduces the concentration of the flacon-steppers. In order to compare gel band intensities and thus the efficiency of the stepping, it is important to normalize the sample concentration loaded onto the gel. This is achieved by estimating the concentration of falcon-steppers in the reaction solution. These prediction can be more precise for the first RGB cycle since it is known that the stepping starts with raw falcon-monomers right after their folding, which provides 20nM of material given that the folding yields are close to 100%. However, the second stepping cycle starts with purified falcon-steppers that have reached state 3. One can only provide a rough estimate on how much material can be retrieved from the purification protocol. A 50% recovery yields was assumed. Based on this assumption, the sample volumes loaded on to the gel were adjusted accordingly. The aspects explained above are important to keep in mind when inspecting figure 7.15.
To summarize, native AGE gels can verify the suggested stepping mechanism to a certain extent, as follows. Intact dimer bands for the intermediate and completed states throughout both cycles together with the controls where dimer bands are specifically dissolved by clip-removal strands are the indicators for proper stepping that can be provided by gels. Certainly, this cannot serve as the only way to prove the principle, which is why TEM imaging will be discussed later as a second route of verification.
For a better overview, figure 7.15 A and B provide illustrations of the falcon-rail with the addressed anchor points highlighted and matched to the appropriate states on the 2% native AGE gels that analyze samples from each state. Lanes (9)-(17) on the gel in 7.15 A refer to samples that have been actuated by the subsequent addition of red, green and blue clip and clip-removal strands. Intermediate states 0-1, 1-2 and 2-3 are highlighted with the colors of the according clip strands involved. For example, state 0-1 corresponds to falcon-monomers that are engaged via the purple clip strands from the previous state 0, and via red clip strands for the upcoming state 1. The other intermediate states can be understood analogously. Completed states are highlighted with only one color since they rely on only one class of clip strands. The expectations for these samples and their

appearance on the gel that have been described above have been confirmed. Intermediate states as well as completed states 1, 2, and 3 exhibit distinct dimer bands. The controls (ctrl $^-$ x with x = 0, 1, 2, 3) show that the dimer band dissolve once the appropriate clip strand is applied. To give an example, the fact that ctrl$^-$ 1 reveals no dimer band verifies that state 1 dimers can be specifically disassembled with red clip-removal strands. Sections 7.3.10 provides an additional verification for the specificity of the clip strand interactions. In summery, figure 7.15 A shows that state 3 dimers can be purified using magnetic bead purification, upon which they successfully transit into the red state of the second RGB cycle. This can be judged by dimer bands that are present for intermediate state 3-4 and state 4 in lanes (18) and (19), respectively.
Following the same argumentation, figure 7.15 B shows that falcon-steppers promote through a whole second cycle of RGB actuation. Lanes (6)-(11) refer to the same sample as shown in the gel above and are included as controls at this point. Any multimer band that appears in the following higher-order states and that runs at the same height as the dimer bands present in the controls can thus BE associated with a dimer band. Dimer band intensities decrease especially for the state 4 dimers shown in lane (11) in 7.15 B. These are the dimers that have been subjected to blue clip-removal strands. Since the monomer bands in lane (11) are of similar intensities compared to state 3-4 dimers in lane (10), one cannot argue that the concentration estimate was off and thus too little sample volume was loaded onto the gel. One reason could be that some dimers miss out on some of the four bonds between the monomer and thus fall apart more easily upon clip-removal strand addition. Consequently, fewer steppers can be actuated onto state 5. However, lane (12) and (13) still exhibit a dimer band. Further falling apart for states 4-5 and state 5 can be excluded since the monomer band intensities remain the same. In the case of the rail monomer band, one can say that the rails remain completely depleted. Since the bands become more faint for state 4-5 and state 5, it is easier to understand the undergoing processes by including the monomer bands into the discussion. The relevant ones are indicated by red arrows in figure 7.15 B, C and D. State 4-5 in B still exhibits a dimer band and rail monomers are completely depleted. On the other hand, for state 5 a rail monomer band appears, meaning that a portion of dimers has fallen apart upon the addition of green clip-removal strands. At this stage, it is not possible to completely understand why the dimers fall apart. Further investigations need to be pursued to elucidate possible reasons for this. However, one can conclude that steppers successfully reach state 4-5. All controls (ctrl$^-$) again verify the specificity of the interactions. Figure 7.15 C and D refer to the same areas highlighted in green and red on the gel in 7.15 B. For a better visibility of the dimer and monomer bands, the contrast and brightness of these sections have been adjusted accordingly. Finally, it is to note that staple strand clouds have been cut as they do not add important information to the discussion. The complete gels can be found in appendix B.2.

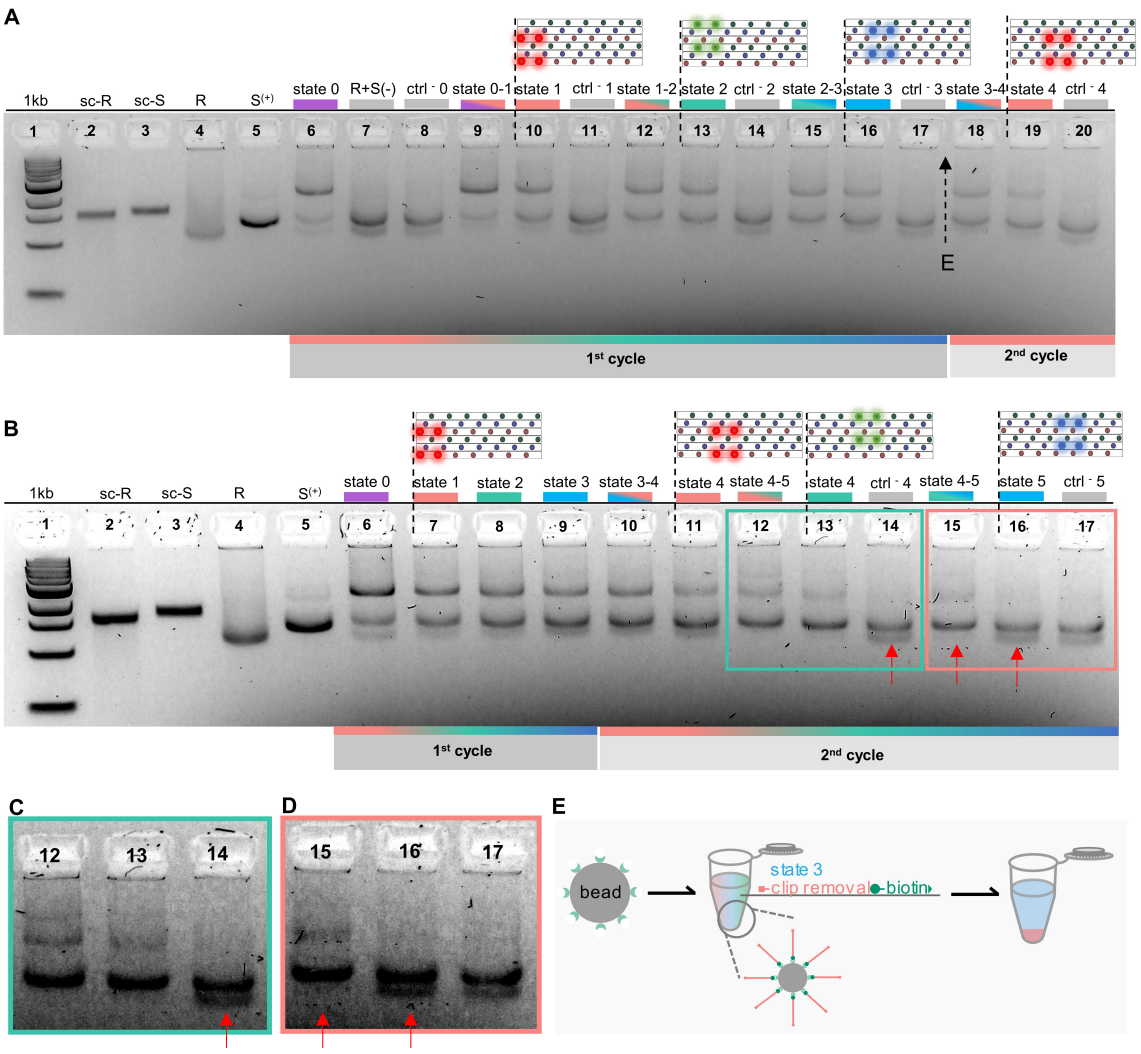

Figure 7.15.: 2% native AGE gels to analyze RGB stepping across two, symmetric cycles. **A** Gel evaluation for PRGBR-stepping. Falcon-monomers heterodimerized *via* purple clip strands (state 0 in lane (6)) and subsequently actuated through the cyclic addition of red, green and blue clip and clip-removal strands. Intermediate states 0-1, 1-2, 2-3 and 3-4 refer to dimers that are engaged *via* two types of clip strands highlighted with the according colors. Falcon-steppers reach states 1, 2, 3, and 4 through the addition of the clip-removal strand displacing the clip strand from the previous state. Controls (ctrl$^-$ x, with x = 0, 1, 2, 3, 4) refer to state x-dimers subjected to the clip-removal strand that addressed the remaining engaged clip strands. Vanishing dimer bands in the control samples indicate that interactions are specific. **B** After magnetic bead purification that eliminate removal strands from state 3-dimers, they can be actuated further into a second cycle of RGB stepping relying on the same clip and clip-removal sequences as in the previous cycle.**C**, **D** Contrast enhanced sections from gel in **B** highlighted in green and red accordingly for a better visibility of the dimer and monomer bands. **E** Illustration of magnetic bead purification. Clip-removal strands are functionalized with biotin and can be captured by streptavidin-coated magnetic beads. Subjected to a magnetic field the beads that are covered with the clip-removal strands can be collected in a pellet on a Eppendorf tube bottom. the supernatant contains purified state 3 dimers that can be further processed.

Gel running parameters: 1x TAE + 11 mM $MgCl_2$ + SYBR gold pre-staining 1:10 000 dilution; 70V for 2h 30min in ice bath

7.3.7. Backward stepping

Backward motion of the falcon-steppers can be achieved by a reverse addition of clip and clip-removal strands. The 2% native AGE gel in figure 7.16 shows that reverse actuation of state 3 dimers is possible. Again, this is confirmed by dimer bands that remain intact over the course of clip and clip-removal strand addition. Backward stepping is also symmetric, meaning that the functional strands have the same sequences. Magnetic bead purification was performed again for state 3 dimers before clip strands were applied in reverse order. Dimer bands for revisited state 2 and 1 are present but very faint.
Figures 7.16 B and C provide contrast enhanced gel sections to better visualize the dimer bands in lanes (11) and (12) as well as (14) and (15). The controls did not reveal any dimer bands as expected. The fact that the gel evidence for backward stepping coincides with what has been seen for previous stepping evaluations indicates that falcon-steppers are also able to step backward.

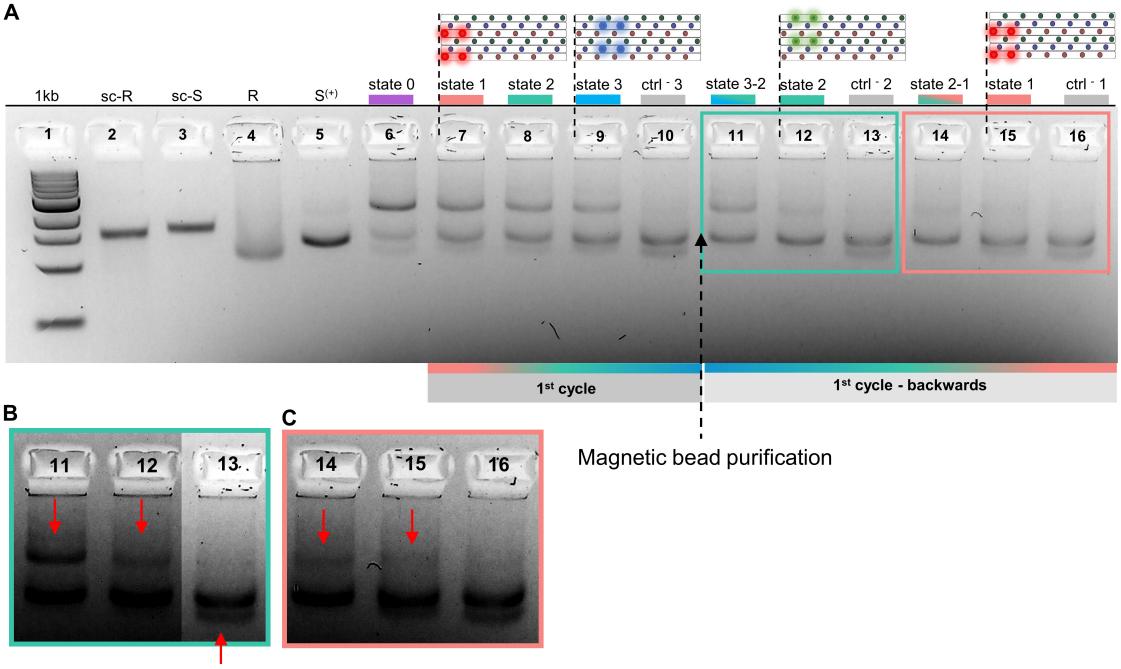

Figure 7.16.: A 2% native AGE gel analysis for the backward actuation of state 3 dimers (cf. text). **B**, **C** Contrast enhanced sections from gel in **A** highlighted in green and red accordingly for a better visibility of the dimer and monomer bands.

Gel running parameters: 1x TAE + 11 mM $MgCl_2$ + SYBR gold pre-staining 1:10 000 dilution; 70V for 2h 30min in ice bath

7.3.8. Optimization of the TEM staining protocol for a higher image contrast

It has been shown that falcon dimers can be specifically addressed with clip and clip-removal strands. Those are designed to drag the slider along the rail through visiting the appropriate anchor point exhibited by the rail. Up to this point, gel electrophoresis was the tool to investigate whether falcon-monomers remain dimerized over the course of the actuation. It has been shown that two cycles of forward stepping as well as backward stepping are achievable with the system under study. However, gel electrophoresis can only confirm the addressability and intactness of the falcon dimers. For full proof of programmable motion, a second route of verification is needed. One approach is to use TEM to resolve the slider motion on the rail by taking snapshots of each state. Since the step size of the falcon-stepper is quite small, it is challenging to resolve the motion of each step. It is more suitable to image the dimers at their starting position – which is state 0 – after they were treated with red clip strand the first time (state 1) and after they have completed the first RGB cycle and have stepped one step ahead into the second RGB cycle (state 4).
Figure 7.17 illustrates the expected outlines of falcon dimers at the different stages. State 0 sliders are expected to be consecutively aligned with the rails. Introducing red clip strands would cause the slider to flip over and stack on top of the rail, as indicated by the red arrow in figure 7.17. This should lead to a decrease of the overall construct length. While a length of 128 nm would be expected for state 0 dimers, state 1 dimers exhibit only a length of 50 nm. The area that is uncovered by the slider – also referred to as the "rail tail" – decreases with each step taken up until the point where the construct exhibits two tails in state 4.
In order to detect the rail tail, it is crucial that the wing portions of the sliders are well distinguishable from the background. The edges of the wings are the geometric feature that are changing their position upon actuation. It emerged that it is challenging to resolve the slider wings from the grid background using the standard staining protocol. A systematic study on achieving ideal conditions for a high image contrast and good population of falcon dimers from different states was thus performed.

Challenge with TEM imaging of RGB dimers

The standard protocol to stain DNA origami structures for TEM imaging enabled properly imaging falcon-sliders and -rails as well as purple dimers. Thereby, samples are usually diluted down to 1 nM and 3 µL raw sample are added to the grid, incubated for 2 minutes (deposition time) and absorbed by filter paper before another 3 µL of negative staining solution is added and again absorbed into filter paper after several seconds of incubation. Negative staining solution was 2% uranylformate (UFO), which has been complemented with 1 µL 5M sodium hydroxide (NaOH). This protocol usually results in an even distribution of stain across the whole grid and is capable of resolving the desired level of structural detail in most cases. It was remarkable that falcon-sliders especially exhibited a rather uneven distribution of the stain across the structures. Figure 7.18 shows TEM images of raw sliders when stained using the standard protocol. The TEM image on the left shows that sliders tend to accumulate more staining solution in the middle area, which make the wing parts to appear much more faint compared to the rest of the structure. This is one way in which sliders appeared on gels. The TEM image on the right shows

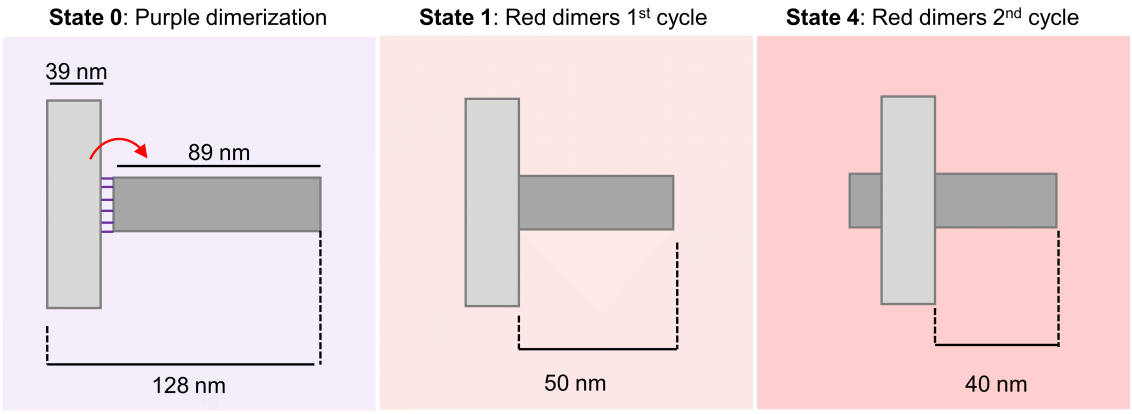

Figure 7.17.: Falcon-sliders are expected to consecutively align with the rails in state 0, which adds up to a total construct lengths of 128 nm. Introducing red clip strands to the system should cause the slider to flip over and stack on top of the rail. Thereby the slider covers a part of the rail. The distance from the lower wing edge of the slider to the end of the rail should measure 50 nm and be used as indicator of properly assembled slider-rail complexes. This rail tail length decrease with each taken step. Sliders in state 4 will reveal 40 nm rail tail in front of them and a shorter rail portion behind them.

that sliders also sometimes appear very faint in general.
These effects do not disrupt imaging of the falcon-monomers or purple dimers, although they become troubling once sliders are stacked on top of the rails. Stacked falcon-monomers form an area of ten DNA layers in the middle while slider wings are still based on three layers only. The middle part of the falcon dimers thus accumulated more stain leading to a much higher staining signals that overloads the signal coming from the slider wings.

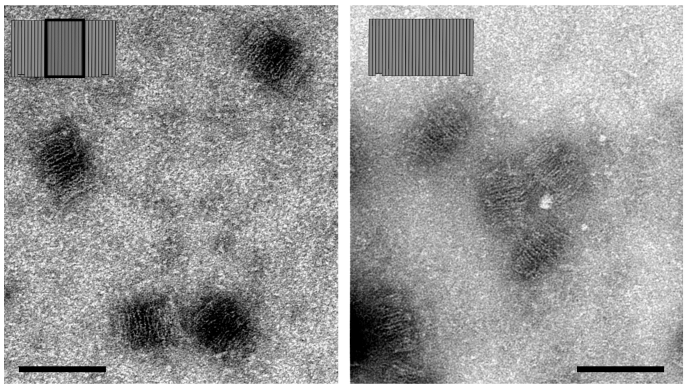

Figure 7.18.: TEM imaging of falcon-sliders with standard staining protocol. Sliders either exhibit an uneven distribution of the staining solution leading to dark areas in the middle, or sliders that are stained even but appear quite faint.

As a result, very often falcon-steppers – once RGB stepping was initiated and higher-order dimers have been formed – appear as dark spots on TEM grids with a low resolution of structural details. Additionally, the standard staining protocol was unsuited to achieve a decent population of falcon-steppers for the higher-order states since the sample con-

centration dropped with each taken step. Especially state 2-4 dimers very often were not detectable on the TEM grid.
Both described situations motivated testing techniques to improve the image contrast by first purifying the falcon-steppers from residual staples and functional handles through gel electrophoresis, second longer depositions times of the samples on the grid and third different techniques to apply the staining solution for the purpose of a better suited distribution of the stain across the constructs.
The following presents representative TEM images referring to different staining techniques. The investigations were performed with state 3 dimers. An important side note is that images taken from this particular sample refer to state 3 dimers with a mistaken handles design. However, this does not influence the results associated with TEM image quality.

TEM images of RGB dimers requires longer depositions times and gel purification

In order to detect any higher-order dimers on TEM grids, it was crucial to gel purify the dimers first using a 1% native AGE gel and ROTI-GelStain and deposit the samples on the grid for 30 min before staining. Details on gel purification can be found in appendix A.3.
After staining was completed, it was important to let the grids dry for no longer than 10 min. Figure 7.19 show the overview and close-up images resulting from different sample deposition times and compares the grid population of unpurified structures in A and purified structures in B and C. TEM images in figure 7.19 A show unpurified state 3 dimers that have been stained using the standard protocol described above. This involves a deposition time of 2 min. During imaging, a huge amount of time had to be invested to screen the grid for structures and very often nothing was detectable. If structures have been detected, most of the them were falcon-monomers and only a few among these were identified as dimers (encircled in red). Those displayed the problematic behavior being almost completely overloaded by the signal coming from the middle area of the dimer. Sliders are almost non-visible. In the rare cases that the dimer displayed an even distribution of stain, as shown in the close-up image in A, the sliders are still so faint that one cannot determine the location of the sliders on the rails.
The situation slightly improves once the sample volume applied to the TEM grids is increased from 3 to 7 µL combined with a prolonged deposition time of 15 min. Moreover, it was tested whether increasing the amount of UFO applied from 3 to 5µL would render the dimers less faint than in A and thus easier to detect. In general, the introduced adjustments of the standard staining protocol helped to increase the detectable number of dimers within the same field of view as shown in A. However, dimers are embedded in a sea of falcon-monomers (encircled black) and although they appeared less faint, they still accumulate more stain in the critical area, as shown by the close-up images in B. Figure 7.19 C shows that if the adjusted staining protocol is performed with gel purified state 3 dimers, it is possible to drastically increase the number of detectable dimers (encircled red). Furthermore, it was easier to identify the sliders due to an improved image contrast. This could be attributed to the absence of the staple strand excess that often render the grid background quite fuzzy. It is not a novel finding that gel purification helps to improve the image quality for DNA origami structures on TEM grids. However, gel purification prior staining is usually performed due to aesthetic reasons. It should be emphasized that

here the combination of gel purification, longer sample deposition times as well as higher volumes of sample and staining solutions is crucial to get from an almost undetectable sample to an even distribution of the construct of interest on the grid. Deviations from the suggested protocol adjustments lead to no or very little detection on the TEM grid. Gel purification of higher-order dimers was not trivial since the concentrations are quite low when more steps are performed. Thus effort had been made to increase the yields of higher-order dimers to achieve a suited concentration on gels. During the process of yield optimization, it has been found that functional staple strands result in slightly better yields when purchased from the company IDT exclusively. This helped to boost the yields to an extend where it was possible to purify the higher-order dimers from a gel.

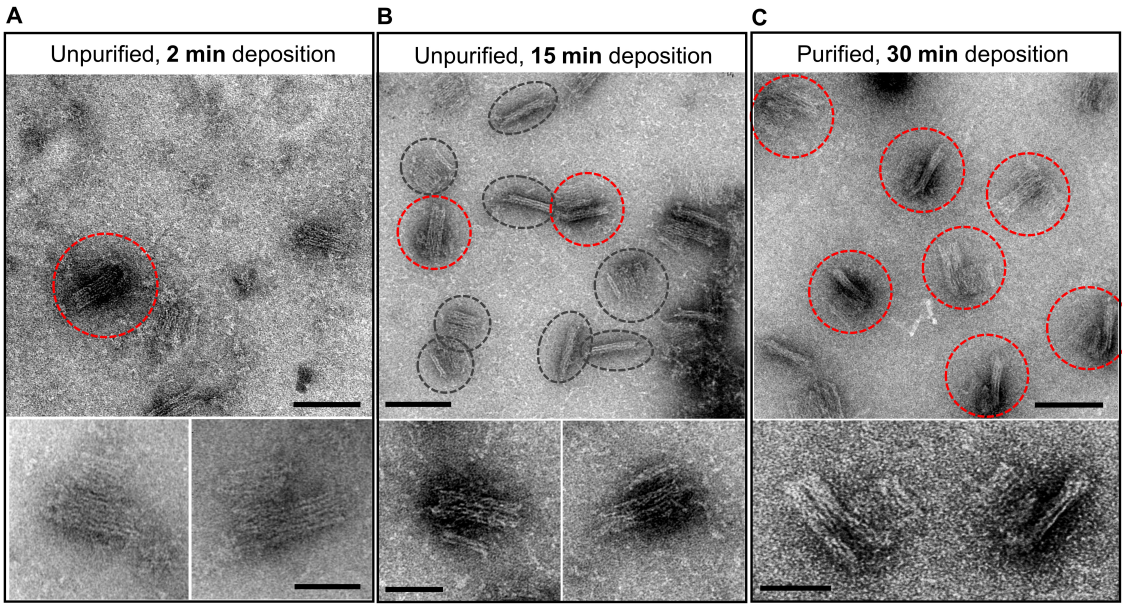

Figure 7.19.: Longer sample deposition times and gel purification help to populate the construct of interest on TEM grids. Scale bars indicate 100nm. **A** TEM images of unpurified state 3-dimers, deposited on TEM grids for 2 min prior staining with the standard protocol, **B** TEM images of unpurified state 3-dimers that have been deposited for 15 min on TEM grids. Increased sample and staining solution volumes have been applied to the grid, **C** TEM images of gel purified state 3-dimers that have been deposited for 30 min on TEM grids. Increased sample and staining solution volumes have been applied to the grid.

Different techniques to apply the staining solutions to the grids effect the image contrast

It has been shown that adjusting the involved volumes of both the sample and staining solution, the sample deposition times as well as the purity of the sample can lead to an all-or-nothing response with respect to the detection of the sample on TEM grids. Although the adjustments to the standard staining procedure enabled detecting higher-order dimers, the image contrast was still unsuited to verify the actual stepping. Sliders were visible but the uneven distribution of the stain across the structures still made it challenging to extract information about the exact location of the slider. However, the latter is crucial to be able to access the rail tail length quantitatively by measuring the distance between the

slider edge and the end of the rail. This motivated investigating different techniques to apply and remove the stain to and from the grid and the effect on its distribution. Thereby, the previously-described adjustments to the protocol have been included. Staining and imaging has been performed on state 3 dimers.

Figure 7.20 presents two methods to apply the stain onto the grid and two to remove it. The standard staining protocol is a combination of release mode and a gentle absorption of the staining solution into the filter paper, as shown in panel 2 and 3. For a systematic study on the effect of different ways to handle the stain, either the technique of how to apply the stain was kept unchanged while the stain removal was adjusted or vise versa. Panel 1 illustrates one way to alter the way to apply stain to the grid. Instead of releasing the droplet form the pipette directly onto the grid, UFO droplets are pipetted on to a piece of parafilm and absorbed by the grid holding it upside down, gently touching the surface of the UFO droplet. For stain removal, the grid holding the UFO droplet was gently held against a filter paper that immediately took up the solution. A TEM image representing the typical outcome of this staining procedure is included below panel 1. The majority of the detected structures were highly overstained and no structural details could be detected. Panel 2 and the TEM image shown for it refer to the standard procedure that has been described in the previous section and was included as frame of reference to study the differences induced by the adjustment in the staining protocol.

Comparing the TEM image of panel 1 and 2 prompts the conclusion that releasing the staining solution from the pipette is a much more suited technique to apply the stain to the grid than the tapping mode. Panel 3 and 4 present variations of the stain removal process. In a gentle approach, staining solution was removed from the grid by holding it in a 90° angle against a filter paper. A method that could be described as harsh uses a filter paper that has been folded in such a way that grids can be pushed against from the bottom, as shown in panel 4. The filter paper and grid thereby align in parallel to each other. The TEM image shown for the gentle method in panel 3 goes back to the same combination of stain application and removal as shown in panel 2, namely the gentle release. Image contrasts are fairly similar, although the representative TEM image for the harsh release shows a drastic improvement in image contrast compared to all other techniques. This technique manages to clearly resolve the slider onto the rails. It seems like the stain permeates the rail, causing them to be much darker compared to the sliders, which are stained a bit lighter. This contrast may be aesthetically less pleasing but is ideal to exactly locate the slider wings and verify their moving edge upon actuation. In general, it is challenging to define the exact reasons for the different outcome of different staining techniques. Researchers strongly rely on empirical knowledge when it comes to TEM sample staining. One possible explanation why the harsh release results in a more uniform distribution of stain could be that the whole grid touches the uranylformate at once with equal forces present between the surface of the grid and the droplet. Soaking the solution from the site as done in panel 3 involves a force implied by the droplet moving to the left, which might not be uniform across the whole grid, resulting in uneven distribution of the stain. The following section presents some TEM images taken from different states of the stepper and shows how the optimized staining can be used to quantitatively verify the motion of the slider on the rail.

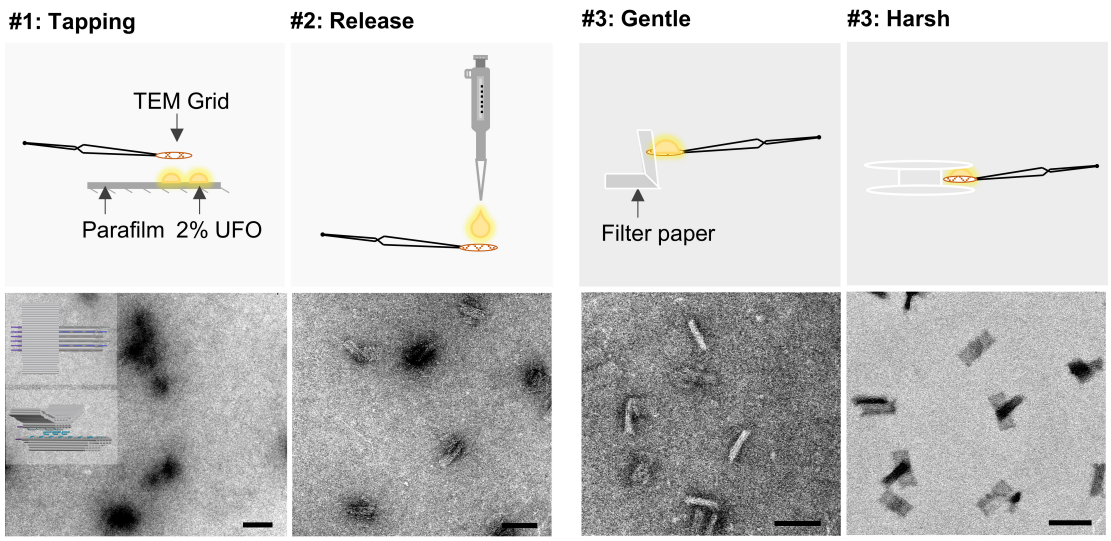

Figure 7.20.: The effect of different staining techniques on the TEM image contrast. A and B Two techniques to apply staining solution to the grid. **A** (top) Illustration of "tapping mode": Stain solution is applied by holding the grid upside down and tapping into a UFO droplet that it pipetted on parafilm. (bottom) Representative TEM image of state 3 dimers. Scale bars indicate 100 nm. **B** (top) Illustration of "release mode": UFO is released on to the grid by pipetting from the top. (bottom) Representative TEM image of state 3 dimers. Scale bars indicate 100 nm. **C** and **D** Two techniques to remove the staining solution form the grid. C (top) Illustration of the "gentle" removal. Grid with the UFO droplet is held against filter paper in 90° angle. (bottom) Representative TEM image of state 3 dimers. Scale bars indicate 100 nm. **D** (top) Illustration of the "harsh" removal. Grid with the UFO droplet is pushed against the filter paper from the bottom. (bottom) Representative TEM image of state 3 dimers. Scale bars indicate 100 nm.

7.3.9. TEM verification of PRGBR-stepping

A systematic investigation of different staining techniques eliminated parameters providing a suited image contrast for verifying the dimer bands observed on gels in previous sections. Figure 7.21 presents a gallery of TEM images taken from different states of the falcon-stepper system such as the state 0 in A, state 1 in B, state 3 in C and state 4 in D. Due to the small step size of 3.4 nm, the difference between state 2 and state 1 dimers is almost non-detectable and thus left out in the gallery. All samples shown on the TEM images have been gel purified and staining followed the already slightly optimized procedure of prolonged sample deposition times and increased sample/stain volumes.

Figure 7.21 A shows TEM images of state 0 dimers. They show the consecutive alignment of the slider and rail that was initially hypothesized. The close-up images even display the gap between slider and rail where purple initialization handles mediate a connection between the monomers illustrated on the top. It is to note, that the illustration shown in A is an exploded view on the purple dimers to show how the connection between falcon-slider and -rail is realized. The gap consists of the 12 nt handles from the rail and the 21 nt handle from the slider. This adds up to around 11 nm distance between slider and rail. The TEM images provided in B confirm the hypothesis that sliders start to flip over once

red clip strands are introduced. The particle observed on TEM grids are more compact and exhibit a reduced rail tail length. Panel B also includes a direct comparison between images obtained with the standard staining protocol and the optimized protocol. The standard protocol thereby refers to the "release-gentle remove" mode described above, while the optimized protocol refers to the "release-harsh-remove" mode. The latter allows observing where the slider is located on top of the rail.
Panel C shows the same, albeit for state 3 dimers. Here, the optimized staining also established an ideal image contrast that allows detecting the edges of the slider wings.
Panel D provides proof that falcon-steppers are able to be actuated with a symmetric set of clip and handle strands. State 4 refers to the first step of a second RGB actuation. Dimers from this state are expected to exhibit a second rail tail behind them since they have overcome 10.2 nm by taking three steps. Panel D shows some candidates of state 4 dimers that match these expectations. However, it should be highlighted that gel purified state 4 dimers are a mixture of three populations. One is the one depicted in panel D, a population that seems to have stepped forward into the center of the rails. The other population seems to have stepped backwards and thus looks similar to what one can observe in panel B. The third population seems to have half of the forward red anchor points engaged, while the other half are engaged with the backward red anchor points, leading to diagonal placement of the slider on top of the rail.
The concentration of gel purified state 4 dimers is too low to generate sufficient data for a statistic evaluation of the occupancy of the three possible population, but their existence should be included in the discussions here. Panel D also only displays TEM images generated with the optimized staining protocol. The reason for this is that all other staining protocols failed to detect state 4 dimers, highlighting the importance of delicate tuning of the staining once again. Overall, these TEM images are proof that the dimer bands on the gels indeed correspond to dimeric structures and that the slider is moving forward upon the cyclic addition of clip and clip-removal strands.

A quantitative analysis of the rail tail length is provided in figure 7.22. Rail tails refer to the longer parts of the rail that is uncovered by the slider. For the presented analysis, only falcon-steppers that landed on the grids facing up – exhibiting the typical T-shape – have been taken into account (see 3D-renders in figure7.22). Dimers that landed on their sides or that looked distorted were excluded from the analysis (see appendix B.2). In total, 50 particles for each state 0, 1 and 4 have been analyzed. Analysis was performed using the measure tool provided by the ImageJ software. As previously highlighted, state 4 reveals a mixture of different dimer populations due to sequence symmetry of applied clip strands. For tail length measurement of dimers in state 4, only forward stepping dimers were included in the analysis. The measured rail tail lengths and their distribution are represented as histograms in figure 7.22 D. The x-axis refers to the lengths in nm starting with the highest measured tail length, while the y-axis refers to the counted particles at a particular length starting with the lowest number of particles. Since state 0 dimers correspond to the initial heterodimerization and sliders are aligned consecutively to the rail, the dimers of state 0 have the longest tail length. This explains the accumulation of data points for state 0 at highest lengths on the very left in the graph of figure 7.22 D. This is followed by the tail lengths of state 1 and state 4 dimers. Despite the length distributions of state 1 and state 4 bordering each other, the peaks of the histograms are well separable in general. A clear cut is observed between state 0 and state 1, which corresponds well to the drastic configurational change caused by the slider flipping over

and terminating the consecutive alignment with the rail. Figure 7.22 D shows that the average of tail length measured for state 1 dimers peaks at 41 ± 4 nm whereas the average tail length for state 4 dimers is at 22 ± 4 nm. These values do not coincide with out theoretical expectations that predict a tail length of around 50 nm for state 1-dimers and 39 nm for state 4 dimers. This deviation can be attributed to image artifacts originating from the fact that DNA origami structures can appear shorter on TEM girds compared to theory due to unavoidable dehydration effects occurring during the drying process on TEM grids. Additionally, we need to consider an error that arises from manually measuring the particles. Approaches like fluorescence microscopy or FRET analysis would be an alternative and appropriate tool to resolve the step size of 3.5 nm. However, at this point of the study we are more broadly interested in whether the stepper can be actuated with a symmetric set of clip strands at all and whether this leads to forward progression of the slider. An overall reduction in tail length of the dimers provides first evidence suggesting that the systems work as hypothesized.

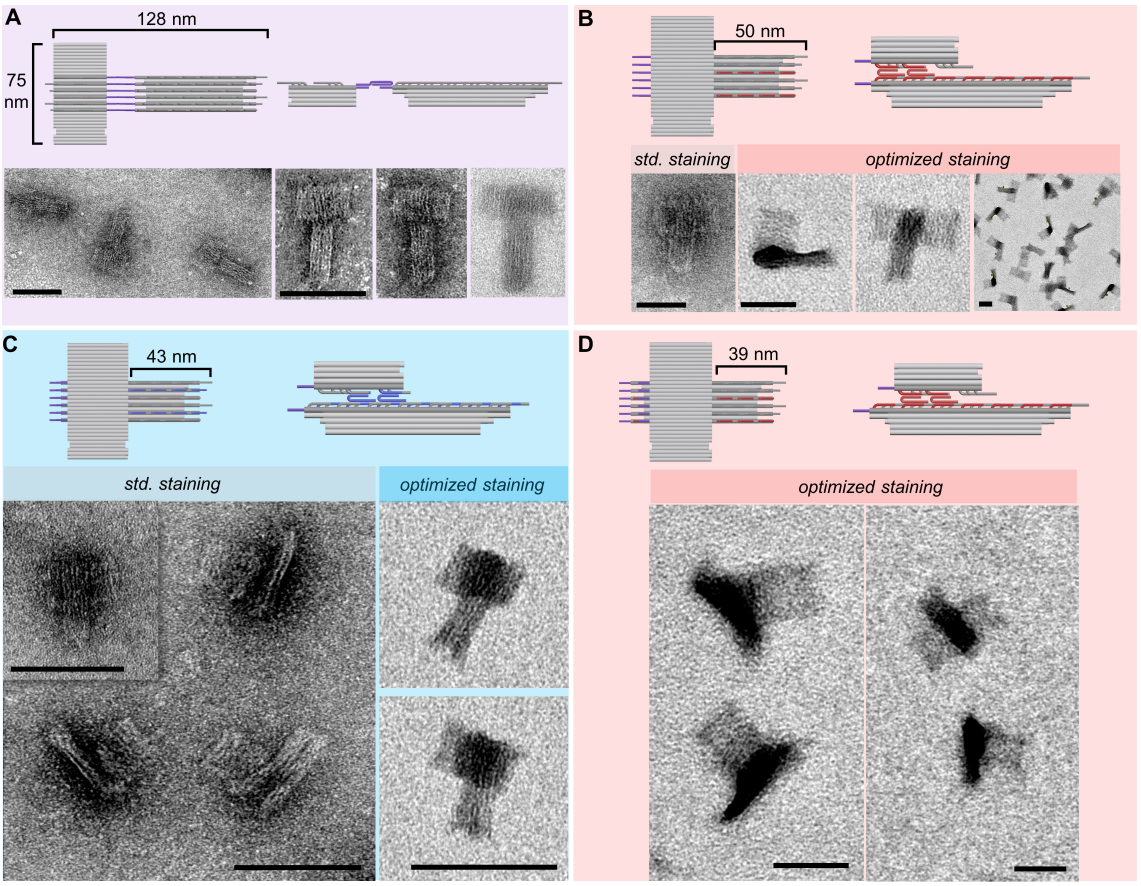

Figure 7.21.: TEM verification of falcon- sliders stepping into a second RGB cycle. Structures have been gel purified for TEM imaging. **A** 3D illustration of state 0-dimers showing the expected dimensions and TEM images. Scale bars indicate 100 nm. **B** 3D illustration of state 1-dimers. Comparison of TEM images of state 1 dimers based on the standard staining protocol (left) and the optimized protocol (right). Scale bars indicate 50 nm. **C** 3D illustrations of state 3-dimers. TEM images based on the standard staining (left) and the optimized staining (right). Scale bars indicate 100 nm. **D** 3D illustration of state 4 dimers. State 4 dimers have been achieved by re-applying red clip strands after red clip-removal strands have been eliminated from the solution using magnetic beads. TEM images based on the optimized staining. Scale bars indicate 50 nm.

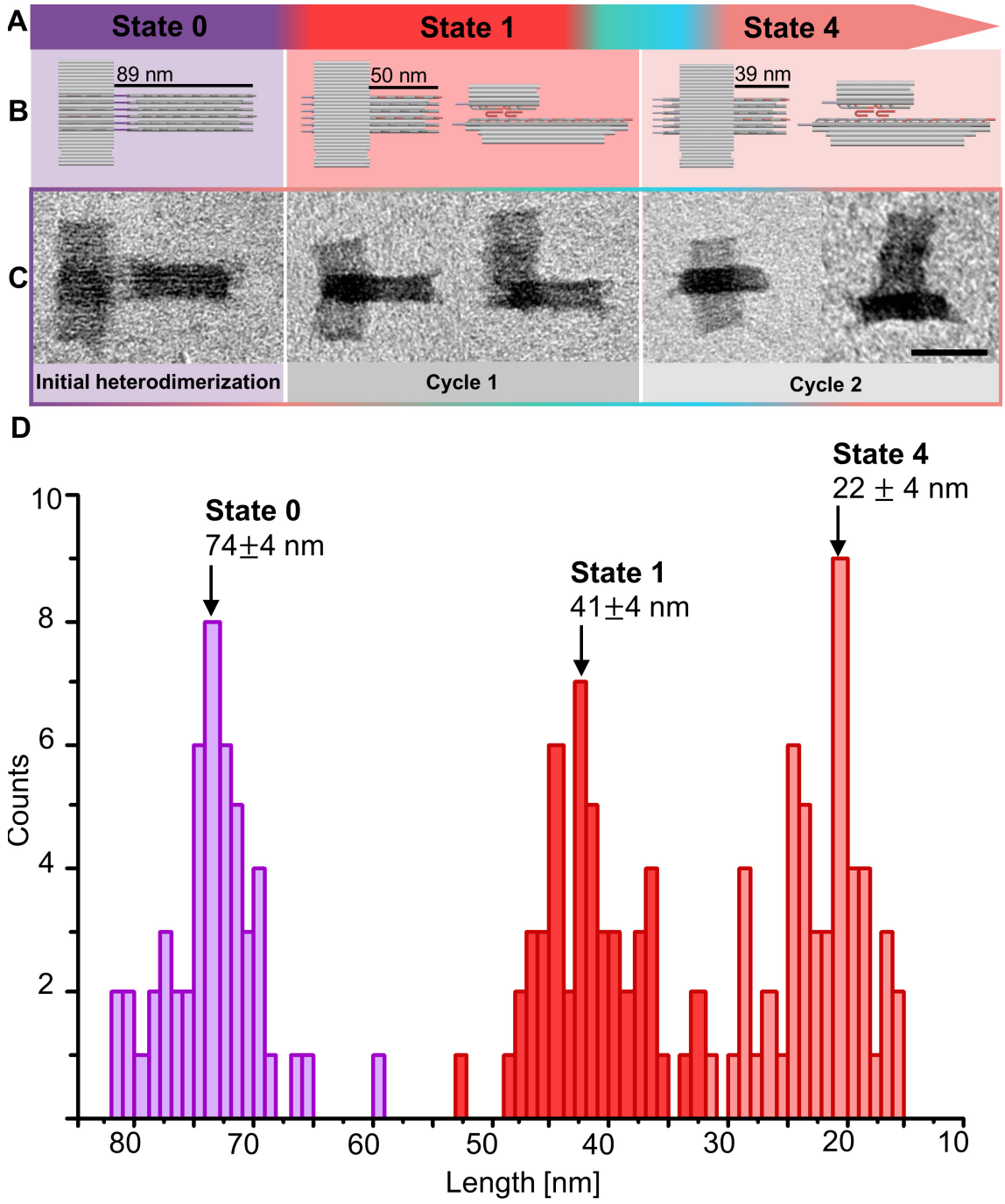

Figure 7.22.: TEM image evaluation of a symmetric, three-phase actuation of falcon dimers. **A** State indicator. Rail-tail lengths of state 0, 1 and 4 have been analyzed, **B** 3D-renders displaying the theoretically expected values of the rail-tail lengths, **C** Representative TEM snapshots of dimers from different states including top- and side-views of state 1 and 4 dimers. Scale bars indicate 50 nm. **D** Histograms showing the distribution of measured rail-tail lengths of 50 particles for the states 0, 1 and 4. The X-axis refers to the lengths in nm starting with the highest measured tail length, y-axis refers to the counted particles at a particular length starting with the lowest number of particles. The overall trend is a reduction in rail-tail length with upon actuation of the slider. The accumulation of data points starts with rail-tail lengths of state 0 dimers (purple), followed by the tail lengths of state 1- and state 4 dimer. The lengths peak at 73 $\pm$ 4 nm for state 0 dimers (purple), at 41 $\pm$ 4 nm for state 1 dimers (dark red) and at 22 $\pm$ 4 nm for state 4 dimers (light red).

7.3.10. Strand interaction specificity

A usual control to show that an interaction between falcon-slider and -rail is specific was to show that the falcon-steppers could be disassembled once the appropriate clip-removal strand was applied. Specific thereby means that the interaction between the falcon- monomers is exclusively mediated by the present and intentionally-applied clip strands. All control samples that have been included in the discussions above showed this kind of exclusive response. For instance, falcon dimers that reside in a state mediated by red clip strands disassembled once red clip-removal strands were applied. This also held true for all other states. Intermediate states that relied on two flavors of clip strands remained intact as long as only one flavor of clip strand has been removed at a time. This already verifies that the dimer bands detected on the gels are a product of specific interactions between the monomers. However, clip strands that have been applied in excess to the amount that is actually binding to falcon-monomers and that have not turned into double-stranded waste products throughout the process of strand displacement might still be in solution and available to mediate interactions between the sliders and rails. This should be a quite unlikely event since the clip-removal strands were applied in a 2.5 excess to the clip strands and should occupy all of them. Nonetheless, the following experiment has been designed to exclude this or other sources of interactions that have not been specifically induced.

Falcon dimers have been subjected to a mixture of removal strands that contained all the removal strand-types, except from the one that is designed to disassemble the complex. If the dimer band is maintained, it implies that the removal strands have no impact on the dimers. In a subsequent step, these dimers are subjected to the appropriate clip-removal strand. This leading to a disassembly of the dimer band suggests that the dimers must have been attached exclusively via the designated clip strand. Figure 7.23 shows the native AGE gel analysis of the experiment. Lanes (8) and (12) in 7.23 correspond to state 0 and 1, respectively, which have been treated with a mixture of clip-removal strands not matching their present clip strand. Both samples maintain a distinct dimer band. These disassembled once the appropriate clip strand is applied as shown in lanes (9) and (13).

The same is true for state 2 and state 3 dimers shown in lane (9) and (13) in 7.23 B. Their dimer bands remain unaffected by the addition of the off-target clip-removal strands (see lanes 10 and 14) but are disassembled upon addition of the correct clip-removal strand (see lanes (11) and (15). It should be noted that due to a pipetting error the sample volume for lanes (6) and (10) were much lower compared to the other lanes and thus exhibit a low band intensity signal. However, the dimer bands for both are still visible when boosting the contrast of the image. Their low intensity does not affect the conclusion about the specificity of the interactions.

These results enable assuming that the dimer bands observed on the previous gels are indeed a product of highly specific interactions based on the controlled attachment and de-attachment of clip and clip-removal strands. This also confirms that, despite the discrepancy of measured and theoretically-predicted displacement values, the displacement of the slider observed on TEM grids can indeed be traced back to the implemented stepping mechanism.

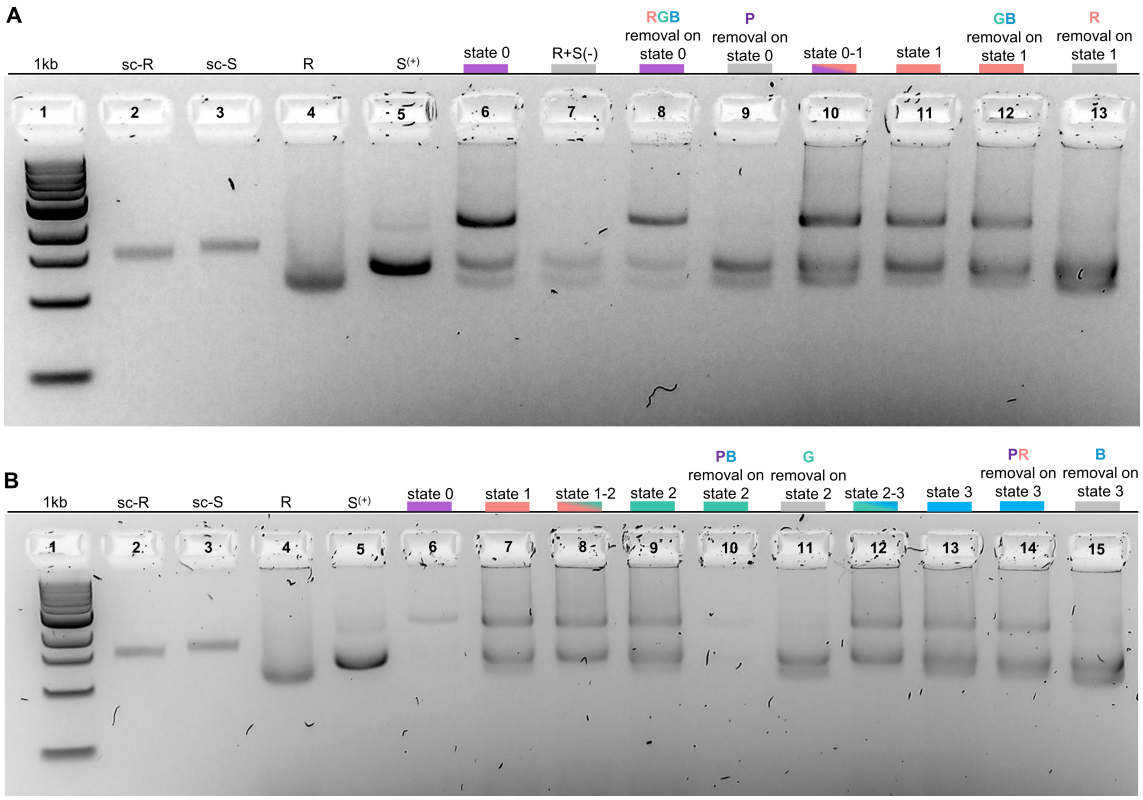

Figure 7.23.: 2% native AGE gel showing the clip strand interaction specificity. Colors refer to interactions mediated by purple ("P"), red ("R"), green ("G") and blue ("B") clip strands. **A** State 0- and state 1 dimers have been subjected to either a mixture of off-target clip-removal strands or the appropriate clip strand-removal. Disassembly is only detected for the target clip-removal strand. **B** State 2 and state 3 dimers subjected to off-target clip-removal strands or target clip-removal strand.

7.3.11. Conclusion

It has been shown that the suggested design for the falcon-slider and -rail successfully folds and that the incorporated functionalities such as the handles can be specifically addressed with appropriate clip and clip-removal strands. Thereby, it has been found that falcon-sliders and -rails are much more robust compared to the previously-approached mini-slider and -rail architecture. It was not necessary to purify the monomers upon dimerization or for the actual actuation, which provides a major benefit compared to mini-steppers.

Moreover, this enabled starting the stepping cycles at a high yield of monomers which – as stated in the very initial premises – combines well with the chosen tools of detection. The monomeric and dimeric stability of the falcon design as well as the high yield allowed testing the proposed symmetric, three-phase stepping mechanism.

First, it was shown that interactions between falcon-sliders and rails are best mediated if the red, green and blue clip strands exhibit a flexible linker comprising six T-bases.

Magnetic bead purification proved to be a valid technique to purify falcon-steppers from residual clip-removal strands and allowed the stepper to be actuated into a second cycle of RGB stepping. Gels confirmed that dimers remain intact over the course of actuation. Imaging the higher-order dimers with TEM has been challenging and required the devel-

opment of a specific staining protocol to make especially the higher-order dimers visible on TEM grids. Through a considerate study of different staining parameters, it was possible to detect the systems of interest. The data collected provides sufficient evidence that a slider displacement is indeed achievable. Together with strand interaction specificity tests provided by the end of the chapter, the displacement observed by TEM can be traced back to the programmed clip and clip-removal strand interactions. In combination, both data sets allow concluding that the sliders are indeed actuated by the cyclic addition of symmetric clip strand sequences.
It is very important to realize that at this point TEM imaging can solely prove that a controlled actuation of the slider is induced, as the level of detail resolvable with TEM is too low to detect the proposed step size of 3.4 nm.
The rail parts detected on TEM grids that are not covered by the slider – the so-called rail tails – served as a measure to show a displacement of around 19 $\pm$ 4 nm from state 1 to state 4. This does not coincide with the theoretical expectations of a displacement of around 10 nm. In general, the measured rail tail-lengths show an increased deviation from the theoretically expected values when more steps are taken. The next step of this project will be to investigate the falcon-stepper with alternative detection methods such as with FRET measurements or super-resolution microscopy with DNA-paint to resolve the designed step size of 3.4 nm.

7.4. Summary

This chapter has presented a novel concept for an artificial, nanoscale stepper whose architecture and mechanism is completely based on DNA. Through the systematic investigation of two stepper candidates – the mini- and the falcon-stepper – it was possible to find an architecture that fulfilled all architectural premises stated initially for the successful implementation of the proposed stepping mechanism.
DNA strand displacement driven steppers that promote individual DNA molecules have been shown many times in the literature. The approaches presented within this thesis extend these established concepts by increasing the scale at which stepping is realized. Instead of single molecule promotion, multi-site interactions are programmed between the surfaces of large DNA arrays.
This is believed to boost the tolerance of the stepper systems towards structural defects and towards missing anchor points. The proposed steppers do not induce a new DNA sequence for each taken step. Instead, an innovative stepping mechanism was developed that relies on only six different fuel strands that are externally applied in regular cycles.
The design of the fuel strands as well as the anchor points have been optimized to meet requirements such a balanced length of the fuel strands that would keep the directional bias of the stepper while maintain the rigidity of the system and sufficient binding energy between fuel strands and anchor strands to hold the DNA arrays together. It was possible to show DNA arrays can interact along and perpendicular to their helical axes despite present repulsion forces arising from the negatively charged, densely packed helical backbones.
Based on optimized strand displacement reactions, controlled forward and backward motion has been shown. Gel electrophoresis and TEM imaging were the methods of choice to detect and verify the proposed architectures. Using those in combination confirmed that symmetric cycling of fuel strands is able to promote the DNA origami structures across

each other. However the resolution of these techniques is too low to confirm the step size of 3.4 nm. To resolve the small step size of 3.4 nm, it is intended to use detection methods such as FRET measurements or super-resolution microscopy with DNA-paint in the future.

8. Summary and outlook

The thesis is part of a project that aims to develop a device for rapid prototyping of nanoscale objects as a promising pathway toward atomically precise manufacturing. Directed DNA self-assembly is especially suited for this implementation since it is highly parallelized allowing to create a trillion copies at the same time within short design cycles. It holds great potential to fulfill the main requirements set out to achieve a similar impact of the 3D printing technology observed on the macroscale. These requirements are:

- Easy accessible building materials
- Transport mechanisms
- Mechanisms for repetitive action

DNA is a readily accessible building material. Methods such as DNA origami folding, and DNA strand displacement allow to construct dynamic DNA nanostructures. Nanoscale stepping based on DNA strand displacement has been shown many times in literature. However, the steppers presented so far are often restricted to irreversible single-molecule interactions and thus limited in terms of travel distances and directions. The latter has been discussed in detail in chapter 4.

This thesis presents a new stepping mechanism extending the functionality of current DNA steppers toward the fulfillment of the above-stated requirements. A central achievement thereby was to show the feasibility of repetitive, multisite interactions between large DNA origami surfaces.
To do so, the first part of the thesis is a systematic study of different design approaches generating DNA origami structures with a high number of functional sites. These studies have been performed for square, honeycomb, and square-holey lattice designs. It was possible to develop stable architectures of different geometries that exhibit up to 200 individually addressable, functional sites with close packing of the nearest neighbors.
In the second part of the thesis, four of these architectures have been used to demonstrate multi-site interactions via a novel stepping mechanism. The stepping mechanism investigated enables a large DNA- array to promote along rigid DNA origami tracks based on the coordination of four legs at the same time. The rigidity of the individual stepper components is given as they are based on multi-layer structures. Stepping relies on a cyclic activation and deactivation of fuel DNA strands that induce strand displacement at designated binding sites. It has been shown that the promotion of the stepper does not require a new sequence for each step but it is possible using a set of six orthogonal sequences as fuel strands that are applied in repetitive cycles. Optimizing the design of the fuel strands allowed control over forward and backward motion.

The main methods to detect and study the systems were gel electrophoresis and transmission electron microscopy. They allow the analysis of the folding and purity of the designed

architectures, the impact of differently designed binding sites as well as fuel strands, and different parameters of the DNA strand displacement reactions. It has been shown that steppers can be promoted based on the proposed, symmetric stepping mechanism. However, insufficient resolution of TEM so far prohibited the verification of the designed step size of 3.4 nm. The steppers are currently equipped with further design features to enable the characterization of step size, speed, and failure rates using alternative detection methods such as FRET measurements or super-resolution fluorescence microscopy with DNA paint.

The results achieved in this thesis are the basis for further ongoing research trajectories of the project. The 1D falcon-steppers presented are currently extended into 2D by introducing a third stepping canvas to the stack architecture of the falcon-stepper. Thereby, 1D falcon-steppers are implemented in a way that one of them performs an up and down motion, while the other promotes from the left to the right. Preliminary data exists, showing that this is a promising approach to realize 2D stepping. Once bidirectional stepping is fully characterized and optimized, molecular analogues to a printhead are aimed to be developed and implemented into the molecular steppers. Ideas are to render the printhead able to recruit DNA "ink" strands from solution and catalyze the hybridization of that ink strand to a DNA origami surface. Patterns could be created by using ink strands that themselves carry a fluorescent dye molecule or metal nanoparticles. As an alternative, one could think about using RNases as printheads that carve out a certain pattern on an RNA covered canvas.
The speed of the steppers remains to be investigated. Since the reaction rates of DNA strand displacement cannot be infinitely boosted by increasing the concentration of the fuel strands, falcon-stepper systems are planned to be integrated into micro-fluidic setups. Switching to such a single-molecule detection method should help to get more insights into the speed and the number of achievable stepping cycles the system can go through. This is hypothesized to support the development of the falcon-steppers toward higher operation rates.

Desirable applications for molecular 2D steppers are, for example, to replace excessive manual pipetting steps currently required to functionalize DNA origami structures. Instead one could imagine mixing the DNA origami structures with the developed molecular 2D steppers that could then decorate the DNA origami structures with the desired functionalizations. Patterning a non-organic canvas such as semiconductor surfaces could be a further long-term application.
In the future, the current mechanism of external stepping control is planned to be replaced with purely concentration-based cycles of activation and de-activation of fuel strands. The design of the fuel strands is going to be modified so that attachment of a certain fuel strand is only energetically stable if the close surrounding provides a high enough concentration of them. Designing the fuel strands much shorter, on the order of 7 bps, will render them to have weak binding energy so that they would easily fall off once concentrations are reduced or once they are under competition with other strands at higher concentrations. This amounts to a hyper-sensitivity of the systems toward changes in concentrations. The fact that stepping is based on multi-site interactions is key to such a hyper-sensitivity as in that way subtle changes in fuel strand concentrations will trigger a multiplied response of the system.
Cycling the concentration of the fuel strands is hypothesized to induce a switch-like be-

havior of strands attaching and detaching. This all-or-nothing response reminds of the concepts of cooperativity and is believed to be a powerful approach to increase the reliability, robustness, and efficiency of the stepper systems. It should be empathized again, that the implementation of such cooperative processes hugely depends on the availability of platforms that allow multivalent interactions and motivates the studies presented in chapter 6 once more.
High-cooperative stepping is currently investigated with the SH-v3 architectures presented in chapter 2. Preliminary data on high-yield dimerization of the SH-v3 structures already exist.
Currently, fuel strands are cycled through manual and external addition. However, a project has been initiated to develop depot systems that could release and capture the required strands upon excitation with light. Gold nanorods for example exhibit a sensitive correlation between their size and their excitation wavelength and thus can be specifically addressed. Studies are available that nanorods can be decorated with DNA strands and release those upon light-induced heat spots [146]. Gold nanorod depot systems of various sizes and strand decoration could thus enable precise and efficient control over the released strand types.

To summarize, the studies pursued within the scope of this thesis are able to positively answer the initially stated research question which was about the feasibility of DNA-based platforms allowing multiple interactions between DNA origami surfaces to happen in tandem for the purpose of high cooperativity stepping. In this context, cooperativity is implemented to the presented systems by disfavoring intermediate states of the steppers through optimized fuel strand design. It is argued that cooperativity could have an even more direct realization by implementing a hyper-sensitivity of the steppers toward changes in fuel strand concentrations. The DNA-based platforms and the 1D symmetric, three-phase stepper system presented in this thesis demonstrate very early approaches to implement nanoscale rapid prototyping and show the potential of DNA self-assembly to be an interesting pathway toward first generation APM prototypes.

A. Materials and methods

A.1. Buffers

Raw buffers	Composition
10×TE	50 mM Tris-base, 10 mM EDTA-Na2, pH 8.0
50×TAE	2 M Tris, 1M Acetic acid, 50 mM EdTA-Na2
5×TBE	445 mM Tris-base, 445 mM Boric acid, 8.6 mM EDTA-Na2
2×PPB	15% (w/v) PEG-8000, 510 mM NaCl, 5 mM Tris-base, 1 mM EDTA-Na2; pH 8.0
2×B&W	10 mM Tris-HCL, 1 mM EDTA, 1 mM NaCl, 0.01 M EDTA-Na2
2x FLB	95% deionized formamide, 5 mM EDTA-Na2, 0.025% Orange G
6x AGLB	15 % Ficoll 400, 60 mM Tric-HCL, 6 mM EDTA-Na2, 0.025% Orange G

Table A.1.: Composition of raw buffers

Raw buffers	Diluted to	Used for
10×TE	1×	Folding buffer
50×TAE	1×	Native AGE gel running buffer - No. 1
5×TBE	0.5×, 1×	Native AGE gel running buffer - No. 2, denaturing PAGE gel running buffer
2×PPB	1×	PEG precipitation
2×B&W	1×	Magentic bead purification for falcon steppers
2x FLB	1×	Denaturing PAGE gel sample loading buffer
6x AGLB	1×	Native AGE gel sample loading buffer

Table A.2.: Buffer compositions and application

- Native AGE gel buffer: 1×TAE with 11mM $MgCl_2$, 0.5×w 10mM $MgCl_2$,
- Native AGE gel sample loading buffer: 6x AGLB with $MgCl_2$ (adjusted to $MgCl_2$ conc. of the analyzed sample)

A.2. Reagents

Company	Reagents
Agarose	Biozym Scientific GmbH
Deionized formamide	Fisher Scientific GmbH
DNA sequences	IDT Integrated Technologies
SYBR gold	Invitrogen
Dynabeads™MyOne™Streptavidin T1	Invitrogen
1 kb ladder	New England BioLabs GmbH
Tris-base	Roth
Tris-HCL	Roth
EDTA-Na2	Roth
Ficoll 400	Roth
Polyethylene glycol-8000	Roth
Acetic acid	Roth
NaCL	Roth
ROTIPHORESE®DNA sequencing system	Roth
RotiGelstain	Roth
TEMED	Roth
Orange G	Sigma-Aldrich
Ammonium persulfate (APS)	Sigma-Aldrich
1M MgCl$_{2}$-solution	Sigma-Aldrich

Table A.3.: Information on purchased reagents

A.3. Methods

DNA and DNA origami synthesis

DNA sequences have been purchased from Integrated DNA Technologies (desalted oligos, dissolved in ddH_2O). The scaffolds have been produced in house following published protocols [147]. Except for DC-v0-1 that relies on the p7308 scaffold and DC-v3-2, HC-v1, SH-v2 and -v3 that rely on the p8634 scaffold, all other structures presented within this work rely on the p8064 scaffold. DNA origami folding was performed in 1×TE buffer including $MgCl_2$. The $MgCl_2$ concentrations vary for each structure and are indicated within the main text. The folding solutions contained 20nM scaffold and 200 nM core staple strands, unless stated differently.
For falcon-stepper interacting slider and rail handles have been applied at 400 nM. Falcon-sliders were folded with purple clip strands (except for negative controls) at a concentration of 800 nM.
For mini-stepper monomers all staples including interacting handles have been applied at 200nM final concentration.
Folding was performed at 50 μL reaction volume.
The following folding ramps were used:

- 5040-18h: 80°C for 15 min →; 50° to 40° over 18h in equal temperature and time steps
- 6025-18h: 80°C for 15 min →; 60° to 25° over 18h in equal temperature and time steps
- 5040-66h: 80°C 15 min →; 50°C to 40°C over 66h in equal temperature and time steps
- 6025-66h: 80°C 15 min →; 60°C to 25°C over 66h in equal temperature and time steps

Gel electrophoresis

Native AGE gel electrophoresis was used to analyze folding yield, purity and stability of the DNA origami designs presented in chapter 6. AGE gels were also used to validate the heterodimerization and stepping performance of mini- and falcon-steppers in chapter 7 as well as to purify structures from different falcon-stepper states.
PAGE gels were used to purify falcon-stepper clip stands as well as falcon slider handles that extrude with their 5'-end.

Native agarose Gels

Analysis of DNA origami structures was performed on 2% native AGE gels, purification was performed on 1% AGE gels. Gels were cast by dissolving agarose (1 g/cm^3 density) in 1×TAE or 0.5×TBE buffer and heating it in a microwave. Once dissolve the agarose was complemented with either 11 or 10 mM $MgCl_2$, respectively, and the appropriate gel stain. Samples were prepared with native AGE gel sample loading buffer that contained $MgCl_2$ adjusted to the $MgCl_2$ concentration of the sample.
Analysis gels were stained with the higher sensitive stain SYBR gold (1: 10,000), purification gels were stained with Roti®GelStain (7μL/150 mL buffer). Gels were run on an

Owl™EasyCast™B2 gel casting system (ThermoFisher Scientific). Information on applied voltages and run times can be found in the captions of the respective gel images included in the main text. Gels were imaged using a UVP BioImaging System (EpiChemi^3 Darkroom) with a Canon EOS 1200D camera (EF-S 18-55 mm IS objective)

Denaturing polyacrylamide gels

Single-stranded DNA handles and clip strands for the falcon-stepper were purified with 15% denaturing PAGE gels. These were cast using the ROTIPHORESE®DNA sequencing system (25% acrylamide/bisacrylamide (19:1) in 50% urea (8,3 M), 10×TBE) as well as 10% APS (0.05% final percentage) and TEMED. The gels were run at 150 V for 1h on the Mini-PROTEAN Tetra Vertical electrophoresis system (BioRad). Samples were prepared with denaturing PAGE gel sample loading buffer (2×FLB) and heated with the buffer to 90° C for 2 min prior loading on the gel.

Purification

Gel purification

Gel purification was performed with 1% native AGE gels, pre-stained with Roti®GelStain (see A.3). 12×14 cm gels were cast with four gel pockets that were loaded with 0.5 pmol of sample. Gel bands of interest were cut under UV-shadowing. Samples were recovered from the gel by pushing a parafilm (Roth) wrapped glass slide on top of the gel band until the liquid is released.

PAGE purification

Interacting handles extruding with the 5'-end and clip strands of the falcon-stepper were purified by loading 2 nmol of individual strand sequences across multiple lanes on a 15% denaturing PAGE gel. Bands of interest were cut under UV-shadowing and crushed in a 2 mL eppendorf tube using a pestle. Crushed gel bands were covered with 1×TE buffer and shaken at 1500 rpm overnight at RT. Subsequently, samples were centrifuged in freeze n'squeeze spin columns (BioRad) for 20 min at 10,000 rpm. Eluded solution was then prepared for an ethanol precipitation. Therefore, samples were combined with 3 vol. 100% EtOH and 1/10 vol. 3M NaOAc and incubated at -20°C for 2h, followed by a 2h centrifugation at 20,000 rpm at 4°C. Centrifugation helps to collect the precipitated material in a pellet. Supernatant is discarded and pellets are washed with 200μL of 70% EtOH spinning them another 20 min at 20,000 rpm at 4°C. Pellets were air dried before dissolved in 30μL ddH_2O.
NanoDrop 1000 (ThermoFisher Scientific) was used to measure the concentration of the recovered single strands.

Amicon purification - Standard protocol

Amicon purification was used for DC-v0-1 and v0-2 structures discussed in chapter 6, section 6.2.1. Amicon purification was performed using the Amicon Ultra-0.5 Centrifugal Filter Unit system (Merck, Millipore) consisting of vertical membranes made from regenerated cellulose. 50 kDa and 100 kDa cut-off filters have been tested. The standard procedure was to use 50 μL of sample and dilute it 10×with 450 μL dilution buffer (1x TE with 10 mM $MgCl_2$). Filters were centrifuged at 10,000 rcf for 5 min at RT. The flow

through collected in the tube bottom was discarded and the samples in the filter were combined with further 450 μL dilution buffer. This was repeated four times. Sample was released in a fresh collection tube by spinning the system a fifth time with an inverted filter.

Amicon purification - Refined protocol

The refined amicon purification protocol proceeds similar to the standard protocol described above. For DC-v0 however it has been found that the following changes need to be applied to the standard protocol in order to achieve reasonable yields:

- 25 μL sample volume per filter membrane topped up with 225 μL dilution buffer.
- Dilution buffer: 1x TE with 6 mM $MgCl_2$ concentration.

Typically, the protocol resulted in 25 μL of retrieved sample volume. Filter units thus do only purify away the staple strand but do not additionally concentrated the sample. This is why one can assume that the structures maintain their initial concentration. For gel analysis, recovery yields were judged based on gel band intensity which have been measured using the ImageJ software ([148]). Thereby, it was crucial to load equal volumes on the gel for unpurified and purified structure or take non-normalized concentrations into account.

PEG precipitation protocol - Standard

PEG precipitation was used to purify DC-v2-1 and v0-2 in chapter 6, section 6.3.4. In the standard protocol 200 μL sample was first adjusted to 30 mM $MgCl_2$ concentration before mixed in a 1:2 ration with 2×PPB buffer. The prepared sample was then subjected to a spin at 16,000 rcf for 25 min at RT. Supernatants were either discarded or kept for further analysis. Sample containing pellets were resuspended in 100 μL 1×TE buffer with 12 mM $MgCl_2$ concentration. To equilibrate the samples incubated at RT for 2-3 h before the concentration was measured with the NanoDrop 1000 (ThermoFisher Scientific).

PEG precipitation protocol - Refined

To increase the recovery yields the standard PEG precipitation protocol needs to be adjusted as follows: 2×PPB was prepared fresh each time and pH has been checked prior use with pH indicator strips (Roth). $MgCl_2$ has to be added to the 2×PPB first and an equal amount of 2×PPB was subsequently added to this solution to make sure the $MgCl_2$ was balanced with an equal amount of 2×PPB. This was thoroughly mixed by pipetting up and down and inverting the tubes. THe tubes weres spun for 5 sec with a tabletop centrifuge to collect the rather viscous solution on the tube bottom. Only after then, the folding solution was added and mixed with the buffer by inverting the tubes and pipetting up and down. This was incubated for 30 min before spun at 16,000 rcf for 25 min at RT. Supernatants were either discarded or kept for further analysis. Pellets were dissolve in 100 μL 1×TE buffer with 12 mM $MgCl_2$ concentration but not yet mixed. The samples incubated for 1h at RT covered with a light protection before mixing.

Magnetic bead purification

Magnetic bead purification was used to eliminate residual clip-removal strand from falcon-steppers after one RGB cycle was completed. Therefore, streptavidin coated, magnetic Dynabeads™MyOne™Streptavidin T1 were combined with 2×B&W buffer in a 1:1 ratio, thoroughly mixed and placed on a magnet. Supernatant was discarded and magentic beads were resuspended in the same amount of fresh 2×B&W. This was mixed with state 3 dimers at a 1:1 ratio and incubated for 15 min, slowly rotating on a 360° rotor. Subsequently, magnetic beads were separated from solution by placing the sample on a magnet and waiting 2 min until the beads have completely gathered on the tube bottom. The supernatant was then used to proceed with the stepping experiment.

TEM imaging and standart staining protocol

TEM imaging was performed with a JEM-1011 microscope (JEOL) that was operated at 80 kV and uses a camera from TVIPS (FastScan F114-B). Carbon/Formvar Cu-Grids, 300 mesh for TEM imaging were purchased from Plano GmbH. Grids have been glow discharged prior staining in an argon environment using a the Femto low pressure plasma system from Diener electronic.
Unpurified samples are diluted to 1 nM for imaging. 3 µL of sample is deposited on to the grid for 2 min before adsorbed in a 90° angle into a filter paper. 3 µL of 2% aqueous uranyl formate containing 50 mM NaOH is applied to grid and immediately adsorbed in a 90° angle into a filter paper followed y a second 3 µL of 2% aqueous uranyl formate that rested on teh grid for several seconds before adsorbed again. Grids dried for 10 min before imaging.

ImageJ

ImageJ [148] (ImageJ 1.53c) was used to analyze gel band intensities on agarose gels to judge the folding yields of designed DNA structures, their sample recovery yields after purification as well as their dimerization and stepping yield in case of the falcon-stepper. Thereby, the gel analysis-tool of the software was used.
Folding yields were accessed by comparing the measured band intensity of the respective scaffold control with the raw folding sample. To enable a direct comparison, the sample concentrations loaded onto the gels have been normalized with respect to each other i.e. sample volume have been adjusted to the 20nM scaffold controls. Stepping and dimerization yields were analyzed by comparing dimer band intensities of different stepper states with the gel band intensity of state 0 dimers.
Additionally, ImageJ was used to measure rail-tail lengths to the different stepper states. Therefore, ImagesJ was first calibrated to the images scale bars before the free-hand measure-tool of the software was used to measure the rail-tails.

B. Additional data

B.1. DNA-based platforms for multivalent interactions - Additional Data

Magnesium screening for amicon purification of DC-v0

The following data refers to section 6.2.2 in chapter 6.

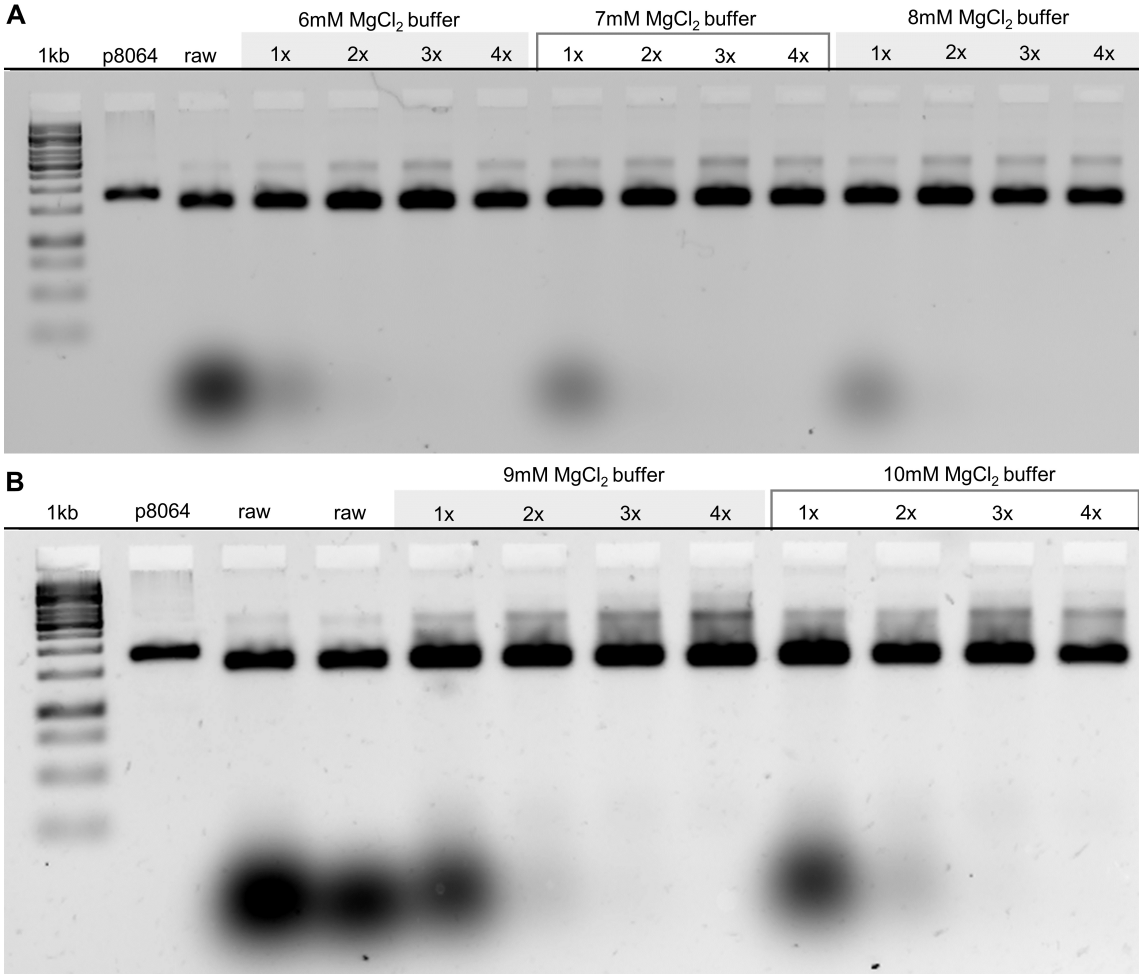

Figure B.1.: 2% native AGE gel analyzing the effect of different magnesium concentrations in the dilution buffers on the recovery yields of DC-v0-2 in amicon filtration. After each spin an aliquot was taken from the sample in the cut-off filters for analysis. 1×-4×refers to the spin number. Sample volumes are not normalized. $MgCl_2$ regime ranging in steps of 1 mM from 6 to 8 mM shown in **A** and 9, 10mM shown in **B**.

Gel running parameters: 0.5×TBE buffer with 10 mM $MgCl_2$, EtBr 0.5 $\mu g/mL$, 65V for 2h at RT

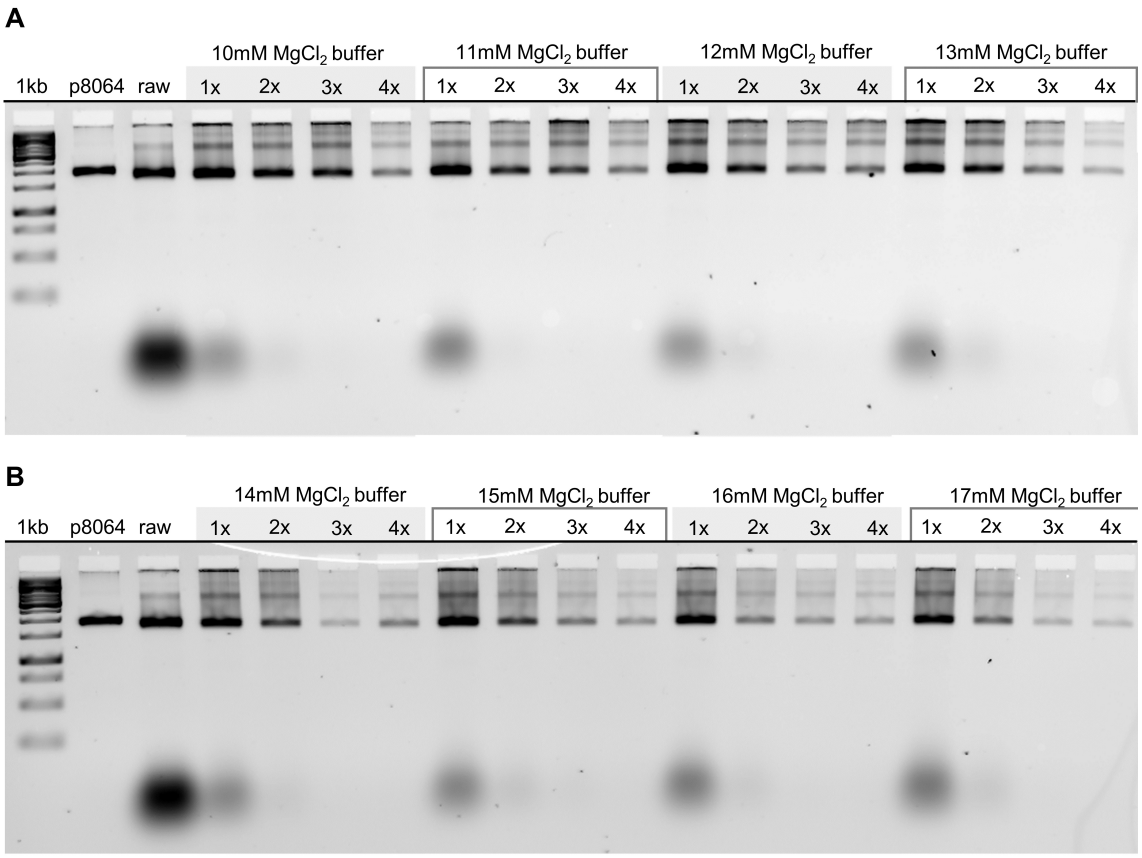

Figure B.2.: 2% native AGE gel analyzing the effect of different magnesium concentrations in the dilution buffers on the recovery yields of DC-v0-2 in amicon filtration. After each spin an aliquot was taken from the sample in the cut-off filters for analysis. 1×-4×refers to the spin number. Sample volumes are not normalized. $MgCl_2$ regime ranging in steps of 1 mM from 10 to 13 mM shown in **A** and 14-17mM shown in **B**.

Gel running parameters: 0.5×TBE buffer with 10 mM $MgCl_2$, EtBr 0.5 $\mu g/mL$, 65V for 2h at RT

Gel evaluation of longer folding ramps for DC-v2-1 and v2-2 and associated PEG purification yields

The following data refers to section 6.3.4 in chapter 6.

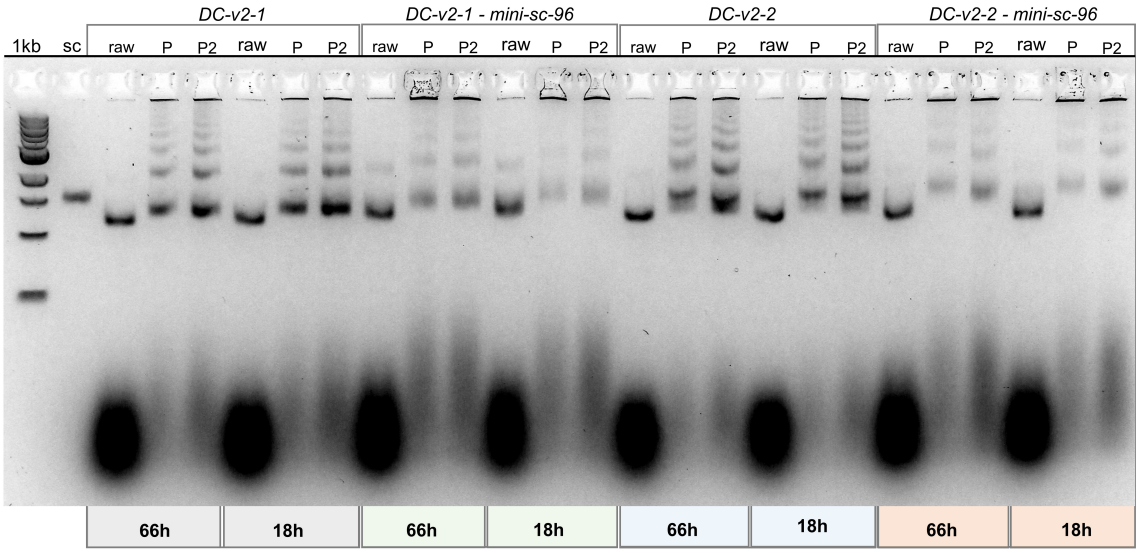

Figure B.3.: Gel evaluation of longer folding ramps for an enhanced stability of DC-v2-1 and v2-2 structures toward PEG purification. **sc** refers to 20 nM p8064 scaffold control, **P** indicates PEG purified sample, **P2** is the same sample as **P** but double the volume was loaded on the gel.

Purification of DC-v2-1 and DC-v2-2 - Complete data Set

The following data refers to section 6.3.4 in chapter 6.

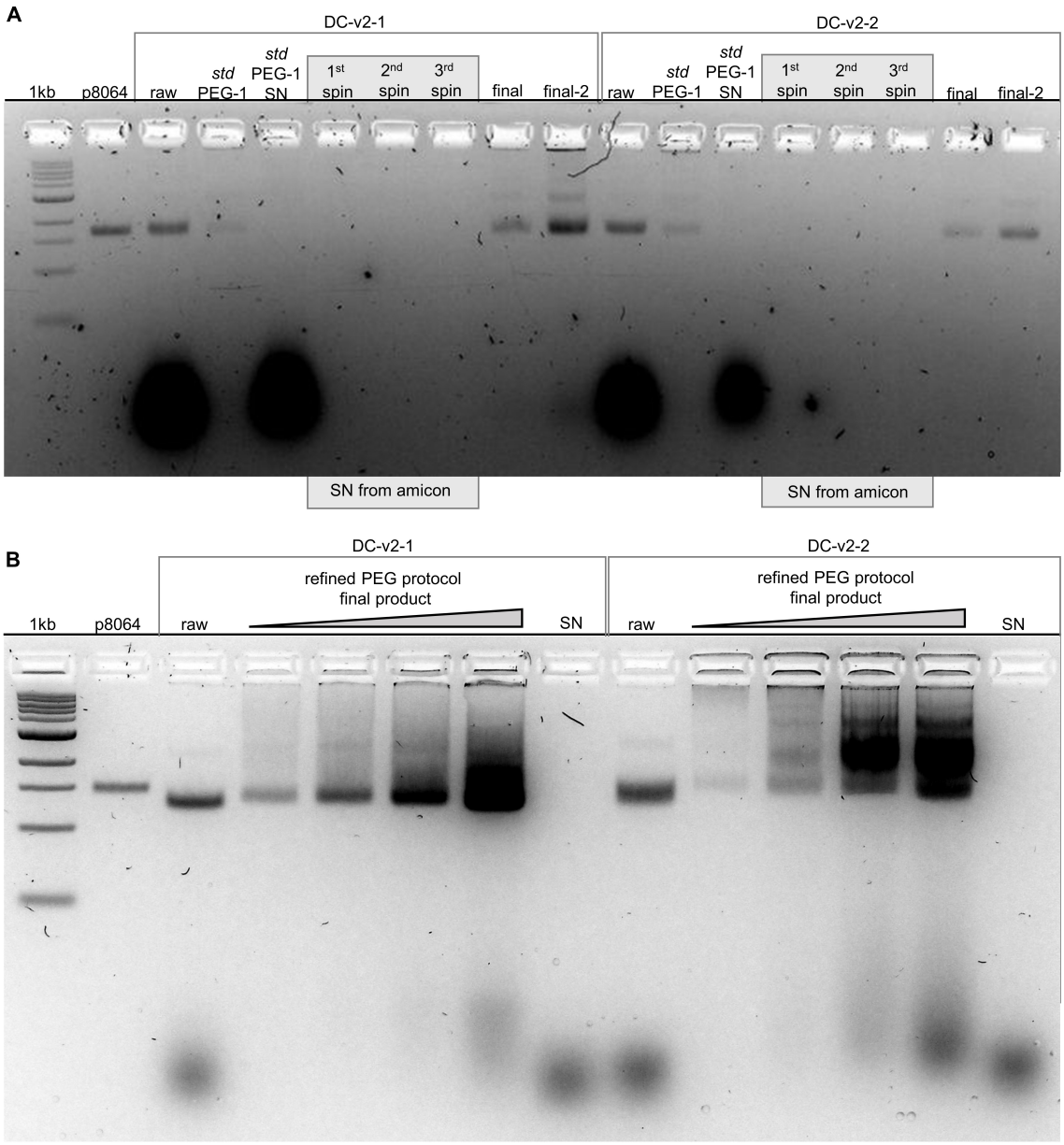

Figure B.4.: 2% native AGE gels to analyze recovery yields of DC-v2-1 and v2-2 structures in different PEG ppt protocols. **A** PEG and amicon purification of DC-v2-1 and v2-2 using the standard protocols. Key: **SN**: supernatant, **final**: samples that have gone through one round of PEG precipitation and three rounds of amicon filtration, **final 2**: Same sample as *final* but double the volume was loaded onto the gel. **B** PEG purification of DC-v2-1 and v2-1 using the refined PEG ppt protocol. Increasing sample volumes of PEG purified DC-v2-1 in lanes (4)-(7) and PEG purified DC-v2-2 in lanes (10)-(13).

Gel running parameters: (A) 1x TAE + 11 mM $MgCl_2$ + SYBR safe staining 0.5 $\mu g/mL$; 65V for 2.5 h at RT, (B) 1x TAE + 11 mM $MgCl_2$ + SYBR gold pre-staining 1:10 000 dilution; 65V for 2.5 h at RT

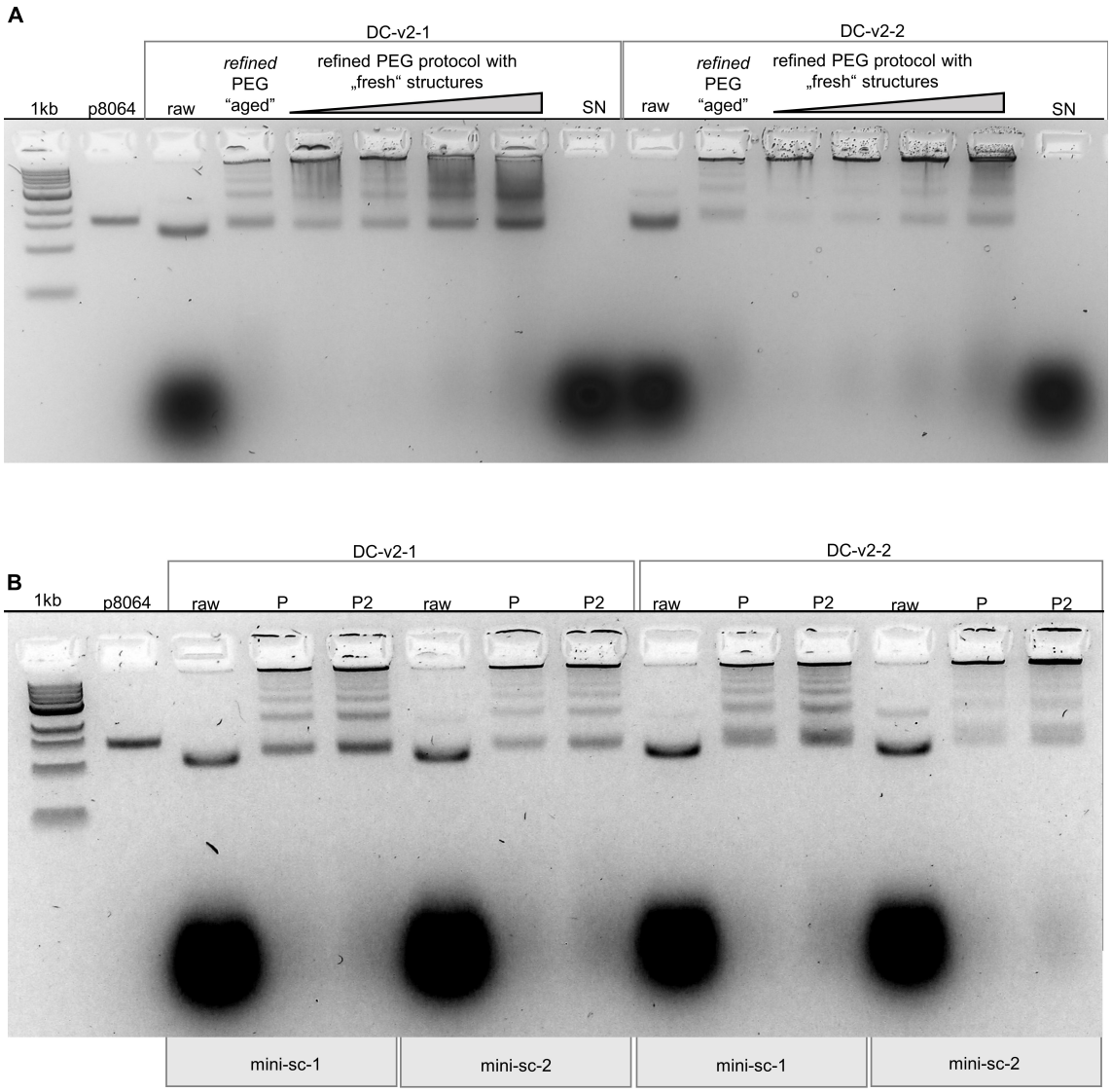

Figure B.5.: 2% native AGE gels to analyze recovery yields of DC-v2-1 and v2-2 structures in different PEG ppt protocols. **A** DC-v2-1 and v2-2 that were purified with the refined PEG ppt protocol but again analyzed after one week at 4C in lane compared to freshly purified DC-v2-1 and v2-2 loaded at increasing sample volumes. **B** DC-v2-1 and v2-2 folded with 56 bps and 96 bps mini-scafs (mini-sc-1 and 2) and purified with refined PEG ppt protocol. Key: **P** indicates PEG purified sample, **P2** is the same sample as **P** but double the volume was loaded on the gel.

Gel running parameters: 1x TAE + 11 mM $MgCl_2$ + SYBR gold pre-staining 1:10 000 dilution; 65V for 2.5 h at RT

Purification of DC-v3-2 - Complete data set

The following data refers to section 6.3.6 in chapter 6.

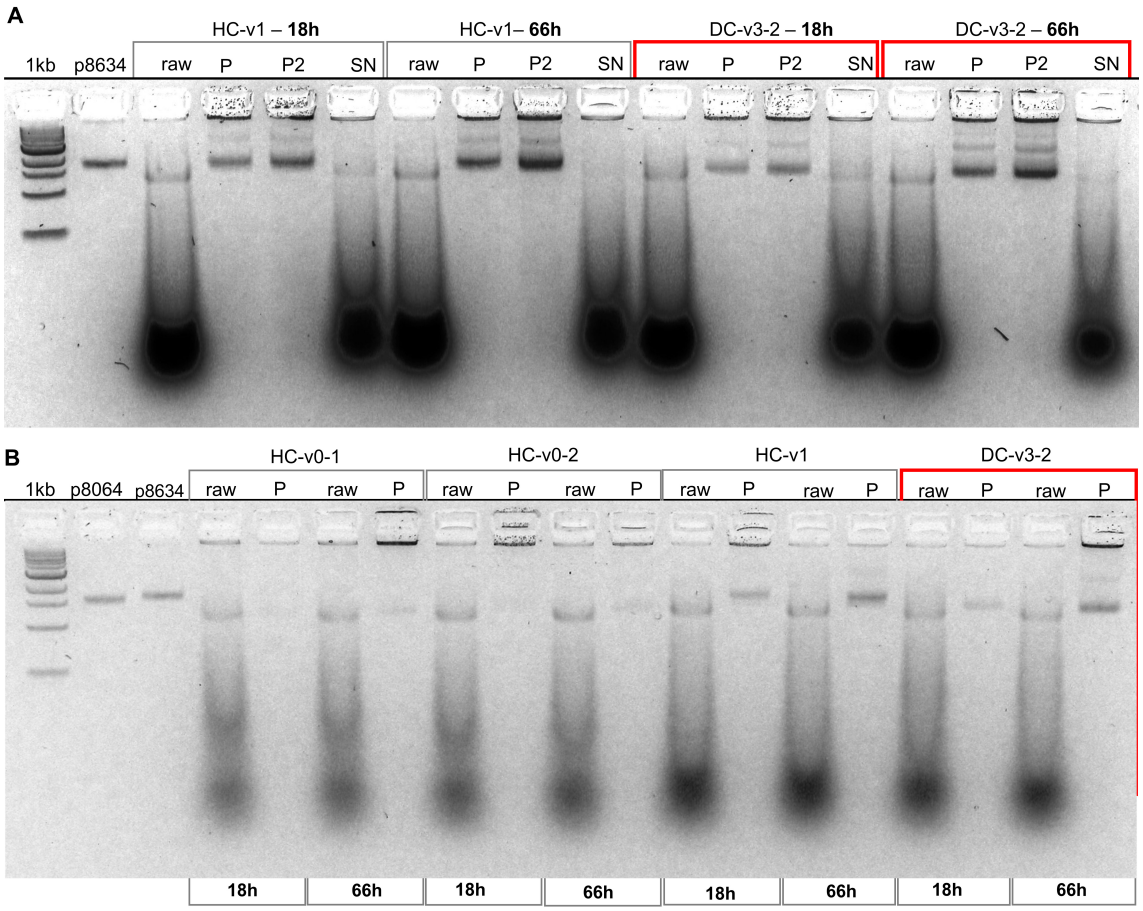

Figure B.6.: A 2% native AGE gels to analyze PEG purification of DC-v3-2 that were folded over 18h vs. 66h (see red boxes), Key: **P** indicates PEG purified sample, **P2** is the same sample as **P** but double the volume was loaded on the gel, **SN** refers to the supernatant. **B** Same samples as in **A** but rested at 4°C overnight (see red box).

Gel running parameters: 1x TAE + 11 mM $MgCl_2$ + SYBR gold pre-staining 1:10 000 dilution; 70V for 2 h in ice bath

Stability of PEG purified HC-v0-1 and v0-2, HC-v1, DC-v3-2

The following data refers to section 6.3.8 in chapter 6.

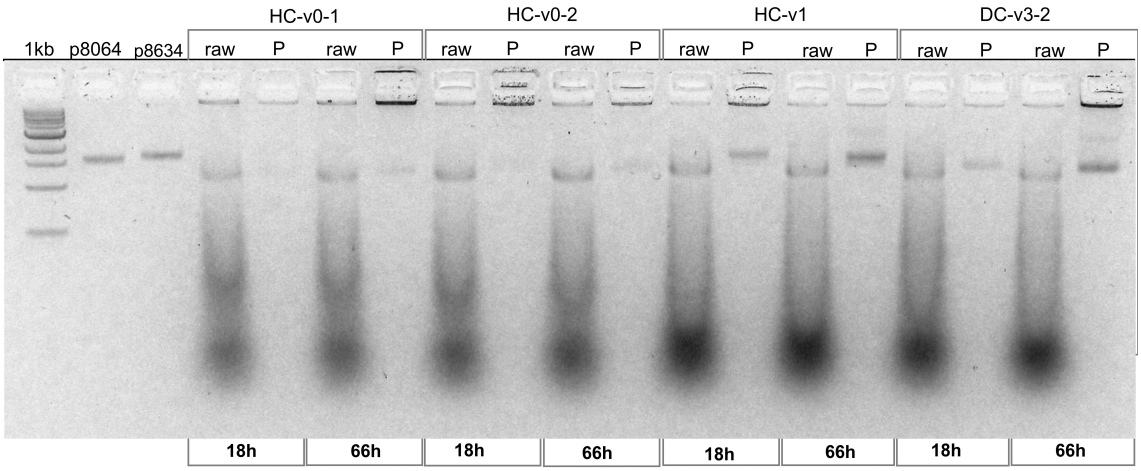

Figure B.7.: 2% native AGE gels analyzing stability of PEG purified HC-v0-1 and v0-2, HC-v1, DC-v3-2 that have rested at 4°C overnight. Thereby 18h and 66h folding ramps are compared. Key: **raw** refers to the sample right after folding, **P** refers to PEG purified sample.

Gel running parameters: 1x TAE + 11 mM $MgCl_2$ + SYBR gold pre-staining 1:10 000 dilution; 70V for 2.5 h at cooled in ice bath

B.2. Symmetric, three-phase DNA origami stepper - Additional Data

Mini-stepper: Investigation of different interacting handle lengths - Amicon purification of monomers

The following data refers to section 7.2.2 in chapter 7.

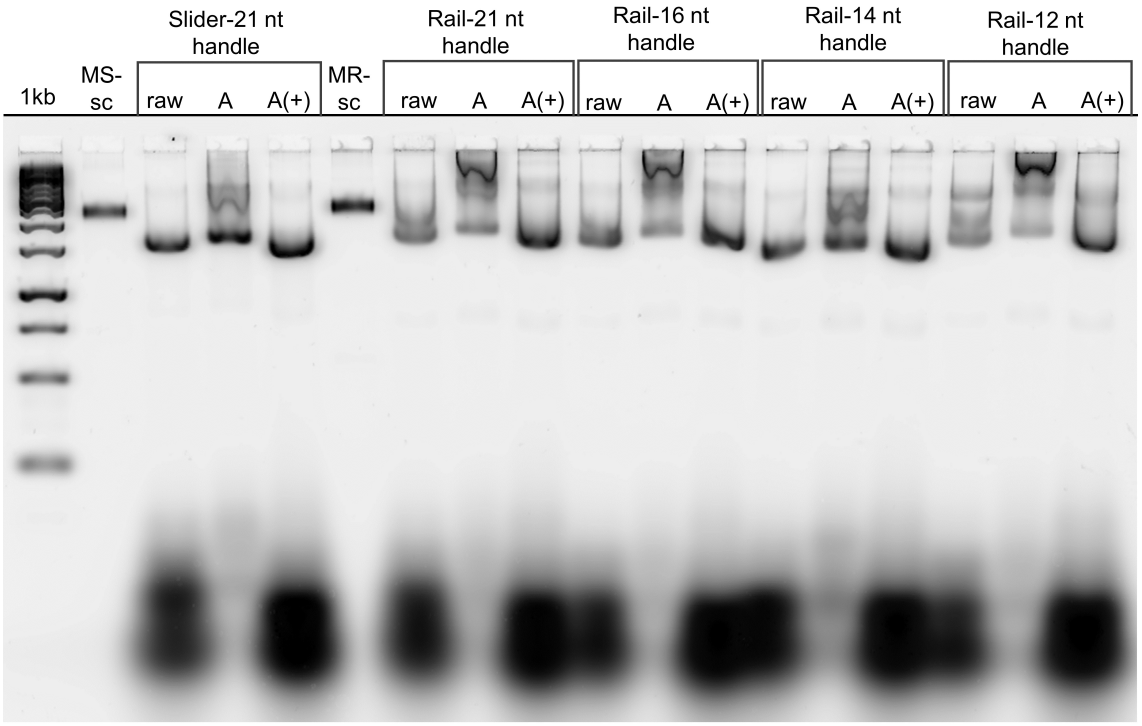

Figure B.8.: 2% native AGE gel for the analysis of amicon purified mini-monomers bearing handles of different lengths. Key: Mini-slider (MS), mini-rail (MR), raw folding samples (raw), amicon purified samples following the standard protocol (A), amicon purified samples following refined protocol and additional core staple strands added (A(+)).

Gel running parameters: 2% native AGE gel; 0.5x TBE + 10 mM $MgCl_2$ + SYBR gold pre-staining 1:10 000 dilution; 65V for 3h at RT

Falcon-stepper: Accessing T-linker length for purple clip strands

The following data refers to section 7.3.5 in chapter 7.

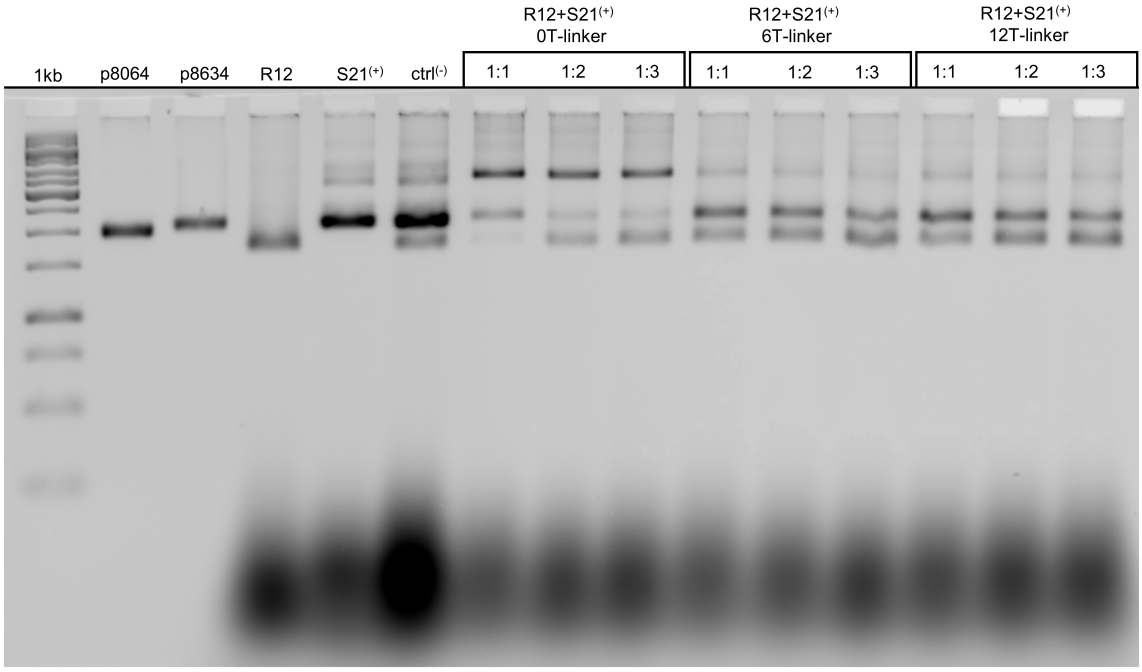

Figure B.9.: Heterodimerization of falcon-monomers at different ratios and using clip strands with 6T- or 12T-linkers vs. clip strand without T-linkers. (1) 1kb ladder, (2) p8064 scaffold control for falcon-rails, (3) p8634 scaffold control for falcon-sliders, (4) Raw falcon-rails with 12 nt handles, (5) Raw slider with 21 nt handles and clip strands included in the folding, (6) Combination of falcon-rails and -sliders without clip strands, (7)-(9) Combination of falcon-rails and -sliders with purple clip strands that exhibit no T-linker, sliders and rails have been combined at a 1:1, 1:2 and 1:3 ratio, respectively. (10)-(12) Combination of falcon-rails and -sliders with purple clip strands that exhibit 6T-linkers, sliders and rails have been combined at a 1:1, 1:2 and 1:3 ratio, respectively. (13)-(15) Combination of falcon-rails and -sliders with purple clip strands that exhibit 12T-linkers, sliders and rails have been combined at a 1:1, 1:2 and 1:3 ratio, respectively.

Gel running parameters: 2% agarose gel; 0.5x TBE + 10 mM MgCl2 + ethidium bromide 0.5 $\mu g/mL$; 60V for 3.5 h at RT

Falcon-stepper: ImageJ analysis of RGB dimers based on different T-linker length within clip strands

The following data refers to section 7.3.5 in chapter 7.

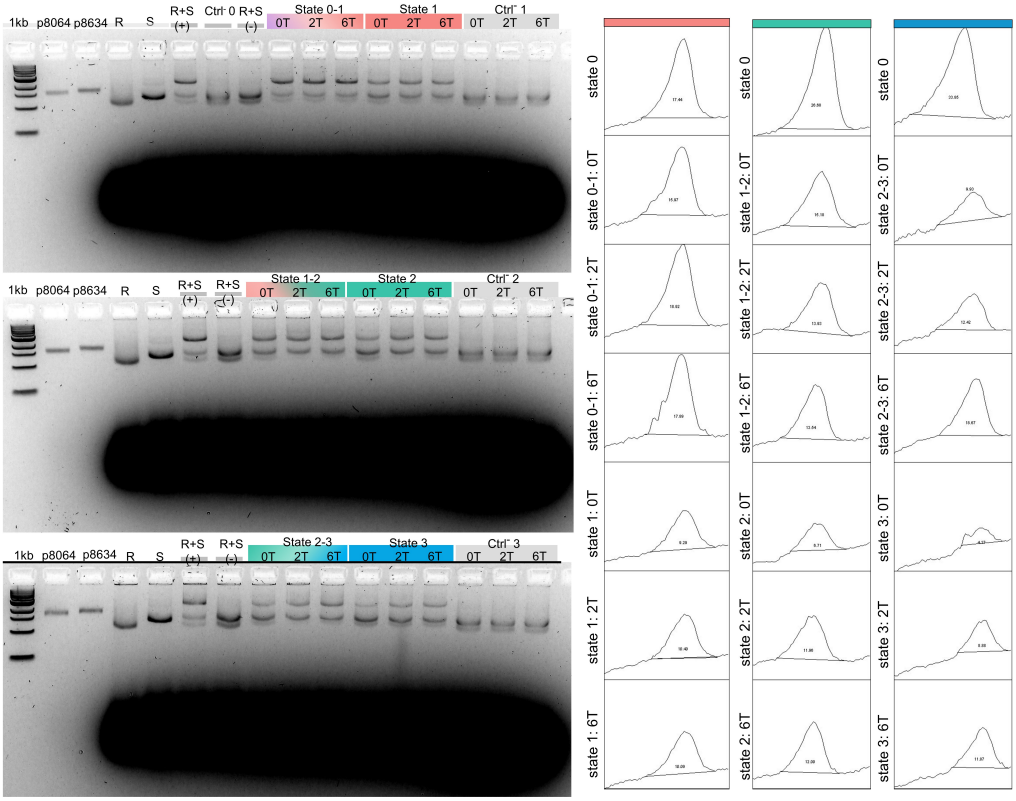

Figure B.10.: (Left) 2% native AGE gel analysis of the effect of T-linker length in clip strands on the performance of RGB stepping. Same gels as in 7.14 but staple clouds are shown. (Right) Intensity peaks of gel bands referring to RGB dimers analyzed with the gel-analysis-tool provided by ImageJ

Lane	Sample	Area under band peak	Percentage [%]
6	state 0	11173.53	100
9	state 0-1_0T	10233.045	92
10	state 0-1_2T	12127.359	109
11	state 0-1_6T	11465.217	103
12	state 1_0T	5954.095	53
13	state 1_2T	6662.217	60
14	state 1_6T	6466.874	58

Table B.1.: ImageJ analysis of dimer gel band intensities for intermediate state 0-1, and state 1

Lane	Sample	Area under band peak	Percentage [%]
6	state 0	15319.359	100
8	state 1-2_0T	8717.945	57
9	state 1-2_2T	8000.702	52
10	state 1-2_6T	7772.51	51
11	state 2_0T	3851.418	25
12	state 2_2T	6870.338	45
13	state 2_6T	6891.51	45

Table B.2.: ImageJ analysis of dimer gel band intensities for intermediate state 1-2, and state 2

Lane	Sample	Area under band peak	Percentage [%]
6	state 0	15220.451	100
8	state 2-3_0T	4465.803	29
9	state 2-3_2T	5584.853	37
10	state 2-3_6T	8395.51	55
11	state 3_0T	1966.79	13
12	state 3_2T	3992.66	26
13	state 3_6T	5339.439	35

Table B.3.: ImageJ analysis of dimer gel band intensities for intermediate state 2-3, and state 3

Falcon-stepper: Symmetric actuation across two RGB cycles - Complete data set

The following data refers to section 7.3.6 in chapter 7.

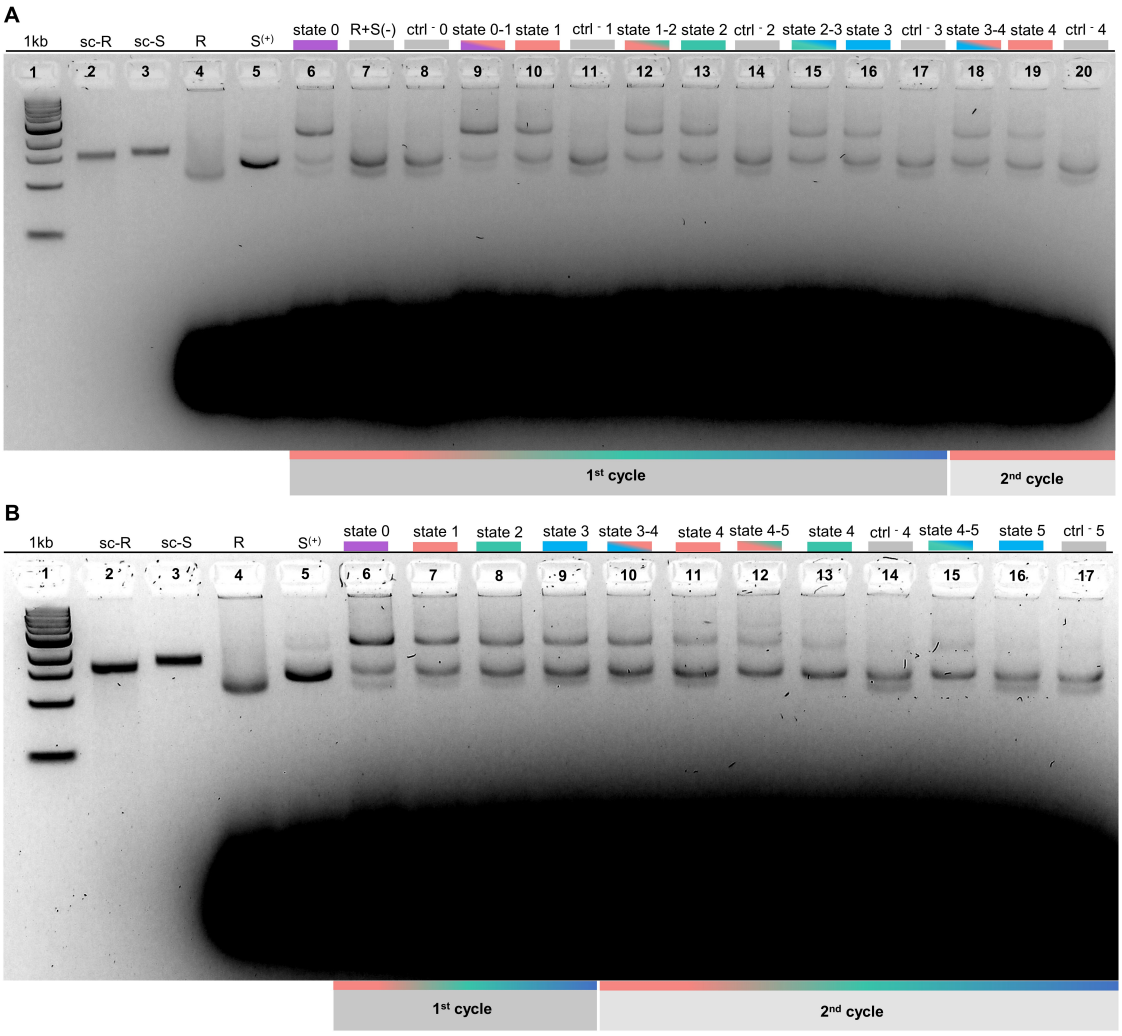

Figure B.11.: 2% native AGE gels to analyze RGB stepping across two, symmetric cycles. Same gels as in 7.15 but staple clouds are shown.

Falcon-stepper: TEM verification of PRGBR-stepping - ImageJ analysis of rail-tail lengths

The following data refers to section 7.22 in chapter 7.
The measure-tool of ImageJ (ImageJ 1.53c) was used to analyze the rail-tail length of the dimers. Images have been calibrated to the appropriate scales. The following figures are a collection of the images used for analysis. Yellow boxes highlight the chosen particles, labels are shown on the sides of the respective boxes and can be matched with the according lengths listed in the tables at the end of this section. Only particles that landed in a top vied on the grids have been used for analysis. Particles that landed on their sides or that looked distorted have been excluded from analysis. The tables list the obtained lengths in nm, the calculated mean values as well as the necessary quantities to calculate standard deviations. To calculate the standard deviation the following formula was used:

$$\sigma = \sqrt{\frac{1}{n}\sum_{i=1}^{n}(x_i - \mu)^2},$$

with n being the total particle number (here: 50), x_i being the measured length in nm of the ith particle and μ being the average length.

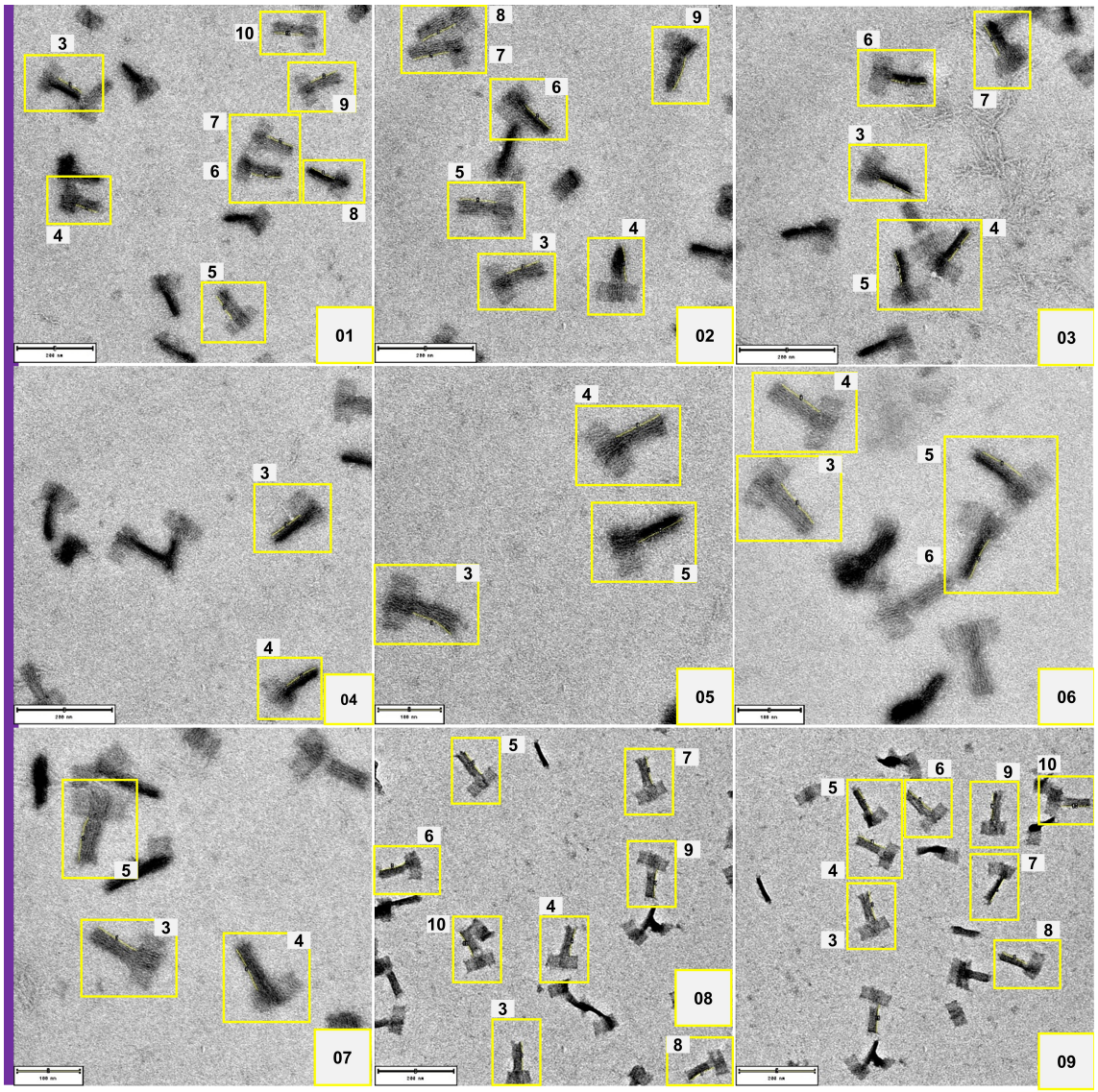

Figure B.12.: Collection of images for state 0 dimers (initial heterodimerization via purple clip strands) used for analysis. Yellow boxes highlight the picked particles. Labels can be used to assign the obtained tail lengths listed in the tables below to the particles.

Table B.4.: Measured tail length x_i in nm for state 0 dimers. Average tail length has been calculated from 50 particles as well as additional quantities necessary to calculate standard deviation.

Std. Deviation – State 0 – Dimers: $\sigma = 4.10$ nm

Image	Label	Measured length $x(i)$ [nm]	Average μ	$x(i) - \mu$	$(x(i) - \mu)^2$	n
01	3	73.63	73.55	0.08	0.01	50
	4	59.86	73.55	-13.70	187.57	50
	5	74.91	73.55	1.36	1.86	50
	6	77.36	73.55	3.80	14.47	50
	7	73.43	73.55	-0.12	0.02	50
	8	66.06	73.55	-7.50	56.19	50
	9	74.40	73.55	0.85	0.72	50
	10	75.51	73.55	1.96	3.83	50
02	3	76.89	73.55	3.34	11.16	50
	4	70.42	73.55	-3.13	9.79	50
	5	65.73	73.55	-7.82	61.21	50
	6	69.62	73.55	-3.94	15.50	50
	7	81.27	73.55	7.71	59.49	50
	8	80.92	73.55	7.36	54.22	50
	9	74.70	73.55	1.15	1.33	50
	10	80.79	73.55	7.23	52.33	50
	11	71.93	73.55	-1.62	2.62	50
03	3	72.17	73.55	-1.38	1.90	50
	4	76.03	73.55	2.48	6.13	50
	5	68.56	73.55	-4.99	24.95	50
	6	72.78	73.55	-0.77	0.60	50
	7	71.98	73.55	-1.58	2.48	50
04	3	74.33	73.55	0.78	0.61	50
	4	71.88	73.55	-1.67	2.79	50
05	3	69.92	73.55	-3.63	13.16	50
	4	78.45	73.55	4.90	23.97	50
	5	77.33	73.55	3.77	14.24	50
06	3	81.62	73.55	8.07	65.05	50
	4	73.46	73.55	-0.10	0.01	50
	5	72.14	73.55	-1.41	1.98	50
	6	71.17	73.55	-2.38	5.65	50
07	3	70.94	73.55	-2.61	6.81	50
	4	72.29	73.55	-1.27	1.60	50
	5	71.76	73.55	-1.79	3.22	50
08	3	73.51	73.55	-0.04	0.00	50
	4	73.46	73.55	-0.10	0.01	50
	5	73.27	73.55	-0.28	0.08	50
	6	72.61	73.55	-0.94	0.88	50
	7	73.83	73.55	0.27	0.08	50
	8	72.44	73.55	-1.11	1.23	50
	9	73.85	73.55	0.30	0.09	50
	10	74.94	73.55	1.39	1.92	50
09	3	77.42	73.55	3.87	14.94	50
	4	78.29	73.55	4.74	22.42	50
	5	75.63	73.55	2.08	4.34	50
	6	79.96	73.55	6.40	41.01	50
	7	70.61	73.55	-2.94	8.65	50
	8	69.56	73.55	-4.00	15.97	50
	9	69.12	73.55	-4.43	19.63	50
	10	74.90	73.55	1.34	1.80	50

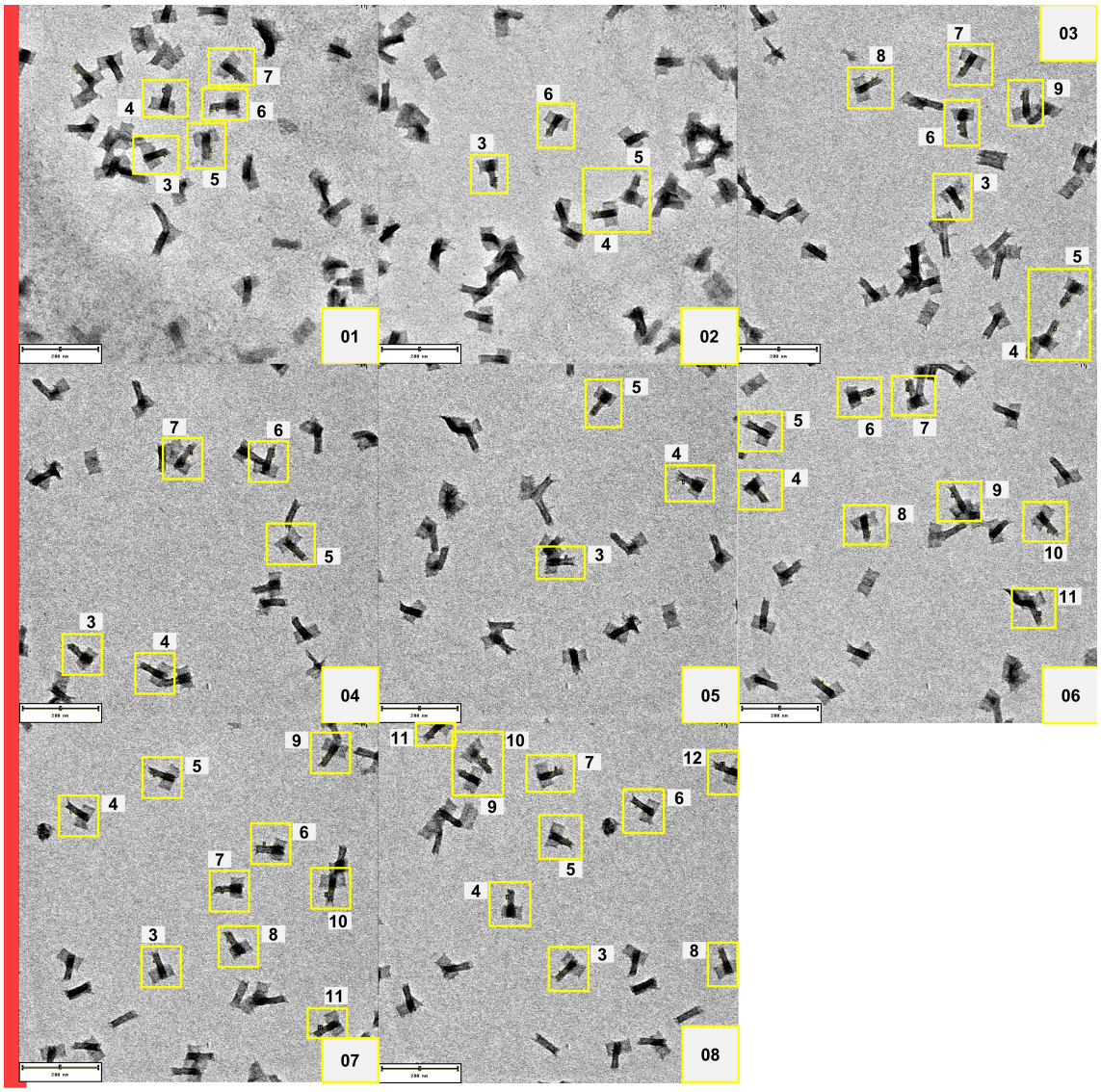

Figure B.13.: Collection of images for state 1 dimers (purple clip strands removed, red clip strand engaged) used for analysis. Yellow boxes highlight the picked particles. Labels can be used to assign the obtained tail lengths listed in the tables below to the particles.

Table B.5.: Measured tail length x_i in nm for state 1 dimers. Average tail length has been calculated from 50 particles as well as additional quantities necessary to calculate standard deviation.

Std. Deviation – State 1 – Dimers: $\sigma = 4.33$ nm

Image	Label	Measured length $x(i)$ [nm]	Average μ	$x(i) - \mu$	$(x(i) - \mu)^2$	n
01	3	37.05	41.37	-4.32	18.66	50
	4	39.49	41.37	-1.88	3.53	50
	5	42.18	41.37	0.81	0.65	50
	6	42.88	41.37	1.51	2.29	50
	7	36.89	41.37	-4.48	20.07	50
	8	41.80	41.37	0.43	0.19	50
02	3	46.53	41.37	5.16	26.63	50
	4	35.97	41.37	-5.40	29.13	50
	5	44.65	41.37	3.29	10.79	50
	6	32.74	41.37	-8.63	74.45	50
03	3	42.66	41.37	1.29	1.65	50
	4	47.43	41.37	6.07	36.79	50
	5	48.15	41.37	6.78	45.96	50
	6	39.02	41.37	-2.35	5.52	50
	7	38.70	41.37	-2.67	7.14	50
	8	36.91	41.37	-4.46	19.87	50
	9	42.31	41.37	0.95	0.89	50
04	3	40.58	41.37	-0.79	0.62	50
	4	38.59	41.37	-2.78	7.73	50
	5	47.39	41.37	6.03	36.30	50
	6	39.17	41.37	-2.20	4.83	50
	7	52.39	41.37	11.02	121.40	50
05	3	36.04	41.37	-5.33	28.42	50
	4	41.79	41.37	0.42	0.17	50
	5	44.18	41.37	2.82	7.93	50
06	3	40.84	41.37	-0.53	0.28	50
	4	43.11	41.37	1.74	3.04	50
	5	37.11	41.37	-4.26	18.17	50
	6	44.20	41.37	2.83	8.02	50
	7	44.43	41.37	3.06	9.38	50
	8	32.34	41.37	-9.03	81.55	50
	9	44.10	41.37	2.73	7.47	50
	10	41.06	41.37	-0.31	0.10	50
	11	42.73	41.37	1.37	1.86	50
07	3	33.98	41.37	-7.38	54.53	50
	4	42.15	41.37	0.78	0.61	50
	5	44.51	41.37	3.14	9.85	50
	6	46.17	41.37	4.80	23.03	50
	7	42.12	41.37	0.75	0.56	50
	8	41.47	41.37	0.10	0.01	50
	9	43.26	41.37	1.89	3.58	50
	10	45.48	41.37	4.11	16.89	50
	11	45.02	41.37	3.65	13.32	50
08	3	46.36	41.37	4.99	24.88	50
	4	45.09	41.37	3.72	13.81	50
	5	36.14	41.37	-5.23	27.36	50
	6	41.67	41.37	0.30	0.09	50
	7	40.08	41.37	-1.29	1.66	50
	8	37.73	41.37	-3.64	13.25	50
	9	31.82	41.37	-9.55	91.27	50

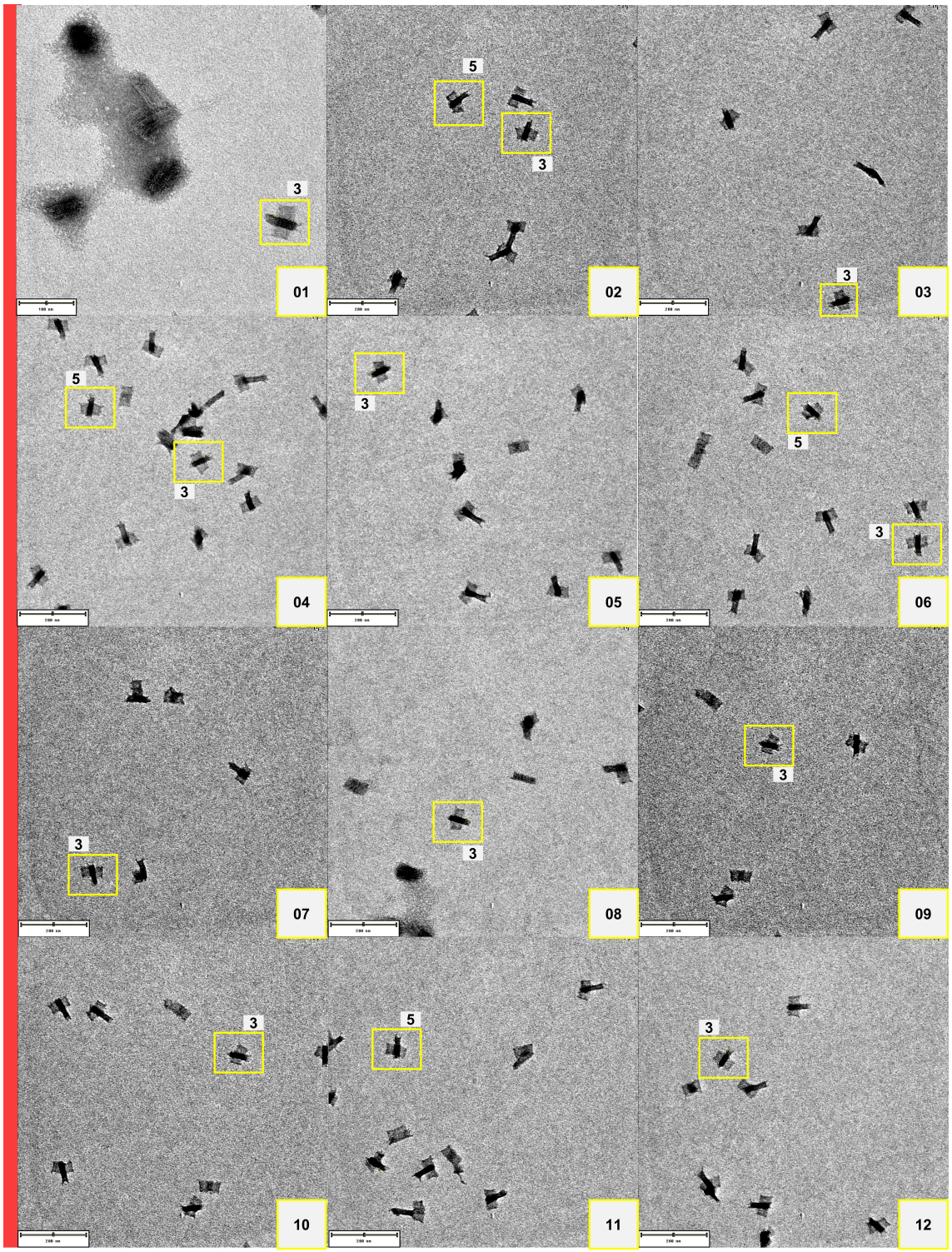

Figure B.14.: Part 1 of the images collection for state 4 dimers (purple clip strands removed, red clip strand engaged) used for analysis. Yellow boxes highlight the picked particles. Labels can be used to assign the obtained tail lengths listed in the tables below to the particles.

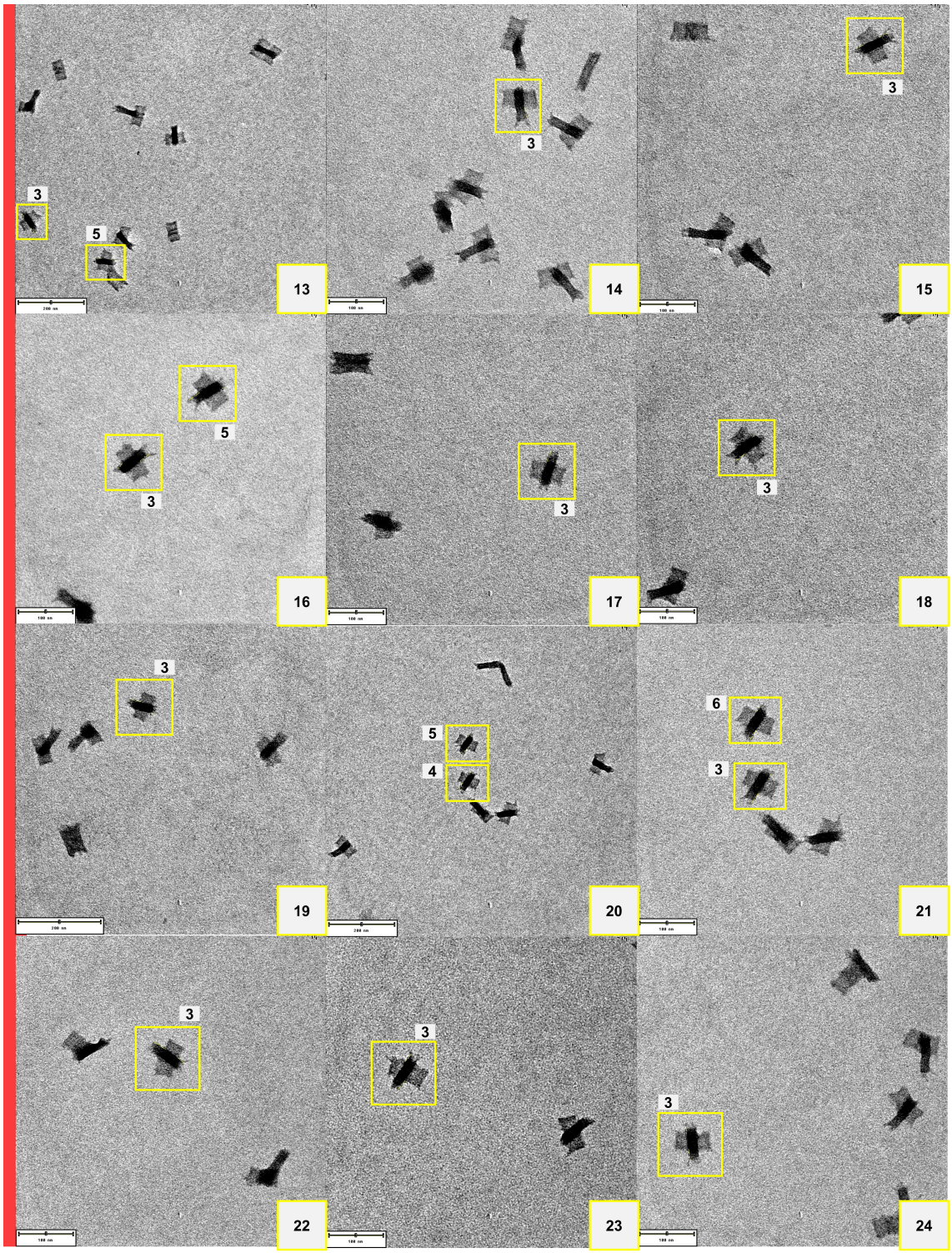

Figure B.15.: Part 2 of the images collection for state 4 dimers used for analysis.

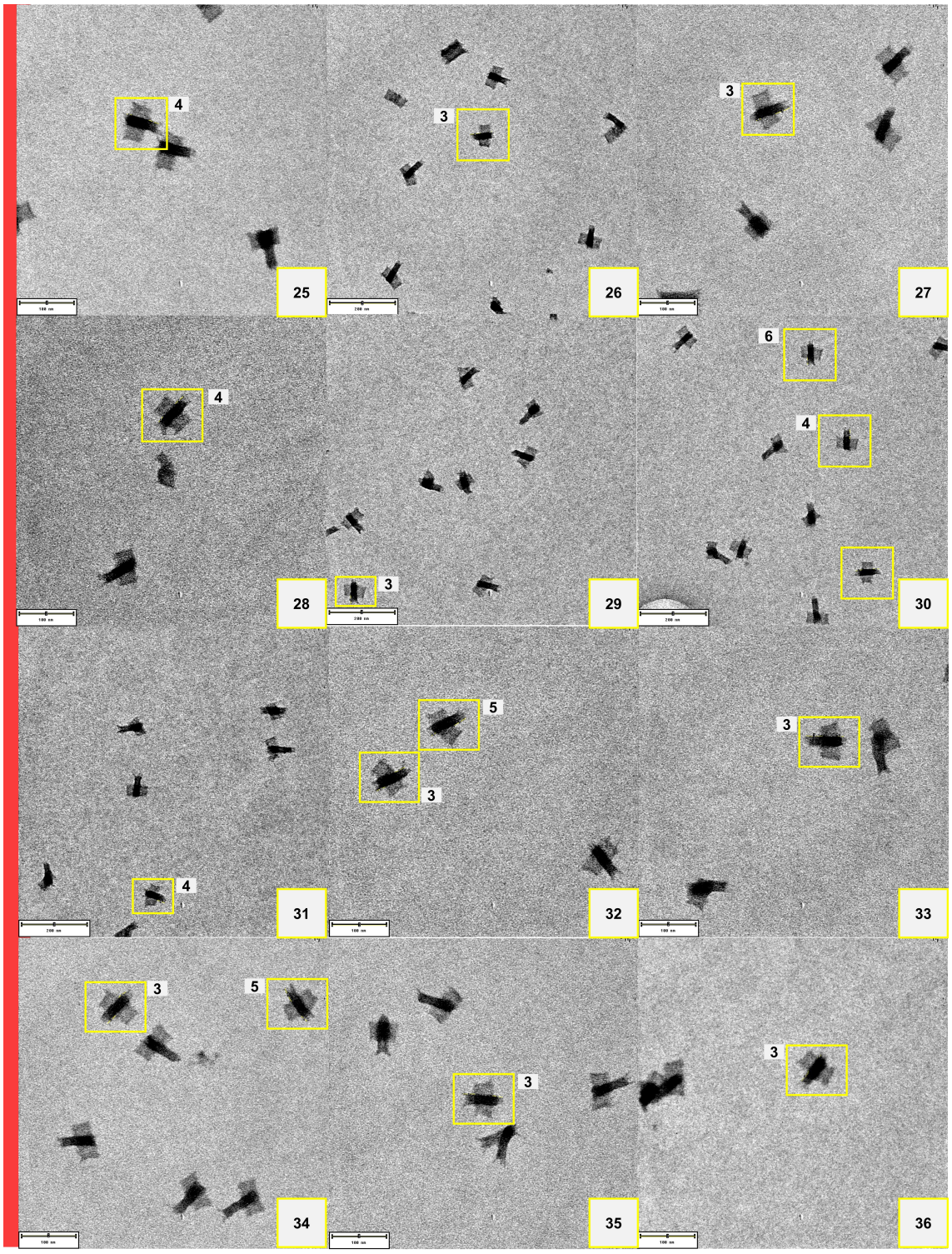

Figure B.16.: Part 3 of the images collection for state 4 dimers used for analysis.

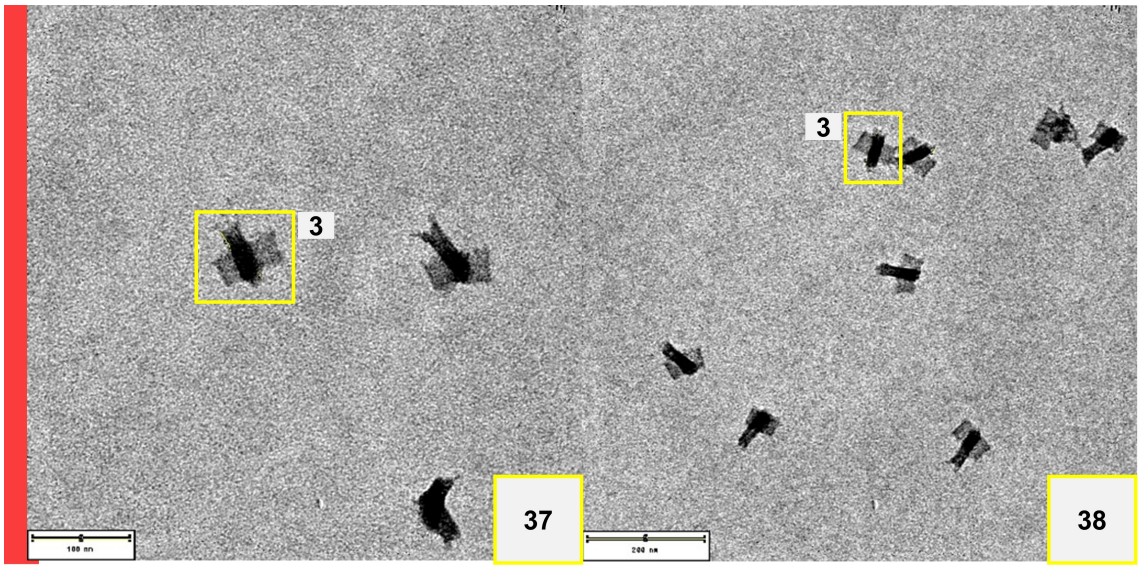

Figure B.17.: Part 4 of the images collection for state 4 dimers used for analysis.

Table B.6.: Measured tail length x_i in nm for state 4 dimers. Average tail length has been calculated from 50 particles as well as additional quantities necessary to calculate standard deviation.
Std. Deviation – State 4 – Dimers: $\sigma = 3.81$ nm

Image	Label	Measured length $x(i)$ [nm]	Average μ	$x(i) - \mu$	$(x(i) - \mu)^2$	n
01	3	19.27	22.32	-3.05	9.28	50
02	3	24.04	22.32	1.72	2.98	50
	5	26.60	22.32	4.29	18.38	50
03	3	20.38	22.32	-1.94	3.77	50
04	3	18.34	22.32	-3.97	15.78	50
	5	20.34	22.32	-1.98	3.91	50
05	3	18.65	22.32	-3.67	13.48	50
06	3	24.68	22.32	2.36	5.58	50
	5	20.41	22.32	-1.90	3.62	50
07	3	28.61	22.32	6.30	39.64	50
08	3	28.04	22.32	5.72	32.73	50
09	3	15.53	22.32	-6.78	46.01	50
10	3	15.08	22.32	-7.24	52.42	50
11	3	25.62	22.32	3.30	10.90	50
	5	27.46	22.32	5.14	26.44	50
12	3	24.59	22.32	2.28	5.18	50
13	3	16.99	22.32	-5.33	28.40	50
	5	16.73	22.32	-5.59	31.25	50
14	3	20.80	22.32	-1.52	2.31	50
15	3	16.81	22.32	-5.50	30.28	50
16	3	21.689	22.32	-0.63	0.39	50
	5	23.494	22.32	1.18	1.39	50
17	3	23.06	22.32	0.74	0.55	50
18	3	19.913	22.32	-2.40	5.78	50
19	3	21.964	22.32	-0.35	0.12	50
20	4	23.72	22.32	1.41	1.98	50
	5	22.63	22.32	0.31	0.10	50
21	3	23.64	22.32	1.33	1.76	50
	6	18.79	22.32	-3.53	12.46	50
22	3	24.67	22.32	2.36	5.55	50
23	3	21.01	22.32	-1.31	1.71	50
24	3	18.77	22.32	-3.55	12.60	50
25	4	19.89	22.32	-2.43	5.91	50
26	3	31.14	22.32	8.83	77.90	50
27	3	28.98	22.32	6.66	44.37	50
28	4	19.63	22.32	-2.68	7.19	50
29	3	24.41	22.32	2.09	4.36	50
30	4	29.00	22.32	6.68	44.61	50
	6	20.69	22.32	-1.63	2.65	50
	7	20.62	22.32	-1.69	2.87	50
31	4	23.80	22.32	1.48	2.19	50
32	3	20.61	22.32	-1.70	2.90	50
	5	24.99	22.32	2.68	7.16	50
33	3	29.68	22.32	7.36	54.20	50
34	3	20.35	22.32	-1.97	3.87	50
	5	26.16	22.32	3.84	14.78	50
35	3	20.90	22.32	-1.42	2.01	50
36	3	22.75	22.32	0.43	0.19	50
37	3	22.21	22.32	-0.10	0.01	50
38	3	17.71	22.32	-4.61	21.24	50

C. Sequences and designs

Scaffold sequences

p7308

AATGCTACTACTATTAGTAGAATTGATGCCACCTTTTCAGCTCGCGCCCCAA
ATGAAAATATAGCTAAACAGGTTATTGACCATTTGCGAAATGTATCTAATGG
TCAAACTAAATCTACTCGTTCGCAGAATTGGGAATCAACTGTTATATGGAAT
GAAACTTCCAGACACCGTACTTTAGTTGCATATTTAAAACATGTTGAGCTAC
AGCATTATATTCAGCAATTAAGCTCTAAGCCATCCGCAAAAATGACCTCTTA
TCAAAAGGAGCAATTAAAGGTACTCTCTAATCCTGACCTGTTGGAGTTTGCT
TCCGGTCTGGTTCGCTTTGAAGCTCGAATTAAAACGCGATATTTGAAGTCTT
TCGGGCTTCCTCTTAATCTTTTTGATGCAATCCGCTTTGCTTCTGACTATAA
TAGTCAGGGTAAAGACCTGATTTTTGATTTATGGTCATTCTCGTTTTCTGAA
CTGTTTAAAGCATTTGAGGGGGATTCAATGAATATTTATGACGATTCCGCAG
TATTGGACGCTATCCAGTCTAAACATTTTACTATTACCCCCTCTGGCAAAAC
TTCTTTTGCAAAAGCCTCTCGCTATTTTGGTTTTTATCGTCGTCTGGTAAAC
GAGGGTTATGATAGTGTTGCTCTTACTATGCCTCGTAATTCCTTTTGGCGTT
ATGTATCTGCATTAGTTGAATGTGGTATTCCTAAATCTCAACTGATGAATCT
TTCTACCTGTAATAATGTTGTTCCGTTAGTTCGTTTTATTAACGTAGATTTT
TCTTCCCAACGTCCTGACTGGTATAATGAGCCAGTTCTTAAAATCGCATAAG
GTAATTCACAATGATTAAAGTTGAAATTAAACCATCTCAAGCCCAATTTACT
ACTCGTTCTGGTGTTTCTCGTCAGGGCAAGCCTTATTCACTGAATGAGCAGC
TTTGTTACGTTGATTTGGGTAATGAATATCCGGTTCTTGTCAAGATTACTCT
TGATGAAGGTCAGCCAGCCTATGCGCCTGGTCTGTACACCGTTCATCTGTCC
TCTTTCAAAGTTGGTCAGTTCGGTTCCCTTATGATTGACCGTCTGCGCCTCG
TTCCGGCTAAGTAACATGGAGCAGGTCGCGGATTTCGACACAATTTATCAGG
CGATGATACAAATCTCCGTTGTACTTTGTTTCGCGCTTGGTATAATCGCTGG
GGGTCAAAGATGAGTGTTTTAGTGTATTCTTTTGCCTCTTTCGTTTTAGGTT
GGTGCCTTCGTAGTGGCATTACGTATTTTACCCGTTTAATGGAAACTTCCTC
ATGAAAAAGTCTTTAGTCCTCAAAGCCTCTGTAGCCGTTGCTACCCTCGTTC
CGATGCTGTCTTTCGCTGCTGAGGGTGACGATCCCGCAAAAGCGGCCTTTAA
CTCCCTGCAAGCCTCAGCGACCGAATATATCGGTTATGCGTGGGCGATGGTT
GTTGTCATTGTCGGCGCAACTATCGGTATCAAGCTGTTTAAGAAATTCACCT
CGAAAGCAAGCTGATAAACCGATACAATTAAAGGCTCCTTTTGGAGCCTTTT
TTTTGGAGATTTTCAACGTGAAAAAATTATTATTCGCAATTCCTTTAGTTGT
TCCTTTCTATTCTCACTCCGCTGAAACTGTTGAAAGTTGTTTAGCAAAATCC
CATACAGAAAATTCATTTACTAACGTCTGGAAAGACGACAAAACTTTAGATC
GTTACGCTAACTATGAGGGCTGTCTGTGGAATGCTACAGGCGTTGTAGTTTG
TACTGGTGACGAAACTCAGTGTTACGGTACATGGGTTCCTATTGGGCTTGCT
ATCCCTGAAAATGAGGGTGGTGGCTCTGAGGGTGGCGGTTCTGAGGGTGGC
GGTTCTGAGGGTGGCGGTACTAAACCTCCTGAGTACGGTGATACACCTATTC

CGGGCTATACTTATATCAACCCTCTCGACGGCACTTATCCGCCTGGTACTGA
GCAAAACCCCGCTAATCCTAATCCTTCTCTTGAGGAGTCTCAGCCTCTTAAT
ACTTTCATGTTTCAGAATAATAGGTTCCGAAATAGGCAGGGGGCATTAACTG
TTTATACGGGCACTGTTACTCAAGGCACTGACCCCGTTAAAACTTATTACCA
GTACACTCCTGTATCATCAAAAGCCATGTATGACGCTTACTGGAACGGTAAA
TTCAGAGACTGCGCTTTCCATTCTGGCTTTAATGAGGATTTATTTGTTTGTG
AATATCAAGGCCAATCGTCTGACCTGCCTCAACCTCCTGTCAATGCTGGCGG
CGGCTCTGGTGGTGGTTCTGGTGGCGGCTCTGAGGGTGGTGGCTCTGAGGG
TGGCGGTTCTGAGGGTGGCGGCTCTGAGGGAGGCGGTTCCGGTGGTGGCTC
TGGTTCCGGTGATTTTGATTATGAAAAGATGGCAAACGCTAATAAGGGGGCT
ATGACCGAAAATGCCGATGAAAACGCGCTACAGTCTGACGCTAAAGGCAAAC
TTGATTCTGTCGCTACTGATTACGGTGCTGCTATCGATGGTTTCATTGGTGA
CGTTTCCGGCCTTGCTAATGGTAATGGTGCTACTGGTGATTTTGCTGGCTCT
AATTCCCAAATGGCTCAAGTCGGTGACGGTGATAATTCACCTTTAATGAATA
ATTTCCGTCAATATTTACCTTCCCTCCCTCAATCGGTTGAATGTCGCCCTTTT
GTCTTTGGCGCTGGTAAACCATATGAATTTTCTATTGATTGTGACAAAATAA
ACTTATTCCGTGGTGTCTTTGCGTTTCTTTTATATGTTGCCACCTTTATGTA
TGTATTTTCTACGTTTGCTAACATACTGCGTAATAAGGAGTCTTAATCATGC
CAGTTCTTTTGGGTATTCCGTTATTATTGCGTTTCCTCGGTTTCCTTCTGGT
AACTTTGTTCGGCTATCTGCTTACTTTTCTTAAAAAGGGCTTCGGTAAGATA
GCTATTGCTATTTCATTGTTTCTTGCTCTTATTATTGGGCTTAACTCAATTCT
TGTGGGTTATCTCTCTGATATTAGCGCTCAATTACCCTCTGACTTTGTTCAG
GGTGTTCAGTTAATTCTCCCGTCTAATGCGCTTCCCTGTTTTTATGTTATTC
TCTCTGTAAAGGCTGCTATTTTCATTTTTGACGTTAAACAAAAAATCGTTTC
TTATTTGGATTGGGATAAATAATATGGCTGTTTATTTTGTAACTGGCAAATT
AGGCTCTGGAAAGACGCTCGTTAGCGTTGGTAAGATTCAGGATAAAATTGTA
GCTGGGTGCAAAATAGCAACTAATCTTGATTTAAGGCTTCAAAACCTCCCGC
AAGTCGGGAGGTTCGCTAAAACGCCTCGCGTTCTTAGAATACCGGATAAGCC
TTCTATATCTGATTTGCTTGCTATTGGGCGCGGTAATGATTCCTACGATGAA
AATAAAAACGGCTTGCTTGTTCTCGATGAGTGCGGTACTTGGTTTAATACCC
GTTCTTGGAATGATAAGGAAAGACAGCCGATTATTGATTGGTTTCTACATGC
TCGTAAATTAGGATGGGATATTATTTTTCTTGTTCAGGACTTATCTATTGTT
GATAAACAGGCGCGTTCTGCATTAGCTGAACATGTTGTTTATTGTCGTCGTC
TGGACAGAATTACTTTACCTTTTGTCGGTACTTTATATTCTCTTATTACTGG
CTCGAAAATGCCTCTGCCTAAATTACATGTTGGCGTTGTTAAATATGGCGAT
TCTCAATTAAGCCCTACTGTTGAGCGTTGGCTTTATACTGGTAAGAATTTGT
ATAACGCATATGATACTAAACAGGCTTTTTCTAGTAATTATGATTCCGGTGT
TTATTCTTATTTAACGCCTTATTTATCACACGGTCGGTATTTCAAACCATTA
AATTTAGGTCAGAAGATGAAATTAACTAAAATATATTTGAAAAAGTTTTCTC
GCGTTCTTTGTCTTGCGATTGGATTTGCATCAGCATTTACATATAGTTATAT
AACCCAACCTAAGCCGGAGGTTAAAAAGGTAGTCTCTCAGACCTATGATTTT
GATAAATTCACTATTGACTCTTCTCAGCGTCTTAATCTAAGCTATCGCTATG
TTTTCAAGGATTCTAAGGGAAAATTAATTAATAGCGACGATTTACAGAAGCA
AGGTTATTCACTCACATATATTGATTTATGTACTGTTTCCATTAAAAAAGGT
AATTCAAATGAAATTGTTAAATGTAATTAATTTTGTTTTCTTGATGTTTGTT
TCATCATCTTCTTTTGCTCAGGTAATTGAAATGAATAATTCGCCTCTGCGCG
ATTTTGTAACTTGGTATTCAAAGCAATCAGGCGAATCCGTTATTGTTTCTCC
CGATGTAAAAGGTACTGTTACTGTATATTCATCTGACGTTAAACCTGAAAAT

CTACGCAATTTCTTTATTTCTGTTTTACGTGCAAATAATTTTGATATGGTAG
GTTCTAACCCTTCCATTATTCAGAAGTATAATCCAAACAATCAGGATTATAT
TGATGAATTGCCATCATCTGATAATCAGGAATATGATGATAATTCCGCTCCT
TCTGGTGGTTTCTTTGTTCCGCAAAATGATAATGTTACTCAAACTTTTAAAA
TTAATAACGTTCGGGCAAAGGATTTAATACGAGTTGTCGAATTGTTTGTAAA
GTCTAATACTTCTAAATCCTCAAATGTATTATCTATTGACGGCTCTAATCTA
TTAGTTGTTAGTGCTCCTAAAGATATTTTAGATAACCTTCCTCAATTCCTTT
CAACTGTTGATTTGCCAACTGACCAGATATTGATTGAGGGTTTGATATTTGA
GGTTCAGCAAGGTGATGCTTTAGATTTTTCATTTGCTGCTGGCTCTCAGCGT
GGCACTGTTGCAGGCGGTGTTAATACTGACCGCCTCACCTCTGTTTTATCTT
CTGCTGGTGGTTCGTTCGGTATTTTTAATGGCGATGTTTTAGGGCTATCAGT
TCGCGCATTAAAGACTAATAGCCATTCAAAAATATTGTCTGTGCCACGTATT
CTTACGCTTTCAGGTCAGAAGGGTTCTATCTCTGTTGGCCAGAATGTCCCTT
TTATTACTGGTCGTGTGACTGGTGAATCTGCCAATGTAAATAATCCATTTCA
GACGATTGAGCGTCAAAATGTAGGTATTTCCATGAGCGTTTTTCCTGTTGCA
ATGGCTGGCGGTAATATTGTTCTGGATATTACCAGCAAGGCCGATAGTTTGA
GTTCTTCTACTCAGGCAAGTGATGTTATTACTAATCAAAGAAGTATTGCTAC
AACGGTTAATTTGCGTGATGGACAGACTCTTTTACTCGGTGGCCTCACTGAT
TATAAAAACACTTCTCAGGATTCTGGCGTACCGTTCCTGTCTAAAATCCCTT
TAATCGGCCTCCTGTTTAGCTCCCGCTCTGATTCTAACGAGGAAAGCACGTT
ATACGTGCTCGTCAAAGCAACCATAGTACGCGCCCTGTAGCGGCGCATTAAG
CGCGGCGGGTGTGGTGGTTACGCGCAGCGTGACCGCTACACTTGCCAGCGCC
CTAGCGCCCGCTCCTTTCGCTTTCTTCCCTTCCTTTCTCGCCACGTTCGCCGG
CTTTCCCCGTCAAGCTCTAAATCGGGGGCTCCCTTTAGGGTTCCGATTTAGT
GCTTTACGGCACCTCGACCCCAAAAAACTTGATTTGGGTGATGGTTCACGTA
GTGGGCCATCGCCCTGATAGACGGTTTTTCGCCCTTTGACGTTGGAGTCCAC
GTTCTTTAATAGTGGACTCTTGTTCCAAACTGGAACAACACTCAACCCTATC
TCGGGCTATTCTTTTGATTTATAAGGGATTTTGCCGATTTCGGAACCACCAT
CAAACAGGATTTTCGCCTGCTGGGGCAAACCAGCGTGGACCGCTTGCTGCAA
CTCTCTCAGGGCCAGGCGGTGAAGGGCAATCAGCTGTTGCCCGTCTCACTGG
TGAAAAGAAAAACCACCCTGGCGCCCAATACGCAAACCGCCTCTCCCCGCGC
GTTGGCCGATTCATTAATGCAGCTGGCACGACAGGTTTCCCGACTGGAAAGC
GGGCAGTGAGCGCAACGCAATTAATGTGAGTTAGCTCACTCATTAGGCACCC
CAGGCTTTACACTTTATGCTTCCGGCTCGTATGTTGTGTGGAATTGTGAGCG
GATAACAATTTCACACAGGAAACAGCTATGACCATGATTACGAATTCGAGCT
CGGTACCCGGGGATCCTTATACGGGTACTAGCCATGCGTATACGGTCGCTAG
CGGACTTGCCTCGCTATCAAAGGTCTAGAGTCGACCTGCAGGCATGCAAGCT
TGGCACTGGCCGTCGTTTTACAACGTCGTGACTGGGAAAACCCTGGCGTTAC
CCAACTTAATCGCCTTGCAGCACATCCCCCTTTCGCCAGCTGGCGTAATAGC
GAAGAGGCCCGCACCGATCGCCCTTCCCAACAGTTGCGCAGCCTGAATGGCG
AATGGCGCTTTGCCTGGTTTCCGGCACCAGAAGCGGTGCCGGAAAGCTGGCT
GGAGTGCGATCTTCCTGAGGCCGATACTGTCGTCGTCCCCTCAAACTGGCAG
ATGCACGGTTACGATGCGCCCATCTACACCAACGTGACCTATCCCATTACGG
TCAATCCGCCGTTTGTTCCCACGGAGAATCCGACGGGTTGTTACTCGCTCAC
ATTTAATGTTGATGAAAGCTGGCTACAGGAAGGCCAGACGCGAATTATTTTT
GATGGCGTTCCTATTGGTTAAAAAATGAGCTGATTTAACAAAAATTTAATGC
GAATTTTAACAAAATATTAACGTTTACAATTTAAATATTTGCTTATACAATC
TTCCTGTTTTTGGGGCTTTTCTGATTATCAACCGGGGTACATATGATTGACA

TGCTAGTTTTACGATTACCGTTCATCGATTCTCTTGTTTGCTCCAGACTCTC
AGGCAATGACCTGATAGCCTTTGTAGATCTCTCAAAAATAGCTACCCTCTCC
GGCATTAATTTATCAGCTAGAACGGTTGAATATCATATTGATGGTGATTTGA
CTGTCTCCGGCCTTTCTCACCCTTTTGAATCTTTACCTACACATTACTCAGGC
ATTGCATTTAAAATATATGAGGGTTCTAAAAATTTTTATCCTTGCGTTGAAA
TAAAGGCTTCTCCCGCAAAAGTATTACAGGGTCATAATGTTTTTGGTACAAC
CGATTTAGCTTTATGCTCTGAGGCTTTATTGCTTAATTTTGCTAATTCTTTG
CCTTGCCTGTATGATTTATTGGATGTT

p8064

ACGTTCTTTAATAGTGGACTCTTGTTCCAAACTGGAACAACACTCAACCCTA
TCTCGGGCTATTCTTTTGATTTATAAGGGATTTTGCCGATTTCGGAACCACC
ATCAAACAGGATTTTCGCCTGCTGGGGCAAACCAGCGTGGACCGCTTGCTGC
AACTCTCTCAGGGCCAGGCGGTGAAGGGCAATCAGCTGTTGCCCGTCTCACT
GGTGAAAAGAAAAACCACCCTGGCGCCCAATACGCAAACCGCCTCTCCCCGC
GCGTTGGCCGATTCATTAATGCAGCTGGCACGACAGGTTTCCCGACTGGAAA
GCGGGCAGTGAGCGCAACGCAATTAATGTGAGTTAGCTCACTCATTAGGCAC
CCCAGGCTTTACACTTTATGCTTCCGGCTCGTATGTTGTGTGGAATTGTGAG
CGGATAACAATTTCACACAGGAAACAGCTATGACCATGATTACGAATTCGAG
CTCGGTACCCGGGGATCCTCAACTGTGAGGAGGCTCACGGACGCGAAGAAC
AGGCACGCGTGCTGGCAGAAACCCCCGGTATGACCGTGAAAACGGCCCGCCG
CATTCTGGCCGCAGCACCACAGAGTGCACAGGCGCGCAGTGACACTGCGCTG
GATCGTCTGATGCAGGGGGCACCGGCACCGCTGGCTGCAGGTAACCCGGCA
TCTGATGCCGTTAACGATTTGCTGAACACACCAGTGTAAGGGATGTTTATGA
CGAGCAAAGAAACCTTTACCCATTACCAGCCGCAGGGCAACAGTGACCCGGC
TCATACCGCAACCGCGCCCGGCGGATTGAGTGCGAAAGCGCCTGCAATGACC
CCGCTGATGCTGGACACCTCCAGCCGTAAGCTGGTTGCGTGGGATGGCACCA
CCGACGGTGCTGCCGTTGGCATTCTTGCGGTTGCTGCTGACCAGACCAGCAC
CACGCTGACGTTCTACAAGTCCGGCACGTTCCGTTATGAGGATGTGCTCTGG
CCGGAGGCTGCCAGCGACGAGACGAAAAAACGGACCGCGTTTGCCGGAACG
GCAATCAGCATCGTTTAACTTTACCCTTCATCACTAAAGGCCGCCTGTGCGG
CTTTTTTTACGGGATTTTTTTATGTCGATGTACACAACCGCCCAACTGCTGG
CGGCAAATGAGCAGAAATTTAAGTTTGATCCGCTGTTTCTGCGTCTCTTTTT
CCGTGAGAGCTATCCCTTCACCACGGAGAAAGTCTATCTCTCACAAATTCCG
GGACTGGTAAACATGGCGCTGTACGTTTCGCCGATTGTTTCCGGTGAGGTTA
TCCGTTCCCGTGGCGGCTCCACCTCTGAAAGCTTGGCACTGGCCGTCGTTTT
ACAACGTCGTGACTGGGAAAACCCTGGCGTTACCCAACTTAATCGCCTTGCA
GCACATCCCCCTTTCGCCAGCTGGCGTAATAGCGAAGAGGCCCGCACCGATC
GCCCTTCCCAACAGTTGCGCAGCCTGAATGGCGAATGGCGCTTTGCCTGGTT
TCCGGCACCAGAAGCGGTGCCGGAAAGCTGGCTGGAGTGCGATCTTCCTGA
GGCCGATACTGTCGTCGTCCCCTCAAACTGGCAGATGCACGGTTACGATGCG
CCCATCTACACCAACGTGACCTATCCCATTACGGTCAATCCGCCGTTTGTTC
CCACGGAGAATCCGACGGGTTGTTACTCGCTCACATTTAATGTTGATGAAAG
CTGGCTACAGGAAGGCCAGACGCGAATTATTTTTGATGGCGTTCCTATTGGT
TAAAAAATGAGCTGATTTAACAAAAATTTAATGCGAATTTTAACAAAATATT
AACGTTTACAATTTAAATATTTGCTTATACAATCTTCCTGTTTTTGGGGCTT
TTCTGATTATCAACCGGGGTACATATGATTGACATGCTAGTTTTACGATTAC

CGTTCATCGATTCTCTTGTTTGCTCCAGACTCTCAGGCAATGACCTGATAGC
CTTTGTAGATCTCTCAAAAATAGCTACCCTCTCCGGCATTAATTTATCAGCT
AGAACGGTTGAATATCATATTGATGGTGATTTGACTGTCTCCGGCCTTTCTC
ACCCTTTTGAATCTTTACCTACACATTACTCAGGCATTGCATTTAAAATATA
TGAGGGTTCTAAAAATTTTTATCCTTGCGTTGAAATAAAGGCTTCTCCCGCA
AAAGTATTACAGGGTCATAATGTTTTTGGTACAACCGATTTAGCTTTATGCT
CTGAGGCTTTATTGCTTAATTTTGCTAATTCTTTGCCTTGCCTGTATGATTT
ATTGGATGTTAATGCTACTACTATTAGTAGAATTGATGCCACCTTTTCAGCT
CGCGCCCCAAATGAAAATATAGCTAAACAGGTTATTGACCATTTGCGAAATG
TATCTAATGGTCAAACTAAATCTACTCGTTCGCAGAATTGGGAATCAACTGT
TATATGGAATGAAACTTCCAGACACCGTACTTTAGTTGCATATTTAAAACAT
GTTGAGCTACAGCATTATATTCAGCAATTAAGCTCTAAGCCATCCGCAAAAA
TGACCTCTTATCAAAAGGAGCAATTAAAGGTACTCTCTAATCCTGACCTGTT
GGAGTTTGCTTCCGGTCTGGTTCGCTTTGAAGCTCGAATTAAAACGCGATAT
TTGAAGTCTTTCGGGCTTCCTCTTAATCTTTTTGATGCAATCCGCTTTGCTT
CTGACTATAATAGTCAGGGTAAAGACCTGATTTTTGATTTATGGTCATTCTC
GTTTTCTGAACTGTTTAAAGCATTTGAGGGGGATTCAATGAATATTTATGAC
GATTCCGCAGTATTGGACGCTATCCAGTCTAAACATTTTACTATTACCCCCT
CTGGCAAAACTTCTTTTGCAAAAGCCTCTCGCTATTTTGGTTTTTATCGTCG
TCTGGTAAACGAGGGTTATGATAGTGTTGCTCTTACTATGCCTCGTAATTCC
TTTTGGCGTTATGTATCTGCATTAGTTGAATGTGGTATTCCTAAATCTCAAC
TGATGAATCTTTCTACCTGTAATAATGTTGTTCCGTTAGTTCGTTTTATTAA
CGTAGATTTTTCTTCCCAACGTCCTGACTGGTATAATGAGCCAGTTCTTAAA
ATCGCATAAGGTAATTCACAATGATTAAAGTTGAAATTAAACCATCTCAAGC
CCAATTTACTACTCGTTCTGGTGTTTCTCGTCAGGGCAAGCCTTATTCACTG
AATGAGCAGCTTTGTTACGTTGATTTGGGTAATGAATATCCGGTTCTTGTCA
AGATTACTCTTGATGAAGGTCAGCCAGCCTATGCGCCTGGTCTGTACACCGT
TCATCTGTCCTCTTTCAAAGTTGGTCAGTTCGGTTCCCTTATGATTGACCGT
CTGCGCCTCGTTCCGGCTAAGTAACATGGAGCAGGTCGCGGATTTCGACACA
ATTTATCAGGCGATGATACAAATCTCCGTTGTACTTTGTTTCGCGCTTGGTA
TAATCGCTGGGGGTCAAAGATGAGTGTTTTAGTGTATTCTTTTGCCTCTTTC
GTTTTAGGTTGGTGCCTTCGTAGTGGCATTACGTATTTTACCCGTTTAATGG
AAACTTCCTCATGAAAAAGTCTTTAGTCCTCAAAGCCTCTGTAGCCGTTGCT
ACCCTCGTTCCGATGCTGTCTTTCGCTGCTGAGGGTGACGATCCCGCAAAAG
CGGCCTTTAACTCCCTGCAAGCCTCAGCGACCGAATATATCGGTTATGCGTG
GGCGATGGTTGTTGTCATTGTCGGCGCAACTATCGGTATCAAGCTGTTTAAG
AAATTCACCTCGAAAGCAAGCTGATAAACCGATACAATTAAAGGCTCCTTTT
GGAGCCTTTTTTTTGGAGATTTTCAACGTGAAAAAATTATTATTCGCAATTC
CTTTAGTTGTTCCTTTCTATTCTCACTCCGCTGAAACTGTTGAAAGTTGTTT
AGCAAAATCCCATACAGAAAATTCATTTACTAACGTCTGGAAAGACGACAAA
ACTTTAGATCGTTACGCTAACTATGAGGGCTGTCTGTGGAATGCTACAGGCG
TTGTAGTTTGTACTGGTGACGAAACTCAGTGTTACGGTACATGGGTTCCTAT
TGGGCTTGCTATCCCTGAAAATGAGGGTGGTGGCTCTGAGGGTGGCGGTTC
TGAGGGTGGCGGTTCTGAGGGTGGCGGTACTAAACCTCCTGAGTACGGTGA
TACACCTATTCCGGGCTATACTTATATCAACCCTCTCGACGGCACTTATCCG
CCTGGTACTGAGCAAAACCCCGCTAATCCTAATCCTTCTCTTGAGGAGTCTC
AGCCTCTTAATACTTTCATGTTTCAGAATAATAGGTTCCGAAATAGGCAGGG
GGCATTAACTGTTTATACGGGCACTGTTACTCAAGGCACTGACCCCGTTAAA

ACTTATTACCAGTACACTCCTGTATCATCAAAAGCCATGTATGACGCTTACT
GGAACGGTAAATTCAGAGACTGCGCTTTCCATTCTGGCTTTAATGAGGATTT
ATTTGTTTGTGAATATCAAGGCCAATCGTCTGACCTGCCTCAACCTCCTGTC
AATGCTGGCGGCGGCTCTGGTGGTGGTTCTGGTGGCGGCTCTGAGGGTGGT
GGCTCTGAGGGTGGCGGTTCTGAGGGTGGCGGCTCTGAGGGAGGCGGTTCC
GGTGGTGGCTCTGGTTCCGGTGATTTTGATTATGAAAAGATGGCAAACGCTA
ATAAGGGGGCTATGACCGAAAATGCCGATGAAAACGCGCTACAGTCTGACGC
TAAAGGCAAACTTGATTCTGTCGCTACTGATTACGGTGCTGCTATCGATGGT
TTCATTGGTGACGTTTCCGGCCTTGCTAATGGTAATGGTGCTACTGGTGATT
TTGCTGGCTCTAATTCCCAAATGGCTCAAGTCGGTGACGGTGATAATTCACC
TTTAATGAATAATTTCCGTCAATATTTACCTTCCCTCCCTCAATCGGTTGAA
TGTCGCCCTTTTGTCTTTGGCGCTGGTAAACCATATGAATTTTCTATTGATT
GTGACAAAATAAACTTATTCCGTGGTGTCTTTGCGTTTCTTTTATATGTTGC
CACCTTTATGTATGTATTTTCTACGTTTGCTAACATACTGCGTAATAAGGAG
TCTTAATCATGCCAGTTCTTTTGGGTATTCCGTTATTATTGCGTTTCCTCGG
TTTCCTTCTGGTAACTTTGTTCGGCTATCTGCTTACTTTTCTTAAAAAGGGC
TTCGGTAAGATAGCTATTGCTATTTCATTGTTTCTTGCTCTTATTATTGGGC
TTAACTCAATTCTTGTGGGTTATCTCTCTGATATTAGCGCTCAATTACCCTC
TGACTTTGTTCAGGGTGTTCAGTTAATTCTCCCGTCTAATGCGCTTCCCTGT
TTTTATGTTATTCTCTCTGTAAAGGCTGCTATTTTCATTTTTGACGTTAAAC
AAAAAATCGTTTCTTATTTGGATTGGGATAAATAATATGGCTGTTTATTTTG
TAACTGGCAAATTAGGCTCTGGAAAGACGCTCGTTAGCGTTGGTAAGATTCA
GGATAAAATTGTAGCTGGGTGCAAAATAGCAACTAATCTTGATTTAAGGCTT
CAAAACCTCCCGCAAGTCGGGAGGTTCGCTAAAACGCCTCGCGTTCTTAGAA
TACCGGATAAGCCTTCTATATCTGATTTGCTTGCTATTGGGCGCGGTAATGA
TTCCTACGATGAAAATAAAAACGGCTTGCTTGTTCTCGATGAGTGCGGTACT
TGGTTTAATACCCGTTCTTGGAATGATAAGGAAAGACAGCCGATTATTGATT
GGTTTCTACATGCTCGTAAATTAGGATGGGATATTATTTTTCTTGTTCAGGA
CTTATCTATTGTTGATAAACAGGCGCGTTCTGCATTAGCTGAACATGTTGTT
TATTGTCGTCGTCTGGACAGAATTACTTTACCTTTTGTCGGTACTTTATATT
CTCTTATTACTGGCTCGAAAATGCCTCTGCCTAAATTACATGTTGGCGTTGT
TAAATATGGCGATTCTCAATTAAGCCCTACTGTTGAGCGTTGGCTTTATACT
GGTAAGAATTTGTATAACGCATATGATACTAAACAGGCTTTTTCTAGTAATT
ATGATTCCGGTGTTTATTCTTATTTAACGCCTTATTTATCACACGGTCGGTA
TTTCAAACCATTAAATTTAGGTCAGAAGATGAAATTAACTAAAATATATTTG
AAAAAGTTTTCTCGCGTTCTTTGTCTTGCGATTGGATTTGCATCAGCATTTA
CATATAGTTATATAACCCAACCTAAGCCGGAGGTTAAAAAGGTAGTCTCTCA
GACCTATGATTTTGATAAATTCACTATTGACTCTTCTCAGCGTCTTAATCTA
AGCTATCGCTATGTTTTCAAGGATTCTAAGGGAAAATTAATTAATAGCGACG
ATTTACAGAAGCAAGGTTATTCACTCACATATATTGATTTATGTACTGTTTC
CATTAAAAAAGGTAATTCAAATGAAATTGTTAAATGTAATTAATTTTGTTTT
CTTGATGTTTGTTTCATCATCTTCTTTTGCTCAGGTAATTGAAATGAATAAT
TCGCCTCTGCGCGATTTTGTAACTTGGTATTCAAAGCAATCAGGCGAATCCG
TTATTGTTTCTCCCGATGTAAAAGGTACTGTTACTGTATATTCATCTGACGT
TAAACCTGAAAATCTACGCAATTTCTTTATTTCTGTTTTACGTGCAAATAAT
TTTGATATGGTAGGTTCTAACCCTTCCATTATTCAGAAGTATAATCCAAACA
ATCAGGATTATATTGATGAATTGCCATCATCTGATAATCAGGAATATGATGA
TAATTCCGCTCCTTCTGGTGGTTTCTTTGTTCCGCAAAATGATAATGTTACT

CAAACTTTTAAAATTAATAACGTTCGGGCAAAGGATTTAATACGAGTTGTCG
AATTGTTTGTAAAGTCTAATACTTCTAAATCCTCAAATGTATTATCTATTGA
CGGCTCTAATCTATTAGTTGTTAGTGCTCCTAAAGATATTTTAGATAACCTT
CCTCAATTCCTTTCAACTGTTGATTTGCCAACTGACCAGATATTGATTGAGG
GTTTGATATTTGAGGTTCAGCAAGGTGATGCTTTAGATTTTTCATTTGCTGC
TGGCTCTCAGCGTGGCACTGTTGCAGGCGGTGTTAATACTGACCGCCTCACC
TCTGTTTTATCTTCTGCTGGTGGTTCGTTCGGTATTTTTAATGGCGATGTTT
TAGGGCTATCAGTTCGCGCATTAAAGACTAATAGCCATTCAAAAATATTGTC
TGTGCCACGTATTCTTACGCTTTCAGGTCAGAAGGGTTCTATCTCTGTTGGC
CAGAATGTCCCTTTTATTACTGGTCGTGTGACTGGTGAATCTGCCAATGTAA
ATAATCCATTTCAGACGATTGAGCGTCAAAATGTAGGTATTTCCATGAGCGT
TTTTCCTGTTGCAATGGCTGGCGGTAATATTGTTCTGGATATTACCAGCAAG
GCCGATAGTTTGAGTTCTTCTACTCAGGCAAGTGATGTTATTACTAATCAAA
GAAGTATTGCTACAACGGTTAATTTGCGTGATGGACAGACTCTTTTACTCGG
TGGCCTCACTGATTATAAAAACACTTCTCAGGATTCTGGCGTACCGTTCCTG
TCTAAAATCCCTTTAATCGGCCTCCTGTTTAGCTCCCGCTCTGATTCTAACG
AGGAAAGCACGTTATACGTGCTCGTCAAAGCAACCATAGTACGCGCCCTGTA
GCGGCGCATTAAGCGCGGCGGGTGTGGTGGTTACGCGCAGCGTGACCGCTA
CACTTGCCAGCGCCCTAGCGCCCGCTCCTTTCGCTTTCTTCCCTTCCTTTCTC
GCCACGTTCGCCGGCTTTCCCCGTCAAGCTCTAAATCGGGGGCTCCCTTTAG
GGTTCCGATTTAGTGCTTTACGGCACCTCGACCCCAAAAAACTTGATTTGGG
TGATGGTTCACGTAGTGGGCCATCGCCCTGATAGACGGTTTTTCGCCCTTTG
ACGTTGGAGTCC

p8634

GAGTCCACGTTCTTTAATAGTGGACTCTTGTTCCAAACTGGAACAACACTCA
ACCCTATCTCGGGCTATTCTTTTGATTTATAAGGGATTTTGCCGATTTCGGA
ACCACCATCAAACAGGATTTTCGCCTGCTGGGGCAAACCAGCGTGGACCGCT
TGCTGCAACTCTCTCAGGGCCAGGCGGTGAAGGGCAATCAGCTGTTGCCCGT
CTCACTGGTGAAAAGAAAAACCACCCTGGCGCCCAATACGCAAACCGCCTCT
CCCCGCGCGTTGGCCGATTCATTAATGCAGCTGGCACGACAGGTTTCCCGAC
TGGAAAGCGGGCAGTGAGCGCAACGCAATTAATGTGAGTTAGCTCACTCATT
AGGCACCCCAGGCTTTACACTTTATGCTTCCGGCTCGTATGTTGTGTGGAAT
TGTGAGCGGATAACAATTTCACACAGGAAACAGCTATGACCATGATTACGAA
TTCGAGCTCGGTACCCGGGGATCCATTCTCCTGTGACTCGGAAGTGCATTTA
TCATCTCCATAAAACAAAACCCGCCGTAGCGAGTTCAGATAAAATAAATCCC
CGCGAGTGCGAGGATTGTTATGTAATATTGGGTTTAATCATCTATATGTTTT
GTACAGAGAGGGCAAGTATCGTTTCCACCGTACTCGTGATAATAATTTTGCA
CGGTATCAGTCATTTCTCGCACATTGCAGAATGGGGATTTGTCTTCATTAGA
CTTATAAACCTTCATGGAATATTTGTATGCCGACTCTATATCTATACCTTCA
TCTACATAAACACCTTCGTGATGTCTGCATGGAGACAAGACACCGGATCTGC
ACAACATTGATAACGCCCAATCTTTTTGCTCAGACTCTAACTCATTGATACT
CATTTATAAACTCCTTGCAATGTATGTCGTTTCAGCTAAACGGTATCAGCAA
TGTTTATGTAAAGAAACAGTAAGATAATACTCAACCCGATGTTTGAGTACGG
TCATCATCTGACACTACAGACTCTGGCATCGCTGTGAAGACGACGCGAAATT
CAGCATTTTCACAAGCGTTATCTTTTACAAAACCGATCTCACTCTCCTTTGA
TGCGAATGCCAGCGTCAGACATCATATGCAGATACTCACCTGCATCCTGAAC

CCATTGACCTCCAACCCCGTAATAGCGATGCGTAATGATGTCGATAGTTACT
AACGGGTCTTGTTCGATTAACTGCCGCAGAAACTCTTCCAGGTCACCAGTGC
AGTGCTTGATAACAGGAGTCTTCCCAGGATGGCGAACAACAAGAAACTGGTT
TCCGTCTTCACGGACTTCGTTGCTTTCCAGTTTAGCAATACGCTTACTCCCA
TCCGAGATAACACCTTCGTAATACTCACGCTGCTCGTTGAGTTTTGATTTTG
CTGTTTCAAGCTCAACACGCAGTTTCCCTACTGTTAGCGCAATATCCTCGTT
CTCCTGGTCGCGGCGTTTGATGTATTGCTGGTTTCTTTCCCGTTCATCCAGC
AGTTCCAGCACAATCGATGGTGTTACCAATTCATGGAAAAGGTCTGCGTCAA
ATCCCCAGTCGTCATGCATTGCCTGCTCTGCCGCTTCACGCAGTGCCTGAGA
GTTAATTTCGCTCACTTCGAACCTCTCTGTTTACTGATAAGTTCCAGATCCT
CCTGGCAACTTGCACAAGTCCGACAACCCTGAACGACCAGGCGTCTTCGTTC
ATCTATCGGATCGCCACACTCACAACAATGAGTGGCAGATATAGCCTGGTGG
TTCAGGCGGCGCATTTTTATTGCTGTGTTGCGCTGTAATTCTTCTATTTCTG
ATGCTGAATCAATGATGTCTGCCATCTTTCATTAATCCCTGAACTGTTGGTT
AATACGCATGAGGGTGAATGCGAATAATAAAGCTTGGCACTGGCCGTCGTTT
TACAACGTCGTGACTGGGAAAACCCTGGCGTTACCCAACTTAATCGCCTTGC
AGCACATCCCCCTTTCGCCAGCTGGCGTAATAGCGAAGAGGCCCGCACCGAT
CGCCCTTCCCAACAGTTGCGCAGCCTGAATGGCGAATGGCGCTTTGCCTGGT
TTCCGGCACCAGAAGCGGTGCCGGAAAGCTGGCTGGAGTGCGATCTTCCTGA
GGCCGATACTGTCGTCGTCCCCTCAAACTGGCAGATGCACGGTTACGATGCG
CCCATCTACACCAACGTGACCTATCCCATTACGGTCAATCCGCCGTTTGTTC
CCACGGAGAATCCGACGGGTTGTTACTCGCTCACATTTAATGTTGATGAAAG
CTGGCTACAGGAAGGCCAGACGCGAATTATTTTTGATGGCGTTCCTATTGGT
TAAAAAATGAGCTGATTTAACAAAAATTTAATGCGAATTTTAACAAAATATT
AACGTTTACAATTTAAATATTTGCTTATACAATCTTCCTGTTTTTGGGGCTT
TTCTGATTATCAACCGGGGTACATATGATTGACATGCTAGTTTTACGATTAC
CGTTCATCGATTCTCTTGTTTGCTCCAGACTCTCAGGCAATGACCTGATAGC
CTTTGTAGATCTCTCAAAAATAGCTACCCTCTCCGGCATTAATTTATCAGCT
AGAACGGTTGAATATCATATTGATGGTGATTTGACTGTCTCCGGCCTTTCTC
ACCCTTTTGAATCTTTACCTACACATTACTCAGGCATTGCATTTAAAATATA
TGAGGGTTCTAAAAATTTTTATCCTTGCGTTGAAATAAAGGCTTCTCCCGCA
AAAGTATTACAGGGTCATAATGTTTTTGGTACAACCGATTTAGCTTTATGCT
CTGAGGCTTTATTGCTTAATTTTGCTAATTCTTTGCCTTGCCTGTATGATTT
ATTGGATGTTAATGCTACTACTATTAGTAGAATTGATGCCACCTTTTCAGCT
CGCGCCCCAAATGAAAATATAGCTAAACAGGTTATTGACCATTTGCGAAATG
TATCTAATGGTCAAACTAAATCTACTCGTTCGCAGAATTGGGAATCAACTGT
TATATGGAATGAAACTTCCAGACACCGTACTTTAGTTGCATATTTAAAACAT
GTTGAGCTACAGCATTATATTCAGCAATTAAGCTCTAAGCCATCCGCAAAAA
TGACCTCTTATCAAAAGGAGCAATTAAAGGTACTCTCTAATCCTGACCTGTT
GGAGTTTGCTTCCGGTCTGGTTCGCTTTGAAGCTCGAATTAAAACGCGATAT
TTGAAGTCTTTCGGGCTTCCTCTTAATCTTTTTGATGCAATCCGCTTTGCTT
CTGACTATAATAGTCAGGGTAAAGACCTGATTTTTGATTTATGGTCATTCTC
GTTTTCTGAACTGTTTAAAGCATTTGAGGGGGATTCAATGAATATTTATGAC
GATTCCGCAGTATTGGACGCTATCCAGTCTAAACATTTTACTATTACCCCCT
CTGGCAAAACTTCTTTTGCAAAAGCCTCTCGCTATTTTGGTTTTTATCGTCG
TCTGGTAAACGAGGGTTATGATAGTGTTGCTCTTACTATGCCTCGTAATTCC
TTTTGGCGTTATGTATCTGCATTAGTTGAATGTGGTATTCCTAAATCTCAAC
TGATGAATCTTTCTACCTGTAATAATGTTGTTCCGTTAGTTCGTTTTATTAA

CGTAGATTTTTCTTCCCAACGTCCTGACTGGTATAATGAGCCAGTTCTTAAA
ATCGCATAAGGTAATTCACAATGATTAAAGTTGAAATTAAACCATCTCAAGC
CCAATTTACTACTCGTTCTGGTGTTTCTCGTCAGGGCAAGCCTTATTCACTG
AATGAGCAGCTTTGTTACGTTGATTTGGGTAATGAATATCCGGTTCTTGTCA
AGATTACTCTTGATGAAGGTCAGCCAGCCTATGCGCCTGGTCTGTACACCGT
TCATCTGTCCTCTTTCAAAGTTGGTCAGTTCGGTTCCCTTATGATTGACCGT
CTGCGCCTCGTTCCGGCTAAGTAACATGGAGCAGGTCGCGGATTTCGACACA
ATTTATCAGGCGATGATACAAATCTCCGTTGTACTTTGTTTCGCGCTTGGTA
TAATCGCTGGGGGTCAAAGATGAGTGTTTTAGTGTATTCTTTTGCCTCTTTC
GTTTTAGGTTGGTGCCTTCGTAGTGGCATTACGTATTTTACCCGTTTAATGG
AAACTTCCTCATGAAAAAGTCTTTAGTCCTCAAAGCCTCTGTAGCCGTTGCT
ACCCTCGTTCCGATGCTGTCTTTCGCTGCTGAGGGTGACGATCCCGCAAAAG
CGGCCTTTAACTCCCTGCAAGCCTCAGCGACCGAATATATCGGTTATGCGTG
GGCGATGGTTGTTGTCATTGTCGGCGCAACTATCGGTATCAAGCTGTTTAAG
AAATTCACCTCGAAAGCAAGCTGATAAACCGATACAATTAAAGGCTCCTTTT
GGAGCCTTTTTTTTGGAGATTTTCAACGTGAAAAAATTATTATTCGCAATTC
CTTTAGTTGTTCCTTTCTATTCTCACTCCGCTGAAACTGTTGAAAGTTGTTT
AGCAAAATCCCATACAGAAAATTCATTTACTAACGTCTGGAAAGACGACAAA
ACTTTAGATCGTTACGCTAACTATGAGGGCTGTCTGTGGAATGCTACAGGCG
TTGTAGTTTGTACTGGTGACGAAACTCAGTGTTACGGTACATGGGTTCCTAT
TGGGCTTGCTATCCCTGAAAATGAGGGTGGTGGCTCTGAGGGTGGCGGTTC
TGAGGGTGGCGGTTCTGAGGGTGGCGGTACTAAACCTCCTGAGTACGGTGA
TACACCTATTCCGGGCTATACTTATATCAACCCTCTCGACGGCACTTATCCG
CCTGGTACTGAGCAAAACCCCGCTAATCCTAATCCTTCTCTTGAGGAGTCTC
AGCCTCTTAATACTTTCATGTTTCAGAATAATAGGTTCCGAAATAGGCAGGG
GGCATTAACTGTTTATACGGGCACTGTTACTCAAGGCACTGACCCCGTTAAA
ACTTATTACCAGTACACTCCTGTATCATCAAAAGCCATGTATGACGCTTACT
GGAACGGTAAATTCAGAGACTGCGCTTTCCATTCTGGCTTTAATGAGGATTT
ATTTGTTTGTGAATATCAAGGCCAATCGTCTGACCTGCCTCAACCTCCTGTC
AATGCTGGCGGCGGCTCTGGTGGTGGTTCTGGTGGCGGCTCTGAGGGTGGT
GGCTCTGAGGGTGGCGGTTCTGAGGGTGGCGGCTCTGAGGGAGGCGGTTCC
GGTGGTGGCTCTGGTTCCGGTGATTTTGATTATGAAAAGATGGCAAACGCTA
ATAAGGGGGCTATGACCGAAAATGCCGATGAAAACGCGCTACAGTCTGACGC
TAAAGGCAAACTTGATTCTGTCGCTACTGATTACGGTGCTGCTATCGATGGT
TTCATTGGTGACGTTTCCGGCCTTGCTAATGGTAATGGTGCTACTGGTGATT
TTGCTGGCTCTAATTCCCAAATGGCTCAAGTCGGTGACGGTGATAATTCACC
TTTAATGAATAATTTCCGTCAATATTTACCTTCCCTCCCTCAATCGGTTGAA
TGTCGCCCTTTTGTCTTTGGCGCTGGTAAACCATATGAATTTTCTATTGATT
GTGACAAAATAAACTTATTCCGTGGTGTCTTTGCGTTTCTTTTATATGTTGC
CACCTTTATGTATGTATTTTCTACGTTTGCTAACATACTGCGTAATAAGGAG
TCTTAATCATGCCAGTTCTTTTGGGTATTCCGTTATTATTGCGTTTCCTCGG
TTTCCTTCTGGTAACTTTGTTCGGCTATCTGCTTACTTTTCTTAAAAAGGGC
TTCGGTAAGATAGCTATTGCTATTTCATTGTTTCTTGCTCTTATTATTGGGC
TTAACTCAATTCTTGTGGGTTATCTCTCTGATATTAGCGCTCAATTACCCTC
TGACTTTGTTCAGGGTGTTCAGTTAATTCTCCCGTCTAATGCGCTTCCCTGT
TTTTATGTTATTCTCTCTGTAAAGGCTGCTATTTTCATTTTTGACGTTAAAC
AAAAAATCGTTTCTTATTTGGATTGGGATAAATAATATGGCTGTTTATTTTG
TAACTGGCAAATTAGGCTCTGGAAAGACGCTCGTTAGCGTTGGTAAGATTCA

GGATAAAATTGTAGCTGGGTGCAAAATAGCAACTAATCTTGATTTAAGGCTT
CAAAACCTCCCGCAAGTCGGGAGGTTCGCTAAAACGCCTCGCGTTCTTAGAA
TACCGGATAAGCCTTCTATATCTGATTTGCTTGCTATTGGGCGCGGTAATGA
TTCCTACGATGAAAATAAAAACGGCTTGCTTGTTCTCGATGAGTGCGGTACT
TGGTTTAATACCCGTTCTTGGAATGATAAGGAAAGACAGCCGATTATTGATT
GGTTTCTACATGCTCGTAAATTAGGATGGGATATTATTTTTCTTGTTCAGGA
CTTATCTATTGTTGATAAACAGGCGCGTTCTGCATTAGCTGAACATGTTGTT
TATTGTCGTCGTCTGGACAGAATTACTTTACCTTTTGTCGGTACTTTATATT
CTCTTATTACTGGCTCGAAAATGCCTCTGCCTAAATTACATGTTGGCGTTGT
TAAATATGGCGATTCTCAATTAAGCCCTACTGTTGAGCGTTGGCTTTATACT
GGTAAGAATTTGTATAACGCATATGATACTAAACAGGCTTTTTCTAGTAATT
ATGATTCCGGTGTTTATTCTTATTTAACGCCTTATTTATCACACGGTCGGTA
TTTCAAACCATTAAATTTAGGTCAGAAGATGAAATTAACTAAAATATATTTG
AAAAAGTTTTCTCGCGTTCTTTGTCTTGCGATTGGATTTGCATCAGCATTTA
CATATAGTTATATAACCCAACCTAAGCCGGAGGTTAAAAAGGTAGTCTCTCA
GACCTATGATTTTGATAAATTCACTATTGACTCTTCTCAGCGTCTTAATCTA
AGCTATCGCTATGTTTTCAAGGATTCTAAGGGAAAATTAATTAATAGCGACG
ATTTACAGAAGCAAGGTTATTCACTCACATATATTGATTTATGTACTGTTTC
CATTAAAAAAGGTAATTCAAATGAAATTGTTAAATGTAATTAATTTTGTTTT
CTTGATGTTTGTTTCATCATCTTCTTTTGCTCAGGTAATTGAAATGAATAAT
TCGCCTCTGCGCGATTTTGTAACTTGGTATTCAAAGCAATCAGGCGAATCCG
TTATTGTTTCTCCCGATGTAAAAGGTACTGTTACTGTATATTCATCTGACGT
TAAACCTGAAAATCTACGCAATTTCTTTATTTCTGTTTTACGTGCAAATAAT
TTTGATATGGTAGGTTCTAACCCTTCCATTATTCAGAAGTATAATCCAAACA
ATCAGGATTATATTGATGAATTGCCATCATCTGATAATCAGGAATATGATGA
TAATTCCGCTCCTTCTGGTGGTTTCTTTGTTCCGCAAAATGATAATGTTACT
CAAACTTTTAAAATTAATAACGTTCGGGCAAAGGATTTAATACGAGTTGTCG
AATTGTTTGTAAAGTCTAATACTTCTAAATCCTCAAATGTATTATCTATTGA
CGGCTCTAATCTATTAGTTGTTAGTGCTCCTAAAGATATTTTAGATAACCTT
CCTCAATTCCTTTCAACTGTTGATTTGCCAACTGACCAGATATTGATTGAGG
GTTTGATATTTGAGGTTCAGCAAGGTGATGCTTTAGATTTTTCATTTGCTGC
TGGCTCTCAGCGTGGCACTGTTGCAGGCGGTGTTAATACTGACCGCCTCACC
TCTGTTTTATCTTCTGCTGGTGGTTCGTTCGGTATTTTTAATGGCGATGTTT
TAGGGCTATCAGTTCGCGCATTAAAGACTAATAGCCATTCAAAAATATTGTC
TGTGCCACGTATTCTTACGCTTTCAGGTCAGAAGGGTTCTATCTCTGTTGGC
CAGAATGTCCCTTTTATTACTGGTCGTGTGACTGGTGAATCTGCCAATGTAA
ATAATCCATTTCAGACGATTGAGCGTCAAAATGTAGGTATTTCCATGAGCGT
TTTTCCTGTTGCAATGGCTGGCGGTAATATTGTTCTGGATATTACCAGCAAG
GCCGATAGTTTGAGTTCTTCTACTCAGGCAAGTGATGTTATTACTAATCAAA
GAAGTATTGCTACAACGGTTAATTTGCGTGATGGACAGACTCTTTTACTCGG
TGGCCTCACTGATTATAAAAACACTTCTCAGGATTCTGGCGTACCGTTCCTG
TCTAAAATCCCTTTAATCGGCCTCCTGTTTAGCTCCCGCTCTGATTCTAACG
AGGAAAGCACGTTATACGTGCTCGTCAAAGCAACCATAGTACGCGCCCTGTA
GCGGCGCATTAAGCGCGGCGGGTGTGGTGGTTACGCGCAGCGTGACCGCTA
CACTTGCCAGCGCCCTAGCGCCCGCTCCTTTCGCTTTCTTCCCTTCCTTTCTC
GCCACGTTCGCCGGCTTTCCCCGTCAAGCTCTAAATCGGGGGCTCCCTTTAG
GGTTCCGATTTAGTGCTTTACGGCACCTCGACCCCAAAAAACTTGATTTGGG
TGATGGTTCACGTAGTGGGCCATCGCCCTGATAGACGGTTTTTCGCCCTTTG

ACGTTG

MeRPy-scaffold strand for SH-v3 - 3158 nt

GAAGTGCCATTCCGCCTGACCTCACACTTGCTATACCGTCATAAACAAGGCC
CTAGCATGTCGATAGGATCCGTATTTTTTTTACGGTACAGAACTGTGAGTCC
GCTATTGTACGTTGAATTGTTGGTACGTTGACAGGTGTTGGATTAGCGCTAG
CATTGTCTGTGGGCCTCTTCAGTAGTGACGACATTACATAACTTCCCATCTA
GTGTCCTTCAGCCATATTCTGGCGTTCATGGTAGAATGCTATTACGCGGAGA
TGCAATTCGTGAGTCAATGCTTCTGGTGCCCACTATTCCTTGCTGCAAACAT
CGGATTTGACAAAGGCCTTATGCATTGTTGGCGCTTACTTGAGTTCCGGCTG
TAGTCATGCTAGTACTCCCTGAAGGCTGAAGATGGTACCTGGTATCACTCCA
CTCACAGAGGTTACGATGGGTTTGGAGCAGTTGTATCCGTGTGCAGTAGTCA
GCTAAACGTTCAGAGGTGTGTGGTTTGTGCCTTGTTGTGAGTTGAGAGTCG
CGGCTAGTAGTACCCATCAAGTAGATCGATCGTCAAGTCCAGTGAGACACTA
GACCGTGGTTTGAGTCAGCTTACCCACTTAGCTCTCCCAGAGGACAACCGTC
GGGAAACATGTATCCGTGTACGTCAAATGTCGCTCATGCAACTGGAGGCTGA
TGGAGATGAAGCAACACCTCGAAGTCATTTGAAACCCATAGCGTTCTGGGTT
TAGTCGCACCGTAAATTGCTTTGTCCGGTCCTTCCTGCTAACACACTCCAGA
ACGTTGCGATTGTCCGCAATAACTGTTAACGCCTCTAAATTGCGCTGGAATC
GGGTTTATGAGGGTTCCGTCATTAGGAACTCCCACTGTCCTTCCCGTTAACT
GCTGAACAACAGGTTCTGGGTACAAAGCCCGACAATACCGGGCTCTCCAAGA
CAACTCAACACCAGTCAAACGCTTGTCGGAGATGAATGCACACGAGACCGAA
GACATAGATCGTACGGTACGGCGATTATCACACTGAGGCGACCGGATATTAA
CCTCTGGAGAGTTAGCCGATCCCACCATTACCAAGGCAATGTAAGAGGGAGT
CTCCAAACAGAACTCGGTTCAAAGTGAATGACGCCGTCCTCAAGAAAGTGAC
CACCTTCCCGTTGATGCACAATAAGGGTAGTTCACCAACAGAGACATCGAAT
TGTGCACAATTCCAAGCAACTGGACCCTATGTGGAATCGGGTTCATGAGGTC
TGACGGGTTAAGTACATGCTCGATTAAACCGACCTCCAAAGGATGCAGTAGG
TGTTGCTGTCAGTTCGTCAAGAGGTCCTCATCCCCTTCAGGTATGCGTAGAA
GTAGCTTGGTTATGTGGCTCAGTGACCACCTATGTTCCGTGTAACAATGGCC
AAAATTTCGTTCGGGTGATACGCTCCTACGTTCAGGAACAATGCTCAAGTCT
TGAGCTACATGCTCGATTGGCGAGTGATACCGACAATGAACGACCCAAATCC
AATTTGCAGGTGCAAGTTGTATGCTTGATGGTGAAGCCAGACTGCCGAAATA
AGTATCGGGTCCATTTCCAACCCATCTCCCAGGATACATTGCCAAGAGAAGG
ACGTGTAAGAGTCCCTACGGGATCCTAAGCCGAAATAAGGTGAACGGGATCA
GAACAGCACAGAAGGACGTGTAATTTCGTTCGACCTCGAAGTCATACCGGAA
TTAAGCGTTTGATTATTCCCCTCTCTAAAGAGCACGCTGGATCTTGCTGTGG
GAAGGAGAGCATATCGGCTAAGAACCGGCGGGCTTAAAGTGTAATTCAGCG
CGAACTTGCAACGAAGACTCTCGATGGACAGGGTATTCCAGGCAAACGGTAC
TTGGGCAATCGTCAAGATGCATCTGTCATGTGGTTGCTGACGGGAAGTCCCT
TGCTACACCTACGTTCAGGGGAAAGACACCGTCTACGAGGTTTCCCGGTTTC
TAGTCATGTCGGTGTCTGCAAAGAAATCACGGCACTTGTCTCCTGACAGTGA
ATGCGGAACCATTCGTTGTGCTGCATTATGAGCTCGTTCCCTCAGATTCCCT
TCCCGTTAGACTAGGAGCAGGTACGCTGATATATCCCGCAATCTTGCCAAAC
GGTGGTATCCCTCTCCGTCACTTGCCATCTCCAATTGGCATTCTGATAGTTC
ACCAGGTAGCTGACACGTGGAAGCTAAACGTCAACAAGGTGAATGACGGTT
GATCGGCTTTTGCCTTCTTGTGAAAGGCTTGCACTCCGCTACTCTGCCTTTG

AGTTGCGTTACGTCAGAGAAGGGAGGACCGTTGGTATGTCCGTCTCCGATGC
TCTCTCGAGGGATGCTTAAGAGAGGTCTGGACCCAGCTAATGGAATGGCTTG
CAAGTTTGTAGAGGAGAGAGCACACCTTTGGTGCATAGTCACCTGTCCCACC
TACGGGAGGAGGTCCTGATGGTGTGACCCAAATACCACTACGGTCTGAGGA
ACTGGTCGTTTGAACGTCCTTCCTGTCAAGACGGGTTAAGAGGCTTTCTCGA
CAGGGACAAGTGCGATGGTAGACCTTTCCTCGATGGTCTAGCTCGATGAAGC
AACGTCGTTGAGACTAAGGGATTCGAGGTAATCGCTCTTGCATGGACAACTA
AGAACCGCTAAGTCCCAAAACTTGGAGGACGCCATCTCCAAGGTACCTCTGC
GATGCTCTCTCTTGAGCTGCTAAATATGCACCCAGAAAGCCAGAGAGGTGGG
AACTATGTGCTTCGAGGTAATGGAGCCCACGACTCACGACGACGTGTGACTT
TGAACGGTTTCTACGCCATGAGCTGCTAACCTGACATAGCAATATGATGCGG
GCCGTTATCCTAACGTTCTTGCACACTCTCGCATTTCACACATGGAGTAGAA
AGCCCATTATCGCCATGCGACTAAGATAATCGCAAAGGATTTAGCGGGAATC
CGACTGATAGGCAGAGGTATTCCAACCCAAGAGCTGCTAAGGAGCTGGTCTA
GCGCCTCTTAACCCCTGATTGACCGCCTCTAGGTACAGACAGAAGCCTGATG
GTGTCGTTTTTTTTTGTAGGATCCATGAGTCTGGTCGGTAAGTGCCTAGAAT
TCAGGAAGATTTGTGTCGAGAAGGCTAGGTGGAGGCTCAGTG

DNA sequences for core staple and interacting handle strands of mini-slider and -rail

Name	Sequence
Mini-rail-Core-Oligo0	CAAAATCGCGCAGAGGCGAATTATGAAACAAAGACAAAGTTAATTTC
Mini-rail-Core-Oligo1	GGATTCGCCTGATTGCTTTGAATAGTAGATTTATATGTAA
Mini-rail-Core-Oligo2	CAGAAATAAAGAATATAATCTTAGATTAAATATATGTTAATTGA
Mini-rail-Core-Oligo3	ATTCATCAAATAGTAACATTATCATTTTGCGGAACAAAGTTCCTGAT
Mini-rail-Core-Oligo4	TTGGATTATACTTCTGAAAATTATATGAATATACAATAAC
Mini-rail-Core-Oligo5	GCAAATCCAATCGCAACATTAATTTTAAAAGTTTGTGCCCAAGTTA
Mini-rail-Core-Oligo6	GTTGGGTTATATAACTTCAGGTTTGCGATAGCCTGATTGT
Mini-rail-Core-Oligo7	TGAGAAGAAGTAATTCCCATATTTCCTTAAATAGCAAATCCAATAGCT
Mini-rail-Core-Oligo8	AGAAAACATACCTTTTTGACCTAAAATAAGGCACAAGAAAGAAACCAA
Mini-rail-Core-Oligo9	CATAAATCAGACCTTTGCCCGAACGTTATCATATCAGATGATGGCA
Mini-rail-Core-Oligo10	TAACCTTGCTTCTGTAAATCCTTGTCAAAATCCGGCTTAG
Mini-rail-Core-Oligo11	ACATGTTCTAGATAAGCCAGCTACGCGTCTTTAAAAGTAACCGAGGAA
Mini-rail-Core-Oligo12	CGACGACAATAAACAATCGACAACTCGTATTAAATCGCATGCTGAT
Mini-rail-Core-Oligo13	TACCGACAAAAGGTAAGTCAATAGAGTAGGGCTGAGTGAA
Mini-rail-Core-Oligo14	CGCTCAACTGAATTTAAAAACATAAACGTCAGTTGCACGTAAAA
Mini-rail-Core-Oligo15	ACACCGGAGAAGACTTTACAAACAATTCTTCTTAATGGAAACAGTA
Mini-rail-Core-Oligo16	ATCATAATCGCGCCCAATCATTCCCCCTGAACTAACGTCACATATGGT
Mini-rail-Core-Oligo17	AAAGCCTGTTTAGTATAAAGCCAAAATTTAGGATATAAAG
Mini-rail-Core-Oligo18	GTTGCTATTTTGCACTCCAGGATTTAGAAGTATTATCGTGTCCAGA
Mini-rail-Core-Oligo19	GCGGGAGGTTTTGAAGAACAACGCATCATTACTACTAGAA
Mini-rail-Core-Oligo20	CTTTCCTTATAAATAGATAATACATTTGTGAGTTAAATAAGAATAA
Mini-rail-Core-Oligo21	GTATTAAACCAAGTACTATTTTCATCCGGTATCCCGACTT
Mini-rail-Core-Oligo22	GAAGCCCTTTTTAAGCCAAATAGATTAGAGCCGTCGCACAAGATTA
Mini-rail-Core-Oligo23	AGAAACAATGAAATAGAGATATAGACTGAACAAAGAACGG
Mini-rail-Core-Oligo24	AGAGGGTAACCGTCACGCGCCAAAGCCAGCATCCTCCCTCGTTGATAT
Mini-rail-Core-Oligo25	CCTAATTTTCCCAATCTAATAACGCCTTATTACCAATGAACAGAATCA
Mini-rail-Core-Oligo26	TTTTTGTTAAATAGGAGCACTAACAACTGAGTCAATAATCGGCTGT
Mini-rail-Core-Oligo27	AATAGCAGCCTTTACATTAGACGGAGAGAGATTAAGAGCA
Mini-rail-Core-Oligo28	GAGCCAGCGGCCGGAAGACGATTGTAAAGCCATCACCGTACGCCACCC
Mini-rail-Core-Oligo29	GCCATTTGGGAATTAACGGTTATCTAAAATATCTTGTCATCTTACC
Mini-rail-Core-Oligo30	TTAAAGGTGAATTATCATTGAGCGAGAAAATTAAAATGAA
Mini-rail-Core-Oligo31	CAATCAATCTAATATCGAGAATTAAAGGCTTATCGTAGGACAACATGT
Mini-rail-Core-Oligo32	AACGTAGATTAGAAAGGAATTGAGGAAGCAACAAATAAGAAACGAT
Mini-rail-Core-Oligo33	AAATACATCACCACCGTAGCGCGTTCTGAAACGTAATAAGCGTCTTTC
Mini-rail-Core-Oligo34	GTGGCAACATATAAAATTTTGTCATCAACCGAATTATTCA
Mini-rail-Core-Oligo35	GGTTGAGGCAGGTCAACGTTGGCAAATCAACAGTTCCACGACTTGA
Mini-rail-Core-Oligo36	CACCACCAGAGCCGCCGACAAAAGACCAGAGCACATAAAG
Mini-rail-Core-Oligo37	TCAGACTGGAAAATCAATATCTGGTCAGTCACGCAGTATGTTAGCA
Mini-rail-Core-Oligo38	GCATTTTCGGTCATAGAATCAAAAGAACCGCCACCAGAAC
Mini-rail-Core-Oligo39	CCCGGAATAGGTGTAGAATCAAATATCAAACCCTCCCGTGACAGGA
Mini-rail-Core-Oligo40	AAGTGCCGTCGAGAGGAGAGCCGCCCTATTATTTTCATCG
Mini-rail-Core-Oligo41	GTATTAAGAATTGCGATTAGTAAAACGAAGGCGGTAGCAAAGGCTTGC
Mini-rail-Core-Oligo42	AAAGCGCAACATGGCTCCGCCACCCAAGCCCATGCTTTCGGTTGCGCC
Mini-rail-Core-Oligo43	GTGTACTGATGCATCACCTTGCTGAACCTGGAGTTTGCCTTTAGCG
Mini-rail-Core-Oligo44	GGGTCAGTGCCTTGAGCCTGCCTAAGAGAAGGAGGCGGAT
Mini-rail-Core-Oligo45	ATCTCCAATCGGTTTAAAAGAATATATACCAAGTAGTAAATCATTGTG
Mini-rail-Core-Oligo46	TTTTTCACGTTGAAATCAAAATGAAAAATCTAAAGAAAAAGTATAG
Mini-rail-Core-Oligo47	AAGGAACAACTAAAGGAGGCTGAGAGTTTTGTTTTTAACG
Mini-rail-Core-Oligo48	CGATCTAAACTCCTCATTTCGGAACACCCTCATCACCGGAGGCGACAT
Mini-rail-Core-Oligo49	CCGTAACACAGCGCTGAGAGCCAGCAGCGAATTTGATGATACAGGA
Mini-rail-Core-Oligo50	CTGAGTTTAGCATCGGACGCATAACAGGCGCACTTAGCCGACGCCAAA
Mini-rail-Core-Oligo51	GTACAAACTACAACGCTAGCGTAAGATTTTGCAGAATAGA
Mini-rail-Core-Oligo52	AAAACGAAAGAGGCATCACGCCTGCAACAGTGCCAACGATAATAAT
Mini-rail-Core-Oligo53	AATACGTAATGCCACTTGAATTTTCGAAAGACCGTCACCA
Mini-rail-Core-Oligo54	CATCGCCCAACGCGGTCAGTATTAACACGCTATAGGAACCCATGTA
Mini-rail-Core-Oligo55	TTCGGTCGCTGAGGCTTCGTCACCGAGGACTAACGGGTAA
Mini-rail-Core-Oligo56	GAAACACCAGAACGAGCGGATAAAACAGAGGTGAGGAGACCAACCT
Mini-rail-Core-Oligo57	GCTCATTCAGTGAATACGGCTACAGTACAGACCCGATATA
Mini-rail-Core-Oligo58	GGCTGACCGAAGTTTTTACGAGGCGAGCTTAAGACCGGAAACTTTTGC
Mini-rail-Core-Oligo59	AACAAAGTTGTGTCGACTTATGCGACGTTGGGCCCCCTCACCATAAAT
Mini-rail-Core-Oligo60	CCATGTTATAGACGAACCACCAGCAGAACGAGACAATGACAACAAC
Mini-rail-Core-Oligo61	CGCAGACGGTCAATCAAGGACAGATTGACAAGACAAAGCT
Mini-rail-Core-Oligo62	GTTTAGACAATATTCACAACATGTAGTTTCATAAGGATAAAATGCCTG
Mini-rail-Core-Oligo63	GGGTAATAGTAAAATAATGCCATTAAAAATACCGAGCTCCTGACGA

Mini-rail-Core-Oligo64	AGAGGCTTTTGCAAAATTCATCAAGATACATAGAACGAGG
Mini-rail-Core-Oligo65	CTAATGCAGAGTAATCTGAACGGTGAGGCTTTCTCAGCAGCTGTATGG
Mini-rail-Core-Oligo66	TAATAAAAAGGGATAGCCCTAAAACATCTACAATCCGCGACCTGCT
Mini-rail-Core-Oligo67	CGAACTAATTCAAAGCCTATTATATAAATCATATAACCTGGCAAACAA
Mini-rail-Core-Oligo68	CATTATTACAGGTAGAACATTCAATATCATAAAAATAGCG
Mini-rail-Core-Oligo69	TATAATGCTGTAGCTTTGTCTTTAATGCGCGAACTAATGCCAGAGG
Mini-rail-Core-Oligo70	TTTTGCGGATGGCTTAATAGTAAGATTCGAGCCGGAACAA
Mini-rail-Core-Oligo71	TACCCTGAGAATTTTGAATGGCTATTAGAATAAGAAAAATCTACGT
Mini-rail-Core-Oligo72	CAAAGCGGATTGCATCCAAATATCCAGGATTAGAGGTCAT
Mini-rail-Core-Oligo73	CCTTTATTTCAACGCTCCCGTGGCACAGACAATATCCATTGCTGAA
Mini-rail-Core-Oligo74	ATTATGACCCTGTAATGCAAACTCACATCCAAGTCAGAAG
Mini-rail-Core-Oligo75	AAGGCAAATAAGCAAACGATGAACAGGCAAAGCCAGTTTGATTTCTGC
Mini-rail-Core-Oligo76	TAACAGTTTTGACCATGTGTAGGTAGTCAAATAGGAACGCAGCCAGCT
Mini-rail-Core-Oligo77	AATGGTCAACACTGAAAGCGTAAGAATAATACAAAAATCAGGTCTT
Mini-rail-Core-Oligo78	TATTTTCATTTGGGGCAATAGTAGGCAATAAACCAAAAAC
Mini-rail-Core-Oligo79	TTTTGTTAATTTTTTACAACTGTTTTACGCCAGGTTGTGTCGCACAGG
Mini-rail-Core-Oligo80	TTGTAAACGTTAATAAGTGATAGAACCCTTCTGACGGCGGGAGAAG
Mini-rail-Core-Oligo81	AAACAGGAAGATTGTAGAATTAGCAGTCTGGATTTAGCTA
Mini-rail-Core-Oligo82	TGCCTGAGAAAATTAATAGCATTACAACAGGTGCGTTTTAAGCAACAC
Mini-rail-Core-Oligo83	ATTCAACCGAGACATTCTGGCCAACAGAAATTAGATACATTTCGCA
Mini-rail-Core-Oligo84	GTTCTAGCTAACCGTGAGTAACAAATGTTTACCGACGGCCAGCAACCG
Mini-rail-Core-Oligo85	TAATGCCGGAGAGGGTCAGGTCATGCATGTCAAGCCCCAA
Mini-rail-Core-Oligo86	GCCATTCAGGCTGCGACCGACCAGTAATAAAAGGGAATTATTTAAA
Mini-rail-Core-Oligo87	TCTGGTGCCGGAAACCGGTAATCGGCGCATCGTGATAAAT
Mini-rail-Core-Oligo88	TGTGAGCGCATAGATTCACCAGTCACACAATCACCATCAATATGAT
Mini-rail-Core-Oligo89	ATTCTCCGTGGGAACAACGTTGGTATCGGCCTGCACCGCT
Mini-rail-Core-Oligo90	CGCCAGCAGTTGGGCGCTGGATTATTTACATTGGCCTGCGCCATTC
Mini-rail-Core-Oligo91	AGCGGATCAAACTTAAAGGGGACGACAGCGCCCCCGTCGG
Mini-rail-Core-Oligo92	CGGAATTTGCTTTCGCTGCCAACGTACCGAGCTTTTCACGTGCCCCAG
Mini-rail-Core-Oligo93	GAAAGGGGCCAGGGTTTTAGTGATTCCGGCAATGCTCGTCATCGTTAA
Mini-rail-Core-Oligo94	TTGTAAAACAGGCTCAATCGTCTGAAATGGCTTCATCAACATTAAA
Mini-rail-Core-Oligo95	GCTTTCAGAGGTGGAGACAATCGGCTCCGTGGGCAGAAAC
Mini-rail-Core-Oligo96	CGGTATGAGGTAAAGGGCTGTTTCCACAACATTGGTTCCGTAGCCCGA
Mini-rail-Core-Oligo97	CGCCGGGCGCGGTTGCGGAATACCTACATTTTGACTCCTCATTTGC
Mini-rail-Core-Oligo98	CGGGGTCATTGCAGGCGTGAGAGATGGTCAGCAGTGCCAA
Mini-rail-Core-Oligo99	TGCTGGTCTAGACTTTCGAAACGTACGACAGTGTAGATGGTAAAACTA
Mini-rail-Core-Oligo100	TCGTCTCGCAAGGAAAAACGCTCATGGACCTTTCCCAGTCACGACG
Mini-rail-Core-Oligo101	TCGCTGGCAATGCGGCGCAGCCAGCGCCAGGGTGCCCGCTGGCGCGTA
Mini-rail-Core-Oligo102	GCCAGAGCACATCCTCCAGCGTGGTGCCATCCAGCATCAG
Mini-rail-Core-Oligo103	GTAATCATGGTCATATTTCGCCAGCCATTGCAACAGAAACTCAATC
Mini-rail-Core-Oligo104	GTTGAGGATCCCCGGGGCAGCACCGCGGCCAGAGCCTCCG
Mini-rail-Core-Oligo105	GGTTACCTGGGATCCAGAACAATATTACCTTACGCGGTCCGTTTTT
Mini-rail-Core-Oligo106	GTGCCCCCTGCATCAGTGCACTCTCTGCCAGCTCCTCACA
Mini-rail-Core-Oligo107	AATCCTGTTTGATGGACGTCGGCCTTGCTGGTAATCCGTCGAATTC
Mini-rail-Core-Oligo108	GCGGTCCACGCTGGTTGTCATACCGTATTGGGCGGTGCCG
Mini-rail-Core-Oligo109	TTCTTTTCAGGAACGGTTGCTTTGACGAGCACGTATAACG
Mini-rail-Core-Oligo110	CGGAAGCAAGCTAACTGTTGAGTGAAGAACGTGGACTCCAACGTCAA
Mini-rail-Core-Oligo111	GCGCTCACTGGTAGAAGAACTCAAACTAAGCCGGCATCAGATGCCG
Mini-rail-Core-Oligo112	GGGAAACCTGTCGTGCGGGAGAGGACAGCTGATGCAGCAA
Mini-rail-Core-Oligo113	TTTTATAAATCACGCAAATTAACCGTTGTAGCAATATGGTACGCCAG
Mini-rail-Core-Oligo114	AATCCTGAGAAGTGTGATAACATCACTTGCCTGAGTTTCAGGCGAA
Mini-rail-Core-Oligo115	TAAAGGGATTTTAGACACCAGTGACGCTACAGTTCCAGTC
Mini-rail-Core-Oligo116	TAATGCGCGACGGGCACGGTTTGCGGGGGTTTGTGGTGCTGTCGGTGG
Mini-rail-Core-Oligo117	AGGGCGAACTACTTCTTTGATTAGTAATAGGCACATTAATTGCGTT
Mini-rail-Core-Oligo118	AAACCGTCTATCATAGGGCGCTGGCAAGTGTAGCCGCGCTTGCTTTCCAGGCCGAT
Mini-rail-Core-Oligo119	TTTTTTTTGAGCAAAAGAAGATGATTCATTTCAATTACCTTTTTTTTT
Mini-rail-Core-Oligo120	TTTTTTTTCGGAATTATCATCATAAAACCACCAGAAGGAGTTTTTTTT
Mini-rail-Core-Oligo121	TTTTTTTTTTCAAATATATTTTAGAACGCGAGAAAACTTTTTTTTTTT
Mini-rail-Core-Oligo122	TTTTTTTTACAATTTCATTTGAATAAATTAATTACATTTATTTTTTTT
Mini-rail-Core-Oligo123	TTTTTTTTGCCTGTTTATCAACAAAGCTAATGCAGAACGCTTTTTTTT
Mini-rail-Core-Oligo124	TTTTTTTTTACCGACCGTGTGATAATTTAATGGTTTGAAATTTTTTTT
Mini-rail-Core-Oligo125	TTTTTTTTTTACCAACGCTAACGAAATTTTATCCTGAATCTTTTTTTT
Mini-rail-Core-Oligo126	TTTTTTTTAATTTACGAGCATGTAAATAATATCCCATCCTTTTTTTTT
Mini-rail-Core-Oligo127	TTTTTTTTAGTTACCAGAAGGAAAGCAGATAGCCGAACAATTTTTTTT
Mini-rail-Core-Oligo128	TTTTTTTTACAGCCATATTATTTAGCCAGTTACAAAATAATTTTTTTT
Mini-rail-Core-Oligo129	TTTTTTTTCCATTACCATTAGCAAAAAATCACCAGTAGCATTTTTTTT
Mini-rail-Core-Oligo130	TTTTTTTTTGGCATGATTAAGACTGAATACCCAAAAGAACTTTTTTTT

Mini-rail-Core-Oligo131	TTTTTTTTACAAATAAATCCTCATGCCTTGATATTCACAATTTTTTTT
Mini-rail-Core-Oligo132	TTTTTTTTCCGTAATCAGTAGCGAACCATCGATAGCAGCATTTTTTTT
Mini-rail-Core-Oligo133	TTTTTTTTCCGCCACCCTCAGAACCTCAGGAGGTTTAGTATTTTTTTT
Mini-rail-Core-Oligo134	TTTTTTTTTTCCAGTAAGCGTCATGTCTCTGAATTTACCGTTTTTTTT
Mini-rail-Core-Oligo135	TTTTTTTTGGAGCCTTTAATTGTAAAAAAAGGCTCCAAAATTTTTTTT
Mini-rail-Core-Oligo136	TTTTTTTTTCATTTTCAGGGATAGCTCAGAGCCACCACCCTTTTTTTT
Mini-rail-Core-Oligo137	TTTTTTTTTTTGACCCCCAGCGATCACTAAAACACTCATCTTTTTTTT
Mini-rail-Core-Oligo138	TTTTTTTTCAGCTTGATACCGATAAGGTGAATTTCTTAAATTTTTTTT
Mini-rail-Core-Oligo139	TTTTTTTTTTAATTTCAACTTTAATTGGGCTTGAGATGGTTTTTTTTT
Mini-rail-Core-Oligo140	TTTTTTTTTCATCGCCTGATAAATACAACGGAGATTTGTATTTTTTTT
Mini-rail-Core-Oligo141	TTTTTTTTCTGCGGAATCGTCATATGGATAGCGTCCAATATTTTTTTT
Mini-rail-Core-Oligo142	TTTTTTTTCATTATACCAGTCAGGATTTTAAGAACTGGCTTTTTTTTT
Mini-rail-Core-Oligo143	TTTTTTTTAAGTACGGTGTCTGGATTTAAATATGCAACTATTTTTTTT
Mini-rail-Core-Oligo144	TTTTTTTTCAGAAAACGAGAATGAAATGCTTTAAACAGTTTTTTTTTT
Mini-rail-Core-Oligo145	TTTTTTTTCATATATTTTAAATGCAAATTTTTAGAACCCTTTTTTTTT
Mini-rail-Core-Oligo146	TTTTTTTTAACGAGTAGATTTAGTGATTCCCAATTCTGCGTTTTTTTT
Mini-rail-Core-Oligo147	TTTTTTTTTTTGTTAAATCAGCTCAAATTCGCATTAAATTTTTTTTT
Mini-rail-Core-Oligo148	TTTTTTTTGAGAAAGGCCGGAGACAAAGATTCAAAAGGGTTTTTTTTT
Mini-rail-Core-Oligo149	TTTTTTTTGCGGGCCTCTTCGCTAGGGAAGGGCGATCGGTTTTTTTTT
Mini-rail-Core-Oligo150	TTTTTTTTCGTCTGGCCTTCCTGTCATCAAAAATAATTCGTTTTTTTT
Mini-rail-Core-Oligo151	TTTTTTTTATCCCGTAAAAAAAGCACATCGACATAAAAAATTTTTTTT
Mini-rail-Core-Oligo152	TTTTTTTTATTAAGTTGGGTAACGGATGTGCTGCAAGGCGTTTTTTTT
Mini-rail-Core-Oligo153	TTTTTTTTCCTGCGGCTGGTAATGGCCGGGTCACTGTTGCTTTTTTTT
Mini-rail-Core-Oligo154	TTTTTTTTCGATGCTGATTGCCGTGAAGGGTAAAGTTAAATTTTTTTT
Mini-rail-Core-Oligo155	TTTTTTTTTCCGCTCACAATTCCACTGTGTGAAATTGTTATTTTTTTT
Mini-rail-Core-Oligo156	TTTTTTTTCTGGTGTGTTCAGCAAATAAACATCCCTTACATTTTTTTT
Mini-rail-Core-Oligo157	TTTTTTTTTTATAAATCAAAAGAAAAATCGGCAAAATCCCTTTTTTTT
Mini-rail-Core-Oligo158	TTTTTTTTGGGTGCCTAATGAGTGTAAAGTGTAAAGCCTGTTTTTTTT
Mini-rail-Core-Oligo159	TTTTTTTTGTAAAAGAGTCTGTCCTCAGTGAGGCCACCGATTTTTTTT
Mini-rail-Core-Oligo160	TTTTTTTTCAAGAGTCCACTATTATTGTTCCAGTTTGGAATTTTTTTT
Mini-rail-Purple-handle1	GAGACGATGTTGACCTTAACCTTTTTACATCGGGAGAAACAGTAACAGTACCTTTTTTTTT
Mini-rail-Purple-handle2	GCTACTCACTCAGATAGGGTATTAGAACCTACCATATCAATAATGGAAGGGTTTTTTTTTT
Mini-rail-Purple-handle3	ACTATATCGGTCGGAAACTGCTTTACCTTTTTAACCTCATAGGTCTGAGAGACTTTTTTTT
Mini-rail-Purple-handle4	GTTTCTCCAAAAGCACTAGGGTTTTAATTTTCCCTTAGAATCGTCGCTATTAATTTTTTTT
Mini-rail-Purple-handle5	CGATCCTGATGTACGAAAGTCTTGCCAGTAATAAGAGACAGAGGCATTTTCGATTTTTTTT
Mini-rail-Purple-handle6	CGTGTAGCCAATTAGACTGACTTAATTCTTACCAGTATCATATGCGTTATACATTTTTTTT
Mini-rail-Red-Handle1	CCTACTGACTTTATCCACCGATTCGTTTTAGCGAACCTTCTAAGAACGCGAGGTTTTTTTT
Mini-rail-Red-Handle2	CACACTTGCTATACCGTCATCTTCAAGCAAGCCGTTTTCGCACTCATCGAGAATTTTTTTT
Mini-rail-Blue-Handle1	TCTCGACACAAATCTTCCTGCTTAGTTAAGCCCAATAAAACCCACAAGAATTGTTTTTTTT
Mini-rail-Blue-Handle2	TTGAACCCCCCCTTAGTTACATTAAACAGGGAAGCGCAGAGAGAATAACATAATTTTTTTT
Mini-rail-Green-Handle1	TCTTCACGCCAAACTATCTCGTTTAAATATTGACGGAATTGAGGGAGGGAAGGTTTTTTTT
Mini-rail-Green-Handle2	CACCTTCGCTTCTACATACAGTTCACGGAATAAGTTTAGAAACGCAAAGACACTTTTTTTT
Mini-rail-Red-Handle3	CCTACTGACTTTATCCACCGATTACCCTCAGAGCCGCCACCCTCAGAGCCACCTTTTTTTT
Mini-rail-Red-Handle4	CACACTTGCTATACCGTCATCTTTTGCCATCTTTTCATCCCCCTTATTAGCGTTTTTTTT
Mini-rail-Blue-Handle3	TCTCGACACAAATCTTCCTGCTTGTTTTGCTCAGTACCATTAGGATTAGCGGGTTTTTTT
Mini-rail-Blue-Handle4	TTGAACCCCCCCTTAGTTACATTAAACAGTTAATGCCCTAACAGTGCCCGTATTTTTTTT
Mini-rail-Green-Handle3	TCTTCACGCCAAACTATCTCGTTAGTTTCAGCGGAGTGTAAACAACTTTCAACTTTTTTT
Mini-rail-Green-Handle4	CACCTTCGCTTCTACATACAGTTGACAGCCCTCATAGTCTGTAGCATTCCACATTTTTTT
Mini-rail-Red-Handle6	CCTACTGACTTTATCCACCGATTGGAAGTTTCCATTAAAAGACTTTTTCATGATTTTTTT
Mini-rail-Red-Handle7	CACACTTGCTATACCGTCATCTTGCCGCTTTTGCGGGATGCAGGGAGTTAAAGTTTTTTTT
Mini-rail-Blue-Handle6	TCTCGACACAAATCTTCCTGCTTACCCAAATCAACGTAAACCGGATATTCATTTTTTTTT
Mini-rail-Blue-Handle7	TTGAACCCCCCCTTAGTTACATTGACCAACTTTGAAAGTAAGGGAACCGAACTTTTTTTT
Mini-rail-Green-Handle6	TCTTCACGCCAAACTATCTCGTTCGACGATAAAAACCACCCTCGTTTACCAGATTTTTTT
Mini-rail-Green-Handle7	CACCTTCGCTTCTACATACAGTTAGATTTAGGAATACCAAGATTCATCAGTTGTTTTTTT
Mini-rail-Red-Handle8	CCTACTGACTTTATCCACCGATTTGCTCCTTTTGATAAGAGAGTACCTTTAATTTTTTTT
Mini-rail-Red-Handle9	CACACTTGCTATACCGTCATCTTAAGCCCGAAAGACTTAAAAAGATTAAGAGGTTTTTTT
Mini-rail-Blue-Handle8	TCTCGACACAAATCTTCCTGCTTGCTAAATCGGTTGTAGCCTCAGAGCATAAATTTTTTT
Mini-rail-Blue-Handle9	TTGAACCCCCCCTTAGTTACATTGGCATCAATTCTACTGCGAGCTGAAAAGGTTTTTTTT
Mini-rail-Green-Handle8	TCTTCACGCCAAACTATCTCGTTGTTGATAATCAGAAAATCATATGTACCCCGTTTTTTT
Mini-rail-Green-Handle9	CACCTTCGCTTCTACATACAGTTATCTACAAAGGCTATAGCTATTTTTGAGAGTTTTTTT
Mini-rail-Red-Handle8	CCTACTGACTTTATCCACCGATTCCAGCCAGCTTTCCGCAGGAAGATCGCACTTTTTTTT
Mini-rail-Red-Handle9	CACACTTGCTATACCGTCATCTTGTAATGGGATAGGTCAACGGCGGATTGACCTTTTTTT
Mini-rail-Blue-Handle8	TCTCGACACAAATCTTCCTGCTTCACGGAAAAAGAGACTGAAGGGATAGCTCTTTTTTTT
Mini-rail-Blue-Handle9	TTGAACCCCCCCTTAGTTACATTATAACCTCACCGGAACCGCCACGGGAACGGTTTTTTTT
Mini-rail-Green-Handle8	TCTTCACGCCAAACTATCTCGTTCGGCTGGAGGTGTCCCACGCAACCAGCTTATTTTTTT
Mini-rail-Green-Handle9	CACCTTCGCTTCTACATACAGTTGGACTTGTAGAACGTATAACGGAACGTGCCTTTTTTTT

Mini-rail-Red-Handle8	CCTACTGACTTTATCCACCGATTTCGCGTCCGTGAGCCACGCGTGCCTGTTCTTTTTTTTT
Mini-rail-Red-Handle9	CACACTTGCTATACCGTCATCTTGTCACTGCGCGCCTGACGATCCAGCGCAGTTTTTTTTT
Mini-rail-Blue-Handle8	TCTCGACACAAATCTTCCTGCTTTGGCCCTGAGAGAGTTTGCCCTTCACCGCCTTTTTTTT
Mini-rail-Blue-Handle9	TTGAACCCCCCCTTAGTTACATTATCGGCCAACGCGCGCAGCTGCATTAATGATTTTTTTT
Mini-rail-Green-Handle8	TCTTCACGCCAAACTATCTCGTTCGGGAGCTAAACAGGTCGTTAGAATCAGAGTTTTTTTT
Mini-rail-Green-Handle9	CACCTTCGCTTCTACATACAGTTGTAACCACCACACCCGCGGTCACGCTGCGCTTTTTTTT
Mini-slider-Core-Oligo0	ATCAAAATCATAGGTCTGAGAGAATATAACTCATTTTCGAAAGGTAA
Mini-slider-Core-Oligo1	TTAAGACGCTGAGAAGAGTCAATATTGCTTCTTAACAACG
Mini-slider-Core-Oligo2	ATATGTGAGTGAAAACATCATTACTAGATCATCTTCCAAGAACG
Mini-slider-Core-Oligo3	GATGAAACATAATTCGCCTGATTGCTTTGAATACCAAGTCAATTACC
Mini-slider-Core-Oligo4	AAATTAATTACATTTAGAAACAGTAATTAATTAGCTTAGA
Mini-slider-Core-Oligo5	TAATTTAGGCAGAGGATAGGGAGAAACAATAACGGACCGTGAATTT
Mini-slider-Core-Oligo6	TGAGAATCGCCATATTGTAAATCGAATCATAAAGAAAACA
Mini-slider-Core-Oligo7	CTGTTTAGCAGATATAAAACCAAGAATTGAGCCAGCCTTTAGACAAAA
Mini-slider-Core-Oligo8	AAATGCTGGAAAACTTTCTGTCCAGCAGAACGATCAAGATTCCTGAAT
Mini-slider-Core-Oligo9	AGTTAATTAAAACAGTACCTTTTACATCTGTTGAGCAAAAGAAGAT
Mini-slider-Core-Oligo10	ATTTAATGGTTTGAAATAAGAATACAAATTCTGGCTTAAT
Mini-slider-Core-Oligo11	AACGCGAGTTTTGAAGCAAGAATTTGAAATAGGAGGGAAGGAATTATC
Mini-slider-Core-Oligo12	ATCCGGTATTCTAAGAGTCAGATGAATATACAGTAAGCCCAACATG
Mini-slider-Core-Oligo13	CCAATAGCAAGCAAATTATCATATTATCATTCTGACCTAA
Mini-slider-Core-Oligo14	TCTTTCCTGCGTTATAAACACCGGTCGCTATTACATAAATCAAT
Mini-slider-Core-Oligo15	AATAGATAGGTATTTTCAGGTTTAACGTAATTTTCAAATATATTTT
Mini-slider-Core-Oligo16	AGTCCTGAAAAAATGATTCCAGAGTACATAAAAAACGCAATTTTCATC
Mini-slider-Core-Oligo17	AATAATATCCCATCCTATCGGCTGAACAAGCATACCGCGC
Mini-slider-Core-Oligo18	CAGAGAGATAACCCACCTATAAAGAAATTGCGTAGATTGAAGGCTT
Mini-slider-Core-Oligo19	AACAAAGTCAGAGGGTTACCGCACTTAACGTCACAAGAAA
Mini-slider-Core-Oligo20	GAGCGTCTAAATTGCACGTAAAACAGAATAACGCCTGTTTATCAAC
Mini-slider-Core-Oligo21	GCCAGTTACAAAATAAAGAAACGAAAAAACAGACACCCTG
Mini-slider-Core-Oligo22	TTCAACCGATTGAGGCAATACCATATCAAAATTATTAGGCTAATAT
Mini-slider-Core-Oligo23	GGTTTACCAGCGCCAAACAGAGAGAAAATACACCTAATTT
Mini-slider-Core-Oligo24	AACATATACAGAGCCGTTCGGTCAGAGGCTGAAGTGCCTTATGAATTT
Mini-slider-Core-Oligo25	CTATCTTAGCCGAACAACCGACTTCCAGTAGCATTGACAGTATTCACA
Mini-slider-Core-Oligo26	AACCGAGGGGTATGGAAGGGTTAGAACCTAGCTTACCAACGCTAAC
Mini-slider-Core-Oligo27	GAATACCCAAAAGAACATGTTAGCACCACGGAATTCATAT
Mini-slider-Core-Oligo28	AGAGCCACGAGCCGCCATTAGCGGTCGAGAGGACTTTCAAACTAAAGG
Mini-slider-Core-Oligo29	AGAACCGCCACCCTCACCGATTATACTTCTGAATAGGCGGGCGACA
Mini-slider-Core-Oligo30	CCGGAACCGCCTCCCTAAAGAAACGTAGCGCGTAATAACG
Mini-slider-Core-Oligo31	GTCAGACTGCAAAGACAAACGTAGAATAACATTTTTTTGTTCATCGAG
Mini-slider-Core-Oligo32	AAGGCCGGGGCATAATCCTGATTGTTTGGTCAAGTTACCAGAAGGA
Mini-slider-Core-Oligo33	AAACGTCAGTTTTAACCAGAATGGTCGTCACCCCTCAGAAACCGATAT
Mini-slider-Core-Oligo34	ACCATCGATAGCAGCACCTTTAGCGTTTGCCAAGCCACCA
Mini-slider-Core-Oligo35	AAGAGAAGGATTAGGGCCGATGGCAATTCATCAATATTCCACCCTC
Mini-slider-Core-Oligo36	AACATGAAAGTATTAATAGCCCCCGGTAATAACCAATGAA
Mini-slider-Core-Oligo37	ATTAAAGCGGGATTCCTGATTATCAGATAGCACCATTACCATTAGC
Mini-slider-Core-Oligo38	GTCTCTGAATTTACCGGATACAGGATAAACAGTATTCTGA
Mini-slider-Core-Oligo39	GGATTTTGCTAAACAGTTAGCGGAATTATCATCATGTCGACTCCTC
Mini-slider-Core-Oligo40	TTCCAGACGTTAGTAAGAGTAACAACTGAGTTAAAGCGCA
Mini-slider-Core-Oligo41	AACTACAAACGGCTACTCGCTGAGCTTCATCAACGGTCAACATAGTAA
Mini-slider-Core-Oligo42	ATAAGTATGGTTTAGTGAATAATAGCTCCAAAGCACCAACACACTCAT
Mini-slider-Core-Oligo43	ACCGCCACAGTAAGAAACCACCAGAAGGGATAACAAATAAATCCTC
Mini-slider-Core-Oligo44	CTCAGAGCCACCACCCACCCATGTCAGACAGCTGTCGTCT
Mini-slider-Core-Oligo45	TTTTCATGATGCCACTATATTCATAGTGAATATTTACCAGTTGCAAAA
Mini-slider-Core-Oligo46	TGAGGACTAAAGACTAATTATCATTTTGCGGAACAACATCTGTATG
Mini-slider-Core-Oligo47	CGGAACGAGGGTAGCACGCCTGTACACGCATACCGCCACC
Mini-slider-Core-Oligo48	CCATCGCCGCATTCCAACCGTAACGTGCCCGTAGTGTACTTTATTAGC
Mini-slider-Core-Oligo49	TATCGGTTATTAAAAGTTTGAGTAACATTGCACCGCCACCCTCAGA
Mini-slider-Core-Oligo50	TATCAGCTGGAACGAGAAGCGCGAACGGAACATGAATTACAGTCAGAA
Mini-slider-Core-Oligo51	AGGTGAATTTCTTAAAGACAACAAAGGCCGCTGACAGCAT
Mini-slider-Core-Oligo52	CTTGACAAGAACCGGACGCGAACGTTATTAATTTTCGGAGAGGCTT
Mini-slider-Core-Oligo53	GCATAGGCTGGCTGACGCTTGCAGACTTAGCCTGCTTTCG
Mini-slider-Core-Oligo54	ATTATACCGCGGTATTAAATCCTTTGCCAAGAGGAGCCTTTAATTG
Mini-slider-Core-Oligo55	ACAACGGAGATTTGTACGACCTGCCTGACCAAGACCAGGC
Mini-slider-Core-Oligo56	CTATCATAACCCTCGAGGAAACAATTCGACAACTCCAGAGAGTAAT
Mini-slider-Core-Oligo57	AAAAGGAATTACGAGGTCATAAGGACGAACTAAACAAAGT
Mini-slider-Core-Oligo58	TTACAGGTAGCAAACTCGGATTGCAGAATTAGTCATTTGGCGGTAATC

Mini-slider-Core-Oligo59	GCCCTGACTGAGATGGTTGCCAGACGTCCAATAATTGCTGATGCAACT
Mini-slider-Core-Oligo60	AATCATTGACAGAAGTATTAGACTTTACCTTCTTTGACCCCCAGCG
Mini-slider-Core-Oligo61	ATTTTAAGAACTGGCTAATCTACGTGAGATTTATAACGCC
Mini-slider-Core-Oligo62	ACCTTTAAATGGCTTAGAGCATAACCTGTAATTGTACCCCAGATTGTA
Mini-slider-Core-Oligo63	TCAGGATTAGAGAGTGAAATACATTTGAGGATTTATTAGAGCAACA
Mini-slider-Core-Oligo64	AGCGAACCAGACCGGAAGAAAGATACTATTATCTTATGCG
Mini-slider-Core-Oligo65	TTACCCTGTCATCAGTTTAATAAAGAACCGAATCCATGTTGGAGTTAA
Mini-slider-Core-Oligo66	TAAATATTGCAAGAGCCGTCAATAGATAGTTTTTAATTTCAACTTT
Mini-slider-Core-Oligo67	CATTGAATGTTTAGCTATTCCATACTGATAAATGAGTAATACCCGTCG
Mini-slider-Core-Oligo68	AATGCTTTAAACAGTTTCAGGTCTGGAAGCCCAGCTTCAA
Mini-slider-Core-Oligo69	AGCAATAAAGCCTCAGAGCTAACAACTAATAGATTAAGCCAACAGG
Mini-slider-Core-Oligo70	CATACAGGCAAGGCAAATCAAAAAAATAACCTCCCCCTCA
Mini-slider-Core-Oligo71	GAAGTTTCATAAAATATCTTTAGGAGCACTTACTGCGGAATCGTCA
Mini-slider-Core-Oligo72	GATTCCCAATTCTGCGCATTTCGCGTGGCATCCAATAAAT
Mini-slider-Core-Oligo73	AGCATGTCAATCATAACTTTGAGGAAGGTTATCTATTTCAAAATTA
Mini-slider-Core-Oligo74	CAAGAGAATCGATGAAGGCGCGAGCGTTCTAGTAACAGTT
Mini-slider-Core-Oligo75	CCGGAGAGGAGGGGACCCGTGGGACCCCGGGTCATGCCTGGCTGGTTT
Mini-slider-Core-Oligo76	GCGGGAGATAGAACCCAATATTTACATTAAATAGCGCCATGCGATCGG
Mini-slider-Core-Oligo77	GCAATGCCTTATCAACAGTTGAAAGGAATTTAAAGTACGGTGTCTG
Mini-slider-Core-Oligo78	AAAGATTCAAAAGGGTCAATATGAAGATCTACGGAGCAAA
Mini-slider-Core-Oligo79	GATCGCACCGGAAACCGGTCATAGAATTCCACTTGATGGTAAAAGAAT
Mini-slider-Core-Oligo80	TATCGGCCTCAGGAATAATCTGGTCAGTTGGCAAAATGGTAAAACT
Mini-slider-Core-Oligo81	GTGCATCTGCCAGTTTGGTAGCTAGAGTAACAGTGTAGGT
Mini-slider-Core-Oligo82	ATGTGAGCTTTTTGAGTATTCAACCTGAAAAGAAATGGTCGATTAAGA
Mini-slider-Core-Oligo83	TCATTTTTGATCAAACCCTCAATCAATAGCATCATATATTTTAAAT
Mini-slider-Core-Oligo84	TAACCAATCAGTGCCACAGCTGGCTATTGGGCCGCTCACTTGGCAGATGGGCGAAA
Mini-slider-Core-Oligo85	CATCAAAAATAATTCGAACATTAACCGTAATGTCGTAACC
Mini-slider-Core-Oligo86	CGAATTCGTAATCATAGGTGCTGAACCTCAAATATTCTGACGACAG
Mini-slider-Core-Oligo87	GTACCCGTATAAGGATACAAACGGACGACGGCAGGAACGC
Mini-slider-Core-Oligo88	TATTACGCAGCAATCTAAAGCATCACCTCAATTTTGTTAAATCAGC
Mini-slider-Core-Oligo89	GATGTGCTGCAAGGCGGTCACGACCTTTGATACATGGCTA
Mini-slider-Core-Oligo90	AGGCGAAAATCCTGTACAGCCAGCAGCAAATGAAATTGACCGAGCT
Mini-slider-Core-Oligo91	GCAGCAAGCGGTCCACCAGGTCGAGGTTTGCGGAAAGGGG
Mini-slider-Core-Oligo92	GTGGTTTTCAATATTTGTCACACGACCAGTAATAAAAGGG
Mini-slider-Core-Oligo93	TACGAGCCATGAGTGAAGATAGGGACTATTAAAGAACGTGGACTCCA
Mini-slider-Core-Oligo94	TTGCGTTGGCCACAGTGCCACGCTGAGAACATGCGGGCCTCTTCGC
Mini-slider-Core-Oligo95	TCCAGTCGGGAAACCTACGCGCGGACGGGCAAAGAGAGTT
Mini-slider-Core-Oligo96	GCGCGAACCGAACGAACCACCAGCAGAAGATAAAACCCATTGAATGG
Mini-slider-Core-Oligo97	CTATTAGTCTTTAATAGCTATTAACACCGCCTGCAAGGGCCCCAGC
Mini-slider-Core-Oligo98	GAATACGTGGCACAGATCTTTTCAATTTACATGCCCGCTT
Mini-slider-Core-Oligo99	AATGGATTCCAGTGAGGGAGAGGCCTCTAGACGTTGTAAACGGATTGA
Mini-slider-Core-Oligo100	ACGTCAAATCAAGAGGTGAGGCGGTCAGCCGGCTAACTCACATTAA
Mini-slider-Core-Oligo101	AACCGTCTATCACAGGAAAAACGCTCGTCTGAACATTCTGAAGCGTAA
Mini-slider-Core-Oligo102	TTTTTTTTTGAAAACATAGCGATTTCCCTTAGAATCCTTTTTTTTT
Mini-slider-Core-Oligo103	TTTTTTTTTTACCTTTTTTAATGACAATTTCATTTGAATTTTTTTT
Mini-slider-Core-Oligo104	TTTTTTTTAACGCTCAACAGTAGTACCAGTATAAAGCCTTTTTTTT
Mini-slider-Core-Oligo105	TTTTTTTTAAATAAGGCGTTAAATACCGACCGTGTGATTTTTTTTT
Mini-slider-Core-Oligo106	TTTTTTTTCATCGTAGGAATCATAGCCGTTTTTATTTTTTTTTTT
Mini-slider-Core-Oligo107	TTTTTTTTAGAAACCAATCAATAAATTTACGAGCATGTTTTTTTTT
Mini-slider-Core-Oligo108	TTTTTTTTGGGAGAATTAACTGAGGAAGCGCATTAGACTTTTTTTT
Mini-slider-Core-Oligo109	TTTTTTTTATCCCAATCCAAATAACAGCCATATTATTTTTTTTTT
Mini-slider-Core-Oligo110	TTTTTTTTCACAATCAATAGAAAATAAGTTTATTTTGTTTTTTTT
Mini-slider-Core-Oligo111	TTTTTTTTTCCTTATTACGCAGTTGGCATGATTAAGACTTTTTTTT
Mini-slider-Core-Oligo112	TTTTTTTTAATCACCGGAACCAGTCTTTTCATAATCAATTTTTTTT
Mini-slider-Core-Oligo113	TTTTTTTTACAGAATCAAGTTTGCCGTAATCAGTAGCGTTTTTTTT
Mini-slider-Core-Oligo114	TTTTTTTTTATTTCGGAACCTATTTAATGCCCCCTGCCTTTTTTTT
Mini-slider-Core-Oligo115	TTTTTTTTTACATGGCTTTTGATTTCCAGTAAGCGTCATTTTTTTT
Mini-slider-Core-Oligo116	TTTTTTTTAACGATCTAAAGTTTCCTCATAGTTAGCGTTTTTTTTT
Mini-slider-Core-Oligo117	TTTTTTTTGCAAGCCCAATAGGATCATTTTCAGGGATATTTTTTTT
Mini-slider-Core-Oligo118	TTTTTTTTCCCTCAGCAGCGAAATTTGCGGGATCGTCATTTTTTTT
Mini-slider-Core-Oligo119	TTTTTTTTAGTTGCGCCGACAATCAGCTTGATACCGATTTTTTTTT
Mini-slider-Core-Oligo120	TTTTTTTTGATGAACGGTGTACACTTTGAAAGAGGACATTTTTTTT
Mini-slider-Core-Oligo121	TTTTTTTTTTGTGTCGAAATCCGTCATCGCCTGATAAATTTTTTTT
Mini-slider-Core-Oligo122	TTTTTTTTAACTAATGCAGATACAGGAATACCACATTCTTTTTTTT
Mini-slider-Core-Oligo123	TTTTTTTTGACGTTGGGAAGAAACATTATACCAGTCAGTTTTTTTT
Mini-slider-Core-Oligo124	TTTTTTTTTCGCGTTTTAATTCGGAAAGACTTCAAATATTTTTTTT

Mini-slider-Core-Oligo125	TTTTTTTTACCATAAATCAAAAACAGAAAACGAGAATGTTTTTTTT
Mini-slider-Core-Oligo126	TTTTTTTTAGTAGCATTAACATCAATTCTACTAATAGTTTTTTTTT
Mini-slider-Core-Oligo127	TTTTTTTTTTTGACCATTAGATAAACGAGTAGATTTAGTTTTTTTT
Mini-slider-Core-Oligo128	TTTTTTTTATTGCCTGAGAGTCTAAAGGCTATCAGGTCTTTTTTTT
Mini-slider-Core-Oligo129	TTTTTTTTCAGTCAAATCACCATGAGAAAGGCCGGAGATTTTTTTT
Mini-slider-Core-Oligo130	TTTTTTTTGTGTAGATGGGCGCAGGATAGGTCACGTTGTTTTTTTT
Mini-slider-Core-Oligo131	TTTTTTTTTAGCCAGCTTTCATCCGTCTGGCCTTCCTGTTTTTTTT
Mini-slider-Core-Oligo132	TTTTTTTTTAGCGACCGTATACGGCGAGGCAAGTCCGCTTTTTTTT
Mini-slider-Core-Oligo133	TTTTTTTTGCCAGGGTTTTCCCAATTAAGTTGGGTAACTTTTTTTT
Mini-slider-Core-Oligo134	TTTTTTTTCACCGCCTGGCCCTGCAGCTGATTGCCCTTTTTTTTTT
Mini-slider-Core-Oligo135	TTTTTTTTTTAATGAATCGGCCAGTCGTGCCAGCTGCATTTTTTTT
Mini-slider-Core-Oligo136	TTTTTTTTACCCTTCTGACCTGAGCCAACAGAGATAGATTTTTTTT
Mini-slider-Core-Oligo137	TTTTTTTTCATTTTGACGCTCAATCATGGAAATACCTATTTTTTTT
Mini-slider-Core-Oligo138	TTTTTTTTCGGCTTAGGTTGGGTTCTACCTTTTTAACCTCTTTTTTTT
Mini-slider-Core-Oligo139	TTTTTTTTGGCGAATTATTCATTTTACAAAATCGCGCAGATTTTTTTT
Mini-slider-Core-Oligo140	TTTTTTTTATATAAAGTACCGACAAGCCAGTAATAAGAGATTTTTTTT
Mini-slider-Core-Oligo141	TTTTTTTTAAGACAAAGAACGCGAATGCAAATCCAATCGCTTTTTTTT
Mini-slider-Core-Oligo142	TTTTTTTTCCCGACTTGCGGGAGGGCGTTTTAGCGAACCTTTTTTTTT
Mini-slider-Core-Oligo143	TTTTTTTTAACATGTTCAGCTAATGACGACGACAATAAACTTTTTTTT
Mini-slider-Core-Oligo144	TTTTTTTTTAAGAGCAAGAAACAAGAGTTAAGCCCAATAATTTTTTTT
Mini-slider-Core-Oligo145	TTTTTTTTCCCAGCTACAATTTTATAGTTGCTATTTTGCATTTTTTTT
Mini-slider-Core-Oligo146	TTTTTTTTATTATTCATTAAAGGTGTAAATATTGACGGAATTTTTTTT
Mini-slider-Core-Oligo147	TTTTTTTTGAAAAGTAAGCAGATACCGAAGCCCTTTTTAATTTTTTTT
Mini-slider-Core-Oligo148	TTTTTTTTACCAGAACCACCACCACACCCTCAGAGCCGCCTTTTTTTT
Mini-slider-Core-Oligo149	TTTTTTTTAGAGCCAGCAAAATCAGAGCCATTTGGGAATTTTTTTTTT
Mini-slider-Core-Oligo150	TTTTTTTTAGGCGGATAAGTGCCGGGTTTTGCTCAGTACCTTTTTTTT
Mini-slider-Core-Oligo151	TTTTTTTTAGACGATTGGCCTTGAGAGGTTGAGGCAGGTCTTTTTTTT
Mini-slider-Core-Oligo152	TTTTTTTTAGAATAGAAAGGAACACAGTTTCAGCGGAGTGTTTTTTTT
Mini-slider-Core-Oligo153	TTTTTTTTATCACCGTACTCAGGAAGCCCGGAATAGGTGTTTTTTTTT
Mini-slider-Core-Oligo154	TTTTTTTTACGGGTAAAATACGTAAGGAAGTTTCCATTAATTTTTTTT
Mini-slider-Core-Oligo155	TTTTTTTTAATCTCCAAAAAAAAGATTTTTTCACGTTGAATTTTTTTT
Mini-slider-Purple-handle1	TTTTTTTTACAAAGCTGCTCATTCTACCCAAATCAACGTATTGGCTGAAAATCTCCTGACATG
Mini-slider-Purple-handle2	TTTTTTTTAAAAGAATACACTAAACTAAAACGAAAGAGGCTTCCATCTTGTCATAACGGGAAG
Mini-slider-Purple-handle3	TTTTTTTTAAATAGCGAGAGGCTTACGACGATAAAAACCATTAACGAGGACTCTTGGACTCTA
Mini-slider-Purple-handle4	TTTTTTTTAGTAGTAAATTGGGCTGAGAAACACCAGAACGTTCGAATTAGGAATACCGTGTCC
Mini-slider-Purple-handle5	TTTTTTTTGAGGTCATTTTTGCGGTTGCTCCTTTTGATAATTCCTGGAACACTTGCTAATGAG
Mini-slider-Purple-handle6	TTTTTTTTTGTTTAGACTGGATAGGGGGGTAATAGTAAAATTTCTAACTTACAGAGCATGGCG
Mini-slider-Red-Handle1	TTTTTTTTCCAAAAACATTATGACAGCTAAATCGGTTGTATTCGTCCCCTTTTAACCCTAGAA
Mini-slider-Red-Handle2	TTTTTTTTTCAACATGTTTTAAATAATATAATGCTGTAGCTTGCTCTGCAATCAACTTATCCC
Mini-slider-Green-Handle1	TTTTTTTTAGCCCCAAAAACAGGAGGTTGATAATCAGAAATTCCTAATTACGATGCTACTCCC
Mini-slider-Green-Handle2	TTTTTTTTCAAGGATAAAAATTTTAGCCTTTATTTCAACGTTCGACTCTCATTCTCTAACAGC
Mini-slider-Blue-Handle1	TTTTTTTTGCACCGCTTCTGGTGCTCCAGCCAGCTTTCCGTTCGTACAACCTTGACCTTACCT
Mini-slider-Blue-Handle2	TTTTTTTTATTTTGTTAAAATTCGAATTGTAAACGTTAATTTCTCACATGGTCTCACATCACT
Mini-rail-Red-Handle3	TTTTTTTTATTGTTATCCGCTCACCTGTTTCCTGTGTGAATTCGTCCCCTTTTAACCCTAGAA
Mini-rail-Red-Handle4	TTTTTTTTGCAACTGTTGGGAAGGTCGCCATTCAGGCTGCTTGCTCTGCAATCAACTTATCCC
Mini-rail-Green-Handle3	TTTTTTTTAAATCCCTTATAAATCGGTTCCGAAATCGGCATTCCTAATTACGATGCTACTCCC
Mini-rail-Green-Handle4	TTTTTTTTAAGCCTGGGGTGCCTAGGAAGCATAAAGTGTATTCGACTCTCATTCTCTAACAGC
Mini-rail-Blue-Handle3	TTTTTTTTTCGCCATTAAAAATACTGATAGCCCTAAAACATTCGTACAACCTTGACCTTACCT
Mini-rail-Blue-Handle4	TTTTTTTTTTTGGAACAAGAGTCCTTGAGTGTTGTTCCAGTTCTCACATGGTCTCACATCACT

DNA sequences for core staples, interacting handle strands, clip and clip removal strands of falcon-slider and -rail

Name	Sequence
Falcon-rail-Core-Oligo0	GTGTTTTTATAATCAGTGAGGCCACCGCGTTGTAGCAATACTTTCACACGAGGGACATT
Falcon-rail-Core-Oligo1	AGACAGGAACGGTACGCCAGAATCCTCATCACTTGCCTGAGAATGGATCTGACCT
Falcon-rail-Core-Oligo2	AGCTAAACAGGAGGCCGATTAAAGGGATCGGCCTTGCTGGTAAAATACCTGACAATAT
Falcon-rail-Core-Oligo3	TAACGTGCTTTCCTCGTTAGAATCAGATTACCGCCAGCGCCCACGATGCATATGCGCGA
Falcon-rail-Core-Oligo4	CGCGTACTATGGTTGCTTTGACGAGCCCAAATCAAGTTTTTACGTCAAGAGAGTT
Falcon-rail-Core-Oligo5	CACCCGCCGCGCTTAATGCGCCGCTATAAAGCACTAAATCGGCAAGAGTCGCCCCAGC
Falcon-rail-Core-Oligo6	AAGTGTAGCGGTCACGCTGCGCGTAACCCCCGATTTAGAGCTTAGATAGGGGGTTCCGA
Falcon-rail-Core-Oligo7	AATTCCACACAACATATGCCTAATGAGTGAGCTGCCACGCGCAAATGAAAAATCTATGTAAATC
Falcon-rail-Core-Oligo8	TGTTTCCTGTGTGAACGTTGCGCTCACTGCAGGCGGTAACCTCAAATATCAAATCAATAT
Falcon-rail-Core-Oligo9	ACCGAGCTCGAATTCGAAACCTGTCGTGCCAGACGAACCATGGTCAGTTGGCAAAAATTACC
Falcon-rail-Core-Oligo10	TGAGCCTCCTCACAGTGGCCAACGCGCGGGGAAGCCCTAAATTGAGGAAGGGAATGCGCAATTA
Falcon-rail-Core-Oligo11	TGCCAGCACGCGTGCTGGGCGCCAGGGTGGCACCAGTCGGTGGTGCCATCCCTCAGCGTG
Falcon-rail-Core-Oligo12	CGGGCCGTTTTCACGGCTCGTCATAAACATCCTGTTGCCCGCTGGAGGTGTCCAGTCATAAC
Falcon-rail-Core-Oligo13	TGCACTCTGTGGTGCTTCAGCAAATCGTTAACCCGGGCGCGCAGGCGCTTTCGCACCGTCGCTG
Falcon-rail-Core-Oligo14	CAACAGCTCACCGCCTGGCCCTGAAGGGCGAAACGTTGAA
Falcon-rail-Core-Oligo15	TTTACGCTTTGAATACCAAGTGTCGCTATCCTTAGAA
Falcon-rail-Core-Oligo16	TAACGGGCGAATTATTCATTATGTGAGAGATTAA
Falcon-rail-Core-Oligo17	GAAATAAGAAGATGATGAAACTTTTTTAAATTTATCA
Falcon-rail-Core-Oligo18	TACCAAAAATTAATTAAATATTCTAACATCTTTTTAA
Falcon-rail-Core-Oligo19	TTATAAACTAATAGATTAGAGTGCTGGAGGCGGC
Falcon-rail-Core-Oligo20	CAATTACATTTGAGGATTTAGGGAACGTGAACGATGC
Falcon-rail-Core-Oligo21	TATCACAAACAATTCGACAACGCAGCCTCGTCCGTTT
Falcon-rail-Core-Oligo22	GCAGCAACCCAACGGCAGCACCGTGAGACGGGCAATTCTG
Falcon-rail-Core-Oligo23	GTAATTCTGTCCAGACGACGACAATAATTTATCAACAATAGATCAAGCAAAGGCTTATC
Falcon-rail-Core-Oligo24	AAGAGAATATAAAGTACCGACAAAAGAAATAATATCCCATCTCATCGTTTTAGCG
Falcon-rail-Core-Oligo25	ATTTAGGCAGAGGCATTTTCGAGCCATAGAAACCAATCAATAACTCATCGTGAAGCCT
Falcon-rail-Core-Oligo26	AGAATCGCCATATTTAACAACGCCAACTTATCATTCCAGGTTGGCTTAAGATGCACCCA
Falcon-rail-Core-Oligo27	AAAGCCAACGCTCAACAGTAGGGCTTGTAAATGCTGATGCAGGGCGGTAATCGGC
Falcon-rail-Core-Oligo28	TCATATGCGTTATACAAATTCTTACCAAAGAACGCGAGAAAACTTAAATTAGTCCCGG
Falcon-rail-Core-Oligo29	AATCATAATTACTAGAAAAAGCCTGTTTTTAGTTAATTTCATCGGAAAAAGCCGTGGTG
Falcon-rail-Core-Oligo30	TCGACATAGTAAAAAAAGCCGCACTCTGGTCACTACGTCA
Falcon-rail-Core-Oligo31	TCCGGCACCGCTTCTGTTCAGGCTGCGCAACTAAATAAGATTTAACGTCAAAAATGCTATCTTA
Falcon-rail-Core-Oligo32	GGCCTCAGGAAGATCGGTGCGGGCCTCTTCAAATAAACAGAGAGAATAACATATAAGAGC
Falcon-rail-Core-Oligo33	ATCTGCCAGTTTGAGGGCGAAAGGGGGATGTGGCGTCTTTATTAGACGGGAGAATATAACCC
Falcon-rail-Core-Oligo34	GTTGGTGTAGATGGGCGTTGGGTAACGCCAGGATTTTATCACAAAGTCAGAAGCTGGTTCTGGG
Falcon-rail-Core-Oligo35	ACGGCGGATTGACCGCGTTGTAAAACGACGAGCTTTCGAGGGTAGCTATTTTTTACAAAT
Falcon-rail-Core-Oligo36	GTAACAACCCGTCGGATTGTATAAGCAAATATCCCGGTTGGCTATCAGGTCATTGCAGACCG
Falcon-rail-Core-Oligo37	GCCAGCTTTCATCAACTAATATTTTGTTAAAAATCGTAAAAAACAAGAGAATCGATTATCGCGT
Falcon-rail-Core-Oligo38	AGCCGCCATAACCTCACCGGAAACTGTGTACACGATGTTA
Falcon-rail-Core-Oligo39	AGCCTACATTATGACCCTGTACCGAAAAAAGTAAGCAGA
Falcon-rail-Core-Oligo40	CAAGGAGCCTTTATTTCAACAAGAAACAATGAAATCAAAGTTA
Falcon-rail-Core-Oligo41	AGTAGTTAGAACCCTCATATAACAAGAATTGAGTTAAAATAATAA
Falcon-rail-Core-Oligo42	CTGAACTGAGTAATGTGTAGGTAATTGAGCGCTAATATGATTAAG
Falcon-rail-Core-Oligo43	CTGTTTGAGAAAGGCCGGAGCACCATCAATATGATAATCAAAA
Falcon-rail-Core-Oligo44	CATTATAATTGCTCCTTTTGAGAAGCAAACTCCAACAATAGTCAG
Falcon-rail-Core-Oligo45	CAATTGCGGATGGCTTAGAGCTTTAATTCGAGCTTCAAGATTAAG
Falcon-rail-Core-Oligo46	TAGCCGAAAGCAATAGAAAATAGCAGCCTTTACAGCCATACCCACTTT
Falcon-rail-Core-Oligo47	CCAGAAGCACGGAATAAGTTTATTTTGTCACAATCttttttt
Falcon-rail-Core-Oligo48	GGAAACGCGCCCAATAAAAAACAGGGAAGCGCCCAGAGCCCCACCCTCTTGGTTCA
Falcon-rail-Core-Oligo49	CGGAATACGGTGGCAACATATAAAAGAAACGCAAAAGGGCGACATTCAATTACCAT
Falcon-rail-Core-Oligo50	AACTGGCATCAGAGAGTAACTGAACACCCTGACTGAATCTCCATGGGC
Falcon-rail-Core-Oligo51	ACTCCTTATGTTAGCAAACGTAGAAAATACATGAAGGTAAATATTGACAATTAGAG
Falcon-rail-Core-Oligo52	TGACCATAATTCAACCATAAATTAATGCCGGAAGAGGTGGAGTGGTGA
Falcon-rail-Core-Oligo53	ATCAGGTAATGCTTTAAACAGTTCAGAAAAAGGTGAATTATGAGCAAGTAACAC
Falcon-rail-Core-Oligo54	TGACTATTGGTCAGGATGAGAGATCTACAAAGATAATCAGTCTATGCTAATCTTGC
Falcon-rail-Core-Oligo55	AAGCAAAGAATCGTCATAAATATTCATTGAATTCGTTTACCAGACGACATACATAA
Falcon-rail-Core-Oligo56	CATCAAAAAAGCGAACCCTGAGAGTCTGGAGCACTAGCATGGGTAATC
Falcon-rail-Core-Oligo57	AGGAAGCCTGTTTAGACTGGATAGCGTCCAATAGCGAGAGGCTTTTGCGATTTAGG
Falcon-rail-Core-Oligo58	GCGAAATAACACCGCCCAGAGATAGAACCCTTTATTTACATTCTGTAT
Falcon-rail-Core-Oligo59	CACAGGTCGTACTCCAGTTAATGCCCCCTTGTACTGGAAGTGTTT
Falcon-rail-Core-Oligo60	ACGGCTAAAGATAAAAAAGAATACGTGGCACAACATTTTGACAGTTTC
Falcon-rail-Core-Oligo61	CGACAAACCATTAAAATGGCTATTAGTCTTTATGCAACAGCAACTAAA
Falcon-rail-Core-Oligo62	GTTAAAAATACCAGGCTGAGACTCCTCAAGAGAAGCGCAGGCCGCCCAACTGAGGG
Falcon-rail-Core-Oligo63	TAGCACGCATCTTTGATTATACCAAGCGCGGACAGATGGTGCATA

Falcon-rail-Core-Oligo64	GATGACTCGTAATGGGCGGTCCACGCTGGTTTCACTATTAAAGGAGCC
Falcon-rail-Core-Oligo65	GCTATAGATATGAGCCAATCCTGTTTGATGGTTTGAGTGTTTGCTTTC
Falcon-rail-Core-Oligo66	TGGCGTTTCGTAATGCCGAAATCCGCGACCTGCTCCAttttttt
Falcon-rail-Core-Oligo67	AAAAAAACCTTGCTTCAAGCATCACCTTGCTGCAGTATTAGAAGCAGA
Falcon-rail-Core-Oligo68	GAGGCCGTAATAAGCCACCAGAGCCGCCGCCACCCTCTCGTGAAA
Falcon-rail-Core-Oligo69	GTTTGTGAGTACATAAACCCTCAATCAATATCCCAGCAGAACTTTTCTAGGCCGTT
Falcon-rail-Core-Oligo70	AGGCTGTCTTCATTTGTCAACAGTTGAAAGGAAACATCGCAAGCCTGG
Falcon-rail-Core-Oligo71	GGAATCGATCTCTGAATTCACAAACAAATAAAATCTTTTCACGACGGCCCCTAATT
Falcon-rail-Core-Oligo72	ATGAACCGAACGGTGGCGCATAGGCTGGCGTTTAATTAGCCTGCA
Falcon-rail-Core-Oligo73	AACGCAACGTAGAACGACGCAACCAGCTTACGTGCGGCTGGGCGGATGCTTGTGTT
Falcon-rail-Core-Oligo74	ATACCCGAGCACATCCCATCAGCGGGGTCATTGGTTGCGGACTGATGC
Falcon-rail-Core-Oligo75	TTTGACTGGAACGAGGCAAATCAACGTAACAAAGCTGttttttt
Falcon-rail-Core-Oligo76	CCACGTCATTACCGCGAACATAGCGATAGCTTTGAATAACTCACCGCT
Falcon-rail-Core-Oligo77	GATTGGAAGAACCGTCAAGTTTGCCTTTACCGGAAACTTTATAGT
Falcon-rail-Core-Oligo78	GCAGTCAGCAAGCCGTGAAGAGTCAATAGTGATGGAAACACCCGATTCATTAGTGG
Falcon-rail-Core-Oligo79	CCGGTTGGTAAACCAAAGGTCTGAGAGACTACTTAACAATTTGATTAT
Falcon-rail-Core-Oligo80	ACGCTACAATAATCAACTTATTAGCGTTTGCCACTTGAGCGAGAGTGACAGATGTT
Falcon-rail-Core-Oligo81	GTTCGTCTCAACTTGAACTGGCTCATTATGGAATTACACCTGGCC
Falcon-rail-Core-Oligo82	CAGACAGCTTTGCCGCATGAAGGGTAAAGTTACCGGACTTTTTGAGTACTACTCCG
Falcon-rail-Core-Oligo83	GGGGTTGAAAACAGCGCGTTCCGGCAAACGCGCGGCCAGATCCGGCTC
Falcon-rail-Core-Oligo84	TCCGGACATAAGGCTTAACGGAACAACATTATTACAGttttttt
Falcon-rail-Core-Oligo85	TTGGCAATTTATTTATTAAGAACGCGAGGCGTAGGAATCAGAACACTA
Falcon-rail-Core-Oligo86	GACGAGCGTCACCAACCAGCGCCAAAGACAAAGACACGAAACCGA
Falcon-rail-Core-Oligo87	GTCTGTCCTAATTTGCGACTTGCGGGAGGTTTAGAACAAGACAGCTGTATTAACTT
Falcon-rail-Core-Oligo88	TATCTCGATACCAACGAGATTAGTTGCTATTTACGGGTATAGGTCTGG
Falcon-rail-Core-Oligo89	GTCCCTACCATTTGGGGGAAATTATTCATTAACGACAGTATTACGGAA
Falcon-rail-Core-Oligo90	TGGCAGAGAGGCATACACTATCATAACCCCCCCCTCACTTTACCC
Falcon-rail-Core-Oligo91	TGCGTATCAAAAGCCCCAGCGCCATGTTTACCTCTGCTCAGGATACTCTCTCGTGT
Falcon-rail-Core-Oligo92	ATGCCGCAGTCAATCAGAGAGATAGACTTTCTAGACGCAGAAAACATT
Falcon-rail-Core-Oligo93	GATCTAGATCAGTTGAAAAAGAAGTTTTGCCATAGTAAAACGAAAGACTTCttttttt
Falcon-rail-Core-Oligo94	GGGATTTAAGTTTTACCGCCACCCTCAGATGTATCACGATGGGCC
Falcon-rail-Core-Oligo95	AGCGGAGTCAGACAGCTCAGGGATAGCAAGCGAGGGTTCCACATA
Falcon-rail-Core-Oligo96	GGAATTGCCAGTACAATACCGTAACACTGAGTTTGCTCAGCTGCTTCCCTACGCTT
Falcon-rail-Core-Oligo97	AATCTCCAGTTAAACGAAAGACAGCATCGAAAACACTCAAATTCA
Falcon-rail-Core-Oligo98	TTTAATTGACCGATATGGCTACAGAGGCTTTACCTAAAGAATCGA
Falcon-rail-Core-Oligo99	GAGGTGAACGACAATGTTCATGAGGAAGTTTCCATTACCGATAGTTGCGCTTTCTTAA
Falcon-rail-Core-Oligo100	tttttttCTCAGAACCGCCACCCTCAGAGTCGTCTTTCCAGACGTTAttttttttt
Falcon-rail-Core-Oligo101	GGAATAGGGCCACCACCCTCATTTCCTCATAGTTAGCGTAACGATCTATGCTAAAC
Falcon-rail-Core-Oligo102	GATATAAGATTATTCTGAAACATGCGTCATTGCAGAA
Falcon-rail-Core-Oligo103	GCCGTCGACCAATAGGAACCCATGACTACAACGCCTGTAGCATTCCAGAGAATA
Falcon-rail-Core-Oligo104	GCGGGGTTTCGTCACCCTCAGCAGGGCCGCTTTTGCGGGATTCGTCACGAATAATA
Falcon-rail-Core-Oligo105	AATACACTGAACGAGGGTAGCAACATTCGGTCGCTGAGGCTTGCAGGGAAAAAAAA
Falcon-rail-Core-Oligo106	ACGAAAGAGAGATTTGTATCATCTAAGGGAACCTACC
Falcon-rail-Core-Oligo107	AGGCACCAGAGGACTAAAGACTTTACAACAACCATCGCCCACGCATATATCGGT
Falcon-rail-Core-Oligo108	tttttttAACGGGTAAAATAGTGCAAGTTGGCGGAT
Falcon-rail-Core-Oligo109	tttttttGAGTAACAGTGCCCGTATAAAAGGAGGTTTAGTACCGCCACCttttttt
Falcon-rail-Core-Oligo110	ACATGGCTGTTGAGGCAGGTCAGGCCACCATCCTATA
Falcon-rail-Core-Oligo111	ACCGAACTTAATCTTGACAAGAACCAGAACTAACACA
Falcon-rail-Core-Oligo112	tttttttTGTTACTTAGCCGGCTCAAAATGAGGAAC
Falcon-rail-Core-Oligo113	tttttttTCAGAGCCGCCACCAGAACCATTTTAACGGGGTCAGTGCCTTttttttt
Falcon-rail-Core-Oligo114	GACAGGAGTTTGATGATACAGGAGGCCTATTTCGGAACCTTATAGCCC
Falcon-rail-Core-Oligo115	CCTTGATATTTACCGTTCCAGTAAGAAAGTATTAAGAGGCGGATAAGT
Falcon-rail-Core-Oligo116	AAAGACCAGTACAGCCAGAATGGAAAGGATTAGGACCAGCGACCCTTA
Falcon-rail-Core-Oligo117	ATCAAGAGGACCAACTTTGAAAGAGAAACAAAGTACAACGGGCAAAAG
Falcon-rail-Core-Oligo118	TCATTACCCGCAGACGGTCAATCAGCCTGATAAATTGTGTCACTACGA
Falcon-rail-Core-Oligo119	CCGGAACCCGTTTTCATCGGCATATCACCACTACATG
Falcon-rail-Core-Oligo120	GAGTAGTAGGAAGAAAAATCTACATTCAACGAGTGGC
Falcon-rail-Core-Oligo121	tttttttCTCATTCAGTGAATGGCCGCGCAATTACA
Falcon-rail-Core-Oligo122	tttttttCCGTAATCAGTAGCGACAGAACCACCCTCAGAGCCACCACCCttttttt
Falcon-rail-Core-Oligo123	TAGCAAGGGCGTCAGACTGTAGCGGCCTCCCTCAGAGCCGCCAGCATT
Falcon-rail-Core-Oligo124	GTAGCACCACCGATTGAGGGAGGACATAAACCAAAAG
Falcon-rail-Core-Oligo125	CCAGCAAATTTCGGTCATAGCCCCAATCACCGGAACCAGAACGATTGG
Falcon-rail-Core-Oligo126	CGTCACCGCCTTATGCGATTTTAATAATCATTGTGAATTATCCTCATT
Falcon-rail-Core-Oligo127	CGCCAAAAACCAGTCAGGACGTTGAATTGGGCTTGAGATGTGACCTTC
Falcon-rail-Core-Oligo128	TAATGCAGGATAAAAACCAAAATACTGCGGCGGATTG
Falcon-rail-Core-Oligo129	AATACCACGTTAATAAAACGAACTGCCCTGACGAGAAACACCGGATAT
Falcon-rail-Core-Oligo130	tttttttGTAGAAAGATTCAAGGAGTGGAGTAGGTA

Falcon-rail-Core-Oligo131	tttttttAATAGAAAATTCATATGGTTTATGAAACCATCGATAGCAGCAttttttt
Falcon-rail-Miniscaf-Oligo0	AGAAAAGTTTAGCCGTGGCCCATCACCTGTGTCTGCTTCTATTTCGCA
Falcon-rail-Miniscaf-Oligo1	GGAAGCAGTTTTTAACCCAGGCTTGTTTGTCGTATGTGGAACGGCCT
Falcon-rail-Miniscaf-Oligo2	CATCCGCCGAGTCATCTGAATTTGCGTGCTACAGAATTGAAGCGTAG
Falcon-rail-Miniscaf-Oligo3	CATCCGCCAACTTGCACAAACGCCAGCATCAGTTCTATAGCTCGATTCAACACAAG
Falcon-rail-Miniscaf-Oligo4	GAATCGGGTCACAAACAAACACTTCGGCCTCAGCGGTGAGTTTTTTTC
Falcon-rail-Miniscaf-Oligo5	TGGGCGGCTCGATTCCATAATCAAGACAGCCTTTCTGCACCACTAAT
Falcon-rail-Miniscaf-Oligo6	TACTCAAAGTTGCGTTTATGCACCGGTTCATTGACGTAGCCCTCAGT
Falcon-rail-Miniscaf-Oligo7	AGTTCCTCATTTTGAGCCAGTCAAAGAGCCGGATCGGGTATGGTAGGTCGGAGTAG
Falcon-rail-Miniscaf-Oligo8	ACAGCTGTCTGACTGCTTTCACGATCCAATCTAGTGTTCTGACGTGGG
Falcon-rail-Miniscaf-Oligo9	GCCGTCGTTGTAGCGTCCAGACCTCCAACCGGTATAGGAAAGTTAAT
Falcon-rail-Miniscaf-Oligo10	GAGTATCCGCTGTCTGTGCAGGCTGACGAACTAACATCGAATTAGGG
Falcon-rail-Miniscaf-Oligo11	ATGTAATTGCGCGGCCATGTCCGGAAATGTTTTTCAACCCCTGTGTTAACACGAGA
Falcon-rail-Miniscaf-Oligo12	GAGGGTGGGGACAGACACTATAAAGCTCGTCAAAGTGGGATTGCCAAC
Falcon-rail-Miniscaf-Oligo13	TCACTCTCGTAGGGACGCCCATGGTCGAGATACATGTAGTGAACCAA
Falcon-rail-Miniscaf-Oligo14	AGCATAGAGATACGCAGGCCAGGTTCTGCCATCACCACTAACATCTG
Falcon-rail-Miniscaf-Oligo15	GTACCTACTCCACTCCTTCTAGATCGATTACCCTGCGGCATGCCACTCGCAAGATT
Falcon-rail-Purple-handle1	tCATCACGCAAATTAACAGTAAAAGAGTCTGTCttGGCTGAAAATCT
Falcon-rail-Purple-handle2	tAGTGTAAAGCCTGGGGCGAGCCGGAAGCATAAttCCATCTTGTCAT
Falcon-rail-Purple-handle3	tACGGATTCGCCTGATTATCGGGAGAAACAATAttAACGAGGACTCT
Falcon-rail-Purple-handle4	tATGCAGAACGCGCCTGACAACATGTTCAGCTAttCGAATTAGGAAT
Falcon-rail-Purple-handle5	tAAAGCGCCATTCGCCAGTGCCGGAAACCAGGCttCCTGGAACACTT
Falcon-rail-Purple-handle6	tATCGGTTGTACCAAAACAGAGCATAAAGCTAAttTCTAACTTACAG
Falcon-rail-Green-Handle1	AATGAATTTTGGCAGATTCACCAGCTTTGATTAGTAATAAGAGAATTCCTAATTACGAT
Falcon-rail-Green-Handle2	AACTTTCAACGCTCAATCGTCTGATAGAAGAACTCAAACTATTTTTTCCTAATTACGAT
Falcon-rail-Green-Handle3	GAAAGGAAGAAAAACGCTCATGGATATCCAGAACAATAGCGGGTTCCTAATTACGAT
Falcon-rail-Green-Handle4	ATTTTTTCAAACCGTCTATCAGGGCTACGTGAACCATCACACGTATTCCTAATTACGAT
Falcon-rail-Green-Handle5	GGCTCCAAAAGAACGTGGACTCCATGGGGTCGAGGTGCCGCAGGGTTCCTAATTACGAT
Falcon-rail-Green-Handle6	TTATCAGCTGTTCCAGTTTGGAAAACCCTAAAGGGAGCCACCATTCCTAATTACGAT
Falcon-rail-Green-Handle7	ACAGCTTGTCAAAAGAATAGCCCGGACGGGGAAAGCCGGCCTGGCTTCCTAATTACGAT
Falcon-rail-Blue-Handle1	CTGGCCAATGCAACAGTAACTCACATTAATTGATTGTTATCCGCTCACTTCGTACAACCTTG
Falcon-rail-Blue-Handle2	GAAAGCGTCAGAGGTGCCGCTTTCCAGTCGGGTAATCATGGTCATAGCTTCGTACAACCTTG
Falcon-rail-Blue-Handle3	TTTTGAAATACCGACTGCATTAATGAATCTGAGGATCCCCGGGTTTCGTACAACCTTG
Falcon-rail-Blue-Handle4	ACTCCCTTGATTGGATGAGGCGGTTTGCGTATCTGTTCTTCGCGTCCGTTCGTACAACCTTG
Falcon-rail-Blue-Handle5	GCAGCAAGTAACTTTTTTTTTAGGTTTCTTTGTCATACCGGGGGTTTCTTCGTACAACCTTG
Falcon-rail-Blue-Handle6	AGGCGAAGGGTCACCTTACACTGGTGTGTGCGGCCAGAATGCGGTTCGTACAACCTTG
Falcon-rail-Blue-Handle7	AATCGGCATCAATCCGGGCATCAGATGCCGGGTGTCACTGCGCGCCTGTTCGTACAACCTTG
Falcon-rail-Red-Handle1	TACAAAATCGCGCAGATCAGATGAATATACAGTAACAGTACCTTTCGTCCCCTTTTA
Falcon-rail-Red-Handle2	TCAATTACCTGAGCAAAAAGAAATTGCGTAGATTTTCAGGTTTTCGTCCCCTTTTA
Falcon-rail-Red-Handle3	AAACATCAAGAAAACTATCAAAATTATTTGCACGTAAAACATTCGTCCCCTTTTA
Falcon-rail-Red-Handle4	CTTTAGGAGCACTAACCTTCTGAATAATGGAAGGGTTAGAACCTTCGTCCCCTTTTA
Falcon-rail-Red-Handle5	GCCGTCAATAGATAATCATCAATATAATCCTGATTGTTTGGATTCGTCCCCTTTTA
Falcon-rail-Red-Handle6	AAGTATTAGACTTTATCATATTCCTGATTATCAGATGATGGTTCGTCCCCTTTTA
Falcon-rail-Red-Handle7	TCGTATTAAATCCTTTCAAAGAAACCACCAGAAGGAGCGGAATTTCGTCCCCTTTTA
Falcon-rail-Green-Handle8	TCCTTGAACCCAATAGAAGTCCTGAACAAGAAGTAAATTCGACTCTCATTC
Falcon-rail-Green-Handle9	GACGCTGATTTTATTTCTAATTTACGAGCATGGTAATTTCGACTCTCATTC
Falcon-rail-Green-Handle10	AAATCATGTACCGCATCGGCTGTCTTTCCATGTATTCGACTCTCATTC
Falcon-rail-Green-Handle11	CCTATCCCAAAAACCGGGTTATATAACTATATAATTGTTCGACTCTCATTC
Falcon-rail-Green-Handle12	CTTTAGTGCAGCAGTTAATCCAATCGCAAGACAGTATTTCGACTCTCATTC
Falcon-rail-Green-Handle13	TGATTGCGATCAAACTTTTTCAAATATATTAGTATTCGACTCTCATTC
Falcon-rail-Green-Handle14	TTTCGTCTGCTCTCACTTCTGACCTAAATTTAACCGGTTCGACTCTCATTC
Falcon-rail-Blue-Handle8	CGGTATTCCCCAATCCGTTGGGAAGGGCGATCGCACTCCAGCCAGCTTTTCTCACATGGTCT
Falcon-rail-Blue-Handle9	AACCTCCCCAGTTACAGCTATTACGCCAGCTGGGACGACGACAGTATCTTCTCACATGGTCT
Falcon-rail-Blue-Handle10	TAAATCACTAACGACTGCAAGGCGATTAAGCATCGTAACCGTGCTTCTCACATGGTCT
Falcon-rail-Blue-Handle11	GCTACGGACGGGAACAGTTTTCCCAGTCACGATAATGGGATAGGTCACTTCTCACATGGTCT
Falcon-rail-Blue-Handle12	GAAACGTACAATGCCAGCCAGAAACAGGAAGATTCTCCGTGGGAACAATTCTCACATGGTCT
Falcon-rail-Blue-Handle13	AATTTGTTATGTACTTAAATTGTAAACGTATTAAATGTGAGCGATTCTCACATGGTCT
Falcon-rail-Blue-Handle14	AAGGGATAGAACGGTATTCGCATTAAATTTTTGTCTGGCCTTCCTGTATTCTCACATGGTCT
Falcon-rail-Red-Handle8	ATACTTTTGCGGGAGACAAAGAATTAGCAAAATTAAGCAATAATTGCTCTGCAATCA
Falcon-rail-Red-Handle9	GCAAGGATAAAAATTTCATTAACATCCAATAAATCATACAGGTTGCTCTGCAATCA
Falcon-rail-Red-Handle10	TTTTAAATGCAATGCAAGGTGGCATCAATTCTACTAATAGTTTGCTCTGCAATCA
Falcon-rail-Red-Handle11	TAAAGATTCAAAAGGGTAGCTATATTTTCATTTGGGGCGCGAGTTGCTCTGCAATCA
Falcon-rail-Red-Handle12	ACAGTGAGAGTACCTTGATACATTTCGCAAATGGTCAATAACTTGCTCTGCAATCA
Falcon-rail-Red-Handle13	TAAGAGGTCATTTTTCTGCGAACGAGTAGATTTAGTTTGACTTGCTCTGCAATCA
Falcon-rail-Red-Handle14	TTAATTGCTGAATATAGTTTCATTCCATATAACAGTTGATTCCTTGCTCTGCAATCA

Falcon-slider-Core-Oligo1	tAAGCGAAAGGAGCGGGCGCTAGGGCGGAACGTGGCGAGAAAGGAAGGGAAGAttttttt
Falcon-slider-Core-Oligo2	tCCCCTGCATCAGACGATCCAGCGCAGTTACCTGCAGCCAGCGGTGCCGGTGCttttttt
Falcon-slider-Core-Oligo3	tTTGAGTAACATTATCATTTTGCGGAAGCCCGAACGTTATTAATTTTAAAAGTttttttt
Falcon-slider-Core-Oligo4	tAAATAAGGCGTTAAATAAGAATAAACATGGTTTGAAATACCGACCGTGTGATttttttt
Falcon-slider-Core-Oligo5	tTAGGAACGCCATCAAAAATAATTCGCGTTAAATCAGCTCATTTTTTAACCAAttttttt
Falcon-slider-Core-Oligo6	tATGCAACTAAAGTACGGTGTCTGGAAATGCTGTAGCTCAACATGTTTTAAATttttttt
Falcon-slider-Core-Oligo7	tttttttAGAGTCCACTATTAAAGTTCCAGTTTGGAACAttttttt
Falcon-slider-Core-Oligo8	AGCCCGAATGGTGGTTCCGAAAGCCCTTCACCGCCTGTTTTTCT
Falcon-slider-Core-Oligo9	GAGCTTGACGGCGAACGTGGCGAGCACCACACCCGCCGCGCGCTACAG
Falcon-slider-Core-Oligo10	tttttttCCGTAAAGCACTAAATCGGAAAGCGAAAGGAGCGGGCGCTAGttttttt
Falcon-slider-Core-Oligo11	tttttttTGGTTTGCCCCAGCAGAGCAAGCGGTCCACGCttttttt
Falcon-slider-Core-Oligo12	ATCAAAGCCGGGGCCTTATAAATCACCGTCTATCATTTTT
Falcon-slider-Core-Oligo13	tttttttGGCGCTGGCAAGTGTAGCGGTCGAGCACGTATAACGTGCTTTttttttt
Falcon-slider-Core-Oligo14	tttttttAGAGGCGGTTTGCGTACGGCCAACGCGCGGGGttttttt
Falcon-slider-Core-Oligo15	TTTCACCAGAAACCTGTCGTGCCTTAATTGCGTTGCGCGCTCACAA
Falcon-slider-Core-Oligo16	GGCTGCGCCTTAAAACAGCTGATTTCGGCAAAATCTGTCG
Falcon-slider-Core-Oligo17	GGCGCGTACGATTAAAGGGATTTTGGTACGCCAGAATCCTCAATACTT
Falcon-slider-Core-Oligo18	tttttttCCTCGTTAGAATCAGAGCGGGAATCAGTGAGGCCACCGAGTAttttttt
Falcon-slider-Core-Oligo19	tttttttCCTGGGGTGCCTAATGAGCATAAAGTGTAAAGttttttt
Falcon-slider-Core-Oligo20	CGCGGAACAGACATTTCCAGTCGGGTGAGACGCCATTCTG
Falcon-slider-Core-Oligo21	TTCCACACATGGTCATAGCTGTTTTTGTTTTATGGAG
Falcon-slider-Core-Oligo22	CTTTGATTTCACTTGCCTGAGTAGCGCTCATGGAAATACC
Falcon-slider-Core-Oligo23	tttttttAAAGAGTCTGTCCATCACGCACGGCCTTGCTGGTAATATCCAttttttt
Falcon-slider-Core-Oligo24	tttttttGGATCCCCGGGTACCGCGAGTCACAGGAGAATttttttt
Falcon-slider-Core-Oligo25	TGATAACAAGTAAAATTGTTATCCTCACTGCCACCATAAA
Falcon-slider-Core-Oligo26	tttttttGAACAATATTACCGCCAGCCATGGACAGTCTGCACAG
Falcon-slider-Core-Oligo27	ATTCACCACCGAACGAACCACCAGCAGAAGATAAAACAGAGGTGAttttttt
Falcon-slider-Core-Oligo28	tttttttGGCGGTCAGTATTAACACCGCGCCACGCTGAGAGttttttt
Falcon-slider-Core-Oligo29	tttttttTAAACCCAATATTACAAAAACATATAGATGATttttttt
Falcon-slider-Core-Oligo30	CGCGGGGACCCTTCTGACCTGATTGAATGGCTATTAG
Falcon-slider-Core-Oligo31	CTCTTTGATACATGCTACGGCGGGTTCCTGTGGCCAATCA
Falcon-slider-Core-Oligo32	CGCTCAATATAAAAGGGACATTCTTGATAGCCCTAAAACA
Falcon-slider-Core-Oligo33	AACGATAGAAATGAAGCCGTCAATAGATAACAAACAATTCGACAACTCGTATTAA
Falcon-slider-Core-Oligo34	AAATATCACAATATCTATCTTTAGGAGCACTATTGCCCGAACGTTATTAATTTTAAAA
Falcon-slider-Core-Oligo35	tttttttCCAGCAGCAAATGAAAAATCTGAACTGATTATTCAGG
Falcon-slider-Core-Oligo36	AATTGAGGAGTAACATTATCATTTTGCGGAACAAAGAAACCACCAttttttt
Falcon-slider-Core-Oligo37	tttttttGAAGGAGCGGAATTATCATCATATCAGATGATGGttttttt
Falcon-slider-Core-Oligo38	tttttttATGAAGACAAATCCCCAAGGTTTATAAGTCTAttttttt
Falcon-slider-Core-Oligo39	TTATCAATAACCCTTATCACGAGTTATCTGAAGACTCCTC
Falcon-slider-Core-Oligo40	AGTCGGCGCAGACACCTTTTACATCGGGAATACC
Falcon-slider-Core-Oligo41	TAATGGAACTACCATAGTTTAACGTCAGATGATTATT
Falcon-slider-Core-Oligo42	tttttttCAATTCATCAATATAATCCTGAGATTTTTTACCTAAT
Falcon-slider-Core-Oligo43	AAAGAAATATGATGAAACAAACATCAAGAAAACAAAATTAATTACttttttt
Falcon-slider-Core-Oligo44	tttttttATTTAACAATTTCATTTGAATAATGGAAACAGTAttttttt
Falcon-slider-Core-Oligo45	tttttttAATGTTGTGCAGATCCAAGATTGGGCGTTATCttttttt
Falcon-slider-Core-Oligo46	TCACGAAGATGAGTATCAATGAGTTTAGCTCTACCTTTTTAACCTAATGCTGATGCAAAT
Falcon-slider-Core-Oligo47	GTAAGAACGGGTTGATGAAGGTATGTGCAAAATTCAACTT
Falcon-slider-Core-Oligo48	TCAAAATTTGTAAATCGTCGCTATTCCCTTAGAGTGAATTTATCAAAAGAACGCGAGAAAACTT
Falcon-slider-Core-Oligo49	tttttttCATAAATCAATATATGTGAGTCTTCGTTATAAGGAGA
Falcon-slider-Core-Oligo50	TTAAGACGAGTTAATTTCATCTTCTGACCTAAATTTAATGGTTTGttttttt
Falcon-slider-Core-Oligo51	tttttttAAATACCGACCGTGTGATAAAAATAAGAATAAACttttttt
Falcon-slider-Core-Oligo52	tttttttACTGTTTCTTTACATAGGTTGAGTATTATCTTttttttt
Falcon-slider-Core-Oligo53	CAAAATTTTAATTGGAGTTTATAAGTGTTTATTTCAAGAC
Falcon-slider-Core-Oligo54	ATGATGAAATTTCGCCAGTAATAAGAGAAGTCCAGACGACGACAATAAACAACAT
Falcon-slider-Core-Oligo55	CGTTATACCAGTATAACAACATGTAATTTAGGGCTAATGCAGAACGCGCCTGTTTATC
Falcon-slider-Core-Oligo56	tttttttACCGGAATCATAATTACTAGATAACAATACCAATTTG
Falcon-slider-Core-Oligo57	AGAATCGCTAGATAAGTCCTGAACAAGAAAAATAATATCCCATCCttttttt
Falcon-slider-Core-Oligo58	tttttttTAATTTACGAGCATGTAGAAAATCGGCTGTCTTTttttttt
Falcon-slider-Core-Oligo59	tttttttTTTTGTAAAAGATAACAGGAGAGTGAGATCGGttttttt
Falcon-slider-Core-Oligo60	ATGCTTACAAATTCCAGAGTCTGTATACATTGTTGACATA
Falcon-slider-Core-Oligo61	TCTGACGGGAGGTCTTTAGCGAACCTCCCGATTA
Falcon-slider-Core-Oligo62	TCGAGAACTTTTTATTGGCTTATCCGGTATTCTTTAT
Falcon-slider-Core-Oligo63	tttttttCCTTATCATTCCAAGAACGGGGCCATAAGTCCAACAA
Falcon-slider-Core-Oligo64	TAGCAAGCGTCTTTCCAGAGCCTAATTTGCCAGTTACAAAATAAAttttttt
Falcon-slider-Core-Oligo65	tttttttCAGCCATATTATTTATCCCAAAAACGATTTTTTGttttttt
Falcon-slider-Core-Oligo66	tttttttTCGACATCATTACGCAGACCCGTTAGTAACTAttttttt
Falcon-slider-Core-Oligo67	AATGGGTTGGAAGAGTTTCTGCGGGAAGACTCCTGTTAGGGAGTAA

Falcon-slider-Core-Oligo68	AGGAGCCGAAGCATGAGTATCTGCTCACAGCGACCGATGC
Falcon-slider-Core-Oligo69	TTCATCGTGAGAATAACATAAAAACATTAGACGGGAGAATGTTAAGCC
Falcon-slider-Core-Oligo70	ttttttTTTAACGTCAAAAATGAAAATAACAAAGTCAGAGGGTAATTGtttttt
Falcon-slider-Core-Oligo71	tttttttCGGAAACCAGTTTCTTACGAAGTCCGTGAAGAttttttt
Falcon-slider-Core-Oligo72	TGCAAGCGCAGGGACTGGTGACCTCAGGATGCTACTACCA
Falcon-slider-Core-Oligo73	GCGTATTCGAGCAGCGTGAGTAGCGACCAGGAGAACGGATGAAC
Falcon-slider-Core-Oligo74	CAATAATAACAATGAAATAGCAATGAAACGCAATAATAACAAAGAACT
Falcon-slider-Core-Oligo75	tttttAGCGCTAATATCAGAGAGATAGCCCTTTTTAAGAAAAGTAAGttttt
Falcon-slider-Core-Oligo76	tttttttGTTGAGCTTGAAACAGAGTAGGGAAACTGCGTttttttt
Falcon-slider-Core-Oligo77	GTGAAGAAAGAGCTTATCTCGGATTCAAGCACGGGTTGCA
Falcon-slider-Core-Oligo78	tttttCAGATAGCCGAACAAAGTTACCGCAGTATGTTAGCAAACGTAttttt
Falcon-slider-Core-Oligo79	tttttttTGGTAACACCATCGATGACCTTTTCCATGAATttttttt
Falcon-slider-Core-Oligo80	GGGAAAGAGGCAATGCATGACGAAAATTAACTCTCAGGCGTTCAGG
Falcon-slider-Core-Oligo81	ATAACCCAGGAATCATCAAACGCCTTACGAAGTGACGGTC
Falcon-slider-Core-Oligo82	GGCATGATAACGCAAAGACACCACTATTTTGTCACAATCAAAATATTG
Falcon-slider-Core-Oligo83	tttttGAAAATACATACATAAAGGTGGGTTTACCAGCGCCAAAGACAttttt
Falcon-slider-Core-Oligo84	tttttttTTATCAGTAAACAGAGCAGGAGGATCTGGAACttttttt
Falcon-slider-Core-Oligo85	GAAAAGTTGGAATGCGGCAGAGCAAACCAGCAGTACTCAC
Falcon-slider-Core-Oligo86	GTTGTCGAGTGTGGCGATCCGATAGATGAAATTACAGC
Falcon-slider-Core-Oligo87	ACGGAAATAGGTGAATTATCACCGTCACCGATAGCAAG
Falcon-slider-Core-Oligo88	tttttAAAGGGCGACATTCAACCGATATTTGGGAATTAGAGCCAGt
Falcon-slider-Core-Oligo89	tCTATATCTGCCACTCACGCCTGAACCACCAGGt
Falcon-slider-Core-Oligo90	CTTAATTGACTCCAACGTCAAAGGGCGAAAAAAAAGAAT
Falcon-slider-Core-Oligo91	GCGGATGGGCAACTAACAGTTGATTCCCAATGATACATCTCCCAA
Falcon-slider-Core-Oligo92	ATAAGAGGTCAGGGCGATGGCCCACTACGTGACCGATTTA
Falcon-slider-Core-Oligo93	TTAATTGCAGACTTCAAAAAAGATTAAGAGGAAAATATTCGTGTAGTTTAGAACTA
Falcon-slider-Core-Oligo94	GATTAGAGCCCAAATCAAGTTTTTTGGGGTCGAGGTGttttttt
Falcon-slider-Core-Oligo95	tCGGAAGCAAACTCCAATCAAAGCGTATTATAGTCAGAAGCAAACAGTTCCCAAACG
Falcon-slider-Core-Oligo96	GGCCGGCCCCTGTTTGGATAGGGTTGAGTGTTGAACGTGGCTGAATATAATt
Falcon-slider-Core-Oligo97	TGTAGATCTTCGCAAACCTGTTTAGCTATATTCAATTCACAGGGG
Falcon-slider-Core-Oligo98	CTAAAGGCATTGAATCTTTAGACTGGATAGCGCAACACTAGGTGCTCAGGTCAATG
Falcon-slider-Core-Oligo99	AATGACACGGGAAGAACCCTAAAGGGAGCCCACCATCAAGTACCT
Falcon-slider-Core-Oligo100	CTGGCGAACAGAAAACAAGTTTTGCCAGAGGGACGATAAATCATATCG
Falcon-slider-Core-Oligo101	AATCGTCACAGGGTGGGCCCTGAGAGAGTTGCGCGAAAATCCCAATAG
Falcon-slider-Core-Oligo102	TGGGCTATTACTAATATAACATCCAATAAATAGCAATATTGCCCC
Falcon-slider-Core-Oligo103	ACCTCATCTCATAACCTACATAACGCCAAAAGAGTCAGGAACGTCTAGCATATTGT
Falcon-slider-Core-Oligo104	CTTAGGCCTGCTTTGACACGCTGCGCGTAACAAAGGAACAACCAT
Falcon-slider-Core-Oligo105	TCTCAGGAAACCAAAAATTTAGGAATACCACAAATAAAACTTTGCCTA
Falcon-slider-Core-Oligo106	AATCATTCAACTCACAAGCTGCATTAATGAATTTGGGCGCAGGTCTGT
Falcon-slider-Core-Oligo107	GGGTTCGGAAGCCTCAATTATGACCCTGTAAAAGGATACGTGAAA
Falcon-slider-Core-Oligo108	TGCAACATCGTTGGGAACTGGCTCATTATACCGCTCATTCGTTAGCTATTCTAGCG
Falcon-slider-Core-Oligo109	GATACAGCGTTTTTATAGCTAAACAGGAGGCCTATGGTCGTAACT
Falcon-slider-Core-Oligo110	GCCGTTGGGAACTAACTCATTGTGAATTACCTAGAAACACGTGGTCGA
Falcon-slider-Core-Oligo111	GTATCAGATTCGTAATCAACATACGAGCCGGAAGTGAGCTCACGCCGT
Falcon-slider-Core-Oligo112	ACTTCAGGAAAATTTTATATATTTTAAATGCAAGGGTGCTTTCCC
Falcon-slider-Core-Oligo113	GACTAGAGAGTGAATAAACCGGATATTCATTAGGCGCAGAACATTGGGGCCTTTGA
Falcon-slider-Core-Oligo114	TGAATTTCCAAACTATAATTAACCGTTGTAGGAGAAGTCAGTGGT
Falcon-slider-Core-Oligo115	CCATGGTACAGAACGAGCTGACCTTCATCAAGCTGACCAACTAAGCCT
Falcon-slider-Core-Oligo116	GTCCACTTCTCGCACTATGATAAATGCACTTCAGCTCGAACACTCGCT
Falcon-slider-Core-Oligo117	ACTTAGTGAGAAAGGCCAAATCACCATCAATTGCCGGACCAGGTT
Falcon-slider-Core-Oligo118	GACATCCCCGGTCAATAAATCCGCGACCTGCTCTAAAACGCAGTCCTTTTGAATCC
Falcon-slider-Core-Oligo119	TGGCCCGAATTTACATTTGCAACAGGAAAAAAAGAACTCCGCTGT
Falcon-slider-Core-Oligo120	TGTACATCCTTTGAAAGATTTGTATCATCGCCAACACTCAACGGCTGT
Falcon-slider-Core-Oligo121	GGGCTTGGATGTGCGACTTGCCCTCTCTGTACTAACAATCTAGACCCC
Falcon-slider-Core-Oligo122	ATTGCATAGAGGGTAGTCATTGCCTGAGAGTTCGTAAACCAGGGT
Falcon-slider-Core-Oligo123	CCAGAAGAAAAGAGGCCTACGAAGGCACCAACCACCCTCATTCGCACCGTTCATGG
Falcon-slider-Core-Oligo124	GGTCCTCACAACAGTTAAAGCATCACCTTGCATGGATTCTTACGA
Falcon-slider-Core-Oligo125	ATTGTTGTTCTTTGACTTCCATTAAACGGGTAGAGGGTAGGTTAACGT
Falcon-slider-Core-Oligo126	AAGGGCAGGTCTCCATATACAAATATTCCATGATTCTGCATCGGTGCG
Falcon-slider-Core-Oligo127	CTCAACGAACTAGCATTGTACCCCGGTTGATATAAGCAAGGGAGA
Falcon-slider-Core-Oligo128	ACCCCAAGGCAGCGAAGGCTTGCAGGGAGTTATTGTATCGAAACCGGACAGAAAGT
Falcon-slider-Core-Oligo129	TTTCGCTCCGTAAAACATTGTTTGGATTATAGGCAAATACCCGAA
Falcon-slider-Core-Oligo130	CAATAGTGCAACGGCTCCCACGCATAACCGATGAATTTCTGGACCAGG
Falcon-slider-Core-Oligo131	TATGGTCCTGATACCGTTAGAGTCTGAGCAAAGGTGTCTTTATGGATC
Falcon-slider-Core-Oligo132	CTGTGGTCAATATTTAGTTAATATTTTGTTAATTTTTTGTTGTAG
Falcon-slider-Core-Oligo133	TCAAGTAAGTTTATCAAAAATCTCCAAAAAAAGACGTTAGCCTAAAGCGACTCAAG
Falcon-slider-Core-Oligo134	CATTCGAAAGCGATAGGAATAACCTTGCTTCATTTGCAATTTCAC

Falcon-slider-Core-Oligo135	ACTTCAGGTAAACAGCAGGAATTGCGAATAATTTTGCTAAGGCCCTAC
Falcon-slider-Core-Oligo136	GCTACATTAAATGCTGCCGTACTCAAACATCGAACATTGCGCTTGGCG
Falcon-slider-Core-Oligo137	GTGAGCTCAACCAATATTCCTGTAGCCAGCTCCGTCGGGGGCAAT
Falcon-slider-Core-Oligo138	GGATGTTGTAAATGAATTTTGTCGTCTTTCCAGGGATAGCTCTATCTAGAATCCAG
Falcon-slider-Core-Oligo139	CCAAATATGTAGGGCTAAAAGCCTGTTTAGTAAAACATAGCCCTT
Falcon-slider-Core-Oligo140	TGTAACCAACAACTTTCAGCCCTCATAGTTAGCGTAACACCGGAGTTA
Falcon-slider-Core-Oligo141	TGGAACTGACGGGGTTCTGGCATTCGCATCAAGCTTGTGAAGGGAAAG
Falcon-slider-Core-Oligo142	CAGCCTCTATTCTCCGCGGCGGATTGACCGTCATCGTAAGGTCAT
Falcon-slider-Core-Oligo143	CTACGCACAAGCCCAACAGAACCGCCACCCTCTTTTGCTCCTTCATGTAAAGAAAG
Falcon-slider-Core-Oligo144	AAGGCCCAATTACCGCTATTAAACCAAGTACCTCAACAAGAGGCG
Falcon-slider-Core-Oligo145	TCGGGGAATGAGTTTCTTAGTACCGCCACCCTCGAGAGGGTTTCGGTT
Falcon-slider-Core-Oligo146	CGTCTCGACCATCCTGGCAGTTAATCGAACAATCGCTATTAGCTTTCG
Falcon-slider-Core-Oligo147	TCCCATTTACCGTGCATGAGGGGACGACGACAGCTTTCCGGCAGT
Falcon-slider-Core-Oligo148	GTCGTGCGAGTACCAGGCTGAGACTCCTCAAGGTGTACTGTACGGATGCAAGACTA
Falcon-slider-Core-Oligo149	AAGGGTGAACACCCTGAGCAGCCTTTACAGAAGGAATCTATGTGG
Falcon-slider-Core-Oligo150	CGTACAATTTGATATACTATTATTCTGAAACATGCCTTGACTTCGTGC
Falcon-slider-Core-Oligo151	TCGTCACGAAACTCAAGCTAAACTGGAAAGCAGTTGTTCGCAGCGATC
Falcon-slider-Core-Oligo152	TAAGTATCCGGCACCGTCGCCATTCAGGCTGCTCTTCGATCTTGT
Falcon-slider-Core-Oligo153	TACATGCGGTAATAAGTTTTGATGATACAGGAGAGGTTGAGAAGATATCAGAAACA
Falcon-slider-Core-Oligo154	GAAATGCCTTACCGAAACCCACAAGAATTGATAACTGAGTCCAGA
Falcon-slider-Core-Oligo155	AGAATAGCGTAACAGTATTTACCGTTCCAGTAATATTCACACTCCATT
Falcon-slider-Core-Oligo156	AATGCTCGAACTGCTGAGGATATTGCGCTAACCAAAATCATTCGACTG
Falcon-slider-Core-Oligo157	GGGGGTTCCTATTACGAAAGGGGGATGTGCTTTCCCAGCATTCGC
Falcon-slider-Core-Oligo158	GCGAGCGAGGCAGGTCACCAGAACCACCACCAAATCAAAATGAATCATCCGTCATT
Falcon-slider-Core-Oligo159	CATCATCTCCTTATTACAGAAGGAAACCGAGAGCTATCAGGATGT
Falcon-slider-Core-Oligo160	TCGCGGATAAACAAATCACCCTCAGAGCCACCGGAACCGCGGCCTATA
Falcon-slider-Core-Oligo161	TCCAATTGAGTGAGCGCTGGGGATTTGACGCATGTGCTGGGGGTGAAG
Falcon-slider-Core-Oligo162	GGGAAGCATCACGACGACGGCCAGTGCCAAGAACCAACGCAATAA
Falcon-slider-Core-Oligo163	GCAGCCACTCACCGGAGGTCATAGCCCCCTTACAGACATCCATCAGAA
Falcon-slider-Core-Oligo164	TCGTTCAAATTCATATGCAACATATAAAAGATAAGACTGCCTCGA
Falcon-slider-Core-Oligo165	TTGCGGAACTCCCTCACAGACTGTAGCGCGTTACCATCGAGTAGCACC
Falcon-slider-Core-Oligo166	AAATGCGCTTGTTGTGGACTTGTGCAAGTTGCAGGTTCGAGTGAAGAC
Falcon-slider-Core-Oligo167	GCAACACAAGTTCAGGGATTAATGAAAGATGGTTAGCGTT
Falcon-slider-Core-Oligo168	ATAGAAGACGAATTAATATTCAGACGCCTGGTCACTGCGTAATGGTAG
Falcon-slider-Core-Oligo169	GCCTTCAGATTGAGGAAACGTCACCAATGAATTCATCGG
Falcon-slider-Core-Oligo170	ATTACCATCTTGAGCCTGAGGGAGGGAAGGTATAGAAATGAGTGT
Falcon-slider-Core-Oligo171	tCAAAATCACCATAGCAGCACCGTAATCAGTAGCGACAGAttttttt
Falcon-slider-Core-Oligo172	ttttttttCACCCTCATGCGTATTCTTTATTATTCGCATTttttttt
Falcon-slider-Core-Oligo173	TGCAAACGTTGTACATCTTTTCATGAGCCGCCGCCTGGCGCCAGCAGC
Falcon-slider-Core-Oligo174	CATTTTCACCAGAGCCACCACCACCCTCAGAGCCGCCAGACGAT
Falcon-slider-Core-Oligo175	tttttttATCAAGTTTGCCTTTAGCGTGAGCCGCCACCttttttt
Falcon-slider-Core-Oligo176	tttttttGGGTAACGCCAGGGTTGCAAGGCGATTAAGTTttttttt
Falcon-slider-Core-Oligo177	tttttttCTCAGAACCGCAAATCCTCATTAAAGCCAGAttttttt
Falcon-slider-Core-Oligo178	tttttttGGCGATCGGTGCGGGCCGCAACTGTTGGGAAGttttttt
Falcon-slider-Core-Oligo179	ATTGACAGCCAGGCAAAGCGCCATCTTCTGGTGCCGGAAAAGAAGGAT
Falcon-slider-Core-Oligo180	TGGCCTTGAGCGTCATACATGGCTTTTAACGGGGTCAGTGAAAGTA
Falcon-slider-Core-Oligo181	tttttttATGGAAAGCGCAGTCTCTGAGCCCGTATAAACAGTTAATGttttttt
Falcon-slider-Core-Oligo182	tttttttAGATCGCACTCCAGCCAGTATCGGCCTCAGGAttttttt
Falcon-slider-Core-Oligo183	TAGCAGTTTCTGCGATTAGCGGGGAGAGCCACCACACAAATGGGACCT
Falcon-slider-Core-Oligo184	TTAAGAGGCGGATAAGTGCCGTCAGAACCGCCACCCTTAGGAAC
Falcon-slider-Core-Oligo185	tttttttCCCCCTGCCTATTTCGGAACAGTATAGCCCGGAATAGGTGttttttt
Falcon-slider-Core-Oligo186	tttttttTTGGTGTAGATGGGCGAATGGGATAGGTCACGttttttt
Falcon-slider-Core-Oligo187	tttttttTATCACCGTACTCAGGAGGTGTCACCAGTACAAACTACAAttttttt
Falcon-slider-Core-Oligo188	tttttttGTGAGCGAGTAACAACTTCATCAACATTAAATttttttt
Falcon-slider-Core-Oligo189	CATTTTCATAATTCGCGTCTGGCCGGAACGCCATCAAAAAAGGCTCCA
Falcon-slider-Core-Oligo190	CCATGTACCGTAACGATCTAAAGTTTTCTGTATGGGATAATTTTTT
Falcon-slider-Core-Oligo191	tttttttCGCCTGTAGCATTCCACAGACAACAGTTTCAGCGGAGTGAttttttt
Falcon-slider-Core-Oligo192	tttttttTTTGTTAAATCAGCTCAAATTCGCATTAAATTttttttt
Falcon-slider-Core-Oligo193	AAATAAACAATTGGGAGCCTTTAAAAGGCCGCTTTTCATAGTCAATGC
Falcon-slider-Core-Oligo194	CACGTTGGCTTGCTTTCGAGGTATATTCGGTCGCTGAAGACAGC
Falcon-slider-Core-Oligo195	tttttttGAATAGAAAGGAACAACTAATTGATACCGATAGTTGCGCCttttttt
Falcon-slider-Core-Oligo196	tttttttAAAACAGGAAGATTGTAATCAGAAAAGCCCCAttttttt
Falcon-slider-Core-Oligo197	tttttttGACAATGACAACAACCATCGACAGAGGCTTTGAGGACTAAttttttt
Falcon-slider-Core-Oligo198	tttttttAATCGATGAACGGTAACTGGAGCAAACAAGAGttttttt
Falcon-slider-Core-Oligo199	GGGATCGTTACAAAGGCTATCAGGCTATTTTTGAGAGATCCCATGTTA
Falcon-slider-Core-Oligo200	ATCGGAACAAATACGTAATGCCAAAAAGAATACACTAATGATAAAT
Falcon-slider-Core-Oligo201	tttttttAGACTTTTTCATGAGGAAGTCCCCAGCGATTATACCAAGCttttttt

Falcon-slider-Core-Oligo202	tttttttCTAGCTGATAAATTAAATGATATTCAACCGTTttttttt
Falcon-slider-Core-Oligo203	CTTACAGTCGGAGAGCCGGAACGACCCAAATCAACCCCTCTAGAAGTA
Falcon-slider-Core-Oligo204	TGTGTCGCATAAGGGAACCGAAAGTAATCTTGACAAGAGGCTTG
Falcon-slider-Core-Oligo205	tttttttGCGAAACAAAGTACAACGGAGAGGACAGATGAACGGTGTAttttttt
Falcon-slider-Core-Oligo206	tttttttGTAGGTAAAGATTCAAAATGCCTGAGTAATGTttttttt
Falcon-slider-Core-Oligo207	tttttttCAGACCAGGCGCATAGGCTGGTAGTAAATTGGGCTTGAGAttttttt
Falcon-slider-Core-Oligo208	tttttttGCCTTTATTTCAACGCTACTTTTGCGGGAGAAttttttt
Falcon-slider-Core-Oligo209	ACAAAGCTCGGTTGTACCAAAAACGAGCATAAAGCTAAATGAATTACG
Falcon-slider-Core-Oligo210	CCCTGACGTATGCGATTTTAAGAAGAAAAATCTACGTTTTCAACTA
Falcon-slider-Core-Oligo211	tttttttTGGTTTAATTTCAACTTTAAGGAACAACATTATTACAGGTttttttt
Falcon-slider-Core-Oligo212	tttttttAGAATTAGCAAAATTACATACAGGCAAGGCAAttttttt
Falcon-slider-Core-Oligo213	AGGAGCATGTAGTCATAGTAAGAGTCCAATACTGCAATAATGGTCGGA
Falcon-slider-Core-Oligo214	ATGCAGACTCGTTTACCAGACGGGTAATAGTAAAATGCCCCTCA
Falcon-slider-Core-Oligo215	tttttttAGAAAGATTCATCAGTTGAGTAGCGAGAGGCttttttt
Falcon-slider-Core-Oligo216	tttttttAGCTGAAAAGGTGGCATTTCATTTGGGGCGCGttttttt
Falcon-slider-Core-Oligo217	tttttttTTTTGCAAAAGGAGAATGACCATAAATCAAAttttttt
Falcon-slider-Core-Oligo218	tttttttTTTAGTTTGACCATTATCTGCGAACGAGTAGAttttttt
Falcon-slider-Core-Oligo219	ATCGTCATGTTTCATTCCATATAAAGTACGGTGTCTGGAAAGCCCGAATCCTTTTG
Falcon-slider-Core-Oligo220	AATGCTTTAAAGCGGATTGCATCAATATCGCGTTTTAATTCGAGCTCAGGTCAG
Falcon-slider-Core-Oligo221	tttttttAATCAGGTCTTTACCCTGACAACCAGACt
Falcon-slider-Core-Oligo222	tGCTGTAGCTCAACATGTTTTAAATATCTTAGAG
Falcon-slider-Miniscaf-Oligo1	ACTATTGGGGGCCGGCCTTGGGAGGATCTACACGACAGATTAGTTCTA
Falcon-slider-Miniscaf-Oligo2	AACTACACGCCTTTAGATGGTTGGTGTCATTCGTTTGGGTTCGCCAGT
Falcon-slider-Miniscaf-Oligo3	TACAGACCTTGACGATTCCCCTGTATAGCCCACAGAATGGCATTGACC
Falcon-slider-Miniscaf-Oligo4	TGAGCACCGATGAGGTAGTTACGGGCCTAAGCGATATGATCCTGAGAG
Falcon-slider-Miniscaf-Oligo5	TACGGCGTGGAATGATTGGGGCAACCGAACCCTTTATGGTACAATATG
Falcon-slider-Miniscaf-Oligo6	CTAGACGTATGTTGCAACCACTGGCTGTATCTAGGCAAACCAACGGCA
Falcon-slider-Miniscaf-Oligo7	GAGCGAGTGTCTGATACTTTCACGCCTGAAGTTGATTGGCCGCTAGAA
Falcon-slider-Miniscaf-Oligo8	TAGCTAACCTCTAGTCACAGCGGGAAATTCATCGACCACTACCATGGC
Falcon-slider-Miniscaf-Oligo9	AGGGGTCTAAAGTGGACGGGAAAGCACTAAGTGAGGAGTCTCAAAGGC
Falcon-slider-Miniscaf-Oligo10	CCCAATGTGGGATGTCTCGTAAGTCGGGCCAAGGCTTAGGATGTACAT
Falcon-slider-Miniscaf-Oligo11	ACGCACCGACCAAGCCCAACCTGGTATGCAATAAGTTGAAGGATTCAA
Falcon-slider-Miniscaf-Oligo12	AAGGACTGTCTTCTGGTTCGGGTTGAGGACCACAGCCGTACAACAATA
Falcon-slider-Miniscaf-Oligo13	CGATCCATACTGCCCTTACCCTGGTCGTTGAGGTCTTGAACCATGAAC
Falcon-slider-Miniscaf-Oligo14	GGTGCGAACTTGGGGTGTGAAATGAGCGAAAACGTTAACCACTATTGC
Falcon-slider-Miniscaf-Oligo15	ACGCCAAGCGGACCATATCTCCCTGACCACAGTATGTCAAACTTTCTG
Falcon-slider-Miniscaf-Oligo16	TCCGGTTTTTACTTGAAAGGGCTTTCGAATGCCTGGTCCCCTGAAGTT
Falcon-slider-Miniscaf-Oligo17	TCTTTCCCTAATGTAGCCTACAACGAGCTCACGCATCGGTCTTGAGTC
Falcon-slider-Miniscaf-Oligo18	GCTTTAGGCAACATCCCGCCTCTATATTTGGGTAGGGCCTGGTTACAG
Falcon-slider-Miniscaf-Oligo19	TCGAAAGCTCAGTTCCAATTGCCCAGAGGCTGTGGTAGTACTGGATTC
Falcon-slider-Miniscaf-Oligo20	TAGATAGAGTGCGTAGCCACATATGGGCCTTTAACTCCGTTCCCCGAA
Falcon-slider-Miniscaf-Oligo21	CGATCGCTGTCGAGACGATGACCTAAATGGGATGCAACCCCTTTCTTT
Falcon-slider-Miniscaf-Oligo22	ACATGAAGCGCACGACTCTGGACTCACCCTTAACCGAAAATTGTACGT
Falcon-slider-Miniscaf-Oligo23	TCAGTCGAACGTGACGAACTGCCGGATACTTAGACCGTCATAGTCTTG
Falcon-slider-Miniscaf-Oligo24	CATCCGTACGCATGTAACATCCTGGCATTTCGCACGAAGGCTATTCTT
Falcon-slider-Miniscaf-Oligo25	TCTTCACCCCGAGCATTACAAGATGAACCCCCGTGAGTACTGTTTCTG
Falcon-slider-Miniscaf-Oligo26	ATATCTTCTCGCTCGCTCGAGGCAGATGATGAATGGAGTATCCGCGAT
Falcon-slider-Miniscaf-Oligo27	CGTCTTCACCAATTGGAGCGAATGTGCTTCCCCTACCATTAATGACGG
Falcon-slider-Miniscaf-Oligo28	ATGATTCAGTGGCTGCACACTCATTGAACGATATAGGCCTTCCGCAAC
Falcon-slider-Purple-Handle1	GAGACGATGTTGACCTTAACCttGGCACAGACAATATTTAAGCGTAAGAATACGTt
Falcon-slider-Purple-Handle2	GCTACTCACTCAGATAGGGTAttAGAAGTATTAGACTTTATACATTTGAGGATTTt
Falcon-slider-Purple-Handle3	ACTATATCGGTCGGAAACTGCttCGCCTGATTGCTTTGAGAAACAATAACGGATTt
Falcon-slider-Purple-Handle4	GTTTCTCCAAAAGCACTAGGGttTATATAACTATATGTACCGGCTTAGGTTGGGTt
Falcon-slider-Purple-Handle5	CGATCCTGATGTACGAAAGTCttAAGGTAAAGTAATTCTTATAAAGTACCGACAAt
Falcon-slider-Purple-Handle6	CGTGTAGCCAATTAGACTGACttGAAGCCTTAAATCAAGACTTGCGGGAGGTTTt
Falcon-slider-Green-Handle1	TTGAACCCCCCCTTAGTTACATTTCTTTAATGCGCGAACGGCCAACAGAGATAGAATTTATTTACGGTGGA
Falcon-slider-Green-Handle2	ttTTGAACCCCCCCTTAGTTACATTTCGCCATTAAAAATAGTCACACGACCAGTACGTCTGAATGAACCTC
Falcon-slider-Blue-Handle1	CACCTTCGCTTCTACATACAGTTATCCTACAACTAATAGATTAGCTGATACCAGATATAG
Falcon-slider-Blue-Handle2	tCACCTTCGCTTCTACATACAGTTGTTTGAAGGTTATCTAAAATGGTCAGTTCTTCTGAA
Falcon-slider-Red-Handle1	CACACTTGCTATACCGTCATCTTAAGTTACAAAATCGCGCAGAGGCGAAATATACAGTAACAGTA
Falcon-slider-Red-Handle2	tCACACTTGCTATACCGTCATCTTCATTTCAATTACCTGAGCAAAAGAAGTGCGTAGATTTTCAG
Falcon-slider-Green-Handle3	TCTCGACACAAATCTTCCTGCTTCCAATCGCAAGACAAATCATAGGTCTGAGAGAGAAACGACAGTGTCAG
Falcon-slider-Green-Handle4	ttTCTCGACACAAATCTTCCTGCTTTTTCAAATATATTTTCTGAGAAGAGTCAATAATCCTTGATCATATG
Falcon-slider-Blue-Handle3	TCTTCACGCCAAACTATCTCGTTGTTCACAGAGGCATTTTCGAGCGTCGTCTATATGATG
Falcon-slider-Blue-Handle4	tTCTTCACGCCAAACTATCTCGTTAACAACATATTTAACAACGCAGCCAACGCGCACTCA

Falcon-slider-Red-Handle3	CCTACTGACTTTATCCACCGATTGTTGCTATTTTGCACCCAGCTACAATTAAGAACGCGAGGCGT
Falcon-slider-Red-Handle4	tCCTACTGACTTTATCCACCGATTCCTGAATCTTACCAACGCTAACGAGCAAATCAGATATAGAA
Falcon-Purple-Clip-Strand1	AGATTTTCAGCCGGTTAAGGTCAACATCGTCTCGTACTCAATT
Falcon-Purple-Clip-Strand2	ATGACAAGATGGTACCCTATCTGAGTGAGTAGCCCATTAACAT
Falcon-Purple-Clip-Strand3	AGAGTCCTCGTTGCAGTTTCCGACCGATATAGTCATCCTAATT
Falcon-Purple-Clip-Strand4	ATTCCTAATTCGCCCTAGTGCTTTTGGAGAAACGATCCATTAT
Falcon-Purple-Clip-Strand5	AAGTGTTCCAGGGACTTTCGTACATCAGGATCGCACCTTATTA
Falcon-Purple-Clip-Strand6	CTGTAAGTTAGAGTCAGTCTAATTGGCTACACGGCTCTAACTA
Falcon-Purple-Clip-Removal-Strand1	**AATTGAGTACGAGACGATGTTGACCTTAACCGGCTGAAAATCT**
Falcon-Purple-Clip-Removal-Strand2	**ATGTTAATGGGCTACTCACTCAGATAGGGTACCATCTTGTCAT**
Falcon-Purple-Clip-Removal-Strand3	**AATTAGGATGACTATATCGGTCGGAAACTGCAACGAGGACTCT**
Falcon-Purple-Clip-Removal-Strand4	**ATAATGGATCGTTTCTCCAAAAGCACTAGGGCGAATTAGGAAT**
Falcon-Purple-Clip-Removal-Strand5	**TAATAAGGTGCGATCCTGATGTACGAAAGTCCCTGGAACACTT**
Falcon-Purple-Clip-Removal-Strand6	**TAGTTAGAGCCGTGTAGCCAATTAGACTGACTCTAACTTACAG**
Falcon-Red-Clip-Strand1	TAAAAGGGGACGttttttGATGACGGTATAGCAAGTGTGGTAGATTCAT
Falcon-Red-Clip-Strand2	TGATTGCAGAGCttttttTCGGTGGATAAAGTCAGTAGGCTAGATGTAT
Falcon-Green-Clip-Strand1	ATCGTAATTAGGTTTTTTTGTAACTAAGGGGGGGTTCAACTTTACCTAA
Falcon-Green-Clip-Strand2	GAATGAGAGTCGTTTTTTTGCAGGAAGATTTGTGTCGAGAGTAATGAAGA
Falcon-Blue-Clip-Strand1	CAAGGTTGTACGTTTTTTCTGTATGTAGAAGCGAAGGTGGATACATTGA
Falcon-Blue-Clip-Strand2	AGACCATGTGAGTTTTTTCGAGATAGTTTGGCGTGAAGATATGTAGATC
Falcon-Red-Clip-Removal-Strand1	**ATGAATCTACCACACTTGCTATACCGTCATCCGTCCCCTTTTA/3BioTEG/**
Falcon-Red-Clip-Removal-Strand2	**ATACATCTAGCCTACTGACTTTATCCACCGAGCTCTGCAATCA/3BioTEG/**
Falcon-Green-Clip-Removal-Strand1	**TTAGGTAAAGTTGAACCCCCCCCTTAGTTACACCTAATTACGAT/3BioTEG/**
Falcon-Green-Clip-Removal-Strand2	**TCTTCATTACTCTCGACACAAATCTTCCTGCCGACTCTCATTC/3BioTEG/**
Falcon-Blue-Clip_Removal-Strand1	**tCAATGTATCCACCTTCGCTTCTACATACAGCGTACAACCTTG/3BioTEG/**
Falcon-Blue-Clip_Removal-Strand2	**GATCTACATATCTTCACGCCAAACTATCTCGCTCACATGGTCT/3BioTEG/**

DNA sequences for staple strands and interacting handles common to both SH-v2 and SH-v3

Green-handle-1	GTACCACGACAATAAACAACAACCAATCAGTCTTTCCTTATCATTCTTTTCATACAGAATCAAGTTTGCCCAGTttTAACCCT
Green-handle-2	GCATTAACGCGCCTGTTTATCAATATCCCAACCAAGTACCGCACCGGTCATTAGCGCGTTTTCATCAGCCAttTAACCCT
Green-handle-3	TTAACAACAGTACCTTTTACACAGATGAAAGCCGTTTTTATTTTCTTGCTATTACCAACGCTAACGAGCATTAAttTAACCCT
Green-handle-4	CAACACGGATTCGCCTGATTAAGAAATTACCGCGCCCAATAGCAGGGAGGTTAATTTGCCAGTTACAAGAGGGttTAACCCT
Green-handle-5	TACAATACAAAATCGCGCAGATATCAAAAAAGGCTTATCCGGTAGCGAGGCATTTATCCCAATCCAAGACAttTAACCCT
Green-handle-6	AGAAATCAATTACCTGAGCAAATTAACTCCAGTGCCAAGCTTTATCCAGGGTTTTGTTTAACGTCAAAAAATAGttTAACCCT
Green-handle-7	AAATAAAACATCAAGAAAACTCAGTAAATCATGCGTATTAACCAATGTGCTGTTTACAGAGAGAATAACACCAt
Green-handle-8	GAAATAACAATTTCATTTGAATTGTGCAATGAAAGATGGCAGACCTTCGCTCGCATTAGACGGGAGAAGGTt
Green-handle-9	ATTTCGAAACAGTACATAAATGAAGACGCCAGAAATAGAAGAATTCAACTGTTTGAACAAAGTCAGAGGGTATGt
Green-handle-10	GCGAGATAACCTTGCTTCTGTGTTGTGAAATAAAAATGCGCCGCAGGCAAAGTATCAGAGAGATAACCAACTGt
Green-handle-11	CGCAATAATAACGGAATACCCAAAAGCACAAGAATTGAGTTAAGCCCAATAATAAGAGGAAAt
Green-handle-12	CGAACAAAGTTACCAGAAGGAAACCGAGCAAGAAACAATGAAATAGCAATAGCTATCTTATAGCt
Blue-handle-13	TCAAAGGGTATCAGGGCGATGGCCTCCTTTGCCTAATAGATTAGAGCCATATCTGGTCAGTTGGttCTTACCA
Blue-handle-14	GAGTCCACACCCAAATCAAGTTTCTTTACATTTGAGGATTTAGAATGCTGAACCTCAAATttCTTACCA
Blue-handle-15	TTAGAGTCCGTAAAGCACTAAATCACCACACCACTATGGTTGCTTTGACAGCAGCAAATGAAAAttCTTACCA
Blue-handle-16	TGCAAGGAGCCCCCGATTTAGAGCGGCAAGTGTGCTTTCCTCGTTAGAACACCGCCTGCAACAGttCTTACCA
Blue-handle-17	TGCTGATAGCGAACGTGGCGAGAAGAAAGCAACAGGAGGCCGATTAGATAAAACAGAGGTttCTTACCA
Blue-handle-18	GTATTATCTGTTATCAAGCACTGCAACCAGTTGGAACGGTACGCCAGACCATTAAAAATACCGAttCTTACCA
Blue-handle-19	AGATGATGGAGTTTCTGCGGCAGTACTGGAAATTTATAATCAGTGAGGTAATGCGCGAACTGATt
Blue-handle-20	GTCTTCACGTTAGTAACTATCGATTATCTCTCTGTCCATCACGCACAGACAATATTTTTGt
Blue-handle-21	TAACGCTTTATTACGGGGTTGGAGACTCAACGAATACTTCTTTGATTACTTCTGACCTGAAAGCt
Blue-handle-22	CAAAGGAGATGCAGGTGAGTATCTTGCGTGTTGCCTGAGTAGAAGAACAAGGGACATTCTGGCCt
Blue-handle-23	AATCAAAACAGAGCCACCACCGGATGAGGAAGGGGATCGTCACCCTCAAATGACAACAACCATCttTACTCCA
Blue-handle-24	AGCCCCCTCCGCCACCCTCAGAAACAGAGGTCGGAACGAGGGTAGTAAACAGCTTGATACttTACTCCA
Blue-handle-25	TTGCACCCCACCACCCTCAGAGCCCGTTCCAGAGTGTACTGGTAATAAGGTTTATCAGCTTGCTttTACTCCA
Blue-handle-26	TTGAAGCCACCAGAGCCGCCGCCACCAGAATGGTGCCTTGAGTAACAGAAAGGCTCCAAAAGGAttTACTCCA
Blue-handle-27	GTTTTAGCGAGGCAGGTCAGACGATATTCATAATGCCCCCTGCCTATAATTTTTTCACGTttTACTCCA
Blue-handle-28	TTCCCAGTGTGGGAACAAACGGCGCATTAAATTTCTGAAACATGAAAGATAGAAAGGAACAACTttTACTCCA
Blue-handle-29	CAAGGCGAGATAGGTCACGTTGGTGTCTGGCCACTCCTCAAGAGAAGGAACAACTTTCAACAGTt
Blue-handle-30	ATTACGCCTAACCGTGCATCTGCACCAATATTTTGCTCAGTACCAGTAAATGAATTTTCTt
Blue-handle-31	GGGAAGGGCGACAGTATCGGCCTCATTAAATTCGAGAGGGTTGATATAGATCTAAAGTTTTGTCt
Blue-handle-32	CGCCATTCCAGCCAGCTTTCCGGCTTGTAAACAGGTGTATCACCGTACTTCCACAGACAGCCCTt
Blue-handle-33	ACACGACCAGTAATAATCAAACTATCGGCCTTGCTGGTAATATCCAGGCAGATTCACCAGTCt
Blue-handle-34	TGGATTATTTACATTGAACAATATTACCGCCAGCCATTGCAACAGGAAGCTCAATCGTCTGAAAt
Blue-handle-35	TACAACGCCTGTAGCATCAGGAGGTTTAGTACCGCCACCCTCAGAACGTCACCAGTACAAACt
Blue-handle-36	CGTAACACTGAGTTTCCGCCACCCTCAGAACCGCCACCCTCAGAGCCAATAGGAACCCATGTACt
Red-handle-1	AAAAGTTTGAGTAACAATGTAGAATGTTCAGCTAATGCAGTTCGAGCCAGTAATAAGAGAATATAAAttTCACCTA
Red-handle-2	CAAAGAAACCACCAGGAAAAATAACAATAGATAAGTCAACGCCAACATGTAATTTAGGCAGAGttTCACCTA
Red-handle-3	ATCATATTCCTGATTATTTAACGTTCGGGAGAAACAATAAGTAGGGCTTAATTGAGAATCGCCATATTtTCACCTA
Red-handle-4	TCATCAATATAATCCTCAGAAATAGCTTTGAATACCAAGTATTCTTACCAGTATAAAGCCAACGCTttTCACCTA
Red-handle-5	CTTCTGAATAATGGACCTACCAGGCGAATTATTCATTAAGCCTGTTTAGTATCATATGCGTTAttTCACCTA
Red-handle-6	GAGCAGGCAATGCATGTGAGCGAAAAGAAGATGATGAAACAGAATAAACACCGGAATCATAATTACTttTCACCTA
Red-handle-7	ACGCAGACCTTTTCCAGGAACTTAAAAATTAATTACATTTACCGACCGTGTGATAAATAAGGCGTTt
Red-handle-8	TCGATTGTGCTGGAAGTCGGACTTACCTTTTTTAATGATCTTCTGACCTAAATTTAATGGTTTt
Red-handle-9	AAAGAAACCAGCAATAAGATGAACCAATATATGTGAGTGAAAAACTTTTTCAAATATATTTTAGTTAt
Red-handle-10	CCAGGAGAACGAGGATCCACTCATTAAATCGTCGCTATTAGCAAATCCAATCGCAAGACAAAGAACt
Red-handle-11	AATACGTAATGCCACTGCTCAACAATTAGAGAGTACCTTTCCCGAAAGACTTCAAATATCGCGTTTTttCCCATTA
Red-handle-12	AAAACGAAAGAGGCATTAGAGCAAGAGGTCATTTTTGAGCGGATTGCATCAAAAAGATTAAGAttCCCATTA
Red-handle-13	CACTCATCTTTGACCCCGAACTGACAGACCAGGCGCATAGGTCTTTACCCTGACTATTATAGTCAGAttCCCATTA
Red-handle-14	AGCGCGAAACAAAGTAACGAGGCGTCAAGAGTAATCTTGAAAAACGAGAATGACCATAAATCAAAAttCCCATTA
Red-handle-15	CATCGCCTGATAAATTCCGCGAATTACCCAAATCAACGAATCCCCCTCAAATGCTTTAAACAGttCCCATTA
Red-handle-16	TTTGAGAGATCTACAATTCTAGCTTTCAGTGAATAAGGCTCCAATACTGCGGAATCGTCATAAATATTttCCCATTA
Red-handle-17	TGCCTGAGAGTCTGGAGTCAAATCCACCAGAACGAGTAGTGTAATAGTAAAATGTTTAGACTGGATt
Red-handle-18	ATGAACGGTAATCGTAGATTCAGGTTTAATTTCAACTGGCTTTTGCAAAAGAAGTTTTGCCAGt
Red-handle-19	TCATATGTACCCCGGTTTAAATGCACCTTATGCGATTTTAACCAGACGACGATAAAAACCAAAATAGt
Red-handle-20	CCCCAAAAACAGGAAGAGGATAAATACCAGTCAGGACGTTAGTAAGAGCAACACTATCATAACCCTt
Red-handle-21	CTGATATTAATTTTCCCTTAGAATCCTTGAAAACATTTGGGTTATATAACTATATGTAAATGt
Red-handle-22	TTAGGAGCGATAGCTTAGATTAAGACGCTGAGAAGAGTGAGAGACTACCTTTTTAACCTCCGGCt
Red-handle-23	GGCATGGGAAGAAAAATCTACGTTAATAAAACGAACATACATAACGCCAAAAGGAATTACGAt
Red-handle-24	TGCAGTAACGGAACAACATTATTACAGGTAGAAAGATAGATTTAGGAATACCACATTCAACTAAt
Purple-handle-1	tttttttCCTGTTTGATGGTGGCCAGCAGGCGAAAATtttttGGCTGAAAATCT
Purple-handle-2	tttttttTTATCTAAAATATCTAGGAATTGAGGAAGGtttttCCATCTTGTCAT

Purple-handle-3	tttttttttAATTCTGTCCAGACGGACAAAAGGTAAAGTtttttttAACGAGGACTCT
Purple-handle-4	tttttttttACCATCGATAGCAGCAACGTCACCAATGAAtttttttCGAATTAGGAAT
Purple-handle-5	tttttttttAGGCTTGCAGGGAGTTATATTCGGTCGCTGtttttttCCTGGAACACTT
Purple-handle-6	tttttttttCCAGACCGGAAGCAAGAGCTTCAAAGCGAAtttttttTCTAACTTACAG
Core-staple-1	TCAGGGTTCTGCTGGATGAACGGGGAGTATTAATCTGTCG
Core-staple-2	ttttttGCCGGAAAACCCTGAACCACCAttttttttttGGCTATATCTGATTGCGCTAACttttttttttAGTAGGGAAAC
Core-staple-3	GAGAAGCCTTTttttttttttATTTCAACGCAATTGTATAAGCttttttttttAAATATTTAAAACCGCTTCTGGttttt
Core-staple-4	GCAGCAAGCGGTCCACGCTGGTTTGCCTTCCGAAATCGGCAAA
Core-staple-5	TTGCCCTTCACCGCCTGGCCCTGAGAAAGAATAGCCCGAGAT
Core-staple-6	TTCTTTTCACCAGTGAGACGGGCAACAAAGATTGGGCGTTATC
Core-staple-7	GCGGTTTGCGTATTGGGCGCCAGGGTGGTGTCTTGTCTCCA
Core-staple-8	CATTAATGAATCGGCCAACGCGCGGGGTGTTTATGTAGATGA
Core-staple-9	CTTTCCAGTCGGGAAACCTGTCGTGCCGTCGGCATACAAATAT
Core-staple-10	CTCACATTAATTGCGTTGCGCTCACTAGTCTAATGAAGACA
Core-staple-11	TAAAGCCTGGGGTGCCTAATGAGTGATGTGCGAGAAATGACT
Core-staple-12	CCACACAACATACGAGCCGGAAGCATATATTATCACGAGTACG
Core-staple-13	TCCTGTGTGAAATTGTTATCCGCTCACCCTCTCTGTACAAA
Core-staple-14	tttttttttGAGATGATAAATGCAGGGTTTTGTTTTATGttttttttt
Core-staple-15	CAAATCAACAGTTGAATTAGGAGCACTAACAACCGAACGT
Core-staple-16	ATCAAACCCTCAATCAGTCAATAGATAATACAAACAATTC
Core-staple-17	ATCTAAAGCATCACCTCCGCTACAGGGCGCGTCGCCGCGC
Core-staple-18	TGCCACGCTGAGAGCCGAGCACGTATAACGTAGCGGTC
Core-staple-19	GAGGCGGTCAGTATTAATCAGAGCGGGAGCTAGAAAGGAG
Core-staple-20	ACGAACCACCAGCAGAAAAGGGATTTTAGACATCTTGTTG
Core-staple-21	AGCCCTAAAACATCGATCCTGAGAAGTGTTGCAACGAA
Core-staple-22	AATGGCTATTAGTCTTCCACCGAGTAAAAGAGGGATGGGA
Core-staple-23	GTAAGAATACGTGGCAAATTAACCGTTGTAGCAGCAGCGT
Core-staple-24	AACAGAGATAGAACCGTAATAACATCACTTGAGCTTGA
Core-staple-25	tttttttttTACCTACATTTTGACAAACGCTCATGGAAAttttttttt
Core-staple-26	tttttttttTCAAAATCATAGGTCTCAATAGTGAATTTAttttttttt
Core-staple-27	AGCACCATTACCATTAGCAAGGCCGGAACCGTAATCAGTAGCG
Core-staple-28	TTTGGGAATTAGAGCCAGCAAAATCACTTTAGCGTCAGACTG
Core-staple-29	AGGTGAATTATCACCGTCACCGACTTGTTTTATCCTGAATCTT
Core-staple-30	AAGGTAAATATTGACGGAAATTATTCGTCTTTCCAGAGCCT
Core-staple-31	AAAGGGCGACATTCAACCGATTGAGGAATAAACAGCCATATT
Core-staple-32	AAAATTCATATGGTTTACCAGCGCCAAAATAAGAAACGATTTT
Core-staple-33	CGGAATAAGTTTATTTTGTCACAATCATGAAAATAGCAGCC
Core-staple-34	GGCAACATATAAAAGAAACGCAAAGACATAAAAACAGGGAAG
Core-staple-35	TTAGCAAACGTAGAAAATACATACATAAATTAACTGAACACCC
Core-staple-36	GCATGATTAAGACTCCTTATTACGCAGTAATTGAGCGCTAA
Core-staple-37	tttttttttAAGAAAAGTAAGCAGACCGAAGCCCTTTTTttttttttt
Core-staple-38	GCCCACGCATAACCGATAAAGGCCGCTTTTGCTTTCCATT
Core-staple-39	CGATAGTTGCGCCGACGCAGCGAAAGACAGCACTTTGAGG
Core-staple-40	TTCGAGGTGAATTTCTCTTTTGATGATACAGGTAAGCGTC
Core-staple-41	GCCTTTAATTGTATCGTTTTAACGGGGTCAGAAAGCGC
Core-staple-42	TGAAAATCTCCAAAAATGCCCGTATAAACAGTCAAACAAA
Core-staple-43	AAAGGAATTGCGAATAATTTCGGAACCTATTAGTGAGCGA
Core-staple-44	TTCAGCGGAGTGAGATATTAAGAGGCTGAGTTCCTGTA
Core-staple-45	GTATGGGATTTTGCTAATTAGGATTAGCGGGGGGAACGCC
Core-staple-46	GTCTTTCCAGACGTTAGGCGGATAAGTGCCGTTTTGTTAA
Core-staple-47	CATAGTTAGCGTAACAGTATAGCCCGGAATGTTAATAT
Core-staple-48	tttttttttGGGATAGCAAGCCCACCACCCTCATTTTCAttttttttt
Core-staple-49	AATTCACTCCAACAGGTCAGGTGTTTTAAAAAGTACGGTGTCTGG
Core-staple-50	GGAAGAATTGCTCCTTTTGATTTAATTGCAACAGTTGATTCCCA
Core-staple-51	AGCAAACAGATGAACGGTGTACCAACTTTGATTTAGTTTGACCAT
Core-staple-52	ATCAGGCTGGCTGACCTTCACAGACGGTAATGGTCAATAACCTG
Core-staple-53	TTCAGCAAGAACCGGATATTCCCTGCTCCTTTGGGGCGCGAGCT
Core-staple-54	TCATTGTAACAAAGCTGCTCAGATAAATTTTCTACTAATAGTAGT
Core-staple-55	AGCGTTGCCCTGACGAGAAAACCATCAATAAATCATACAGGCAA
Core-staple-56	AGGGGAAATTGGGCTTGAGATAAAGGGTGAATTAAGCAATAAAG
Core-staple-57	CGAGATTAATCATTGTGAATTAATGCCTGTAAATCGGTTGTACCA
Core-staple-58	CGTTTAGAACTGGCTCATTAAATTTTTATGTAATACTTTTGCGG

DNA sequences specific to SH-v3

Miniscaf-strand-1	CGGGTGTAGCTTGATAAAACTGCGCGTACGTCATATAGGC
Miniscaf-strand-2	GGAAGCAGTTTTTAACCCAGGCTTGTTTGTCGTATGTGGAACGGCCT
Miniscaf-strand-3	CATCCGCCGAGTCATCTGAATTTGCGTGCTACAGAATTGAAGCGTAG
Miniscaf-strand-4	TGGGCGGCTCGATTCCATAATCAAGACAGCCTTTCTGCACCACTAAT
Miniscaf-strand-5	TACTCAAAGTTGCGTTTATGCACCGGTTCATTGACGTAGCCCTCAGT
Miniscaf-strand-6	AGAAAAGTTTAGCCGTGGCCCATCACCTGTGTCTGCTTCTATTTCGCA
Miniscaf-strand-7	CAACCCGTTACTTTATTTCGCCACTGTTACCAGGCCGGAT
Miniscaf-strand-8	GCCGTCGTTGTAGCGTCCAGACCTCCAACCGGTATAGGAAAGTTAAT
Miniscaf-strand-9	GAGTATCCGCTGTCTGTGCAGGCTGACGAACTAACATCGAATTAGGG
Miniscaf-strand-10	TCACTCTCGTAGGGACGCCCATGGTCGAGATACATGTAGTGAACCAA
Miniscaf-strand-11	AGCATAGAGATACGCAGGCCAGGTTCTGCCATCACCACTAACATCTG
Miniscaf-strand-12	GAATCGGGTCACAAACAAACACTTCGGCCTCAGCGGTGAGTTTTTTTC
Miniscaf-strand-13	TGGTTCTTTACTGGGCGGACTTTACGTTCACGAGCGAATT
Miniscaf-strand-14	CAGTCACCTACACATAAGTTGGAGACACCTAGGGAGCACGGCCATAC
Miniscaf-strand-15	CAAGCGGGTGAAAATGAGCGTCCCCTAGTCCACAACTCTTGTAGAAG
Miniscaf-strand-16	AACGATGGCTTGCTCCGCACAGGTCAAAGCATGGTCTTGTTTCATAT
Miniscaf-strand-17	AGGTCAGGGAGAGACTTGTCCCGAAATCGTGGTCCTGGGAGATAGAA
Miniscaf-strand-18	ACAGCTGTCTGACTGCTTTCACGATCCAATCTAGTGTTCTGACGTGGG
Miniscaf-strand-19	CCTCCTGCACTTGTTGTCCAATTGGAACGCTCACAGTAGA
Miniscaf-strand-20	CAAAAGAGGAACCAGATGATGCATATTGCGCCAGGTTTCCGTGTAGC
Miniscaf-strand-21	CGGGCCAACGCTCAAAAAAGTCCACCGATAATAACACGCTCTTCCTA
Miniscaf-strand-22	ATGAATCACGTTTGCCATTGGAGTCGGTCCCGGAGTACATGTCATTC
Miniscaf-strand-23	GCAGCTATAGAACAGGCCAGAGATCAGTCAGAGGTGGACTTTTCCGG
Miniscaf-strand-24	GAGGGTGGGGACAGACACTATAAAGCTCGTCAAAGTGGGATTGCCAAC
Miniscaf-strand-25	CTAGCGTAGAAATCAGGTTTAAGCGCGCGTACCTCAAGTG
Miniscaf-strand-26	CAAGCCCGCCTGTCTTCCTCGCCAGGGTATTATAACAGTACAATCGA
Miniscaf-strand-27	GCCAAGTGTACAAATGCAGCATAGTGTAGATCCCGAGCTACCCTCGT
Miniscaf-strand-28	GGTTTCTTCATTTTTTTAACGCGCAATCTTACGACAGGCCGCCGAGA
Miniscaf-strand-29	GGAACGGGGATGGAGCGGAGAATTTACCAATGTGACAAGCCTAACCA
Miniscaf-strand-30	ACTATTGGGGGCCGGCCTTGGGAGGATCTACACGACAGATTAGTTCTA
Miniscaf-strand-31	GAACGGTATCAGGGAGCGATATGACGAAAGCTTACCCCAG
Miniscaf-strand-32	ACATCTGAATACAGCATTGGCCAGTGTGCAAATGTTACGCGATGGGA
Miniscaf-strand-33	CCCGCGTCGTCTTGGTCTTTAAGCTAAAGCGACTTCCCCATATTGTT
Miniscaf-strand-34	GATGGCTGCGTCTACTAGCCGATTAGTGCGAGATTCTAGGGTGGAAG
Miniscaf-strand-35	TAGGTCCATCCAGATCCCATTGGTTTATCCTTACGTCGTAGAGCCCG
Miniscaf-strand-36	AACTACACGCCTTTAGATGGTTGGTGTCATTCGTTTGGGTTCGCCAGT
Core-staple-SH-v3-1	CCTATATGACGTACGCATGCTGTAACGAAGGCACCAACCTACTAAAGATGGCGAAA
Core-staple-SH-v3-2	TTAAAAACAAGGGAACCCAGCGATTATACCAAGTCTCTCGACGGCCCCTAATT
Core-staple-SH-v3-3	TAGCACGCTAGCCGGACAACGGAGATTTGTATTAAATCCTGCCTGCAC
Core-staple-SH-v3-4	GAATCGAGTTCAACCGAGGCTATCAGGTCATGCCAGCTAGAGTGACAGATGTT
Core-staple-SH-v3-5	ATGAACCGCGGAGACAGCAAACAAGAGAATCGATCAAAAACCTGGCCT
Core-staple-SH-v3-6	ACGGCTAACATATATTTGATAATCAGAAAAGTTTGTTACCCGATT
Core-staple-SH-v3-7	TCCGGCCTGGTAACAGCTTTTTCAACCGCCTCCCTCAGAGTATTAGCGAAAGTCCG
Core-staple-SH-v3-8	CGCTACAAGAATTTACGCCACCAGAACCACCTTAAATCGTGACTGCTTCTACA
Core-staple-SH-v3-9	GTTCGTCACATTAAAGGCATTGACAGGAGGTTGAACCTCCGGACGCTC
Core-staple-SH-v3-10	TCCCTACGTTCATCAAGATTGACCGTAATGGTTAAGTTCATCGTTTTCTATCT
Core-staple-SH-v3-11	TGGCAGAATAATTCGCGTAGATGGGCGCATCGAGCTGGCGCGGGACAA
Core-staple-SH-v3-12	GTTTGTGAAAATTCGCAGGAAGATCGCACTCGCCATTCACAGCTG
Core-staple-SH-v3-13	ATTCGCTCGTGAACGTTTTGCCATCCAAGAACGGGTATTAATCCTAATAATTGGAC
Core-staple-SH-v3-14	ATGTGTAGAAGATTAGATCGTAGGAATCATTGCGTAGATCTTTTGTAGGAAGA
Core-staple-SH-v3-15	GGACTAGGCGACTTGCAGCAAATCAGATATAGTTATTTGCGGACTTTT
Core-staple-SH-v3-16	GAGCAAGCGGGTAACGTATTCGCATTCACCCCAGAGAGGATTCATCCGGAAAA
Core-staple-SH-v3-17	CACGATTTAAAGGGGGACAGTTCAGGGATTAAGTTGCCAGTCTCTGGC
Core-staple-SH-v3-18	GCAGTCAGAGGCTGCGACAGCGCAACACAGCGTGTGGCCCACCCT
Core-staple-SH-v3-19	CTACTGTGAGCGTTCCTTACGAGCTTATCATTTTGCGGAAGACAACTCCTTAAACC
Core-staple-SH-v3-20	CTGGTTCCTTTTCAGGTCAGATGATGGCAATACGCTGCGGGCTTGACGAGGGT
Core-staple-SH-v3-21	TTATCGGTACGTAAAAGATTGTTTGGATTATACGGGCGCTTATGCTGC
Core-staple-SH-v3-22	GCAAACGTGTTCGAAGACGACTGGGGATTTGGTCCGTGAGAAACCTGGTTAGG
Core-staple-SH-v3-23	CTGACTGAGAGGATCTTGAATTGGTAACACCAGTAAGCGTATTCTCCG
Core-staple-SH-v3-24	GTCTGTCCGATCCGATCATCAAACGCCGCGAAACAGCACCAATAG
Core-staple-SH-v3-25	ACTTGAGGTACGCGCGGTATTAAACACTACGTGAACCATCTATTAAAGCATATCGC
Core-staple-SH-v3-26	AGACAGGCGCGTAACCGGAACCCTAAAGGGAGTTTATACAGATGTAACAATAT
Core-staple-SH-v3-27	ATCTACACAGGGCGCTTTGACGGGGAAAGCCGCCGTTTAGCTTAAAGA
Core-staple-SH-v3-28	AAAAATGAAAGACGGAACTGGTGACCTGGAAACCGTACAGCCATCCGGGCTCT

Core-staple-SH-v3-29	ATTGGTAAATTGCTAATAATCGAACAAGACCCAGCGATGCCCAATGGG
Core-staple-SH-v3-30	GCCGGCCCAAATCAAAGTCAATGGGTTCAGGAGTGAGAGTGTAGT
Core-staple-SH-v3-31	GTATTAGATTTGGGGTCGAGGTGCTGAGCAAACGTAACAT
Core-staple-SH-v3-32	CCTAGGGAAAGGAGGGAAGACTCCTTACTGTTCTAGAATC
Core-staple-SH-v3-33	CGAAGGTGCATCATTACGCATCGCGTGAAAATACCCAAAC
Core-staple-SH-v3-34	CTGAACAAAAGGAGCGGAATTATCTTAATGCGACTGTTAT
Core-staple-SH-v3-35	TGCTAGAAAGGGTGTGAAGCGGCATTCGCCATGCCTGTCG
Core-staple-SH-v3-36	GGCATTTTTCATCGAGAACAAGCATATACAGTGAAACCTG
Core-staple-SH-v3-37	TGTAGAACTTCTAAAAACGACGGCTCAGGCACTGTACTCC
Core-staple-SH-v3-38	GCGGGCCTATCATTGATTCAGCATCTGGTCGTTCCCACTT
Core-staple-SH-v3-39	CAACGGCTCCGCCACCCTCAGAGCAGCTACAAGTGCTCCC
Core-staple-SH-v3-40	CCGCCTTGATTGGTCGGATTCTCCCACGACGTCAAGACCA
Core-staple-SH-v3-41	ATTTTTTACAGTTTGAGGGGACGACGATCGGTAGAACACT
Core-staple-SH-v3-42	CGGATGGCAAAGAATACACTAAAAATACATGGTCCTATAC
Core-staple-SH-v3-43	AGACGAAATGTGTGGGTAGCTATTGTAACAACCTACATGT
Core-staple-SH-v3-44	GTAGGTAAAAAACTAGCATGTCAAATCAGCTCCTCACCGC
Core-staple-SH-v3-45	AAGTTTCATTCCATATTGAATATAGCAGTTTT
Core-staple-SH-v3-46	ATTCTGCGAACGAGTAGAAAGAGGCCACATAC
Core-staple-SH-v3-47	TAGATACATTTCGCACAATCATTGCTTCCCTACGCTT
Core-staple-SH-v3-48	TTTAGCTATATTTTCAATGTTACTAAATTCAG
Core-staple-SH-v3-49	GAAAAGGTGGCATCAAAATGCCGGTGCAGAAA
Core-staple-SH-v3-50	AGCATTAACATCCAATATGATACCGCCCAACTGAGGG
Core-staple-SH-v3-51	GGCAAAGAATTAGCAAAGAAAGGCGTGCATAA
Core-staple-SH-v3-52	CCTCAGAGCATAAAGCAGTAATGTAGAAGCAG
Core-staple-SH-v3-53	AAAACATTATGACCCGAACCCTACTTTTC
Core-staple-SH-v3-54	CGCCGGTTCCTTCTCTTGGCAATGCCTGAACGAGCTCGGG
Core-staple-SH-v3-55	TGCATCTTCGTACCTGCTCCTAGTTTGCGGGACTTGTCAC
Core-staple-SH-v3-56	tttttttttGCAGACACCGACATGAGTGCCGTGATTTCTTTttttttt
Core-staple-SH-v3-57	tttttttttGAGGTCGAACGAAATTACACGTCCTTCTCAAACGC
Core-staple-SH-v3-58	TAGGAGCGAGCATGTACTTAACCCCTTTGAACGCGTGTTA
Core-staple-SH-v3-59	TATATCAGCATACCAACGGTCCTCCTCTTAAGGTCCACCT
Core-staple-SH-v3-60	tttttttttACGTTTAGCTTCCACGGTCATTCACCTTGTTGttttttt
Core-staple-SH-v3-61	tttttttttGCATACCTGAAGGGGAACCAAGCTACTTCTACttttttt
Core-staple-SH-v3-62	AGCAACACCACGGAACATAGGTGGCCGTTCACCTTATTTCGATCCAGC
Core-staple-SH-v3-63	TTAATCGTATCACCCGAACGAAGGGACTCTTACACGTCTTAGCC
Core-staple-SH-v3-64	TCATGAACAGACTTGAGCATTGTTTATCCTGGGAGATGGGTCGCGCTG
Core-staple-SH-v3-65	GCTTGGAAGGTATCACTCGCCAATATACTTATTTCGGCAGACCCTGTC
Core-staple-SH-v3-66	AGACGGACCTGCAAATTGGATTAGCATACAACTTGCAGACGATT
Core-staple-SH-v3-67	GACGTAACCCACCGTTTGGCAAGACTAACGGGAAGGGAATTCCCGTCA
Core-staple-SH-v3-68	AGTGCAAGAATTGGAGATGGCAAGCATAATGCAGCACAACTTTCCCCT
Core-staple-SH-v3-69	ATCAACCTGTCAGCTACCTGGTACTGTCAGGAGACAACTAGAAA
Core-staple-SH-v3-70	CGAGTTCTGTATTGTCGGGCTTTGGTTAGCAGAGAGTTGT
Core-staple-SH-v3-71	CATCCCTCACCATCGCACTTGTCCGTTGCTTCCCCAGGAC
Core-staple-SH-v3-72	tttttttttCCTCCTCCCGTAGGTGGGTCACACCATCAGGAttttttt
Core-staple-SH-v3-73	CGTACCGTACGATCTATGTCTTCGAATATCCGGTCGCCTCAGTGTGAT
Core-staple-SH-v3-74	ATGGGTTTATCTCCGACAAGCGTTAATGGTGGGATCGGCTGAACTGAC
Core-staple-SH-v3-75	GCAATTTAGTCTTGGAGAGCCCGGTTTGGAGACTCCCTAGGTCGGT
Core-staple-SH-v3-76	GAAGGACCTGGGTAAGCTGACTCACTCTGTGACGATGTTA
Core-staple-SH-v3-77	TGGAGTGTTACCCAGAACCTGTTGAGGACGGCGTCATTCAGTCAGACC
Core-staple-SH-v3-78	TTAACAGTGAAGGACAGTGGGAGTGTGCATCAACGGGAAGGTCCAGTT
Core-staple-SH-v3-79	CGAAAACCCTCATGGAAAGGTCTGAGAGAGCATTGTTGGTCTCCGG
Core-staple-SH-v3-80	ATCGAGCTAGTCACACGTCGTCGTCGTAGAAAAGTGGTGA
Core-staple-SH-v3-81	TCAACGACCTGTCGAGAAAGCCTCAGCTGGGTCCAGACCTCCTTCTCT
Core-staple-SH-v3-82	TGCAAGAGAGGAAGGACGTTCAAATCTCCTCTACAAACTTAGTAGCGG
Core-staple-SH-v3-83	AGTTTTGGCCGTAGTGGTATTTGGGACAGGTGACTATGAAAAGCCG
Core-staple-SH-v3-84	tttttttttTACCTTGGAGATGGCGGAGAGCATCGCAGAGGttttttt
Core-staple-SH-v3-85	tttttttttTCAGCCTCCAGTTGCATGTTGCTTCATCTCCAttttttt
Core-staple-SH-v3-86	GTGGAGTGGTAATAGCATTCTACCCTCACAGTCAATTCTG
Core-staple-SH-v3-87	CCGTTCAATTAAGAGGCGCTAGACGGCTTCTGCTACGTCA
Core-staple-SH-v3-88	tttttttttGGGCTTTCTACTCCATGTCGCATGGCGATAATttttttt
Core-staple-SH-v3-89	tttttttttAAGGCCTTTGTCAAATAGCGCCAACAATGCATttttttt
Core-staple-SH-v3-90	TGGGCACCTACTAGCATGACTACAGTACACGGATACATGTAGAACGCT
Core-staple-SH-v3-91	TCTCCGCATACCAGGTACCATCTCTGGGAGAGCTAAGGGACAAA
Core-staple-SH-v3-92	CAGAATATCCAAACCCATCGTAACAACCACGGTCTAGTGTCAACGTTC
Core-staple-SH-v3-93	GTTATGTATAGCTGACTACTGCACGATCGATCTACTTGATTAGAGGCG
Core-staple-SH-v3-94	TCAGGGGACAAGGCACAAACCAGACTCTCAACTCACAAGACCAT

Core-staple-SH-v3-95	TAGCAGCTGGTTAGCAGCTCATGGGAGTCGTGGGCTCCATCCTTAGTC
Core-staple-SH-v3-96	ATCAGTCGGGATAACGGCCCGCATAGTTCCCACCTCTCTGGTTGTCCA
Core-staple-SH-v3-97	TATCTTAGTGTGAAATGCGAGATTTAGCAGCTCAAGATCCTCCA
Core-staple-SH-v3-98	TCTGTACCGTAAAAAAAATACGGGAATTGCA
Core-staple-SH-v3-99	TCTGTACCTAGAGGCGGTCCCACAGAGGCAA
Core-staple-SH-v3-100	AGCCTCCACCTAGCCTTCTCGACACAAATCTTTTGCGAT
Core-staple-SH-v3-101	ATCAAGCTGCAAGTGTGAGGTCAGGCGGAATG
Core-staple-SH-v3-102	GACAAACAGACATGCTAGGGCCTTGTTTATGAAGGAATAG
Core-staple-SH-v3-103	ATGACTCGAACAATTCAACGTACAATAGCGGAATGAACGC
Core-staple-SH-v3-104	GGCTGTCTCTAGCGCTAATCCAACACCTGTCAGATGGGAA
Core-staple-SH-v3-105	ACGCAACTCTACAAAAAAAAACGACACCATCACAGCTCCT
Core-staple-SH-v3-106	ACACAGGTTCTAGGCACTTACCGACCAGACTCCTCTGCCT
Core-staple-SH-v3-107	TAAAGTAACTCAAGTACCGATGTTTGCAGCACGGTATAACACCCGAGGCCGTT
Core-staple-SH-v3-108	CGGTTGGATCAGGGAGAGAAGCATTGACTCACATCCTATCAGCCTGGG
Core-staple-SH-v3-109	AGACAGCGCAACTGCTGGCTGAAGGACACTAACGTACCGCGGATGATTAGTGG
Core-staple-SH-v3-110	ATCTCGACTGAACGTTATGTCGTCACTACTGAAGACAATGTGATTATG
Core-staple-SH-v3-111	GCGTATCTCTATGTCACTTGGGTTGGAATACATGGATCTTGAGTATGCGAAAT
Core-staple-SH-v3-112	TGAGGCCGGAACGTTAGATTCCCGCTAAATCCTCCTGAATGATGGGCC
Core-staple-SH-v3-113	CCCAGTAACTTCGAGGTGAGCGACATTTGACGCCGGAACGGGTTGATTAACTT
Core-staple-SH-v3-114	TAGGTGTCCTAAACCCTTCCCGACGGTTGTCCTTCAGCCTGGTCTGGA
Core-staple-SH-v3-115	ATTTTCACGACAATCGCTCACTGGACTTGACACGGATAGATACTCTTGGTTCA
Core-staple-SH-v3-116	TGCTTTGAGCGCAATTGGGTACTACTAGCCGCCACACCTCCATGGGCG
Core-staple-SH-v3-117	GTCTCTCCCTCGAATCTACCTCGAAGCACATCATATTGCTATGCTGAAAAAAA
Core-staple-SH-v3-118	AGATTGGAGGTTCTTAGCTTTCTGGGTGCATAGTGTGCAAAAGTGTTT
Core-staple-SH-v3-119	AACAAGTGCAGAGGTTGTCTCGTGTGCATTCCAAATGAAGAACCAGTATGGCC
Core-staple-SH-v3-120	GCGCAATAGCCTTGGTTGACTGGTGTTGAGTTCGGTGCGATCCAACTT
Core-staple-SH-v3-121	TTGAGCGTCTTTCTTGTTCAGCAGTTAACGGTATTGCGCCGCTTGATATGAAA
Core-staple-SH-v3-122	GGGACCGACCCTTATTTCCTAATGACGGAACCCGATTCCACCTGTGCG
Core-staple-SH-v3-123	CTGTTCTAATTCCATTTTAACCCGTCTTGACCGATTACCTGACCTCCCACGTC
Core-staple-SH-v3-124	TGACGAGCGTGTGCTCCGACCAGTTCCTCAGAGACTTAGCTCGTGAAA
Core-staple-SH-v3-125	TGATTTCTGCCACATATGAGGACCTCTTGACAACTCTCCAGGAGGGCTACACG
Core-staple-SH-v3-126	AATACCCTCATTGTTACTACTGCATCCTTTGGCTTACATTTGCATCAT
Core-staple-SH-v3-127	ATTTGTACGTAGCTCACCGATTCCACATAGGGTGGTCATGGCCCGGAATGACA
Core-staple-SH-v3-128	TAAGATTGTCATTGTCTTGTGCACAATTCGATGTGAACTACTCCAATG
Core-staple-SH-v3-129	CTCCATCCGAGGGATAGCAACTCAAAGGCAGGCAAGCCTAGCTGCGTTGGCAA
Core-staple-SH-v3-130	TGTAGATCAGAATGCCCCTTTCACAAGAAGGCCACCAAAGTTTATAGT
Core-staple-SH-v3-131	TCCCTGATGGGAATAATGTGCTGTTCTGATCTCACTGAACGCTAGTCGATTGT
Core-staple-SH-v3-132	TTGCACACCACAGCAAGGCTTAGGATCCCGTAATTTTGGCGGCGAGGA
Core-staple-SH-v3-133	CCAAGACGTTGCAAGTTTGGAAATGGACCCGCGAGCATACTTGGCTCTCGGCG
Core-staple-SH-v3-134	TCGCACTACCTGGAATTCTGGCTTCACCATCATGGGTCGTCGCGTTAA
Core-staple-SH-v3-135	ATCTGGATAAGGGACTCTGAGGGAACGAGCTTGACGGACCGTTCCTAGAACTA
Core-staple-SH-v3-136	GAATGACAACGGTGTCGAATGGTTCCGCATTCGAACTATCCTCCCAAG
Core-staple-SH-v3-137	TTAATTCCGGTATGACTGGGGTAAGCTTTCGTAACGTGGACTCCAACGATCCCTTATAAATCAAGAGTTttCTCTAAC
Core-staple-SH-v3-138	GTGCTCTTTAGAGAGACCGTTCTCCCATCGTCCAGTTTGGAACAAAGGGTTGAGTGTTGTGCTGAttCTCTAAC
Core-staple-SH-v3-139	GATATGCTCTCCTTCCTGGCCAATGCTGTATTAATGAGTATCAATGAGAATGTTGTGCAGATCCGGTTTttCTCTAAC
Core-staple-SH-v3-140	AATTACACTTTAAGCCGGGGAAGTCGCTTTAGCTGAAACGACATACATTGCAGACATCACGAAGGAGAGttCTCTAAC
Core-staple-SH-v3-141	CATCGAGAGTCTTCGACGCGGGCTTCCACCTCTTTACATAAACATAGGTATAGATATAGAAGCTGttCTCTAAC
Core-staple-SH-v3-142	GCCCAAGTACCGTTTGATCGGCTAGTAGACGCTCAAACATCGGGTTGATCCATGAAGGTTTATAGCCCGttCTCTAAC
Core-staple-SH-v3-143	GCAACCACATGACAGAACGACGTAAGGATAAACAGAGTCTGTAGTGTCAATCCCCATTCTGCAAGCTAAt
Core-staple-SH-v3-144	GAACGTAGGTGTAGCGGACCTAACTGGCGAGCTGAATTTCGCGTCGATACCGTGCAAAATAAGTGt
Core-staple-SH-v3-145	CCGGGAAACCTCGTAGCCAACCATCTAAAGGCTCGGTTTTGTAAAAGAGTGGAAACGATACTTGCAATTt
Core-staple-SH-v3-146	GCATATGATGTttttttttttCTGACGCTGGCATTCGCATACATATAGATGATTAACTGTTt
Core-staple-SH-v3-147	GCTCGAATTCGTAATCATGGTCATAGACCCAATATTACATAACAATCCTCGCACTCGACCGAt
Core-staple-SH-v3-148	GAGTCACAGGAGAATGGATCCCCGGGTCGGGGATTTATTTTATCTGAACTCGCTACGGCCTTCCt

DNA sequences specific to SH-v2

Core-staple-SH-v2-1	ATGCTGTAACGAAGGCACCAACCTACTAAAGA
Core-staple-SH-v2-2	AAGGGAACCCAGCGATTATACCAAGTCTCT
Core-staple-SH-v2-3	TAGCCGGACAACGGAGATTTGTATTAAATCCT
Core-staple-SH-v2-4	TTCAACCGAGGCTATCAGGTCATGCCAGCT
Core-staple-SH-v2-5	CGGAGACAGCAAACAAGAGAATCGATCAAAAA
Core-staple-SH-v2-6	CATATATTTGATAATCAGAAAAGTTTGTTA
Core-staple-SH-v2-7	CTTTTTCAACCGCCTCCCTCAGAGTATTAGCG
Core-staple-SH-v2-8	GAATTTACGCCACCAGAACCACCTTAAATC

Core-staple-SH-v2-9	CATTAAAGGCATTGACAGGAGGTTGAACCTCC
Core-staple-SH-v2-10	TTCATCAAGATTGACCGTAATGGTTAAGTT
Core-staple-SH-v2-11	TAATTCGCGTAGATGGGCGCATCGAGCTGGCG
Core-staple-SH-v2-12	AAATTCGCAGGAAGATCGCACTCGCCATTC
Core-staple-SH-v2-13	TTTGCCATCCAAGAACGGGTATTAATCCTAAT
Core-staple-SH-v2-14	AAGATTAGATCGTAGGAATCATTGCGTAGA
Core-staple-SH-v2-15	CGACTTGCAGCAAATCAGATATAGTTATTTGC
Core-staple-SH-v2-16	GGGTAACGTATTCGCATTCACCCCAGAGAG
Core-staple-SH-v2-17	AAAGGGGGACAGTTCAGGGATTAAGTTGCCAG
Core-staple-SH-v2-18	AGGCTGCGACAGCGCAACACAGCGTGTGGC
Core-staple-SH-v2-19	TTACGAGCTTATCATTTTGCGGAAGACAACTC
Core-staple-SH-v2-20	TTTTCAGGTCAGATGATGGCAATACGCTGC
Core-staple-SH-v2-21	ACGTAAAAGATTGTTTGGATTATACGGGCGCT
Core-staple-SH-v2-22	GTTCGAAGACGACTGGGGATTTGGTCCGTG
Core-staple-SH-v2-23	GAGGATCTTGAATTGGTAACACCAGTAAGCGT
Core-staple-SH-v2-24	GATCCGATCATCAAACGCCGCGAAACAGCA
Core-staple-SH-v2-25	GTATTAAACACTACGTGAACCATCTATTAAAG
Core-staple-SH-v2-26	GCGTAACCGGAACCCTAAAGGGAGTTTATA
Core-staple-SH-v2-27	AGGGCGCTTTGACGGGGAAAGCCGCCGTTTAG
Core-staple-SH-v2-28	AAGACGGAACTGGTGACCTGGAAACCGTAC
Core-staple-SH-v2-29	ATTGCTAATAATCGAACAAGACCCAGCGATGC
Core-staple-SH-v2-30	AAATCAAAGTCAATGGGTTCAGGAGTGAGA
Core-staple-SH-v2-31	GTATTAGATTTGGGGTCGAGGTGCTGAGCAAA
Core-staple-SH-v2-32	CCTAGGGAAAGGAGGGAAGACTCCTTACTGTT
Core-staple-SH-v2-33	CGAAGGTGCATCATTACGCATCGCGTGAAAAT
Core-staple-SH-v2-34	CTGAACAAAAGGAGCGGAATTATCTTAATGCG
Core-staple-SH-v2-35	TGCTAGAAAGGGTGTGAAGCGGCATTCGCCAT
Core-staple-SH-v2-36	GGCATTTTTCATCGAGAACAAGCATATACAGT
Core-staple-SH-v2-37	TGTAGAACTTCTAAAAACGACGGCTCAGGCAC
Core-staple-SH-v2-38	GCGGGCCTATCATTGATTCAGCATCTGGTCGT
Core-staple-SH-v2-39	CAACGGCTCCGCCACCCTCAGAGCAGCTACAA
Core-staple-SH-v2-40	CCGCCTTGATTGGTCGGATTCTCCCACGACGT
Core-staple-SH-v2-41	ATTTTTTACAGTTTGAGGGGACGACGATCGGT
Core-staple-SH-v2-42	CGGATGGCAAAGAATACACTAAAAATACATGG
Core-staple-SH-v2-43	AGACGAAATGTGTGGGTAGCTATTGTAACAAC
Core-staple-SH-v2-44	GTAGGTAAAAAACTAGCATGTCAAATCAGCTC
Core-staple-SH-v2-45	AAGTTTCATTCCATATTGAATATA
Core-staple-SH-v2-46	ATTCTGCGAACGAGTAGAAAGAGG
Core-staple-SH-v2-47	TAGATACATTTCGCACAATCAT
Core-staple-SH-v2-48	TTTAGCTATATTTTCAATGTTACT
Core-staple-SH-v2-49	GAAAAGGTGGCATCAAAATGCCGG
Core-staple-SH-v2-50	AGCATTAACATCCAATATGATA
Core-staple-SH-v2-51	GGCAAAGAATTAGCAAAGAAAGGC
Core-staple-SH-v2-52	CCTCAGAGCATAAAGCAGTAATGT
Core-staple-SH-v2-53	AAAACATTATGACCCGAACCCT
Core-staple-SH-v2-54	AACGTGGACTCCAACGATCCCTTATAAATCAAGAGTTttCTCTAAC
Core-staple-SH-v2-55	TCCAGTTTGGAACAAAGGGTTGAGTGTTGTGCTGAttCTCTAAC
Core-staple-SH-v2-56	AATGAGTATCAATGAGAATGTTGTGCAGATCCGGTTTttCTCTAAC
Core-staple-SH-v2-57	CTGAAACGACATACATTGCAGACATCACGAAGGAGAGttCTCTAAC
Core-staple-SH-v2-58	TCTTTACATAAACATAGGTATAGATATAGAAGCTGttCTCTAAC
Core-staple-SH-v2-59	TCAAACATCGGGTTGATCCATGAAGGTTTATAGCCCGttCTCTAAC
Core-staple-SH-v2-60	CAGAGTCTGTAGTGTCAATCCCCATTCTGCAAGCTAAt
Core-staple-SH-v2-61	GCTGAATTTCGCGTCGATACCGTGCAAAATAAGTGt
Core-staple-SH-v2-62	TCGGTTTTGTAAAAGAGTGGAAACGATACTTGCAATTt
Core-staple-SH-v2-63	GCATATGATGTttttttttttCTGACGCTGGCATTCGCATACATATAGATGATTAACTGTTt
Core-staple-SH-v2-64	GCTCGAATTCGTAATCATGGTCATAGACCCAATATTACATAACAATCCTCGCACTCGACCGAt
Core-staple-SH-v2-65	GAGTCACAGGAGAATGGATCCCCGGGTCGGGGATTTATTTTATCTGAACTCGCTACGGCCTTCCt

Path diagrams exported from cadnano v1:
DC-v1-1 (left), DC-v1-2 (middle), DC-v1-3 (right)

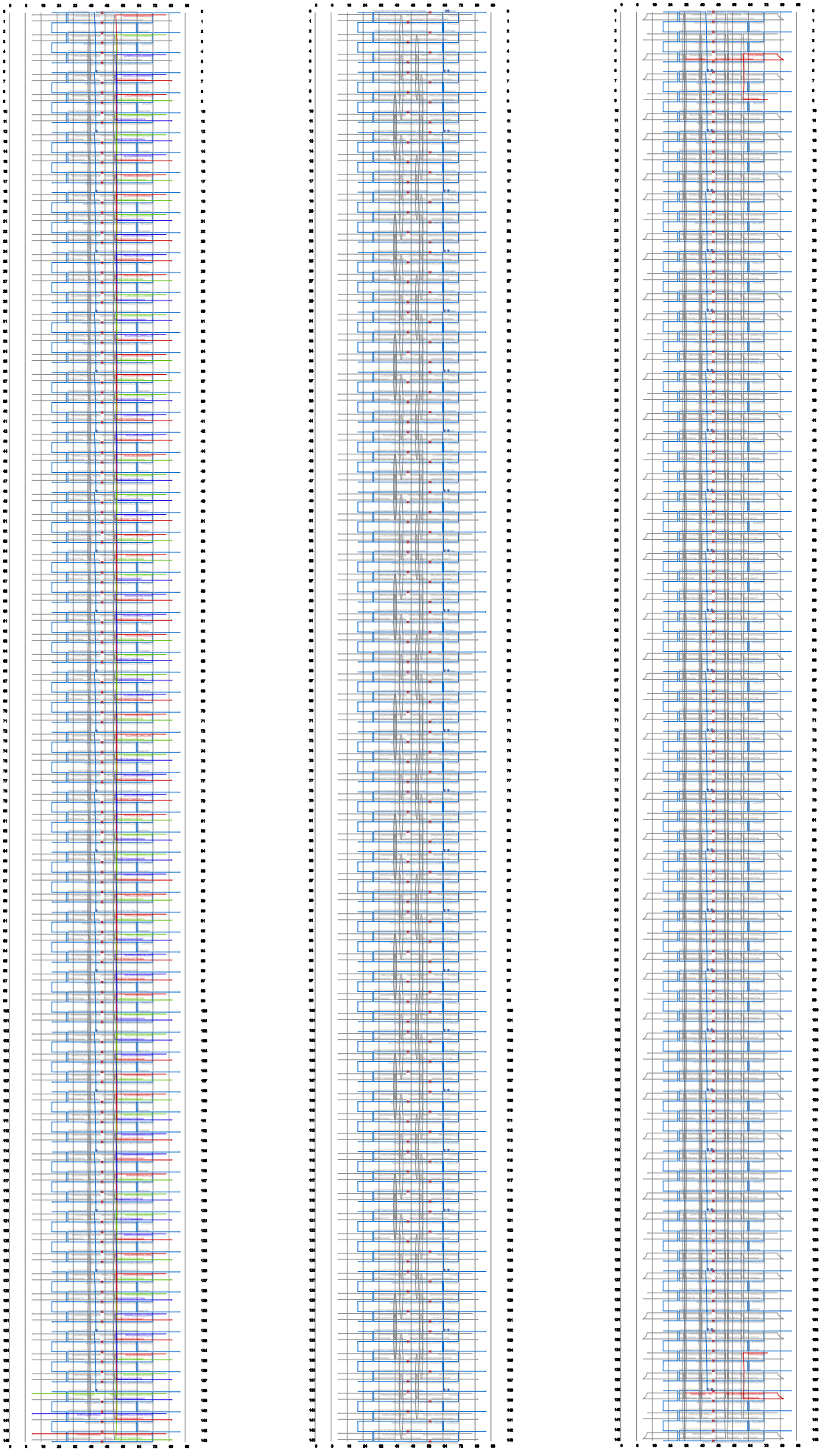

Path diagrams exported from cadnano v1:
DC-v2-1 (left), DC-v2-2 (right)

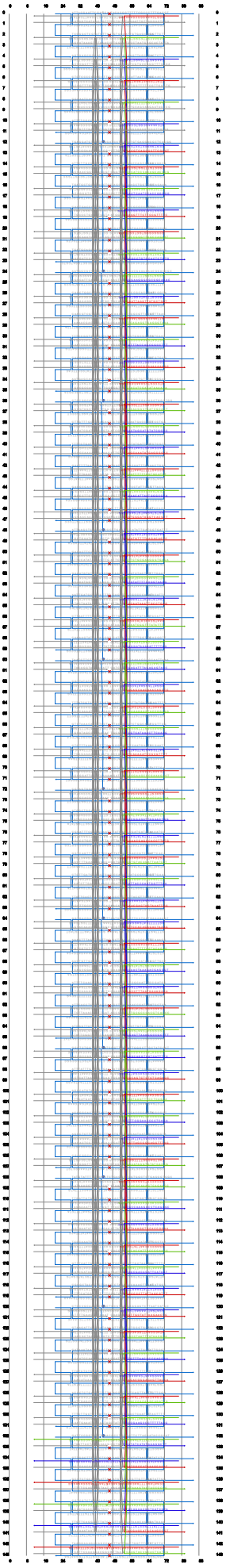

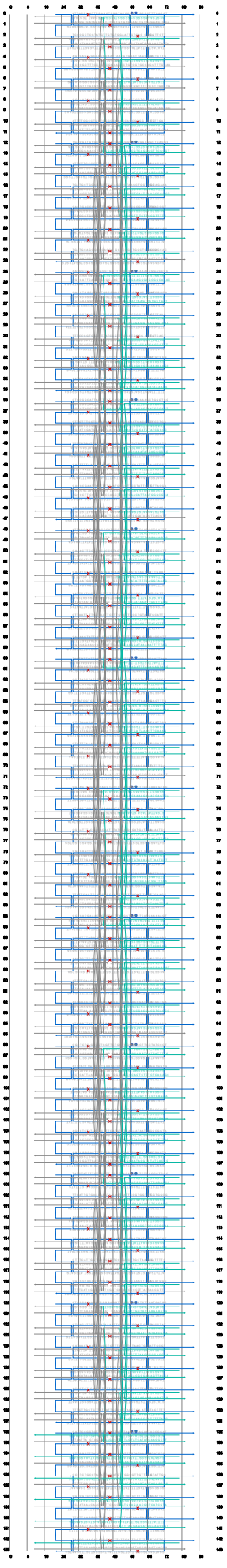

Path diagrams exported from cadnano v1:
DC-v3-1 (left), DC-v3-2 (right)

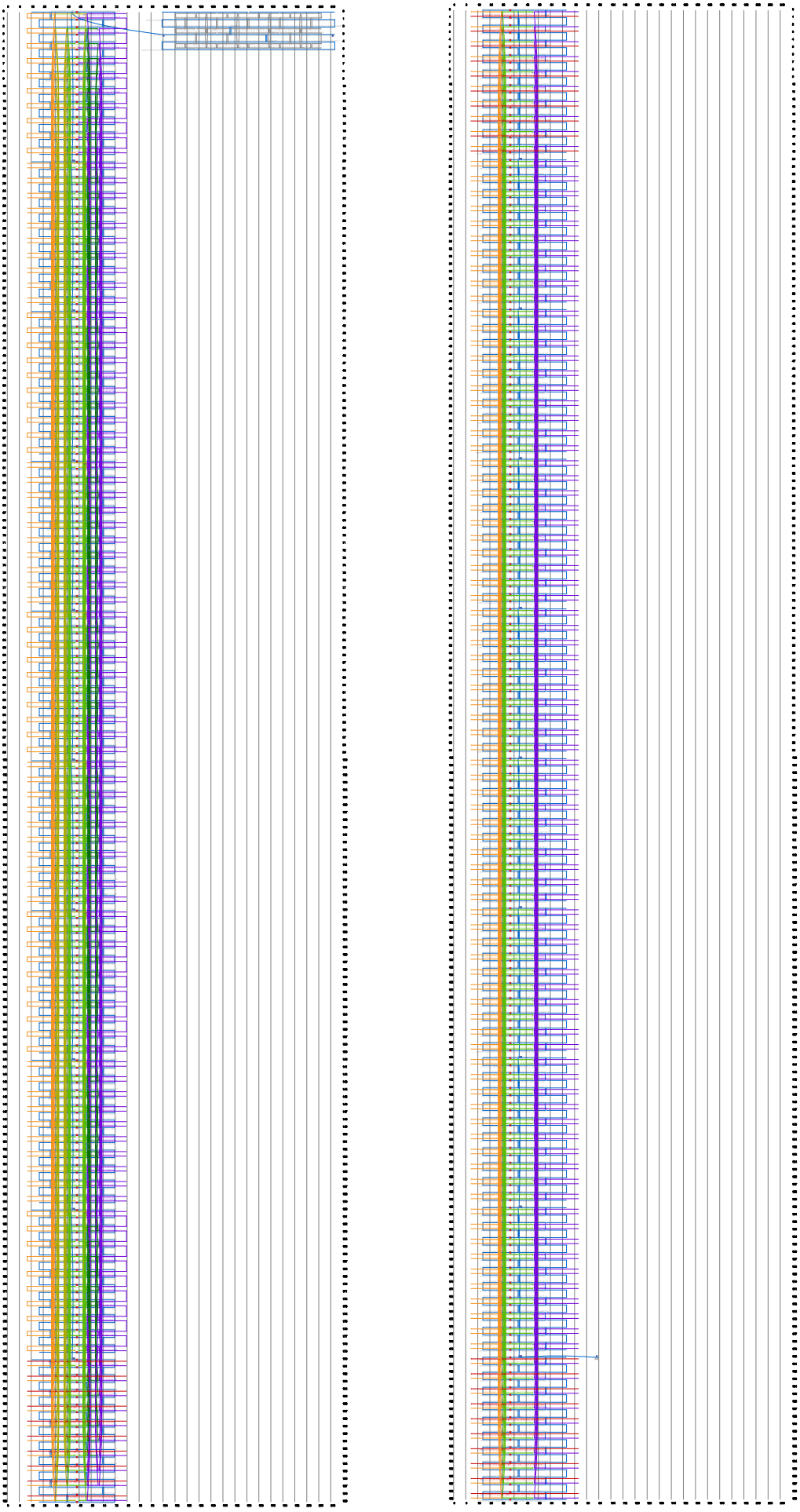

Path diagrams exported from cadnano v1:
HC-v0-1 (left), HC-v0-2 (middle), HC-v1 (right)

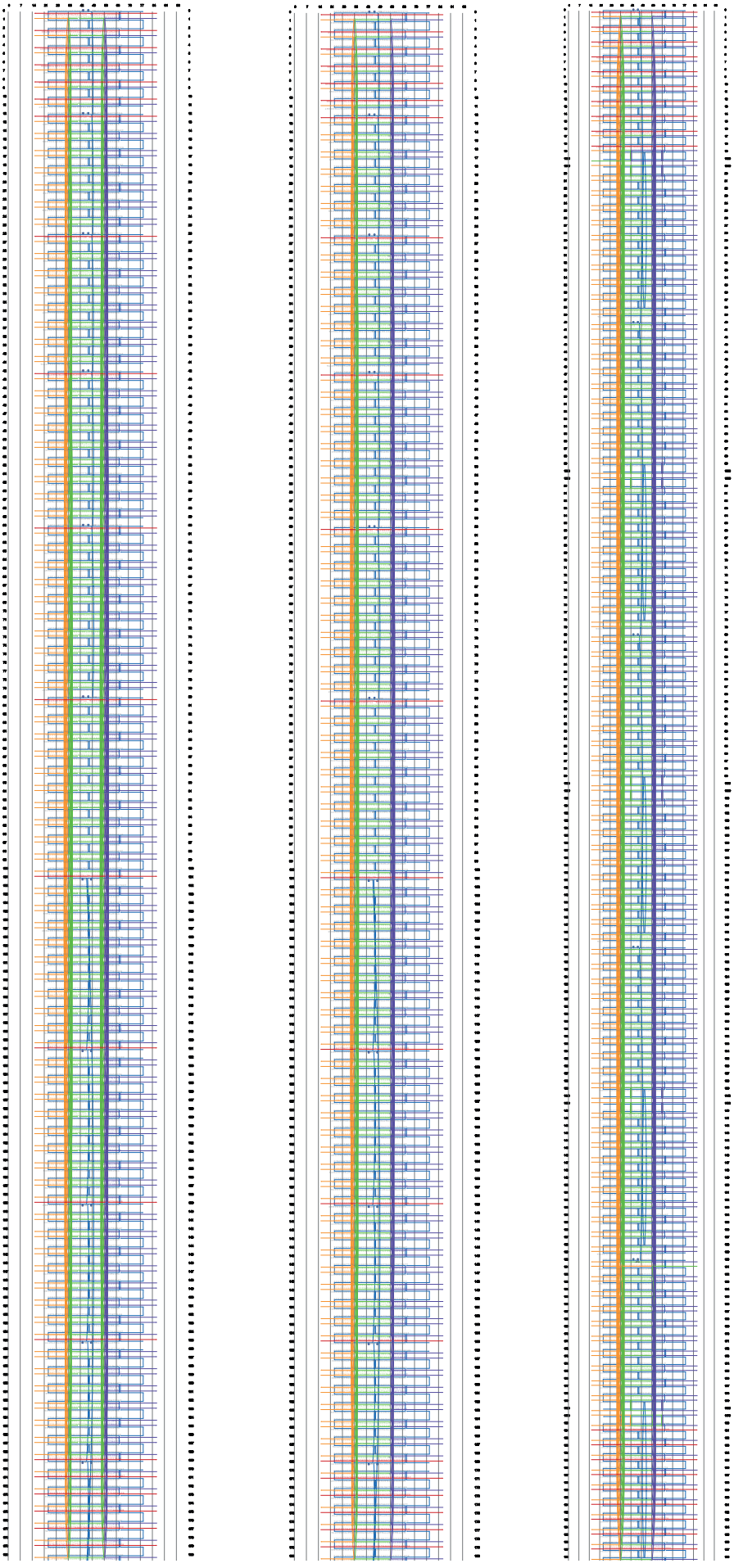

Bibliography

[1] Letcher, T. M. *Climate change: Observed Impacts on Planet Earth* (Elsevier, 2021).

[2] World Resource Institute. Climate action must progress far faster to achieve 1.5 c goal. https://www.wri.org/insights/climate-action-must-progress-far-faster-achieve-15-c-goal (2020). Accessed September 06, 2021.

[3] World Resources Institute. 4 charts explain greenhouse gas emissions by countries and sectors. https://www.wri.org/insights/4-charts-explain-greenhouse-gas-emissions-countries-and-sectors (2021). Accessed August 30, 2021.

[4] Moore, G. E. Cramming more components onto integrated circuits. *Proceedings of the IEEE* **86**, 82–85 (1998).

[5] Zhang, Z., Yan, J. & Kuriyagawa, T. Manufacturing technologies toward extreme precision. *International Journal of Extreme Manufacturing* **1**, 022001 (2019).

[6] Randall, J. N. *et al.* Digital atomic scale fabrication an inverse moore's law–a path to atomically precise manufacturing. *Micro and Nano Engineering* **1**, 1–14 (2018).

[7] Umbrello, S. & Baum, S. D. Evaluating future nanotechnology: The net societal impacts of atomically precise manufacturing. *Futures* **100**, 63–73 (2018).

[8] Caruthers, M. H. Gene synthesis machines: Dna chemistry and its uses. *Science* **230**, 281–285 (1985).

[9] Rothemund, P. W. Folding dna to create nanoscale shapes and patterns. *Nature* **440**, 297–302 (2006).

[10] Jungmann, R., Liedl, T., Sobey, T. L., Shih, W. & Simmel, F. C. Isothermal assembly of dna origami structures using denaturing agents. *Journal of the American Chemical Society* **130**, 10062–10063 (2008).

[11] CollegeOpenStax. *Biology* (Rice University, 2013).

[12] Eisenberg, D. & Crothers, D. *Physical chemistry with applications to the life sciences* (The Benjamin/Cummings Publishing Commpany, Inc., 1979).

[13] Berg, J. M., Stryer, L. & Tymoczko, J. L. *Stryer Biochemie* (Springer-Verlag, 2018).

[14] Carraher Jr, C. E. *Introduction to polymer chemistry* (CRC press, 2012).

[15] Blanco, A. & Blanco, G. *Medical Biochemistry* (Academic Press, 2017).

[16] Seeman, N. C. *Structural DNA nanotechnology* (Cambridge University Press, 2015).

[17] BarCharts Inc. *Periodic Table Advanced* (BarCharts, Inc, 2014).

[18] Seeberger, F. Educhem - pse. http://www.educhem.eu/PSE.html (2017). Accessed June 11, 2021.

[19] Lemieux, S. & Major, F. Rna canonical and non-canonical base pairing types: a recognition method and complete repertoire. *Nucleic acids research* **30**, 4250–4263 (2002).

[20] Leontis, N. B. & Westhof, E. Geometric nomenclature and classification of rna base pairs. *Rna* **7**, 499–512 (2001).

[21] Nikolova, E. N. *et al.* A historical account of hoogsteen base-pairs in duplex dna. *Biopolymers* **99**, 955–968 (2013).

[22] Largy, E., Mergny, J.-L. & Gabelica, V. Role of alkali metal ions in g-quadruplex nucleic acid structure and stability. In *The Alkali Metal Ions: Their Role for Life*, 203–258 (Springer, 2016).

[23] Dettler, J. M. *et al.* Biophysical characterization of an ensemble of intramolecular i-motifs formed by the human c-myc nhe iii1 p1 promoter mutant sequence. *Biophysical journal* **99**, 561–567 (2010).

[24] Gargallo, R. Hard/soft hybrid modeling of temperature-induced unfolding processes involving g-quadruplex and i-motif nucleic acid structures. *Analytical biochemistry* **466**, 4–15 (2014).

[25] Holliday, R. A mechanism for gene conversion in fungi. *Genetics Research* **5**, 282–304 (1964).

[26] Schwacha, A. & Kleckner, N. Identification of double holliday junctions as intermediates in meiotic recombination. *Cell* **83**, 783–791 (1995).

[27] SantaLucia, J., Allawi, H. T. & Seneviratne, P. A. Improved nearest-neighbor parameters for predicting dna duplex stability. *Biochemistry* **35**, 3555–3562 (1996).

[28] Hsu, H.-P., Paul, W. & Binder, K. Breakdown of the kratky-porod wormlike chain model for semiflexible polymers in two dimensions. *EPL (Europhysics Letters)* **95**, 68004 (2011).

[29] Gordon, R. *Encyclopedia of Biophysics* (Springer Berlin Heidelberg, 2013).

[30] Seeman, N. C. Nucleic acid junctions and lattices. *Journal of theoretical biology* **99**, 237–247 (1982).

[31] Wang, X. & Seeman, N. C. Assembly and characterization of 8-arm and 12-arm dna branched junctions. *Journal of the American Chemical Society* **129**, 8169–8176 (2007).

[32] Chen, J. & Seeman, N. C. Synthesis from dna of a molecule with the connectivity of a cube. *Nature* **350**, 631–633 (1991).

[33] Winfree, E., Liu, F., Wenzler, L. A. & Seeman, N. C. Design and self-assembly of two-dimensional dna crystals. *Nature* **394**, 539–544 (1998).

[34] LaBean, T. H. *et al.* Construction, analysis, ligation, and self-assembly of dna triple crossover complexes. *Journal of the American Chemical Society* **122**, 1848–1860 (2000).

[35] Yan, H., Park, S. H., Finkelstein, G., Reif, J. H. & LaBean, T. H. Dna-templated self-assembly of protein arrays and highly conductive nanowires. *science* **301**, 1882–1884 (2003).

[36] He, Y. *et al.* Sequence symmetry as a tool for designing dna nanostructures. *Angewandte Chemie International Edition* **44**, 6694–6696 (2005).

[37] He, Y., Chen, Y., Liu, H., Ribbe, A. E. & Mao, C. Self-assembly of hexagonal dna two-dimensional (2d) arrays. *Journal of the American Chemical Society* **127**, 12202–12203 (2005).

[38] He, Y. & Mao, C. Balancing flexibility and stress in dna nanostructures. *Chemical communications* 968–969 (2006).

[39] Zheng, J. *et al.* From molecular to macroscopic via the rational design of a self-assembled 3d dna crystal. *Nature* **461**, 74–77 (2009).

[40] Goodman, R. P. *et al.* Rapid chiral assembly of rigid dna building blocks for molecular nanofabrication. *Science* **310**, 1661–1665 (2005).

[41] Zhang, Y. & Seeman, N. C. Construction of a dna-truncated octahedron. *Journal of the American Chemical Society* **116**, 1661–1669 (1994).

[42] He, Y. *et al.* Hierarchical self-assembly of dna into symmetric supramolecular polyhedra. *Nature* **452**, 198–201 (2008).

[43] Shih, W. M., Quispe, J. D. & Joyce, G. F. A 1.7-kilobase single-stranded dna that folds into a nanoscale octahedron. *Nature* **427**, 618–621 (2004).

[44] Yan, H., LaBean, T. H., Feng, L. & Reif, J. H. Directed nucleation assembly of dna tile complexes for barcode-patterned lattices. *Proceedings of the National Academy of Sciences* **100**, 8103–8108 (2003).

[45] Schreiber, R. *et al.* Hierarchical assembly of metal nanoparticles, quantum dots and organic dyes using dna origami scaffolds. *Nature nanotechnology* **9**, 74–78 (2014).

[46] Saccà, B. *et al.* Orthogonal protein decoration of dna origami. *Angewandte Chemie* **122**, 9568–9573 (2010).

[47] Rafat, A. A., Sagredo, S., Thalhammer, M. & Simmel, F. C. Barcoded dna origami structures for multiplexed optimization and enrichment of dna-based protein-binding cavities. *Nature chemistry* **12**, 852–859 (2020).

[48] Williams, N. D. *et al.* Dna-origami-based fluorescence brightness standards for convenient and fast protein counting in live cells. *Nano Letters* **20**, 8890–8896 (2020).

[49] Yurke, B., Turberfield, A. J., Mills, A. P., Simmel, F. C. & Neumann, J. L. A dna-fuelled molecular machine made of dna. *Nature* **406**, 605–608 (2000).

[50] Arbona, J.-M., Aimé, J.-P. & Elezgaray, J. Cooperativity in the annealing of dna origamis. *The Journal of chemical physics* **138**, 01B606 (2013).

[51] Wei, X., Nangreave, J., Jiang, S., Yan, H. & Liu, Y. Mapping the thermal behavior of dna origami nanostructures. *Journal of the American Chemical Society* **135**, 6165–6176 (2013).

[52] Dunn, K. E. *et al.* Guiding the folding pathway of dna origami. *Nature* **525**, 82–86 (2015).

[53] Andersen, E. S. *et al.* Self-assembly of a nanoscale dna box with a controllable lid. *Nature* **459**, 73–76 (2009).

[54] Douglas, S. M. *et al.* Self-assembly of dna into nanoscale three-dimensional shapes. *Nature* **459**, 414–418 (2009).

[55] Ke, Y. *et al.* Multilayer dna origami packed on a square lattice. *Journal of the American Chemical Society* **131**, 15903–15908 (2009).

[56] Han, D. *et al.* Dna gridiron nanostructures based on four-arm junctions. *Science* **339**, 1412–1415 (2013).

[57] Liedl, T., Högberg, B., Tytell, J., Ingber, D. E. & Shih, W. M. Self-assembly of three-dimensional prestressed tensegrity structures from dna. *Nature nanotechnology* **5**, 520–524 (2010).

[58] Ke, Y., Voigt, N. V., Gothelf, K. V. & Shih, W. M. Multilayer dna origami packed on hexagonal and hybrid lattices. *Journal of the American Chemical Society* **134**, 1770–1774 (2012).

[59] Benson, E. *et al.* Dna rendering of polyhedral meshes at the nanoscale. *Nature* **523**, 441–444 (2015).

[60] Benson, E. *et al.* Computer-aided production of scaffolded dna nanostructures from flat sheet meshes. *Angewandte Chemie* **128**, 9015–9018 (2016).

[61] Matthies, M., Agarwal, N. P. & Schmidt, T. L. Design and synthesis of triangulated dna origami trusses. *Nano letters* **16**, 2108–2113 (2016).

[62] Han, D. *et al.* Dna origami with complex curvatures in three-dimensional space. *Science* **332**, 342–346 (2011).

[63] Dietz, H., Douglas, S. M. & Shih, W. M. Folding dna into twisted and curved nanoscale shapes. *Science* **325**, 725–730 (2009).

[64] Majikes, J. M., Liddle, J. A. *et al.* Dna origami design: A how-to tutorial. *J. Res. Natl. Inst. Stan* **126**, 126001 (2020).

[65] MIT. Cando - about. https://cando-dna-origami.org/about/ (2018). Accessed August 24, 2021.

[66] Ke, Y., Bellot, G., Voigt, N. V., Fradkov, E. & Shih, W. M. Two design strategies for enhancement of multilayer–dna-origami folding: underwinding for specific intercalator rescue and staple-break positioning. *Chemical science* **3**, 2587–2597 (2012).

[67] Wei, B., Dai, M. & Yin, P. Complex shapes self-assembled from single-stranded dna tiles. *Nature* **485**, 623–626 (2012).

[68] Ke, Y., Ong, L. L., Shih, W. M. & Yin, P. Three-dimensional structures self-assembled from dna bricks. *science* **338**, 1177–1183 (2012).

[69] Park, S. H. *et al.* Finite-size, fully addressable dna tile lattices formed by hierarchical assembly procedures. *Angewandte Chemie* **118**, 749–753 (2006).

[70] Yin, P., Choi, H. M., Calvert, C. R. & Pierce, N. A. Programming biomolecular self-assembly pathways. *Nature* **451**, 318–322 (2008).

[71] Rothemund, P. W. & Winfree, E. The program-size complexity of self-assembled squares. In *Proceedings of the thirty-second annual ACM symposium on Theory of computing*, 459–468 (2000).

[72] Ong, L. L. *et al.* Programmable self-assembly of three-dimensional nanostructures from 10,000 unique components. *Nature* **552**, 72–77 (2017).

[73] Minev, D., Wintersinger, C. M., Ershova, A. & Shih, W. M. Robust nucleation control via crisscross polymerization of highly coordinated dna slats. *Nature communications* **12**, 1–9 (2021).

[74] Pohl, F. M. & Jovin, T. M. Salt-induced co-operative conformational change of a synthetic dna: equilibrium and kinetic studies with poly (dg-dc). *Journal of molecular biology* **67**, 375–396 (1972).

[75] Gerling, T., Wagenbauer, K. F., Neuner, A. M. & Dietz, H. Dynamic dna devices and assemblies formed by shape-complementary, non–base pairing 3d components. *Science* **347**, 1446–1452 (2015).

[76] Liedl, T. & Simmel, F. C. Switching the conformation of a dna molecule with a chemical oscillator. *Nano letters* **5**, 1894–1898 (2005).

[77] Shu, W. *et al.* Dna molecular motor driven micromechanical cantilever arrays. *Journal of the American Chemical Society* **127**, 17054–17060 (2005).

[78] Liu, D. & Balasubramanian, S. A proton-fuelled dna nanomachine. *Angewandte Chemie International Edition* **42**, 5734–5736 (2003).

[79] Li, T. & Famulok, M. I-motif-programmed functionalization of dna nanocircles. *Journal of the American Chemical Society* **135**, 1593–1599 (2013).

[80] Idili, A., Vallée-Bélisle, A. & Ricci, F. Programmable ph-triggered dna nanoswitches. *Journal of the American Chemical Society* **136**, 5836–5839 (2014).

[81] Modi, S. *et al.* A dna nanomachine that maps spatial and temporal ph changes inside living cells. *Nature nanotechnology* **4**, 325–330 (2009).

[82] Kamiya, Y. & Asanuma, H. Light-driven dna nanomachine with a photoresponsive molecular engine. *Accounts of chemical research* **47**, 1663–1672 (2014).

[83] Zhou, M., Liang, X., Mochizuki, T. & Asanuma, H. A light-driven dna nanomachine for the efficient photoswitching of rna digestion. *Angewandte Chemie International Edition* **49**, 2167–2170 (2010).

[84] Turberfield, A. J. *et al.* Dna fuel for free-running nanomachines. *Physical review letters* **90**, 118102 (2003).

[85] Bath, J. & Turberfield, A. J. Dna nanomachines. *Nanoscience And Technology: A Collection of Reviews from Nature Journals* 124–133 (2010).

[86] Ouldridge, T. E., Louis, A. A. & Doye, J. P. Dna nanotweezers studied with a coarse-grained model of dna. *Physical Review Letters* **104**, 178101 (2010).

[87] Simmel, F. C. & Yurke, B. Using dna to construct and power a nanoactuator. *Physical Review E* **63**, 041913 (2001).

[88] Simmel, F. C. & Yurke, B. A dna-based molecular device switchable between three distinct mechanical states. *Applied Physics Letters* **80**, 883–885 (2002).

[89] Yan, H., Zhang, X., Shen, Z. & Seeman, N. C. A robust dna mechanical device controlled by hybridization topology. *Nature* **415**, 62–65 (2002).

[90] Ding, B. & Seeman, N. C. Operation of a dna robot arm inserted into a 2d dna crystalline substrate. *Science* **314**, 1583–1585 (2006).

[91] Feng, L., Park, S. H., Reif, J. H. & Yan, H. A two-state dna lattice switched by dna nanoactuator. *Angewandte Chemie* **115**, 4478–4482 (2003).

[92] Yin, F., Wang, F., Fan, C., Zuo, X. & Li, Q. Biosensors based on dna logic gates. *View* **2**, 20200038 (2021).

[93] Sherman, W. B. & Seeman, N. C. A precisely controlled dna biped walking device. *Nano letters* **4**, 1203–1207 (2004).

[94] Shin, J.-S. & Pierce, N. A. A synthetic dna walker for molecular transport. *Journal of the American Chemical Society* **126**, 10834–10835 (2004).

[95] SantaLucia, J. A unified view of polymer, dumbbell, and oligonucleotide dna nearest-neighbor thermodynamics. *Proceedings of the National Academy of Sciences* **95**, 1460–1465 (1998).

[96] Seelig, G., Yurke, B. & Winfree, E. Catalyzed relaxation of a metastable dna fuel. *Journal of the American Chemical Society* **128**, 12211–12220 (2006).

[97] Bois, J. S. *et al.* Topological constraints in nucleic acid hybridization kinetics. *Nucleic acids research* **33**, 4090–4095 (2005).

[98] Green, S. J., Lubrich, D. & Turberfield, A. J. Dna hairpins: fuel for autonomous dna devices. *Biophysical journal* **91**, 2966–2975 (2006).

[99] Bath, J., Green, S. J. & Turberfield, A. J. A free-running dna motor powered by a nicking enzyme. *Angewandte Chemie International Edition* **44**, 4358–4361 (2005).

[100] Yin, P., Yan, H., Daniell, X. G., Turberfield, A. J. & Reif, J. H. A unidirectional dna walker that moves autonomously along a track. *Angewandte Chemie* **116**, 5014–5019 (2004).

[101] Green, S., Bath, J. & Turberfield, A. Coordinated chemomechanical cycles: a mechanism for autonomous molecular motion. *Physical review letters* **101**, 238101 (2008).

[102] Omabegho, T., Sha, R. & Seeman, N. C. A bipedal dna brownian motor with coordinated legs. *Science* **324**, 67–71 (2009).

[103] Tian, Y., He, Y., Chen, Y., Yin, P. & Mao, C. A dnazyme that walks processively and autonomously along a one-dimensional track. *Angewandte Chemie* **117**, 4429–4432 (2005).

[104] Chen, Y., Wang, M. & Mao, C. An autonomous dna nanomotor powered by a dna enzyme. *Angewandte Chemie* **116**, 3638–3641 (2004).

[105] Bath, J., Green, S. J., Allen, K. E. & Turberfield, A. J. Mechanism for a directional, processive, and reversible dna motor. *Small* **5**, 1513–1516 (2009).

[106] Wang, Z.-G., Elbaz, J. & Willner, I. Dna machines: bipedal walker and stepper. *Nano letters* **11**, 304–309 (2011).

[107] You, M., Huang, F., Chen, Z., Wang, R.-W. & Tan, W. Building a nanostructure with reversible motions using photonic energy. *ACS nano* **6**, 7935–7941 (2012).

[108] Chiang, Y. *et al.* Inchworm bipedal nanowalker. *Nanoscale* **10**, 9199–9211 (2018).

[109] Tomov, T. E. *et al.* Dna bipedal motor achieves a large number of steps due to operation using microfluidics-based interface. *Acs Nano* **11**, 4002–4008 (2017).

[110] Khara, D. C. *et al.* Dna bipedal motor walking dynamics: an experimental and theoretical study of the dependency on step size. *Nucleic acids research* **46**, 1553–1561 (2018).

[111] Pei, R. *et al.* Behavior of polycatalytic assemblies in a substrate-displaying matrix. *Journal of the American Chemical Society* **128**, 12693–12699 (2006).

[112] Lund, K. *et al.* Molecular robots guided by prescriptive landscapes. *Nature* **465**, 206–210 (2010).

[113] Wickham, S. F. *et al.* Direct observation of stepwise movement of a synthetic molecular transporter. *Nature nanotechnology* **6**, 166–169 (2011).

[114] Bazrafshan, A. *et al.* Tunable dna origami motors translocate ballistically over μm distances at nm/s speeds. *Angewandte Chemie International Edition* **59**, 9514–9521 (2020).

[115] Bazrafshan, A. *et al.* Dna gold nanoparticle motors demonstrate processive motion with bursts of speed up to 50 nm per second. *ACS nano* **15**, 8427–8438 (2021).

[116] Zhou, C., Duan, X. & Liu, N. A plasmonic nanorod that walks on dna origami. *Nature communications* **6**, 1–6 (2015).

[117] Urban, M. J., Zhou, C., Duan, X. & Liu, N. Optically resolving the dynamic walking of a plasmonic walker couple. *Nano Letters* **15**, 8392–8396 (2015).

[118] Xin, L., Duan, X. & Liu, N. Dimerization and oligomerization of dna-assembled building blocks for controlled multi-motion in high-order architectures. *Nature communications* **12**, 1–9 (2021).

[119] Gu, H., Chao, J., Xiao, S.-J. & Seeman, N. C. A proximity-based programmable dna nanoscale assembly line. *Nature* **465**, 202–205 (2010).

[120] He, Y. & Liu, D. R. Autonomous multistep organic synthesis in a single isothermal solution mediated by a dna walker. *Nature nanotechnology* **5**, 778–782 (2010).

[121] Cha, T.-G. *et al.* A synthetic dna motor that transports nanoparticles along carbon nanotubes. *Nature nanotechnology* **9**, 39–43 (2014).

[122] Valero, J. & Škugor, M. Mechanisms, methods of tracking and applications of dna walkers: A review. *ChemPhysChem* **21**, 1971–1988 (2020).

[123] Douglas, S. M. *et al.* Rapid prototyping of 3d dna-origami shapes with cadnano. *Nucleic acids research* **37**, 5001–5006 (2009).

[124] Doty, D., Lee, B. L. & Stérin, T. scadnano: A browser-based, scriptable tool for designing dna nanostructures. *arXiv preprint arXiv:2005.11841* (2020).

[125] Jones, R. & Agacinski, G. Main page. https://dna.physics.ox.ac.uk/index.php/Main_Page (2021). Accessed September 02, 2021.

[126] Doye, J. P. *et al.* The oxdna coarse-grained model as a tool to simulate dna origami. *arXiv preprint arXiv:2004.05052* (2020).

[127] Beattie, K. L., Wiegand, R. C. & Radding, C. M. Uptake of homologous single-stranded fragments by superhelical dna: Ii. characterization of the reaction. *Journal of molecular biology* **116**, 783–803 (1977).

[128] Radding, C. M., Beattie, K. L., Holloman, W. K. & Wiegand, R. C. Uptake of homologous single-stranded fragments by superhelical dna: Iv. branch migration. *Journal of molecular biology* **116**, 825–839 (1977).

[129] Morrison, L. E. & Stols, L. M. Sensitive fluorescence-based thermodynamic and kinetic measurements of dna hybridization in solution. *Biochemistry* **32**, 3095–3104 (1993).

[130] Panyutin, I. G. & Hsieh, P. The kinetics of spontaneous dna branch migration. *Proceedings of the National Academy of Sciences* **91**, 2021–2025 (1994).

[131] Simmel, F. C., Yurke, B. & Singh, H. R. Principles and applications of nucleic acid strand displacement reactions. *Chemical reviews* **119**, 6326–6369 (2019).

[132] Srinivas, N. *et al.* On the biophysics and kinetics of toehold-mediated dna strand displacement. *Nucleic acids research* **41**, 10641–10658 (2013).

[133] Ouldridge, T. E., Louis, A. A. & Doye, J. P. Structural, mechanical, and thermodynamic properties of a coarse-grained dna model. *The Journal of chemical physics* **134**, 02B627 (2011).

[134] Viovy, J.-L. Electrophoresis of dna and other polyelectrolytes: Physical mechanisms. *Rev. Mod. Phys.* **72**, 813–872 (2000). URL https://link.aps.org/doi/10.1103/RevModPhys.72.813.

[135] von Smoluchowski, M. Contribution à la théorie de l'endosmose électrique et de quelques phénomènes corrélatifs. *Bull. Akad. Sci. Cracovie.* **8**, 182–200 (1903).

[136] Slater, G. W. & Noolandi, J. The biased reptation model of dna gel electrophoresis: mobility vs molecular size and gel concentration. *Biopolymers: Original Research on Biomolecules* **28**, 1781–1791 (1989).

[137] Bio-Rad Laboratories. The bio-rad literature library. https://www.bio-rad.com/de-de/literature-library (2021). Accessed August 31, 2021.

[138] ThermoFisher Scientific. Nucleic acid electrophoresis workflow-5 main steps. https://www.thermofisher.com/de/de/home/life-science/cloning/cloning-learning-center/invitrogen-school-of-molecular-biology/na-electrophoresis-education/na-electrophoresis-workflow.html (2021). Accessed September 02, 2021.

[139] Integrated DNA Technologies. Which type of oligo purification should i choose? https://eu.idtdna.com/pages/education/decoded/article/which-type-of-purification-should-i-choose- (2021). Accessed August 22, 2021.

[140] Wagenbauer, K. F. *et al.* How we make dna origami. *ChemBioChem* **18**, 1873–1885 (2017).

[141] Merck KGaA. Amicon ultra-0.5 ml centrifugal filters for dna and protein purification and concentration. https://www.merckmillipore.com/DE/de/product/Amicon-Ultra-0.5mL-Centrifugal-Filters-for-DNA-and-Protein-Purification-and-Concentration,MM_NF-C82301 (2021). Accessed August 31, 2021.

[142] Egerton, R. F. *et al. Physical principles of electron microscopy*, vol. 56 (Springer, 2005).

[143] Minev, D. *et al.* Rapid in vitro production of single-stranded dna. *Nucleic acids research* **47**, 11956–11962 (2019).

[144] Fischer, S. *et al.* Shape and interhelical spacing of dna origami nanostructures studied by small-angle x-ray scattering. *Nano letters* **16**, 4282–4287 (2016).

[145] Strauss, M. T., Schueder, F., Haas, D., Nickels, P. C. & Jungmann, R. Quantifying absolute addressability in dna origami with molecular resolution. *Nature communications* **9**, 1–7 (2018).

[146] Ogura, Y., Onishi, A., Nishimura, T. & Tanida, J. Optically controlled release of dna based on nonradiative relaxation process of quenchers. *Biomedical optics express* **7**, 2142–2153 (2016).

[147] Douglas, S. M., Chou, J. J. & Shih, W. M. Dna-nanotube-induced alignment of membrane proteins for nmr structure determination. *Proceedings of the National Academy of Sciences* **104**, 6644–6648 (2007).

[148] Abràmoff, M. D., Magalhães, P. J. & Ram, S. J. Image processing with imagej. *Biophotonics international* **11**, 36–42 (2004).

List of Figures

1.1. The development of machine accuracy according to Norio Taniguchi 4

2.1. Spontaneous vs. non-spontaneous chemical reactions 8
2.2. Kinetics of DNA duplex formation 11
2.3. Chemical DNA bases and their binding mechanism 13
2.4. Sugar-phosphate backbone of the DNA 14
2.5. The DNA double helix - Interaction forces and geometry 17
2.6. Non-canonical base pairing - Three edges for interaction 19
2.7. Cis- and trans-orientation of glycosidic bonds in DNA base pairs 19
2.8. Hoogsteen base pairs (AT and GC^+) and DNA motifs 21
2.9. Holliday junctions and branch migration 22
2.10. Polymers as continuous chains in the WLC model 23

3.1. DNA junctions for the assembly of higher-order structures 26
3.2. Folding process of DNA-Origami 27
3.3. 3D extension of DNA origami 28
3.4. Honeycomb-pleat-based vs. square-lattice DNA origami design strategies . . 30
3.5. Recommended helix arrangement-angles and relaxed crossover distances for relaxed DNA origami structures 31
3.6. Counteracting twist in a single-layer, square-lattice DNA origami sheet . . . 32
3.7. Scaffold-free assembly of DNA nanostructures 33

4.1. Using DNA as fuel for nanodevices 36
4.2. DNA strand displacement and enzymically driven DNA biped walkers . . . 38
4.3. Boosting DNA walkers toward higher efficiency 41
4.4. DNA walkers for cargo transport 42

5.1. CaDNAno user interface and path diagram 46
5.2. oxDNA - coarse-grained model to simulate DNA origami structures 47
5.3. Working principle of toehold mediated strand displacement 48
5.4. Dependency of toehold mediated strand displacement reaction rates on the toehold length 49
5.5. Schematic representation of a charged sphere in an ionic solution 51
5.6. Amicon®Ultra filter system 55
5.7. First cycle of a standard PCR 57
5.8. Working principle of MeRPy-PCR 58

6.1. Lattice spacing: Standard square-lattice vs. diagonal-cut 60
6.2. Overview of the designed and evaluated architectures for multi-site interactions 62

6.3. Design approach 1: Diagonal-cut architectures based on a square-lattice (DC-v0) . . . 64
6.4. Folding evaluation of diagonal-cut architectures on a square-lattice (DC-v0) 65
6.5. Effect of TWEEN 20 and $MgCl_2$ on recovery yields of DC-v0-2 in amicon purification . . . 67
6.6. Effect of $MgCl_2$ concentration in dilution buffers used for amicon purification on the recovery yield of DC-v0-2 . . . 68
6.7. Impact of handle masking on recovery yields and purity of DC-v0-2 after amicon purification . . . 69
6.8. Effect of added back core strand on recovery yields and purity of DC-v0-1 and v0-2 after amicon purification . . . 70
6.9. Axes of crossover connections and nearest neighbors in square- vs. honeycomb-lattices . . . 72
6.10. Design approach 2: Helices shortened to 50 bps in a 24×3 array (DC-v1-1) 74
6.11. Folding evaluation of DC-v1-1 . . . 75
6.12. Swapping crossover positions for less supertwisting (DC-v1-2) . . . 76
6.13. Folding evaluation of DC-v1-2 . . . 77
6.14. Folding evaluation of DC-v1-3 . . . 78
6.15. Design approach 2: Lowering the aspect ratio for less supertwisting (DC-v2) 79
6.16. Experimental data on DC-v2-1 and v2-2 folding . . . 80
6.17. Gel evaluation of approaches to enhance the stability of DC-v2-1 structures toward PEG purification . . . 81
6.18. Gel evaluation of approaches to enhance the stability of DC-v2-2 structures toward PEG purification . . . 82
6.19. Re-design cycle of DC-v2 for higher stability: Design features of DC-v3 . . 84
6.20. Experimental data on DC-v3-1 folding . . . 85
6.21. Experimental data on DC-v3-2 folding . . . 86
6.22. PEG purification of DC-v3-2 . . . 87
6.23. DC-v3-1 vs. DC-v3-2 - Summary . . . 88
6.24. Design approach 2 on a honeycomb-lattice: Design features of hexagonal-shaped HC-v0-1 and HC-v0-2 . . . 89
6.25. Experimental data on HC-v0-1 folding . . . 90
6.26. Experimental data on HC-v0-2 folding . . . 91
6.27. PEG purification of HC-v0-1 and HC-v0-2 . . . 92
6.28. TEM imaging of HC-v0 structures before and after PEG precipitation . . . 93
6.29. Design approach 2 on a honeycomb-lattice: Design features of square-shaped HC-v1 . . . 94
6.30. Experimental data on HC-v1 folding . . . 95
6.31. PEG purification of HC-v1 . . . 96
6.32. Square- vs. square-holey-lattice . . . 97
6.33. Design approach 3: Square-holey lattice architecture SH-v1 . . . 98
6.34. Experimental data on SH-v1 folding . . . 99
6.35. Design approach 3: Square-holey lattice architecture SH-v2 . . . 100
6.36. Experimental data on SH-v2 folding . . . 101
6.37. Design approach 3: Square-holey lattice architecture SH-v3 . . . 101
6.38. Experimental data on SH-v3 folding . . . 102

7.1. Variations in step size depending on chosen lattice designs . . . 107

7.2. Functional mechanism of symmetric, three-phase stepping 109
7.3. Forward and backward stepping controlled by a bias toward shorter bridging distance 109
7.4. Mini-stepper design and functionalization 111
7.5. Clip strand titration for mini-monomer dimerization 113
7.6. Titration of the ratio between mini-sliders and -rails in dimerization 115
7.7. Effect of different interacting handle length on dimerization yields for mini-stepper 117
7.8. Falcon-stepper design and functionalization 119
7.9. Falcon monomer folding and purification 120
7.10. Effect of handle length variations on falcon heterodimerization 122
7.11. Effect of handle length variations on the disassembly reactions of falcon-dimers 123
7.12. 124
7.13. Investigation of temperature and time dependency of heterodimerization yields for falcon monomers 126
7.14. The effect of T-linker length in clip strands on the performance of RGB stepping 129
7.15. Two cycles of RGB stepping 132
7.16. Backward actuation of falcon-steppers 133
7.17. TEM imaging of PRGB-dimers - Expectations 135
7.18. TEM imaging of falcon-sliders with standard staining protocol 135
7.19. Optimization of the TEM imaging protocol - Longer sample deposition times 137
7.20. The effect of different staining techniques on the image contrast 139
7.21. TEM verification of falcon-sliders stepping across two RGB cycles 142
7.22. TEM image evaluation of a symmetric, three-phase actuation of falcon dimers 143
7.23. Gel verification of specificity of clip strand interactions 145

B.1. Low regime magnesium screening for amicon purification of DC-v0-2 159
B.2. High regime magnesium screening for amicon purification of DC-v0-2 160
B.3. Gel evaluation of longer folding ramps for an enhance stability of DC-v2-1 and v2-2 structures toward PEG purification 161
B.4. Gel evaluation of approaches to enhance stability of DC-v2-1 structures in PEG purification - Complete data set - Part 1 162
B.5. Gel evaluation of approaches to enhance stability of DC-v2-1 structures in PEG purification - Complete data set - Part 2 163
B.6. Purification of DC-v3-2 - Complete data set 164
B.7. Stability of PEG purified HC-v0-1 and v0-2, HC-v1, DC-v3-2 165
B.8. Amicon purified mini-monomers bearing handles of different lengths 166
B.9. Accessing T-linker length for purple clip strands 167
B.10. ImageJ analysis of RGB dimers - Complete data set and intensity peaks . . 168
B.11. Symmetric actuation across two RGB cycles 170
B.12. ImageJ analysis of rail-tail length of state 0 dimers 172
B.13. ImageJ analysis of rail-tail length of state 1 dimers 174
B.14. ImageJ analysis of rail-tail length of state 4 dimers - Part 1 176
B.15. ImageJ analysis of rail-tail length of state 4 dimers - Part 2 177
B.16. ImageJ analysis of rail-tail length of state 4 dimers - Part 3 178
B.17. ImageJ analysis of rail-tail length of state 4 dimers - Part 4 179

List of Tables

2.1. Non-canonical base pairing - Twelve basic geometric families 20

A.1. Composition of raw buffers 153
A.2. Buffer compositions and application 153
A.3. Information on purchased reagents 154

B.1. ImageJ analysis of dimer gel band intensities for intermediate state 0-1, and state 1 168
B.2. ImageJ analysis of dimer gel band intensities for intermediate state 1-2, and state 2 169
B.3. ImageJ analysis of dimer gel band intensities for intermediate state 2-3, and state 3 169
B.4. Measured tail length x_i in nm for state 0 dimers. Average tail length has been calculated from 50 particles as well as additional quantities necessary to calculate standard deviation. Std. Deviation – State 0 – Dimers: $\sigma =$ 4.10 nm 173
B.5. Measured tail length x_i in nm for state 1 dimers. Average tail length has been calculated from 50 particles as well as additional quantities necessary to calculate standard deviation. Std. Deviation – State 1 – Dimers: $\sigma =$ 4.33 nm 175
B.6. Measured tail length x_i in nm for state 4 dimers. Average tail length has been calculated from 50 particles as well as additional quantities necessary to calculate standard deviation. Std. Deviation – State 4 – Dimers: $\sigma =$ 3.81 nm 180